Transactions of the ASME®

Journal of Turbomachinery

Published Quarterly by The American Society of Mechanical Engineers

VOLUME 119 • NUMBER 3 • JULY 1997

TECHNICAL PAPERS

(Contents continued on p. 663)

Technical Editor, **T. H. OKIISHI (1998)**
Associate Technical Editors
Aeromechanical Interaction
R. E. KIELB (1999)
Gas Turbine (Review Chair)
A. KIDD (1997)
Heat Transfer
M. G. DUNN (1999)
Nuclear Engineering
H. H. CHUNG (1996)
Power
D. LOU (1998)
Turbomachinery
R. A. DELANEY (1998)

BOARD ON COMMUNICATIONS
Chairman and Vice-President
R. MATES

OFFICERS OF THE ASME
President, **KEITH B. THAYER**
Executive Director, **D. L. BELDEN**
Treasurer, **J. A. MASON**

PUBLISHING STAFF
Managing Director, Engineering
CHARLES W. BEARDSLEY
Director, Technical Publishing
PHILIP DI VIETRO
Managing Editor, Technical Publishing
CYNTHIA B. CLARK
Managing Editor, Transactions
CORNELIA MONAHAN
Production Coordinator
VALERIE WINTERS
Production Assistant
MARISOL ANDINO

Transactions of the ASME, Journal of Turbomachinery (ISSN 0889-504X) is published quarterly (Jan., Apr., July, Oct.) for $195.00 per year by The American Society of Mechanical Engineers, 345 East 47th Street, New York, NY 10017. Periodicals postage paid at New York, NY and additional mailing offices. POSTMASTER: Send address changes to Transactions of the ASME, Journal of Turbomachinery, c/o THE AMERICAN SOCIETY OF MECHANICAL ENGINEERS, 22 Law Drive, Box 2300, Fairfield, NJ 07007-2300.
CHANGES OF ADDRESS must be received at Society headquarters seven weeks before they are to be effective. Please send old label and new address.
PRICES: To members, $40.00, annually; to nonmembers, $195.00.
Add $24.00 for postage to countries outside the United States and Canada.

STATEMENT from By-Laws. The Society shall not be responsible for statements or opinions advanced in papers or . . . printed in its publications (B7.1, Par. 3).
COPYRIGHT © **1997** by The American Society of Mechanical Engineers. Authorization to photocopy material for internal or personal use under circumstances not falling within the fair use provisions of the Copyright Act is granted by ASME to libraries and other users registered with the Copyright Clearance Center (CCC) Transactional Reporting Service provided that the base fee of $3.00 per article is paid directly to CCC, 222 Rosewood Dr., Danvers, MA 01923. Request for special permission or bulk copying should be addressed to Reprints/Permission Department.

INDEXED by Applied Mechanics Reviews and Engineering Information, Inc.
Canadian Goods & Services Tax Registration #126148048

Copyright © 1997 by ASME

Downloaded 01 Jun 2010 to 171.66.16.52. Redistribution subject to ASME license or copyright; see http://www.asme.org/terms/Terms_Use.cfm

(Contents continued)

ANNOUNCEMENTS

Heat Transfer Committee and Turbomachinery Committee Best Paper of 1996 Award

The Path to Predicting Bypass Transition

R. E. Mayle[1]
Fellow ASME

A. Schulz

Institut für Thermische
Strömungsmaschinen,
Universität Karlsruhe,
Karlsruhe, Federal Republic of Germany

A theory is presented for calculating the fluctuations in a laminar boundary layer when the free stream is turbulent. The kinetic energy equation for these fluctuations is derived and a new mechanism is revealed for their production. A methodology is presented for solving the equation using standard boundary layer computer codes. Solutions of the equation show that the fluctuations grow at first almost linearly with distance and then more slowly as viscous dissipation becomes important. Comparisons of calculated growth rates and kinetic energy profiles with data show good agreement. In addition, a hypothesis is advanced for the effective forcing frequency and free-stream turbulence level that produce these fluctuations. Finally, a method to calculate the onset of transition is examined and the results compared to data.

Introduction

One of the remaining difficulties in calculating laminar-to-turbulent transition in boundary layers is predicting its onset. For natural transition, onset is usually determined using the "e^n" method developed by Smith (1956) and others. This method, which is widely used in the aircraft industry, uses the amplification rate of the most unstable Tollmien–Schlichting wave at each streamwise position to determine a disturbance–amplitude ratio. Onset is then presumed to occur at the position where this ratio attains an experimentally determined critical value related to the free-stream turbulence level (Mack, 1977). For bypass transition, which is the usual mode of transition in gas turbine engines, onset is usually determined without too much regard concerning the physics involved. In this case, empirical correlations providing the best fit to transition data are used, and these are applied either directly to the mean flow (Abu-Ghannam and Shaw, 1980; Mayle, 1991), or indirectly to the production of turbulent-kinetic-energy (from the many examples see the earliest, McDonald and Fish, 1973; one of the latest, Schmidt and Patankar, 1991; and a comparison of several, Sieger et al., 1993). In spite of these methods, however, predicting the onset of either natural or bypass transition is still more of an art than a science (see Savill, 1991, or Sieger et al. for examples).

As pictured in Fig. 1, transition from a practical standpoint may be considered to begin where a quantity such as the surface shear stress first deviates from its laminar value. In 1951, Emmons showed that this corresponds to the first position along the surface where isolated spots of turbulence within the boundary layer are formed. Clearly then, everything before the spots are formed happens in a completely laminar boundary layer. Measurements show, however, that this pretransition flow is not steady (see Fig. 2).

For natural transition, which occurs when the free-stream turbulence level is zero or nearly so, Tollmien–Schlichting waves can be found. For bypass transition, which occurs at high free-stream turbulence levels, "turbulent-looking" fluctuations mimicking those in the free stream are found, and similar to the Tollmien–Schlichting waves, these fluctuations also amplify, eventually forming turbulent spots. Their growth in an unaccelerated flow is shown in Fig. 3.

Although our eventual goal is to predict the onset of transition, our aim in this paper is to calculate the pretransition laminar fluctuations. As will be seen, this is done by developing and solving a laminar-kinetic-energy equation for the fluctuations, but more importantly it is accomplished by recognizing a new mechanism and determining the effective frequency and turbulence level in the free stream that are responsible for both producing and amplifying the fluctuations. The approach is new. It is based on Lin's (1957) analysis for unsteady laminar boundary layers and Dullenkopf and Mayle's (1995) concept of an effective frequency and turbulence level for laminar boundary layers in a turbulent free stream. Because it is easy to incorporate in any modern boundary-layer computer code, the approach is also practical.

The paper is divided into several sections. In the first we briefly review Lin's analysis and high-frequency results. In the next, we develop the laminar-kinetic-energy (LKE) equation, introduce the new mechanism, and propose models for the production and dissipation terms in the equation. After briefly describing how to include the new kinetic energy equation in k–ϵ-type computer codes, we compare the results of our calculations with experimental data. Then we propose a method to determine the effective forcing frequency for the fluctuations and the effective free-stream turbulence level. Finally we examine a criterion for the onset of transition and conclude with suggestions of work yet to be done.

C. C. Lin's Analysis

Lin (1957) examined the effect of free-stream fluctuations on laminar boundary layers by decomposing the velocities and pressure into time-averaged and time-dependent components similar to Reynolds' analysis for turbulent flow, i.e., $u(x, y, t) = \bar{u}(x, y) + u'(x, y, t)$, $v(x, y, t) = \bar{v}(x, y) + v'(x, y, t)$ and $p(x, t) = \bar{p}(x) + p'(x, t)$. In contrast to the usual turbulent approach, however, both the pressure and its fluctuation may be eliminated from the equations of motion by using the unsteady Euler equation, namely,

$$-\frac{1}{\rho}\frac{\partial p}{\partial x} = \frac{\partial U}{\partial t} + U\frac{\partial U}{\partial x} \qquad (1)$$

where ρ is the density and U is the free-stream velocity given by $U(x, t) = \bar{U}(x) + U'(x, t)$. The time-averaged boundary-

---

[1] Professor Emeritus of Mechanical Engineering, Rensselaer Polytechnic Institute, Troy, NY.

Contributed by the International Gas Turbine Institute and presented at the 41st International Gas Turbine and Aeroengine Congress and Exhibition, Birmingham, United Kingdom, June 10–13, 1996. Manuscript received at ASME Headquarters February 1996. Paper No. 96-GT-199. Associate Technical Editor: J. N. Shinn.

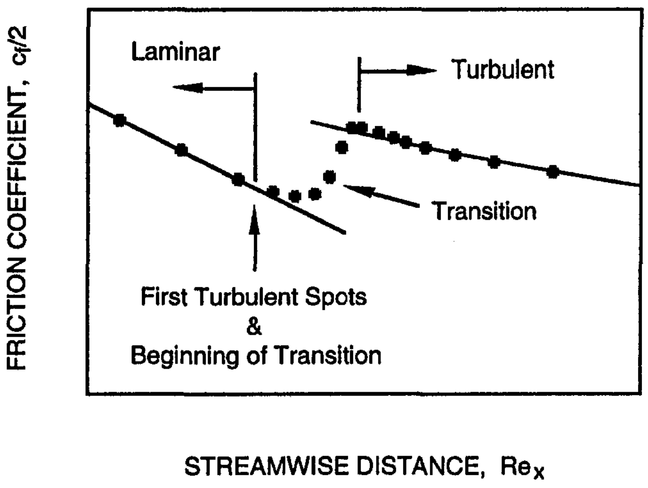

Fig. 1 Transition from laminar to turbulent flow in a boundary layer

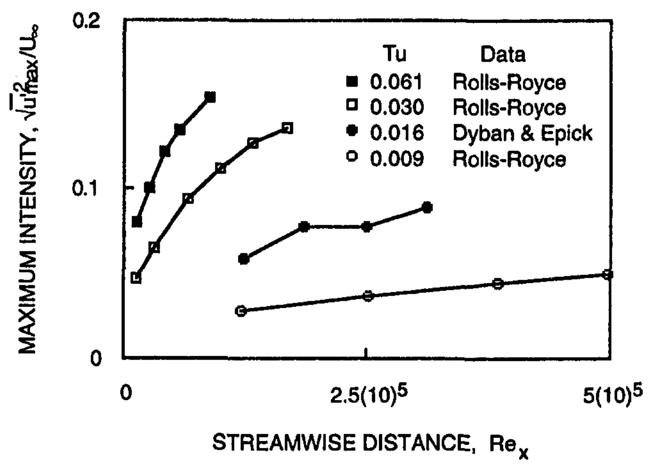

Fig. 3 The growth of fluctuations in a laminar boundary layer before transition

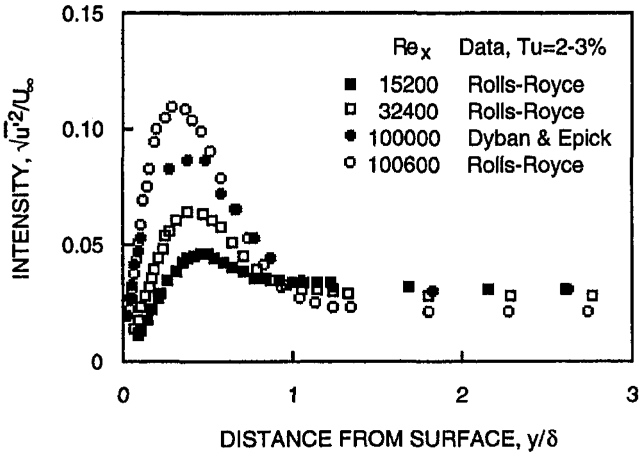

Fig. 2 Fluctuations in a laminar boundary layer before the onset of transition

layer equations for mass and momentum are identical to those for turbulent flow except that the momentum equation contains the additional term $\overline{U'(\partial U'/\partial x)}$ on the right-hand side,[2] and except that now they apply to a time-averaged laminar flow. The equations for the fluctuating components of velocity can be obtained by subtracting the time-averaged equations from the equations for the instantaneous motion and, contrary to the situation for turbulent flow, can be solved once the unsteady free-stream velocity distribution is given.

Solutions are easily obtained when the frequency of the free-stream fluctuations is high enough such that $\omega \gg \nu/\delta^2$, where ω is the frequency, ν is the kinematic viscosity, and δ is the boundary layer thickness. In this case, the fluctuations occur mostly adjacent to the wall within a thickness $\delta_\omega = \sqrt{2\nu/\omega} \leqslant \delta$ independent of the mean flow. Considering the temporal and spatial varying free-stream velocity $U(x, t) = U_\infty(x) + U'_\infty(x) \cdot \sin \omega t$, the solution for the u' component is

$$u'(x, y, t) = U'_\infty \left[\sin \omega t - e^{-(y/\delta_\omega)} \sin \left(\omega t - \frac{y}{\delta_\omega} \right) \right] ;$$

$$(\omega \gg \nu/\delta^2) \quad (2)$$

which can also be obtained from Stokes solution for a plate oscillating parallel to itself in a quiescent fluid (Schlichting, 1979). Since the equation for u' is linear, a solution for an arbitrary free-stream fluctuation may be obtained by superposition. If $U'_\infty \neq$ fnc (x), the normal component of the fluctuating velocity v', which is proportional to dU'_∞/dx, is zero, the apparent shear stress $(\overline{u'v'})$ is zero, and the time-averaged velocities $\bar{u}$ and $\bar{v}$ are exactly those given by the laminar solution. Thus, for unaccelerated flow over a surface with slowly decaying free-stream turbulence, we should expect the mean flow velocity profiles to be those given by Blasius. This result is well documented by Dyban et al. (1976), Sohn and Reshotko (1991), Zhou and Wang (1995), and others.

The kinetic energy for the u' component given in Eq. (2) is

$$k = \frac{1}{2}\overline{u'^2} = k_\infty \left[1 - 2e^{-(y/\delta_\omega)} \cos \left(\frac{y}{\delta_\omega} \right) + e^{-2(y/\delta_\omega)} \right] \quad (3)$$

where, since there is no other fluctuating component in the free

---

[2] See Lin's original paper or Schlichting (1979).

Nomenclature

c_f = skin friction coefficient
k = kinetic energy of the laminar fluctuations, m^2/s^2
$O(q)$ = of order of magnitude q
p = static pressure, N/m^2
$\bar{q}$ = time-averaged component of q
q' = fluctuating component of q, $\bar{q}' = 0$
Re = Reynolds number
t = time, s
Tu = free-stream turbulence level
u = velocity component in the x direction, m/s
u^* = friction velocity, m/s
U = free-stream velocity, m/s
U_∞ = free-stream velocity for unaccelerated flow, m/s
v = velocity component in the y direction, m/s
x = coordinate in the free-stream direction, m
y = coordinate normal to the surface, m
δ = boundary layer thickness, m
ϵ = dissipation of kinetic energy, m^2/s^3
η = Kolmogorov's length scale, m
λ = viscous dissipation length scale, m
Λ = integral length scale of turbulence m
ν = kinematic viscosity, m^2/s
ρ = density, kg/m^3
υ = Kolmogorov's velocity scale, m/s
ω = angular frequency, 1/s

stream for this case, $k_\infty = \overline{U'^2}/2 = U_\infty'^2/4$. This distribution has a maximum of roughly $1.1k_\infty$ near $y = 2\delta_\omega$.

For details regarding higher order approximations, the reader is referred to Lin's original paper. For other approaches to solving laminar-boundary-layer flows with an unsteady free stream, the reader should see Moore (1951), Lighthill (1954), and Ackerberg and Phillips (1972).

Theory

The Laminar-Kinetic-Energy Equation. To the authors' knowledge, the energy equation for laminar fluctuations, henceforth called the "LKE" equation, has never been presented before. It can be obtained in the same way as the turbulent-kinetic-energy equation (see Bradshaw, 1971), except that the pressures $\bar{p}$ and p' can be eliminated by using the time-averaged and instantaneous form of Eq. (1). For boundary layer flows, one obtains

$$\bar{u}\frac{\partial k}{\partial x} + \bar{v}\frac{\partial k}{\partial y}$$

$$= -(\overline{u'}\overline{v'})\frac{\partial \bar{u}}{\partial y} - \frac{\partial}{\partial y}\left[\overline{v'}\bar{k} - \nu\frac{\partial k}{\partial y}\right] - \epsilon + \left\{\overline{u'\frac{\partial U'}{\partial t}}\right\} \quad (4)$$

where k is the kinetic energy of the laminar fluctuations, and ϵ is the viscous dissipation of kinetic energy defined by $\epsilon \equiv \nu\overline{(\partial u'/\partial y)^2}$. All of the terms but the last are similar to those in the TKE equation and represent the convection of laminar kinetic energy (on the left), and the production, diffusion, and dissipation of laminar kinetic energy respectively (on the right). The term in curly brackets arises from taking the average of $u'(dp'/dx)$ and represents the production of laminar kinetic energy by the work of the imposed fluctuating pressure forces. This term is new. It is also the only term in the equation providing a direct link between the fluctuations in the free stream and boundary layer, and as will now be shown, it is the most important production term.

If the kinetic energy is to increase as shown in Fig. 3, then at least one of the production terms must be larger than the dissipation term. Supposing the orders of magnitude for each quantity in Eq. (4) are $u' \approx O(\sqrt{k})$, $v' \approx O(\delta\sqrt{k}/L)$ where L is a distance along the surface and $\delta \approx O(\sqrt{\nu L/U_\infty})$, $\partial/\partial y \approx O(1/\delta)$, $\bar{u} \approx O(U_\infty)$ where U_∞ is the free-stream velocity, $\partial/\partial t \approx O(\omega)$, and $U' \approx O(\sqrt{k_\infty})$ where k_∞ is the free-stream kinetic energy, one obtains

$$\overline{u'v'}\frac{\partial \bar{u}}{\partial y}\Big/\epsilon \approx O(1) \quad \text{and} \quad \overline{u'\frac{\partial U'}{\partial t}}\Big/\epsilon \approx O\left(\frac{\omega\delta^2}{\nu}\sqrt{k_\infty/k}\right)$$

This implies that only the new production term has a chance of overwhelming the dissipation term, and that this occurs when Lin's high-frequency criterion is met, namely, when $\omega \gg \nu/\delta^2$. If the free-stream fluctuations result from turbulence having a broad spectrum of frequencies, this criterion will always be met. Therefore, the main effect of free-stream turbulence on a laminar boundary layer is similar to the high-frequency response examined by Lin.

Using the same order of magnitude analysis, it can also be shown that the diffusion of kinetic energy by the v' component of the fluctuations can be neglected compared to the viscous diffusion. Hence, the relevant LKE equation for a laminar boundary layer with a turbulent free stream becomes

$$\bar{u}\frac{\partial k}{\partial x} + \bar{v}\frac{\partial k}{\partial y} = \overline{u'\frac{\partial U'}{\partial t}} + \nu\frac{\partial^2 k}{\partial y^2} - \epsilon \quad (5)$$

which reveals that the mechanism for producing and amplifying laminar fluctuations in a boundary layer has the form of a forcing function.

The impact of this mechanism can be seen immediately by considering only the first terms on each side of Eq. (5) and setting the production term equal to $\omega\sqrt{k \cdot k_\infty}$. Considering $\omega \neq \text{fnc}(x)$ and $\bar{u} \approx U_\infty/2 \neq \text{fnc}(x)$, the equation may be integrated immediately to yield $\sqrt{k} \approx \sqrt{k_\infty}(\omega x/U_\infty)$. This is a fundamental result, which shows that any free-stream fluctuation produces a fluctuation in the boundary layer directly proportional to itself that initially grows linearly with distance.

Modeling the Kinetic Energy Equation. Measurements by Liepmann (1943), Dyban and Epik (1985), and Rolls-Royce (1993) show that the major contribution of kinetic energy in a laminar boundary layer comes from the u' component of the fluctuations. Hence, to a good approximation, we have $k \approx \overline{u'^2}/2$. (Indeed, for boundary layers, Eq. (4) is the transport equation for $\overline{u'^2}/2$.) In the free stream, $\overline{u'^2} \rightarrow \overline{U'^2}$, which for isotropic turbulence requires that $k \rightarrow k_\infty/3$.

Turning attention first to the production term in Eq. (5), we propose that $\overline{u'\partial U'/\partial t}$ may be modeled by the expression $\omega_{\text{eff}}\sqrt{k \cdot k_{\text{eff}}}$ where, following Dullenkopf and Mayle (1995), ω_{eff} is an effective frequency of turbulence and k_{eff} is an effective free-stream turbulent kinetic energy for forcing the fluctuations. This provides $\overline{u'\partial U'/\partial t} \propto \omega_{\text{eff}}(Tu_{\text{eff}}/Tu_\infty)\sqrt{k \cdot k_\infty}$ where Tu denotes a turbulence level and k_∞ is the measured free-stream kinetic energy. Since any fluctuation in the free stream and its temporal derivative is 90 deg out of phase, the production of kinetic energy must decay as the free stream is approached. The "damping" factor for Lin's problem is e^{-y/δ_ω}. Sharma et al. (1982) noted that the fluctuation intensity profiles always seem to have a maximum near $y+ \equiv u^*y/\nu \approx 25$, where u^* is the friction velocity. Supposing δ_ω is proportional to the position of maximum intensity provides $\delta_\omega u^*/\nu = \text{constant}$, say C^+, and the damping factor becomes $\exp(-y^+/C^+)$. Therefore a suitable expression for the production term might be

$$\overline{u'\frac{\partial U'}{\partial t}} = C_\omega\frac{U_\infty^2}{\nu}\sqrt{k \cdot k_\infty}e^{-y^+/c^+}$$

where $C_\omega = \text{const}\ x(\omega_{\text{eff}}\nu/U_\infty^2)(Tu_{\text{eff}}/Tu_\infty)$, and where both C_ω and C^+ remain to be determined. Although the damping factor in this expression appears similar to Van Driest's (1956) for turbulent boundary layers, and is arrived at through similar considerations, his refers to the viscous damping of fluctuations as the surface is approached while the present factor refers to a decreased interaction caused by a phase shift as the free stream is approached.

Turning attention now to the dissipation term, we have $\epsilon = \nu\overline{(\partial u'/\partial y)^2} \propto \nu k/\lambda^2$, where λ is a viscous dissipation length scale. Knowing that the dissipation remains finite near the surface, indeed a maximum, and that velocity fluctuations near the surface must be proportional to y, the length scale near the surface must be proportional to y. Since the dissipation and diffusion of kinetic energy are equal at the surface, the coefficient of proportionality must equal two. Hence, a suitable expression for the dissipation term might be

$$\epsilon = 2\nu\frac{k}{y^2}$$

This expression is identical to that proposed by Chien (1982) for the viscous dissipation of turbulent kinetic energy.

Substituting these expressions into Eq. (5), the LKE equation becomes

$$\bar{u}\frac{\partial k}{\partial x} + \bar{v}\frac{\partial k}{\partial y} = C_\omega\frac{U_\infty^2}{\nu}\sqrt{k \cdot k_\infty}e^{-y^+/C^+} + \nu\frac{\partial^2 k}{\partial y^2} - 2\nu k/y^2 \quad (6)$$

The boundary conditions are $k = 0$ at $y = 0$ and, for isotropic free-stream turbulence, $k \rightarrow k_\infty/3$ as $y \rightarrow \infty$. In addition, an initial kinetic energy profile must be provided.

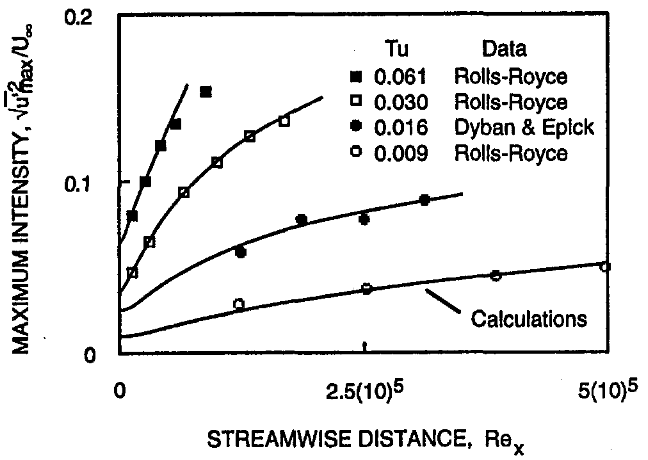

Fig. 4 A comparison of the calculations with measurements

Solution Methodology Using k, ϵ-Codes. Equation (6) can easily be solved by most modern boundary-layer computer codes. For codes based on the Spalding–Patankar algorithms, incorporating an additional transport equation is quite straightforward. Caution is needed only to ensure that the diffusivity of kinetic energy, which is usually calculated from an effective diffusivity using molecular and turbulent Prandtl numbers, is set equal to ν. It is also necessary to provide for the possibility that k diffuses beyond the viscous boundary layer. In addition, all turbulent quantities in the time-averaged equations of motion must be set equal to zero and any transition model must be deactivated such that the flow remains completely laminar. This can usually be accomplished by setting the production of turbulent kinetic energy equal to zero.

For the present calculations, Eq. (3) with $\delta_\omega = \delta/4$ was used as the initial profile. Calculations with other values of δ_ω had virtually no effect on the solutions. In addition, calculations were begun at $Re_x \approx 1000$ and no modifications to the equations of motion for the mean flow were made. Since the streamwise distribution of maximum fluctuation intensity is used for predicting the onset of transition, provisions for obtaining it should also be included in the code.

Comparisons With Experiments

Calculations for this paper were performed using the computer code called "ALFA" (Sieger et al., 1993). This is a standard boundary-layer code of the $k-\epsilon$ variety, which was modified as just described. Three of the following comparisons are made with data obtained by Rolls-Royce (1993) for free-stream turbulence levels of about 1, 3, and 6 percent. Their experiments are well documented and all necessary turbulence data are available (Roach, 1987; Roach and Brierley, 1990). In addition, these data have become standard test cases for transitional flow modeling (Savill, 1991). A comparison with data from Dyban and Epik (1985) is also made for a free-stream turbulence level of about 2 percent.

Preliminary calculations indicated that reasonably good results could be obtained by considering both C_ω and C^+ independent of x. The "best" values for C_ω and C^+ were then obtained by fitting the data by eye, realizing that C_ω has the greatest effect on the growth of kinetic energy, while C^+ has the greatest effect on its growth rate (see Eq. (6)). When no combination of C_ω and C^+ could be found to fit the kinetic energy distributions in both the x and y directions, a compromise was made to fit the streamwise distribution of maximum kinetic energy. With this, the best value for C^+ turned out to be virtually the same for all of the data and was consequently set equal to a constant, namely, $C^+ = 13$.

The calculated and measured maximum intensity distributions are shown in Fig. 4. Agreement is excellent, and although not shown, a good fit for the 1 percent data is found all the way out to $Re_x \approx 1.3(10)^6$. The values of C_ω that provide these results are presented in Table 1. Their variation will be discussed in the next section.

Table 1

Test Case	Tu_∞ [%]	C_ω
Rolls-Royce (1993)	0.9	0.00010
Dyban &Epik (1985)	1.6	0.00014
Rolls-Royce (1993)	3.0	0.00021
Rolls-Royce (1993)	6.0	0.00017

Cross sections of calculated and measured intensity profiles are shown in Figs. 5(*a*) and 5(*b*). While on the average reasonable, the calculated profiles are not quite right. In general, the peaks of the intensity profiles are calculated closer to the wall than measured. This is particularly true for the $Tu_\infty = 1$ percent test case where just before transition (comparison not shown), the peak is predicted to be one-third of the measured distance from the wall. In this case, however, fluctuations at the Tollmien–Schlichting frequency were detected and transition is suspected to be caused by a natural instability. In spite of these discrepancies, the agreement between the calculated and measured intensity profiles is remarkable considering the simplicity of the model and the fact that no transitional boundary-layer

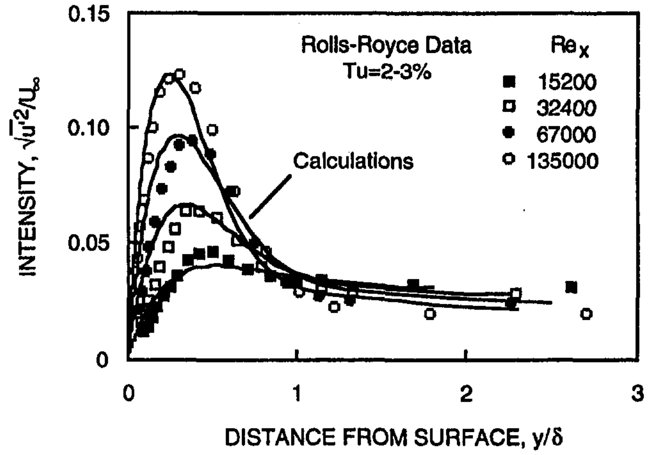

Fig. 5(*a*) Calculated and measured intensity profiles for one set of free-stream conditions

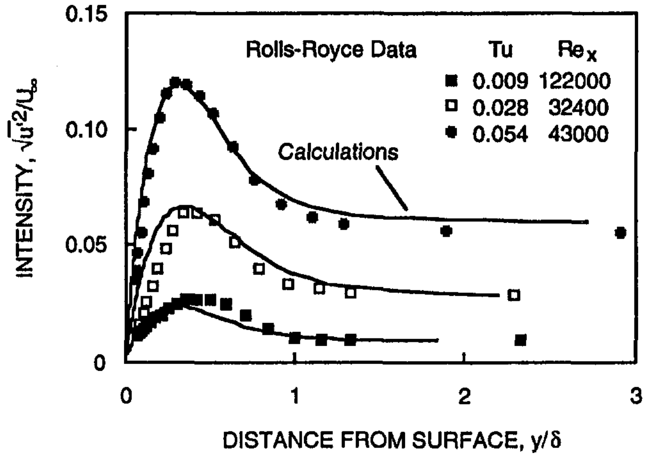

Fig. 5(*b*) Calculated and measured intensity profiles for three different sets of free-stream conditions

code using low-Reynolds-number turbulence modeling has yet been able to calculate these data.

Effective Frequency and Turbulence Level

By definition, C_ω depends on both an effective frequency and turbulence level. Therefore, one may expect that the variation of C_ω with Tu_∞ as shown in Table 1 is not in general valid. In fact we believe that C_ω, and consequently the production of LKE, is intimately connected to the turbulence spectrum characterized at the very least by the turbulence level, integral length scale, and the dissipation length scale.

Since the boundary layer is thinnest at the front of a surface, the first fluctuations in the layer will be produced by turbulence in the free stream having the highest frequencies. The "highest" frequencies are not necessarily "effective," however, since fluctuations at these frequencies will be viscously dissipated. Considering free-stream dissipation is most intense at the frequency ω_d, say, any fluctuations with frequencies near or higher than ω_d will certainly be dissipated in the boundary layer. Thus, the first fluctuations to amplify in the boundary layer will have frequencies less than ω_d, and from Lin's criterion this will occur once $\mathrm{Re}_x \geqslant U_\infty^2/\omega_d\nu$.

The frequency ω_d can be determined from the second moment of the turbulence spectrum (Hinze, 1975) and corresponds roughly to the frequency where the energy begins to fall off from Kolmogorov's equilibrium spectral distribution. An estimate for it, however, can be obtained by dividing the free-stream velocity by the eddy size in the free stream most affected by viscous dissipation. Introducing Kolmogorov's length scale η, one obtains (see Hinze) $\omega_d \approx 0.1U_\infty/\eta = 0.1U_\infty/(\nu^3/\epsilon_\infty)^{1/4}$ where ϵ_∞ is the free-stream dissipation of turbulence. Assuming that the effective frequency for fluctuations in a laminar boundary layer is some fraction of this, one obtains

$$\frac{\omega_{\mathrm{eff}}\nu}{U_\infty^2} \propto \frac{\omega_d\nu}{U_\infty^2} \propto \frac{(\epsilon_\infty\nu)^{1/4}}{U_\infty} = \frac{v}{U_\infty}$$

where v is Kolmogorov's velocity scale.

Following Dullenkopf and Mayle (1995), fluctuations in a laminar boundary layer will only respond to the energy contained within a relatively small band of frequencies near the effective frequency. If the energy spectral distribution near ω_{eff} is that given by Kolmogorov, and only the energy contained within a band near this frequency is important, an estimate for the effective turbulence level can be obtained. According to Dullenkopf and Mayle, the effective turbulence level is

$$\frac{Tu_{\mathrm{eff}}}{Tu_\infty} \propto \left(\frac{\omega_{\mathrm{eff}}\Lambda}{U_\infty}\right)^{-1/3} \propto \left(\frac{\omega_d\Lambda}{U_\infty}\right)^{-1/3} = \left(\frac{\omega_d\nu}{U_\infty^2}\right)^{-1/3}(\mathrm{Re}_\Lambda)^{-1/3}$$

where Λ is the integral length scale of turbulence and $\mathrm{Re}_\Lambda = U_\infty\Lambda/\nu$ is the integral-length-scale Reynolds number.

Substituting these expressions into the definition of C_ω yields

$$C_\omega = C\left(\frac{v}{U_\infty}\right)^{2/3}\mathrm{Re}_\Lambda^{-1/3} \qquad (7)$$

where C is an accumulation of proportionality factors that is expected to be a constant. The quantities v/U_∞ and Re_Λ can be determined directly from the turbulence energy density spectrum. Since v is related to the dissipation of turbulence, it can also be determined from the decay of turbulence, namely $(v/U_\infty)^4 = -(3/2)[d(Tu_\infty^2)/d\,\mathrm{Re}_x]$. Estimating Re_Λ from the dissipation length scale is not recommended, however, since comparisons between these estimates and measurements using the data of Roach (1987) show poor agreement.

The 1, 3, and 6 percent data of Rolls-Royce were obtained using three very different turbulence grids. Since the turbulence field generated by these grids is well documented by Roach (1987), however, one can easily determine the values of v/U_∞ and Re_Λ. These values are listed in Table 2. The values for v/U_∞ were obtained using the equation above together with Roach's correlations for the decay of Tu_∞. The correlation for the 1 and 3 percent test cases, which used grids with round bars, is found in Roach's Fig. 3. The correlation for the 6 percent case, which used a grid with square bars, is found in Roach's Fig. 4. The grid for this test, as for the 3 percent test case, had bars placed in a parallel array. The grid for the 1 percent case had bars placed in a square array. Unlike the correlations given for Tu_∞, the correlation for Λ does not fit the data very well. Therefore the values for Re_Λ in Table 2 were obtained directly from the data plotted in Fig. 9 of Roach's paper, not from his correlation. For Dyban and Epik's test case, v/U_∞ was evaluated from the measured decay of turbulence. No data on length scale, however, are reported.

Table 2

Test Case	v/U_∞	Re_Λ	C
Rolls-Royce (1%)	0.0035	4740	0.073
Dyban &Epik (2%)	0.0080	-	-
Rolls-Royce (3%)	0.0098	3590	0.070
Rolls-Royce (6%)	0.0117	9830	0.071

The values for C in the last column of Table 2 were obtained using Eq. (7) and the values for C_ω given in Table 1. The fact that C is virtually identical for all three cases, in spite of the large variations in Tu_∞, v/U_∞, and Re_Λ, is truly remarkable, and nicely supports our hypotheses for an effective frequency and turbulence level. Making our best estimate for Dyban and Epik's test, however, we obtain $\mathrm{Re}_\Lambda \approx 3000$, which in turn provides $C \approx 0.05$. This difference we believe is in the uncertainty of Re_Λ and perhaps even in the value given for v/U_∞, which had to be extrapolated back to the beginning of the plate. Considering this, we presently suggest using $C = 0.07$ in Eq. (7) and strongly urge using measurements for obtaining both v/U_∞ and Re_Λ. To the experimenter, of course, we strongly encourage measuring the complete spectrum of turbulence in the free stream, paying particular attention to frequency spikes, and ask for streamwise distributions of turbulence intensity, integral- and microlength scales, and dissipation. In addition, all experimenters should measure the intensity and spectral energy distribution of the streamwise component of vibration of the test surface, which, of course, contributes to the "real" turbulence "sensed" by the flow over the surface.

The Onset of Transition

In 1943, Liepmann proposed that transition begins where the maximum Reynolds stress in the boundary layer equals the wall shear stress. According to Sharma et al. (1982) this may be expressed as

$$\sqrt{(\overline{u'^2})_{\max,t}} \approx 3(u^*)_t \qquad (8)$$

where the subscript "t" denotes the condition at the onset of transition, and u^* is the friction velocity.

The calculated values of $\sqrt{(\overline{u'^2})_{\max}}/U_\infty$ from Fig. 4 have been replotted in Fig. 6 together with the quantity $3u^*/U_\infty$. For unaccelerated flow, $u^*/U_\infty = 0.576/\mathrm{Re}_x^{1/4}$. The criterion expressed in Eq. (8) is met where the curves cross. These locations are where transition is "predicted" to begin. The observed locations are marked with arrows. In general, agreement is best for the higher turbulence levels. The discrepancy at the lowest turbulence level is discussed below. Nevertheless, since the calculations of $\sqrt{(\overline{u'^2})_{\max}}$ were correlated to give the best fit to the data, any disagreement here is a result of the criterion.

The $Tu_\infty = 1$ percent test case is interesting and impossible for most transitional boundary layer codes to predict. As re-

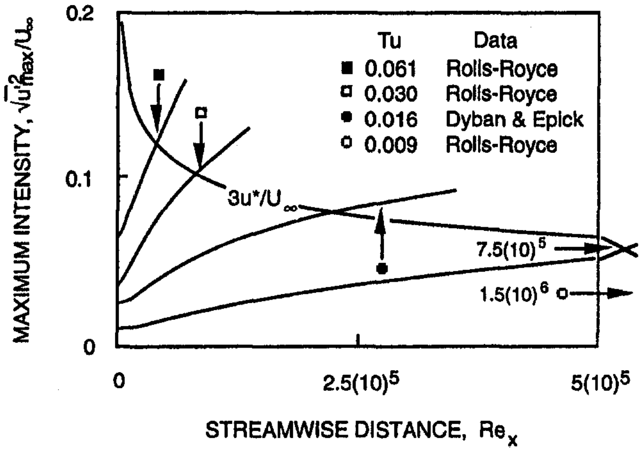

Fig. 6 Calculated and measured locations for the onset of transition

ported by Roach and Brierley (1990), the fluctuations far downstream have a strong component at the Tollmien–Schlichting frequency. While fluctuations of this sort first appear contrary to the concept of an effective frequency and therefore impossible to predict using the present theory, we believe this test is an excellent and perhaps the only documented example of the subtle transformation between bypass and natural transition. Our interpretation of this test is that the initial fluctuations developed according to the present theory for bypass transition, but the growth rate was too low. Thus once the critical Reynolds number was reached, the Tollmien–Schlichting instabilities, which amplify exponentially compared to the linear amplification for bypass transition, dominated, and transition finally occurred "naturally." Since the average growth of the fluctuations, whether forced or natural, was reasonably calculated by the present theory, the effective and Tollmien–Schlichting frequencies must be nearly identical for this case. This suggests that once the effective frequency nears the Tollmien–Schlichting frequency, transition is more likely to occur naturally.

Conclusions

The main idea proposed in this paper is that the laminar fluctuations preceding transition are primarily caused by the work of the imposed fluctuating free-stream pressure forces on the flow in the boundary layer. Based on this thought, we presented a theory for calculating these fluctuations using the laminar-kinetic-energy equation which, after some modeling, assumes the form

$$\bar{u}\frac{\partial k}{\partial x} + \bar{v}\frac{\partial k}{\partial y} = C_\omega \frac{U_\infty^2}{\nu}\sqrt{k \cdot k_\infty}\, e^{-y^+/C^+} + \nu\frac{\partial^2 k}{\partial y^2} - 2\nu k/y^2$$

where $C^+ \approx 13$.

Additional ideas concerning the frequency that drives the fluctuations were also proposed. These ideas permitted us to relate the coefficient C_ω in the equation above to the free-stream turbulence-energy-density spectrum according to

$$C_\omega = C\left(\frac{v}{U_\infty}\right)^{2/3} \mathrm{Re}_\Lambda^{-1/3}$$

where $C \approx 0.07$.

These ideas are new and, we believe, clear the path to predicting the onset of transition. But before onset can reliably be predicted, much more work remains to be done. Some of our suggestions for study are:

- Obtain more data in the pretransitional flow, including the quantities v' and $\overline{u'v'}$, as well as u', comprehensive free-stream turbulence measurements, and surface vibration measurements,
- Develop more sophisticated production and dissipation models, a more universal criterion for turbulent spot formation, and hence the onset of transition, and models for the second-order effects of the fluctuations on the time-averaged velocity and temperature profiles, and
- Investigate the effects of free-stream acceleration, and the transformation between bypass and natural transition.

This list is neither all inclusive nor in an order of priority except, perhaps to say, that more data are clearly needed.

Acknowledgments

The lead author wishes to express his gratitude to Professor S. Wittig for his support and hospitality during the author's recent visits to the Institut für Thermische Strömungsmaschinen as a Visiting Professor. The work presented herein was conducted during several visits beginning January 1994 while this author was on sabbatical. The same author is also grateful to Rensselaer Polytechnic Institute for granting him a sabbatical at that time and to the German Sonderforschungsbereich 167 which funded part of the work.

The authors also wish to thank their good friend and colleague Dr. -Ing. K. Dullenkopf for his part in the many helpful discussions during the course of this work.

References

Abu-Ghannam, B. J., and Shaw, R., 1980, "Natural Transition of Boundary Layers—The Effects of Turbulence, Pressure Gradient and Flow History," *J. Mech. Engng. Sci.*, Vol. 22, pp. 213–228.

Ackerberg, R. C., and Phillips, J. H., 1972, "The Unsteady Laminar Boundary Layer on a Semi-infinite Flat Plate Due to Small Fluctuations in the Magnitude of the Free-Stream," *J. Fluid Mech.*, Vol. 51, pp. 137–157.

Bradshaw, P., 1971, *An Introduction to Turbulence and Its Measurement*, Pergamon Press, Braunschweig.

Chien, K. Y., 1982, "Predictions of Channel and Boundary Flows With a Low-Reynolds-Number Turbulence Model," *AIAA Journal*, Vol. 20, pp. 33–38.

Dullenkopf, K., and Mayle, R. E., 1995, "An Account of Free-Stream-Turbulence Length Scale on Laminar Heat Transfer," ASME JOURNAL OF TURBOMACHINERY, Vol. 117, pp. 401–406.

Dyban, E., Epik, E., and Suprun, T. T., 1976, "Characteristics of the Laminar Boundary Layer in the Presence of Elevated Free-Stream Turbulence," *Fluid Mech.—Soviet Res.*, Vol. 5, pp. 30–36.

Dyban, E., and Epik, E., 1985, *Thermal/Mass Transport and Hydrodynamics of Turbulent Flows*, Kiev [in Russian].

Emmons, H. W., 1951, "The Laminar–Turbulent Transition in a Boundary Layer—Part I," *J. Aero. Sci.*, Vol. 18, pp. 490–498.

Hinze, J. O., 1975, *Turbulence*, McGraw-Hill, New York.

Liepmann, H. W., 1943, "Investigations on Laminar Boundary-Layer Stability and Transition on Curved Boundaries," NACAACR 3H30 (NACA-WR-W-107).

Lighthill, M. J., 1954, "The Response of Laminar Skin Friction and Heat Transfer to Fluctuations in the Stream Velocity," *Proc. Roy. Soc.*, Vol. A224, pp. 1–23.

Lin, C. C., 1957, "Motion in the Boundary Layer With a Rapidly Oscillating External Flow," *Proc. 9th Int. Congress Appl. Mech.*, Brussels, Vol. 4, pp. 155–167.

Mack, L. M., 1977, "Transition Prediction and Linear Stability Theory," AGARD CP 224, pp. 1-1 to 1-22.

Mayle, R. E., 1991, "The Role of Laminar–Turbulent Transition in Gas Turbine Engines," 1991 ASME International Gas Turbine Institute Scholar Award Paper, ASME JOURNAL OF TURBOMACHINERY, Vol. 113, pp. 509–537.

McDonald, H., and Fish, R. W., 1973, "Practical Calculations of Transitional Boundary Layers," *Int. J. Heat Mass Transfer*, Vol. 16, pp. 1729–1744.

Moore, F. K., 1951, "Unsteady, Laminar Boundary-Layer Flow," NACA TN 2471.

Roach, P. E., 1987, "The Generation of Nearly Isotropic Turbulence by Means of Grids," *Int. J. Heat Fluid Flow*, 8, pp. 82–92.

Roach, P. E., and Brierley, D. H., 1990, "The Influence of a Turbulent Free-Stream on Zero Pressure Gradient Transitional Boundary Layer Development Including the T3A & T3B Test Case Conditions," *Proc. 1st ERCOFTAC Workshop on Numerical Simulation of Unsteady Flows, Transition to Turbulence and Combustion*, Lausanne.

Rolls-Royce, 1993, transmittal by J. Coupland of data from the Rolls-Royce Applied Science Laboratory.

Savill, A. M., 1991, "Synthesis of T3 Test Case Computations," *Proc. 1st ERCOFTAC Workshop on Numerical Simulation of Unsteady Flows, Transition to Turbulence and Combustion*, Lausane.

Schlichting, H., 1979, *Boundary-Layer Theory*, McGraw-Hill, New York.

Schmidt, R. C., and Patankar, S. V., 1991, "Simulating Boundary Layer Transition With Low-Reynolds-Number $k-\epsilon$ Turbulence Models, Part I & II," ASME JOURNAL OF TURBOMACHINERY, Vol. 113, pp. 10–26.

Sharma, O. P., Wells, R. A., Schlinker, R. H., and Bailey, D. A., 1982, "Boundary Layer Development on Turbine Airfoil Suction Surfaces," ASME *Journal of Engineering for Power*, Vol. 104, pp. 698–706.

Sieger, K., Schulz, A., Wittig, S., and Crawford, M. E., 1993, "An Evaluation of Low-Reynolds-Number $k-\epsilon$ Turbulence Models for Predicting Transition Under the Influence of Free-Stream Turbulence and Pressure Gradient," *Proc. 2nd Int. Symp. Engng. Turb. Modeling & Measurements*, Florence, Italy, pp. 593–602.

Smith, A. M. O., 1956, "Transition, Pressure Gradient and Stability Theory," presented at the IIX Int. Congr. Appl. Mech., Brussels.

Sohn, K. H., and Reshotko, E., 1991, "Experimental Study of Boundary Layer Transition With Elevated Freestream Turbulence on a Heated Plate," NASA CR 187068.

Van Driest, E. R., 1956, "On Turbulent Flow Near a Wall," *J. Aerosp. Sci.*, Vol. 23, pp. 1007–1012.

Zhou, D., and Wang, T., 1995, "Effects of Elevated Free-Stream Turbulence on Flow and Thermal Structures in Transitional Boundary Layers," ASME JOURNAL OF TURBOMACHINERY, Vol. 117, pp. 407–417.

DISCUSSION

M. W. Johnson[3]

The authors in their paper recognize that the velocity fluctuations appearing in the laminar boundary layer are the precursor to bypass transition. Furthermore, he shows that the mechanism through which these fluctuations are generated in the boundary layer is the unsteady pressure field resulting from the freestream turbulent eddies. This is, I believe, an important step forward in both understanding and predicting bypass transition.

A similar model to that presented here, but using empirical correlations rather than analytical theory for the induction of the velocity fluctuations through the unsteady pressure field, has been used to predict transition previously (Savill, 1993, 1994, 1995a, b; Johnson, 1994; Johnson and Ercan, 1996). In this work it was found that the model could be extended to adverse/favorable streamwise pressure gradients using the same unsteady pressure field model, as it is the effect of the streamwise pressure gradient on the time mean laminar boundary layer profile that results in an increase or decrease in the velocity fluctuation levels in an adverse or favorable pressure gradient, respectively. Can the authors comment on how their model might be modified to account for streamwise pressure gradients?

In the paper, Lin's theory is used to show that the "fluctuations in a laminar boundary layer will only respond to the energy contained within a relatively small band of frequencies near the effective frequency." The wavelength of this effective frequency is relatively long at approximately 16 δ (Dullenkopf and Mayle, 1995). Measured frequency spectra (e.g., Blair, 1992) indeed show that the laminar boundary layer responds most strongly to low frequencies, but over a wide band with no discernible lower limit. The lowest frequencies measured by Blair had wavelengths of approximately 200 δ. Do the authors believe this discrepancy is due to the frequency limitation of Lin's theory ($\omega\delta^2/\nu \gg 1$, equivalent to wavelengths $\ll (2\pi\,\mathrm{Re}_\delta)\delta$) or can they offer some other explanation?

The paper also raises the question as to how a laminar fluctuation can be distinguished from a turbulent fluctuation. Laminar fluctuations do not significantly modify the boundary layer profile and hence have negligible Reynolds stress associated with them. In contrast, the significant Reynolds stresses resulting from turbulent fluctuations modify the time mean boundary layer profile through momentum transport. Would the authors therefore agree that a laminar fluctuation is best defined as one with negligible (or zero) Reynolds stress?

References

Blair, M. F., 1992, "Boundary Layer Transition in Accelerating Flows With Intense Freestream Turbulence. Parts 1 and 2," ASME *Journal of Fluids Engineering*, Vol. 114, pp. 313–332.

Johnson, M. W., 1994, "A Bypass Transition Model for Boundary Layers," ASME JOURNAL OF TURBOMACHINERY, Vol. 116, pp. 759–764.

Johnson, M. W., and Ercan, A., 1996, "A Boundary Layer Transition Model," ASME Paper 96-GT-444.

Savill, A. M., 1993, "Transition Modelling for Turbomachinery," *Proc. 1st Workshop of the ERCOFTAC Transition SIG*, Manchester, England.

Savill, A. M., 1994, *Proc. 2nd Workshop of the ERCOFTAC Transition SIG*, Brussels.

Savill, A. M., 1995a, *Proc. 3rd Workshop of the ERCOFTAC Transition SIG*, Prague.

Savill, A. M., 1995b, *Proc. 4th Workshop of the ERCOFTAC Transition SIG*, Thessaloniki.

Authors' Closure

We sincerely appreciate Dr. Johnson's comment regarding our paper and hope in answering his questions we may also clarify some issues.

First, we are aware of his and others' previous work in this area and wish to thank him for pointing out our oversight and adding the references for us. We would not, however, call the "models" similar except in that both recognize the importance of the pretransitional velocity fluctuations to the transition problem. Whereas the empirical methods correlate the growing fluctuations, generally within a frequency range, which, as discussed below, we believe is too low, ours is a model for the overall process leading to their growth. This process should be the same for flows with or without pressure gradients. Therefore, since the link between free-stream turbulence and fluctuations in the boundary layer is the production term in our LKE equation, extending the model to flows with a pressure gradient should be possible by properly accounting for its effect on this term, as well as, of course, by calculating the mean laminar flow corresponding to the pressure gradient.

Regarding Dr. Johnson's second question, the discrepancy is even worse than he states, but we don't understand what Lin's theory has to do with it. The discrepancy has to do with the transfer of energy from higher frequencies, on which we show the production of laminar kinetic energy depends, to the lower frequencies where most of the energy is observed, and only when this mechanism is understood can the "discrepancy" be explained. In regard to his question, however, we also wish to clarify some of his statements. First, the concept of an effective frequency came directly from the work of Dullenkopf and Mayle (1995). Lin's theory was used in our paper as the most practical way of approaching the problem. As it turns out, his frequency criterion also happens to be the necessary condition for amplifying fluctuations in the boundary layer. Second, the effective frequency for augmenting laminar heat transfer, as examined by Dullenkopf and Mayle, is not the same frequency effective in amplifying laminar kinetic energy. The latter is about one to two orders of magnitude larger, implying that the important wavelength of turbulence for pretransitional flow is one to two orders of magnitude smaller than that found by Dullenkopf and Mayle. (This issue is treated in more detail in a paper entitled "The Turbulence That Matters" by R. E. Mayle, K. Dullenkopf, and A. Schulz, which will also be published in a future volume of this journal.)

Distinguishing between laminar and turbulent fluctuations will be difficult, but we don't agree with Dr. Johnson's definition. According to Lin's theory, the Reynolds stress for laminar fluctuations will only be zero when the free-stream fluctuations are independent of the streamwise distance (see Lin, 1957, or Schlichting, 1979). For the low free-stream turbulence levels, such as we examined, the decay of turbulence over the pretransitional region of flow is negligible. For high free-stream turbulence, however, say 6 percent or more, and this was not pointed out in our paper, it cannot be neglected, the Reynolds stress is not negligible, and as shown by Dyban et al. (1976), the mean velocity profiles are definitely affected.

---

[3] Department of Mechanical Engineering, The University of Liverpool, Liverpool L69 3BX, United Kingdom.

Schmidt, R. C., and Patankar, S. V., 1991, "Simulating Boundary Layer Transition With Low-Reynolds-Number $k-\epsilon$ Turbulence Models, Part I & II," ASME JOURNAL OF TURBOMACHINERY, Vol. 113, pp. 10–26.

Sharma, O. P., Wells, R. A., Schlinker, R. H., and Bailey, D. A., 1982, "Boundary Layer Development on Turbine Airfoil Suction Surfaces," ASME *Journal of Engineering for Power*, Vol. 104, pp. 698–706.

Sieger, K., Schulz, A., Wittig, S., and Crawford, M. E., 1993, "An Evaluation of Low-Reynolds-Number $k-\epsilon$ Turbulence Models for Predicting Transition Under the Influence of Free-Stream Turbulence and Pressure Gradient," *Proc. 2nd Int. Symp. Engng. Turb. Modeling & Measurements*, Florence, Italy, pp. 593–602.

Smith, A. M. O., 1956, "Transition, Pressure Gradient and Stability Theory," presented at the IIX Int. Congr. Appl. Mech., Brussels.

Sohn, K. H., and Reshotko, E., 1991, "Experimental Study of Boundary Layer Transition With Elevated Freestream Turbulence on a Heated Plate," NASA CR 187068.

Van Driest, E. R., 1956, "On Turbulent Flow Near a Wall," *J. Aerosp. Sci.*, Vol. 23, pp. 1007–1012.

Zhou, D., and Wang, T., 1995, "Effects of Elevated Free-Stream Turbulence on Flow and Thermal Structures in Transitional Boundary Layers," ASME JOURNAL OF TURBOMACHINERY, Vol. 117, pp. 407–417.

DISCUSSION

M. W. Johnson[3]

The authors in their paper recognize that the velocity fluctuations appearing in the laminar boundary layer are the precursor to bypass transition. Furthermore, he shows that the mechanism through which these fluctuations are generated in the boundary layer is the unsteady pressure field resulting from the freestream turbulent eddies. This is, I believe, an important step forward in both understanding and predicting bypass transition.

A similar model to that presented here, but using empirical correlations rather than analytical theory for the induction of the velocity fluctuations through the unsteady pressure field, has been used to predict transition previously (Savill, 1993, 1994, 1995a, b; Johnson, 1994; Johnson and Ercan, 1996). In this work it was found that the model could be extended to adverse/favorable streamwise pressure gradients using the same unsteady pressure field model, as it is the effect of the streamwise pressure gradient on the time mean laminar boundary layer profile that results in an increase or decrease in the velocity fluctuation levels in an adverse or favorable pressure gradient, respectively. Can the authors comment on how their model might be modified to account for streamwise pressure gradients?

In the paper, Lin's theory is used to show that the "fluctuations in a laminar boundary layer will only respond to the energy contained within a relatively small band of frequencies near the effective frequency." The wavelength of this effective frequency is relatively long at approximately 16 δ (Dullenkopf and Mayle, 1995). Measured frequency spectra (e.g., Blair, 1992) indeed show that the laminar boundary layer responds most strongly to low frequencies, but over a wide band with no discernible lower limit. The lowest frequencies measured by Blair had wavelengths of approximately 200 δ. Do the authors believe this discrepancy is due to the frequency limitation of Lin's theory ($\omega\delta^2/\nu \gg 1$, equivalent to wavelengths $\ll (2\pi\,\mathrm{Re}_\delta)\delta$) or can they offer some other explanation?

The paper also raises the question as to how a laminar fluctuation can be distinguished from a turbulent fluctuation. Laminar fluctuations do not significantly modify the boundary layer profile and hence have negligible Reynolds stress associated with them. In contrast, the significant Reynolds stresses resulting from turbulent fluctuations modify the time mean boundary layer profile through momentum transport. Would the authors therefore agree that a laminar fluctuation is best defined as one with negligible (or zero) Reynolds stress?

---

[3] Department of Mechanical Engineering, The University of Liverpool, Liverpool L69 3BX, United Kingdom.

References

Blair, M. F., 1992, "Boundary Layer Transition in Accelerating Flows With Intense Freestream Turbulence. Parts 1 and 2," ASME *Journal of Fluids Engineering*, Vol. 114, pp. 313–332.

Johnson, M. W., 1994, "A Bypass Transition Model for Boundary Layers," ASME JOURNAL OF TURBOMACHINERY, Vol. 116, pp. 759–764.

Johnson, M. W., and Ercan, A., 1996, "A Boundary Layer Transition Model," ASME Paper 96-GT-444.

Savill, A. M., 1993, "Transition Modelling for Turbomachinery," *Proc. 1st Workshop of the ERCOFTAC Transition SIG*, Manchester, England.

Savill, A. M., 1994, *Proc. 2nd Workshop of the ERCOFTAC Transition SIG*, Brussels.

Savill, A. M., 1995a, *Proc. 3rd Workshop of the ERCOFTAC Transition SIG*, Prague.

Savill, A. M., 1995b, *Proc. 4th Workshop of the ERCOFTAC Transition SIG*, Thessaloniki.

Authors' Closure

We sincerely appreciate Dr. Johnson's comment regarding our paper and hope in answering his questions we may also clarify some issues.

First, we are aware of his and others' previous work in this area and wish to thank him for pointing out our oversight and adding the references for us. We would not, however, call the "models" similar except in that both recognize the importance of the pretransitional velocity fluctuations to the transition problem. Whereas the empirical methods correlate the growing fluctuations, generally within a frequency range, which, as discussed below, we believe is too low, ours is a model for the overall process leading to their growth. This process should be the same for flows with or without pressure gradients. Therefore, since the link between free-stream turbulence and fluctuations in the boundary layer is the production term in our LKE equation, extending the model to flows with a pressure gradient should be possible by properly accounting for its effect on this term, as well as, of course, by calculating the mean laminar flow corresponding to the pressure gradient.

Regarding Dr. Johnson's second question, the discrepancy is even worse than he states, but we don't understand what Lin's theory has to do with it. The discrepancy has to do with the transfer of energy from higher frequencies, on which we show the production of laminar kinetic energy depends, to the lower frequencies where most of the energy is observed, and only when this mechanism is understood can the "discrepancy" be explained. In regard to his question, however, we also wish to clarify some of his statements. First, the concept of an effective frequency came directly from the work of Dullenkopf and Mayle (1995). Lin's theory was used in our paper as the most practical way of approaching the problem. As it turns out, his frequency criterion also happens to be the necessary condition for amplifying fluctuations in the boundary layer. Second, the effective frequency for augmenting laminar heat transfer, as examined by Dullenkopf and Mayle, is not the same frequency effective in amplifying laminar kinetic energy. The latter is about one to two orders of magnitude larger, implying that the important wavelength of turbulence for pretransitional flow is one to two orders of magnitude smaller than that found by Dullenkopf and Mayle. (This issue is treated in more detail in a paper entitled "The Turbulence That Matters" by R. E. Mayle, K. Dullenkopf, and A. Schulz, which will also be published in a future volume of this journal.)

Distinguishing between laminar and turbulent fluctuations will be difficult, but we don't agree with Dr. Johnson's definition. According to Lin's theory, the Reynolds stress for laminar fluctuations will only be zero when the free-stream fluctuations are independent of the streamwise distance (see Lin, 1957, or Schlichting, 1979). For the low free-stream turbulence levels, such as we examined, the decay of turbulence over the pretransitional region of flow is negligible. For high free-stream turbulence, however, say 6 percent or more, and this was not pointed out in our paper, it cannot be neglected, the Reynolds stress is not negligible, and as shown by Dyban et al. (1976), the mean velocity profiles are definitely affected.

Transition Over C4 Leading Edge and Measurement of Intermittency Factor Using PDF of Hot-Wire Signal

B. K. Hazarika

C. Hirsch

Department of Fluid Mechanics,
Vrije Universiteit Brussel,
Brussels, Belgium

The variation of intermittency factors in the transition region of a C4 leading edge flat plate is measured at three incidence angles in a low-turbulence free stream. During the determination of intermittency factor, the threshold value of the detector function and the validity of conditional averaging are verified by a method based on the direct application of PDF of the hot-wire output. As the angle of incidence is increased, the transition progressively moves through all the three modes on the suction surface: at zero incidence the bypass transition, at 2 deg incidence the natural transition, and at 4 deg incidence the separated-flow transition occur, respectively. All three modes of transition exhibited the chordwise intermittency factor variation in accordance with Narasimha's universal intermittency distribution; thus, the method based on spot production rate is applicable to all the three modes of transition. In the transition zone of the attached boundary layers, the conditionally averaged interturbulent profiles are fuller than the Blasius profile, while the conditionally averaged turbulent profiles follow a logarithmic profile with a variable additive parameter.

Introduction

The behavior of the transition region in zero-pressure-gradient flows is well documented and the confidence on the correlation is high due to the presence of a large number of experimental data. Klingman et al. (1993) have shown that a locally adverse pressure gradient in the leading edge region has a strong influence on the stability of the boundary layer over a flat plate even when there is no pressure gradient over a considerable distance upstream of the critical point. Therefore, the correlation for a transition region in a zero pressure gradient should be examined carefully for its suitability before it is used to predict transition over a flat plate with a leading edge profile, even when there is no pressure gradient in the transition region.

Earlier estimations of the intermittency factors were made by a number of indirect methods, for example, by comparing the variation of shape factors with laminar and fully turbulent boundary layers, or by relating the variation of output of a surface pitot to the length of the transition region, etc. In the case of the separation bubbles, the onset and the extent of the transition region are estimated from the extent of the pressure plateau and the variation of turbulence intensity along the center of the shear layer. With the advent of high-speed digital data acquisition, the use of direct methods has become more common. Measurement of intermittency factor and conditionally averaged profiles, both parallel and normal to the surface, using digital data acquisition in the zero-pressure-gradient transition region, are reported by Sohn et al. (1989).

In the accelerating flows it is difficult to create a transition zone in the Reynolds number range normally achievable in most wind tunnels; this is the reason for paucity of data in accelerating flows. In the adverse pressure gradients the transition may occur through the natural or the separation path. In these cases the difference between the hot-wire signals of interturbulent and turbulent portions is very small. This is one of the reasons that intermittency measurements in adverse pressure gradient cases are still rare. In accelerating flows Blair (1982, 1992) and Keller and Wang (1995) reported the intermittency factor variations through the transition region. Gostelow and Blunden (1989) used an on-line intermittency meter, facilitating a large number of measurements in flows with various pressure gradients and free-stream turbulence levels. The intermittency factors and the correlations in the transition zones at various adverse pressure gradients are given by Gostelow et al. (1994). Walker and Solomon (1992) and Walker et al. (1993) reported the measurement of the intermittency factors in the wake-induced transition in the flow over a compressor blade including separated flow. The investigation reported by Malkiel (1994) is the only set of data in a leading edge separation bubble where the intermittency factor is directly measured normal to the surface at several stations in the transition region.

The method used here is based on digital data acquisition and examination of the distribution of a suitable detector function derived from the hot-wire output to discriminate between turbulent and interturbulent portions of the signal. The method is used to map the intermittency factor distribution and conditional averaging in the transition zone on a C4 profile leading edge plate at three incidence angles in a low-turbulence free stream. All three modes, natural, bypass, and separated flow transition, are observed.

Experimental Arrangement and Method of Measurement

The experimental investigations are carried out in an open return wind tunnel driven by a centrifugal blower. The tunnel has a contraction ratio of 9.2:1. The end of the contraction section is 1350 mm wide and 450 mm high. The 8-m-long test section has a flexible roof, which is arranged to create a zero pressure gradient over a flat surface set parallel to the axis. The nonuniformity in the free stream is less than 0.5 percent and free-stream turbulence is around 0.03 percent. The smooth aluminum flat plate used for the experiment has overall dimensions of 1245 × 435 × 10 mm^3. The 50-mm-long leading edge has

---

Contributed by the International Gas Turbine Institute and presented at the 40th International Gas Turbine and Aeroengine Congress and Exhibition, Houston, Texas, June 5–8, 1995. Manuscript received by the International Gas Turbine Institute March 10, 1995. Paper No. 95-GT-294. Associate Technical Editor: C. J. Russo.

a typical C4 thickness distribution, given by Eq. (1). The maximum thickness is at $x = 50$ mm where the surfaces blend tangentially. There are 28 static pressure taps of 0.5 mm diameter distributed on both sides along the plate and staggered about the midspan. Most of these pressure taps are clustered near the leading edge.

$$t = 2(28.110l^3 - 25.281l^2 - 6.563l + 15.492\sqrt{l})\frac{t_m}{10} \quad (1)$$

where

$$l = \frac{x}{166.67} \quad \text{and} \quad t_m = 10$$

The free-stream turbulence is increased to 0.35 percent at the leading edge by placing a galvanized iron screen of 0.7 mm wire diameter and 12 mm mesh size, 1600 mm upstream of the leading edge at the exit of the contraction section (Fig. 1). The plate is placed in the test section with its span in the vertical plane and held in place with four bolts. This leaves gaps between the edges of the plate and the roof and the floor of the test section. The reference pressure gradients over the plate are determined at various angles of incidence and in the range $3 \times 10^3 < \text{Re} < 3 \times 10^4$ by positioning the plate at the required angle in the test section (when the downstream screen is not present). For the measurements reported here, the gaps between the edges of the plate and the floor and the roof are closed with Styrofoam profiles and thin adhesive tapes. Screens of selected blockage are introduced near the trailing edge (shown in Fig. 1) to create pressure gradients on the leading edge same as those at 2 and 4 deg incidence angles.

The measurements are taken with a normal single-sensor hot-wire probe connected to a constant-temperature anemometer. The probe has a 3 mm prong separation and the sensor has a diameter of 5 μm. The prongs and a portion of the sensing wire are gold plated to leave a 1.25 mm sensing length. All the pressures are measured with one pressure transducer connected to the taps and the pitot tubes through a Scannivalve. The two-channel data acquisition system (DAS) used for these measurements has a 16 bit processor and is set at ±4 volts span. The DAS digitizes the data and is capable of finding average, rms, correlation, spectra, etc., of the input signals. On-line monitoring of the signal is also carried out with a spectrum analyzer and an oscilloscope connected in parallel to the DAS. A personal computer is used as the principal controller to coordinate the probe traverse and data acquisition.

The hot-wire is calibrated in-situ before and after each experiment. In addition, reference readings are taken frequently to compensate for change in the hot-wire sensitivity due to fouling and room temperature change. The minimum free-stream velocity that can be achieved in the test section is around 1 m/s; therefore, the calibration is conducted in the range from 1 m/s to the maximum velocity that is encountered for the particular test case. At each incidence the mean velocity and the rms values of fluctuating velocity profiles are measured at a number of streamwise locations using the hot-wire probe. The profiles give indications of the extent of the transition region. The stations for transition survey and conditional averaging are selected from the results of the mean survey. For most of these measurements the DAS is operated at 10 kHz low-pass filter setting at which 2048 data acquisition (a record) is completed in 0.08 second. To determine the intermittency factors, 40 records of data are stored at each measurement point, making a total of 3.2 seconds of data for each point. The data stored in a hard disk are later analyzed in a work station using an interactive program, the procedure for which is given in the following section. The spectra of the fluctuating output of the hot-wire are taken at selected positions based on the results of mean and transition measurements. Several mean velocity profile measurements are also performed with a pneumatic boundary layer probe for comparison.

Procedure for Signal Processing. Various investigators have reported that the probability density function (PDF) of the fluctuating component of a velocity in a fully turbulent region is normally distributed. Therefore, if the turbulence intensity is relatively small, the PDF of the hot-wire signal from the turbulent region will be normally distributed about the mean. If the instrumentation noise of the anemometer system used is negligible compared to the disturbance diffused from free stream into a laminar boundary layer, the PDF of the hot-wire output signals from these regions will also be normally distributed. However, if derivatives of the signals are used, they deviate progressively from the Gaussian distribution with the order of the derivative (Hedley and Keffer, 1974).

The procedure for the signal processing is based on the assumption that the PDF of the hot-wire output signal from the intermittent region is a combination of two Gaussian functions with a large difference in the standard deviations. Since the average velocities of the turbulent and interturbulent portions are not known separately a priori, the use of a derivative of the output as the detector function β, instead of the output itself,

Nomenclature

A = constant in the logarithmic profile
B = additive parameter in the logarithmic profile
b = displacement height of the separated layer
C_p = pressure coefficient
c = wave speed
E = instantaneous hot-wire output
K = acceleration parameter = $(\nu/U_e^2)(\partial U_e/\partial x)$
N = nondimensional spot formation rate
n = spot formation rate, numbers/s/m
$\hat{n}$ = spot production rate
P = stagnation pressure
p = static pressure
Re = reference Reynolds number = Vt_m/ν
Re_θ = momentum Reynolds number = $U_e\theta/\nu$
Re_{δ_*} = displacement Reynolds number = $U_e\delta^*/\nu$
t = plate thickness
U = mean velocity
U_e = maximum mean velocity at a station
u = rms of fluctuating component
V = reference velocity
x = chordwise distance
y = distance from the surface
α = wave number
β = detector function = $(\partial E/\partial \tau)^2$ or $(\partial^2 E/\partial \tau^2)^2$
γ = intermittency factor
δ = boundary layer thickness
δ^* = displacement thickness
δ_{sh} = shear layer thickness
θ = momentum thickness
λ = transition length scale = $(x_{\gamma=0.75} - x_{\gamma=0.25})$
λ_θ = pressure gradient parameter = $(\theta^2/\nu)(\partial U_e/\partial x)$
ν = kinematic viscosity
σ = dependence area
σ_i = standard deviation (interturbulent)
σ_τ = standard deviation (turbulent)
τ = time
ω = angular frequency

Subscripts

0 = free-stream
m = maximum
s = reference
T = completion of transition
t = onset of transition

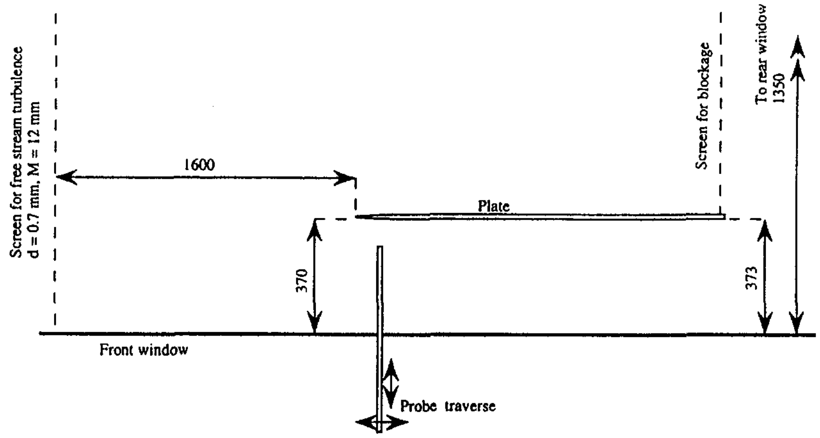

All dimensions are in mm.
Not to scale.

PLAN

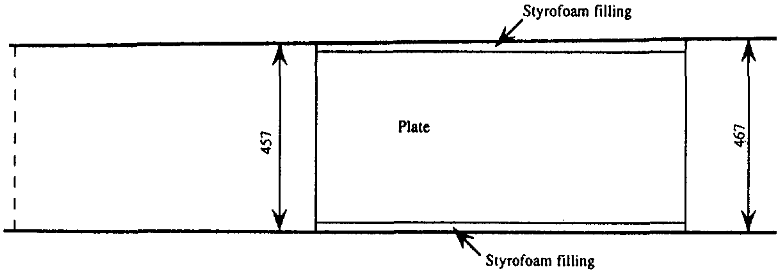

FRONT VIEW

Fig. 1 Schematic diagram of the flat plate in the test section

removes the need of a priori knowledge. If the square of the derivative of the velocity or the hot-wire output from the transition region is used to amplify the difference, the distribution could be given by:

$$f(\beta) = (1-\gamma)\frac{\sqrt{2}}{\pi\sigma_i}\exp\left\{-\frac{1}{2}\left(\frac{\beta}{\sigma_i}\right)^2\right\} + (\gamma)\frac{\sqrt{2}}{\pi\sigma_T}\exp\left\{-\frac{1}{2}\left(\frac{\beta}{\sigma_T}\right)^2\right\};\ \beta > 0 \quad (2)$$

In the transition and turbulent regions of a boundary layer, the distributions of the turbulent parts of the signal are not truly Gaussian (due to the presence of coherent structures, etc.). Therefore, Eq. (2) does not truly represent the distribution. However, it does not become an insurmountable obstacle if the standard deviations differ considerably. The value of the detector function at which a sudden change in the distribution occurs will indicate the threshold (cutoff) value. The correct threshold value and the drop-off time are determined by observing the PDFs of the detector function for the interturbulent and the turbulent portions of the signal after they are separated. In bypass transition, the standard deviations differ by a few orders of magnitude. This method has been successfully used by Hazarika and Hirsch (1993) to measure intermittency factors and to average the interturbulent and the turbulent profiles conditionally.

The flow chart of the interactive program for the analysis of the signals is shown in Fig. 2. Either $(\partial E/\partial\tau)^2$ or $(\partial^2 E/\partial\tau^2)^2$ can be used as the detector function. In case of noisy (instrumentation noise, etc.) signals, it may be necessary to carry out smoothing (digital filtering) of the signal before the derivative is calculated. All these possibilities are included in this flow chart. A plot of the PDF of the detector function will reveal the threshold value for determining whether the signal is from interturbulent or turbulent events. However, portions of the signal from turbulent events could show the detector function value to be smaller than the threshold since the distribution is continuous until zero; in the same way the interturbulent portion of the signal could have values larger than threshold. Two assumptions are made to overcome this dilemma: (1) An isolated portion of a turbulent signal can have values of the detector function less than cutoff continuously for a duration (drop-off time) given by the largest time scale for turbulence. (2) The smallest period of time for which a portion should be turbulent continuously to be considered turbulent is the smallest time scale of turbulence. A series of switches tagged to the data points are now set at "on" (value 1) for turbulent and at "off" (value 0) for interturbulent data points after applying these assumptions. This series of switches forms the discriminator function for the set of data at the measurement point.

In bypass transition, due to the large difference in the standard deviations of the detector functions for the interturbulent and the turbulent portions of the signal, the selection of drop-off time is not critical. The threshold value can also be easily identified even at high intermittency factor. However, in the adverse pressure gradient case, when natural or separation mode of transition occurs, the standard deviations of the turbulent portion of the signal could be only slightly larger (4–5 times, not an order of magnitude) than that for the interturbulent portions. The distributions of the data (called PDF for brevity) at a point of measurement where the intermittency factor is around 15 percent, for a test case (transition of a separation bubble) are shown in Figs. 3(*a*) and 3(*b*). The abscissa in these figures represents β calculated by taking the time interval between consecutive data taken as unity ($\partial\tau = 1$). The ordinates represent the number of occurrences at various values of β out of a total of 40 records of data points. The distribution of the detector function before the separation of interturbulent and turbulent portions is shown in Fig. 3(*a*). The continuous curves in the

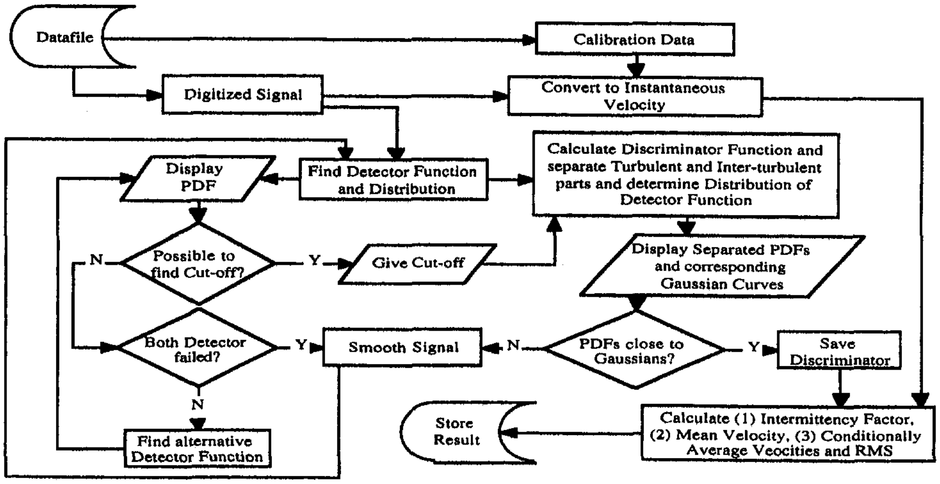

Fig. 2 Flow chart for analysis of transition data

PDF plots represent Gaussian distributions with the same area under the curve and total number of occurrence at zero value as the measured distribution. The distributions after separation of the signal are shown in Fig. 3(*b*). The ratio σ_T/σ_i is about 4.2 for this case. In such situations, at higher intermittency factor the threshold value is completely masked and the correct value could be determined only after analyzing the PDFs at several points covering the whole shear layer at that axial station. The best value for the drop-off time is found to be in the range between δ_{sh}/U_e and $2\delta_{sh}/U_e$. Various investigators have used a time window in the range 0.4 to 3.5 (Walker and Solomon, 1992); the range (1 to 2) found suitable for the present series of measurements lies in the middle of this range.

The effectiveness of this method can be seen from the analysis of signals for the natural mode of transition (Re = 3500 at 2 deg incidence, for example) from a station prior to transition. Part of a velocity signal from a station upstream of the onset of transition is shown in Fig. 4. Large amplification in velocity oscillation is quite noticeable in this figure; the spectra taken at the position (Fig. 14) show a large increase in energy in the frequency range 150 to 400 Hz. However, examination of the PDF of the detector function (Fig. 5) proves it to be a single Gaussian distribution by its closeness to the theoretical curve and absence of discontinuity. All the PDFs upstream of onset of transition show similar characteristics.

Estimated Error. The uncertainty in mean velocity (outside the reverse flow region) is 1 percent and the uncertainty in rms value of the fluctuating component is 0.5 percent of the nominal velocity.

The uncertainties in the transition onset length and the transition length scale for the worst case (separated flow) reported here are 10 percent. For the rest of the cases they are less than 5 percent.

Results and Discussion

The transition of boundary layers over the C4 leading edge plate at three angles of incidence, namely 0, 2, and 4 deg, are reported here. At 0 deg incidence the measurements are taken

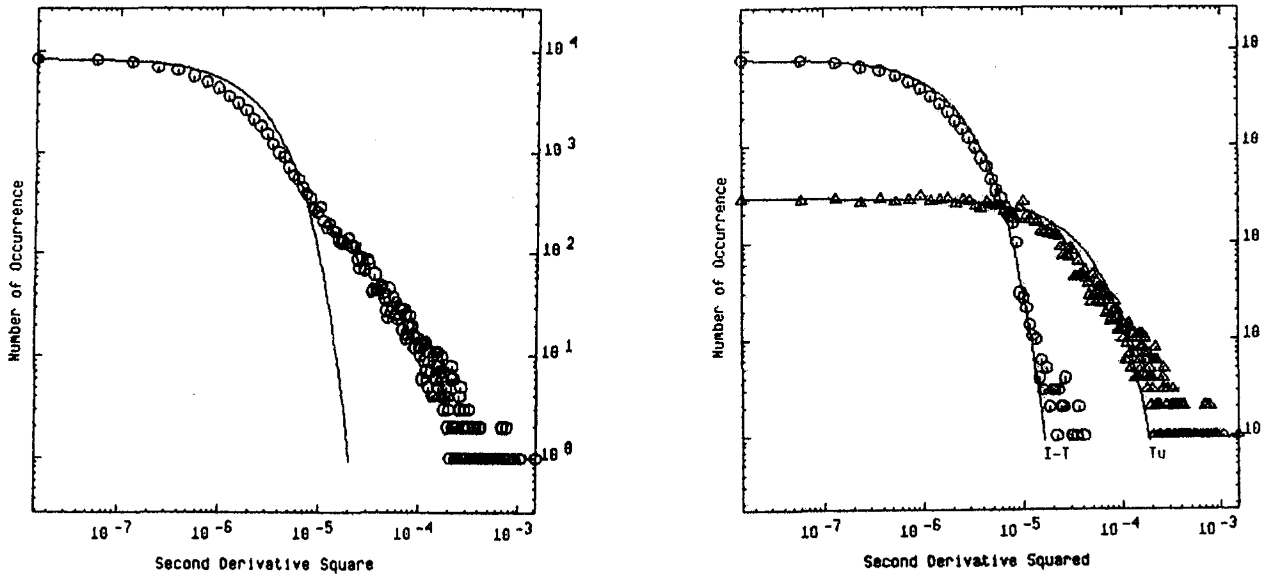

(a) COMPLETE SIGNAL BEFORE SEPARATION (b) SEPARATED INTER-TURBULENT AND TURBULENT

Fig. 3 PDF of the detector functions of a signal from the transitional shear layer

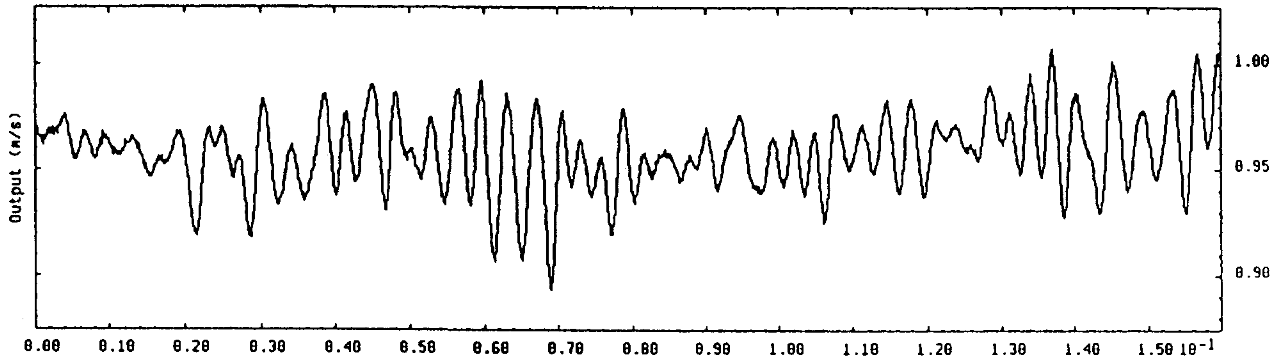

Fig. 4 Velocity trace from a record at $X = 50$ mm, $Y = 0.2$ mm for case B

at $Re = 21.5 \times 10^3$. The measurements at 2 deg incidence conducted at $Re = 3.5 \times 10^3$ and $Re = 6.9 \times 10^3$, and the measurements at 4 deg incidence conducted at $Re = 3.6 \times 10^3$, are presented. The turbulence intensity at the leading edge ($x = 0$), in the free stream ($y = 55$ mm) is close to 0.35 percent at all Re and incidence angles. The free-stream turbulence drops to 0.32 percent at $x = 560$ mm, where p_S is measured. The reference dynamic pressure ($\rho V^2/2$) and the reference velocity (V) are evaluated from the difference between the free-stream total pressure (P_0) and p_S. For the sake of convenience, the test cases are designated as case A, case B, case C, and case D, respectively as shown in Table 1, and figures are labeled accordingly.

At the low value of turbulence intensity (0.35 percent) used for the experiments, the length scales of turbulence could not be measured accurately, thus they are not reported. Instead, the free-stream ($x = 0$, $y = 55$ mm) turbulence spectra for the four test cases are shown in Fig. 6. All the spectra shown here are the spectra of the hot-wire output signals. If velocity information is needed, the procedure outlined by Ramamoorthy et al. (1993) should be employed. The ordinate is normalized by making the area under the curve for power against frequency equal to unity and is termed "spectral density." This figure shows that the spectrum in case D is slightly different from those of the other cases. The difference occurred due to the curvature of the streamlines. The energy distribution for the other three cases is quite similar.

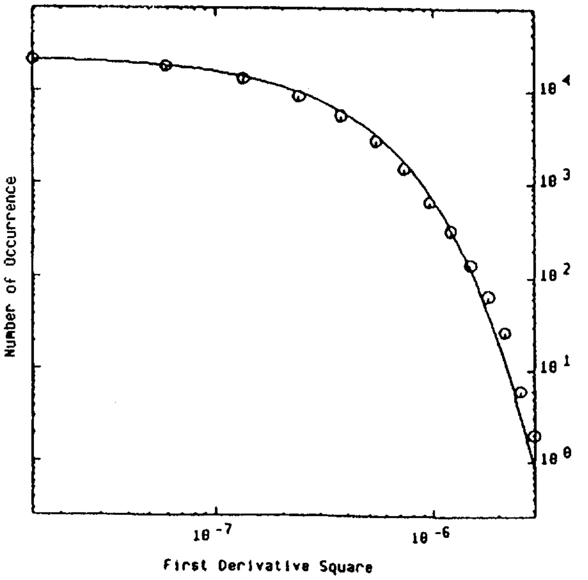

Fig. 5 PDF of the detector function of a signal recorded at $X = 50$ mm, $Y = 0.2$ mm for case B

The pressure coefficients over the plate at the three angles of incidence are shown in Fig. 7. In all the test cases, far downstream of the leading edge ($x > 30$ cm), the static pressure on the flat plate remains practically constant ($C_p = \pm 0.005$). The dotted lines are used to show the continuation of data points. At zero incidence (case A) the pressure coefficient has a minimum on the leading edge and there is no difference in pressure between the front and the rear surfaces. Downstream of 175 mm, in the transition zone, the static pressure remains practically constant. At 2 deg incidence (cases B and C are similar), away from the leading edge, the difference between the C_p of the front and rear surfaces is about 0.2. Significant pressure gradient is present up to $x = 175$ mm. Intermittency measurements show that the transition takes place in this region of adverse pressure gradient. At 4 deg incidence (case D) the suction peak is detected at the nose of the plate and the plateau exists in the region where $3 \text{ mm} < x < 24$ mm, downstream of which rapid pressure recovery takes place. Downstream of 300 mm, where pressure levels off, the difference between the C_p of the front and the rear surface is about 0.45. A significant pressure gradient is present up to $x = 175$ mm in this case also. The reattachment takes place in the region where $90 \text{ mm} < x < 175$ mm. The intermittency measurement showed that the transition region lies within the region of the pressure plateau.

The profiles of U/V and u/V through the transition region for three test cases are shown in Figs. 8, 9, and 10 on a shifted abscissa. The first curves on these plots truly correspond to the abscissa, the rest of the curves are shifted equally along the abscissa. A point is plotted at (0, 0) of each curve to indicate the origin (also the theoretical value) for the particular curve,

Table 1 Test cases and quantities related to the transition over the suction surface

Quantity	Case A	Case B	Case C	Case D
Incidence	0°	2°	2°	4°
Re	21.5×10^3	3.5×10^3	6.9×10^3	3.6×10^3
FST (%)	0.35	0.35	0.35	0.35
x_t (mm)	212	58	43	5
λ (mm)	39	31	13.5	4
x_T(mm)	343	162	88	18.4
$\lambda_{\theta t}$	0	-0.06	-0.07	0
$\lambda_{\theta T}$	0	-0.035	-0.05	0
K_t ($\times 10^6$)	0	-4.3	-3.8	0
K_T ($\times 10^6$)	0	-0.6	-0.7	0
$Re_{\delta^* t}$	890	314	424	435
$Re_{\theta t}$	375	118	142	73
$Re_{\theta T}$	716	253	258	220
U_e (m/s)	32.57	5.56	11.18	7.30
$\hat{n}$	5.88×10^{-11}	3.18×10^{-9}	4.15×10^{-9}	1.11×10^{-7}
N	3.14×10^{-3}	4.69×10^{-3}	10.79×10^{-3}	48.97×10^{-3}

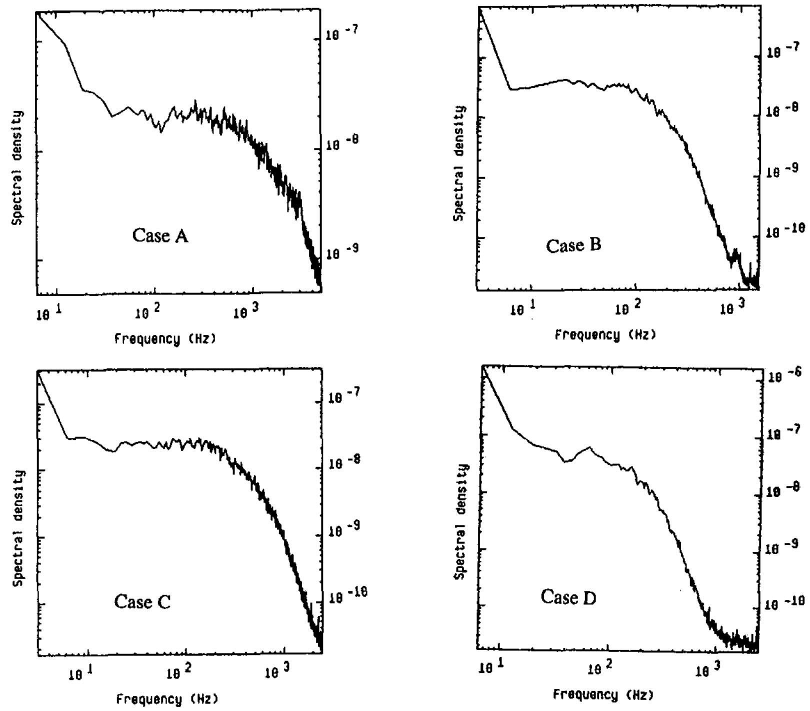

Fig. 6 Free-stream turbulence spectra for the four test cases

and does not represent a data point. At the top of each curve the chordwise position is shown in mm.

The profiles for case A (Fig. 8) show that the typical double peak formation in the profiles of u/V appears in the transition region. However, these double peaks appear after the peak intermittency factor exceeds 0.5 (x = 270 mm). The double peak formation completely disappears at the completion of transition. The velocity traces near the onset of transition in case A show some oscillations, but their contribution to the spectra is negligible as seen in Fig. 13(a). The peak value of u/V increases through the transition, reaches a maximum at x = 270 mm, then reduces to level off at the completion.

The profiles for cases B and C show a significant increase in u/V early in the transition region. The development of the profiles through the transition region for case B are shown in Fig. 9. The velocity signal near the onset of transition (Fig. 4) shows significant oscillations. The contribution of these oscillations to the spectra (Fig. 14) could be seen around a particular frequency determined by the boundary layer parameters as shown later. No double peak is observed in this case. The peak value of $u/$

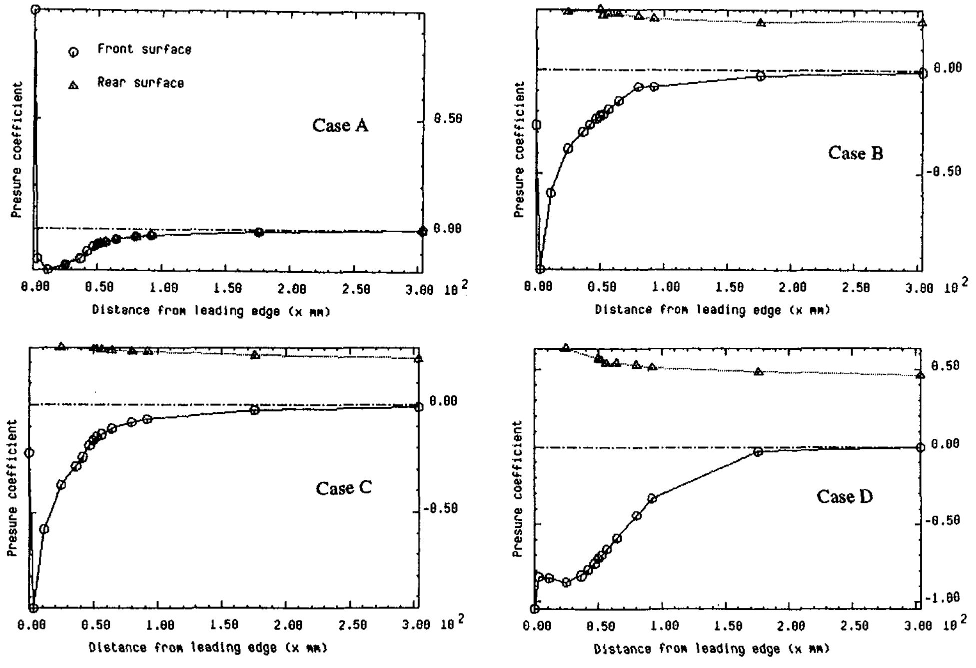

Fig. 7 Variation of wall static pressure near the leading edge

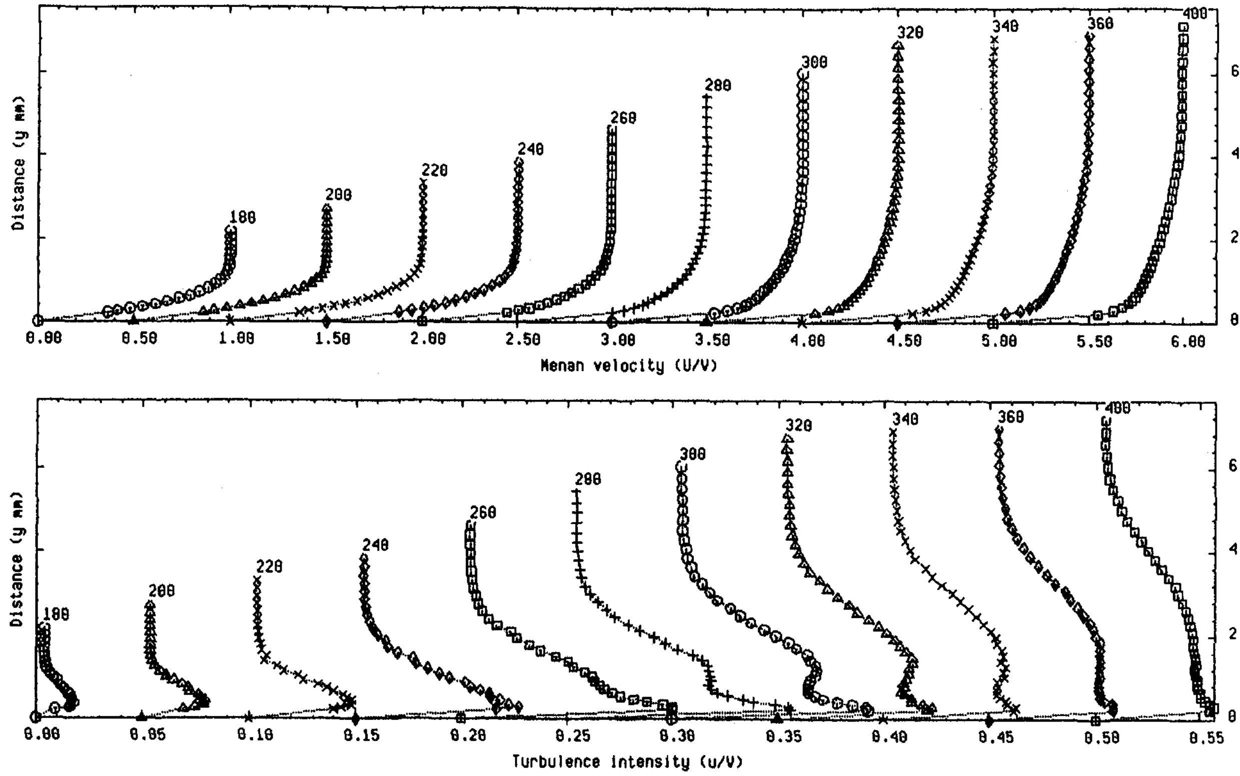

Fig. 8 Development of the profiles of mean velocity and rms of fluctuating velocity through the transition region for case A

V increases through the transition and reaches a maximum in the early transition region ($x = 90$ mm, $\gamma \sim 0.35$) then reduces gradually toward the completion of transition.

The profiles of *U*/*V* for case D (Fig. 10) show the typical profiles of a thick separation bubble close to the nose. In the early part of the bubble ($x < 20$ mm) a smooth velocity profile

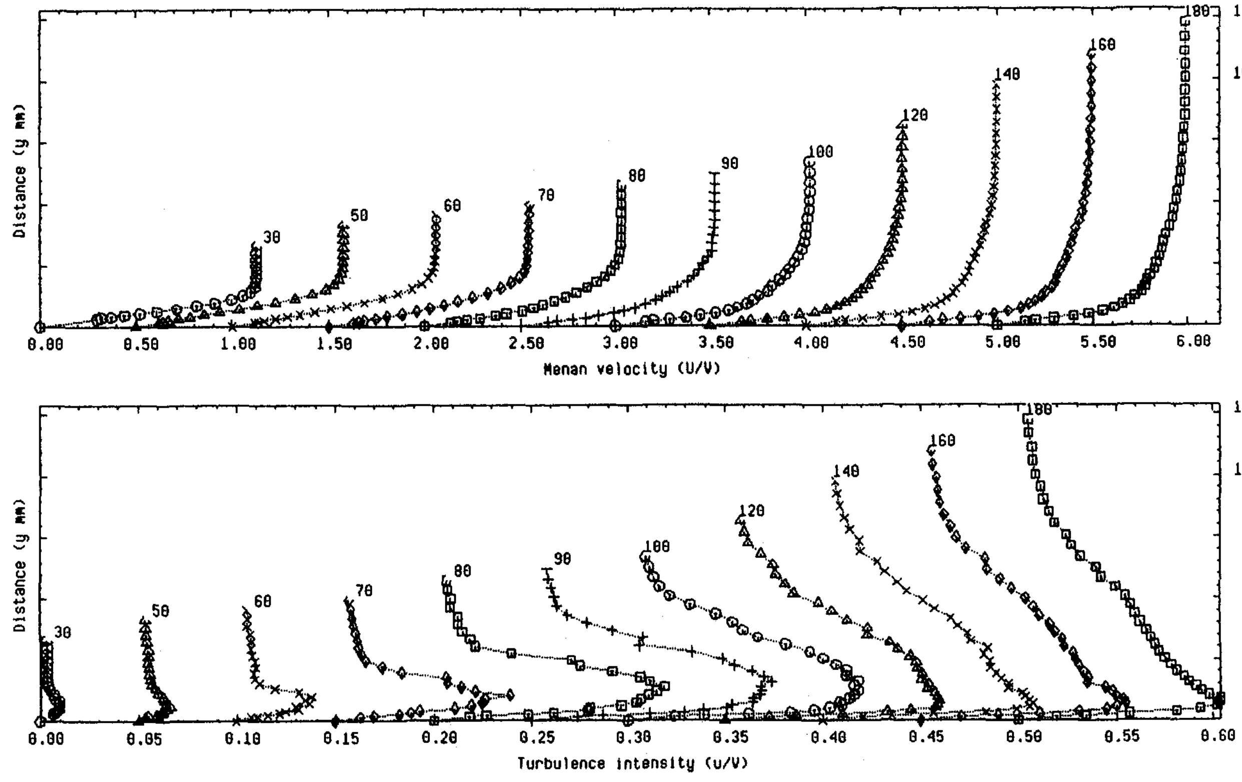

Fig. 9 Development of the profiles of mean velocity and rms of fluctuating velocity through the transition region for case B

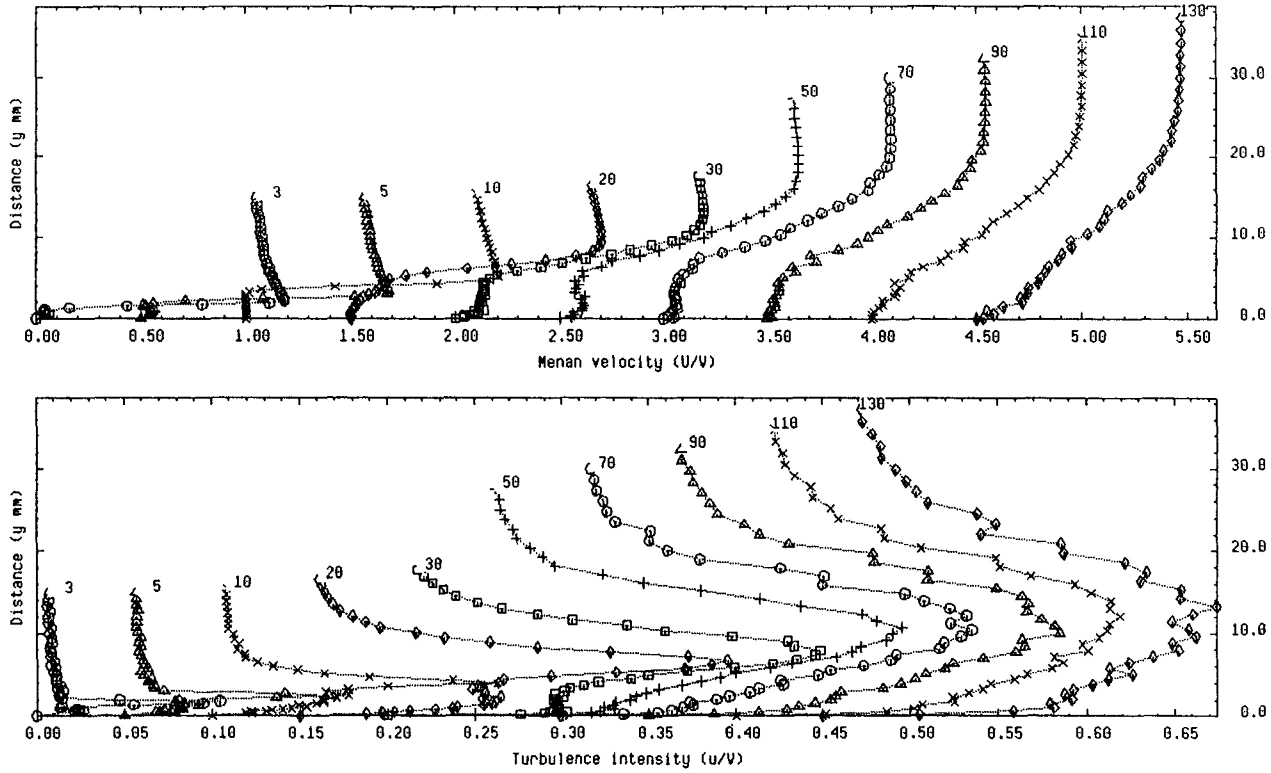

Fig. 10 Development of the profiles of mean velocity and rms of fluctuating velocity through the transition region for case D

could be obtained through the reverse flow region by using the method given by Hazarika and Hirsch (1994). Downstream of 20 mm it is not possible to obtain a smooth velocity profile, thus all velocities are left as positive. The mean velocity profiles show that the reattachment takes place in the region around 110 mm. The peak value of u/V is measured at the center of the shear layer. The peak value of u/V reaches 12 percent at the onset of transition. Through the transition it increases to 25 percent and stays close to that value until after reattachment. Large values ($\sim$20 percent) of u/V are detected at the last measurement station ($x = 180$ mm). It is seen that strong harmonic oscillations are present in the velocity signals for this case also.

The intermittency factors measured in the transition region normal to the axis across the shear layer show that for all the test cases, the peak value of γ appears at a distance away from the surface, as reported by many investigators (for example, Sohn et al., 1989). The peaks appear around $y/\delta = 0.3$ for the attached flow transition, and near the center of the shear layer for the separated flow transition. For the four test cases, the variations of peak γ in the chordwise direction are shown in Fig. 11. The broken curves in these figures represent the universal intermittency distribution found by using the method given by Narasimha (1985). These figures show that for all four test cases investigated here the intermittency distribution can be given by:

$$\gamma = 1 - \exp\left\{-0.412\left(\frac{x - x_t}{\lambda}\right)^2\right\} \quad (3)$$

The analysis of the data for cases B and C shows that the transition is through the natural mode, whereas for case A the transition is through the bypass mode and for case D the transition is through separated flow. The scatter in the results for cases B, C, and D reflects the difficulty in the measurement of γ for these cases as well as the difficulty in traversing the probe along the locus of the peak γ and the limited time of data acquisition. In spite of the scatter, it is clear that Narasimha's universal distribution is a practical basis for expressing intermittency distribution for all the three types of transition.

The peak value of u/V for the mean measurements (not conditionally averaged) for cases A, B, and C appears relatively away from the surface in the laminar and transition regions as compared to the turbulent region. In the separated layer it appears in the center of the shear layer. For the attached flow the peak value approaches 3.5 percent as the onset of transition is approached. In separated flow u/V approached 11 percent before the breakdown occurred; the breakdown of the instability waves could be clearly distinguished by observing the PDF of the detector function.

The distributions of γ normal to the chordwise direction at several measurement stations in the transition regions for the four cases are shown in Fig. 12. As reported by a number of investigators, the general trend is a reducing intermittency close to the surface. The reduction in intermittency factor close to the surface is very severe in cases B and D. In case B, the measurement point closest to the surface is in the viscous sublayer ($y^+ < 5$); therefore, the behavior in this region is more like a highly disturbed laminar layer rather than a turbulent layer. Therefore, γ at this point has value close to zero. For test cases A and C, measurements are not taken in the viscous sublayer; therefore such low values of γ are not measured. However, case C shows a sharper reduction relative to case A because the points closest to the surface are in the buffer layer.

In case D, the reverse flow region below the transitioning shear layer shows a very small intermittency. In the pressure recovery region the fluid in the reverse flow region experiences a favorable pressure gradient. At the same time the velocity of reverse flow below the transitioning shear layer is extremely small: This gives an extremely low transverse gradient of velocity. Therefore, the possibility of relaminarization in the reverse flow region could not be ruled out. The intermittency factor measured normal to the chord, near the middle of the separation bubble ($x = 50$ mm, where $\gamma = 1$ in a large portion around the

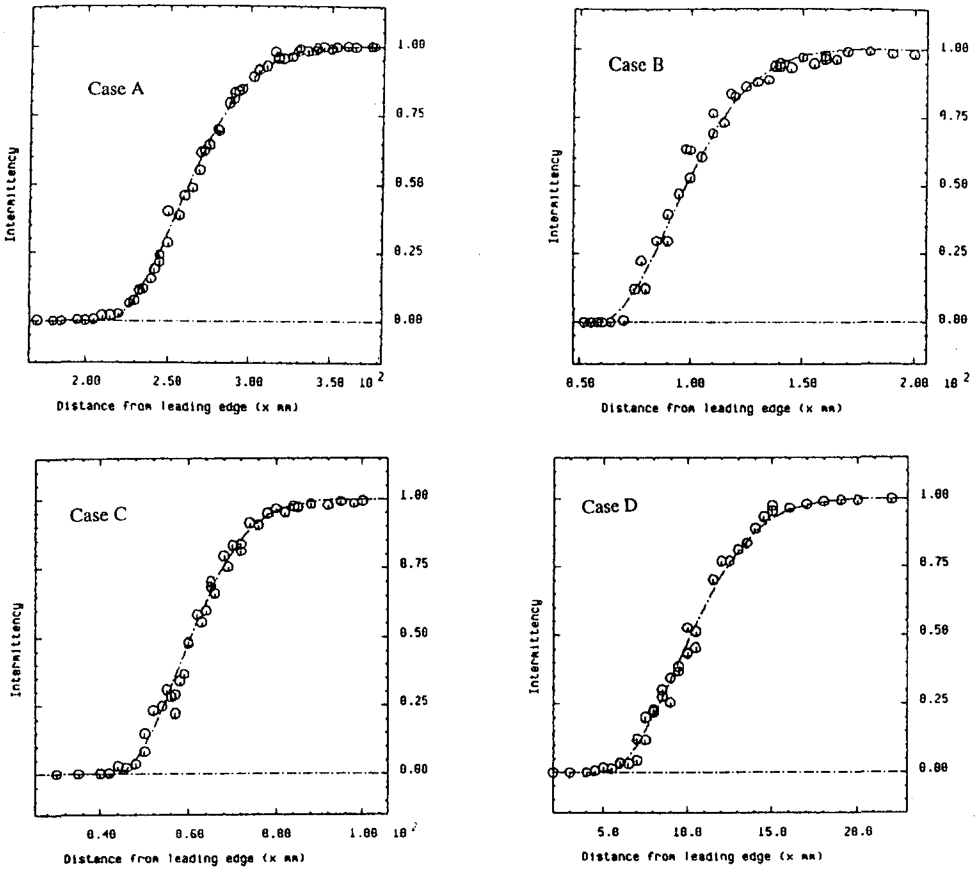

Fig. 11 Chordwise distribution of peak intermittency for the four test cases

center of the shear layer) shows that in the reverse flow region the intermittency factor drops from unity in the shear layer to zero towards the surface, almost linearly.

For Falkner–Skan profiles, an approximate relation for the locus of the frequency for maximum disturbance amplification in terms of the boundary layer parameters is given by Walker and Gostelow (1990). The flow conditions studied here do not give rise to similarity profiles; however Eq. (4) they suggested gave quite good predictions even for cases A, B, and C considered here.

$$\frac{\omega\nu}{U_e^2} = 3.2\,\mathrm{Re}_{\delta_*}^{-3/2} \qquad (4)$$

For case A, it is observed that in the hot-wire output signal occasional spikes appeared at $x = 170$ mm. The amplification of velocity signal in the selected frequency range given by Eq. (4) is 1350 Hz; but no significant oscillations in this frequency range (similar to those seen in Fig. 4) could be seen in the output. The spectrum at $x = 160$ mm, shown in Fig. 13(*a*) in a logarithmic plot, reveals a peak around 1400 Hz. However spectral density at this peak is an order of magnitude smaller than that at lower frequency. At downstream stations, the spectral density at lower frequencies increases at a faster rate due to the turbulent spots and obliterates this peak, which can be seen in Fig. 13(*b*).

The velocity signals prior to the appearance of the turbulent spots for the test cases B and C show very large and well-ordered oscillations similar to those shown in Fig. 4. For case B, Eq. (4) shows that at the onset of transition ($x_t = 58$ mm) the oscillations around 200 Hz have the highest rate of amplification. A combined plot of the raw spectra at different chordwise positions, at a constant height above the surface ($y = 0.2$ mm), is shown in Fig. 14 on a shifted axis. The chordwise positions for the curves are printed at the data points for 0 Hz on all the curves. The spectrum of the free-stream turbulence (designated FST) is also plotted at the beginning of the figure to show a rough comparison. These spectra show that the Tollmien–Schlichting (T–S) instability waves amplify quite rapidly in the chordwise direction. The bell-shaped forms suggest a normal mixture of all the frequencies around the most favored one. The distribution of detector function, which is Gaussian (Fig. 5), proves this point. As turbulent spots appear in the boundary layer, a sudden increase in energy takes place at lower frequencies. The spectra of the hotwire output along the locus of the peak turbulence intensity for case C are shown in Fig. 15 in a manner similar to that of Fig. 14. The amplification around the most favored frequency and the sudden increase in energy at lower frequencies with the appearance of turbulent spots are displayed in this case also.

The bell-shaped spectra seen in cases B and C (natural transition) upstream of the transition onset point cannot be seen in the transition of separated shear layer of case D when the probe is traversed along the center of the shear layer. However, when the spectra are taken near the outer edge (intermittency factor less than 0.1) of the shear layer, similar shapes are observed. The spectra at three stations in the transition region for three values of (peak) γ, 0, 0.5, and 0.9 are shown in Figs. 16, 17, and 18, respectively. At all three stations in the reverse flow region the spectra are basically similar (Figs. 16(*a*), 17(*a*), and 18(*a*)). In all the other spectra a sharp increase in energy around the frequency 750 Hz is noticed, but a relatively small fraction of total energy is contributed by the oscillations around this peak except near the edge of the shear layer at transition onset (Fig. 16(*c*)).

Malkiel's (1994) theoretical analysis of simplified shear layer above a separation bubble shows that the amplification of the

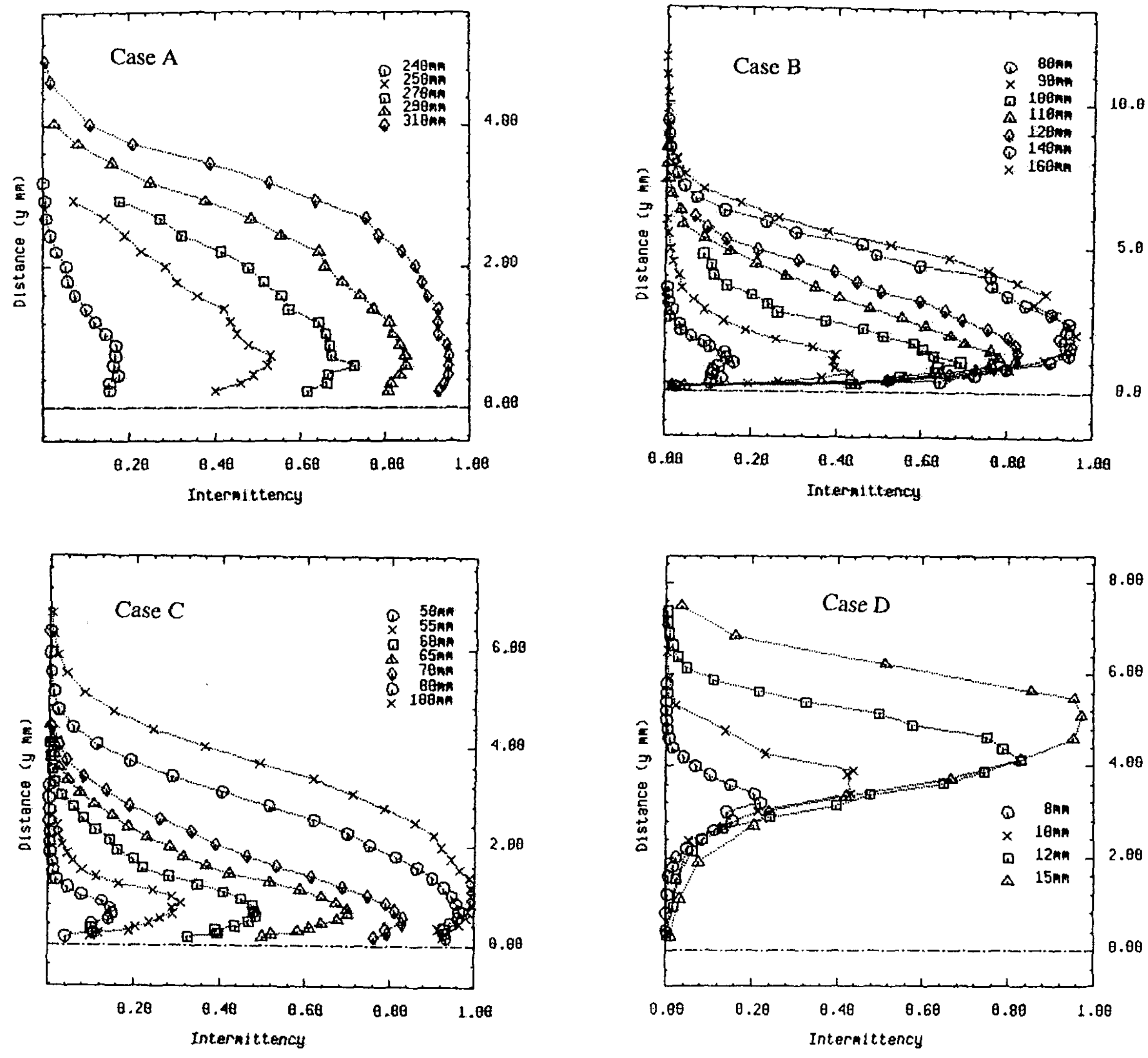

Fig. 12 Distribution of intermittency normal to the chord for the four test cases

instabilities is high and quite close to that for free shear layer, when the ratio b/δ_{sh} exceeds 2. In case D of the present study, prior to transition onset the ratio exceeds 2 and approaches 3 in the transition region. When the peak γ exceeds 0.5, the ratio drops to about 1.8 and stays around that value until completion of transition. For this particular case the free-stream velocity

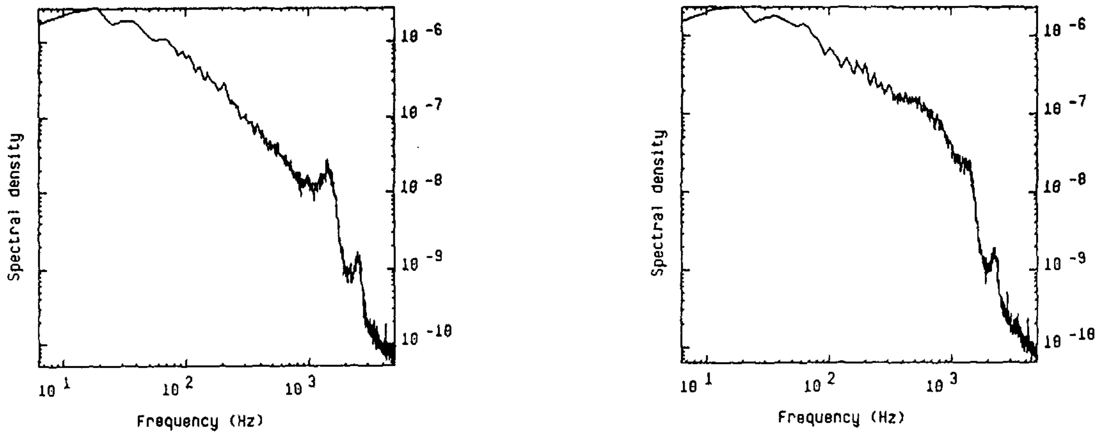

(a) AT X=160MM, Y=0.2MM

(b) AT X=180MM, Y=0.2MM

Fig. 13 Spectra at onset of transition for case A

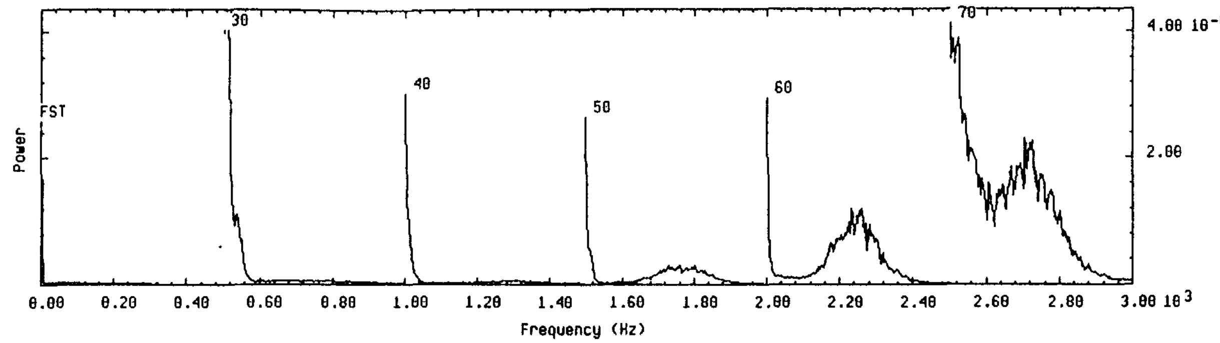

Fig. 14 Spectra at several stations in the laminar and the transition region for case B

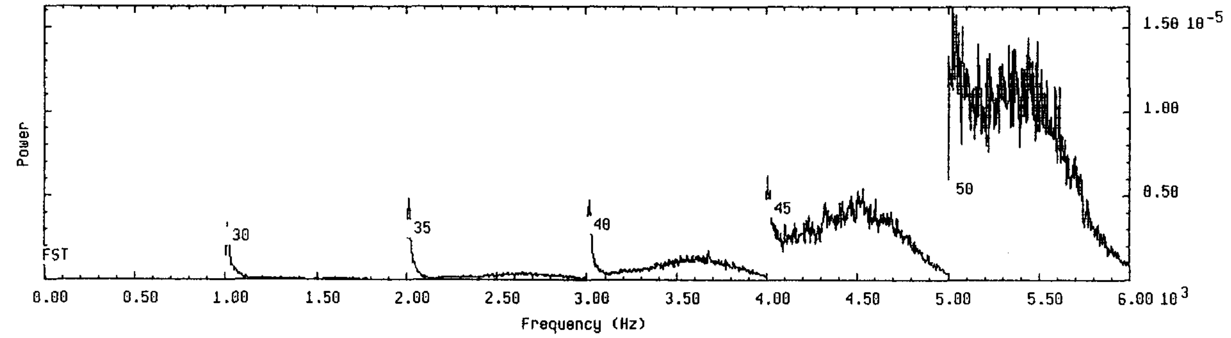

Fig. 15 Spectra at several stations in the laminar and the transition region for case C

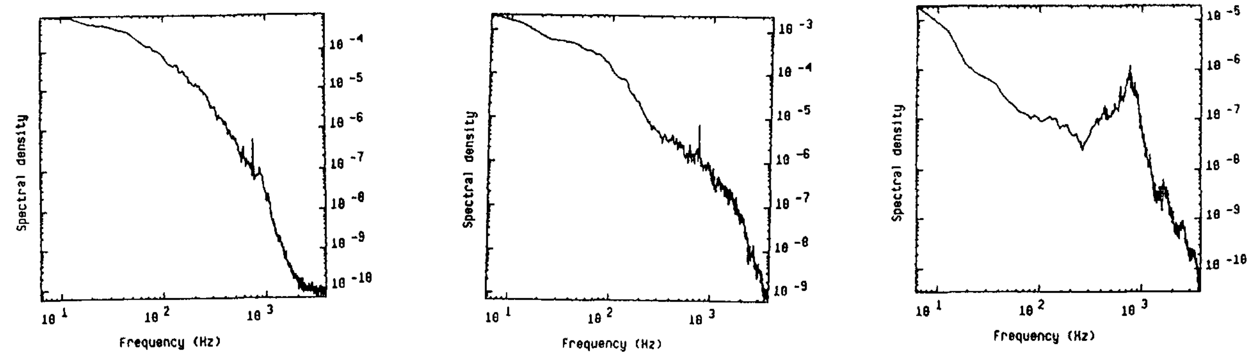

(a) REVERSE FLOW REGION
u/V=0.02

(b) CENTRE OF THE SHEAR LAYER
u/V=0.12

(c) EDGE OF THE SHEAR LAYER
u/V=0.02

Fig. 16 Spectra for case D at X = 5 mm

over the plateau region of the separation bubble is around 7.3 m/s. At the onset of transition, δ_{sh} is 0.8 mm; using these values with $\alpha\delta_{sh} = 0.79$ and $c/U_e = 0.5$ (for maximum rate of amplification) the frequency obtained is 575 Hz. Considering that for amplification the cutoff wave number in this case is given by $\alpha\delta_{sh} = 1.25$, amplification of disturbance up to the frequency 900 Hz is predicted, which includes the peak seen at 750 Hz. At the downstream stations (Figs. 17(c), 18(c)), a bell-shaped peak shifts to a lower frequency, which is expected since δ_{sh} increases.

Figure 19 shows two velocity traces taken close to the positions where spectra in Figs. 17(b) and 17(c) are taken. At the grid point for the upper curve in Fig. 19, $\gamma = 0.005$ and $u/V = 0.05$. Large amplification of the oscillations between 0.03 s–0.045 s and 0.06 s–0.075 s and breakdown of a few peaks can be seen in this trace. At the grid point for the lower trace in Fig. 19, $\gamma = 0.25$ and $u/V = 0.16$. Large amplification of the oscillations and eventual breakdown can be seen between 0.0 s–0.01 s and 0.02 s–0.035 s in this trace. Some superimposed low-frequency oscillations are also visible in this trace. For the spectrum in Fig. 17(c) most of the energy is contributed by the oscillations in the frequency range between 200–800 Hz. For the spectrum in Fig. 17(b), most of the energy is contributed by the oscillations in the frequency range below 500 Hz.

The spectral analysis shows that in bypass transition, the increase in energy in the subharmonic range is an indication of turbulent breakdown. In natural transition, the increase in energy upstream of onset of transition is around the harmonic for Falkner-Skan profile. After turbulent breakdown the energy in the whole range of frequency (about 150 percent of harmonic) increases rapidly. In the case of separated flow transition, along the edge of the shear layer, energy increase is around the harmonic range even at the station with a peak intermittency factor of 1. Along the center of the shear layer the subharmonic range

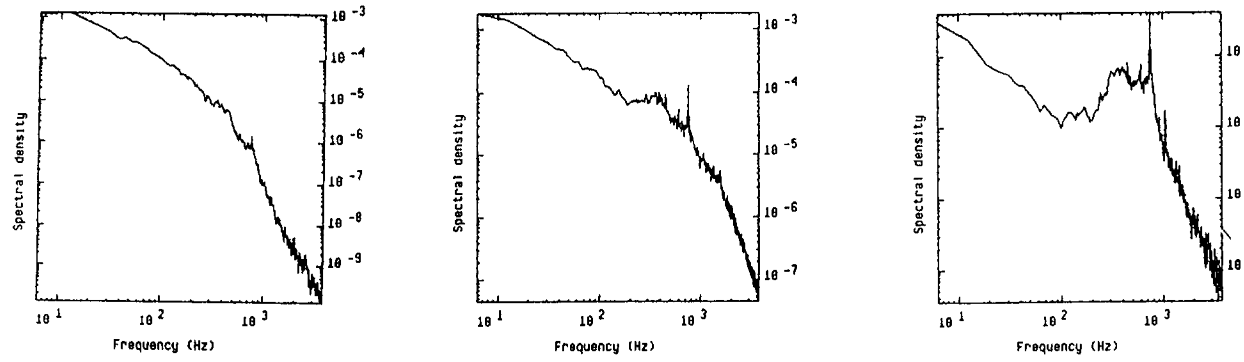

(a) REVERSE FLOW REGION
u/V=0.02

(b) CENTRE OF THE SHEAR LAYER
u/V=0.15

(c) EDGE OF THE SHEAR LAYER
u/V=0.05

Fig. 17 Spectra for test case D at X = 10 mm

initially contains a very large proportion of the energy. Through the transition zone the energy around the harmonic frequency increases. The reason may be the flapping of the shear layer and unsteadiness of the bubble, which is expected to have a lower frequency, this being the largest contribution to the velocity fluctuation where the transverse gradient of velocity is high.

The velocity profiles obtained by conditionally averaging the interturbulent and turbulent portions of the signals in the transition region of attached boundary layers follow a general trend. In all three cases of attached boundary layer transition (cases A, B, and C) with the increase in intermittency factor, the interturbulent velocity profiles become progressively fuller and approach a similarity profile for accelerating flow. Upstream of transition onset the velocity profiles for case B and C have the typical shape for adverse pressure gradient with a point of inflection away from the surface. Figure 20 shows a plot of the interturbulent profiles through the transition region for case B in similarity parameters. The solid line in this figure represents the Blasius profile. The general trend shown in this case is followed by all three cases A, B, and C. The conditionally averaged turbulent velocity profiles follow a family of curves given by:

$$\frac{U}{u^*} = A \log_{10} \frac{yu^*}{\nu} + B \qquad (5)$$

The parameter A is the usual constant in the universal profile 5.616. The quantity u^* and the parameter B are found from the curve of best fit through the measured points. At low intermittency the additive parameter B has a negative value, but toward the completion of transition, the parameter approaches the constant value 5 for the universal logarithmic profile. It is to be noted that the velocity scale u^* is not the friction velocity u_τ used in the universal profile. For the test case B, the measured profiles and the curves of best fit at several stations are shown in Fig. 21. These profiles show that the transition zone model based on linear combination may have a large error unless the development of the profiles is taken into account.

The transition zone parameters for the four cases are summarized in Table 1. The position of completion of transition in this table is calculated from the relation $x_T = x_t + 3.36\lambda$. The acceleration and the pressure gradient parameters are calculated from the mean velocity and surface pressure measurements. The quantity b/δ_{sh} for the shear layer above the separation bubble in the early part of the transition lies between 2 and 3 for case D. Therefore, the influence of the wall on the behavior of the shear layer is negligible. For this reason, the displacement and momentum thicknesses shown in Table 1 are calculated for the shear layer rather than the separation bubble.

For case A, where transition onset and completion occur at constant pressure, Narasimha's (1985) correlation between transition onset Reynolds number and transition length scale Reynolds number is not found to be suitable. The reason for

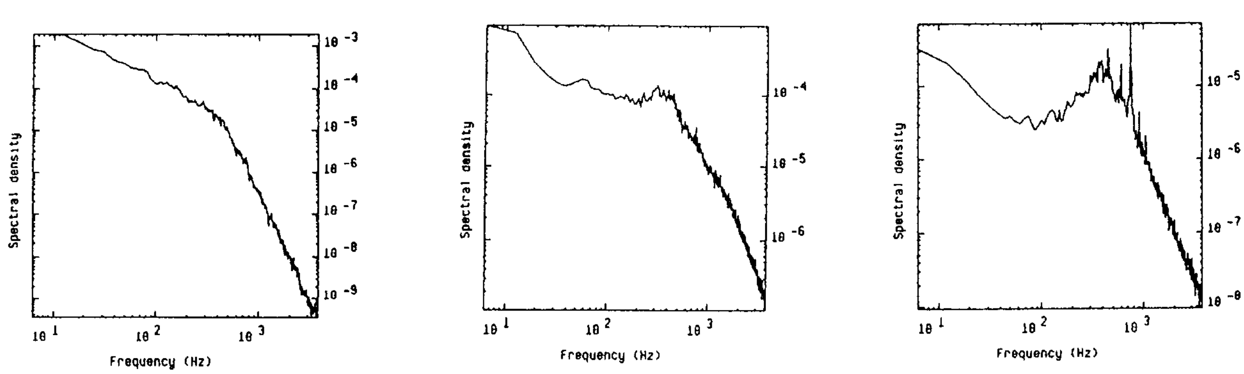

(a) REVERSE FLOW REGION
u/V=0.04

(b) CENTRE OF THE SHEAR LAYER
u/V=0.20

(c) EDGE OF THE SHEAR LAYER
u/V=0.08

Fig. 18 Spectra for case D at X = 15 mm

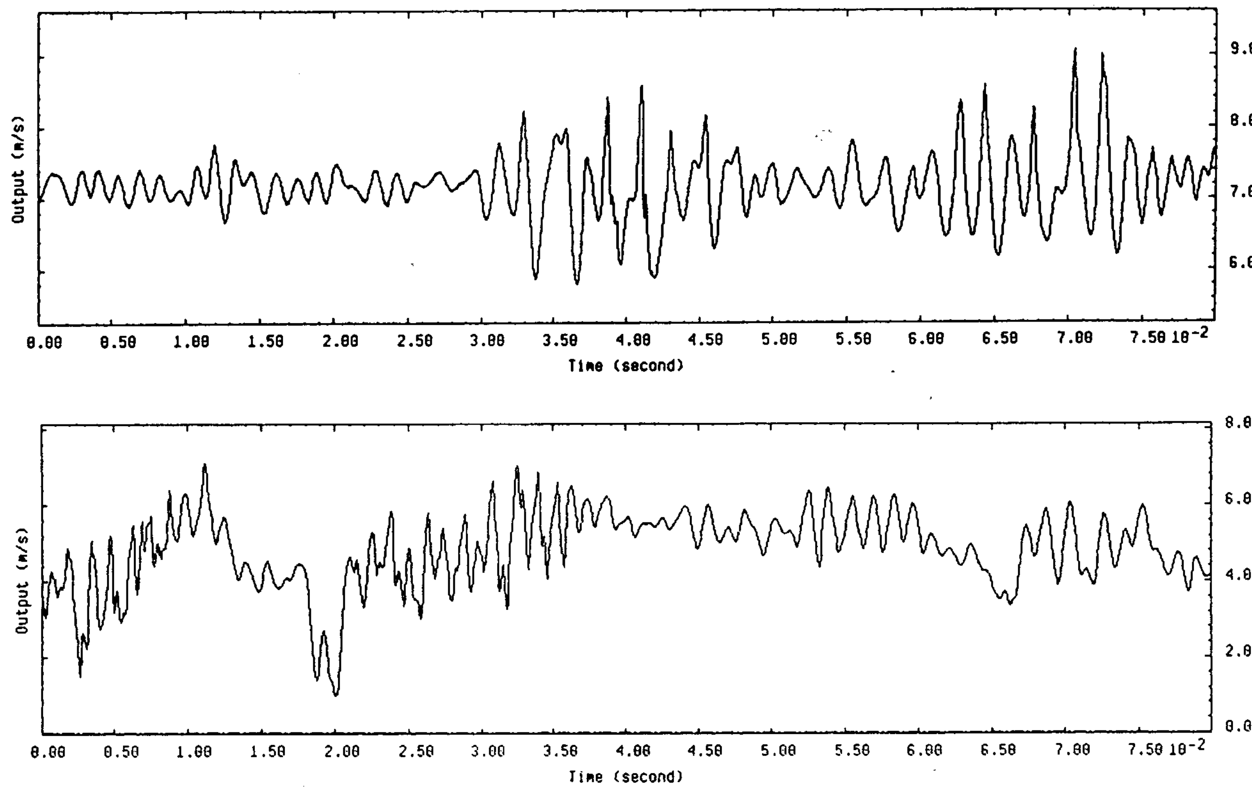

Fig. 19 Velocity trace from a record near the center of the shear layer (lower plot, corresponds to spectrum 17(*b*)) and near the edge of the shear layer (upper plot, corresponds to spectrum 17(c)) for case D, showing instability wave and turbulent breakdown

this discrepancy is the pressure gradient at the leading edge in this case. Klingmann et al. (1993) showed that small differences in pressure gradient near the leading edge have large effects on the neutral stability curve. Therefore, for the present case, where turbulence intensity is low, the pressure gradient at the leading edge makes considerable difference in the transitional behavior. A comparison of the profiles of velocity and rms of velocity for case A with that in an accelerating flow at the leading edge (Hazarika and Hirsch, 1993) shows that in the second case (strong bypass transition) the rms profiles have a double peak as early as $\gamma = 0.1$, as against $\gamma = 0.5$ for case A. In an adverse pressure gradient, the difference between velocities is reduced near the surface. The conditional averaging of the hot-wire signals from cases B and C show that the interturbulent and turbulent velocities differ very little. This is the reason for the absence of the peak closer to the surface, therefore the absence of the double peak shape.

Comparison of the transition data for cases B and C with those reported by Walker and Gostelow (1990) shows that for the same pressure gradient parameters at the onset of transition, the transition length in the C4 leading edge profile is much longer. It should be pointed out that for the C4 profile at incidence, the pressure gradient parameter changes considerably over the transition region as shown in Table 1. At the same incidence the increase in Reynolds number affects the transition length scale more severely than the onset length. Between cases

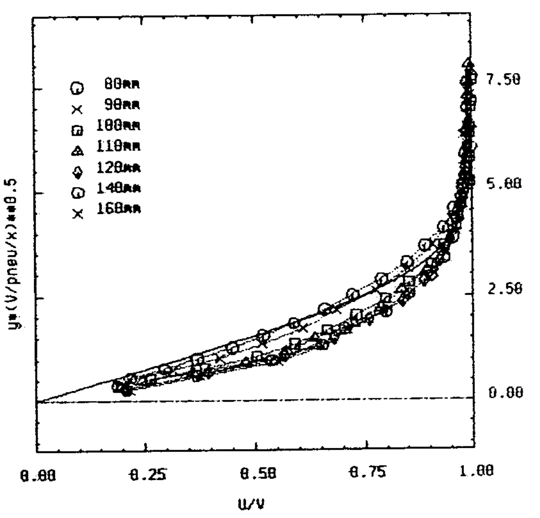

Fig. 20 Development of interturbulent velocity profiles for case B

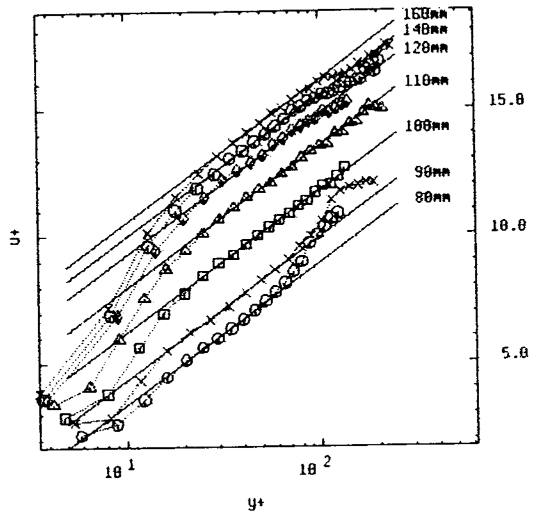

Fig. 21 Development of turbulent velocity profiles for case B

B and C (twofold increase in Reynolds number), x_t decreases by 26 percent whereas λ by 56 percent.

Since all four cases considered here follow Narasimha's universal intermittency distribution quite well, the chordwise variation of the peak value of γ can be given by spot production rate. The equations given by Narasimha (1985):

$$N = n\sigma \frac{\theta_t^3}{\nu} \text{ and } \hat{n} = n\sigma \frac{\nu^2}{U_e^3}\,;\text{ where } n\,\sigma = 0.412\,\frac{U_e}{\lambda^2} \quad (6)$$

are used as the nondimensional spot formation rate and spot production rate in Table 1. For cases A and D, the free-stream velocity over the transition region remains constant. For flows with a pressure gradient, Mayle (1991) recommends that the mean velocity over the transition region be used as the free-stream velocity. In the present case the transition region is short, therefore the variation of velocity is small and the value at the section with 0.5 peak γ is used. These values show that for each 2 deg increase in incidence the nondimensional spot formation rate jumps by two orders of magnitude. The increase (30 percent) between cases B and C is caused by the increase in the pressure gradient parameter, not by the increase in Reynolds number.

Conclusions

Transitions of boundary layers on a flat plate with C4 profile shape leading edge in a low-turbulence free stream at various angles of incidence are reported. These studies show that natural, bypass, and separated flow mode are responsible for transition of the boundary layer on the suction surface, depending on the angle of incidence.

The peak value of the rms of fluctuating velocity approaches 3.5 percent for the cases of attached transition before onset of transition; for separated flow it approaches 11 percent before the turbulent breakdown is detected.

Distinct spectral peaks appear upstream of the transition onset indicating amplification of a favorable range of frequencies in all the cases studied. For bypass transition the energy content in the subharmonic range increases before transition prior to significant amplification in the harmonic frequency could be seen. Walker and Gostelow's correlation adequately represent the most favorable frequency for attached flow. In the case of separated flow, Malkiel's formulation is found to be appropriate. For natural and separated flow transition downstream of onset of transition, rapid increase of energy over the whole range of frequency is observed.

For all three modes of transition, Narasimha's universal intermittency distribution adequately represents the peak intermittency distribution along the length of the plate. For the attached flow, the peak intermittency factor appears between $\frac{1}{4}$ to $\frac{1}{3}$ boundary layer thickness. For separated flow the peaks appear around the center of the shear layer; in the transition zone the reverse flow region shows negligible intermittency.

The spot production rates calculated from the test cases show that for each 2 deg increase in incidence, spot production rate goes up by around 2 orders of magnitude.

The conditionally averaged interturbulent and turbulent velocity profiles in the transition region of an attached flow are significantly different from those in the laminar and turbulent zones. For modeling the transition region by linear combination, these modifications should be considered.

Acknowledgments

This work is supported by CEC through BRITE/EURAM project contract AERO-CT92-0050.

References

Blair, M. F., 1982, "Influence of Free-Stream Turbulence on Boundary Layer Transition in Favourable Pressure Gradients," ASME *Journal of Engineering for Power,* Vol. 104, pp. 743–750.

Blair, M. F., 1992, "Boundary Layer Transition in Accelerating Flows With Intense Freestream Turbulence: Part 2—The Zone of Intermittent Turbulence," ASME *Journal of Fluids Engineering,* Vol. 114, pp. 322–332.

Gostelow, J. P., and Blunden, A. R., 1989, "Investigation of Boundary Layer Transition in an Adverse Pressure Gradient," ASME JOURNAL OF TURBOMACHINERY, Vol. 111, pp. 366–375.

Gostelow, J. P., Blunden, A. R., and Walker, G. J., 1994, "Effects of Free-Stream Turbulence and Adverse Pressure Gradients on Boundary Layer Transition," ASME JOURNAL OF TURBOMACHINERY, Vol. 116, pp. 392–404.

Hazarika, B. K., and Hirsch, Ch., 1993, "Boundary Layer Transition on a Sharp Leading Edge Plate," *Proc. 5th International Conference on Refined Flow Modelling and Turbulence Measurements,* pp. 277–284.

Hazarika, B. K., and Hirsch, Ch., 1994, "Behavior of Separation Bubble and Reattached Boundary Layer Around a Circular Leading Edge," ASME Paper No. 94-GT-385.

Hedley, T. B., and Keffer, J. F., 1974, "Turbulent/Nonturbulent Decision in an Intermittent Flow," *Journal of Fluid Mechanics,* Vol. 64, Part 4, pp. 625–644.

Keller, F. J., and Wang, T., 1995, "Effects of Criterion Functions on Intermittency in Heated Transitional Boundary Layers With and Without Streamwise Acceleration," ASME JOURNAL OF TURBOMACHINERY, Vol. 117, pp. 154–165.

Klingmann, B. G. B., Boiko, A. V., Westin, K. J. A., Kozlov, V. V., and Alfredsson, P. H., 1993, "Experiments on the Stability of Tollmien–Schlichting Waves," *The European Journal of Mechanics, B/Fluids,* Vol. 12, No. 4, pp. 493–514.

Malkiel, E., 1994, "An Experimental Investigation of a Separation Bubble," Ph.D. Thesis, Rensselaer Polytechnic Institute, Troy, New York.

Mayle, R. E., 1991, "The Role of Laminar–Turbulent Transition in Gas Turbine Engines," ASME JOURNAL OF TURBOMACHINERY, Vol. 113, pp. 509–537.

Narasimha, R., 1985, "Role of Laminar–Turbulent Transition Zone in Boundary Layer," *Progress in Aerospace Science,* Vol. 22, pp. 29–80.

Ramamoorthy, S., Munukutla, S., and Rajan, P. K., 1993, "Relation Between Spectra of Hot-Wire and Velocity Fluctuation," *AIAA Journal,* Vol. 31, No. 5, pp. 968–970.

Sohn, K. S., O'Brien, J. E., and Reshotko, E., 1989, "Some Characteristics of Bypass Transition in a Heated Boundary Layer," NASA Technical Memorandum 102126.

Walker, G. J., and Gostelow, J. P., 1990, "Effects of Adverse Pressure Gradients on the Nature and Length of Boundary Layer Transition," ASME JOURNAL OF TURBOMACHINERY, Vol. 112, pp. 196–205.

Walker, G. J., and Solomon, W. J., 1992, "Turbulent Intermittency Measurement on an Axial Compressor Blade," *Proc. 11th Australian Fluid Mechanics Conference,* Vol. II, pp. 1277–1280.

Walker, G. J., Solomon, W. J., and Gostelow, J. P., 1993, "Observations of Wake-Induced Turbulent Spots on an Axial Compressor Blade," ASME Paper No. 93-GT-378.

D. E. Halstead

D. C. Wisler
GE Aircraft Engines,
Cincinnati, OH 45215

T. H. Okiishi
Iowa State University,
Ames, IA 50011

G. J. Walker
University of Tasmania,
Hobart, Tasmania

H. P. Hodson
University of Cambridge,
Cambridge, United Kingdom

H.-W. Shin
GE Aircraft Engines,
Cincinnati, OH 45215

Boundary Layer Development in Axial Compressors and Turbines: Part 2 of 4—Compressors[1]

This is Part Two of a four-part paper. It begins with Section 6.0 and continues to describe the comprehensive experiments and computational analyses that have led to a detailed picture of boundary layer development on airfoil surfaces in multistage turbomachinery. In this part, we present the experimental evidence used to construct the composite picture for compressors given in the discussion in Section 5.0 of Part 1. We show the data from the surface hot-film gages and the boundary layer surveys, give a thorough interpretation for the baseline operating condition, and then show how this picture changes with variations in Reynolds number, airfoil loading, frequency of occurrence of wakes and wake turbulence intensity. Detailed flow features are described using raw time traces. The use of rods to simulate airfoil wakes is also evaluated.

6.0 Multistage Effects

After a brief description of the format we use to present our experimental results, this section describes the dramatic difference between boundary layer development along a first-stage rotor airfoil and that along an embedded, third-stage rotor airfoil. It then describes how we identify the transition regions in our data.

6.1 Format for Data Presentation

Space–Time (s–t) Diagrams. The time history of the developing boundary layer is described on s–t diagrams by using contour plots of ensemble-averaged random unsteadiness and skew measured by the surface hot-film gages. Examples are shown in Figs. 11(a, b) and 12(a, b) where airfoil surface length is plotted along the abscissa and time, in units of wake passing period, is plotted along the ordinate. Although spanwise wakes convect over the entire surface of the airfoil, measurements were obtained only at midspan.

The color red on the contour plot represents the highest values of the variable measured, and the color blue represents the lowest. There is a linear variation of ten equal increments (changes in color) between red and blue. Reference color legends are shown only in Fig. 13. For all other color contour plots, the highest value of the quantity (plotted in red) is given in the figure caption as Q_{10} and the lowest value (plotted in blue) as Q_0. The reader can refer to the reference color legends to decode the values the colors represent.

Important regions of the s–t diagram are identified on the contour plots by letters A, B, etc., and points of specific interest within these regions are identified by numbers 1, 2, etc. Trajectories W, X, Y, and Z, which are drawn at selected percentages of the wake passing period, are also shown. Trajectory W always extends along the wake-induced path.

Line Plots. Distributions of quasi wall shear stress, random unsteadiness, and skew are also shown as line plots. Black lines through the black symbols on the plots denote the time-average of the data, as seen in Fig. 12(c). Colored lines denote values along trajectories W, X, Y, and Z. The dashed lines, shown for quasi wall shear stress only, denote the minimum and maximum values of the unsteady data. These dashed lines do not represent error bars.

6.2 Multistage Effects. The dramatic difference between boundary layer development on an airfoil in the first rotor and that on an airfoil in an embedded rotor is seen by comparing Figs. 11 and 12. The airfoils on both rotors have identical shapes and were operating at Test Point 2B. The lightly loaded IGV is relatively far upstream of the first rotor as shown in Fig. 1.

The boundary layer on Rotor 1 is characterized in Fig. 11 by the following features: (1) a laminar boundary layer that extends without interruption from the leading edge to about 50 percent SSL. It has low random unsteadiness (blue color in Fig. 11(a)), zero skew (green color in Fig. 11(b)), and decreasing wall shear stress in Fig. 11(c); (2) a laminar separation bubble that begins at about 45 percent SSL. Flow separation is indicated by zero shear stress in Fig. 11(c). This is followed by a very rapid rise in shear stress and random unsteadiness (yellow/red colors in Fig. 11(a)) as reattachment occurs. Transition length is very short; and (3) a reattached turbulent boundary layer that has decreasing wall shear stress in Fig. 11(c) and extends to the trailing edge. Note that the weak IGV wakes exert only a modulating effect in the upper portion of Fig. 11(a). This would be the picture for an isolated rotor or cascade.

In contrast, the boundary layer on the multistage embedded Rotor 3 in Fig. 12 changes significantly with time and is characterized by distinct features that correlate with wake-passing events. The region of laminar flow, A, is now penetrated by

---

[1] Parts 1 and 4 of this four-part paper appeared in the January 1997 edition of the JOURNAL OF TURBOMACHINERY, pp. 114–139. Part 3 appeared in the April 1997 issue, pp. 234–246.

Contributed by the International Gas Turbine Institute and presented at the 40th International Gas Turbine and Aeroengine Congress and Exhibition, Houston, Texas, June 5–8, 1995. Manuscript received by the International Gas Turbine Institute April 7, 1995. Paper No. 95-GT-462. Associate Technical Editor: C. J. Russo.

wake-induced strips, B, having high random unsteadiness as indicated by the yellow/red colors in Fig. 12(a) and varying skew in Fig. 12(b). Transition is identified by the manner in which skew and random unsteadiness vary, as will be described in Section 6.3. No flow separation occurs anywhere on the airfoil as shear stress remains well above zero in Fig. 12(c); however, differences in shear stress levels along trajectories W, X, Y, and Z are evident. Transition without separation occurs over a long region from about 20 to 80 percent SSL. A turbulent boundary layer continues from there to the trailing edge.

6.3 Identifying Transition. Throughout this paper we will use the variation in skew and the variation in random unsteadiness along the airfoil surface to identify the transition region and to infer values of intermittency. Since skew provides a measure of the asymmetry in fluctuations of wall shear stress about the mean, its value is positive when the transitional flow is more laminar than turbulent. Its value is negative when the transitional flow is more turbulent than laminar. Therefore as shown in Fig. 12(d), skew is zero prior to transition onset (intermittency $\gamma = 0$), skew reaches a maximum positive value at $\gamma \approx 0.25$, skew is zero at the midpoint of transition $\gamma \approx 0.50$, skew is a negative maximum at $\gamma \approx 0.75$, and skew is zero when transition is complete, $\gamma = 1.0$. At the same time skew is varying in this manner, the random unsteadiness increases from a laminar level at $\gamma = 0$ to a peak value at $\gamma \approx 0.50$. It then decreases in value as transition is completed. Thus peak random unsteadiness occurs near zero skew and 50 percent intermittency.

Since it is easy to identify where intermittency is 0.75 from skew data, we have selected $\gamma = 0.75$ as a figure of merit for identifying the location where the wake-induced strips are capable of generating effective calmed regions. This provides consistency for comparison purposes.

7.0 Boundary Layer Development for Compressors

This section presents the development of the boundary layer along the embedded, third-stage rotor and stator airfoils of the compressor operating at the baseline Test Point 2B. It provides the evidence for Fig. 10(a) of the discussion in Section 5.0. For completeness, we have tabulated the locations of the laminar, transitional, and turbulent regions for our compressor test cases in Table 5 at the end of this paper.

The s–t diagrams, presented in Figs. 13(a, b) for the suction surface of the stator, were constructed from the surface hot-film data as described in Section 6.1. Four trajectories, labeled W, X, Y, and Z, are drawn at a speed of 0.7 V_∞, which is an average of the leading and trailing boundary speeds of a turbulent spot. These trajectories are not straight lines because the free-stream velocity, V_∞, varies through the airfoil passage. Trajectory W is drawn through the wake-induced transitional/turbulent strips. Trajectories X, Y, and Z are located in time at 20, 44, and 72 percent of the wake passing period behind trajectory W. The temporal variation in turbulence intensity measured at the stator inlet is superimposed as curve "TI" on Fig. 13(a). Along rotor wake avenues this turbulence intensity was about 5.5 percent. Between wake avenues, it falls to about 2.5 percent. An example of the temporal variation in shear stress across the calmed region is superimposed as curve "S" on Fig. 13(b).

Related line plots of shear stress characteristics along the specific trajectories W, X, Y, and Z are shown in Figs. 13(c, d, e).

The composite picture in Fig. 10(a) described the boundary layer as developing along two separate but coupled paths: the wake-induced path, which consists of regions A, B, and C; and the path between wakes, which consists of regions A, D, E, and F. These paths are examined below.

7.1 The Wake-Induced Path. As wakes from the upstream airfoil row convect along the downstream airfoil, a boundary layer on the downstream airfoil develops along a wake-induced path, which lies approximately under the convecting wake. The wake-induced path begins at the leading edge in Figs. 13(a, b), goes through points 2–3 in laminar region A and continues through both the wake-induced transitional strip B and the wake-induced turbulent strip C to the trailing edge of the airfoil.

The Laminar Region (A). For the baseline test condition, a laminar boundary layer begins at the leading edge of the suction surface and extends downstream. This region is identified as laminar because it has low random unsteadiness and zero skew, seen respectively as the blue region A in Fig. 13(a) and the green region A in Fig. 13(b).

The portion of region A that is of interest here occupies only about 15–20 percent of the wake passing period. It lies approximately beneath the convecting wakes and extends from

Nomenclature

A = laminar region on s–t diagram
B = wake-induced transitional strip on s–t diagram
C = wake-induced turbulent strip on s–t diagram
d = diameter of cylindrical rod
D = calmed region on s–t diagram
E = region of transition between wakes on s–t diagram
F = region of turbulent boundary layer between wakes on s–t diagram
h = height through boundary layer normal to surface
l = distance from rod centerline to measurement plane
LE = leading edge
PSL = pressure surface length from LE to TE of airfoil
Q_0 = lowest value (blue) of quantity in reference color legend for color figures
Q_{10} = highest value (red) of quantity in reference color legend for color figures
Re = Reynolds number for compressor = V_{in} (SSL)/ν
$\overline{\text{Re}}$ = stage-averaged Reynolds number = $0.5(\text{Re}_{\text{rotor}} + \text{Re}_{\text{stator}})$
s = distance, the abscissa in the distance–time (s–t) diagram
SSL = suction surface length from LE to TE of airfoil
t = time, the ordinate in the distance–time (s–t) diagram
t^* = time normalized by wake-passing period
TE = trailing edge
TI = turbulence intensity
u = streamwise velocity within boundary layer
V = velocity
V_∞ = velocity at edge of boundary layer (free-stream velocity)
w = wake width
W, X, Y, Z = trajectories on s–t diagrams at constant fraction of free-stream velocity
γ = intermittency
Δ = difference
δ = boundary layer thickness
δ^* = displacement thickness
θ = momentum thickness or tangential direction
${}_q\tau_w$ = quasi wall shear stress

Subscripts

avg = average
z = axial direction

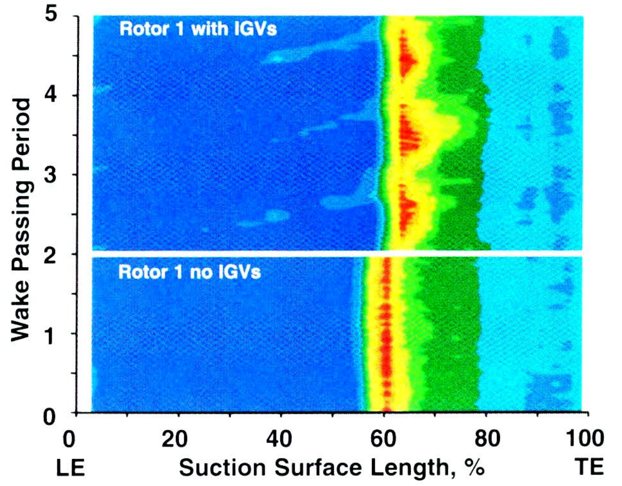

a) Random unsteadiness, top = IGVs present, bottom = No IGVs, $Q_0 = 0.1$, $Q_{10} = 11.5$

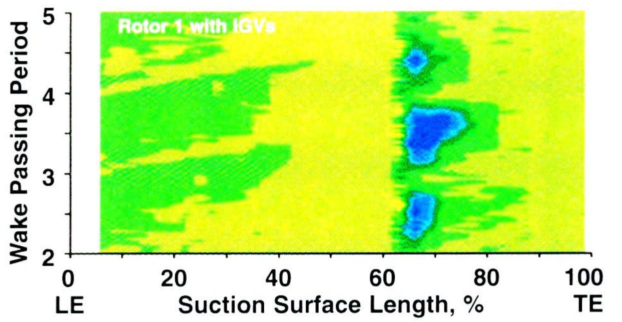

b) Skew, IGVs present, $Q_0 = -2.5$, $Q_{10} = 2.5$

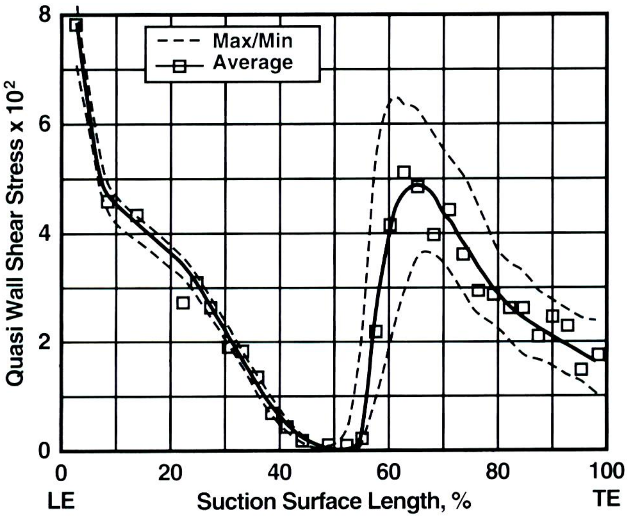

c) Quasi wall shear stress, no IGVs

Fig. 11 Shear stress characteristics on suction surface of first-stage rotor. $\overline{Tl} = 1.4$ percent, $\overline{Re} = 3.35 \times 10^5$, compressor baseline Test Point 2B.

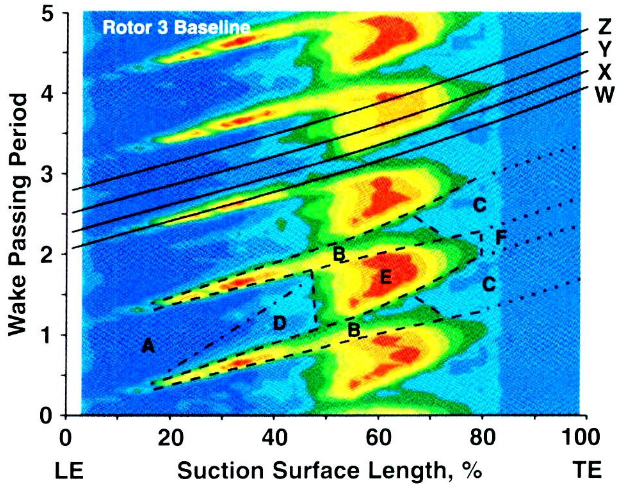

a) Random unsteadiness, $Q_0 = 0.7$, $Q_{10} = 17.0$

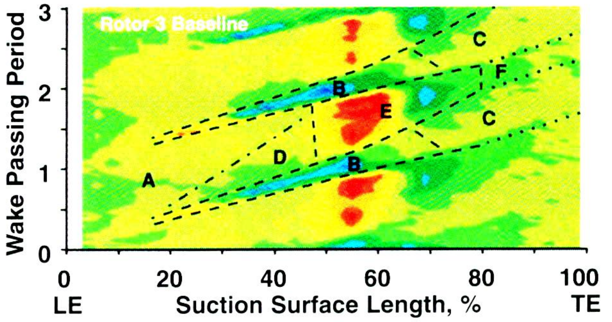

b) Skew, $Q_0 = -2.5$, $Q_{10} = 2.5$

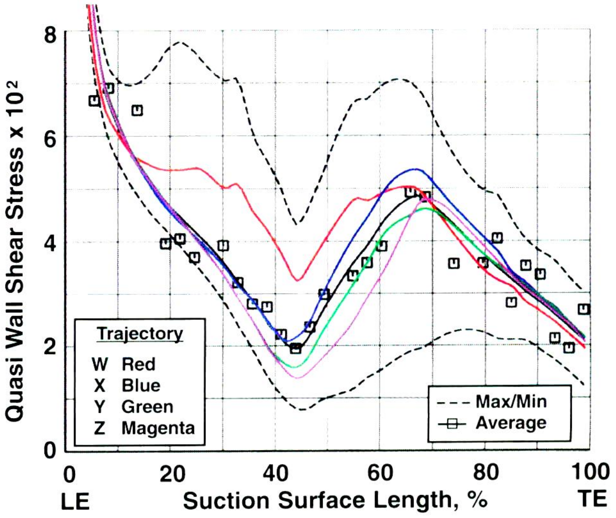

c) Quasi wall shear stress

Fig. 12 Shear stress characteristics on suction surface of third-stage rotor. $\overline{Tl} = 3.4$ percent, $\overline{Re} = 3.35 \times 10^5$, compressor baseline Test Point 2B.

the leading edge along points 2–3 to about 19 percent SSL. Along 2–3, the laminar boundary layer is subjected to periodic and random unsteadiness from the passage of Rotor 3 wakes. This is identified from the slightly higher (but still low) level of random unsteadiness seen as the lighter blue area along points 2–3 in Fig. 13(*a*). Wake-induced Trajectory *W* passes through this portion. The skew along 2–3 is still near zero in Fig. 13(*b*) and wall shear stress is decreasing, as shown for trajectory *W* in Fig. 13(*c*). This portion of region *A* constitutes the beginning of the wake-induced path.

Wake-Induced Transitional Strip (B). Near 19 percent SSL at point 3 in Fig. 13(*a*) and along the red wake-induced trajectory *W* in Fig. 13(*d*), there begins a significant increase in

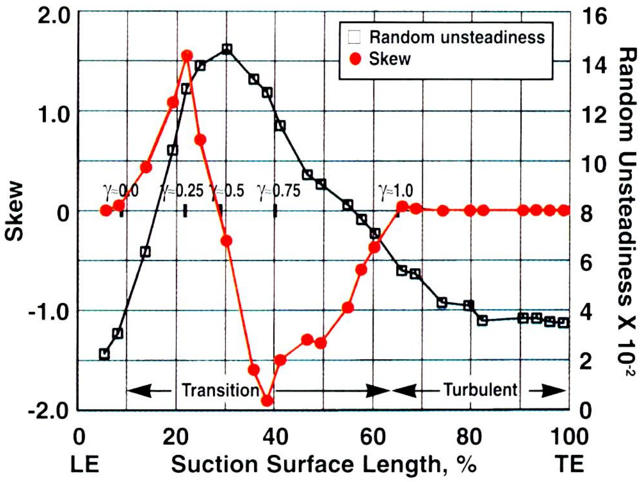

d) Random unsteadiness and skew along trajectory W

Fig. 12 (Continued)

random unsteadiness. This occurs when disturbances in the convecting rotor wakes penetrate into the laminar boundary layer of region *A* and initiate turbulent spots. In Figs. 13(*b, e*), the skew along trajectory *W* becomes increasingly positive. These changes mark the onset of wake-induced transition, which occurs in phase with the peak values of inlet turbulence intensity shown as curve **TI** in Fig. 13(*a*).

This transitional flow appears convecting in time as region *B* in the *s–t* diagrams in Figs. 13(*a, b*). We have named this region a wake-induced transitional strip. For this stator, the strip extends from 19 to 62 percent SSL, as determined from the variation in skew.

The detailed evidence showing that wake-induced transition begins as a transitional strip *B* and not as a turbulent strip is given below.

- The variation of skew along trajectory *W* in Figs. 13(*b, e*) is typical of transition. The skew is near zero just ahead of point 3 (19 percent SSL) and intermittency is zero. Skew becomes yellow-red positive along 3–4–5, reaching a maximum at 4 (25–30 percent SSL) and falling to zero around 5 (35 percent SSL). The intermittency is inferred to be about 0.5 at this location. The skew subsequently becomes negative, reaching a blue minimum around 6 (45 percent SSL) where intermittency is inferred to be about 0.75. It then increases to zero by 7 (62 percent SSL) where intermittency is about one. Thus, during the early development of the strip, there is an occasional turbulent spot. Much later, there is only occasional laminar flow. The results for the rotor in Fig. 12 are similar.
- The variation of random unsteadiness is characteristic of transition. The unsteadiness in Fig. 13(*a*) increases along 3–4–5 to a maximum (red) at 5, after which it decays in amplitude along 5–6–7. By 7 the levels are down to those seen in the turbulent (green-blue) regions of the boundary layer on this airfoil. Maximum random unsteadiness occurs at point 5 in Fig. 13(*a*) where skew is near zero in Fig. 13(*b*), indicating that the intermittency is about 0.5. Comparing red trajectories *W* in Figs. 13(*d, e*) shows these details in line plots. The results for the rotor in Fig. 12 are similar.
- The boundary layer profile for trajectory *W* in Fig. 14 is transitional in shape. It was obtained at 34 percent SSL where the intermittency is 0.5.
- The raw data from both the spanwise- and chordwise-distributed gages clearly show the creation and coalescence of individual turbulent spots typical of transitional behavior.
- The quasi wall shear stress along red trajectory *W* in Fig. 13(*c*) is suggestive of transition. This is even more pronounced for the rotor in Fig. 12(*c*), where the shear stress decreases, reaches a minimum at 44 percent SSL, increases to a maximum and then begins to fall. The levels of shear stress remain well above zero, indicating the flow is attached in region *B*.

The discovery that these strips are transitional in nature and not turbulent means that the process of wake-induced transition does not immediately produce a fully turbulent strip with an intermittency of one, as assumed by some researchers.

The velocities of the leading and trailing boundaries of region *B* are inferred from the figure to be about 0.9 V_∞ and 0.5 V_∞, respectively. These velocities are equal to those typically reported for turbulent spots, as will be seen in our raw data. Outside the boundary layer, the wake convects at the free-stream velocity V_∞, which in Fig. 13(*a*) is greater than (i.e., leads) the leading boundary of transitional strip *B*.

Wake-Induced Turbulent Strip (C). When transition is complete, the wake-induced transitional strip *B* becomes a wake-induced turbulent strip, identified as region *C* in Figs. 13(*a, b*). Region *C* extends along points 7–8 from 62 percent SSL to the trailing edge of the airfoil. The random unsteadiness has returned to lower relative levels, as shown by the lighter blue color in Fig. 13(*a*), and the skew has returned to zero in Fig. 13(*b*). This indicates that the transition process has been completed and the boundary layer is turbulent. The results for the rotor in Fig. 12 are similar.

Turbulent strip *C* has leading and trailing boundary velocities of 0.90 V_∞ and 0.40 V_∞, respectively, as inferred from the figure. The trajectories for these two convection velocities form the boundaries of *C* up to about 85 percent SSL, giving it a wedge-shape appearance for this case. Thus region *C* expands more rapidly than region *B*, which may be caused by the decreased stability of the surrounding flow. Beyond 85 percent SSL, the region boundaries are shown as dotted lines, as will be discussed later.

7.2 The Path Between Wakes.

The development of the boundary layer is now described along the path between wakes. This path begins at the leading edge of the airfoil, goes through both point 1 in laminar region *A* and the calmed region *D*. It then continues through the transition and turbulent regions between wakes, *E* and *F*, as it goes to the trailing edge.

The Laminar Region (A). The portion of laminar region *A* that is of interest here occupies most of the wake-passing period. It lies between the avenues created by the passing rotor wakes where the laminar boundary layer is subjected only to disturbances from other than the upstream rotor wakes. It extends from the leading edge near point 1 to about 52 percent SSL. It is characterized by low levels of random unsteadiness (darker blue area in Fig. 13(*a*)), zero skew (green area in Fig. 13(*b*)) and decreasing wall shear stress for trajectories *X*, *Y*, and *Z* in Fig. 13(*c*).

The Calmed Region (D). As described in Section 4.2 and associated Fig. 9 of Part 1, the turbulent spots produced within wake-induced transitional strip *B* generate a calmed region that follows the transitional strip in time. This calmed region appears in the path between wakes and is identified in Figs. 13(*a, b*) as region D. Thus, boundary layer development in the path between wakes is influenced by (i.e., coupled to) the flow in the wake-induced path by means of the calmed region. An example of this influence is provided in Fig. 14. The boundary layer profile for trajectory X at 34 percent SSL, located within the calmed region, is seen to be characteristically laminar when compared to a Blasius profile. It is apparent that the effect of the adverse pressure gradient is offset by a small calmed effect in this region.

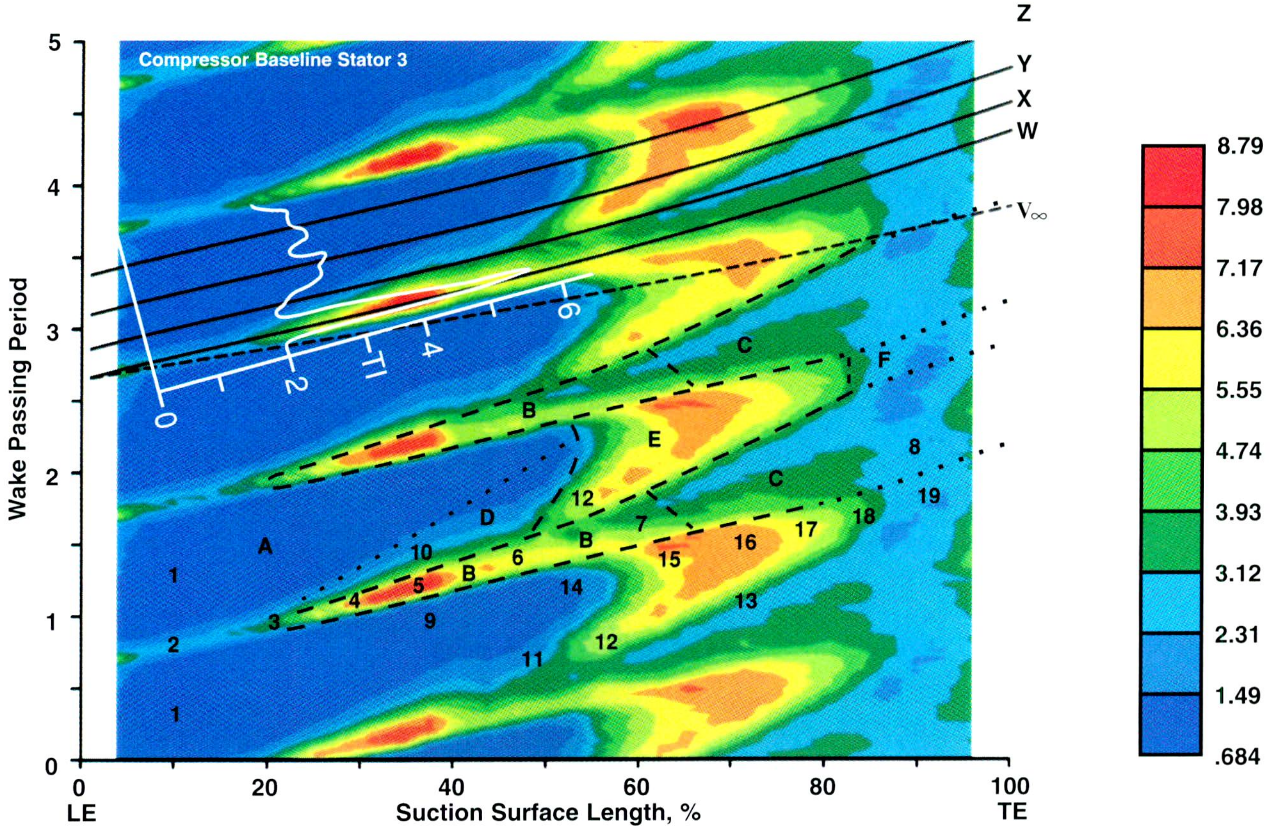

a) Random unsteadiness, $Q_0 = 0.68$, $Q_{10} = 8.79$

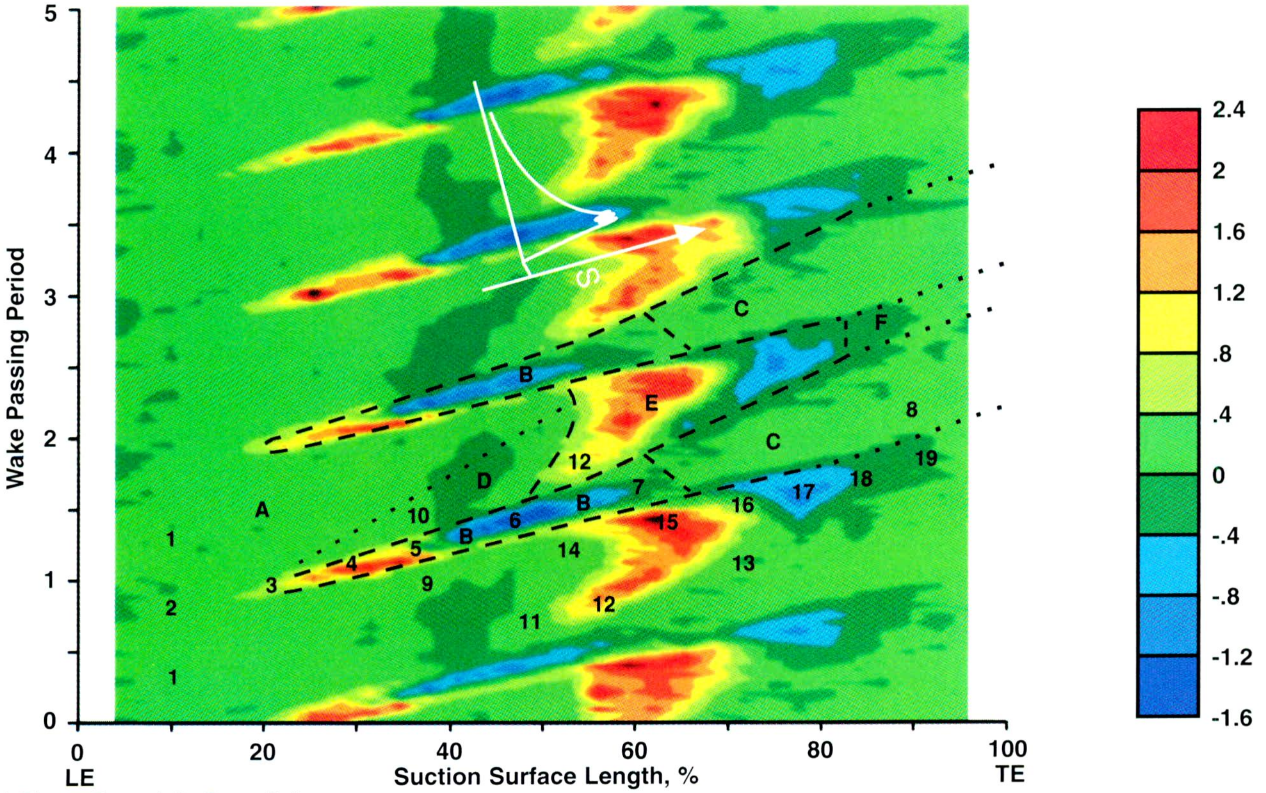

b) Skew, $Q_0 = -1.6$, $Q_{10} = 2.4$

Fig. 13 Shear stress characteristics on suction surface of third-stage stator. (*a–b*) *s–t* diagram, (*c–e*) trajectories *W*, *X*, *Y*, *Z*. $\overline{Re} = 3.35 \times 10^5$, compressor baseline Test Point 2B.

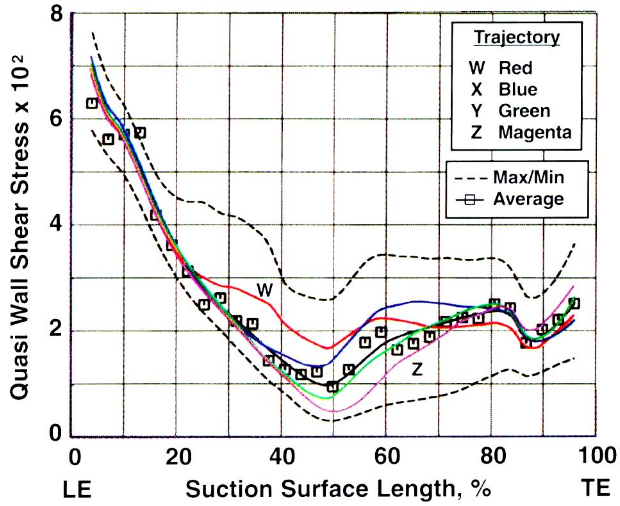

c) Quasi wall shear stress

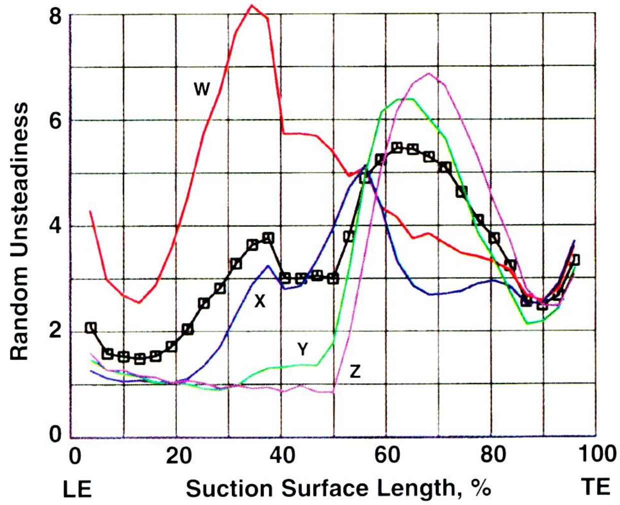

d) Random unsteadiness

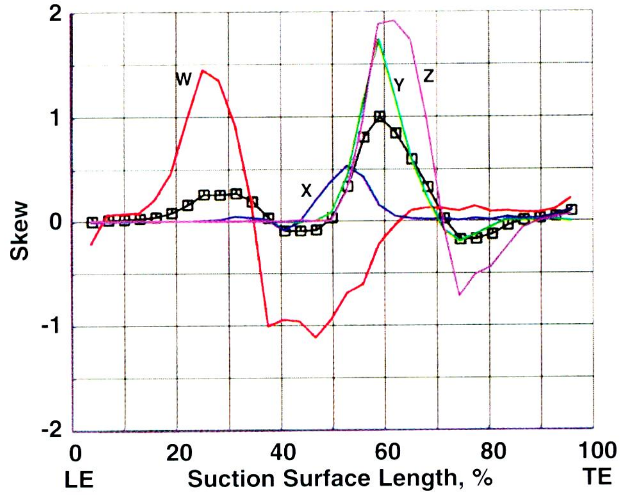

e) Skew

Fig. 13 (Continued)

Although there is no visual evidence that allows us to identify the calmed region from the ensemble-average random unsteadiness and skew presented in Figs. 13(*a, b*), its existence is clearly seen in the raw data. A time segment of raw data for shear stress when a turbulent spot and calming is present is superimposed on Fig. 13(*b*) and marked as curve "*S*." The area of high nonturbulent shear stress is located at the leading boundary of region *D*, which adjoins the trailing boundary of transitional strip *B*. The high shear gradient relaxes asymptotically across the calmed region *D*. The entire area of calmed region *D* has some degree of elevated shear stress and low shape factor. These important features tend to make the flow between wakes more resistant to separation and can delay transition onset.

The boundary of region *D* is defined from raw data traces as the limit where the high shear relaxes asymptotically to low-shear values. For our data, this boundary lies along an average trajectory of 0.30 V_∞, which is marked as the dotted line in Figs. 13(*a, b*). The boundary has some uncertainty since the relaxation is asymptotic and the appearance of turbulent spots is random.

Transition Between Wakes (E). In the region between wakes, the flow undergoes transition that is induced by disturbances other than those associated with wakes immediately upstream of the blading. This region is labeled "*E*" in Figs. 13(*a, b*). It has high random unsteadiness and varying skew. Transition between wakes begins on average at 52 percent SSL, which is 33 percent SSL farther downstream than that for region *B*. This difference is consistent with the lower levels of inlet turbulence intensity of 2.5 percent. Transition is completed by about 84 percent SSL as determined from random unsteadiness and skew.

The differences in the transition processes in region *E* are described by following the three trajectories *X*, *Y*, and *Z* in Figs. 13(*a, b*) and in the more detailed line plots in Figs. 13(*c, d, e*).

Along trajectory *X*, which is just behind transitional strip *B*, transition along points 11–12–13 is indicated by positive (red) skew at point 12 in Fig. 13(*b*). The skew returns to near zero shortly after 12 and, significantly, remains zero to the trailing edge. The blue curve in Fig. 13(*e*) does not subsequently become negative as the others do. Thus the process of transition is not actually completed along trajectory *X*. Instead, transition is terminated between 12 and 13 by the growth into region *E* of the adjacent wake-induced turbulent strip *C*.

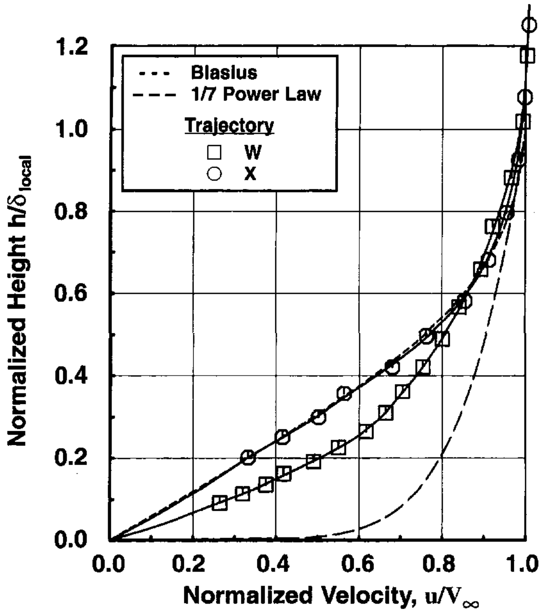

Fig. 14 Boundary layer profiles at 34 percent SSL for Trajectories *W* (wake-induced strip) and *X* (between wake-induced strips) in Fig. 13. Compressor Test Point 2B.

Along green trajectory Y the transition process is similar to that for trajectory X except that a small amount of negative skew is seen in Fig. 13(*e*) before the growth of the turbulent strip C terminates transition.

Along trajectory Z, the transition process occurs in a more conventional manner. In Fig. 13(*a*), the random unsteadiness along 14–18 increases to a maximum around 16 and then falls to a low level by 18. The skew in Fig. 13(*b*) increases to a maximum positive value around 15, drops to zero near 16, reaches a negative maximum at 17, and returns to near zero by 18. At point 16, maximum unsteadiness occurs at zero skew.

The quasi wall shear stress along trajectories X, Y, and Z in Fig. 13(*c*) remains positive throughout, indicating that the flow remains attached. However, proceeding from trajectory X to Y to Z near 50 percent SSL, one notices the shear stress becoming progressively lower because the calmed effect is diminishing. This lowest shear region along Z is the region where flow separation would most likely first appear with changes in operating conditions or design.

An important feature of region E in Figs. 13(*a, b*) is the slope of its boundary marking transition onset near 52 percent SSL. This boundary, which ends at point 6, has a positive slope. There is also transitional activity at point 12. Since the region near 12 lies in the most calmed portion of calmed region D, one would expect that transition should be delayed along path 11–12–13 relative to that along path 14–18, which is much farther removed from the calmed effect. This would cause the slope of the transition onset line to be negative. But this is not the case.

The positive slope of the boundary of transition onset and the transitional activity at point 12 occur in region E because region B, which generates the calmed region, is a transitional strip, not a turbulent one. In a transitional strip there is considerable variation in the formation of turbulent spots. Consequently the flow near point 12 alternates between laminar and turbulent on successive wake passings depending on whether a wake-induced transitional strip (i.e., turbulent spot) is present or absent. This profile switching, or transitional unsteadiness, explains the high level of random disturbance at point 12 and the positive slope of the onset line. This will be seen in the raw data.

From these observations, we reason that the effectiveness of the calmed region in suppressing flow separation and transition onset between wakes is a function of the level of intermittency through the transitional strip B. The closer the location of high intermittency within the strip is to the leading edge, the more effective the calmed region will become. For this operating condition, intermittency of strip B does not reach 0.75 until about 45 percent SSL, which is close to the region of transition between wakes. Therefore the calmed effect is judged to be only moderate.

Turbulent Region Between Wakes (F). The region of turbulent boundary layer downstream of the flow that undergoes transition between wakes is labeled F in Figs. 13(*a, b*). The flow at

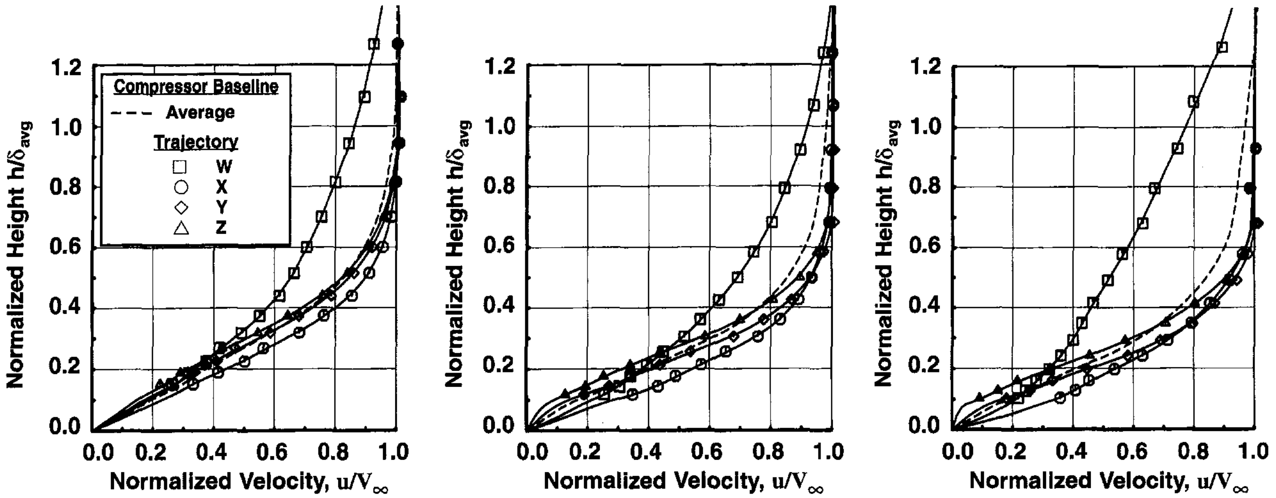

a) 34 percent SSL b) 49 percent SSL c) 56 percent SSL

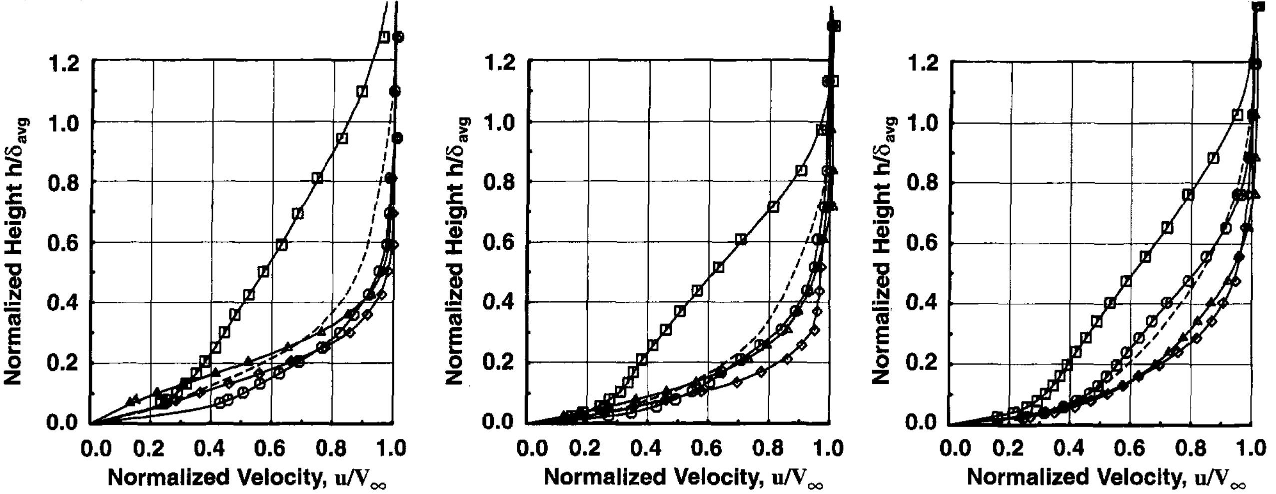

d) 60 percent SSL e) 75 percent SSL f) 90 percent SSL

Fig. 15 Boundary layer profiles for compressor baseline along Trajectories *W*, *X*, *Y*, and *Z* in Fig. 13. Suction surface of third-stage stator, profiles normalized by time-average boundary layer thickness, $\overline{Re} = 3.35 \times 10^5$, Test Point 2B.

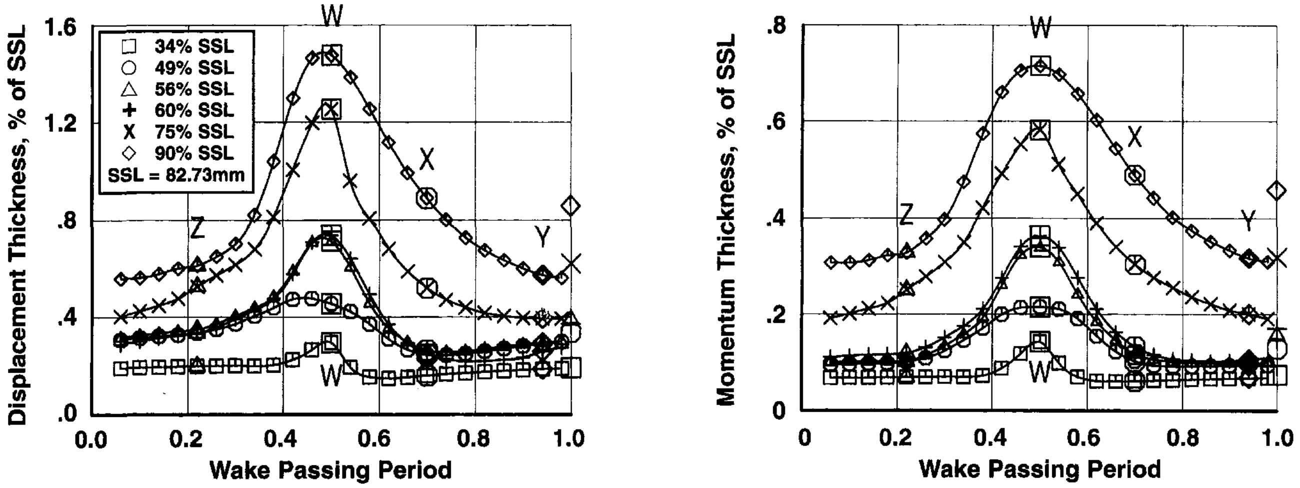

a) Displacement thickness

b) Momentum thickness

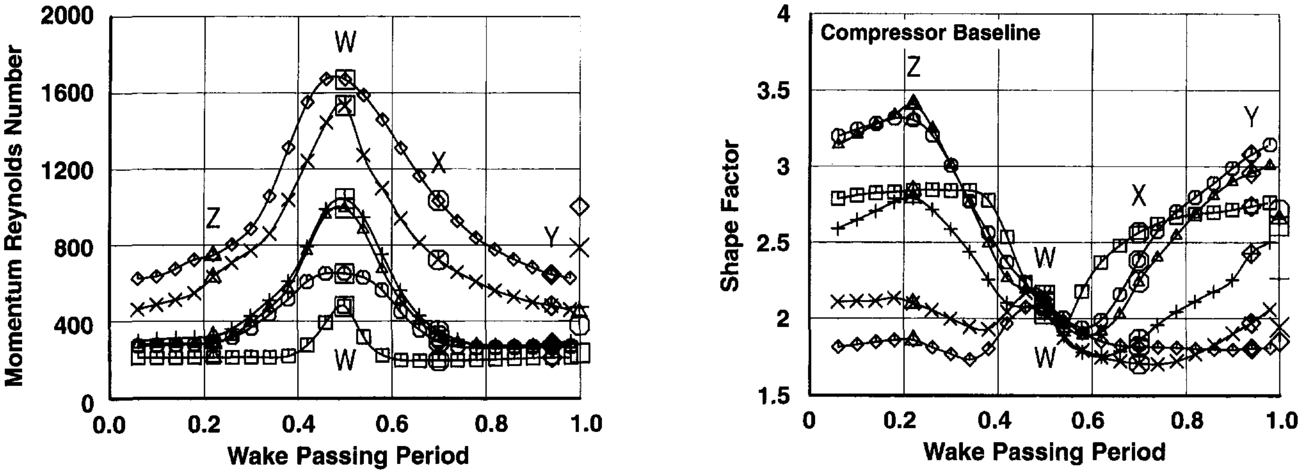

c) Momentum Reynolds number

d) Shape factor

Fig. 16 Variation of integral boundary layer parameters across wake-passing period for compressor baseline, suction surface third-stage stator. Trajectories *W*, *X*, *Y*, and *Z* from Figs. 13 and 15 are identified. $\overline{Re} = 3.35 \times 10^5$. Test Point 2B.

point 19 is similar to that at point 8. The random unsteadiness is low, albeit above that for the laminar flow in region *A*, and the skew is near zero. The boundaries between regions *C* and *F* from 84 percent SSL to the trailing edge cannot be distinguished by the fluctuations in the surface hot-film (shear stress) data. However, they can be distinguished in the integral boundary layer parameters seen in the surveys through the turbulent boundary layer and are therefore shown in Fig. 13 as parallel dotted lines.

7.3 Boundary Layer Surveys. The results presented so far show only what is happening on the airfoil surface. A complete understanding of the state of the boundary layer can only be achieved by also studying the boundary layer profiles.

Surveys of the boundary layer were obtained at midspan on the stator suction surface at streamwise locations 34, 49, 56, 60, 75, and 90 percent SSL. Boundary layer profiles for trajectories *W*, *X*, *Y*, and *Z* of Fig. 13(*a*) are presented in Fig. 15(*a*–*f*). The time-averaged profile is shown as a dashed line. Height above the stator surface is normalized by the time-averaged boundary layer thickness measured at the given streamwise location instead of the local time-varying value. This allows the thickness of the various boundary layers to be distinguished. Velocity is normalized by the local free-stream value of each individual profile. Curve fits of the data were done systematically using a spline fit with weighted averaging and zero velocity imposed at the wall. No custom-tailoring was employed.

Ensemble-averaged distributions of the boundary layer integral parameters, obtained by integration of the profile curve fits, are given in Figs. 16(*a*–*d*) for one wake passing period. Displacement and momentum thicknesses are normalized by stator suction-surface length. Time-averaged values are provided along the right-hand side of each figure.

Profile Characteristics–34 percent SSL. Both laminar and transitional profiles occur across a wake-passing period at 34 percent SSL in Fig. 15(*a*). Profiles *X*, *Y*, and *Z* are laminar and Profile *W*, within the wake-induced transitional strip *B*, is transitional.

Profile *W* in Figs. 15(*a*) and Fig. 16(*a*, *b*) is thicker than the others and is clearly distinguishable from them. Being transitional, its shape factor of 2.1 in Fig. 16(*d*) is markedly lower than those for surrounding laminar trajectories *X*, *Y*, and *Z*.

For trajectory *X*, the profile shape and the shape factor of 2.55 are those of a Blasius laminar boundary layer in spite of the adverse pressure gradient (see Fig. 14). The effects of relaxation through the calmed region are evident as trajectories *Y* and *Z* in Fig. 15(*a*) take on an increasing degree of inflection relative to *X*.

Momentum thickness Reynolds numbers of profiles *X*, *Y*, and *Z* are about 200, which are below that at which transition onset would be expected for the background level of free-stream turbulence (Abu-Ghannam and Shaw, 1980).

Profile Characteristics–49, 56, and 60 percent SSL. The wake-induced profiles *W* remain clearly distinguishable from the others in Figs. 15(*b*, *c*, *d*). These profiles are filling with lower momentum fluid and are seen in Figs. 16(*a*, *b*) to occupy

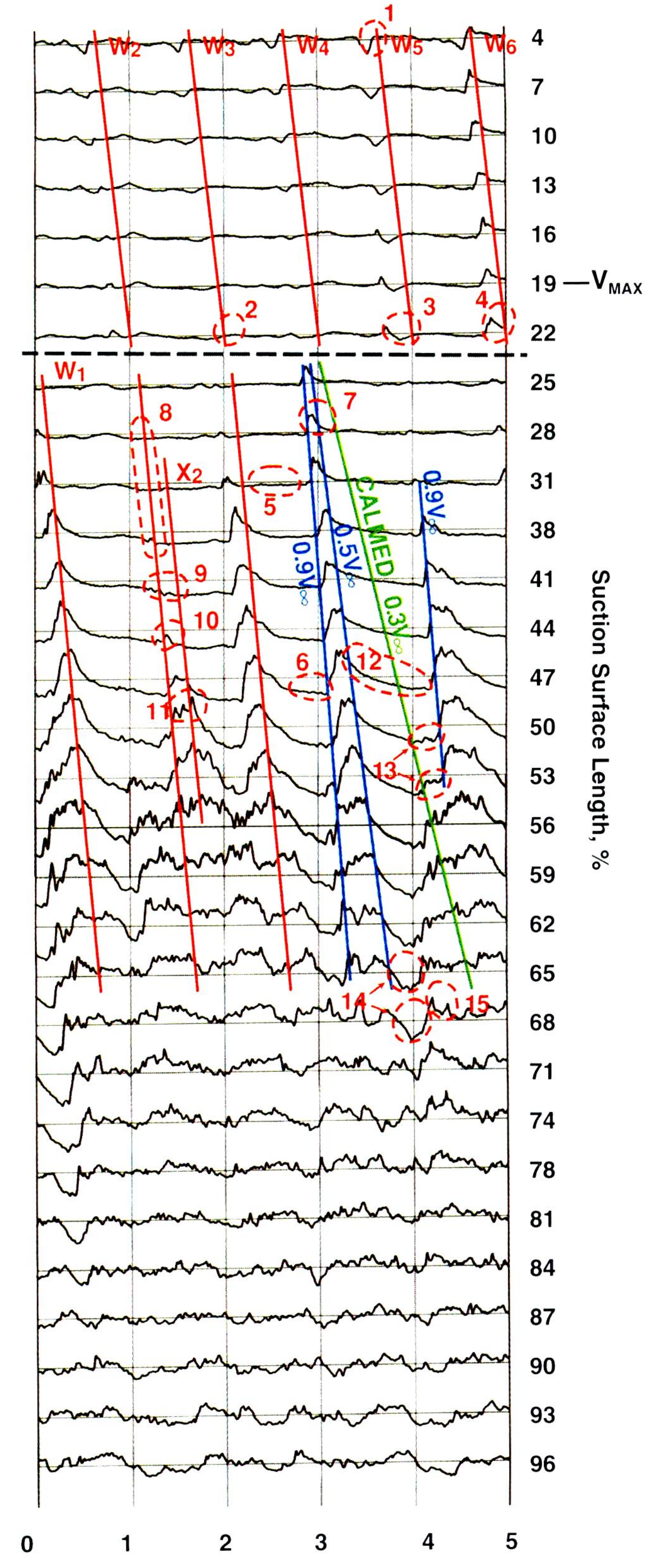

a) Raw time traces

a larger percentage of the wake passing period. Their shape factors in Fig. 16(*d*) remain virtually unchanged from those at 34 percent SSL. Along the wake-induced strip, the tendency of shape factor to decrease as transition progresses is offset by the effects of the positive pressure gradient, which maintains high shape factors.

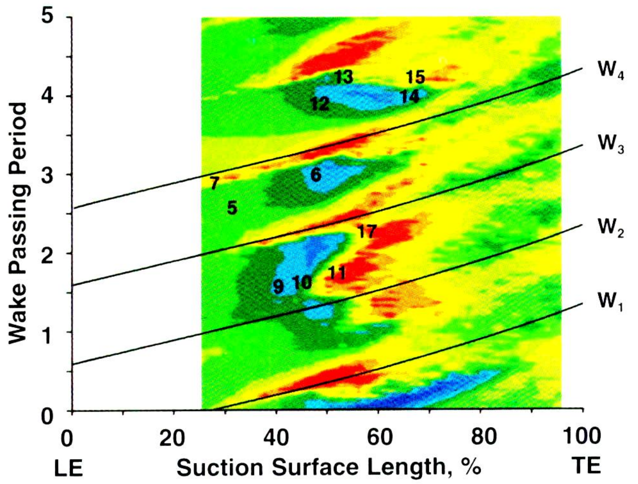

b) s-t diagram of instantaneous quasi wall shear stress from Fig. 17a. $Q_0 = -0.1$, $Q_{10} = 0.1$

Fig. 17 Raw time traces from surface hot-film gages operated simultaneously on the suction surface of third-stage stator S3, Compressor Test Point 2B

The profiles along trajectories *X* in Figs. 15(*b–d*) have begun to fill in noticeably near the wall as transition progresses. Shape factors in Fig. 16(*d*) are decreasing accordingly with a sharp drop from 56 to 60 percent SSL.

Profile Y remains laminar-like in appearance although slightly inflectional due to the adverse pressure gradient. The degree of inflectionality increases from Y to Z as the calming effect diminishes. The shape factor for Z has increased significantly to a value of 3.4 at 56 percent SSL. This suggests that, on average, the associated boundary layer is on the verge of separation; however, the surface velocity distributions in Fig. 3(*b*) show no signs of this. By 60 percent SSL, the shape factors are decreasing and the Z profile is much less inflectional.

Profile Characteristics–75 and 90 percent SSL. Along the wake-induced path, Profiles *W* in Figs. 15(*e, f*) continue to fill with lower momentum fluid as they respond to the adverse pressure gradient. By 90 percent SSL, profile *W* has the highest value of shape factor of any profile at these streamwise locations in Fig. 16(*d*). This boundary layer, contained in wake-induced turbulent strip *C*, completed transition earliest and will be the first to separate under continued conditions of adverse pressure gradient.

For profile *X* at 75 percent SSL, the shape factor has reached a minimum value suggesting completion of transition. By 90 percent, its value has increased in a manner consistent with a diffusing turbulent boundary layer. Along *Y* and *Z*, significant profile filling occurs from 75 to 90 percent SSL. Values of shape factors stabilize near minimum values by 90 percent SSL. Consequently, all layers are fully turbulent by 90 percent SSL.

General Observations. The peak values of displacement and momentum thickness and momentum Reynolds number, in Figs. 16(*a–c*), occur along wake-induced trajectory *W* in which transition was completed farther forward. Along trajectories *X*, *Y*, and *Z* where transition was completed farther aft, the more newly formed turbulent layers at 90 percent SSL have momentum Reynolds numbers of 650–1000. In contrast at the same location, those along wake-induced trajectory *W* are 1700.

There is little variation in values of shape factor of about 2.1 all along trajectory *W*. Outside the wake-induced strip and upstream of midchord, the values of shape factor are significantly greater than those along *W*, characterizing the laminar and transitional nature of the diffusing boundary layers. By 90 percent SSL, transition between wake-induced strips is complete. Shape factors of these newly

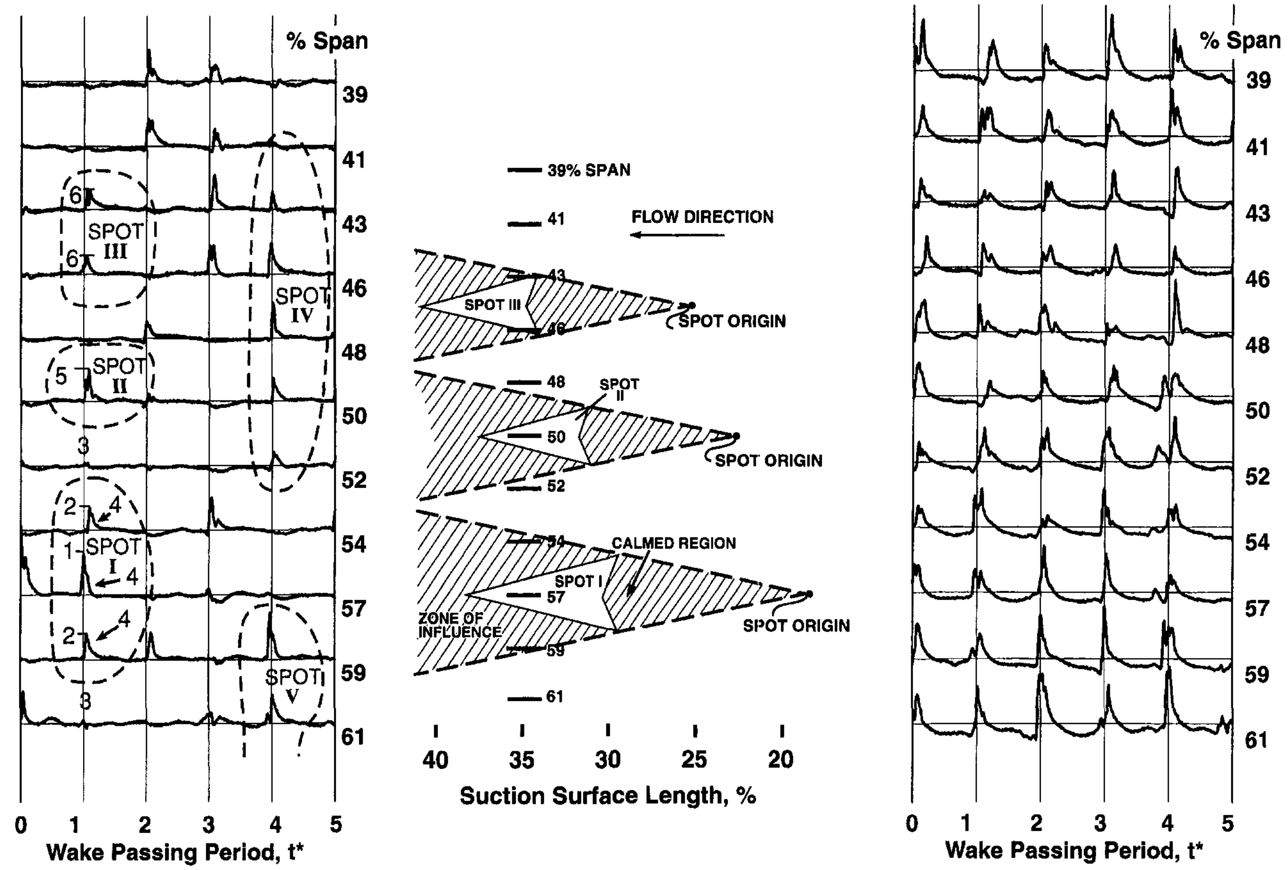

a) Raw time traces from spanwise array of surface hot-films operated simultaneously on the suction surface of third-stage compressor stator. $\overline{Re} = 3.35 \times 10^5$, Test Point 2B.

b) Schematic illustrating convection of turbulent spots past spanwise array of sensors. t*=1.0, overhead view.

c) Raw time traces from spanwise array for the suction surface of third-stage compressor stator at increased loading. $\overline{Re} = 3.00 \times 10^5$, Test Point 3.

Fig. 18 Raw time traces from spanwise array of surface hot films at 35 percent SSL

formed turbulent boundary layers are at levels below those within the wake-induced strip, where transition was completed earlier.

7.4 Analysis of Raw Data. The raw data are examined because they show evidence for important flow features, such as the calmed effect and velocities of turbulent spots, that cannot be seen in ensemble-averaged data.

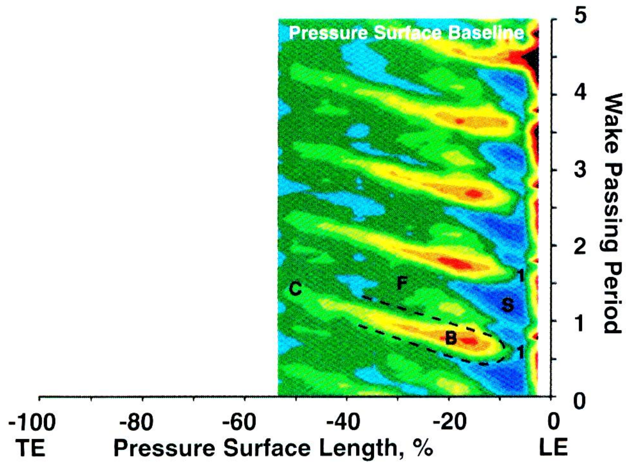

a) Random Unsteadiness $Q_0 = 0.75$, $Q_{10} = 5.5$

Fig. 19 Shear stress characteristics on pressure surface of third-stage stator, $\overline{Re} = 3.35 \times 10^5$, compressor baseline, Test Point 2B

Instantaneous time traces of quasi wall shear stress, presented in A–C coupled format, are shown in Fig. 17(*a*) for the suction surface of the third-stage stator. The traces were obtained simultaneously in two groups. A dashed line drawn at 23 percent SSL separates the two groups. Trajectories *W* through successive wake passing periods are given numerical subscripts. Areas of importance are encircled and identified with a number. An instantaneous *s*–*t* diagram, shown in Fig. 17(*b*), was constructed from the data in Fig. 17(*a*).

The Laminar Region A. Close to the leading edge at 4 percent SSL in Fig. 17(*a*), the fluctuations in wall shear stress, like those in encircled area 1, correlate with wake passing events. These fluctuations result from the local increase in both unsteadiness and incidence angle as the wake moves past the leading edge.

From the leading edge to about 22 percent SSL, this wake influence sometimes dies out as in area 2, sometimes persists as in area 3, and sometimes develops into a turbulentlike event as in area 4. Such an event is distinguished by a sharp and distinct rise in shear stress. These variations lead to the slightly elevated levels of random unsteadiness extending along points 2–3 for the wake-induced path in Fig. 13(*a*).

In between the wake-induced paths, there are low-amplitude, low-frequency variations in wall shear stress indicative of laminar boundary layers responding to free-stream disturbances. Encircled area 5 at 31 percent SSL is an example. The perturbed laminar flow like that in area 5 persists well past maximum velocity, which occurs at 20 percent SSL, as it extends to area 6 near midchord. Tollmien–Schlichting waves were not observed in the raw data.

Table 5 Effect of Reynolds number and loading on boundary layer development for compressors. Tabulated numbers give locations of regions along suction surface of airfoil in percent SSL.

REGION	$\overline{Re} \times 10^{-5}$ OR LOADING LEVEL	TEST POINT	A LAMINAR REGION		B WAKE-INDUCED TRANSITIONAL STRIP			C WAKE-INDUCED TURBULENT STRIP		D CALMED REGION	E TRANSITION BETWEEN WAKES			F TURBULENT BETWEEN WAKES	
			L	T_B/T_E	*L*	$0.5\gamma/0.75\gamma$	*T*	*L*	*T*	*Effective*	*L*	0.5γ	*T*	*L*	*T*
COMPRESSOR STATOR	4.19	2A	LE	12/50	12	28/38	56	56	TE	Moderate	50	64	80	80	TE
	3.35	2B	LE	19/52	19	35/45	62	62	TE	Moderate	52	70	84	84	TE
	1.87	2C	LE	25/56	25	48/55	63	63	TE	Low	56	70	83	83	TE
	0.93	2D	LE	46*/46*	52	—	≈85	≈85	TE	No	55	—	≈85	≈85	TE
COMPRESSOR ROTOR	3.35	2B	LE	10/48	10	29/40	66	66	TE	Moderate	48	64	80	80	TE
	1.87	2C	LE	44*/44*	46	–/–	76	76	TE	Low	50	—	80	80	TE
STATOR	Low	1	LE	30/60	30	55/62	70	70	TE	Low	60	73	89	89	TE
	Design	2B	LE	19/52	19	35/45	62	62	TE	Moderate	52	70	84	84	TE
	High	3	LE	0/50	0	30/35	42	42	TE	High	50	60	77	77	TE
	Near Stall	4	*	—	—	—	—	LE	TE	—	—	—	—	LE	TE

∗ Separation
L ≡ Leading boundary of region
T ≡ Trailing boundary of region
γ ≡ Intermittency

T_B ≡ Trailing boundary of laminar region along wake-induced transitional strip B (Trajectory W)
T_E ≡ Trailing boundary of laminar region for transition between wakes E (Trajectory Y)

Wake-Induced Transitional Strip B. Evidence of wake-induced transition is seen by the positive spikes (turbulent spots) in wall shear stress that appear along the *W* trajectories in Fig. 17(*a*). A typical spot that develops into a wake-induced transitional strip along W_4 is shown in area 7. The convection rates of the leading and trailing boundaries of this spot are 0.9 V_∞ and 0.5 V_∞, respectively, as shown by blue lines in the figure. These velocities are consistent with those reported for individual

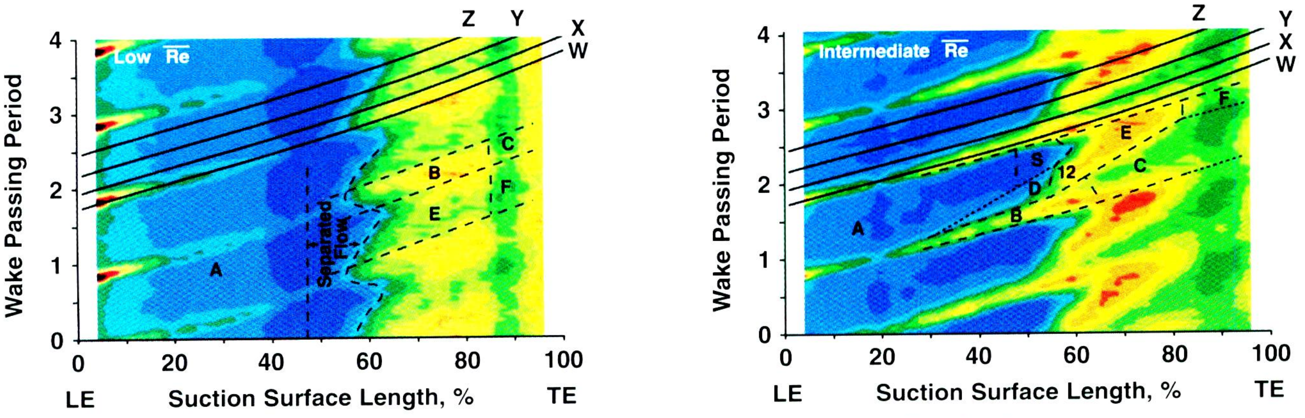

a) $\overline{Re}$ = 0.93 x 10^5, Test 2D, Q_0 = 0.01, Q_{10} = 0.60

b) $\overline{Re}$ = 1.87 x 10^5, Test 2C, Q_0 = 0.15, Q_{10} = 2.46

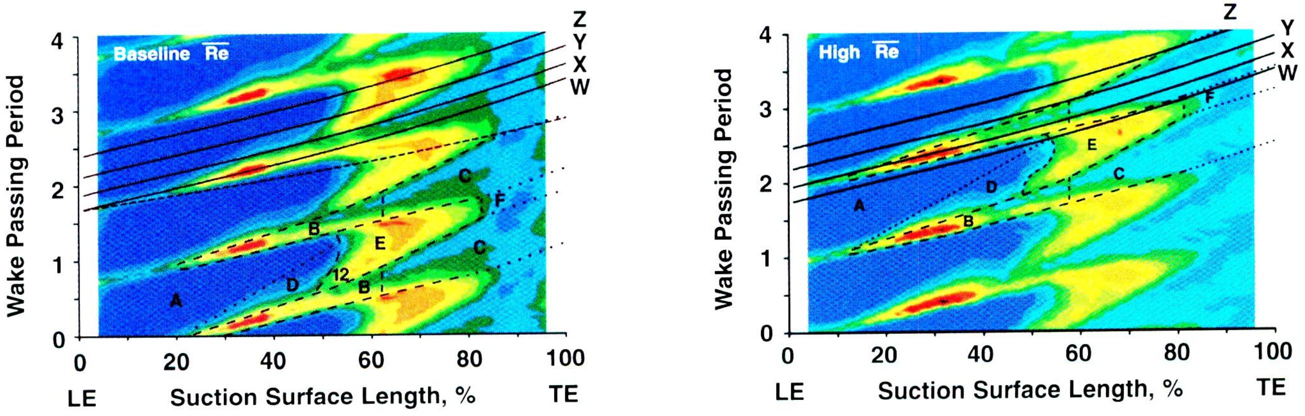

c) $\overline{Re}$ = 3.35 x 10^5, Test 2B, Q_0 = 0.68, Q_{10} = 8.79

d) $\overline{Re}$ = 4.19 x 10^5, Test 2A, Q_0 = 1.65, Q_{10} = 19.00

Fig. 20 Reynolds number effect on boundary layer development. Suction surface, compressor third-stage stator, *s*–*t* diagrams of random unsteadiness for Test Points 2D, 2C, 2B, and 2A.

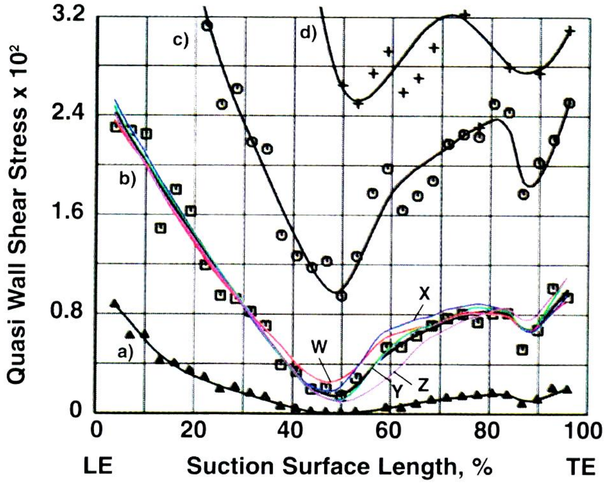

Fig. 21 Reynolds number effect on time-averaged, quasi-wall shear stress. Suction surface, compressor third-stage stator. (*a*) $\overline{Re} = 0.93 \times 10^5$, (*b*) $\overline{Re} = 1.87 \times 10^5$, (*c*) $\overline{Re} = 3.35 \times 10^5$, (*d*) $\overline{Re} = 4.19 \times 10^5$, trajectories *W*, *X*, *Y*, and *Z* also shown for $\overline{Re} = 1.87 \times 10^5$.

turbulent spots. On the other hand for area 8 along W_2, turbulent spots are missing.

Calmed Region D. The calmed regions are identified in Fig. 17(*a*) as areas of elevated but decaying shear stress following turbulent spots. An example is seen as area 12. The downstream boundary of the region is determined by locating where flow breakdown occurs, as in area 13, and constructing a trajectory from the origin of the strip to the breakdown point. The green trajectory of 0.3 V_∞ is an example.

Transition Between Wakes E. Transition between wakes is described for two different trajectories in Fig. 17(*a*): one along W_4, which has a distinct turbulent spot and a strong calmed region, and the other along W_2, where the spot and calmed region are missing.

Transition between wakes along W_4 is suppressed by the calmed effect in area 12 until turbulent spots originate primarily in the least-calmed, lowest-shear-stress areas such as 13. Note that downstream areas 14, which are strongly influenced by the calmed region, are still laminarlike. Areas 12–15 are also shown as points 12–15 in the instantaneous *s*–*t* diagram of Fig. 17(*b*). Clearly low-shear, laminar-like flow (blue region) persists quite far aft to point 14 when calming is present. The slope of the line connecting points 13 and 15 is negative.

As transition develops along W_2 in Fig. 17(*a*), the wake-induced strip (spot) is completely absent along area 8. By area 9 the calmed effect from the previous wake-induced strip W_1 has completely decayed and offers no assistance in suppressing transition. Bypass transition begins in area 10 and by area 11, significant breakdown appears. This is also seen as the red-orange area at point 11 in Fig. 17(*b*). The slope of the line connecting points 17 and 11 is now positive in contrast to the negative slope of line 13–15. This intermittent switching of the boundary layer is responsible for the change in slope and for the lobe of increased unsteadiness denoted as point 12 in Fig. 13(*a*).

The Turbulent Strips C and Region F. The traces extending from 80 percent SSL to the trailing edge are predominantly of a low-amplitude, high-frequency turbulent nature.

7.5 Analysis of Raw Data From the Spanwise Array. The two-dimensional transitional nature of the wake-induced strips *B* is clearly shown by the instantaneous (raw) time traces obtained from the spanwise-oriented array of surface hot-films on the third-stage stator. The data, obtained at 35 percent SSL, are shown in Fig. 18(*a*). All traces were acquired simultaneously. The number to the right of each trace corresponds to percent span. Areas of significance are encircled and identified by Roman numeral. Other points of interest are numbered. Since the spanwise array is approximately parallel to the convecting wakes, turbulent spots from a specific wake segment arrive at the sensors at about the same instant in normalized time. For example, spots I, II, and III arrive at about $t^* = 1.0$ while spots IV and V arrive at $t^* = 4.0$.

The sketch in Fig. 18(*b*) is drawn to scale and shows turbulent spots I, II, and III passing over the sensors at $t^* = 1.0$. The hatched region indicates the area swept out by each spot as it convects downstream. The "zone of influence" was drawn as it would occur for a conventional turbulent spot.

Spot I in Fig. 18(*b*) completely covers the sensor located at 57 percent span. The corresponding magnitude of wall shear (point 1 in Fig. 18(*a*)) is at a peak value. The zone of influence for spot I is such that, at a slightly later instant in time, its lateral edges, seen as points 2 in Fig. 18(*a*), will pass over the sensors at 54 and 59 percent span in Fig. 18(*b*). The sensors at 52 and 61 percent span are outside all zones of influence, hence the traces are quiet at points 3, Fig. 18(*a*). Evidence of the calmed region behind spot I is labeled as points 4.

Only a single spike occurs at point 5 as spot II convects past the sensor array in Fig. 18(*b*). Spot III at point 6 is centered about the sensors and only its lateral edges actually pass over them. The traces for the remaining spanwise locations are quiet.

Using the zones of influence, we determine that spots I, II, and III originate from about 18 to 25 percent SSL, as suggested in Fig. 18(*b*). This agrees well with previous conclusions regarding the onset location of wake-induced transition seen in Fig. 13(*a*).

At later instances in time, for example $t^* = 4.0$ in Fig. 18(*a*), spots IV and V will move over the sensors. This random occurrence of turbulent spots is a classical picture of transition.

Spanwise traces were obtained at other loading conditions. For increased loading Test Point 3 shown in Fig. 18(*c*), the high rate of occurrence of turbulent spots suggests that transition is nearly complete, the wake-induced strips are nearly turbulent, and the calmed regions are well developed.

7.6 The Pressure Surface. Boundary layer transition on the pressure surface, shown for Test Point 2B in Fig. 19, occurs closer to the leading edge because of the adverse pressure gradient in that region (see Fig. 3). Transition between the wakes begins in the shear layer over a leading-edge separation bubble, which corresponds to the blue area marked "*S*." The size of *S* varies over the wake period. The raw data (not shown) exhibit a separational character. Transitional flow in region E extends to about 40 percent PSL, followed by a turbulent boundary layer in region *F*, which remains attached to the trailing edge.

The flow in the wake path remains attached. Flow separation is suppressed at point 1 by the intermittent increase in local incidence angle as the wake crosses the leading edge. Wake-induced transition begins rapidly in region *B* and is completed by 20 percent PSL. Expansion of the subsequent wake-induced turbulent strip, *C*, partially terminates the region of transitional flow *E* between wakes. Similar regions were observed on the suction surface.

8.0 Reynolds Number Effects on Compressor Boundary Layers

This section examines the influence of Reynolds number on compressor boundary layers. It provides the evidence for Fig. 10(*c*) of the discussion in Section 5.0. It shows that lowering the Reynolds number substantially weakens and eventually eliminates wake-induced transitional strips and any associated

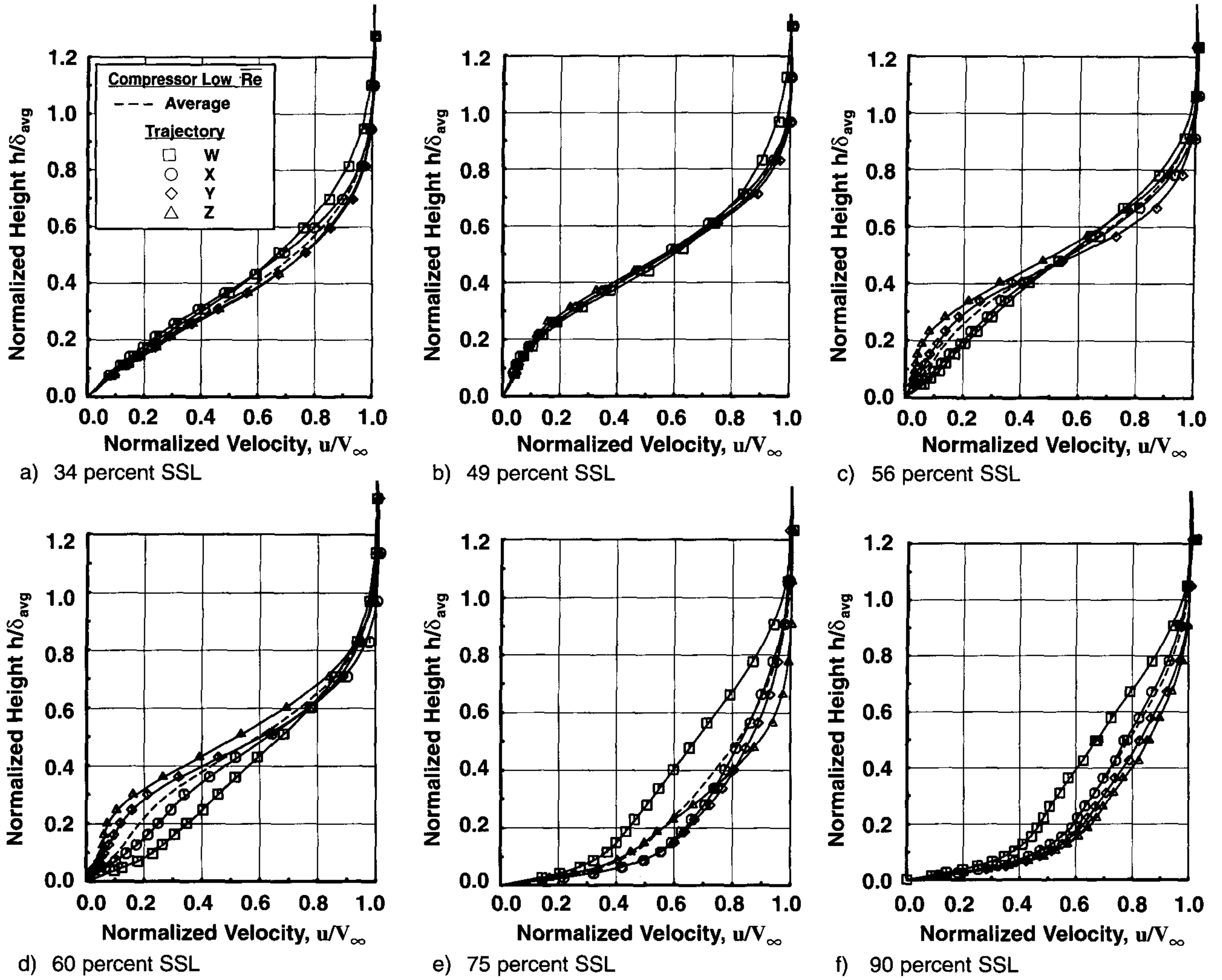

Fig. 22 Boundary layer profiles for compressor low Reynolds number along Trajectories *W*, *X*, *Y*, and *Z* in Fig. 20(*a*). Suction surface of third-stage stator, profiles normalized by time-average boundary layer thickness, $\overline{Re} = 0.93 \times 10^5$, Test Point 2D.

calming effect. In the process, separated-flow transition increasingly replaces bypass transition as the dominate transition mechanism. The findings are evaluated relative to those for the baseline. The results are listed in Table 5.

The Reynolds number tests for the third stage were conducted at design-point flow coefficient for stage-averaged, aerodynamic Reynolds numbers of 4.19×10^5, 3.35×10^5, 1.87×10^5 and 0.93×10^5 based on airfoil surface length and inlet velocity. These are Test Points 2A, 2B, 2C, and 2D, respectively, in Figs. 2 and 3(*b*) and Table 2 of Part 1.

8.1 Picture Constructed From Surface Film Data

Low Reynolds Number. The $s-t$ diagram of random unsteadiness for the low Reynolds number of 0.93×10^5 is shown in Fig. 20(*a*). The flow picture is now markedly different from that at the baseline Reynolds number of 3.35 × 105 shown in Fig. 13 and in an abbreviated form in Fig. 20(*c*).

The striking feature of Fig. 20(*a*) is the absence of any appreciable wake-induced transitional strips penetrating the extensive laminar region *A*. Instead, laminar separation of the flow occurs near 46 percent SSL as shown by the wall shear stress falling to zero for this Reynolds number in Fig. 21 and by the boundary layer surveys shown later. The presence of separation complicates the data interpretation, as separated-flow transition begins above the surface in the separated shear layer. This makes the surface film data in this region less distinct and subject to lag effects. Dashed lines in Fig. 20(*a*) mark the zone of separated flow. The downstream boundary of the separation zone modulates between 55 and 62 percent SSL as the wakes pass. This line indicates where intermittent reattachment begins. From the measurements of static pressure, a laminar separation bubble is clearly inferred from the change in the velocity distributions on the suction surface between 50 and 65 percent SSL for Test Point 2D in Fig. 3(*b*) of Part 1.

The boundaries of the regions in the figure are less distinct. The wake-"influenced" and nonwake-"influenced" transitional regions *B* and *E* are marked in Fig. 20(*a*) along with the associated turbulent regions *C* and *F*.

The data in Fig. 20(*a*) indicate that from 45 percent SSL to the trailing edge both the separated laminar region and the transitional/turbulent regions *B*, *E*, *C*, and *F* are oscillating in sync with the passing wakes. Thus, the wakes exert only a modulating effect on the boundary layer rather than a mode-switching effect.

The picture is similar to that shown for the first rotor at the top of Fig. 11(*a*).

Intermediate Reynolds Number. At the intermediate Reynolds number of 1.87×10^5 shown in Fig. 20(*b*), the boundary layer develops features more identifiable with those seen at the higher Reynolds number in Fig. 20(*c*). However the structure

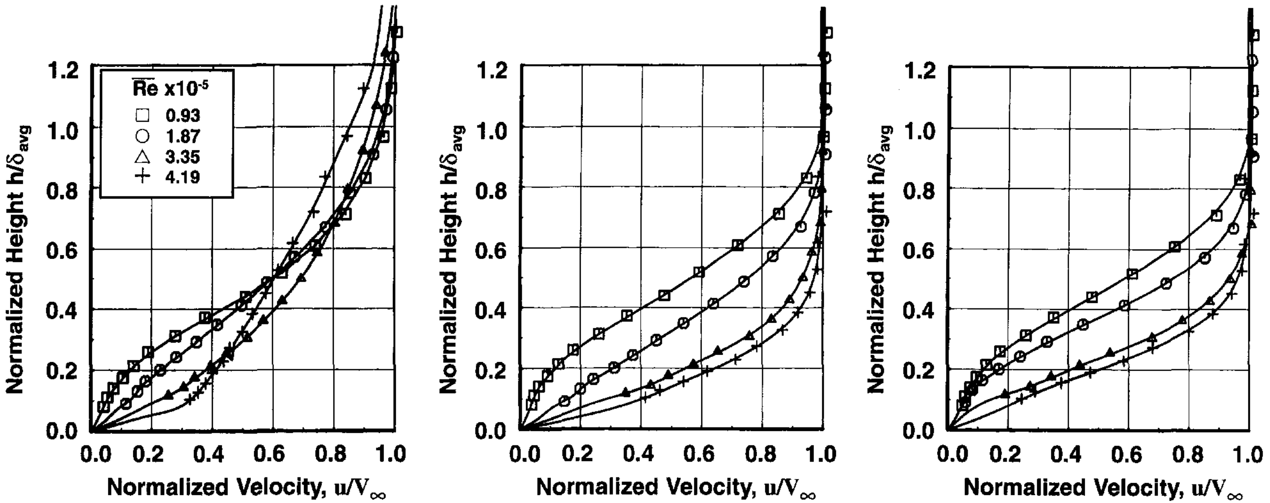

a) Trajectory W b) Trajectory X c) Trajectory Y

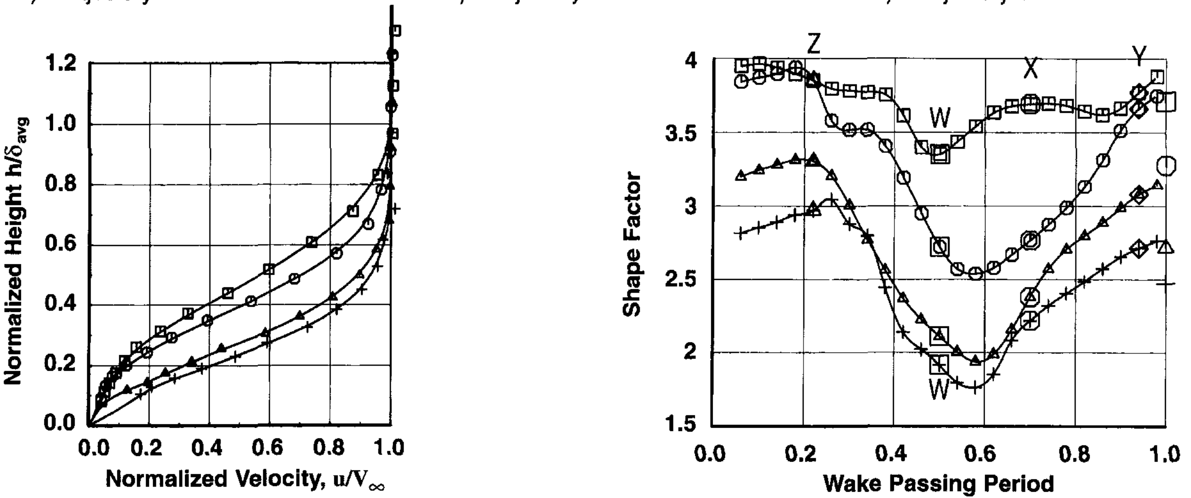

d) Trajectory Z e) Shape factor

Fig. 23 Effect of Reynolds number on boundary layer profiles and shape factor at 49 percent SSL. Suction surface of the third-stage compressor stator, Test Points 2A, 2B, 2C, and 2D.

of the various regions *A* through *F* and the whole development picture look more diffuse.

The wake-induced transitional strips *B* in the laminar region *A* are readily seen in Fig. 20(*b*). However they are more diffuse and begin near 25 percent SSL, which is about 6 percent farther downstream than for the baseline. Intermittency along *W* does not reach 0.75 until about 55 percent SSL, or 10 percent farther downstream than for the baseline. The transitional strips are weak and therefore so is the calmed effect in region D. The shear stress along the red trajectory *W* in Fig. 21 hardly departs from the others which is unlike that in Figs. 12(*c*) and 13(*c*). The flow probably remains attached along *W*, but just barely, as will be confirmed by boundary layer surveys.

Between wakes, the flow is intermittently separational in the region marked "*S*" in Fig. 20(*b*), as will be seen in the boundary layer surveys. Flow separates at about 48 percent and reattaches by 57 percent SSL. The surface velocity distribution for this Test Point 2C, shown in Fig. 3(*b*) of Part 1, gives evidence of a small laminar separation at about 50 percent SSL, but it is not nearly so pronounced as that for the lowest Reynolds number. Transition in region *E* between wakes is completed by about 83 percent SSL. The lobe at point 12 in Fig. 20(*b*) is very evident and results from the transitional nature of the weak wake-induced strip *B*.

The turbulent regions *C* and *F* are fundamentally the same as those for the baseline.

High Reynolds Number. The boundary layer development at the highest test Reynolds number of 4.19×10^5 in Fig. 20(*d*) looks similar to that shown for the baseline in Fig. 20(*c*) with the following exceptions. The locations of the wake-induced transitional and turbulent strips *B* and *C* and the locations where 0.75 intermittency occur have moved about 8 percent closer to the leading edge. Consequently their associated calmed regions are somewhat stronger and the lobe of region *E* (point 12 in Figs. 13(*a*) and 20(*c*)) is not quite so prominent. This follows directly from the increased strength (intermittency) of the wake-induced strip.

The nonzero shear stress in Fig. 21 (curve *d*) indicates that no separated flow is present, as boundary layer surveys will confirm. Bypass transition in the region between wakes occurs at about 50 percent SSL. The surface velocity distributions for this Reynolds number in Fig. 3(*b*) of Part 1 show no signs of a separation bubble.

8.2 Boundary Layer Surveys. Surveys of the boundary layer were obtained for the low Reynolds number of 0.93×10^5, Test Point 2D, to remove uncertainties associated with interpreting surface film gages in regions of separated flow. The results, presented in Figs. 22 and 23, are in the same format as those for the baseline in Fig. 15.

Profile Characteristics–34 percent SSL. All of the profiles at low Reynolds number for trajectories W, X, *Y*, and Z in Fig. 22(*a*) are laminar ones with shape factors between 2.6 and 3.0.

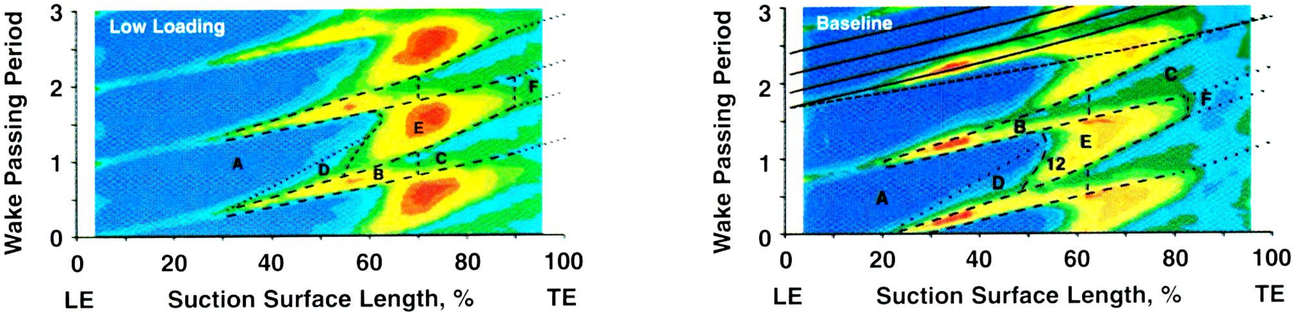

a) Low loading, Test 1, $Q_0 = 0.91$, $Q_{10} = 13.80$

b) Design Pt., Test 2B, $Q_0 = 0.68$, $Q_{10} = 8.80$

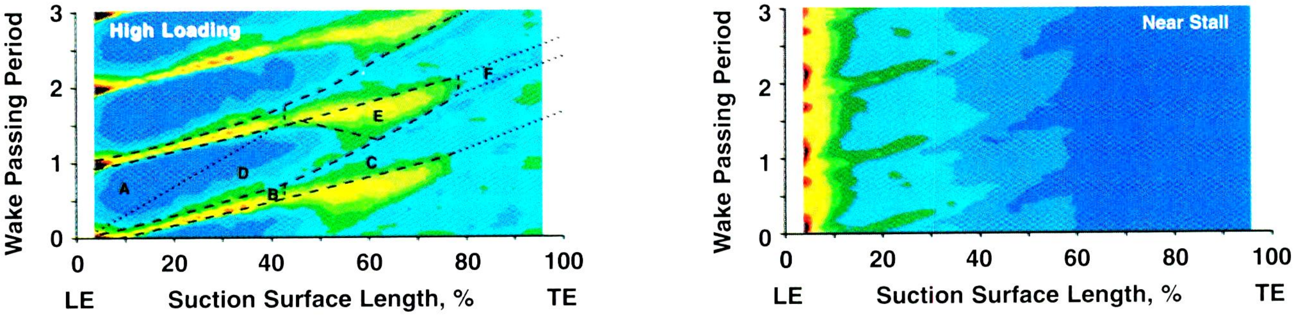

c) High loading, Test 3, $Q_0 = 1.00$, $Q_{10} = 10.50$

d) Near stall, Test 4, $Q_0 = 1.31$, $Q_{10} = 20.50$

Fig. 24 Loading effect on boundary layer development. Suction surface, compressor third-stage stator, *s–t* diagrams of random unsteadiness for Test Points 1, 2B, 3, and 4.

This is consistent with the lack of wake-induced transitional strips forming in laminar region A. It is in contrast with the trajectory *W* profile in Figs. 14 and 15(*a*), which has a nonlaminar character caused by the wake-induced strip B.

Profile Characteristics–49, 56 and 60 percent SSL. At 49 percent SSL all of the profiles for trajectories *W* through Z in Fig. 22(*b*) indicate separated flow, as evidenced by the strong inflection of the profiles near the airfoil surface. For 56 and 60 percent SSL in Figs. 22(*c, d*), the profiles for trajectories *W* and *X* show attached flow, the profile for trajectory *Y* shows reattaching flow, and that for trajectory *Z* still shows separated flow. This is consistent with the modulating shape of the reattachment line across a wake-passing period in Fig. 20(*a*). The separational profiles in Figs. 22(*b, c, d*) are in contrast to the attached baseline profiles in Figs. 15(*b, c, d*) where only trajectory Z is on the verge of separation.

Profile Characteristics–75 and 90 percent SSL. Although not as full and developed as their more turbulent counterparts in Figs. 15(e, f), the profiles for trajectories *X*, *Y*, and *Z* in Figs. 22(*e, f*) are similar in character. Profiles for trajectory *W* are beginning to thicken as they respond to the adverse pressure gradient.

The Integral Parameters. Although similar in structure to their baseline counterparts in Fig. 16, the integral parameters for low Reynolds number (not shown) exhibit the following differences. The boundary layers are thicker at the lower Reynolds numbers than they are at the baseline with maximum values of $\delta^* = 1.9$ percent SSL and $\theta = 0.97$ percent SSL in the wake-induced region near the trailing edge. Momentum Reynolds numbers are as low as 100 at 34 percent SSL and as high as 600 in the wake-induced region near the trailing edge. The maximum-to-minimum values of both displacement thickness and momentum Reynolds number differ by only a factor of 1.7, compared to 2.6 at the baseline Reynolds number.

Varying the Reynolds Number. The effect of varying Reynolds number on the boundary layer profiles at 49 percent SSL is presented in Fig. 23. For each of the individual trajectories *W–Z* in Figs. 23(*a–d*), respectively, the clear trend is from a separated-flow profile shape at low $\overline{\text{Re}} = 0.93 \times 10^5$ to an attached profile shape at the high $\overline{\text{Re}} = 4.19 \times 10^5$. For the intermediate $\overline{\text{Re}} = 1.87 \times 10^5$, profiles for trajectories *W* and *X* in Figs. 23(*a, b*) have an attached character, while profiles for trajectories *Y* and *Z* in Figs. 23(*c, d*) are still separational. This is consistent with the appearance of wake-induced strips *W* and the regions of separated flow between wakes in Fig. 20(*b*). The profile shapes at the two highest Reynolds numbers are similar.

The values of shape factor for $\overline{\text{Re}}$ 3.35×10^5 in Fig. 23(*e*) indicate attached flow across the whole wake passing period, although trajectory *Z* is on the verge of separation. At lower Reynolds numbers, the shape factors indicate separated flow for some or all of the wake passing period.

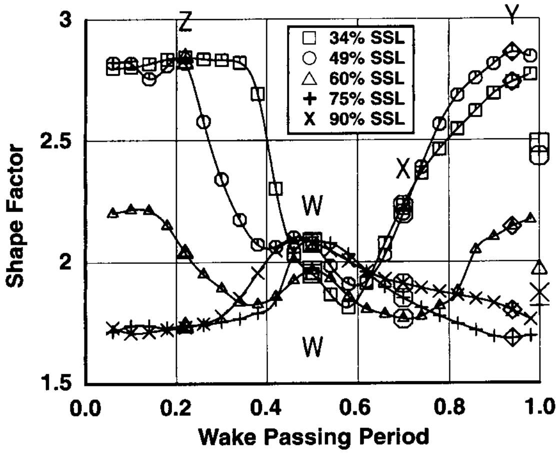

Fig. 25 Variation of shape factor across wake-passing period for compressor high loading, suction surface of the third-stage stator. Trajectories *W*, *X*, *Y*, and *Z* are identified, Test Point 3.

9.0 Loading Effects on Boundary Layers

This section examines the influence of airfoil loading on boundary layer development. It provides the evidence for Fig. 10e of the discussion in Section 5.0. It shows that increasing the loading strengthens both the wake-induced transitional/turbulent strips and the associated calmed effect. The transitional and turbulent strips move closer to the leading edge as the calming becomes more effective in suppressing flow separation and delaying transition. The turbulent strips eventually dominate in the wake-induced regions as their trailing boundaries increasingly terminate the region of transition between wakes. The findings are evaluated relative to those for the baseline. The results are listed in Table 5.

Loading effects were evaluated at Test Points 1, 2B, 3 and 4 shown in Figs. 2 and 3(*a*) and in Table 2 of Part 1.

9.1 Picture Constructed From Surface Film Data

Low Loading. The *s*–*t* diagram of random unsteadiness is shown for the low-loading Test Point 1 in Fig. 24(*a*). Although all of the regions *A*–*F* are identifiable, boundary layer development has shifted downstream compared to that for the baseline loading in Fig. 24(*b*).

A large region *A* of perturbed laminar flow extends to about 60 percent SSL in Fig. 24(*a*). Along the wake path W, the wake-induced transitional strips *B* are visible, but they are weak and their onset at 30 percent SSL is 11 percent SSL farther downstream than those for the baseline. Consequently the associated calmed region is hardly present. The wake-induced turbulent strip *C* begins at 70 percent SSL, which is 8 percent SSL farther downstream than for the baseline.

Along the path between wakes, the regions of transitional and turbulent boundary layers, regions *E* and *F* respectively, are clearly identifiable. Transition begins in region E at about 60 percent SSL, with the onset boundary having a positive slope.

High Loading. As loading is increased past the baseline to near peak pressure Test Point 3, the entire picture of boundary layer development shown in Fig. 24(*c*) has shifted toward the leading edge.

Along the wake path, the wake-induced transitional strips *B* are stronger and start near the leading edge. The location of 0.75 intermittency has likewise moved upstream to about 35 percent SSL. Consequently the associated calmed regions begin sooner and are stronger. The wake-induced turbulent strip, *C*, begins at about 42 percent SSL.

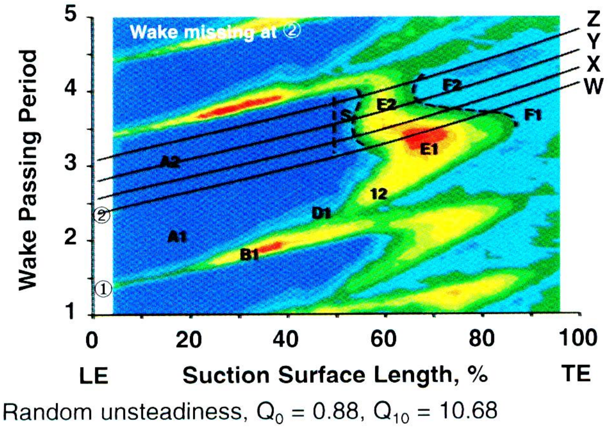

Fig. 26 Effect of reduced wake frequency on boundary layer development. Suction surface, compressor stator S3. The one airfoil removed from the stage three rotor eliminates the wake-induced strip for event ②. Nominal rotor solidity = 1.11. Decreased solidity = 0.56.

Along the nonwake path, the calmed region is very effective in suppressing flow separation and delaying transition. The boundary of transition onset for region *E* now has a negative slope and the lobe that was present at point 12 in Fig. 13(*a*) and Fig. 24(*b*) is gone in Fig. 24(*c*). This is consistent with the location of 0.75 intermittency in the wake-induced strip having moved upstream. The region of transition between wakes, *E*, has moved upstream to about 50 percent SSL. The trailing boundary of wake-induced turbulent strip *C*, having moved forward, terminates region *E* sooner in Fig. 24(*c*) than it does for the baseline loading in Fig 24(*b*). Turbulent region *F* begins at about 77 percent SSL.

Near-Stall Loading. The random unsteadiness for the near stall loading (Test Point 4) is shown in Fig. 24(*d*). At this high incidence and high loading (see Fig. 3(*a*)), the boundary layer undergoes separated-flow transition near the leading edge with turbulent reattachment at about 5 percent SSL. Except for small periodic imprints, the figure is otherwise featureless. The time-average wall shear stress (not shown) continuously decreases for the near stall loading downstream of reattachment.

9.2 Boundary Layer Surveys. The boundary layer profiles at high loading (not shown) are similar in structure to those for the baseline loading in Fig. 15, except for the following distinctions. All of the profiles at high loading show the effects of being under an adverse pressure gradient for a longer extent of the airfoil suction surface. For example, the high loading profiles at 49 percent SSL are nearly identical to those at 60 percent SSL for the baseline.

The integral parameters at high loading are also similar in shape to those of the baseline in Fig. 16. However, the boundary layers at high loading are about 12 percent thicker, with maximum thickness occurring in the wake-induced region. Importantly, the shape factors in Fig. 25 are below 2.8 everywhere, indicating an attached boundary layer across the entire wake passing period.

9.3 The Pressure Surface. The effect of loading on boundary layer development along the pressure surface is described without figures. At low loading, separated flow occurs on the pressure surface at the leading edge due to the negative incidence angle and very adverse pressure gradient seen in Fig. 3(*a*). Turbulent reattachment occurs at about 8 percent PSL and a turbulent boundary layer continues to the trailing edge. At high loading the turbulence intensity is higher and a turbulent boundary layer develops near the leading edge and continues to the trailing edge.

10.0 Effects of Wake Frequency, Turbulence Level and Rods

This section examines the effects of changing the frequency of occurrence of the incoming wakes on boundary layer development of embedded stages. It also examines the use of rods to simulate the effects of airfoil wakes and shows how the picture changes when the level of turbulence intensity in the wake is changed. This section provides the evidence for Figs. 10(*g*, *i*) of the discussion in Section 5.0 of Part 1.

10.1 Effect of Wake Frequency. The frequency of occurrence of the upstream wakes was reduced by removing one airfoil from the third-stage rotor, R3, leaving all other airfoils in the stage unchanged. This reduced the local solidity of the affected rotor passage from 1.11 to 0.56. The *s*–*t* diagram of random unsteadiness along the stator suction surface is shown for this test configuration in Fig. 26. Two wake-passing events are marked along the ordinate. Event 1, with wake-induced strip B_1, calming D_1 and transition/turbulent regions between wakes E_1 and F_1, is identical to the baseline in Fig. 13(*a*). Event 2 is clearly the passage for the missing rotor airfoil.

Since the wake is missing for event 2, so is the wake-induced strip and therefore so is the associated calming. In addition, the calming from region D_1 has by this time subsided. Yet, a large laminar region A_2 still persists in the passage. The location of transition onset has not moved appreciably toward the leading edge. However, the transition process for event 2 is now quite different. Flow separation occurs at 50 percent SSL as indicated by shear stress (not shown) going to zero. The region of separated flow between wakes is marked as "*S*" in Fig. 26. Separated-flow transition develops, the transition region is short, the flow reattaches in E_2 and a turbulent boundary layer appears in region F_2, as determined from raw data. This confirms the sketch in Fig. 10(*g*) in Section 5.0 of Part 1.

Thus, when the wake frequency (reduced frequency) is high enough that calming does not decay to zero before the appearance of the next wake, bypass transition dominates, as in region E_1. As calming runs out when wake frequency is reduced, separated-flow transition dominates, as in region E_2.

10.2 Effect of Wake-Turbulence Intensity and Rods.

In an effort to simulate periodic wake effects in turbomachines, some investigators have placed moving rods ahead of stationary cascades or stationary rods ahead of single rotor facilities (Pfeil and Herbst, 1979; Orth, 1993; Wittig et al., 1988; O'Brien and Capp, 1989; McFarland and Tiderman, 1992). The wakes from the rods then impinge periodically on the downstream airfoils.

We used this scheme in the multistage environment to evaluate the effects of changing the wake-turbulence intensity while leaving other test conditions the same. In these tests, a rod was inserted into the Rotor 3 disk at the location where the airfoil had previously been removed for the test results presented in Section 10.1. As described in the appendix, measurements of rod wake characteristics were made and two rods, identified as rod 1 and rod 2 in Table A1 of the appendix, were selected for these tests. The rods gave measured wake-turbulence intensities of 16 and 7.3 percent, respectively, at measurement Plane 3.5 in Fig. 1. The tests were conducted at baseline Test Point 2B.

The *s–t* diagram shown in Fig. 27(*a*) contains results for rod 1, which produced the high wake TI of 16 percent. The results are shown for the same blade passing periods as those in Fig. 26. Event 1 in Fig. 27(*a*) is caused by the rotor airfoil wake (TI ≈ 5.5 percent). Event 2 is caused by the rod wake, whose velocity defect was only about 12 percent greater than that of the airfoil. The high turbulence intensity in the rod wake produces a very strong wake-induced transitional strip, B_2, which already has high intermittency near the leading edge. The calmed region for the rod-generated wake, D_2, is now extensive and strong. The calming effect eliminates any tendency for flow separation and significantly delays transition onset in Region E_2 between wakes until about 67 percent SSL. As a result of strong calming, the slope of the onset boundary is negative. The trailing boundary of the wake-induced turbulent strip from the rod, C_2, progressively terminates the region of transition between wakes in E_2. Clearly the picture for Event 2 is much different from that for Event 1, with the fundamental differences resulting from the differences in turbulence intensity of the wakes. This confirms the picture in Fig. 10(*i*) of the discussion in Section 5.0 of Part 1.

The *s–t* diagram shown in Fig. 27(*b*) contains results for rod 2, which produced the much lower wake TI of 7.3 percent. Event 2 in Fig. 27(*b*) is caused by this rod wake, whose velocity defect is about the same as that of the airfoil. Although the wake-induced strip B_2 is still somewhat stronger than strip B_1 produced by the airfoil, it is now much weaker than that in Fig. 27(*a*) and its maximum unsteadiness is located farther aft. Consequently, the transition picture in region E_2 of Fig. 27(*b*) is now much closer in shape to that produced by the airfoil wake, as seen by the positive slope of the line of transition onset. However, the level of unsteadiness in the lobe at point 12 for event 2 is lower than that produced by the airfoil wake for event 1. Also, region E_2 develops farther aft than region E_1. These features are indicative of stronger calming effects from the rod wake.

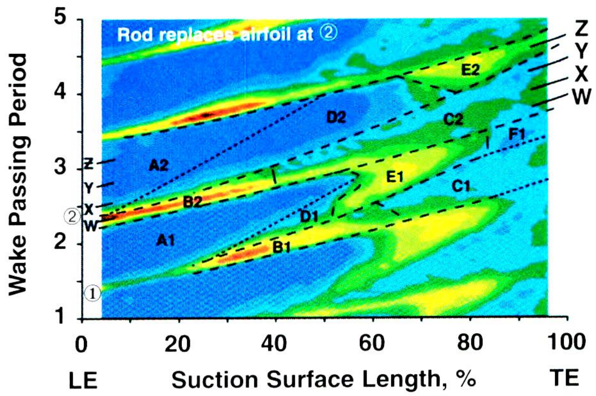

a) Wake-generating rod, l/d = 7.0, TI = 16%, $Q_0 = 0.70$, $Q_{10} = 10.00$

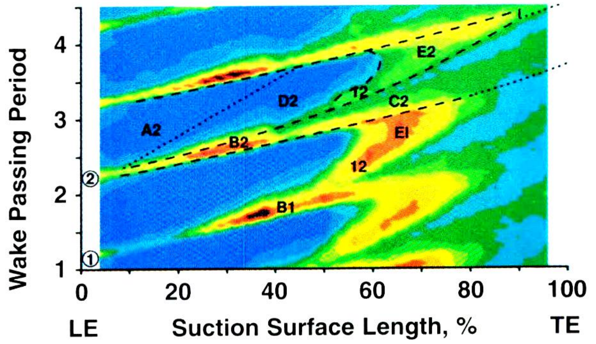

b) Wake-generating rod, l/d = 21, TI = 7.3%, $Q_0 = 0.75$, $Q_{10} = 9.00$

Fig. 27 Random unsteadiness showing effect of wake turbulence intensity on boundary layer development. Suction surface, compressor stator S3. A rod for event ② replaces the rotor airfoil removed in Fig. 26.

The results in Fig. 27 clearly show that as turbulence intensity is increased, the wake-induced strips and the location of high intermittency move toward the leading edge, calming becomes more effective and the region of transition between wakes moves aft.

Based on these findings, we conclude that the level of turbulence intensity of the incoming wakes, rather than the level of the velocity defect, is the dominant factor not only in producing the wake-induced strips found in turbomachinery but also in determining their strength and the effectiveness of calmed regions they produce. Selecting a rod size and location based solely upon the criterion of duplicating the velocity defect of the incoming wake, as some papers have reported, can easily result in turbulence intensities from the rods being too high relative to those from airfoils in high efficiency turbomachines. This difference can alter the transitional picture significantly and can mislead one about the nature of transition in multistage turbomachinery. Great care should be exercised when using rods to simulate airfoil wakes.

Conclusions

Conclusions about boundary layer development in compressors drawn from our experiments are given at the end of Part 1.

References

McFarland, V. E., and Tiderman, W. G., 1992, "Viscous Interaction Upstream and Downstream of a Turbine Stator Cascade With a Periodic Wake Effect," ASME Paper No. 92-GT-162.

O'Brien, J. E., and Capp, S. P., 1989, "Two-Component Phase-Averaged Turbulence Statistics Downstream of a Rotating Spoked-Wheel Wake Generator," ASME JOURNAL OF TURBOMACHINERY, Vol. 111, pp. 475–482.

Orth, U., 1993, "Unsteady Boundary Layer Transition in Flow Periodically Disturbed by Wakes," ASME JOURNAL OF TURBOMACHINERY, Vol. 15, pp. 707–713.

Pfeil, H., and Herbst, R., 1979, "Transition Procedure of Instationary Boundary Layers," ASME Paper No. 79-GT-128.

Wittig, S., Schulz, A. Dullenkopf, K., and Fairbank, J., 1988, "Effects of Free-Stream Turbulence and Wake Characteristics on the Heat Transfer Along a Cooled Gas Turbine Blade," ASME Paper No. 88-GT-179.

APPENDIX

Tests were conducted to measure the wake characteristics of cylindrical rods. The measurements were made in a calibration jet having a diameter of 76.2 mm (3.00 in.). This diameter was large enough to assure that all testing was conducted well within the potential core of the jet. Rods having diameters, *d*, of 1.60 mm (0.063 in.), 1.88 mm (0.074 in.), 2.11 mm (0.085 in.), and 2.36 mm (0.093 in.) were tested. Profiles of velocity and turbulence intensity through the wake were measured at various distances downstream from the rod, l, using an "X" hot-film probe. The results, which are presented in Fig. A1, were normalized to be independent of rod diameter.

These plots were used to select the appropriate size rod as follows: (1) For the criterion of matching peak wake-turbulence intensity of the airfoil, find the level of turbulence intensity of the airfoil to be matched along the ordinate of Fig. A1(*a*). This sets the rod l/d. One can then determine the velocity defect in the rod wake and the width of the rod wake by using Figs. A1(*b, c*), respectively; or, (2) for the criterion of matching wake velocity defect, find the wake defect of the airfoil to be matched along the ordinate of Fig. A1(*b*). This sets the rod l/d. One can then find the other wake characteristics in Figs. A1(*a, c*).

The results of these tests were used for selecting appropriately sized rods that would replace the airfoil removed from the third-stage rotor. Two rod diameters of 2.36 mm (0.093 in.) and 1.88 mm (0.074 in.) were used. For reference, the trailing edge thickness of our rotor airfoil was 1.83 mm (0.072 in.). The placement of the rods and other parameters are shown in Table A1, where l_z is the axial distance from measurement Plane 3.5 in Fig. 1 to the rod location. The larger rod was located in the trailing edge plane of the rotor airfoils. Values of l/d of 7.0, 21 and 40 were achieved with the rods, where the value of "l" is the computed streamwise distance from the rod to Plane 3.5. In general, the characteristics of the rod-generated wakes measured at Plane 3.5 were consistent with those from Figs. A1(*a, b*), except for the rod located farthest upstream inside the rotor passage.

Rods 1 and 2 in Table A1 had very different levels of turbulence intensity but nearly the same velocity defect in the wake. Test results from these two rods are presented in Section 10.2 to show the effects of turbulence intensity on wake-induced strips and calming.

Based upon our calibration test results in Fig. A1, we selected rod 3 to produce a slightly lower turbulence intensity than that of the airfoil. However in the actual embedded stage environment, this rod produced a somewhat higher turbulence intensity than of the airfoil and a much wider wake than expected. This may result from one or both of the following reasons: First, the unsteadiness level of the compressor flowfield in which the rod was installed is much greater than that of the calibration jet. Second, the rod was located about 0.35 chord downstream of the leading edge such that the rod wake developed in a diffusing flowfield. This rod produced a picture about the same as that shown in Fig. 27(*b*) with a somewhat wider Region B.

Table A1 Parameters for rod tests

	d mm	l_z mm	l/d	TI (Fig. A1a)	TI (Pl 3.5)	ΔV/V
Airfoil	1.83*	12.7	—	—	5.5%	22%
rod 1	2.36	12.7	7.0	14%	16%	25%
rod 2	1.88	31.8	21	7.4%	7.3%	22%
rod 3	1.88	61.0	40	4.6%	6.2%	16%

*trailing edge thickness

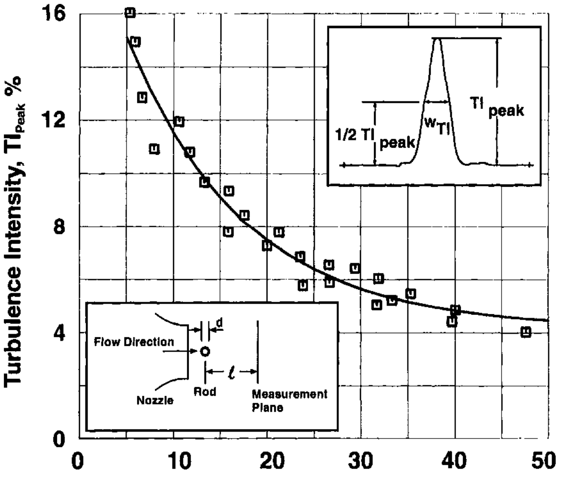

a) Peak turbulence intensity

Fig. A1 Wake characteristics of cylindrical rods

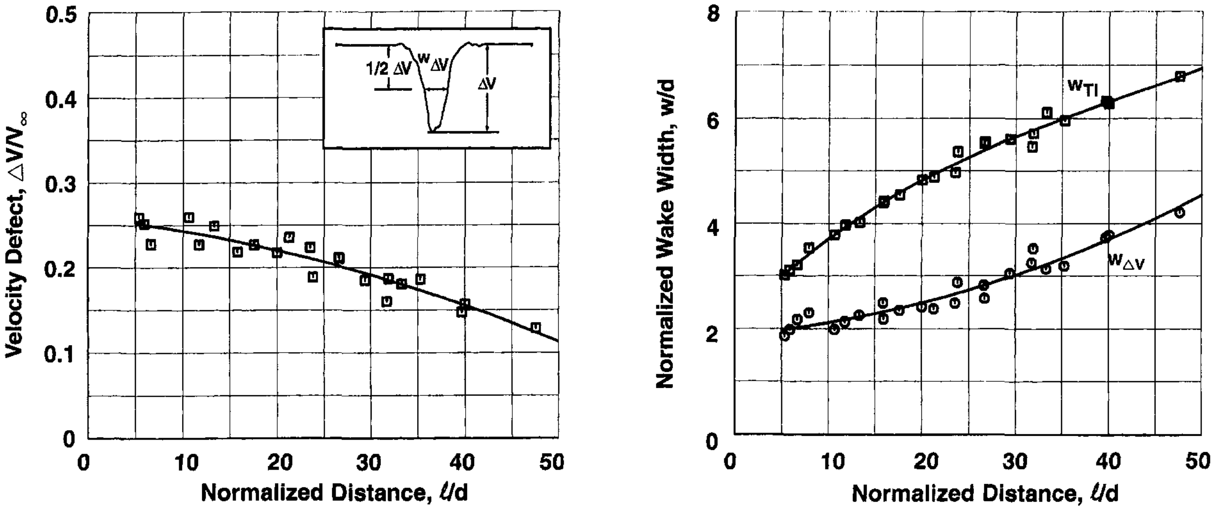

b) Normalized maximum velocity defect of wake

c) Normalized wake width for turbulence intensity and velocity defect

Fig. A1 (Continued)

Evaluation of Flow Field Approximations for Transonic Compressor Stages

D. J. Dorney
Western Michigan University,
Kalamazoo, MI 49008

O. P. Sharma
Pratt and Whitney,
East Hartford, CT 06108

The flow through gas turbine compressors is often characterized by unsteady, transonic, and viscous phenomena. Accurately predicting the behavior of these complex multi-blade-row flows with unsteady rotor–stator interacting Navier–Stokes analyses can require enormous computer resources. In this investigation, several methods for predicting the flow field, losses, and performance quantities associated with axial compressor stages are presented. The methods studied include: (1) the unsteady fully coupled blade row technique, (2) the steady coupled blade row method, (3) the steady single blade row technique, and (4) the loosely coupled blade row method. The analyses have been evaluated in terms of accuracy and efficiency.

Introduction

Experimental data from jet-engine tests have indicated that unsteady blade row interaction effects can have a significant impact on the performance of compressor stages. Modern compressors can experience three types of unsteady flow mechanism associated with the interaction between adjacent blade rows. The first interaction mechanism is referred to as potential-flow interaction, and results from the variations in the velocity potential or pressure fields associated with the blades in adjacent rows. This type of interaction is of serious concern when the axial spacing between adjacent blade rows is small or the flow Mach number is high. The second interaction mechanism is wake interaction. Wake interaction is the effect upon the flow through a downstream blade row of the vortical and entropic wakes shed by one or more upstream rows. The third interaction mechanism is called shock wave interaction, and is caused by the shock system in a given blade row extending into the passage of an adjacent blade row.

The different blade row interaction mechanisms require different levels of viscous flow modeling complexity to capture the physics associated with a given flow field. In the unsteady fully coupled blade row (FCBR) techniques, the flow fields of multiple blade rows are solved simultaneously and the relative position of one or more of the blade rows is varied to simulate blade motion (e.g., Rai, 1989; Rao et al., 1994a, b). FCBR solution techniques can accurately predict the unsteady flow phenomena in compressor stages (within the limits of turbulence and transition modeling), but can also require enormous computer resources. The next level in the modeling heirarchy includes steady coupled blade row (SCBR) techniques. In a SCBR simulation, a steady solution is obtained for each blade row, and the effects of adjacent blade rows are included through the use of mixed-out steady boundary conditions (e.g., Dawes, 1992). Additionally, several of the SCBR methods incorporate deterministic stresses to model the unsteady effects of neighboring blade rows approximately (Adamczyk, 1985; Rhie et al., 1995; Le-Jambre et al., 1995). Perhaps the least sophisticated modeling techniques for multiple-blade row geometries are the steady single blade row (SSBR) methods (e.g., Denton and Singh, 1979; Denton, 1986; Chima, 1987; Davis et al., 1988; Crook and Delaney, 1992). In SSBR simulations, each blade row of a turbomachinery stage is solved in isolation. Thus, each blade row operates in the absence of interaction effects. More recently, the concept of unsteady loosely coupled blade row (LCBR) simulations has been introduced (Chen et al., 1994; Dorney et al., 1995). In the LCBR method, which builds upon an underlying SSBR or average-passage solution, unsteady boundary conditions are specified at the inlet and exit of each blade row to account for the interaction mechanisms. The inter-blade-row boundary conditions are periodically updated to couple the unsteady flow effects from the upstream and downstream blade rows. The LCBR method has been shown to be computationally efficient, while retaining a significant amount of the unsteady flow physics.

The focus of the present effort has been to evaluate the accuracy of each of the four modeling techniques in predicting the performance and losses of a transonic high-pressure compressor stage. For the purposes of this investigation, the results of the FCBR simulations will be considered the benchmark data. The modeling comparison has been accomplished using a quasi-three-dimensional Navier–Stokes procedure.

Numerical Integration Procedure

The governing equations considered in this study are the time-dependent, quasi-three-dimensional Reynolds-averaged Navier–Stokes equations:

$$Q_t + F_x + G_y = 0 \qquad (1)$$

where the vector Q represents the primary variables, ρ, ρu, ρv, and e_t. The variables F and G represent the components of the inviscid and viscous mass, momentum, and energy fluxes, as well as streamtube contraction terms. The viscous fluxes are simplified by incorporating the thin layer assumption (Baldwin and Lomax, 1978). In the current study, viscous terms are retained in the direction normal to the blade surface. To extend the equations of motion to turbulent flows, an eddy viscosity formulation is used and the turbulent viscosity is calculated using the Baldwin–Lomax (1978) algebraic turbulence model.

The numerical procedure used in the computational analysis consists of a time-marching, implicit, finite-difference scheme. The procedure is third-order spatially accurate and second-order temporally accurate. The inviscid fluxes are discretized according to the scheme developed by Chakravarthy and Osher (1982). The viscous fluxes are calculated using standard central differences. An alternate direction, approximate-factorization technique is used to compute the time rate changes in the primary variables. In unsteady simulations, Newton subiterations are used at each global time step to increase stability and reduce

---

Contributed by the International Gas Turbine Institute and presented at the 41st International Gas Turbine and Aeroengine Congress and Exhibition, Birmingham, United Kingdom, June 10–13, 1996. Manuscript received at ASME Headquarters February 1996. Paper No. 96-GT-371. Associate Technical Editor: J. N. Shinn.

linearization errors. For the unsteady simulations performed in this study, two Newton subiterations were performed at each time step. Further details of the numerical technique can be found in Dorney and Verdon (1994) and Dorney et al. (1995).

Boundary Conditions

The theory of characteristics is used to determine the boundary conditions at the inlet and exit of the computational domain. For subsonic inlet flow, the total pressure, total temperature, and flow angle are specified, while the upstream running Riemann invariant, $R_2 = u - (2a/(\gamma - 1))$, is extrapolated from the interior of the computational domain. For subsonic outflow, the v velocity component, entropy, and the downstream running Riemann invariant are extrapolated from the interior of the computational domain. The average pressure ratio in the circumferential direction, P_2/P_{t1}, is specified at the computational exit. In the LCBR simulations, nonreflecting unsteady boundary conditions are implemented at the inlet and exit of each blade row (Dorney and Verdon, 1994; Dorney et al., 1995). A periodicity condition is enforced at midpassage in the circumferential (y) direction.

No-slip boundary conditions are enforced along the surfaces of the inlet guide vane (IGV) and rotor airfoils. It is assumed that the normal derivative of the pressure is zero at solid wall surfaces. In addition, a specified (zero) heat flux distribution is held constant in time along the solid surfaces. The flow variables of Q at zonal boundaries are explicitly updated after each time step by interpolating values from the adjacent grid.

Grid Generation

The Navier–Stokes analysis uses O- and H-type zonal grids to discretize the flow field and facilitate relative motion of the rotor. Algebraically generated H-grids are used in the regions upstream of the leading edge, downstream of the trailing edge, and in the interblade region. The O-grids, which are body-fitted to the surfaces of the airfoils and generated using an elliptic equation solution procedure, are used to resolve the viscous flow properly in the blade passages and to apply the algebraic turbulence model easily (see Fig. 1).

Results

Experimental and Computational Models. The experimental geometry modeled in this investigation is a high-pressure transonic compressor stage containing 76 IGV air-foils and 40 rotor airfoils. The design Mach number at the IGV inlet is $M_1 = 0.650$ and the design flow angle is $\alpha_1 = 19.3$ deg. The inlet total pressure is approximately $P_{t1} = 98.5$ kPa and the total temperature is approximately $T_{t1} = 298$ K. The rotor rotates at $\Omega = 8267$ rpm, the ratio of the exit static pressure to the inlet total pressure is $P_3/P_{t1} \approx 1.028$, and the free-stream unit Reynolds number is 88,400/cm. The axial gap between the IGV and rotor airfoils is 14.3 percent of the rotor axial chord.

In the numerical simulations the compressor is modeled using 2 IGVs and 1 rotor blade. Thus, the number of IGVs in the first row was increased to 80 and the size of the airfoils was reduced by a factor of 76/80 to maintain the same blockage. The IGV passages have been discretized with 151 × 45 computational grid points in each O-grid and 130 × 45 grid points in each H-grid, for a total of 25,290 grid points in the two IGV passages. The rotor passages have been discretized with 201 × 51 in the O-grid and 210 × 45 in the H-grid, for a total of 19,701 grid points. The entire compressor stage was modeled with a total of 44,991 grid points. The grid spacing at the airfoil surface resulted in an average value of y^+, the nondimensional distance of the first grid point above the surface, of approximately 1.0 for the both the IGV and rotor airfoils. Figure 1 illustrates the computational grid for the compressor stage. For the SSBR and LCBR simulations, the appropriate grid sections from the topology shown in Fig. 1 were used.

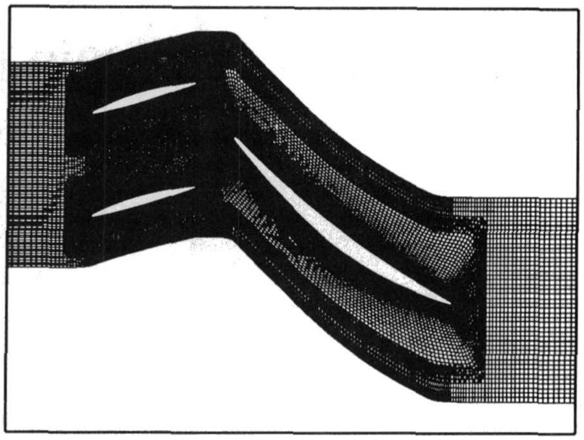

Fig. 1 **Computational grid for the IGV-R5 compressor stage**

The numerical flow simulations were performed on a Digital Equipment Corporation Alpha 3000-300 workstation. The unsteady FCBR simulation was run for 25 global cycles at 6000 iterations/cycle. A global cycle corresponds to the rotor blade rotating through an angle of $2\pi n/N$ where n is the number of IGV airfoils in the simulations (i.e., $n = 2$) and N is the total number of IGVs assumed to be in the actual machine ($N = 80$). The unsteady LCBR simulations for the IGV were run for 5 global cycles at 1500 iterations/cycle, while the rotor simulations were run for 5 global cycles at 2500 iterations/cycle. Typical calculations required 0.00027 seconds per grid point per time step computation time. Note that the steady solutions were deemed to be converged when the residual of the total energy was reduced four orders of magnitude. The unsteady solutions were considered to be time-periodic when the amplitude of the unsteady pressure variations at several test points (near the airfoil leading and trailing edges, and in the vicinity of the rotor shock) did not change more than 3 percent from one blade-passing cycle to the next.

FCBR Simulation. The results of the FCBR simulation, which captures all three interaction mechanisms, have been chosen to serve as the baseline results. The primary drawback to

Nomenclature

a = speed of sound
e_t = total energy
M = Mach number
P = static pressure
Re = inlet reference Reynolds number
S = entropy
T = static temperature

u, v = x, y components of velocity
α = absolute flow angle
β = relative flow angle
ρ = density
ω = loss coefficient = $2(P_{t1} - P_{t2})/(\gamma P_1 M_1^2)$
Ω = rotor rotational speed

Subscripts

rel = relative reference frame quantity
t = stagnation quantity
x, y = first derivative with respect to x, y
1 = stator inlet quantity
2 = rotor inlet quantity
3 = rotor exit quantity
∞ = free-stream quantity

Table 1 Comparison of computational requirements

CPU TIME (min)	FCBR	SCBR	SSBR	LCBR
IGV	—	—	1,704	2,454
ROTOR	—	—	2,401	3,391
Total	33,744	7,582	4,105	5,845

the FCBR technique is that it requires significantly more computation time than any of the other three methods (see Table 1).

Figures 2–5 illustrate the static pressure contours at 25, 50, 75, and 100 percent of a blade-passing cycle, respectively. The flow field is characterized by a strong shock wave at approximately 40 percent of the axial chord on the suction surface of the rotor. The shock system extends upstream of the rotor and into the IGV passage, where it intersects the suction-surface trailing edge region of an IGV (see Fig. 2). As the blade-passing cycle continues, the shock moves farther upstream along the suction surface of one IGV, and intersects the pressure-surface trailing edge region of the adjacent IGV (see Fig. 3). In addition, the shock is reflected as it impacts the suction and pressure surfaces of the adjacent IGVs (see Figs. 3 and 4). The shock system slowly dissipates as it propagates upstream through the IGV passage (see Figs. 4 and 5). The movement of the rotor shock into the IGV passage causes the losses in the IGV to be nearly as large as those in the rotor (see Table 2).

Figures 6–9 show the entropy contours from the same increments during the blade-passing cycle. The entropy contours highlight the convection of the IGV wakes through the rotor passage, as well as the development of the airfoil boundary layers. The rotor suction-surface boundary layer separates at approximately 70 percent of the axial chord, although the separation point varies during the blade-passing cycle. Shedding is evident from the separated flow region to the trailing edge of the suction surface. The shed fluid results in high-loss regions, which are convected downstream as discrete eddies.

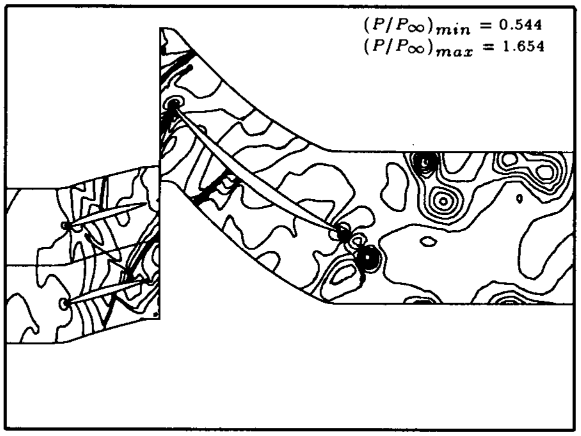

Fig. 2 Static pressure contours from the FCBR simulation: 25 percent cycle

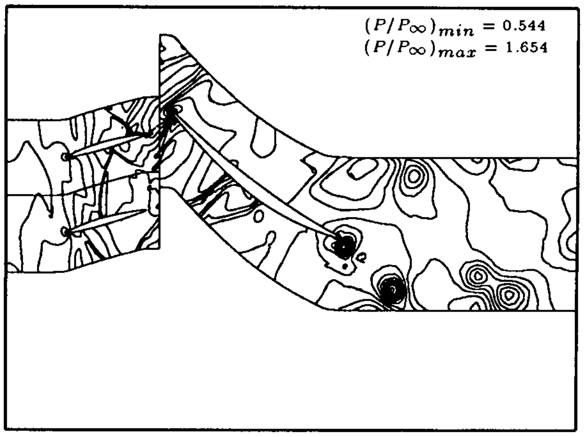

Fig. 4 Static pressure contours from the FCBR simulation: 75 percent cycle

The unsteady pressure envelopes (i.e., minimum, maximum, and time-averaged) for the surfaces of the IGV and rotor are illustrated in Figs. 10 and 11, respectively. A considerable amount of unsteadiness is observed over the entire surface of the IGV (see Fig. 10). The unsteadiness is primarily due to the impingement of the rotor shock system, although interaction with the rotor potential field contributes to the unsteadiness near the IGV trailing edge. The rotor experiences significant pressure fluctuations along the pressure surface, and downstream of the shock on the suction surface (see Fig. 11). Much less unsteadiness is evident from the leading edge of the suction surface to the location of the shock. The location of the shock varies approximately 18 percent during the blade-passing cycle. The unsteadiness in the rotor passage is mainly due to the IGV wakes, and to a lesser extent due to the IGV potential field and the unsteady movement of the suction-surface shock.

Table 2 contains the time-averaged quantities at the inlet and exit of each blade row. The FCBR quantities presented in Table 2 were time-averaged over 5 blade-passing cycles. Of particular interest are the high loss in the IGV and the predicted total-to-

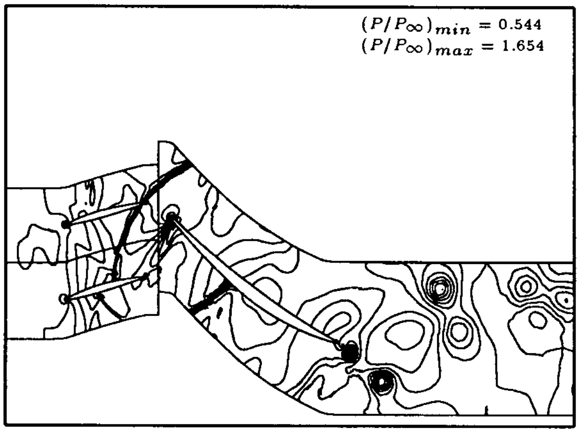

Fig. 3 Static pressure contours from the FCBR simulation: 50 percent cycle

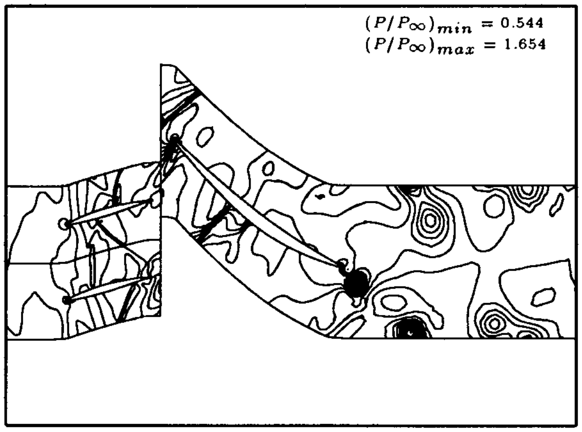

Fig. 5 Static pressure contours from the FCBR simulation: 100 percent cycle

Table 2 Inlet and exit flow quantities for the IGV-R5 compressor

	IGV FCBR	IGV SCBR	IGV SSBR	IGV LCBR	ROTOR FCBR	ROTOR SCBR	ROTOR SSBR	ROTOR LCBR
$M_{in}(abs)$	0.6618	0.6549	0.6674	0.6519	0.6641	0.6474	0.5905	0.6420
$M_{in}(rel)$	0.6618	0.6549	0.6674	0.6519	0.9715	0.9607	0.9228	0.9230
$M_{out}(abs)$	0.6641	0.6494	0.6634	0.6573	0.7559	0.7488	0.7107	0.7062
$M_{out}(rel)$	0.6641	0.6494	0.6634	0.6573	0.5816	0.5772	0.5901	0.5879
$(T_t)_{in}(K\ abs)$	297.58	297.64	297.63	297.63	297.48	296.58	301.87	301.42
$(T_t)_{in}(K\ rel)$	297.58	297.64	297.63	297.63	326.50	324.22	326.03	326.10
$(T_t)_{out}(K\ abs)$	296.58	296.58	297.62	297.03	335.84	337.76	335.39	334.17
$(T_t)_{out}(K\ rel)$	296.58	296.58	297.62	297.03	327.52	323.89	325.20	325.90
$\beta_{in}(abs)$	19.29°	19.30°	19.30°	19.40°	16.50°	16.61°	17.05°	17.20°
$\beta_{in}(rel)$	19.29°	19.30°	19.30°	19.40°	−49.48°	−49.60°	−49.50°	−49.18°
$\beta_{out}(abs)$	16.50°	16.58°	16.30°	16.90°	46.80°	49.59°	47.36°	47.94°
$\beta_{out}(rel)$	16.50°	16.58°	16.30°	16.90°	−36.05°	−33.19°	−32.87°	−35.06°
ω	0.0931	0.0270	0.0261	0.0420	0.0947	0.1168	0.0991	0.1005
$(y^+)_{avg}$	1.15	0.98	0.98	1.15	1.10	1.25	1.25	0.95
η_{tt}	--	--	--	--	0.894	0.902	0.915	0.904

total efficiency of $\eta_{tt} = 0.894$. Note that the loss in the IGV passage is calculated between the computational inlet and the interface between the IGV and rotor grids, while the rotor loss is calculated between the interface of the grids and the computational exit.

SCBR Simulation. The SCBR technique is an attractive alternative to the FCBR method because of its computational efficiency (see Table 1). The SCBR technique used in this investigation employs steady, mixed-out boundary conditions to transfer information between the IGV and rotor passages. Specifically, the conserved fluxes are mixed out on both sides of the interface between the IGV and rotor grids (Giles, 1991). Mixing out the conserved fluxes has a solid foundation in the physics of the flow, but also generates an entropy rise across the mixing plane.

The IGV and rotor surface pressure distributions obtained with the SCBR technique are compared to the time-averaged results of the FCBR method in Figs. 12 and 13, respectively. The pressure distribution along the IGV exhibits reasonable agreement with the FCBR results, although the SCBR technique overpredicts the pressure on the aft portion of the pressure surface. The pressure distribution along the pressure surface of the rotor displays fair agreement with the FCBR results, with the SCBR technique underpredicting the pressure over the first 30 percent of the chord. Along the suction surface of the rotor the shock location is predicted approximately 14 percent too far downstream and the strength of the shock is greater than in

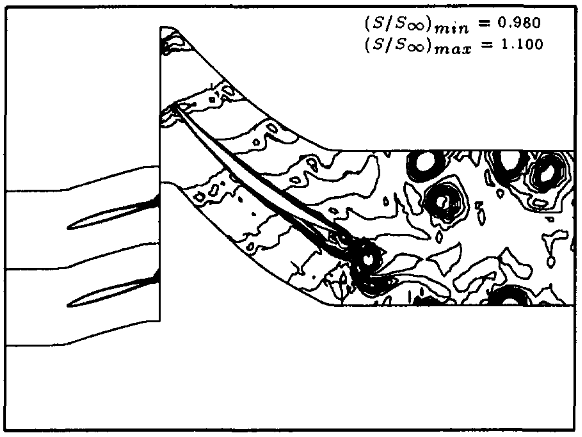

Fig. 6 Entropy contours from the FCBR simulation: 25 percent cycle

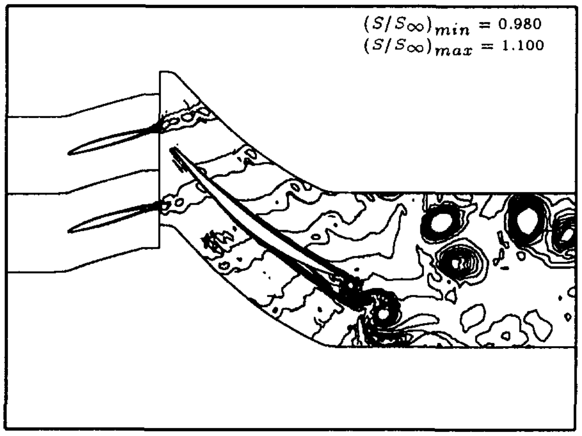

Fig. 7 Entropy contours from the FCBR simulation: 50 percent cycle

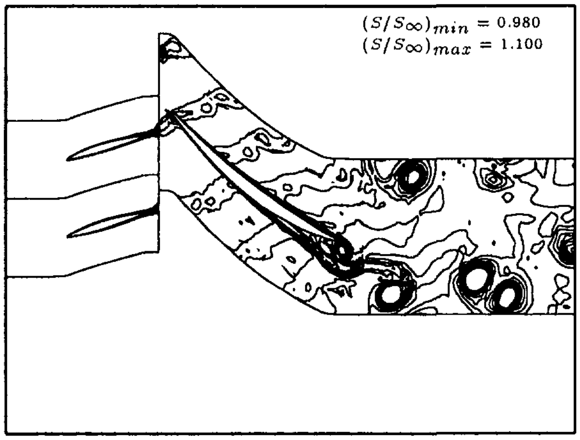

Fig. 8 Entropy contours from the FCBR simulation: 75 percent cycle

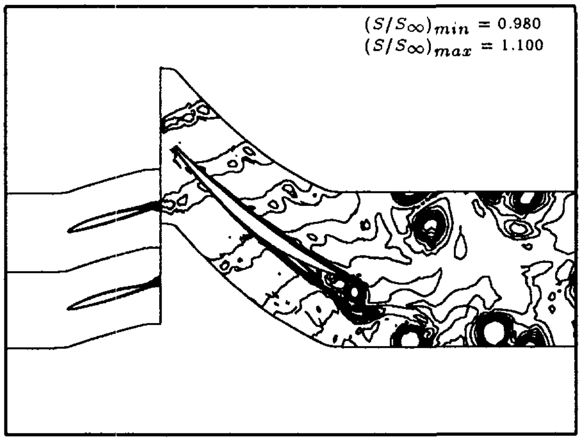

Fig. 9 Entropy contours from the FCBR simulation: 100 percent cycle

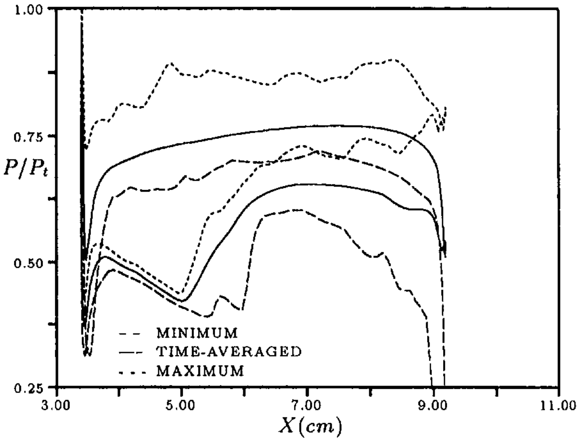

Fig. 11 Unsteady pressure envelope along the rotor: FCBR simulation

the FCBR simulation. It is hypothesized that the discrepancies in the rotor surface pressure are caused by differences in the IGV flow field; i.e., in the FCBR simulation there is strong interaction between the IGV wake and the rotor shock. Figure 14 contains the pressure contours for the rotor passage predicted using the SCBR technique. Figure 14 again shows that the SCBR technique predicts the shock too far downstream.

Table 2 contains the flow quantities at the inlet and exit of each blade row. The loss in the IGV is approximately 29 percent of the value predicted in the FCBR simulation, which is due to the mixing-out of the rotor shock at the IGV/rotor interface. The predicted loss in the rotor is similar the FCBR value. The loss in the rotor predicted using a SCBR method will, in general, be greater than that predicted by a FCBR technique because of the losses introduced by the mixing process used at the IGV/rotor boundary. The predicted efficiency, $\eta_{tt} = 0.902$, is higher than the FCBR value because of the underprediction of the IGV losses. Note that the losses in the steady (SCBR and SSBR)

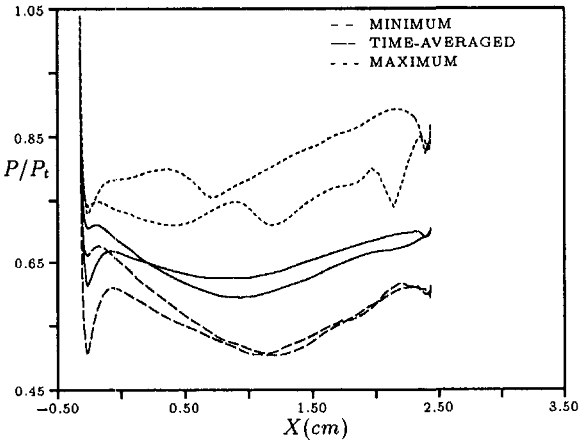

Fig. 10 Unsteady pressure envelope along the IGV: FCBR simulation

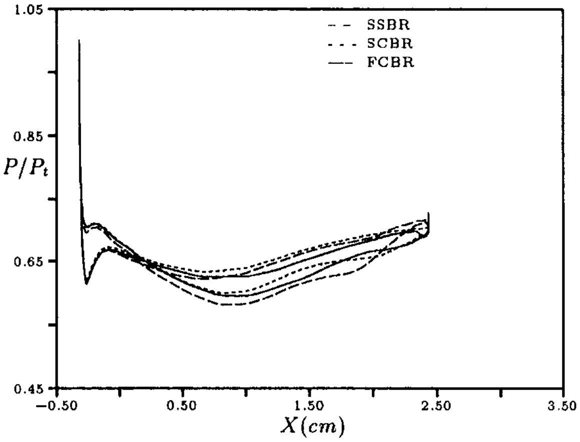

Fig. 12 IGV steady/time-averaged pressure distributions from the SSBR, SCBR, and FCBR simulations

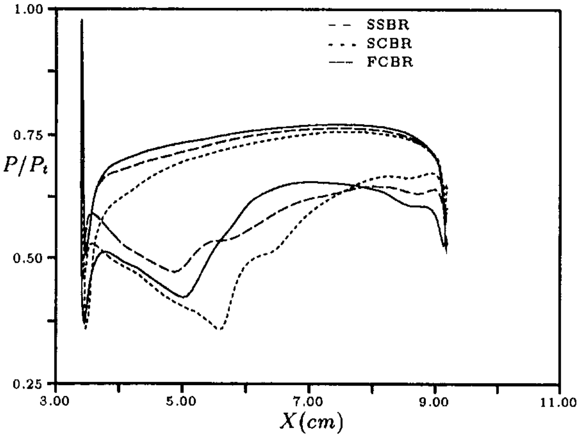

Fig. 13 Rotor steady/time-averaged pressure distributions from the SSBR, SCBR, and FCBR simulations

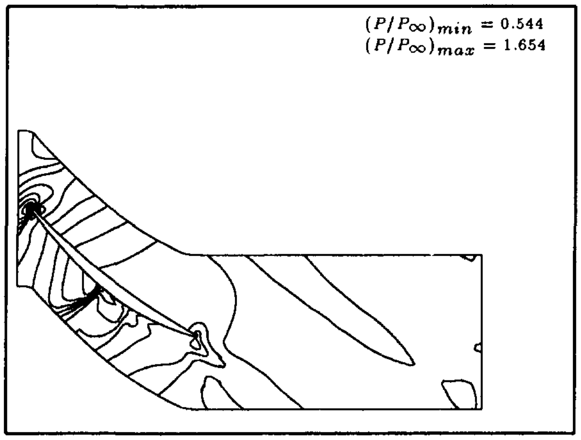

Fig. 14 Pressure contours from the SCBR simulation

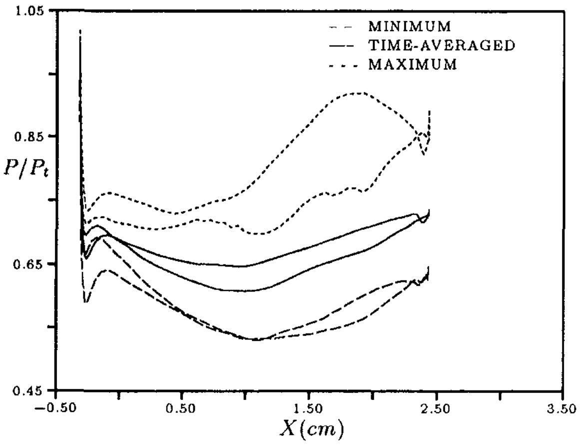

Fig. 16 Unsteady pressure envelope along the IGV: LCBR simulation

simulations are calculated between the same locations as in the FCBR simulation.

SSBR Simulation. The SSBR method requires much less computation time than the FCBR and SCBR methods (see Table 1), but also retains the least amount of interaction-related physics. In the SSBR method, each blade row is computed in isolation. Thus, no interaction mechanisms are included. Note, in the current SSBR simulations the flow variables at the exit of the IGV and the inlet of the rotor were specified based on a quasi-one-dimensional flow analysis, and were not modified based on the FCBR results.

The IGV and rotor surface pressure distributions obtained with the SSBR technique are compared to the results of the FCBR and SCBR methods in Figs. 12 and 13, respectively. The IGV pressure distribution exhibits fair agreement with the results of the other techniques on the pressure surface, but somewhat underpredicts the pressure on the suction surface. The pressure distribution along the rotor shows surprisingly good agreement with the FCBR data. The rotor results are fortuitous; in transonic simulations the SSBR technique does not always provide such accurate results when the shock is terminated at the interface between blade rows. Figure 15 contains the pressure contours for the rotor passage predicted by using the SSBR techniques. The position of the shock in the SSBR computation (see Fig. 15) is similar to that predicted in the FCBR simulation.

Table 2 contains the flow quantities at the inlet and exit of each blade row. Using the SSBR technique, the loss in the IGV is only 28 percent of that predicted using the FCBR method. The rotor loss is similar to that predicted in both the FCBR and SCBR techniques. The efficiency, $\eta_{tt} = 0.915$, is higher than both the FCBR and SCBR techniques because of the low losses predicted in the IGV and the absence of mixed-out boundary conditions. The results of the FCBR, SCBR, and SSBR simulations indicate that the effects of the rotor shock must be included in the IGV simulation to predict the losses and the stage efficiency accurately.

LCBR Simulation. A design-type solution method for turbomachinery stages should retain the physics of the FCBR simulation, but at the computational expense of an SSBR simulation. In the LCBR method, which builds upon an SSBR solution, unsteady boundary conditions (which are translated in time in the circumferential direction) are specified at the inlet and exit of each blade row to model the adjacent-blade-row interaction mechanisms. For example, the wake profile (in pertubation form) from the exit of the IGV passage is superimposed upon the flow variables at the inlet of the rotor boundary. The superimposed wake profile is translated in the time in the circumferential direction to simulate blade rotation. The unsteady boundary conditions are intermittently updated to allow for changes in the underlying steady flow solutions. The total computation time associated with the LCBR simulation is the sum of the steady (SSBR) and unsteady (LCBR) solution times, 5845 minutes, because the LCBR technique uses the SSBR solution for the initial flow field. Still, the LCBR technique requires significantly less computation time than either the FCBR or SCBR methods. It is worth noting that the LCBR solution depends on SSBR solution; therefore the SSBR solution must be reasonable to expect an accurate solution from the LCBR simulation.

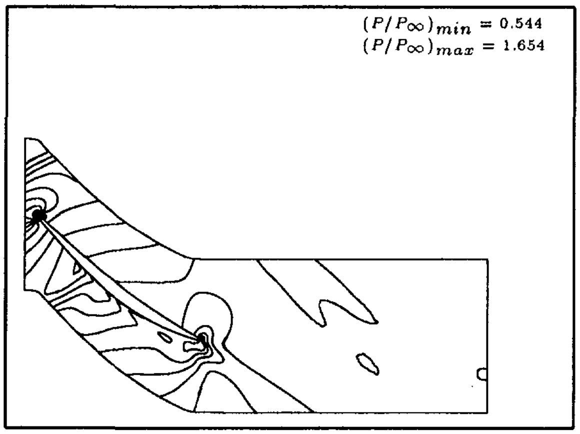

Fig. 15 Pressure contours from the SSBR simulation

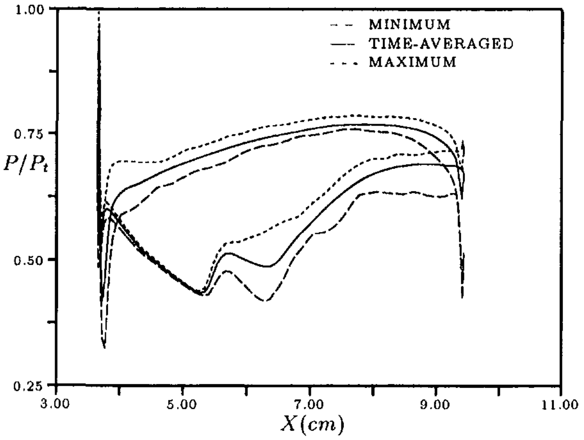

Fig. 17 Unsteady pressure envelope along the rotor: LCBR simulation

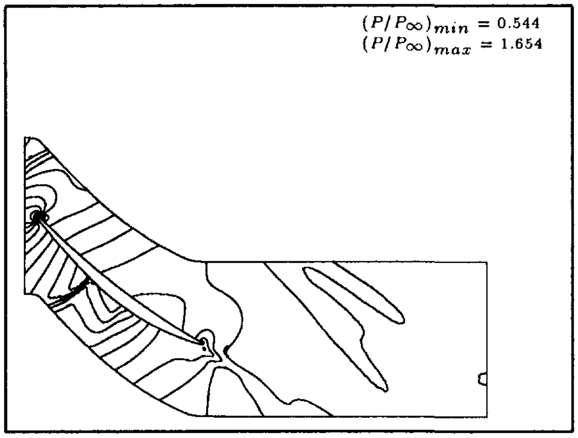

Fig. 18 Time-averaged pressure contours from the LCBR simulation

Figure 16 illustrates the unsteady pressure envelope along the surface of the vane. The time-averaged pressure distribution is nearly identical to the one predicted in the SSBR simulation. The magnitude of the unsteady pressure envelope shows satisfactory agreement with the results of the FCBR simulation (see Fig. 10). Figure 17 contains the unsteady pressure envelope for the rotor. Similar to the FCBR results, the LCBR solution exhibits little unsteadiness upstream of the shock on the suction surface (see Fig. 11). Downstream of the shock the LCBR solution exhibits a moderate amount of unsteadiness, although less than in the FCBR solution. The LCBR technique predicts less unsteadiness on the pressure surface of the rotor than is observed in the FCBR solution. While the LCBR technique is currently capable of modeling the linear unsteadiness in the transonic compressor stage, more work is necessary to model the nonlinear unsteadiness accurately in such complex flow fields. The time-averaged static pressure contours in the rotor passage are illustrated in Fig. 18. The pressure contours predicted in the LCBR simulation show reasonable agreement with the FCBR results.

Table 2 contains the flow quantities at the inlet and exit of each blade row. The predicted loss in the IGV is greater than that predicted using the SCBR method, but only about half of that predicted by the FCBR method. The rotor loss is similar to that predicted by both the FCBR and SCBR techniques. The efficiency, $\eta_{tt} = 0.904$, is about the same as that predicted using the SCBR technique. Comparing the results in Table 2, the SCBR and LCBR solutions exhibit similar agreement with the FCBR results, except for the IGV loss. The LCBR technique, however, is more computationally efficient and gives a qualitative (if not quantitive) estimation of the unsteady loading and viscous quantities.

Conclusions

Several methods for predicting the flow field, losses, and performance quantities in a transonic compressor stage have been investigated. The methods studied include: (1) the unsteady fully coupled blade row (FCBR) technique, (2) the steady coupled blade row (SCBR) method, (3) the steady single blade row (SSBR) technique, and (4) the loosely coupled blade row (LCBR) method. The predicted results highlight the fact that it is necessary to model the effects of the rotor shock on the IGV flow field to determine the losses and stage efficiency accurately. The SCBR and LCBR techniques provide a reasonable representation of the FCBR results (except for the IGV loss), while the SSBR method significantly underpredicts the IGV losses and overpredicts the stage efficiency. The LCBR technique requires approximately 23 percent less computation time than the SCBR method, and also supplies a qualitative estimation of the unsteady blade loadings. Work is underway to improve the inter-blade-row unsteady boundary conditions in the LCBR technique for transonic flow fields. Fourier series may be used to construct the boundary conditions at the interface between blade rows, similar to the techniques used by several research groups for periodic boundary conditions. Techniques for improving the accuracy of the initial SSBR solution are also being studied. Finally, the LCBR technique is being extended to three-dimensional flow fields.

References

Adamczyk, J. J., 1985, "Model Equation for Simulating Flows in Multistage Turbomachinery," ASME Paper No. 85-GT-226.

Baldwin, B. S., and Lomax, H., 1978, "Thin-Layer Approximation and Algebraic Model for Separated Turbulent Flows," AIAA Paper No. 78-257.

Chakravarthy, S., and Osher, S., 1982, "Numerical Experiments With the Osher Upwind Scheme for the Euler Equations," AIAA Paper No. 82-0975.

Chen, J. P., Celestina, M. L., and Adamczyk, J. J., 1994, "A New Procedure for Simulating Unsteady Flows Through Turbomachinery Blade Rows," ASME Paper No. 94-GT-151.

Chima, R. V., 1987, "Explicit Multigrid Algorithm for Quasi-Three-Dimensional Viscous Flows in Turbomachinery," *AIAA Journal of Propulsion and Power*, Vol. 3, No. 5, pp. 397–405.

Crook, A. J., and Delaney, R. A., 1992, "Investigation of Advanced Counterrotation Blade Configuration Concepts for High Speed Turboprop Systems: Task IV—Advanced Fan Section Aerodynamic Analysis Final Report," NASA CR-187128, Nov.

Davis, R. L., Hobbs, D. E., and Weingold, H. D., 1988, "Prediction of Compressor Cascade Performance Using a Navier–Stokes Technique," ASME JOURNAL OF TURBOMACHINERY, Vol. 110, pp. 520–531.

Dawes, W. N., 1992, "Toward Improved Throughflow Capability: The Use of 3D Viscous Flow Solvers in a Multistage Environment," ASME JOURNAL OF TURBOMACHINERY, Vol. 114, pp. 8–17.

Denton, J. D., and Singh, U. K., 1979, "Time Marching Methods for Turbomachinery Flow Calculations," VKI Lecture Series, 1979–7.

Denton, J. D., 1986, "The Use of a Distributed Body Force to Simulate Viscous Flow in 3D Flow Calculations," ASME Paper No. 86-GT-144.

Dorney, D. J., and Verdon, J. M., 1994, "Numerical Simulations of Unsteady Cascade Flows," ASME JOURNAL OF TURBOMACHINERY, Vol. 116, pp. 665–675.

Dorney, D. J., Davis, R. L., and Sharma, O. P., 1995, "Unsteady Multi-stage Analysis Using a Loosely-Coupled Blade Row Approach," AIAA Paper No. 95-0179; to be published in the *AIAA Journal of Propulsion and Power*.

Giles, M., 1991, "UNSFLO: A Numerical Method for the Calculation of Unsteady Flow in Turbomachinery," MIT Gas Turbine Laboratory Report No. 205.

LeJambre, C. J., Zacharias, R. M., Biederman, B. P., Gleixner, A. J., and Yetka, C. J., 1995, "Development and Application of a Multistage Navier–Stokes Solver—Part II: Application to a High Pressure Compressor Design," ASME Paper No. 95-GT-343, to appear in the ASME JOURNAL OF TURBOMACHINERY.

Rai, M. M., 1989, "Three-Dimensional Navier–Stokes Simulations of Turbine Rotor–Stator Interaction," *AIAA Journal of Propulsion and Power*, Vol. 5, No. 3, pp. 307–319.

Rao, K. V., Delaney, R. A., and Dunn, M. G., 1994a, "Vane-Blade Interaction in a Transonic Turbine: Part I—Aerodynamics," *AIAA Journal of Propulsion and Power*, Vol. 10, No. 3, pp. 305–311.

Rao, K. V., Delaney, R. A., and Dunn, M. G., 1994b, "Vane-Blade Interaction in a Transonic Turbine: Part II—Heat Transfer," *AIAA Journal of Propulsion and Power*, Vol. 10, No. 3, pp. 312–317.

Rhie, C. M., Gleixner, A. J., Spear, D. A., Fischberg, C. J., and Zacharias, R. M., 1995, "Development and Application of a Multistage Navier–Stokes Solver—Part I: Multistage Modeling Using Body Forces and Deterministic Stresses," ASME Paper No. 95-GT-342; to appear in the ASME JOURNAL OF TURBOMACHINERY.

A Three-Dimensional Shock Loss Model Applied to an Aft-Swept, Transonic Compressor Rotor

S. L. Puterbaugh

W. W. Copenhaver

Wright Laboratory,
Wright-Patterson Air Force Base, OH 45432

C. Hah

NASA Lewis Research Center,
Cleveland, OH 44135

A. J. Wennerstrom

Engineering Consultant,
Hot Springs Village, AR 71909

An analysis of the effectiveness of a three-dimensional shock loss model used in transonic compressor rotor design is presented. The model was used during the design of an aft-swept, transonic compressor rotor. The demonstrated performance of the swept rotor, in combination with numerical results, is used to determine the strengths and weaknesses of the model. The numerical results were obtained from a fully three-dimensional Navier–Stokes solver. The shock loss model was developed to account for the benefit gained with three-dimensional shock sweep. Comparisons with the experimental and numerical results demonstrated that shock loss reductions predicted by the model due to the swept shock induced by the swept leading edge of the rotor were exceeded. However, near the tip the loss model underpredicts the loss because the shock geometry assumed by the model remains swept in this region while the numerical results show a more normal shock orientation. The design methods and the demonstrated performance of the swept rotor are also presented. Comparisons are made between the design intent and measured performance parameters. The aft-swept rotor was designed using an inviscid axisymmetric streamline curvature design system utilizing arbitrary airfoil blading geometry. The design goal specific flow rate was 214.7 kg/s/m^2 (43.98 lbm/sec/ft^2), the design pressure ratio goal was 2.042, and the predicted design point efficiency was 94.0. The rotor tip speed was 457.2 m/s (1500 ft/sec). The design flow rate was achieved while the pressure ratio fell short by 0.07. Efficiency was 3 points below prediction, though at a very high 91 percent. At this operating condition the stall margin was 11 percent.

Introduction

High-performance aircraft gas turbine engines must employ compression systems that provide maximum performance at minimum weight. This requirement, in addition to maintainability and fabrication issues, has led to the development of compressors that maximize pressure ratio per stage while maintaining high efficiency. In response to these timeless requirements, state-of-the-art gas turbines have employed the transonic compressor stage for many years. The transonic stage is defined as one that includes a rotor that operates at supersonic tip speeds with some portion of the span operating at subsonic relative blade speed.

The shock generated by this type of rotor increases diffusion in the relative frame and, hence, does work on the fluid by turning the flow in the absolute frame. However, along with the benefit, the shock also presents challenges that have been the subject of research and development programs for decades. These include reducing the magnitude of loss generated by the shock system, managing the shock–boundary layer interaction at the suction surface, and providing proper area relationships within the passage to achieve the desired flow and to allow the shock to start.

This study seeks to evaluate a model that was utilized in an attempt to reduce shock loss. The model describes the salient features of the three-dimensional shock structure present in transonic compressor rotors. The availability of such a model allows the compressor designer to exploit the physical characteristics of the three-dimensional shock surface to enhance compressor performance. Specifically, the loss due to the shock may be reduced by inducing a shock surface that is oblique to the relative flow. This is done by sweeping the leading edge of the rotor away from the direction of rotation. Since the Mach number normal to the shock surface sets the strength of the shock, the more the shock is swept relative to the incoming flow, the weaker the shock and its attendant loss.

The experimental hardware that is the subject of the current work was also the subject of a paper by Hah and Wennerstrom (1991). The emphasis of the earlier paper was to demonstrate a numerical technique applied to an advanced, swept, transonic rotor and to investigate the shape of the shock surface. The intent of the current work is to (1) evaluate the shock model first used during the subject rotor design, (2) provide details of the design and the design process, and (3) provide experimental measurements and test analysis results.

Background

The concept of using backward sweep to reduce shock losses began as a result of some observations made by Prince (1980) about research fans that demonstrated higher efficiency than expected. He proposed the idea that a swept shock surface could be responsible for the increase. Each of the rotors reviewed by Prince incorporated a modest amount of sweep that was an incidental result of design procedures that sought to optimize other parameters, such as midspan solidity. The logical next step was to intentionally design a swept rotor in order to determine how far this concept might be extended.

However, additional information was required to guide the many choices that impact the leading edge profile, or the sweep, of the rotor. A model was therefore developed by Wennerstrom and Puterbaugh (1984) that relates shock loss to the three-dimensional shape of the shock surface. The model extended the well-known two-dimensional shock loss model of Miller et al. (1961) to include the effect of the spanwise sweep of the shock surface. The new approach was to compute the angle of the three-dimensional shock surface relative to the local flow

---

Contributed by the International Gas Turbine Institute and presented at the 41st International Gas Turbine and Aeroengine Congress and Exhibition, Birmingham, United Kingdom, June 10–13, 1996. Manuscript received at ASME Headquarters February 1996. Paper No. 96-GT-354. Associate Technical Editor: J. N. Shinn.

Table 1 Rotor design point predictions and geometric parameters

Pressure Ratio	2.042	
Adiabatic Efficiency	94.0	
Corrected Specific Flow	214.7 (43.98	kg/sec/m^2 lbm/sec/ft^2)
Corrected Tip Speed	457.2 (1500	m/sec ft/sec)
Tip Inlet Relative Mach Number	1.65	
Mean Rotor Aspect Ratio	1.26	
Rotor Inlet Hub/Tip Ratio	0.312	
Rotor Diameter	43.18 (17.0	cm in)
Number of Blades	20	

vectors on each streamsurface. The shock surface was assumed to be formed by normal (when viewed in the cascade plane), attached shocks on each streamsurface. This modeling approach allowed the resulting assumed shock surface to be swept all the way to the casing. It was recognized at the time that it did not satisfy the correct boundary conditions at the outer case.

After implementing the three-dimensional shock loss model into the design system, a rotor was designed that utilized sweep to minimize losses generated by the shock. The intent was to evaluate the overall effect of blade sweep on compressor performance. Therefore the swept rotor was designed as a derivative of a rotor having a more conventional leading edge profile as a baseline. The "baseline" rotor, the sweep of which was small and unintentional, was one of the subjects of Prince's study. The swept rotor was tested in a single-stage configuration during a research program conducted by Wright Laboratory's Compressor Aero Research Lab at Wright-Patterson Air Force Base. Though the stator influences rotor performance to various degrees, it is felt that the results presented here can be generalized to stages incorporating well-designed stators.

Design Approach

A detailed description of the approach and tools used for the research compressor design was given by Law and Wadia (1993). A brief description is given here. Typically a two-phase approach is used where a preliminary design is followed by a detailed design. The preliminary design defines fundamental geometric characteristics such as annulus shape, blade speed, solidity, etc. The detailed design phase takes these parameters along with fully defined aerodynamic information, obtains a flow field solution using the streamline curvature computational scheme, and generates the airfoil shape in the form of blade surface coordinates. In the subject effort, the detailed design phase was used exclusively since the new design was derived from the "baseline" rotor design.

The optimization criterion used during detailed design was to obtain a chordwise circumferentially averaged static pressure distribution that rises linearly from the leading edge to about $\frac{3}{4}$ chord and then smoothly transitions to zero slope. "Arbitrary" airfoils were used rather than a specific family of airfoils, such as double-circular-arc. The airfoils were developed from relative flow angles and assumed incidence and deviation angle distributions at different chordwise computing stations. This approach to airfoil definition gives the designer the flexibility to closely achieve an optimum static pressure distribution without constraints on blade shape. The validity of this approach has been demonstrated through the generation of several very successful designs (Wennerstrom, 1984; Law and Wadia, 1993; Law and Wennerstrom, 1987).

The rotor design point performance predictions along with the pertinent geometric parameters are shown in Table 1. The application of this type of rotor to an engine would be as a fan stage or as an inlet stage to a turbojet. High flow per frontal area required by these applications is achieved by the combination of the high specific flow and the low hub/tip ratio. A cut-away view of the test stage is shown in Fig. 1. The rotor is cantilevered with support provided by four struts located two stator chord lengths downstream of the stator trailing edge. The rotors used in the test rig are the integral blade and disk, or "blisk," type. The blisk was made of 6A14V titanium.

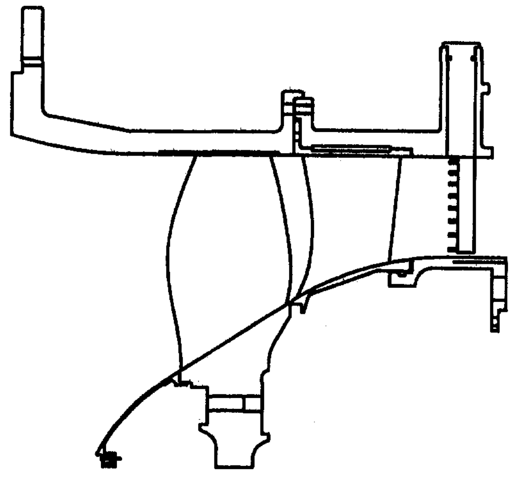

Fig. 1 Research vehicle diagram

The aerodynamic parameter changes were guided by earlier experience with rotors of similar geometry. The spanwise work and deviation angle distribution obtained from earlier experiments were used in the swept rotor design. However, the work distribution internal to the blade row was modified to achieve the optimum static pressure distribution according to the criteria described earlier. The incidence angles were also determined from earlier design experience. In order to achieve the design flow rate, the spanwise incidence angle distribution (relative to the suction surface) was set at 2 deg inboard of 66 percent span and smoothly transitioning to 3.5 deg at the tip. The estimate of relative total pressure loss was obtained from a combination of a diffusion factor/loss parameter correlation (Fig. 2) and the three-dimensional shock loss model (Wennerstrom and Puterbaugh, 1984). The aerodynamic blockage distribution was established from earlier design experience.

Previous experience had revealed that low-aspect-ratio, high-tip-speed rotor designs undergo a significant three-dimensional deformation of the manufactured geometry from rest to design speed. Specifically, the camber line is deformed in addition to the familiar untwist of the airfoil. Therefore, a three-dimensional mechanical design procedure was used to account for the complex deformation. An iterative technique was used where

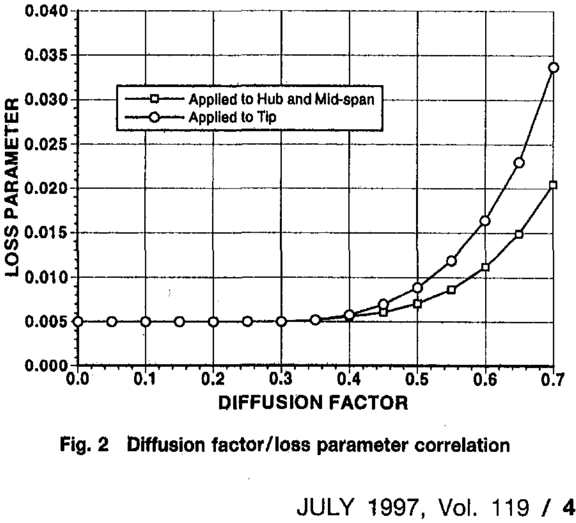

Fig. 2 Diffusion factor/loss parameter correlation

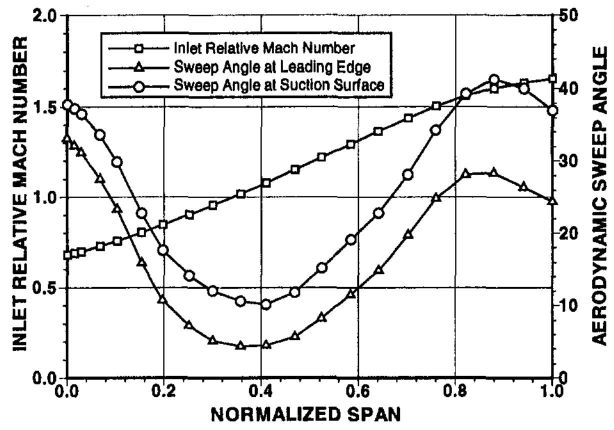

Fig. 3 Inlet relative Mach number and sweep angles

the three-dimensional displacements obtained from the structural analysis were subtracted from the design intent to create the cold geometry. The structural analysis was rerun with new cold geometry and the resulting geometry was compared with the design intent. If the differences exceeded a tolerance of 0.0762 mm (0.003 in.), then new cold-hot displacements were computed and another iteration was begun.

Incorporation of Blade Sweep. The intent of the use of sweep was to decrease the shock loss generated in the rotor. Therefore, it was most important to introduce sweep in increasing amounts beginning just outboard of the sonic radius. Figure 3 shows the spanwise distribution of aerodynamic sweep angles that was obtained after optimizing the leading edge profile for minimum shock loss. Two distributions of angles are shown, labeled leading edge sweep and suction surface sweep. Both angles are computed as the difference between the local air angle and a normal to the local shock surface. The leading edge sweep angles are computed at the intersection of the leading edge of the blade and the shock surface. The suction surface sweep angles are computed at the intersection of the shock surface and the suction surface of the adjacent blade. Both distributions reach peaks between 85 and 90 percent span. The meridional view of the leading edge does not change shape in this region. The decrease outboard of this location is due to changes in streamsurface slope and blade stagger. Figure 3 also includes a distribution of the inlet relative Mach number as a reference. The sonic radius occurs at about 35 percent span.

The structural challenges associated with the swept rotor design concept required that the mechanical design be considered simultaneously with the aerodynamic design. Therefore, an iteration between the blade design procedure and a simple finite element analysis was used to keep stresses within allowable limits. The steady-state stress limit was set to allow for a minimum of a 103.4 MPa (15 ksi) dynamic stress margin.

The initial attempt to introduce more sweep was to add midspan chord symmetrically so that section centroids would remain approximately on the stacking axis. This resulted in exceptionally high blade lean angles, especially near the hub, and very high stress levels. The second approach was to hold the trailing edge to its original baseline configuration in the meridional plane and to examine the impact on stress of the new leading edge plus nonradially stacked centroids. This offered an improvement but still produced unacceptably high stresses. The third and successful approach was to again hold the trailing edge to its original baseline configuration and, in addition, to introduce a reflex curvature in the meridional view of the leading edge bringing it from its new swept profile in the tip region back tangent to the original baseline configuration where the leading edge intersects the hub platform. This resulted in lean angles at the platform comparable to the baseline and acceptable stress levels in spite of the off-axis centroids. The resulting leading edge profile is evident in Fig. 1.

Test Facility, Instrumentation, and Data Reduction

The facility and instrumentation were described in detail by Law and Wadia (1993). The facility has a closed-loop airflow path and is powered by a 1.49 MW (2000 hp) electric motor. Facility flow rate is measured using a calibrated venturi. The test article instrumentation consisted of over 150 steady-state pressure measurements, over 130 steady-state temperature measurements, and 10 high-frequency response static pressure measurements over the rotor tip. Radial clearance between the rotor tip and the casing was measured on-line by spark discharge type clearance probes. A clearance of 0.43 mm (0.017 in.), or 0.44 percent of chord, was measured at design speed. The measurement uncertainty of individual measurements along with computed quantities for a 95 percent confidence interval are given in Table 2.

The data presented in this paper are for rotor performance. The rotor exit conditions, in terms of spanwise distributions of total pressure and total temperature, were determined using stator leading edge instrumentation. These distributions were input directly to a streamline curvature type computer program to generate the data match for subsequent analysis. The particular computer program used in the analysis did not simulate effects due to mixing or secondary flow.

The stator leading edge instrumentation consisted of nine total pressure and nine total temperature vane-mounted probes. The probes were located at even increments in the spanwise direction on the vane. A total of four vanes were instrumented, chosen at approximately even circumferential spacing. The pressure probes were mounted on two different vanes at alternating spanwise locations on each vane. The temperature probes were mounted similarly.

The performance analysis is based on stator leading edge results to minimize the impact of the stator on the conclusions drawn about the rotor losses. The focus of this work is on shock sweep and a loss model developed to predict advantages of swept shocks. Therefore, it was important to reduce the uncertainty regarding shock loss that would be added if stage exit results were used. Although stator leading edge measurements add their own level of uncertainty because they are sensing a highly unsteady flow field, they provide a clearer view of the shock losses than interpretations made from stage discharge measurements.

Numerical Method

The numerical method described here was not available during the design phase of this rotor and therefore did not influence the design. The numerical method is from Hah (1987). This approach utilizes a fully three-dimensional, steady-state formulation of the Reynolds-averaged Navier–Stokes equations. The equations are solved using a finite-volume approach. The overall numerical scheme is second-order accurate in the physical domain.

The system of equations is closed using a $k-\epsilon$ type turbulence model to provide the Reynolds stresses. A low-Reynolds-num-

Table 2 Measurement uncertainty for instrumentation used in the current study

Mass Flow	±0.5% Reading
Pressure Ratio	±0.1% Reading
Efficiency	±1.1 Points
Pressure	±206.8 Pa (0.03 psi)
Temperature	±0.78° C @ 10° C, ±1.17° C @ 121.1° C (±1.4° F @ 50° F, ±2.1° F @ 250° F)
Tip Clearance	±0.051 mm (0.002 in.)

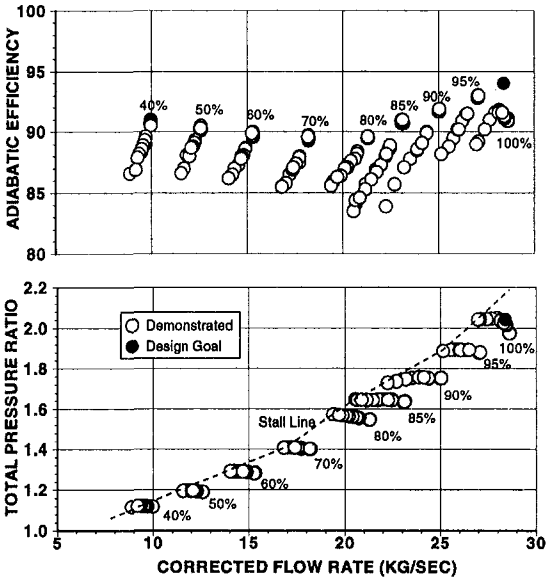

Fig. 4 Rotor performance map

ber correction was employed to extend the validity of the model to the viscous sublayer. This approach allows the numerical scheme to be utilized in situations where strong secondary flow and flow separation are present. The constants in the turbulence transport equations are the same as those used in many earlier computations of the flow field in transonic fans and compressors (Hah and Puterbaugh, 1992; Copenhaver et al., 1993, 1996).

At the inflow plane, total temperature, total pressure, and flow angle are defined. At the outflow plane, static pressure is specified at a point and asymptotic conditions are imposed on the remaining dependent variables. Nonreflective boundary conditions are imposed at both the inflow and outflow boundaries. Periodicity is enforced at the periodic boundaries and no-slip is enforced at solid walls.

For the current study, a total of 347,300 nodes make up the blade-centered, I-type grid. Fifty nodes are used in the pitchwise direction, 46 nodes in the spanwise direction, and 151 nodes in the streamwise direction. The blade chord has 95 nodes distributed from leading edge to trailing edge. In order to resolve the clearance flow, seven nodes are distributed from suction surface to pressure surface with six nodes in the clearance gap. The clearance gap was set to the value measured during the experiment, 0.43 mm (0.017 in.). The design, hot-running blade shape was modeled by the grid.

Results

Overall Results. The rotor performance map is shown in Fig. 4. The stall line was fully characterized without encountering stall flutter. The minimum back pressure condition capable of being run in the facility did not allow operation at a fully choked condition. Choke flutter was not encountered in the region tested. Full speedlines were obtained from 40 to 100 percent design speed. Peak efficiency on speedlines below 100 percent speed was not determined due to the facility back pressure limit. The very high design speed efficiency peaked just under 92 percent, whereas pressure ratio peaked at about 2.05. The design system prediction is indicated on the figure by the filled circle symbol. The design flow rate was exceeded slightly but the demonstrated peak efficiency was about 2 points below the predicted value. While this difference is significant from an engine performance point of view, it must be kept in mind that the predicted absolute level is very high.

The maximum stall margin demonstrated was nearly 11 percent at an efficiency of 91 percent and a pressure ratio of 1.97.

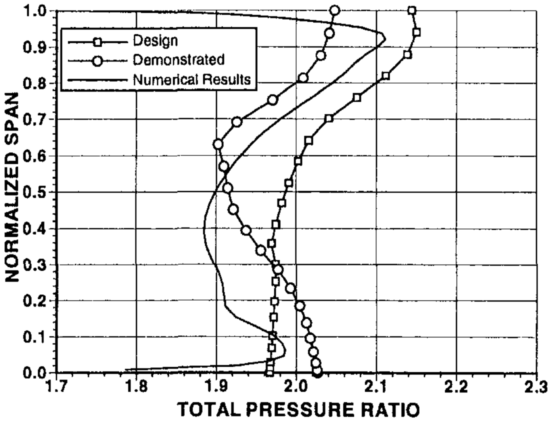

Fig. 5 Comparison of spanwise distributions of total pressure ratio at design speed, maximum stall margin operating point

The facility back pressure limit restricted the maximum demonstrated stall margin to this value. Since a stall margin of 11 percent is closer to acceptable levels for military designs, this operating condition was chosen for detailed analysis and comparisons with design predictions.

The spanwise distributions of total pressure ratio and adiabatic efficiency as compared to design intent are shown in Figs. 5 and 6, respectively. These and subsequent plots show comparisons between predicted and demonstrated quantities along with results from the numerical analysis. The numerical results will be discussed later. Pressure was underpredicted in the inboard 30 percent and overpredicted outboard. Recall that the sonic radius is about 35 percent span; therefore the underprediction reflects the performance of the subsonic blade sections. The perceived underprediction near the hub is reflected in the unreasonably high efficiencies, as seen in Fig. 6. This condition is believed to be produced by strong secondary flow within the suction surface boundary layer and blade wake, which was not accounted for when analyzing the measurements. This secondary flow is not unusual in a highly loaded configuration with high hub ramp angle and is very evident in the numerical results (not shown here). In the midspan, the efficiency is somewhat underpredicted. However, in the tip region the efficiency is significantly overpredicted. Hah and Wennerstrom (1991) demonstrated graphically that the shock surface transitions to a normal orientation relative to the casing wall as it approaches the tip. The shock is less oblique in this region and therefore will produce more loss. It is therefore not surprising that loss is underpredicted in the tip region. This is clearly a weakness in the model, which should be addressed in the future. It must also

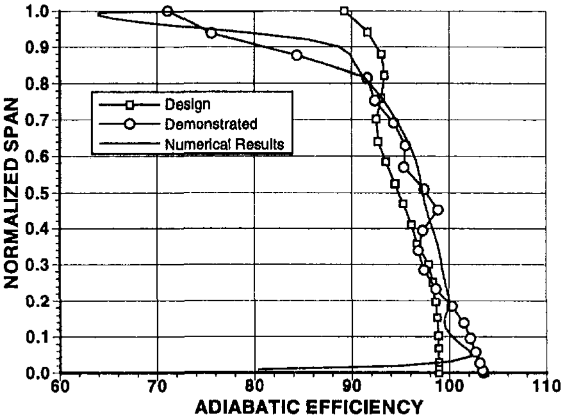

Fig. 6 Comparison of spanwise distributions of adiabatic efficiency at design speed, maximum stall margin operating point

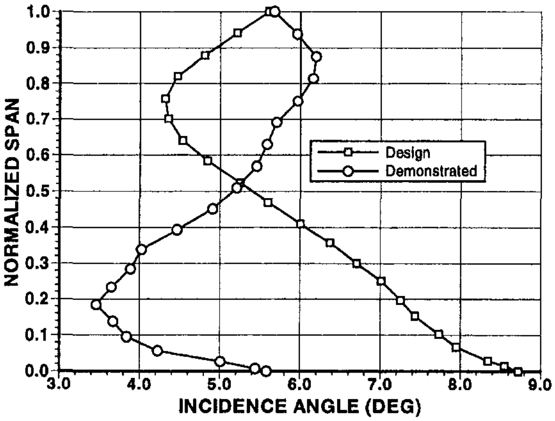

Fig. 7 Comparison of spanwise distributions of incidence angles at maximum stall margin operating point

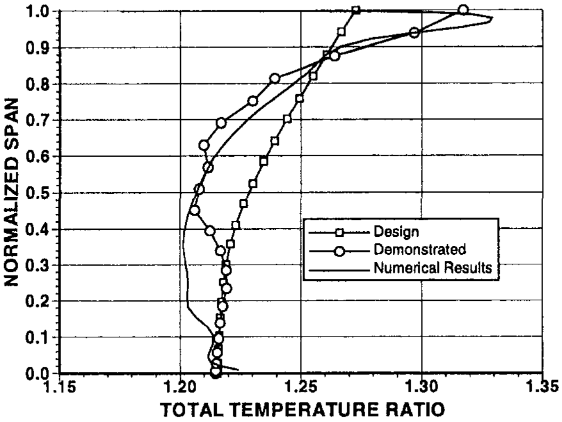

Fig. 9 Comparison of spanwise distributions of total temperature ratio at maximum stall margin operating point

be kept in mind that the design system does not use a tip clearance loss model and, therefore, a fraction of the increased loss is attributable to clearance loss.

Figures 7 and 8 show comparisons of spanwise distributions of incidence and deviation angles. Note that this plot shows incidence relative to the camber line, whereas the comments in the Design Approach section referred to incidence relative to the suction surface. Incidence is significantly overpredicted in the inboard half of the span and underpredicted in the outboard half. Since the design suction surface incidence angles were patterned after the baseline rotor test results, this discrepancy implies that the changes in leading-edge sweep angle caused a significant change in the inlet wave pattern in the supersonic region. The deviation angle distribution (Fig. 8) shows a fairly constant overprediction across the span with the exception of between 40 and 70 percent span. In this region the two distributions agree fairly well. This is also in the region of highest solidity and longest chord.

Total temperature ratio distributions are compared in Fig. 9. Near the hub, the distributions agree quite closely but begin to diverge at about 30 percent span. This location also coincides closely with the sonic radius. Moving outboard of 30 percent span the demonstrated total temperature ratio first is less than design and then, at about 85 percent span, crosses the design distribution and is much greater than design at the tip. Consider the midspan region in more detail, between 45 and 70 percent span. In this region, the design and demonstrated deviation angles agree fairly well (Fig. 9). This requires that the relative flow angles agree as well. It then follows that the absolute flow angles, and turning, agree but the work done does not agree. The only way for the work to be overpredicted at the same relative flow angle is for the diffusion of the flow to be reduced while maintaining the same flow direction in the relative frame. A potential cause for this condition is the presence of a shock that is weaker (produces less diffusion), than what was expected.

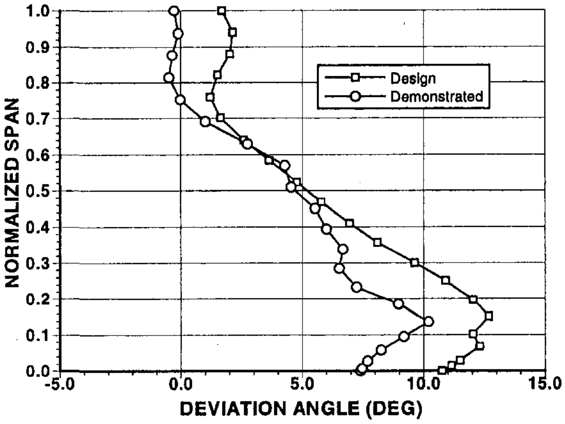

Fig. 8 Comparison of spanwise distributions of deviation angles at maximum stall margin operating point

Numerical Solution Validation. The numerical method described previously has been the subject of several prior studies of rotors with similar loading and relative Mach number levels (Hah and Puterbaugh, 1992; Copenhaver et al., 1993, 1996). In all cases where the rotor performance is concerned, the comparisons were very favorable. Therefore, this method was considered to be an excellent tool, in conjunction with the experimental results, for use in evaluating the performance of the swept shock model.

For the case currently under study, the validity of the numerical results will be evaluated in three ways. First, the integrated performance obtained from the numerical solution in terms of pressure ratio and efficiency versus corrected flow rate will be compared with the experimental results. Second, various spanwise distributions will be compared to experimental results. The comparisons were done at the maximum stall margin operating point for convenience of presentation on Figs. 5, 6, and 9. Finally, the tip shock structure is compared at peak efficiency to lend credence to the evaluation of the shock structure geometry assumed by the model.

Computations were carried out for six different operating points at 100 percent speed. The exit pressure and temperature results were area-averaged to obtain integrated performance characteristics for comparison with the measured data. Experimental integrated performance values were obtained from the measurements of fixed frame probes in a nonsteady rotor exit flow field. There is no obvious approach to sampling numerical results in a similar manner. Therefore, area-averaging was selected simply for convenience in determining integrated quantities.

The integrated performance obtained from numerical results is compared with the measured experimental results in Fig. 10. The general shapes of the characteristics agree very well. The numerical results give a lower flow rate and higher peak pressure ratio than that seen with the measurements. In both flow and pressure ratio the agreement is within 2 percent. The agreement in peak efficiency is within 1 percent.

The spanwise distributions of quantities were computed from the numerical solution by area-averaging the circumferential distributions at various spanwise radii. A comparison of total pressure ratio is shown in Fig. 5. Agreement between the numerical solution and experiment is quite good in terms of the shape

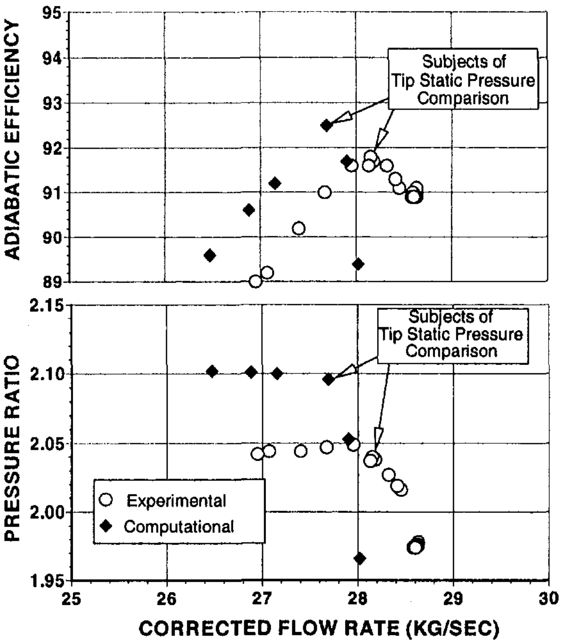

Fig. 10 Performance comparisons at 100 percent speed

of the distribution. The numerical results underpredict near the hub and overpredict near the tip, however. Efficiency is compared in Fig. 6. The agreement between the numerical solution and experimental results is quite evident. Finally, total temperature is compared in Fig. 9. The largest discrepancy appears at the hub, but the overall character of the experimental distribution is reflected in the numerical results, i.e., a reduction of work in midspan and an increase of work near the tip as compared to the design distribution.

The analysis in the remainder of the paper will center around the peak efficiency operating point in order to more fairly evaluate the shock loss model's accuracy in the light of assumptions made during development. The assumed shock orientation in the cascade plane, i.e., an attached, normal shock, corresponds to that typically found at the tip when operating at peak efficiency.

Figure 11 compares static pressure contours in the cascade plane obtained from the numerical solution with experimental measurements at the peak efficiency operating point. The measurements were made with high-response pressure transducers positioned on the rotor casing at equal axial increments of 6.35 mm (0.25 in.). The measurement method is described by Sellin et al. (1993). The shock locations as measured and computed at the blade tip agree very well. In both cases the shock stands off the leading a small distance and is oriented normal to the flow in the cascade plane. In addition the absolute values of the static pressure downstream of the passage shock agree.

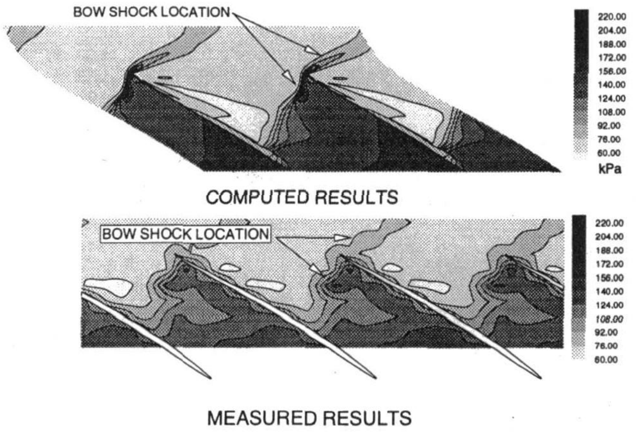

Fig. 11 Tip static pressure distribution comparisons at design speed, peak efficiency operating point

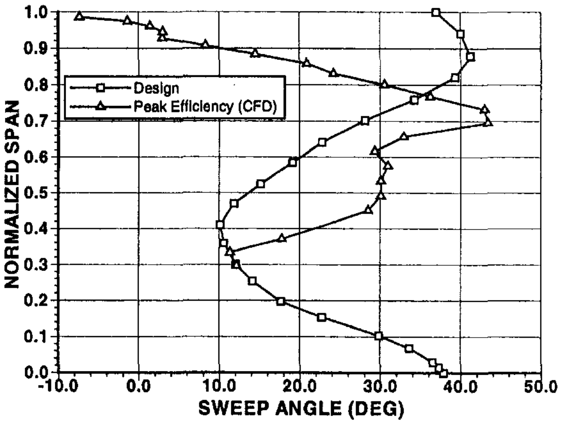

Fig. 12 Shock sweep angles at the shock/suction surface intersection at peak efficiency operating point

The integrated performance and detailed comparisons shown in Figs. 5, 6, 9, 10 and 11 serve to establish the credibility of the numerical results for use in extended analysis of the swept shock loss model. On the basis of these comparisons and the prior studies cited, the computation was deemed to be an excellent tool for evaluating the swept shock loss model in more detail. Comparisons will now be made between the modeled shock structure and the computed structure along with the losses these structures produce.

Assessment of Swept Shock Model. An integral factor in the design of the aft-swept rotor was the use of the three-dimensional shock loss model. This model provided criteria for tailoring the leading edge profile to minimize shock losses. The model's strengths and weaknesses must be assessed before improvements can be made. However, a detailed evaluation from test data is difficult because of the inability to directly measure shock loss. Losses result from many mechanisms and measurements only provide the ability to compute an overall loss. Furthermore, spanwise transport within the flow field via secondary flow and mixing masks the location of loss production. This makes it difficult to assign loss generation to a specific location and, therefore, a specific mechanism. Therefore, the approach taken to analyze the model will be to compare detailed information derived from numerical results with design information, the credibility of the numerical solution for the subject rotor having already been established.

The three-dimensional shock loss model's assumed shock geometry is compared to the actual shock geometry (as computed numerically) in Fig. 12 by comparing shock sweep angles at the suction surface. The design sweep angles were obtained directly from the compressor design computer program, which uses the three-dimensional shock loss model. The method used to compute the sweep angles from the numerical solution was similar to the design method once the shock surface and the local velocity vector were defined. The shock surface was determined by locating the sonic line on each streamsurface near the suction surface. The local velocity vector was computed from the solution such that the vector component normal to the stream surface was zero. This was done by transforming the Cartesian vector to an intrinsic coordinate system relative to the stream surface, setting the normal velocity component to zero, and then transforming back to the Cartesian system. This approach was taken to provide a similar basis of comparison between the throughflow-based design information and numerical results. In

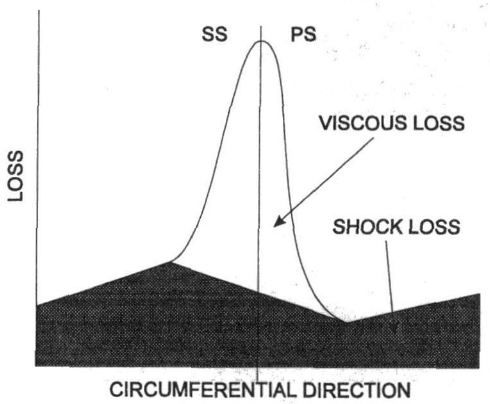

Fig. 13 Diagram of wake showing losses associated with viscous phenomena and shocks

the midspan region, where the loss was slightly overpredicted (Fig. 6), the design suction surface sweep angle is significantly less than the angle obtained from the numerical results. This implies that the shock surface is swept back by a greater amount than was assumed during the design. Recall that the model assumed an attached, normal shock (when viewed in the cascade plane) from the tip all the way to the sonic radius. Several papers published since the completion of the model and design illustrate that, at least at some locations inboard of the tip region, the shock is actually oblique in the cascade plane even when the shock at the tip is in a normal orientation (Pierzga and Wood, 1985; Strazisar, 1985; Bloch et al., 1995). This is an area of improvement necessary for the three-dimensional shock model.

The most important area for improvement is near the tip region. This was a known weakness of the model. Figure 12 clearly shows the disagreement in shock shape near the tip (normalized span approaching 1.0). The sweep from the numerical results approach zero whereas the design values remain at about 40 deg. Further study is required to determine where, in the spanwise sense, the modeled shock surface should transition to a more normal orientation near the tip. The decrease in shock sweep results in a stronger shock, and therefore increased loss. This effect is seen in the spanwise distribution of efficiency in Fig. 6. It must be kept in mind that the increase in losses in the tip region are also due in part to the losses associated with the clearance flow.

The numerical results were further analyzed to shed some light on the fraction of the overall loss which can be attributed to shocks in a transonic compressor rotor. Using a method from Schreiber (1987), an analysis of the blade wake was used to provide the required information. It is recognized that this is an approximate method that may be more applicable to cascades since secondary flows that exit in the rotating compressor environment can distort the interpretation. However, this approach can at least give an approximate means for attempting the very difficult task of determining losses due to shocks. The viscous loss is assumed to be contained within the peak of the circumferential loss distribution, whereas the shock loss was assumed to be contained within the "base" of the distribution as diagrammed in Fig. 13. The method is not usable at the endwalls, however. At the hub, the nonzero "base" loss cannot be attributed to shocks, since the blade section operates in the subsonic regime. The false shock loss contribution seen there is presumed to be a result of secondary flow and the hub boundary layer, though it was not investigated fully in this work. The shock loss component is arbitrarily set to zero in this region. At the tip, the clearance flow and its interaction with the shock invalidates the method.

Figure 14 shows the spanwise distribution of the fraction of overall loss, which is attributable to the shock system from design data and the numerical results. The fraction of overall loss was chosen as the value for comparison in order to normalize the difference in integrated efficiency between the measured and numerical results. In the midspan region, where the design sweep was underpredicted, the fraction of overall loss associated with the shock was overpredicted. Whereas the design predicted that the shock loss would account for 35 to almost 50 percent of the overall loss, the numerical results showed that the shock actually accounts for only up to 30 percent. Outboard of about 75 percent span, the numerical results indicate that the shock accounts for a larger fraction of the loss than predicted by the design. These findings are consistent with the improper assumption of shock shape.

Conclusions

The goal of this study was to evaluate the three-dimensional shock loss model used during the rotor's design and examine the performance of a highly swept transonic compressor rotor relative to its design intent. Experimental and numerical results provided the means to conduct the investigation. The following conclusions with regard to the design and performance of the swept rotor can be drawn:

1 A rotor utilizing a high degree of leading edge sweep at very high tip speeds can be designed for safe operation. Design optimization utilizing an iterative aerodynamic and structural analysis approach allowed for adequate structural margins for safe operation of an aggressive blading geometry.

2 The design flow rate goal was achieved, but the demonstrated pressure ratio and efficiency fell short of design predictions. At the point selected for analysis, pressure ratio was about 3 percent low and efficiency was about 3 points low relative to the prediction. The peak demonstrated efficiency fell about 2 points short of the predicted efficiency. It must be kept in mind that the efficiency prediction was extremely high. The efficiency prediction was established in large part by the swept shock model, which is the main focus of this study.

3 Measured spanwise work distributions indicate that the design fell short of work in the midspan region and was high near the tip.

The following conclusions can be drawn from the experimental and numerical evaluations of the swept shock loss model:

4 In the tip region, modifications are required in the swept shock model to accommodate the change in shock sweep. The shock sweep angle reduces significantly toward the tip, resulting in a significant reduction in obliquity at the casing.

5 The midspan shock sweep angle is underpredicted with the swept shock model. The model requires modification to

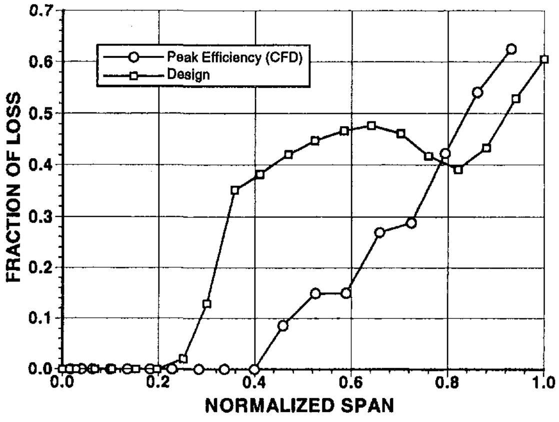

Fig. 14 Fraction of overall loss due to the shock at peak efficiency operating point

reflect the oblique orientation of the shock in the cascade plane. The model currently assumes a normal shock in the cascade plane.

Acknowledgments

The authors would like to acknowledge the Compressor Aero Research Lab staff for their excellent support in obtaining the data presented here. We also thank the management at Wright Lab and NASA for allowing us to present this work.

References

Bloch, G. S., Copenhaver, W. W., and O'Brien, W. F., 1995, "Development of an Off-Design Loss Model for Transonic Compressor Design," AGARD *Loss Mechanisms and Unsteady Flows in Turbomachines,* AGARD-CP-571, Paper No. 16.

Copenhaver, W. W., Hah, C., and Puterbaugh, S. L., 1993, "Three-Dimensional Flow Phenomena in a Transonic, High-Through-Flow, Axial-Flow Compressor Stage," ASME JOURNAL OF TURBOMACHINERY, Vol. 115, pp. 240–248.

Copenhaver, W. W., Mayhew, E. R., Hah, C., and Wadia, A. R., 1996, "The Effect of Tip Clearance on a Swept Transonic Compressor Rotor," ASME JOURNAL OF TURBOMACHINERY, Vol. 118, pp. 230–239.

Hah, C., 1987, "Calculation of Three-Dimensional Viscous Flows in Turbomachinery With an Implicit Relaxation Method," AIAA *Journal of Propulsion and Power,* Vol. 3, No. 5, pp. 415–422.

Hah, C., and Wennerstrom, A. J., 1991, "Three-Dimensional Flowfields Inside a Transonic Compressor With Swept Blades," ASME JOURNAL OF TURBOMACHINERY, Vol. 113, April pp. 241–251.

Hah, C., and Puterbaugh, S. L., 1992, "A Critical Evaluation of a Three-Dimensional Navier–Stokes Method as a Tool to Calculate Transonic Flows Inside a Low-Aspect-Ratio Compressor," AGARD *CFD Techniques for Propulsion Applications,* AGARD-CP-510, Paper No. 10.

Law, C. H., and Wennerstrom, A. J., 1987, "Performance of Two Transonic Axial Compressor Rotors Incorporating Inlet Counterswirl," ASME JOURNAL OF TURBOMACHINERY, Vol. 109, pp. 142–148.

Law, C. H., and Wadia, A. R., 1993, "Low Aspect Ratio Transonic Rotors: Part I—Baseline Design and Performance," ASME JOURNAL OF TURBOMACHINERY, Vol. 115, pp. 218–225.

Miller, G. R., Lewis, G. W., Jr., and Hartmann, M. J., 1961, "Shock Losses in Transonic Blade Rows," ASME *Journal of Engineering for Power,* Vol. 83, pp. 235–242.

Pierzga, M. J., and Wood, J. R., 1985, "Investigation of the Three-Dimensional Flow Field Within a Transonic Fan Rotor: Experiment and Analysis," ASME *Journal of Engineering for Gas Turbines and Power,* Vol. 107, pp. 436–449.

Prince, D. C., Jr., 1980, "Three-Dimensional Shock Structures for Transonic/Supersonic Compressor Rotors," AIAA *Journal of Aircraft,* Vol. 17, pp. 28–37.

Schreiber, H. A., 1987, "Experimental Investigations on Shock Losses of Transonic and Supersonic Compressor Cascades," AGARD *Transonic and Supersonic Phenomena in Turbomachines,* AGARD-CP-401, Paper No. 11.

Sellin, M. D., Puterbaugh, S. L., and Copenhaver, W. W., 1993, "Tip Shock Structures in Transonic Compressor Rotors," AIAA/SAE/ASME/ASEE 29th Joint Propulsion Conference, Monterey, CA, Paper No. AIAA-93-1869.

Strazisar, A. J., 1985, "Investigation of Flow Phenomena in a Transonic Fan Rotor Using Laser Anemometry," ASME *Journal of Engineering for Gas Turbines and Power,* Vol. 107, pp. 427–436.

Wennerstrom, A. J., 1984, "Experimental Study of a High-Throughflow Transonic Axial Compressor Stage," ASME *Journal of Engineering for Gas Turbines and Power,* Vol. 106, pp. 552–560.

Wennerstrom, A. J., and Puterbaugh, S. L., 1984, "A Three-Dimensional Model for the Prediction of Shock Losses in Compressor Blade Rows," ASME *Journal of Engineering for Gas Turbines and Power,* Vol. 106, No. 2, pp. 295–299.

F. Kameier
BMW Rolls-Royce Aeroengines,
Eschenweg,
15827 Dahlewitz,
Federal Republic of Germany

W. Neise
Deutsche Forschungsanstalt für Luft- und
Raumfahrt e.V.,
Abteilung Turbulenzforschung Berlin
Müller-Breslau-Straße 8,
10623 Berlin, Federal Republic of Germany

Experimental Study of Tip Clearance Losses and Noise in Axial Turbomachines and Their Reduction

An experimental study is described to investigate the negative effects of the tip clearance gap on the aerodynamic and acoustic performance of axial turbomachines. In addition to the increased broadband levels reported in the literature when the tip clearance is enlarged, significant level increases were observed within narrow frequency bands below the blade passing frequency. Measurements of the pressure and velocity fluctuations in the vicinity of the blade tips reveal that the tip clearance noise is associated with a rotating flow instability at the blade tip, which in turn is only present under reversed flow conditions in the tip clearance gap. A turbulence generator inserted into the tip clearance gap is found to be effective in eliminating the tip clearance noise and in improving the aerodynamic performance.

Introduction

The present paper is concerned with the negative effects of the radial clearance between the casing wall and the blade tip upon the aerodynamic and acoustic performance characteristics of axial turbomachines like jet engines, axial compressors, and axial fans.

It is well known that a small tip clearance is beneficial for both the aerodynamic performance and the noise characteristic of axial turbomachines. The pressure rise increases and the onset of rotating stall moves to lower flow rates as the clearance is reduced; compare Hutton (1955) and Cumpsty (1989). Tip clearance noise can be a significant source of noise when the tip clearance exceeds a certain limit. While Marcinowski (1953), Longhouse (1978), Stütz (1988), and Fukano et al. (1986) reported increased broadband noise levels as a result of an enlarged tip clearance, Kameier et al. (1992) observed, on top of the higher broadband noise, drastic level increases within limited almost narrow-band frequency regions below the blade passing frequency. This narrow-band noise component was found when the dimensionless gap width became larger than $\tau = s/D = 0.0027$ (D = impeller diameter) and at flow rates equal to or smaller than the optimum. The generation mechanism of the tip clearance noise, however, is still widely unknown.

In turbomachinery sciences, the flow around the blade tip is generally known as tip clearance vortex, and is schematically shown in Fig. 1. This tip vortex corresponds to the vortex at the end of an aircraft wing. In an axial turbomachine such vortices are generated on each blade. As in the case of aircraft wings, the tip vortices of axial turbomachines are generated by the pressure difference between the pressure and suction sides of the airfoil (rotor blades). The flow field between two adjacent blades is not affected much by the presence of the vortices attached to the blade tips, from where they are convected downstream with the main flow. In addition to the classical tip vortex, the pressure difference between the suction side and the pressure side of the impeller disk of an axial fan or compressor drives a secondary flow through the tip clearance in the axial direction; see the flow sketch in Fig. 2. Differently from the blade tip vortex, the reversed flow condition in the blade tip regime extends over the entire circumference of the rotor, as will be shown later when discussing the results of hot-wire measurements. The size of the radial gap between blade tip and casing wall is decisive for the strength of the secondary flow, which in turn influences the mean flow field in the tip region including the flow separation processes at the blade tips.

To investigate the unsteady flow processes in the blade tip region that are responsible for the aerodynamic losses as well as for the generation of the tip clearance noise, measurements are made in this study of the pressure fluctuations at the casing wall in the vicinity of the impeller, of the pressure fluctuations on the impeller blades, and of the steady and unsteady velocity fluctuations around the blade tips as well as in the tip clearance gap itself. In this way, some aspects of stall inception on the blade tips could be clarified. Finally, a simple method is described to diminish the negative effect of the tip clearance gap while maintaining its nominal width.

Experimental Apparatus

The test fan is a low-speed high-pressure axial fan with outlet guide vanes. The design is similar to an axial fan manufactured by J. M. Voith GmbH, Heidenheim, Germany (now Voith Howden GmbH) who kindly supplied the impeller blades. The impeller diameter was kept constant throughout all experiments, and the tip clearance was varied by changing the casing diameter: Four different casing segments were used to give gap widths of 0.3, 0.6, 1.2, and 2.4 mm, which correspond to tip clearance ratios of $\tau = s/D = 0.00066, 0.0013, 0.0027$, and 0.0053. The principal impeller dimensions are summarized below:

- Rotor diameter $D = 452.4$ mm
- Hub-to-tip ratio $\varepsilon = 0.62$
- NACA 65 blade profile
- Rotor blade number $Z = 24$
- Blade chord length at the tip $c = 43$ mm
- Blade stagger angle at the tip $\theta = 27$ deg

The stator row comprises $V = 17$ nonprofiled vanes. Figure 3 shows the experimental setup along with its major dimensions. The measurement facility meets the requirements of DIN 24 163 (1985) for measurement of the aerodynamic fan performance. On the inlet side there is a short duct section with a bellmouth nozzle; there are no flow straighteners nor screens in the inlet duct. The anechoically terminated outlet duct is in

---

Contributed by the Turbomachinery Division for publication in the JOURNAL OF TURBOMACHINERY. Manuscript received at ASME Headquarters February 17, 1995. Associate Technical Editor: N. A. Cumpsty.

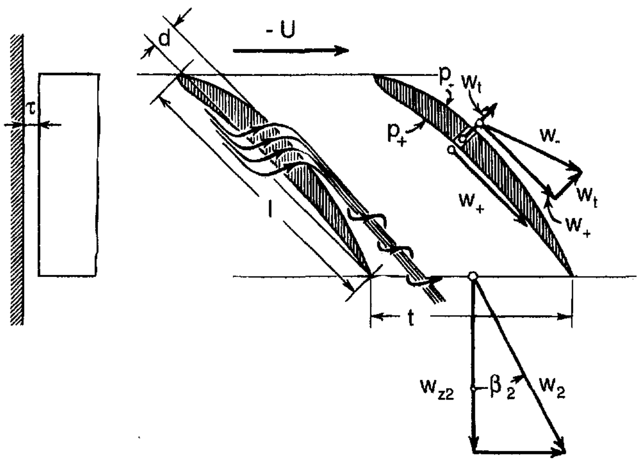

Fig. 1 Tip vortex at the impeller blade tip of an axial turbomachine (from Vavra, 1969)

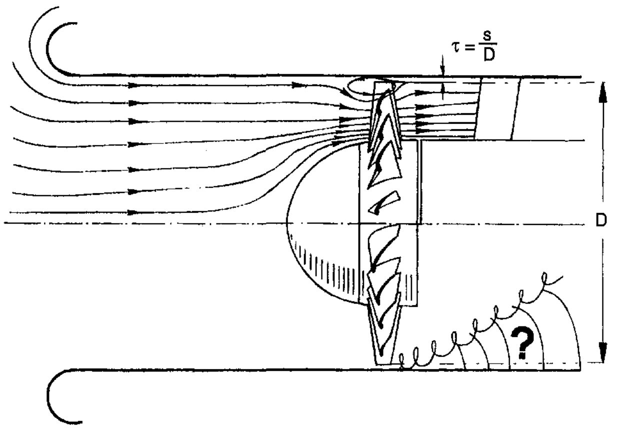

Fig. 2 Schematic view of secondary flow driven by the pressure difference between suction and pressure side in the tip region

accordance with the standardized in-duct method (DIN 45 635 Part 9, 1989; ISO 5136, 1990). A $\frac{1}{2}$-in. microphone equipped with a turbulence screen (slit-tube) is mounted in a rotatable duct section to measure the circumferentially averaged sound pressure level at a specified radial distance from the duct axis. The pressure fluctuations on the interior casing wall are monitored by using $\frac{1}{8}$-in. microphones (Bruel & Kjaer type 4138), which are mounted flush with the inner wall; see Fig. 4. To measure the unsteady blade pressures, four miniature pressure sensors (Kulite type LQ 47-5-SG) are mounted in small recesses of the impeller blades so that the original outer blade contour is retained; see the schematic in Fig. 5. The low-voltage output signals of the sensors are amplified within the rotating system and then transmitted into the fixed frame of reference via a two-channel telemetry-system (Datatel).

A special hot-wire probe (Fig. 6) is used to measure the flow field in the blade tip region as well as in the 2.4-mm-wide tip clearance gap. The probe shaft is placed in a cylindrical hole of the fan casing and can be rotated around its axis. Four prongs hold two parallel wires at distance of 2.8 mm, which are driven by constant-temperature anemometers. To vary the radial measurement position, the prongs are moved in and out of the fan casing while the probe shaft maintains its position. With this arrangement a minimal distortion of the flow field by the presence of the hot-wire probe is ensured. The velocity components in the axial and azimuthal directions are determined by performing measurements at different yaw angles between the hot wires and the mean flow. At any given yaw angle, the flow direction is detected by comparing the signals from the two wires, i.e., the signal from the first wire in the direction of the flow is larger than that from the second wire.

More details about the experimental equipment and measurement techniques are given by Kameier (1994).

Effect of the Tip Clearance on the Aerodynamic and Acoustic Fan Performance

In Fig. 7 are shown the aerodynamic and acoustic fan performance curves for four tip clearance ratios in terms of the pres-

Nomenclature

a_0 = speed of sound
c_z = flow velocity in the z direction
$\overline{C_z}$ = average axial flow velocity = $4Q/\pi(D_G^2 - D_{\text{hub}}^2)$
D = impeller diameter = 452 mm
D_G = casing diameter = $D + 2s$
f = frequency
Δf_B = filter bandwidth
G_{11} = power spectrum
G_{12} = cross spectrum
Lp = pressure level = $20 \lg p/p_0$ ($p_0 = 2 \times 10^{-5}$ Pa)
Lw = sound power level = $10 \lg P/P_0$ ($P_0 = 1\ pW$)
Lw_s = specific sound power level = $Lw - 20 \lg \Delta p/\Delta p_0 - 10 \lg Q/Q_0$
M = rotor tip Mach number = U/a_0
n = rotor shaft speed = $\Omega/2\pi$
p = pressure (p' = pressure fluctuation)
Δp = total fan pressure rise (Δp_0 = 1 Pa)
P = sound power
Q = volume flow ($Q_0 = 1$ m^3/s)
R = impeller radius = $D/2$
R_G = casing radius = $D/2 + s$

s = tip clearance gap
St = Strouhal number = $(fD/U)(\pi/Z)$
Δt = time delay
U = rotor tip speed = $\Omega\ D/2$
V = number of stator vanes
Z = number of rotor blades
β = flow angle
γ^2 = coherence function = $|G_{12}|^2/(G_{11}G_{22})$
ζ = nondimensional z coordinate = z/D (ζ = 0 at blade leading edge)
ε = hub-to-tip ratio = 0.62
λ = wavelength
θ = stagger angle = 27 deg
φ = phase angle or coordinate direction ($\Delta\varphi$ = azimuthal distance)
$\hat{\varphi}_{12}$ = phase angle of the cross spectrum G_{12}
Φ = flow coefficient = $4Q/\pi D_G^2 U$
Φ_{opt} = flow coefficient at the point of maximum efficieny
η = efficiency
Ψ = pressure coefficient = $2\Delta p/\rho U^2$
ρ = density
ω = angular frequency

Ω = angular rotor speed
Ω_{RI}^F = angular velocity of the rotating instability component relative to the fixed frame of reference
Ω_{RI}^R = angular velocity of the rotating instability component relative to the rotating frame of reference (impeller)
τ = tip clearance ratio = s/D

Superscripts

F = fixed frame of reference
R = rotating frame of reference (impeller)

Subscripts

RI = rotating instability

Abbreviations

BPF = blade passing frequency
CN = clearance noise
RF = rotor shaft frequency
RI = rotating instability (RIF = rotating instability frequency)
RS = rotating stall (RSF = rotating stall frequency)

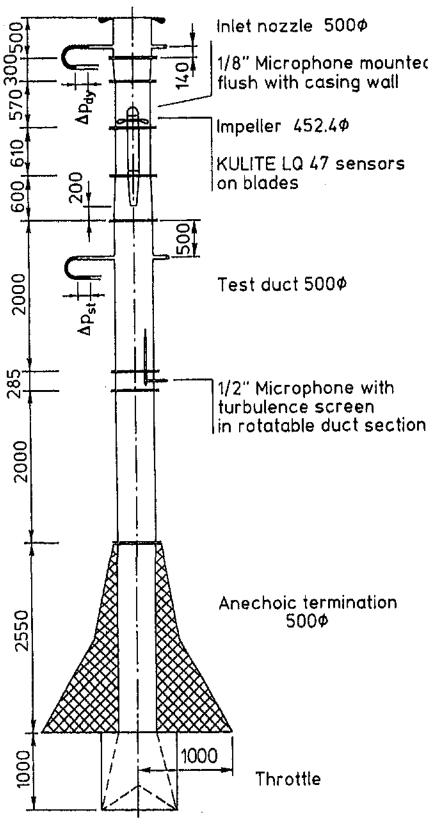

Fig. 3 Experimental setup (dimensions in mm)

sure coefficient Ψ, efficiency η, and specific sound power level L_{W_S} as functions of the flow coefficient Φ (for definitions see the nomenclature). Except for the largest tip clearance, the fan performance curves are characterized by pronounced hysteresis loops with sudden drops in flow rate, fan pressure, and efficiency, and accompanying increases in the specific sound power level when the fan is throttled into the stall region. The larger the hysteresis loop, the larger the drop in fan pressure and efficiency, as was demonstrated earlier by Hutton (1955). Note that the rise in specific sound power level is as much as 20 dB at small tip clearances. The smaller the tip clearance, the further the fan can be throttled before the blade flow is stalled but, on the other hand, the stronger the hysteresis type behavior. At the largest tip clearance (τ = 0.0053), the hysteresis loop is reduced to a very small regime, which is visible only in the specific sound power level distribution, while there is only a discontinuous change in the fan pressure and efficiency curve.

The hysteresis loop is always fairly close to the point of maximum efficiency. Decreasing the tip clearance ratio from τ = 0.0053 to τ = 0.00066 increases the optimum efficiency by as much as 7 percent points. On the other hand, there is hardly any change in the specific sound power level with tip clearance at optimum fan operation. Incidentally, the efficiency data shown in Fig. 7 are somewhat lower than commonly found in these types of flow machines, but this is due to the fact that the stator vanes were designed for a higher impeller speed (n = 3000/min).

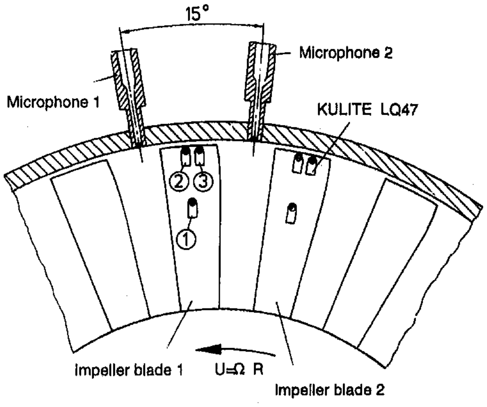

Fig. 4 Sectional view of the fan with pressure transducers KULITE LQ 47 mounted on the impeller blades and of the $\frac{1}{8}$-in. microphones B&K 4138, mounted flush with the inner casing wall

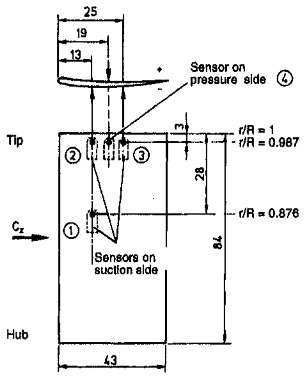

Fig. 5 Schematic of pressure sensors mounted on the impeller blade

Pressure Spectra in the Acoustic Far Field and Near Field

In earlier papers by Marcinowski (1953), Longhouse (1978), Fukano et al. (1986), and Stütz (1988), increases in broadband noise are reported as the result of an enlarged tip clearance. The sound pressure spectra depicted in Fig. 8, which were measured in the fan outlet duct, support this finding. The rotor speed is 1400/min, which corresponds to a rotor tip speed of U = 33.16 m/s and a rotor tip Mach number of M = 0.10. The blade passing frequency component is BPF = 560 Hz. According to Tyler and Sofrin's (1962) analysis, the azimuthal mode order m of the spinning modes generated by rotor/stator interaction is given by $m = h\,Z \pm vV$, where $h = 1, 2, 3, \ldots$ for the blade passing frequency component and its harmonics, and $v = 1, 2, 3, \ldots$. From this follows for the present case that the lowest azimuthal mode order of the blade passing frequency

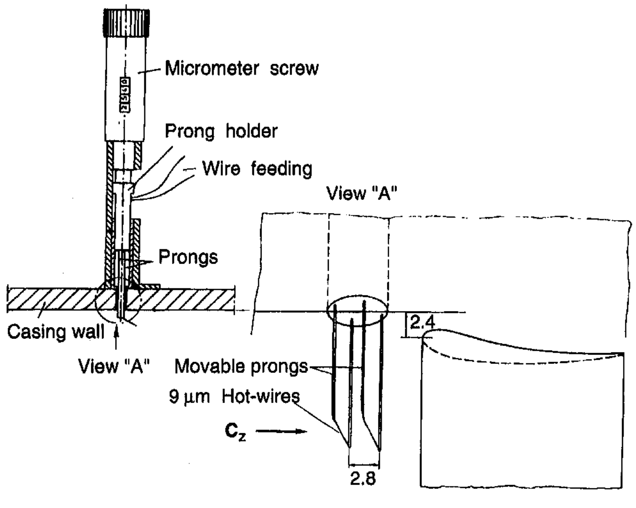

Fig. 6 Schematic of hot-wire probe

component produced by rotor/stator interaction is $m = 7$, the cut-off frequency of which in a 500-mm-dia duct is 1873 Hz under standard atmospheric conditions ($a_0 = 343$ m/s), i.e., this mode is cut off. Since the blade passing frequency component is visible in the spectrum, though of low level, one concludes that it must be the interaction of the rotor with inlet flow distortions (nonuniformities of the intake flow and/or inflow turbulence, see the review paper by Cumpsty (1977)), that causes the blade tone fundamental. The lowest azimuthal mode order of the second blade tone harmonic 2 × BPF = 1120 Hz is $m = -3$, the cut-off frequency of which in the fan duct is 917 Hz; hence, the rotor/stator interaction at 2 × BPF contributes to the sound field in the test duct.

Figure 9 shows only the low frequency range of the spectra with enhanced frequency resolution; there it is obvious that enlarging the tip clearance results in drastic level increases of the radiated sound pressure within limited, almost narrow-band frequency regions. A particularly steep level increase of 15 dB occurs at 370 Hz when the tip clearance ratio is raised from $\tau = 0.0027$ to $\tau = 0.0053$.

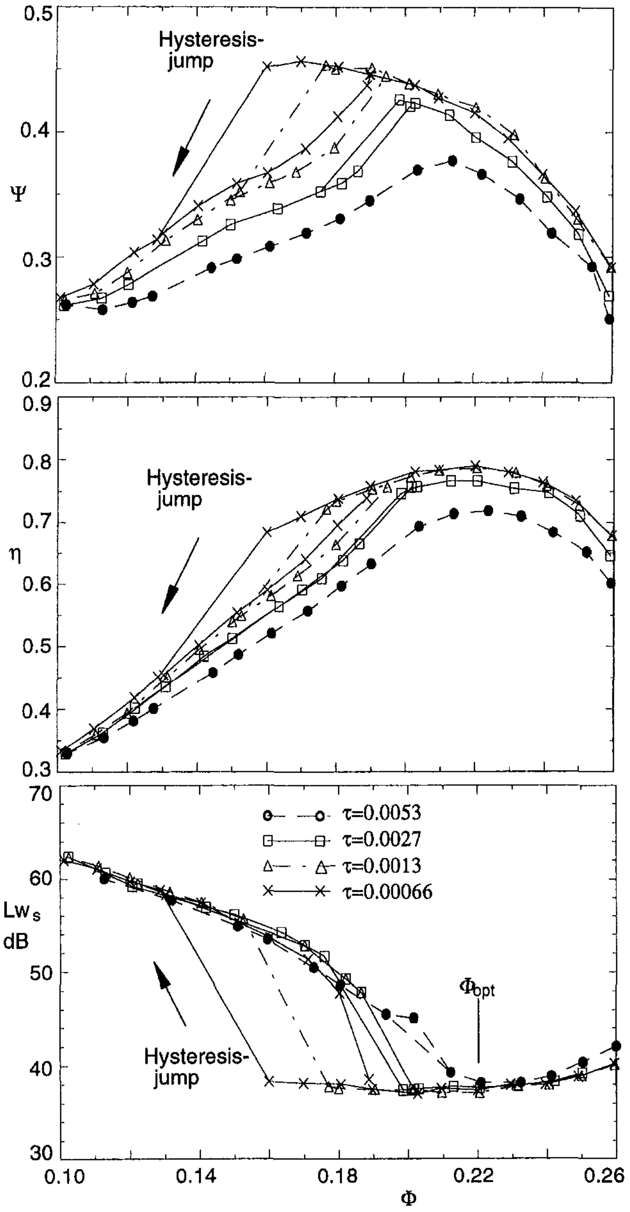

Fig. 7 Effect of tip clearance on the aerodynamic and acoustic performance, $n = 1400$/min ($U = 33.16$ m/s; $M = 0.10$)

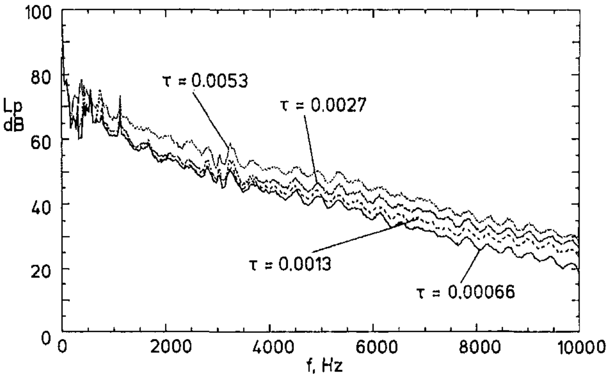

Fig. 8 Sound pressure spectra in the outlet duct as a function of tip clearance, $\Phi/\Phi_{opt} = 1$, $n = 1400$/min, $\Delta f_B = 12.5$ Hz

Nawrot (1991) and Kameier et al. (1992) performed measurements with the short inlet duct shown in Fig. 3 replaced by an anechoic test duct, which had about the same dimensions as the outlet duct. The various fan performance curves measured with this arrangement were slightly different from the ones reported here, but the effect of the tip clearance was found to be unaltered. This statement holds also true for the sound spectra radiated. From these results it appears that the tip clearance effects discussed here are largely independent of the flow conditions at the fan inlet.

In Fig. 10 pressure spectra are compared that were measured in the outlet duct (acoustic far field, curves labeled "*B*") and at the casing wall at an axial location $\zeta = z/D = -0.007$ upstream of the leading edge of the impeller blades (acoustic near field, curves labeled "*A*"). The diagrams in the left column show the results for the largest tip clearance ratio ($\tau = 0.0053$) where the tip clearance noise is most prominent in the spectrum, and the right column is for the smallest tip clearance ratio ($\tau = 0.00066$). The outlet duct spectra were obtained as before by using a $\frac{1}{2}$-in. slit-tube microphone, and $\frac{1}{8}$-in. microphones mounted flush with the inner duct wall were used to measure the near-field pressures; compare Fig. 4. The flow coefficient Φ is reduced from the top to the bottom diagram. The blade passing frequency component (BPF) is clearly visible in the wall pressure spectra, and multiples of the rotor frequency (RF) appear to both sides of this component.

The tip clearance noise component (CN) measured for $\tau = 0.0053$ in the duct is shifted toward lower frequencies as the flow rate is reduced. In the wall pressure spectra another component termed rotating instability (RI) appears, which increases in level as the flow rate is throttled. The term rotating instability noise is discussed further in the following section. At some operating conditions, tone components exist at frequencies

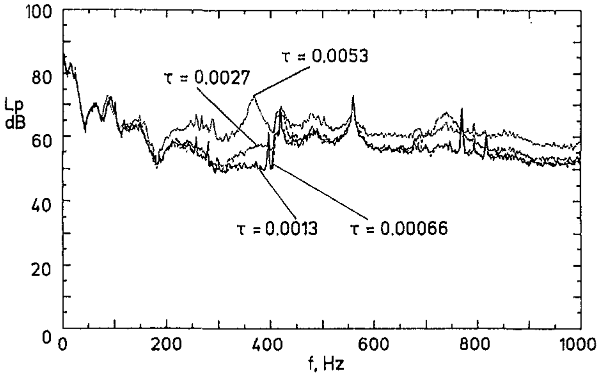

Fig. 9 Sound pressure spectra in the outlet duct as a function of tip clearance, $\Phi/\Phi_{opt} = 1$, $n = 1400$/min, $\Delta f_B = 1.56$ Hz

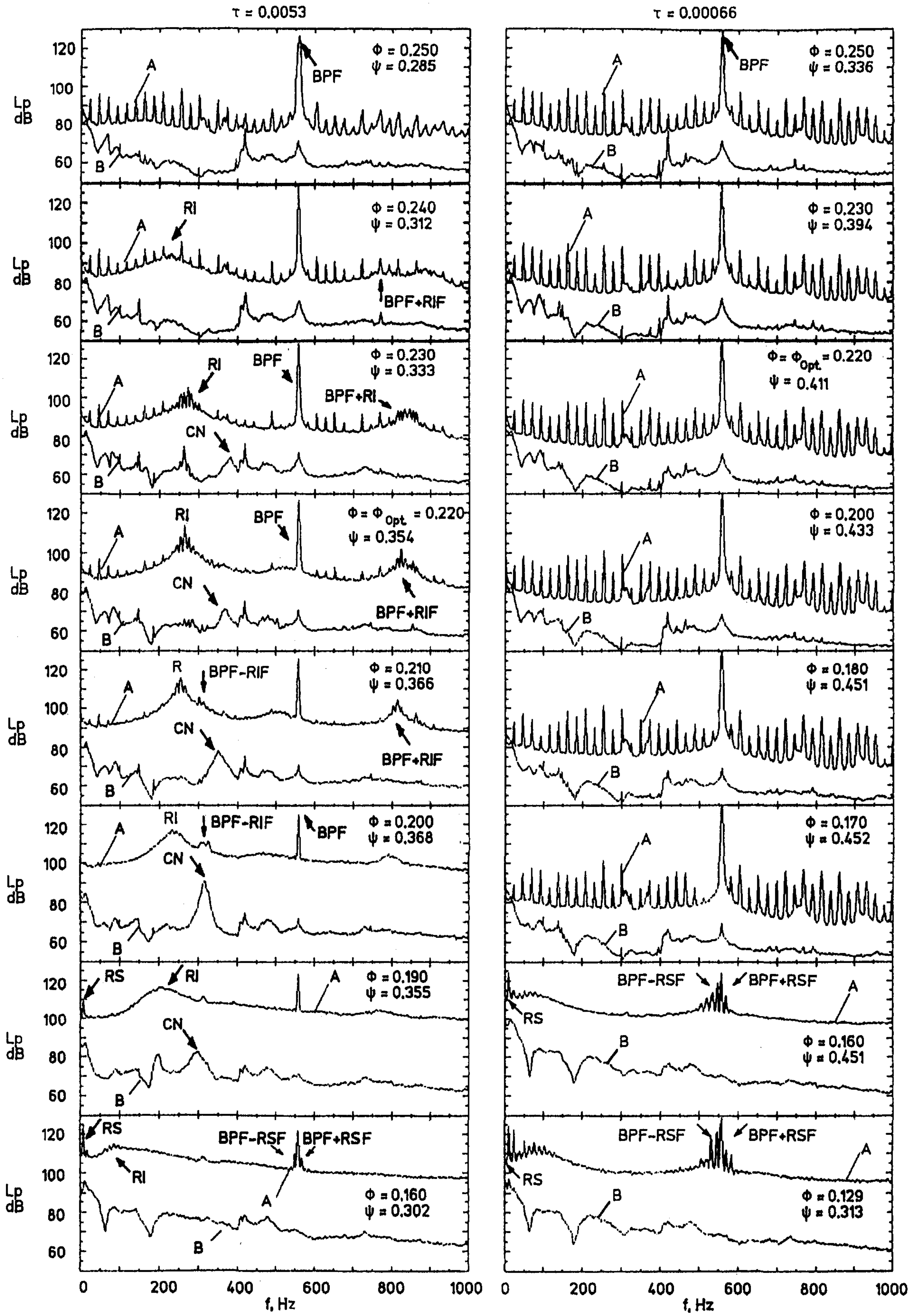

Fig. 10 Pressure spectra in the outlet duct ("B", far field) and at the casing wall ("A", $\zeta = -0.007$, near field) for various operating conditions, $\tau = 0.0053$ (left column) and $\tau = 0.00066$ (right column), $n = 1400$/min, $\Delta f_B = 1.56$ Hz

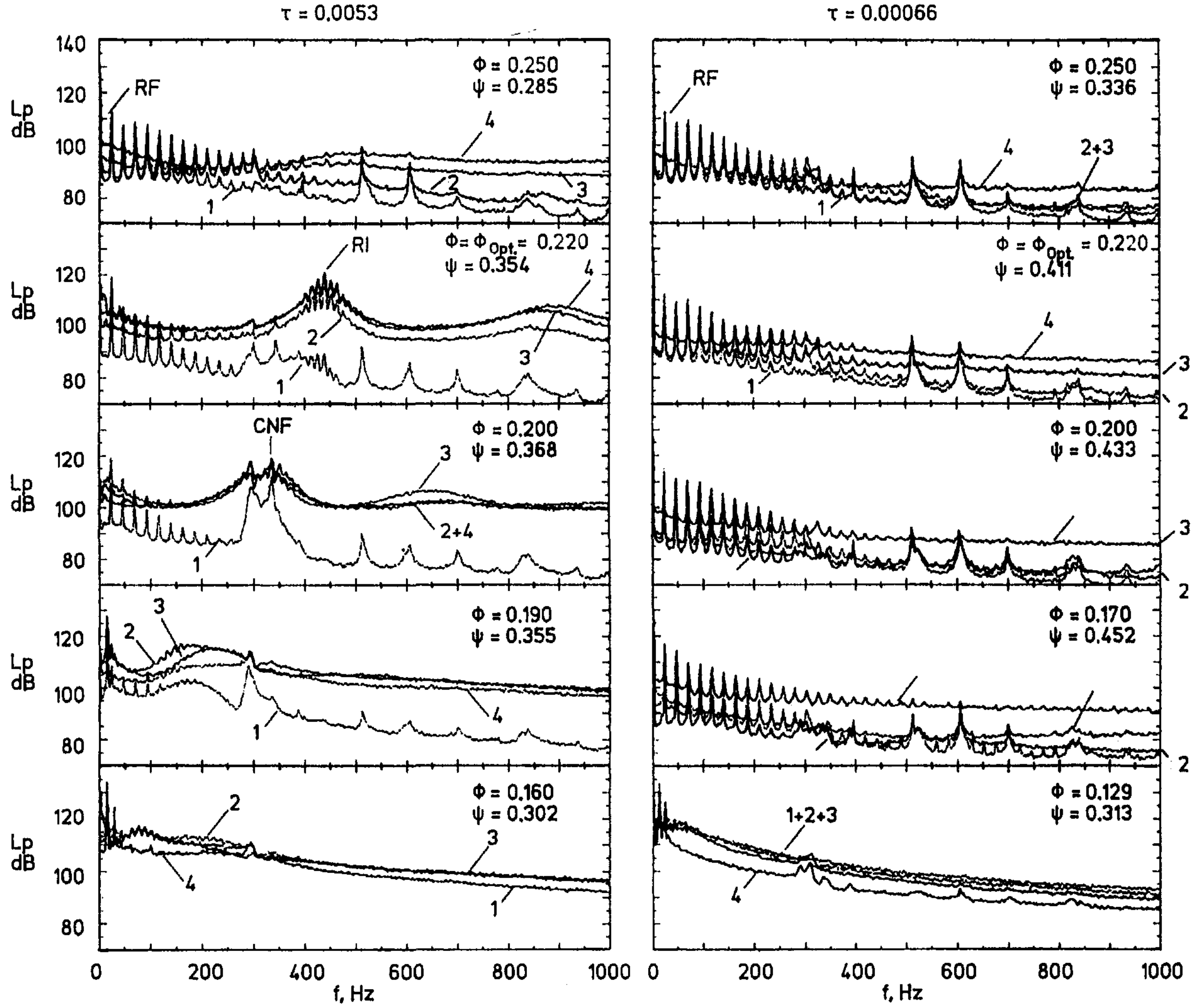

Fig. 11 Spectra of the impeller blade pressures for various operating conditions, $\tau = 0.0053$ (left column) and $\tau = 0.00066$ (right column), $n = 1400$/min, $\Delta f_B = 1.56$ Hz

equal to the sum or difference of the blade passing frequency and the frequency of the rotating instability component, i.e., at BPF + RIF and BPF − RIF. At $\Phi = 0.200$ (third diagram from the bottom) the tip clearance noise reaches its highest level. At flow rates below $\Phi = 0.200$, the fan operation becomes unstable, and a tonal component below the rotor shaft frequency is generated in the outlet duct spectra as well as in the wall pressure spectra that are associated with rotating stall (RS). This also results in a frequency modulation of the blade passing frequency, and consequently side bands at BPF + RSF and BPF − RSF appear in the wall pressure spectrum.

With a tip clearance ratio of $\tau = 0.00066$ (right column in Fig. 10), the clearance noise component and rotating instability component are missing in the spectra throughout the range of operating conditions. Rotating stall occurs at much lower flow rates than before, i.e., $\Phi \leq 0.16$.

Pressure Fluctuations on the Impeller Blades

To measure the fluctuating blade pressures, two impeller blades were equipped with four miniature pressure sensors each; see the arrangement in Fig. 5. A comparison of the pressure spectra measured at the four blade positions is given in Fig. 11, where the left column is again for the largest tip clearance ($\tau = 0.00053$) and the right column for the smallest $\tau = 0.00066$).

The upper three diagrams in the left column ($\tau = 0.0053$) correspond to stable fan operating conditions, and the lower two to the rotating stall regime. At all four measurement positions the spectra are dominated by spikes at the rotor shaft frequency and multiples thereof, which indicates that the flow environment of the rotor is not quite uniform. Since the tone levels are highest at the rotor shaft frequency Ω and decrease monotonously with increasing frequency, it is concluded that these tones are generated by the interaction of the rotor with inlet flow distortions; compare the discussion of the origin of the blade passing frequency component in the context of Fig. 8. Knowledge of the exact origin of the shaft order frequency components, however, is not of importance for the present study. For most of the flow rates tested, the "stator passing frequency" $V \cdot \Omega = 397$ Hz is not visible but buried in the random noise. When the fan is operated just near the maximum efficiency point ($\Phi = 0.220$), a broad-band hump with superimposed multiple peaks appears in the spectrum, which moves to lower frequencies when the flow is further throttled. This behavior is similar to that of the rotating instability component in the wall pressure spectra; compare Fig. 10. The frequencies measured in the fixed and in the rotating frame of reference are different. Closer to the hub ($r/R = 0.876$, sensor #1), the pressure fluctuations of the rotating instability component are much lower in level than at the blade tip, which reveals that the cause for this phenomenon lies in the tip flow region. Mongeau (1991), Bent et al. (1992), and Mongeau et al. (1993) reported similar pressure spectra on the blades of a casingless centrifugal pump impeller and interpreted them as the result of a rotating "almost-frozen" discharge flow instability pattern, which rotates relative to the blades, similar to the cells of separated flow in case of rotating stall. The term rotating flow instability is also used in the present paper; however, it was shown by Kameier (1994) and in another paper by the present authors (1997) that the rotating instability components found in the blade tip region of axial fans are not caused by a frozen flow disturbance but rather by a rotating source or vortex mechanism. As the fan pressure is increased, the rotating flow instability components are moved to lower frequencies.

As in the case of the wall pressure spectra shown in Fig. 10, the rotating instability component is missing in the blade pressure spectra when the tip clearance is small; compare the diagrams in the right column of Fig. 11.

With the onset of rotating stall, the low-frequency random noise levels are increased, and the harmonics of the stator frequency are masked. The spectra are now dominated by the rotating stall component with the highest levels at sensor location #2 and #3, i.e., on the blade suction side at a radial distance from the axis of $r/R = 0.987$. This indicates that the blade flow is stalled first at the tip. When the flow is further reduced, the stalled flow regime extends deeper down to the hub. Note that the frequency of the rotating stall component is different from the one found in the wall pressure fluctuations (see Fig. 10); the sum of the two frequencies is, of course, equal to the rotor shaft frequency.

In Fig. 12 the nondimensional frequencies (Strouhal numbers $St = (fD/U)(\pi/Z)$) of the tip clearance noise in the outlet duct (CN) and of the rotating instability component (RI) are plotted as functions of the flow coefficient; the data for the latter component were measured on the rotating impeller blades as well as on the stationary casing. Note that with this definition of the Strouhal number, the blade passing frequency assumes the value $St = 1$. In the case of the large tip clearance ($\tau = 0.0053$), a fan operating condition exists at which the frequency difference BPF − RIF measured in the fixed frame of reference is equal to the frequency CNF of the tip clearance noise component. This is the operating condition of maximum tip clearance noise ($\Phi = 0.20$). Before such a condition can be reached in the case of the small tip clearance ($\tau = 0.0027$, lower diagram in Fig. 12) the blade flow is already stalled.

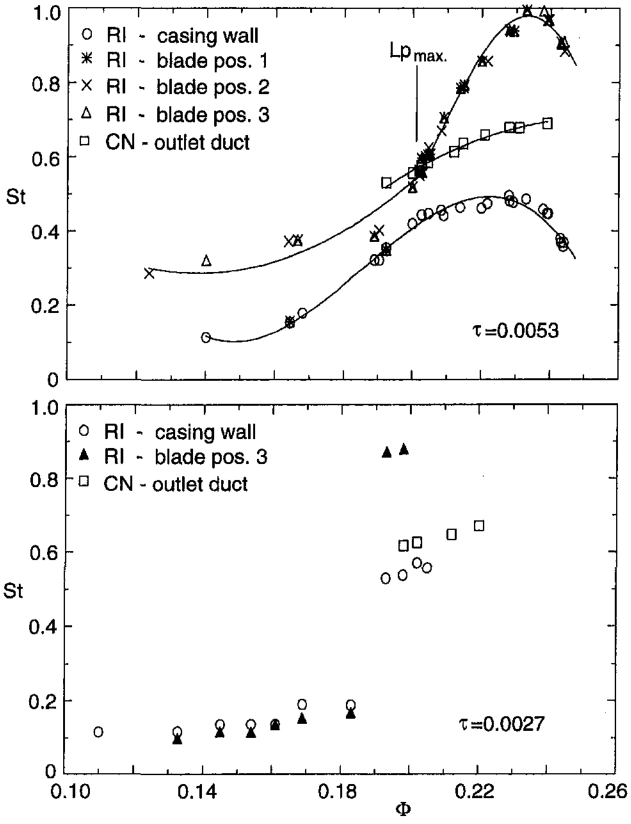

Fig. 12 Variation of the nondimensional frequency of various spectral components with the flow rate in the outlet duct, at the casing wall and on the impeller blade, *n* = 1400/min (RI = rotating instability component; CN = tip clearance noise

Azimuthal Propagation of the Rotating Instability Component

Bendat and Piersol (1980) describe a source location method, which is adapted here to determine the azimuthal propagation velocity of the rotating instability component. On the premises that auto power spectra of the pressure signals measured at two different locations have the same magnitude ($G_{11} = G_{22}$), the cross-spectrum G_{12} between the two signals can be written as

$$G_{12}(\omega) = G_{11}(\omega)e^{i\omega\Delta t}. \qquad (1)$$

Here G_{11} is the auto power spectrum at location 1, ω the angular frequency, and Δt the time delay between the two signals. In Eq. (1) the phase angle $\hat{\varphi}_{12}$ of the cross-spectrum is expressed as a function of the propagation time

$$\hat{\varphi}_{12} = \omega\Delta t. \qquad (2)$$

The speed of propagation is determined by the displacement between the sensors and the delay time Δt. In the present experiments, the azimuthal propagation velocity Ω_{RI} is determined by using two azimuthally spaced sensors in the casing walls and two sensors mounted on adjacent impeller blades; compare Fig. 4. The angular displacement of the two sensors is $\Delta\varphi = 15$ deg for the casing wall microphones as well as for the blade pressure sensors. The azimuthal propagation velocity Ω_{RI} is given by the following relation:

$$\Omega_{RI} = \Delta\varphi/\Delta t = \Delta\varphi\omega/\hat{\varphi}_{12} \qquad (3)$$

As an example, in Fig. 13 are shown the auto power spectrum Lp of one of the two sensors, the coherence γ^2 of the two sensor signals, and the phase angle $\hat{\varphi}_{12}$ of the cross spectrum; the diagrams on the left-hand side are for the casing wall pressures and the ones on the right-hand side for the impeller blade pressures. Clearly, the frequencies of the rotating instability component are different in the fixed and rotating frames of reference. The coherence of the signals of the two microphones or, respectively, the two pressure sensors on the blades, is high in the frequency range of the rotating instability component. The gradient of the phase angle in that frequency range is different for the fixed and the rotating system, which indicates that the propagation velocity of the rotating instability component is positive in one coordinate system and negative in the other. The angular propagation velocity is now determined by applying Eq. (3) to the spectral line with the highest coherence. This was done for different operating conditions, and the result is plotted in Fig. 14 for the tip clearance ratios $\tau = 0.0027$ and $\tau = 0.0053$; the rotating instability phenomenon does not exist at the two other, smaller tip clearances.

The data in Fig. 14 reveal that the rotating instability components move relative to the impeller blades as well as relative to the fixed coordinate system. Note that differently from the rotating stall case, the sum of the frequencies of the various spikes measured in the fixed and rotating frames of reference is not equal to the rotor shaft frequency. On the other hand, the sum of the magnitudes of the propagation velocities in the two coordinate systems is equal to the impeller angular velocity or, in other words:

$$\Omega^F_{RI} = \Omega^R_{RI} + \Omega \qquad (4)$$

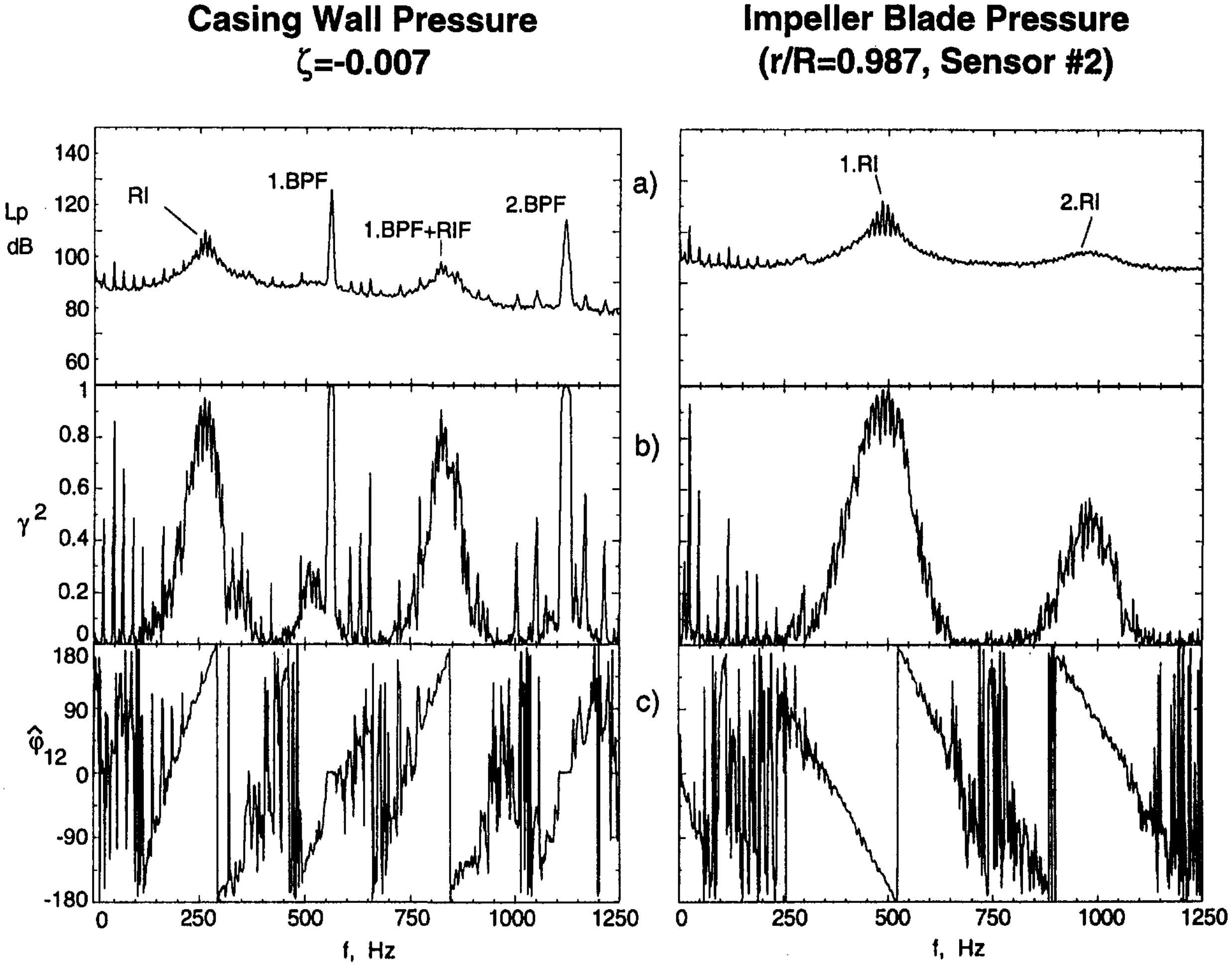

Fig. 13 Comparison of the pressure fluctuations at the casing wall ($\zeta = -0.007$, left column) and on the impeller blade (sensor #2, right column), compare the arrangement shown in Fig. 4 ($\Phi/\Phi_{opt} = 1$, $\tau = 0.0053$, $n = 1400/\mathrm{min}$, $\Delta f_B = 1.56$ Hz): (*a*) pressure spectra, (*b*) coherence, (*c*) phase angle of the cross-spectrum

where the superscripts F and R denote the fixed and the rotating frames of reference, respectively. Since the angular displacement of the two sensors $\Delta\varphi$ is the same in the fixed and rotating frames of reference, a simple relation can be derived for the frequencies of the rotating instability component measured in the two coordinate systems:

$$f^F/\hat{\varphi}^F_{12} - f^R/\hat{\varphi}^R_{12} = \Omega/2\pi\Delta\varphi. \tag{5}$$

Modification of the Tip Clearance Gap

Up to this point, the experimental results do not give a decisive clue as to what the exact relation is between the tip clearance noise and the rotating instability component found in the impeller blade pressures and the casing wall pressures. To examine whether the tip clearance noise is generated by the flow over the blade tip, i.e., by the blade tip vortex, which is driven by the pressure difference between the pressure and the suction side of the blade profile, a thin self-adhesive plastic tape was wrapped around the impeller from blade to blade to suppress the flow over the blade tip. The tape formed a polygon with the impeller blades placed in the corners. With this configuration, however, the tip clearance noise level was higher than before, despite the fact that the flow rate and the fan pressure were reduced (Kameier, 1994).

From this result it was concluded that it is not the blade tip flow that generates the tip clearance noise but rather the secondary flow through the gap, which is driven by the static pressure difference between inlet and outlet of the impeller disk and extends over the entire circumference. To help block or at least impede this gap flow, a tape of 2-mm-thick Velcro tape material was inserted into the 2.4-mm-wide ($\tau = 0.0053$) tip clearance gap; see the schematic presentation shown in Fig. 15. The Velcro tape is bonded to the inner casing wall; its axial width is 15 mm, and its axial position is that of the maximum thickness of the impeller blade profile, which is presumably the location of the maximum pressure difference between suction and pressure side of the blade profile (Fig. 16). Incidentally, in experimental fluid dynamics Velcro tape is frequently used as a tripping device for the generation of turbulent boundary layers.

Figure 17 shows a comparison of the sound pressure spectra in the fan outlet duct and the pressure spectra at the casing wall for the cases with and without the Velcro tape. The fan operating point is that of maximum tip clearance noise ($\Phi = 0.200$). The effect of the Velcro material is to diminish the tip clearance noise component by more than 30 dB, which practically eliminates this component from the radiated far field spectrum. The rotating instability component in the near field pressures is suppressed as well. At the same time the fan pressure coefficient is improved from $\Psi = 0.368$ to 0.419. A comparison of the aerodynamic and acoustic fan performance curves is depicted in Fig. 18. Clearly, the fan with the modified tip clearance gap reaches a distinctly higher fan pressure and widens the useful range of operating conditions. The hysteresis loop is comparable to that of a fan with about half the gap width, and the stall behavior is similar to that with the two smallest tip clearance ratios $\tau = 0.0013$ and $\tau = 0.00066$; compare Fig. 7.

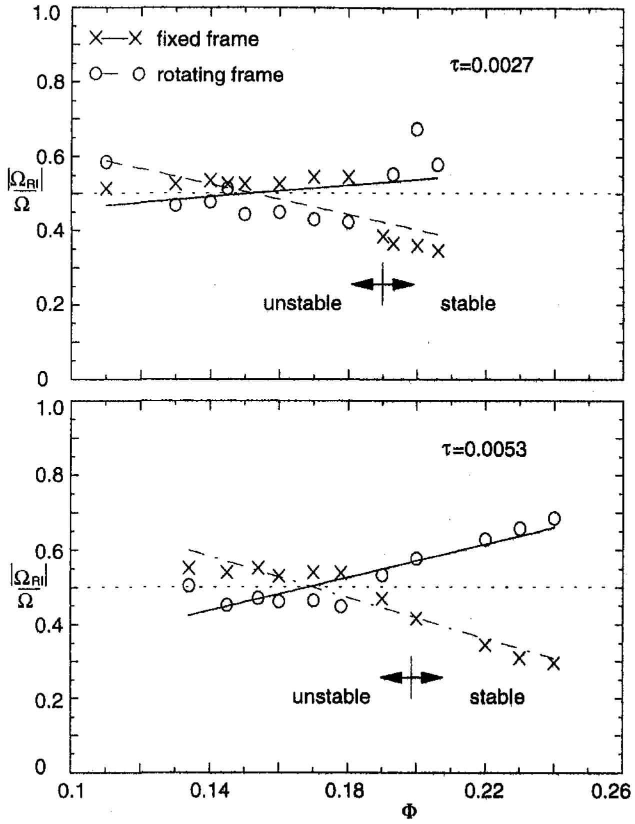

Fig. 14 Normalized angular propagation velocity of the rotating instability component as a function of flow rate for two tip clearance ratios, n = 1400/min

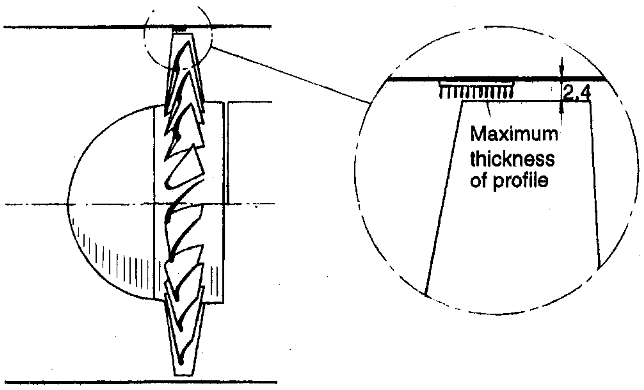

Fig. 15 Schematic view of tip clearance gap with Velcro tape inserted

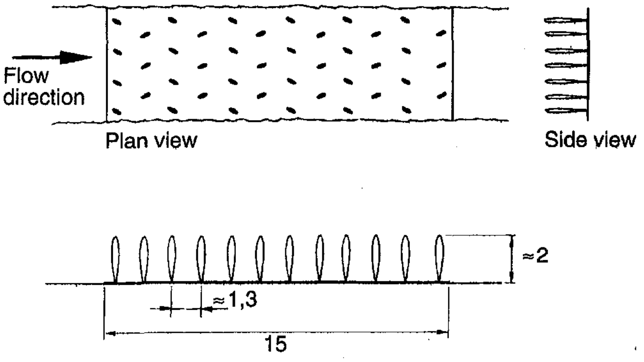

Fig. 16 Sketch of the Velcro tape geometry (dimensions in mm)

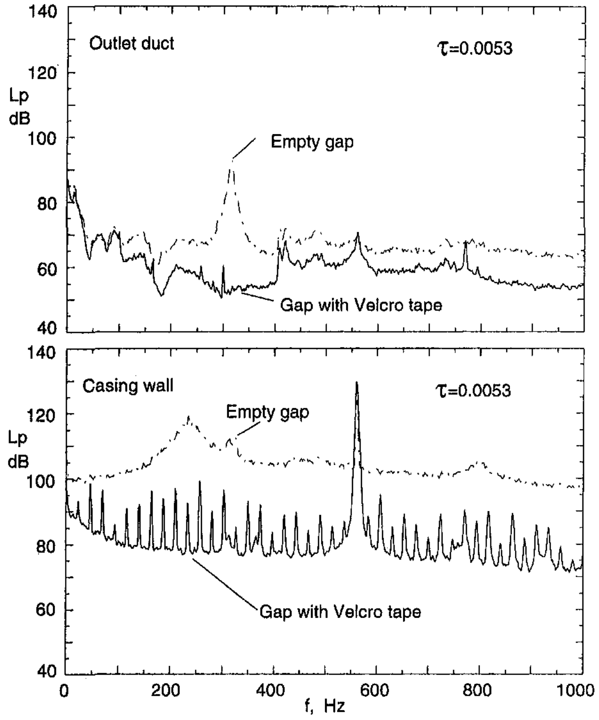

Fig. 17 Sound pressure spectra in the outlet duct and on the casing wall at the operating conditions with maximum tip clearance noise (empty gap: Φ = 0.200, Ψ = 0.368, gap with Velcro tape: Φ = 0.200, Ψ = 0.419); n = 1400/min, Δf_B = 1.56 Hz, τ = 0.0053

Hot-Wire Measurements in the Blade Tip Region

To investigate the influence of the Velcro tape on the flow conditions in the blade tip region and in the tip clearance gap, hot-wire measurements were made in that area with the aid of the hot-wire probe depicted in Fig. 6. In this environment, hot-wire measurements are extremely difficult and subject to larger measurement errors because close to the rotating impeller blades both the magnitude and the angle of the mean flow velocity vector vary periodically by significant amounts. In addition, there is a superimposed secondary flow in the gap region, the direction of which depends on the fan operation condition. Nevertheless, the experimental results presented in the following provide at least a qualitative picture of the blade tip flow field. As was mentioned before, the two-wire hot-wire probe permitted measurements of the axial and circumferential components of the absolute velocity at different radial distances from the casing wall. The radial velocity component could not be measured.

In Fig. 19 is shown a comparison of the flow fields for the cases with and without the Velcro tape in the 2.4-mm-wide gap (τ = 0.0053) for a fan operating condition to the right of the design point (Φ/Φ_{opt} = 1.1) where the tip clearance noise component does not exist. At this flow rate, the effect of the Velcro tape on the fan performance curves is small (compare Fig. 18), and consequently there is hardly any change in the flow field. A similar comparison is shown in Fig. 20 for the optimum efficiency point (Φ/Φ_{opt} = 1). With the conventional tip clearance geometry, the flow velocity in the gap is reversed (upper sketch) while it is in the direction of the main flow when the Velcro tape is inserted. This result reveals that the effect of the Velcro tape is not to block the reversed tip clearance flow, because in that case the axial flow velocity component in the gap would become zero. Also, the area of the tip annulus blocked by the loops of the Velcro tape is small compared to the total. For comparison, experiments with other flow obstructions upstream of the blade tips, which in fact blocked the tip clear-

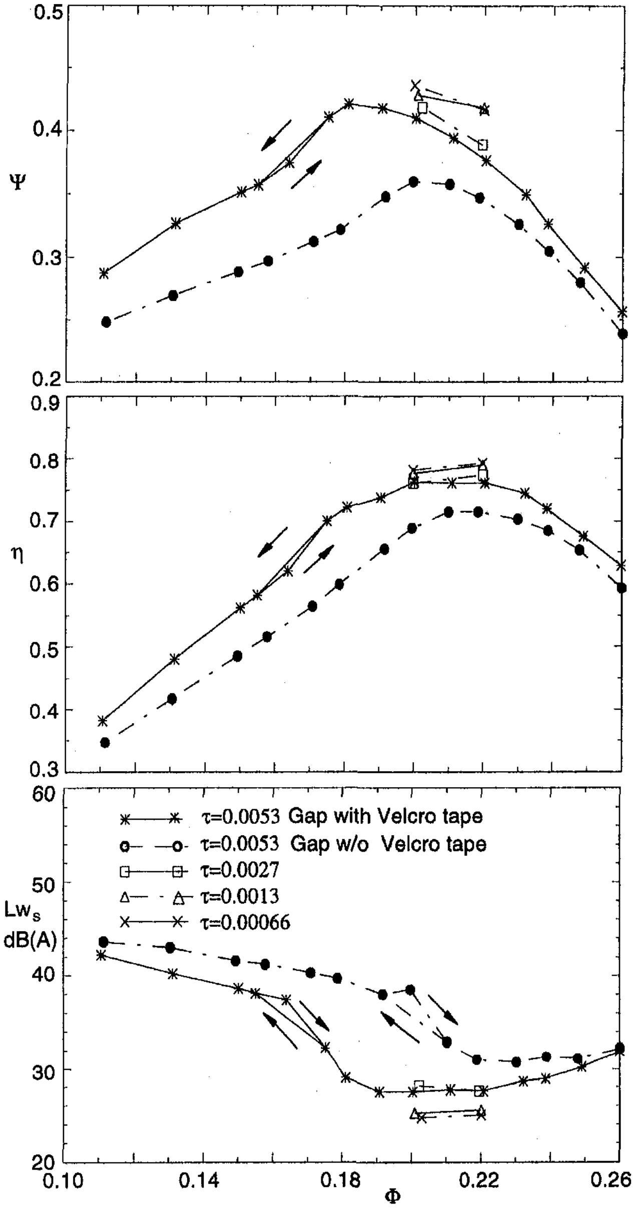

Fig. 18 Influence of the Velcro tape inserted into the tip clearance gap on the aerodynamic and acoustic fan performance curves, n = 1400/min

ance flow, did not improve the fan performance and the noise. For these reasons, it is assumed that the Velcro tape acts to trip the duct wall boundary layer flow, like a turbulence generator, and thereby improves the energy exchange between the low-momentum fluid particles at the wall and those of the main flow. Admittedly, however, how exactly the Velcro tape affects the flow in the blade tip regime is not known. Note that the flow vectors shown in Figs. 19 and 20 were obtained by continuous time averaging of the hot-wire signals and therefore represent the flow components averaged over the impeller circumference. Hence, the reversed flow in the tip clearance gap at flow rates $\Phi/\Phi_{\mathrm{opt}} \leq 1$ extends over the entire circumference.

Figure 21 shows the radial distribution of the axial and the azimuthal velocity component in tip clearance gap at an axial position downstream of the blade tip ($\zeta = z/D = 0.009$). The azimuthal component is normalized by the impeller tip speed U and the axial component by the average flow velocity $\bar{C}_z$ in the fan annulus. The azimuthal velocity component increases when the flow rate is reduced while the axial component is reversed. The more the fan is throttled, the higher the reversed flow velocity. In conclusion we note that reversed flow conditions exist at those operating conditions where the tip clearance noise appears in the sound pressure spectrum.

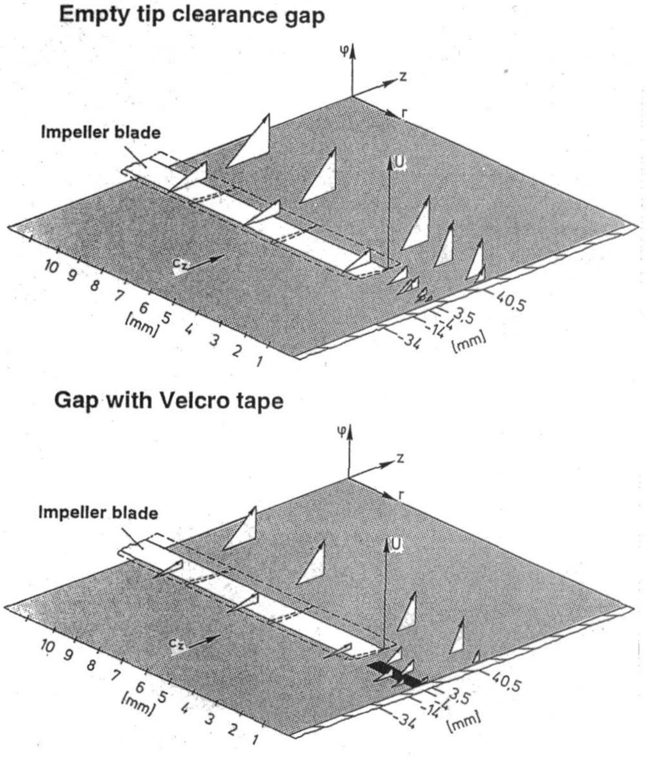
Empty tip clearance gap

Gap with Velcro tape

Fig. 19 Vectors of the absolute flow velocity in the blade tip area (the radial dimensions are enlarged by a factor 5), Φ/Φ_{opt} = 1.1, n = 1400/min

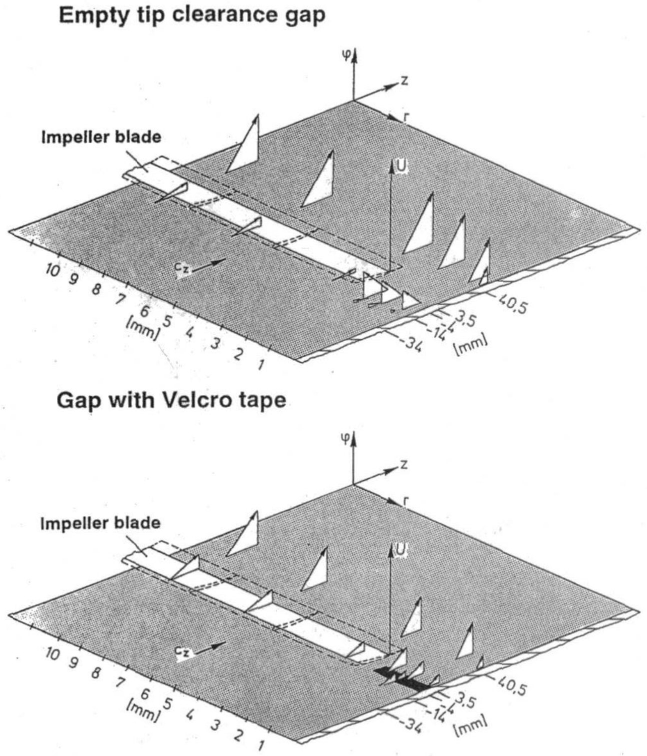
Empty tip clearance gap

Gap with Velcro tape

Fig. 20 Vectors of the absolute flow velocity in the blade tip area (the radial dimensions are enlarged by a factor 5), Φ/Φ_{opt} = 1.0, n = 1400/min

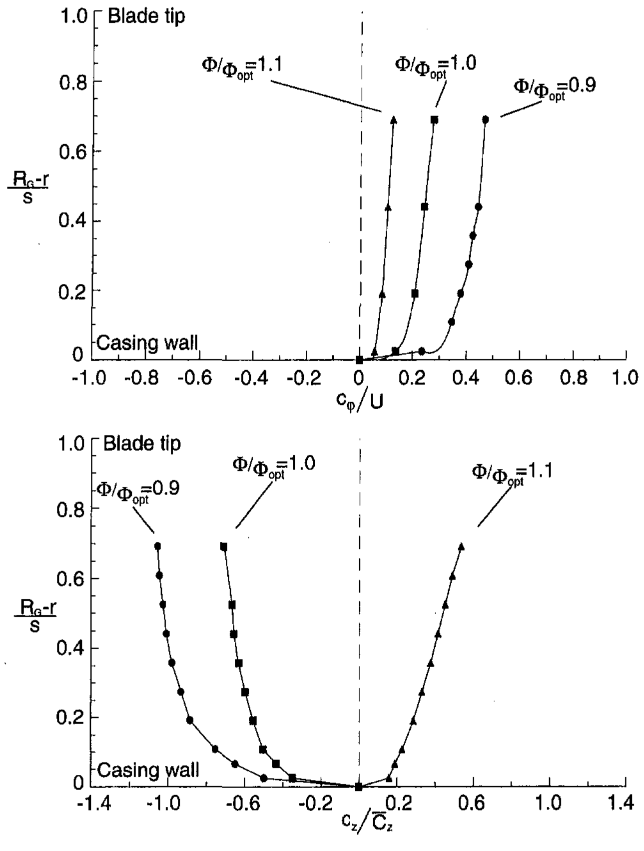

Fig. 21 Radial distribution of the axial and azimuthal velocity component in the tip clearance gap (empty gap), $\zeta = 0.009$, $\tau = 0.0053$, $n = 1400$/min

When the Velcro tape is inserted into the gap, compare Fig. 22, the flow reversal in the gap is suppressed. At this point it is worth mentioning that large measurement errors may have occurred in the determination of the axial velocity component downstream of the Velcro tape due to the increased turbulence intensity. In particular the data for $\Phi/\Phi_{opt} = 0.9$ are probably in error because they show values larger than the average flow velocity in the fan annulus.

Conclusions

An experimental study is described to investigate the negative effects of the tip clearance gap on the aerodynamic and acoustic performance of axial turbomachines. The experiments were made with a high-pressure low-speed axial fan with $D = 452$ mm impeller diameter, $\varepsilon = 0.62$ hub-to-tip ratio, $Z = 24$ blades (NACA 65 profile), and $V = 17$ outlet guide vanes. The impeller diameter was kept constant throughout the tests, and the tip clearance was varied in the range $s = 0.3$ to 2.4 mm by using casing segments of different size.

In the published literature higher broad-band levels were reported when the tip clearance was enlarged. The present results show that in addition to that, significant sound pressure level increases occur within limited, almost narrow frequency bands in a region below the blade passing frequency component. This tip clearance noise component, which is a particularly effective noise source, was observed when the tip clearance ratio was larger than or equal to $\tau = s/D = 0.0027$ and if there is a high enough pressure difference between suction and pressure side of the impeller, i.e., at flow rates equal to or smaller than the design flow rate.

Measurements of the pressure fluctuations on the casing wall close to the impeller and on the rotating blades have shown that a flow instability mechanism occurs at the blade tip associated with the tip clearance noise. These rotating instability components move in azimuthal direction, relative to the impeller blade row. Hot-wire measurements in the tip region have shown that this rotating instability only occurs if a reversed flow condition exists in the tip clearance gap. The effect of the reversed flow is to increase the thickness of the casing wall boundary layer at the fan intake and to eliminate the axial component of the absolute flow velocity in the gap. As a result, vortex separation takes place at the blade tip, similar to part span stall. If the azimuthal wavelength of the shed vortices is equal to the blade spacing, there is a strong interaction of the vortex separation on individual blades, which results in drastic increases of the radiated noise. When the mean flow is throttled even further, the blade flow is separated over the entire radial span over part of the impeller circumference, which is the well-known phenomenon of rotating stall.

The rotating flow instability phenomenon found in the present study was also observed in high-speed axial compressors. Recent engine tests (Baumgartner et al., 1995) revealed that vibrations of the first-stage rotor blades were caused by flow pressure fluctuations in the frequency region below the blade passing frequency, which show a spectral characteristic similar to the rotating instability components described here.

As a modification of the tip clearance geometry, a turbulence generator (Velcro tape) is inserted into the 2.4-mm-wide tip clearance gap ($\tau = 0.0053$) to obstruct the secondary flow through the gap. With this device, the tip clearance noise component is diminished in the acoustic far field spectrum by more than 30 dB at the operating point where maximum tip clearance noise is found otherwise. At the same time the fan pressure is improved by 14 percent, the fan efficiency by 7 percent points, the specific sound power level is reduced by 11 dB(A), and the onset of rotating stall is shifted to lower flow rates so that

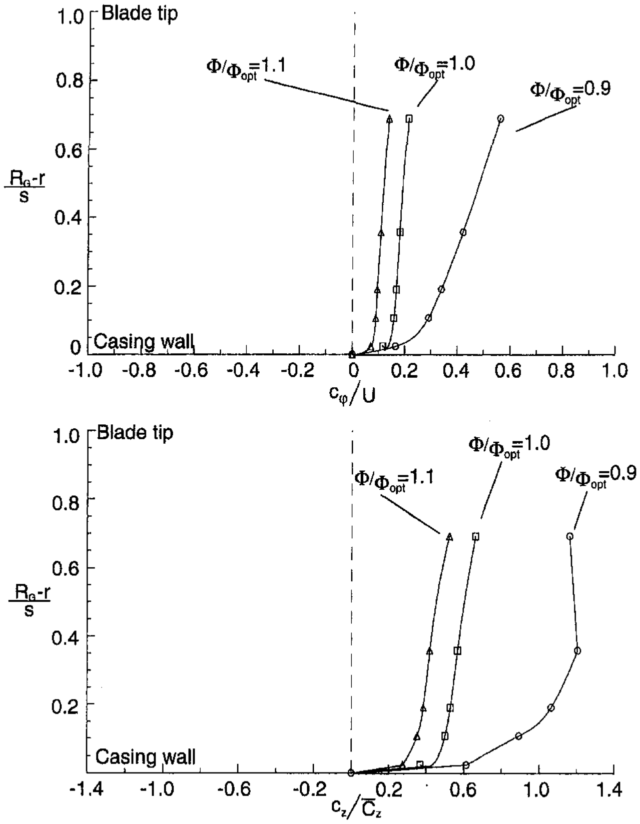

Fig. 22 Radial distribution of the axial and azimuthal velocity component in the tip clearance gap with Velcro tape inserted, $\zeta = 0.009$, $\tau = 0.0053$, $n = 1400$/min

the useful range of the characteristic curve is comparable to the case of a much smaller tip clearance ratio, i.e., $\tau = 0.0013$ and $\tau = 0.00066$. The turbulence generator device is suggested for fan installations where the tip clearance cannot be reduced further for reasons such as blade stagger angle variation, relative motion between impeller and casing, blade deformation under thermal or acceleration forces, or spark generation; it can be used for retrofitting existing axial turbomachines as well as for new installations.

References

Baumgartner, M., Kameier, F., and Hourmouziadis, J., 1995, "Non Engine Order Blade Vibration in a High Speed Compressor," *Twelfth International Symposium on Airbreathing Engines,* Melbourne, Australia, Sept. 10–15.

Bendat, J. S., and Piersol, A. G., 1980, *Engineering Applications of Correlation and Spectral Analysis,* Wiley, New York.

Bent, P. H., McLaughlin, D. K., and Thompson, D. E., 1992, "The Influence of Discharge Configuration on the Generation of Broadband Noise in Centrifugal Turbomachinery," *Proc. 14th DGLR/AIAA-Aeroacoustics Conference Aachen,* DGLR Bericht 92-03, pp. 607–614, Paper No. 92-02-099, Bonn, Germany.

Cumpsty, N. A., 1977, "Review—A Critical Review of Turbomachinery Noise," ASME *Journal of Fluids Engineering,* Vol. 99, pp. 278–293.

Cumpsty, N. A., 1989, *Compressor Aerodynamics,* Longman Scientific & Technical, pp. 343–345.

DIN 24 163, Parts 1, 2, and 3, 1985, "Ventilatoren, Leistungsmessung," German Standard, Deutsches Institut für Normung, Berlin, Germany.

DIN 45 635, Part 9, 1989, "Geräuschmessungen an Maschinen, Luftschallmessung, Kanal-Verfahren, Rahmen-Meßverfahren für Genauigkeitsklasse 2," German Standard, Deutsches Institut für Normung, Berlin, Germany.

Fukano, T., Takamatsu, Y., and Kodama, Y., 1986, "The Effect of the Tip Clearance on the Noise of Low Pressure Axial and Mixed Flow Fans," *Journal of Sound and Vibration,* Vol. 105, pp. 291–308.

Hutton, S. P., 1955, "Three-Dimensional Motion in Axial Flow Impellers," *Proc. IMechE,* No. 25, Vol. 170, pp. 863–873.

ISO/DIS 5136, 1990, "Acoustics—Determination of Sound Power Radiated into Duct by Fans—In-Duct Method," International Standard, International Organisation for Standardization.

Kameier, F., Geuer, U., and Neise, W., 1991, "Untersuchung zur Entstehung des Blattspitzen-Wirbellärms an einer axialen Strömungsmaschine," *VDI Berichte,* No. 872, pp. 343–358.

Kameier, F., Nawrot, T., and Neise, W., 1992, "Experimental Investigation of Tip Clearance Noise in Axial Flow Machines," *Proc. 14th DGLR/AIAA-Aeroacoustics Conference Aachen,* DGLR Bericht 92-03, pp. 250–259, Paper No. 92-02-040, Bonn, Germany.

Kameier, F., 1994, "Experimentelle Untersuchung zur Entstehung und Minderung des Blattspitzen-Wirbellärms axialer Strömungsmaschinen," *Fortschritt Berichte VDI Reihe* 7, No. 243, Verein Deutscher Ingenieure, VDI Verlag GmbH, Düsseldorf, Germany (Doctoral Dissertation, Technische Universität Berlin).

Kameier, F., and Neise, W., 1997, "Rotating Flow Instability as a Source of Noise in Axial Turbomachines," to be published in *Journal of Sound and Vibration.*

Longhouse, R. E., 1978, "Control of Tip-Vortex Noise of Axial Flow Fans by Rotating Shrouds," *Journal of Sound and Vibration,* Vol. 58, pp. 201–214.

Marcinowski, H., 1953, "Einfluß des Laufradspaltes und der Luftführung bei einem Kühlgebläse axialer Bauart," *Motortechnische Zeitschrift (MTZ),* No. 14, pp. 259–262.

Mongeau, L., 1991, "Experimental Study of the Mechanism of Sound Generation by Rotating Stall in Centrifugal Turbomachines," PhD thesis, The Pennsylvania State University.

Mongeau, L., Thompson, D. E., and McLaughlin, D. K., 1993, "Sound Generation by Rotating Stall in Centrifugal Turbomachines," *Journal of Sound and Vibration,* Vol. 163, pp. 1–30.

Nawrot, T., 1992, "Experimentelle Untersuchung zum Entstehungsmechanismus des Spitzenwirbellärms an einer axialen Strömungsmaschine," Diploma-thesis; Hermann-Föttinger-Institut für Thermo- und Fluiddynamik, Technische Universität Berlin, Germany.

Stütz, W., 1988, "Experimentelle Untersuchung zum Radialspalteinfluß auf das aerodynamische und akustische Verhalten eines Axialventilators," *Strömungsmechanik und Strömungsmaschinen,* No. 39, Verlag G. Braun, Karlsruhe, Germany, pp. 153–160.

Tyler, J. M., and Sofrin, T. G., 1962, "Axial Flow Compressor Noise Studies," *Transactions of the Society of Automotive Engineers,* Vol. 70, pp. 309–332.

Vavra, M. H., 1969, *Aero-thermodynamics and Flow in Turbomachines,* Wiley, New York.

Navier–Stokes and Potential Calculations of Axial Spacing Effect on Vortical and Potential Disturbances and Gust Response in an Axial Compressor

M.-H. Chung

A. M. Wo

Institute of Applied Mechanics,
National Taiwan University,
Taipei 106, Taiwan

The effect of blade row axial spacing on vortical and potential disturbances and gust response is studied for a compressor stator/rotor configuration near design and at high loadings using two-dimensional incompressible Navier–Stokes and potential codes, both written for multistage calculations. First, vortical and potential disturbances downstream of the isolated stator in the moving frame are defined; these disturbances exclude blade row interaction effects. Then, vortical and potential disturbances for the stator/rotor configuration are calculated for axial gaps of 10, 20, and 30 percent chord. Results show that the potential disturbance is uncoupled locally; the potential disturbance calculated from the isolated stator configuration is a good approximation for that from the stator/rotor configuration upstream of the rotor leading edge at the locations studied. The vortical disturbance depends strongly on blade row interactions. Low-order modes of vortical disturbance are of substantial magnitude and decay much more slowly downstream than do those of potential disturbance. Vortical disturbance decays linearly with increasing mode except very close to the stator trailing edge. For a small axial gap, e.g., 10 percent chord, both vortical and potential disturbances must be included to determine the rotor gust response.

1.0 Introduction

An understanding of blade unsteady force is vital for design considerations of structural integrity in turbomachines. This unsteady loading is due to two effects: response to flow unsteadiness on a rigid blade and vibratory blade motion. In general, the flow unsteadiness, acting as a forcing function, includes wakes and the potential field from the upstream blade row, the potential effect from the downstream row, and all other time-varying flow features. Disastrous blade failure can occur when the flow excitation frequency matches the blade natural frequency. Thus, a sound understanding of the sources of unsteadiness is vital for prediction of unsteady blade force.

Many researchers have undertaken the study of gust and gust response in axial compressors. Since an exhaustive list of excellent contributions is not feasible here, the reader is referred to AGARD (1987) for reference. Kielb and Chiang (1992) provided a summary of recent advances in forced response analyses. Verdon (1993) reviewed unsteady aerodynamic methods for turbomachinery aeroleastic and aeroacoustic applications.

As the axial space between blade rows is decreased, blade row flow interaction increases. Aerodynamically, limited data seem to suggest a beneficial effect, but the underlying physics is unclear. Smith (1969) reported an increase in the peak static pressure rise by about 6 percent and design efficiency of 1 percent in a four-stage compressor with a blade average axial gap decrease from 36.5 to 7.0 percent chord. Mikolajczak (1976) confirmed this view by showing data with an increase in peak isentropic enthalpy rise of 4 percent and design adiabatic efficiency of about 1 percent when axial spacing is decreased. However, Hetherington and Moritz (1976) argued that blade rows should be separated sufficiently so that most of the wake mixing can occur between rows. Aeromechanically, the present understanding of axial gap effect also needs clarification. Among others, Fleeter et al. (1981) carried out an important experimental study on the effect of axial spacing on gust response for a rotor/stator configuration and reported that the unsteady blade surface pressure increases significantly with decreased spacing at 100 percent speed but not at 70 percent speed. They also observed wave-related phenomenon from unsteady pressure data. Gallus et al. (1982) undertook extensive investigation of the blade number ratio and blade row spacing on stator dynamic loading and stage sound pressure level. They found that both vortical and potential effects are important in determining the blade response for very small gap. Recently, Manwaring and Wisler (1993) made a substantial contribution in comparing current state of the art gust response analyses with experimental data. They showed that an approach in which the unsteady gust is linearized about the time mean nonlinear flow is appropriate. Among other conclusions, they highlighted the importance of properly accounting for both vortical and potential disturbances in predicting gust response.

2.0 Objectives and Approach

The goal of this paper is to examine effects of axial spacing on vortical and potential disturbances and rotor gust response. We seek to answer, in part, the following questions:

- How large are the vortical and potential disturbances for various axial gaps and time-mean loadings?
- How does the axial gap affect rotor gust response?

Both Navier–Stokes and potential codes are used to address these questions for a stator/rotor configuration with axial gaps

---

Contributed by the International Gas Turbine Institute and presented at the 40th International Gas Turbine and Aeroengine Congress and Exhibition, Houston, Texas, June 5–8, 1995. Manuscript received by the International Gas Turbine Institute March 10, 1995. Paper No. 95-GT-301. Associate Technical Editor: C. J. Russo.

of 10, 20, and 30 percent chord and at two loadings. The approach taken is as follows. First, Navier–Stokes and potential calculations for an isolated stator are performed to determine vortical and potential disturbances as seen in the moving frame. This also serves to define disturbances without the presence of the rotor, thus without blade row interaction effects. Then, calculations are done for a stator/rotor configuration at all three axial gaps and two loadings. Flow variables in the gap region are presented. Vortical and potential disturbances are computed in the rotor frame at a *fixed* axial distance upstream of the rotor, along the extension of its camber line at the leading edge. This allows comparison of disturbances for different axial spacings on an equal basis. Finally, the amplitude and phase of unsteady rotor surface pressure are presented and discussed.

3.0 Navier–Stokes Calculation

This calculation is largely based on the work of Patankar and Spalding (1972). The following briefly describes the code. The unsteady flow in the blade passage is governed by the transformed incompressible continuity equation:

$$\nabla \cdot \mathbf{u} = 0 \qquad (1)$$

with a reference frame attached to either stator or rotor. The form of the Reynolds-averaged Navier–Stokes equation used is:

$$\frac{\partial \mathbf{u}}{\partial t} + \nabla \cdot [(\mathbf{u} - \mathbf{u}_b)\mathbf{u}] = -\nabla P + \nabla \cdot [(\mu + \mu_t)\nabla \mathbf{u}]. \qquad (2)$$

The modified Launder–Sharma (LS) low-Re version of $k-\epsilon$ two-equation model (Morse, 1991) is used to close these equations via the eddy viscosity coefficient μ_t. The equations governing these two variables are:

$$\frac{\partial k}{\partial t} + \nabla \cdot \; [(u - u_b)k]$$

$$= \nabla \cdot \left[\left(\mu + \frac{u_t}{\sigma_k} \nabla k \right) \right] + G_k - \epsilon - D \qquad (3)$$

$$\frac{\partial \epsilon}{\partial t} + \nabla \cdot [(u - u_b)\epsilon] = \nabla \cdot \left[\left(\mu + \frac{\mu_t}{\sigma_\epsilon} \right) \nabla \epsilon \right]$$

$$+ C_1 f_{\mu_1} G_k \frac{\epsilon}{k} - C_2 f_{\mu_2} \frac{\epsilon^2}{k} + E - F \qquad (4)$$

where $G_k = \mu_t\,(\partial u_i/\partial x_k)\,(\partial u_i/\partial x_k + \partial u_k/\partial x_i)$, $D = 2\mu(\partial\sqrt{k}/\partial x_j)^2$, $E = 2\mu\mu_t(\partial^2 u_i/\partial x_j^2)$, $F = 2\mu(\partial\sqrt{\epsilon}/\partial x_j)^2$, $C_\mu = 0.09$, $C_1 = 1.44$, $C_2 = 1.92$, $\sigma_\kappa = 1$, $\sigma_\epsilon = 1.22$, $f_\mu = [1 - \exp(-y^+/A^+)]^2$, $A^+ = 25$, $f_{\mu_1} = 1$ and $f_{\mu_2} = 1 - .21875 \exp(-R_t^2/36)$ with the eddy viscosity coefficient $\mu_t \equiv$

Nomenclature

A = coefficient of harmonic potential disturbance

C = chord

C_p = static pressure coefficient

D = coefficient of harmonic vortical disturbance

h_k = k^{th} data in a series analyzed by FFT

H_n = amplitude of the n^{th} harmonic from FFT

$\mathbf{i}/\mathbf{j}$ = unit vector in the axial/circumferential direction

L = 2π/disturbance pitch

M = Mach number

p = static pressure

$\hat{p}_i^+$ = i^{th} harmonic static pressure

Re = Reynolds number based on inlet flow velocity and blade chord

R_t = turbulence Re

S = circumferential blade pitch

s = solidity

T = rotor blade passing period

Tu = turbulence intensity

t = time

U_∞ = inlet uniform velocity

u^+ = streamwise component of periodic unsteady velocity

u_{NS}^+ = streamwise component of periodic unsteady velocity from *NS* code

u_p^+ = streamwise component of periodic unsteady velocity from potential code

u_v^+ = vortical part of streamwise component of periodic unsteady velocity

$\hat{u}_i^+$ = i^{th} harmonic streamwise gust

$|\hat{u}_i^+|$ = amplitude of the i^{th} harmonic streamwise gust

$\mathbf{u} = u\mathbf{i} + v\mathbf{j}$ = absolute flow velocity vector

$\mathbf{u}_b$ = rotor blade wheel velocity vector

V = periodic unsteady absolute velocity

V_b = rotor blade wheel speed

V_e = velocity outside the war layer in the far wake test case (see caption of Fig. 5)

$\bar{V}_z$ = axial component of time-mean velocity

v^+ = transverse component of periodic unsteady velocity

v_{NS}^+ = transverse component of periodic unsteady velocity from *NS* code

v_p^+ = transverse component of periodic unsteady velocity from potential code

v_v^+ = vortical part of transverse component of periodic unsteady velocity

$\hat{v}_i^+$ = i^{th} harmonic transverse gust

$|\hat{v}_i^+|$ = amplitude of the i^{th} harmonic transverse gust

W = periodic unsteady relative velocity from *NS* code

W_{NS} = periodic unsteady relative velocity from *NS* code

W_p = periodic unsteady relative velocity from potential code

$\bar{W}$ = time-mean relative velocity from *NS* code

$\bar{W}_{NS}$ = time-mean relative velocity from *NS* code

$\mathbf{x}$ = position vector

x/y = axial/circumferential coordinate

Z_g = axial gap (Fig. 9)

Z_s = axial coordinate downstream from stator trailing edge (Fig. 9)

Z_r = axial coordinate upstream from rotor leading edge (Fig. 9)

β_1 = inlet relative air angle

β_2 = exit relative air angle

Φ = flow coefficient

ϕ = velocity potential

ΔP = static pressure rise across compressor

ρ = density of fluid

κ = turbulence kinetic energy

Γ = circulation

ϵ = dissipation rate of turbulence kinetic energy

λ = normalized turbulence length scale

Ω = reduced frequency ($=\omega C/2\bar{W} = \pi s \cos \beta_1/\Phi$)

ω = rotor blade wheel angular frequency

Subscripts

∞ = inlet condition

b = blade

g = axial gap

i = harmonic number

NS = Navier–Stokes calculation

p = potential disturbance

r = rotor

s = stator

t = turbulence

v = vortical disturbance

Superscripts

$+$ = periodic unsteadiness or wall variable

$\rho C_\mu f_\mu(k^2/\epsilon)$, the turbulence Reynolds number $R_t \equiv (\rho k^2/\mu\epsilon)$, the wall variable $y^+ \equiv (\rho y U_\tau/\mu)$, and the wall shear velocity $U_\tau \equiv \sqrt{\tau_w/\rho}$.

3.1 Computational Domain and Discretization of Governing Equations. The computational domain is bounded by various boundaries as shown in Fig. 1. In this paper, each blade row is associated with a body-fitted embedded H-type grid. The GRAPE code (Sorenson, 1980) constitutes the majority of grid generation. For the isolated stator calculation, cells of 196 × 78 is used. For the stator/rotor configuration, 160 × 78, 172 × 78 and 184 × 78 cells per row is used for axial gaps of 10, 20, and 30 percent chord, respectively. The blade surface discretization contains 108 cells per blade surface. The resolution in time is 200 steps per blade-to-blade period.

Equations (1) to (4) are discretized and solved by SIMPLEC on a nonstaggered grid (Miller and Schmidt, 1988). We use the Crank–Nicolson scheme for time discretization, QUICK scheme (Leonard, 1979) for the convection term in momentum equations, and the first-order upwind scheme for $k-\epsilon$ equations. To avoid "checkerboard oscillation" of the pressure on nonstaggered grids, the pressure-weighted interpolation method (PWIM) of Miller and Schmidt is used to evaluate mass fluxes on control volume faces. This renders the converged solution independent of the underrelaxation factor.

3.2 Initial and Boundary Conditions. Various boundary conditions are specified as follows. The initial condition is a uniform flow imposed on impulsively started compressor blade rows with all flow variables having free-stream values. At the inflow boundary, which is 1.5 chord upstream of the stator leading edge, the potential influence of the stator row can be neglected, so it is reasonable to assume a uniform flow there. The turbulence kinetic energy and dissipation rate are specified through turbulence intensity Tu and its length scale λ nondimensionalized by the blade pitch, with $Tu = 4$ percent and $\lambda = 0.003$ corresponding to $R_t = 25$. At the outflow boundary, which is also 1.5 chord axially downstream of the rotor trailing edge, simple extrapolation boundary conditions, which assume that the flow does not evolve further in the axial direction, are imposed for all variables. On the blade surface, the no-slip condition is imposed. To avoid using very fine grids, the wall function approach is used to evaluate the wall shear stress τ_w.

The boundary treatment at the interface between two relatively moving grids is elucidated in Fig. 2, which shows an enlarged view of an instantaneous grid system near the interface. At this instant, the boundary value at the node P of the moving grid is found by interpolating the values at the solid-circle nodes of the stationary grid, which are known from the last iteration of the stator calculation. Linear interpolation is used for turbulence variables k, ϵ, μ_t, and cubic spline interpolation for all other variables. To reduce the error due to grid line skewness, Cartesian mesh is used near the interface. To ensure global mass continuity, the mass flux across the rotor grid boundary $\overline{AC}$ must equal to the sum of that across the stator grid boundaries $\overline{AB}$ and $\overline{BC}$. On periodic boundaries, direct periodic conditions are imposed for all variables. For the pressure and pressure correction, their normal derivatives vanish on the blade surface, or inflow/outflow boundaries.

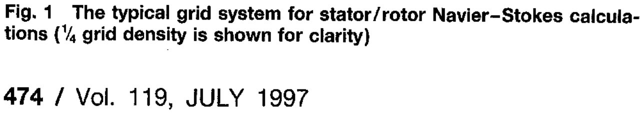

Fig. 1 The typical grid system for stator/rotor Navier–Stokes calculations (¼ grid density is shown for clarity)

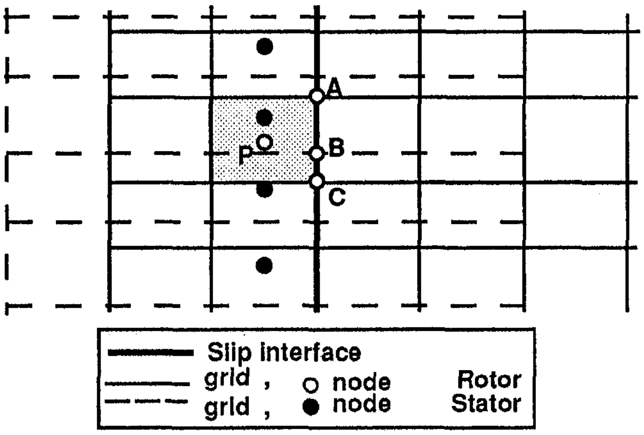

Fig. 2 Schematic showing data transfer between stator grid and rotor grid

3.3 Convergence Criteria. To determine convergence at the current iteration, the sum of the absolute residual of each finite difference equation for each variable is calculated. Convergence is reached when this sum is below 1 percent of that at the first iteration for all variables. For problems periodic in time, the whole flow field will approach a periodic steady state, after which the time-mean values are calculated for one further cycle. Such a state is defined by the smallest number of cycles, n_{cycle}, so that the following convergence criterion is satisfied:

$$\frac{\dfrac{1}{N_{CV}}\sum_{i_{CV}}^{N_{CV}}\left|u_{i_{CV}}^{n_{\text{cycle}}} - u_{i_{CV}}^{n_{\text{cycle}}-1}\right|}{\underset{i_{CV}}{\mathrm{Max}}(u_{i_{CV}}^{n_{\text{cycle}}}) - \underset{i_{CV}}{\mathrm{Min}}(u_{i_{CV}}^{n_{\text{cycle}}})} \le 10^{-4}, \qquad (5)$$

where i_{cv} is the index for the control volume and N_{CV} is the total number of control volumes. Computation is performed in an inhouse Cray YMP/EL four-processor machine. Typical calculation for stator/rotor configuration requires 3×10^{-4} CPU second per iteration per cell, with approximately 10 iterations per time step. About 20 to 30 blade to blade periods is required from impulsive start to periodic steady state. Thus, the total computational time is about 120 CPU hours.

4.0 Potential Calculation

For incompressible irrotational flow, the governing equation is

$$\nabla^2\phi = 0 \qquad (6)$$

with boundary condition $(\partial\phi/\partial n) = \mathbf{u}_b \cdot \mathbf{n}$. The Kelvin's theorem also holds, i.e., $(D\Gamma/Dt) = 0$. The Kutta condition used is that the velocity at the trailing edge is finite. The pressure is found using the unsteady Bernoulli's equation.

4.1 Solution Procedure. The vortex panel method with linearly varying strength is distributed on each panel. Each blade is composed of 64 surface panels. The resolution in time is 50 steps per blade-to-blade period. The influence coefficient of each surface panel is obtained by ten-point Gauss–Legendre integration. The Kutta condition is implemented by enforcing zero vorticity strength at blade trailing edges. With the bound circulation defined to be positive clockwise on both stator and rotor, Kelvin's theorem is satisfied by shedding vortices at each instant near the stator trailing edge from the pressure surface if the bound circulation is decreasing and from the suction surface if increasing. For the rotor, vortices are shed from the suction surface for decreasing circulation and from the pressure surface for increasing circulation (Basu and Hancock, 1978).

5.0 Validations

To verify the Navier–Stokes and potential codes, four test cases are presented. Two are taken from well-accepted data of AGARD (1990) and two from UTRC data.

5.1 Cascade Calculations. First, data from the UTRC subsonic cascade (Hobbs et al., 1980), tested near design point are used to validate both the Navier–Stokes and potential calculations. The test condition is $\mathrm{Re} = 4.78 \times 10^5$ and $M = 0.113$, which is appropriate for validation of incompressible codes. For the Navier–Stokes calculation, a 164×88 embedded H-type grid with 216 grid points per blade is used. At the inlet, $Tu = 2$ percent and $\lambda = 0.003$ is prescribed as the input to numerical simulation. For potential calculation, 46 surface panels per blade are used, and note that in this steady calculation, the strength of bound vortices is determined such that there is no upwash far upstream.

Figure 3 shows the distribution of the static pressure coefficient on the blade surface. The computational result agrees well with data along the whole blade surface except for regions near the separation bubbles where laminar–turbulent transition occurs at this Reynolds number, which is not modeled in the present study. Nevertheless, the overall pressure distribution seemed to be not greatly affected by the details of transition, and our assumption that the flow field is fully turbulent applies.

5.2 UTRC Multistage Compressor. Data from the UTRC low-speed multistage compressor, test case E/CO-5 in AGARD (1990), are used for comparison with the present calculation. This case is to test the capability of treating unsteady terms and interfacial boundaries in the Navier–Stokes calculations. The experimental compressor geometry consists of an inlet guide vane (IGV) followed by two nearly identical stages. Although in the experiment the IGV has 50 blades, rotor 44 blades, and stator 44 blades, equal blade number for all rows is assumed, as in Gundy-Burlet et al. (1991). The test condition is $\mathrm{Re} \approx 3 \times 10^5$, $M \leq 0.2$, $\Phi = 0.51$ and $Tu = 0.5$ percent. At the inlet, $\lambda = 0.001$ is prescribed as the input of numerical simulation. A grid system of 105×48 cells is attached to each blade row with 68 grid points per blade surface. The resolution in time is 200 steps per blade to blade period.

Figure 4 shows the distribution of time mean pressure coefficient on the rotor and stator of the second stage. The overall agreement with data is good except near the leading edge region. This is mainly due to lack of accuracy of the Navier–Stokes code near the leading edge and partly due to lack of information about the leading edge radius used in the experiment.

5.3 Far Wake Velocity Profile. This case involves the far-wake velocity profile of a low-speed compressor NACA 65 cascade, test case E/CA-1 in AGARD (1990). This and the following case are used to compare the two turbulence models considered. The ability to calculate wake profiles accurately lies mainly in the quality of the turbulence model used. The result is shown in Fig. 5. It can be seen that the Launder–Sharma (LS) model (Morse, 1991) and the standard high-Re (HR) model (Launder and Spalding, 1974) are about equal in capturing the far wake profile. The LS model seems to calculate the wake width slightly better than the HR model. Both predict the wake deficit on about an equal basis; the LS model slightly undershoots and the HR model slightly overshoots.

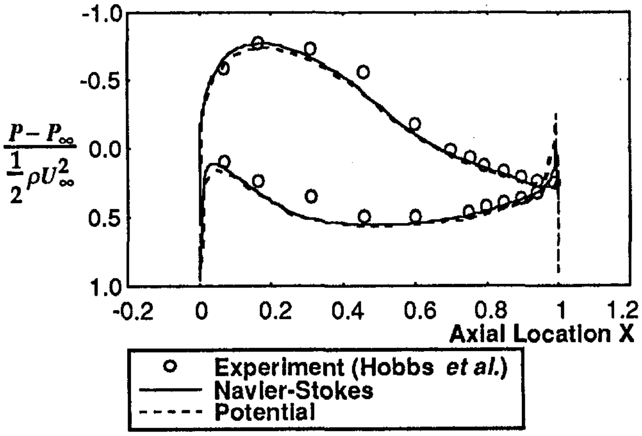

Fig. 3 Comparison between numerical results and surface pressure data on the UTRC low-speed cascade (Hobbs et al., 1980)

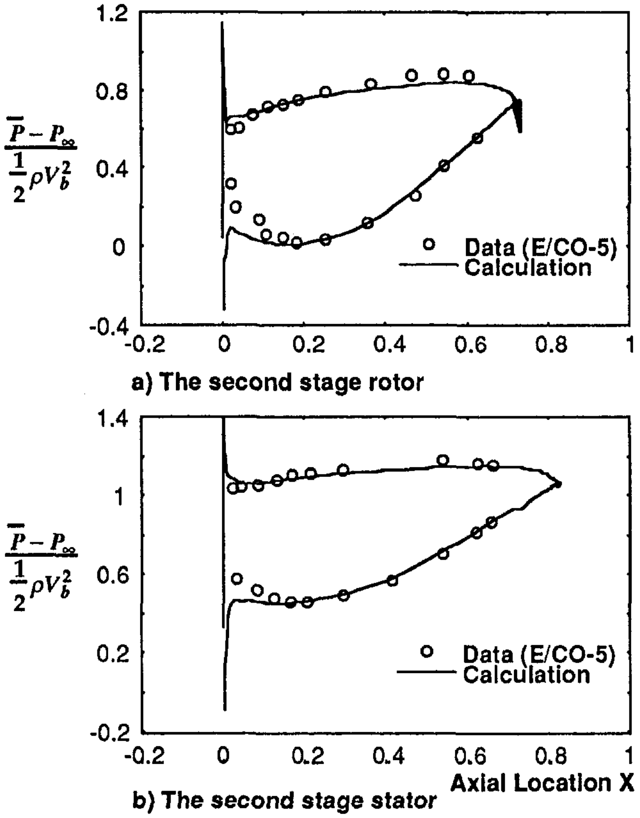

Fig. 4 Comparison between Navier–Stokes calculation and the second-stage time-mean surface pressure data on the UTRC low speed multistage compressor (test case E/CO-5 in AGARD, 1990)

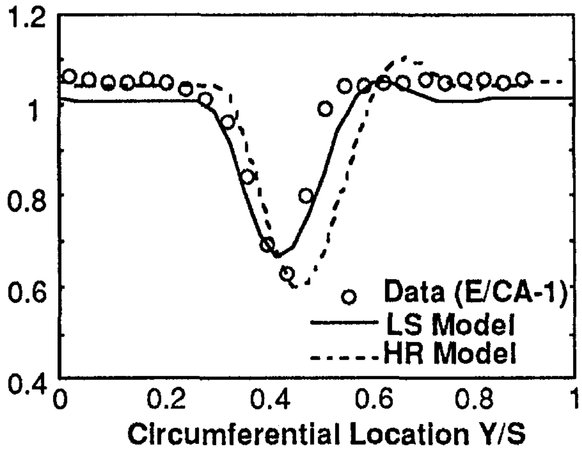

Fig. 5 Comparison between predictions by two turbulence models with data for the far wake total velocity at axial location 1.5 true chord aft of the blade leading edge at midspan (test case E/CA-1 in AGARD, 1990). Ve is the velocity at the midspan and midpitch location in the axial measuring plane used in the test case data.

5.4 Near-Wake Velocity Profile. The near-wake data, 0.1 chord downstream, in a single-rotor rig of UTRC (Dring, 1982), is also compared, as shown in Fig. 6. The LS model gives excellent prediction of the wake deficit but underpredicts the potential region. The HR model grossly overpredicts the deficit and does worse than the LS model on predicting the wake width. In light of calculations required for axial gaps of 10, 20, and 30 percent chord in this paper, the quality of the turbulence model in the near wake is more important than that in the far wake; thus the Launder–Sharma model is adopted.

6.0 Relationship Between Navier–Stokes and Potential Calculations

In this paper, both Navier–Stokes and potential codes are used to calculate vortical and potential disturbances; thus some comments are needed on the definition of the disturbances and the manner in which they are computed. The key approach taken here is that the potential disturbance, as defined below, calculated by the potential code, represents the potential disturbance included in the Navier–Stokes results, i.e.,

$$u_{NS}^{+} = u_{v}^{+} + u_{p}^{+} \tag{7}$$

$$v_{NS}^{+} = v_{v}^{+} + v_{p}^{+} \tag{8}$$

where u_{NS}^{+} and v_{NS}^{+} are streamwise and transverse gusts, respectively, from the Navier–Stokes code, u_{p}^{+} and v_{p}^{+} are potential disturbances from the potential code, and u_{v}^{+} and v_{v}^{+} are vortical disturbances from the difference between the Navier–Stokes and potential codes. Figure 7 illustrates this graphically. It is important to note that all disturbances are treated such that they are normal to and parallel with the local time-mean relative velocity vector, as computed by the Navier–Stokes code.

The manner in which the potential disturbances, u_{p}^{+} and v_{p}^{+}, are extracted from the potential code do not include contributions from shed vortices. (Of course, in the calculation procedure vortices are shed as dictated by the Kelvin's theorem.) For a stator/rotor unsteady calculation, if the disturbance includes contributions from shed vortices, this potential disturbance would persist far downstream, which is not physical, since there is no mechanism for the shed vortices to decay. Thus, disturbances due to shed vortices are viewed as a viscous phenomenon due to the Kutta condition, and are included in the vortical disturbances, u_{v}^{+} and v_{v}^{+}.

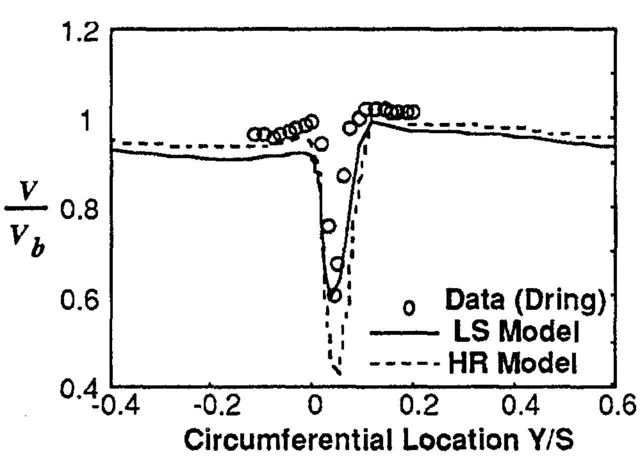

Fig. 6 Comparison between predictions by two turbulence models with data for the near-wake total velocity at axial location 0.1 axial chord aft of the blade trailing edge at midspan with Φ = 0.85 (Dring et al., 1982)

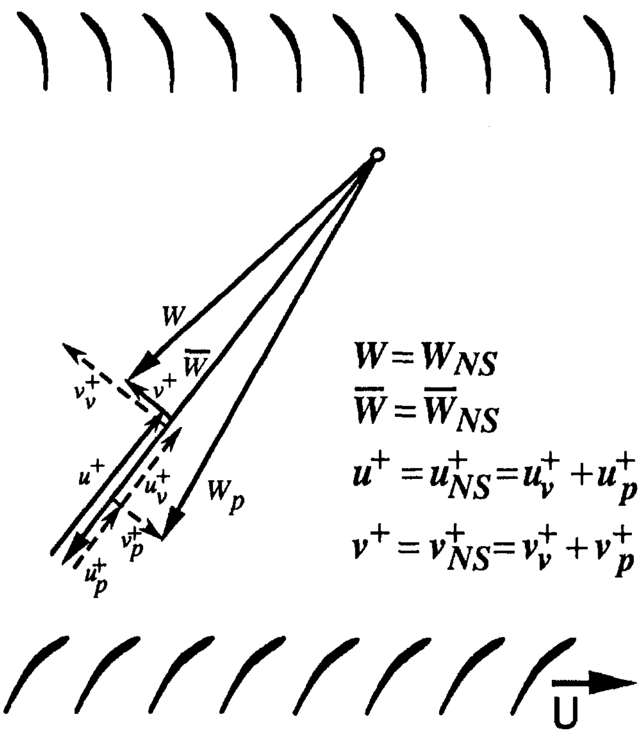

Fig. 7 Relative velocity vector diagram showing decomposition of vortical and potential disturbances from Navier–Stokes and potential code results (subscripts: *NS* = Navier–Stokes, *p* = potential, *v* = vortical)

To justify our splitting procedure, the vortical and potential disturbances by Giles (see Appendix II of Manwaring and Wisler, 1993), which satisfy the splitting procedure of Goldstein (1978), are used to compare with the present calculated disturbances for flow downstream of the isolated stator. In Giles' formulation, disturbances from the rotor as seen in the stator frame are considered. For this paper, we consider disturbances from the stator as seen in the relative frame. Modifying Giles' formulation, the vortical disturbances in the relative frame are[1]

$$\tilde{u}_{v} = \overline{V}_{z} D e^{-iL(\theta - \overline{V}_{\theta}/\overline{V}_{z} z)} \tag{9}$$

$$\tilde{v}_{v} = \overline{V}_{\theta} D e^{-iL(\theta - \overline{V}_{\theta}/\overline{V}_{z} z)} \tag{10}$$

and the potential disturbances are

$$\tilde{u}_{p} = -LAe^{(-iL\theta - Lz)} \tag{11}$$

$$\tilde{v}_{p} = -iLAe^{(-iL\theta - Lz)} \tag{12}$$

Thus, their complex constants D and A in the relative frame are

$$D = \frac{i\hat{u} - \hat{v}}{i\overline{V}_{z} - \overline{V}_{\theta}} \tag{13}$$

$$A = -\frac{\overline{V}_{z}\hat{v} - \overline{V}_{\theta}\hat{u}}{L(i\overline{V}_{z} - \overline{V}_{\theta})}\,. \tag{14}$$

Numerically, we computed Giles' formulation by first finding the values for D and A, from Eqs. (13) and (14), using results from the Navier–Stokes calculations. With D and A known, vortical and potential disturbances are found from Eqs. (9) to (12). The location $z = 0$ in Eqs. (9) to (14) is taken to be $Z_s/C = 0.058$ near design and 0.051 at high loading, since at these locations the two comparisons match for the transverse gust. (In the original analysis, the $z = 0$ point is arbitrarily taken to

---

[1] Notations in Eqs. (9) to (14) are based on the original paper; u is the disturbance in the axial direction and v the disturbance in the tangential direction (the tilde and headed quantities represent the periodic unsteady and its first harmonic, respectively).

be the location of the hot wire.) Figure 8 shows the comparison between disturbances obtained from the present splitting procedure and those from Giles' formulation. Results show excellent agreement for the potential disturbances, which decay exponentially. The vortical disturbances do not agree as well since no viscous diffusion is considered in Eqs. (9) and (10), thus do not decay downstream. The flow physics will be discussed in more detail in Sec. 10.0. In summary, the present splitting procedure using results from the Navier–Stokes and potential codes to extract vortical and potential disturbances is believed to be physically sound.

7.0 Axial Coordinates

Two axial coordinates are used in this paper—one with the origin at the stator trailing edge extending aft, Z_s, and the other with the origin at the rotor leading edge extending forward, Z_r. Figure 9 provides a sketch of Z_s and Z_r. An example using stator/rotor configuration should help to clarify the need for the two axial coordinates when the axial gap varies. Consider Point *A* located 5 percent *C* axially upstream of the rotor leading edge for a gap, Z_g, of 30 percent *C*; then Point *A* is located at Z_s = 25 percent *C* and Z_r = 5 percent *C*. If the gap is reduced to 20 percent *C* with the Point *A* relative to the rotor held stationary, then the Point *A* is located at Z_s = 15 percent *C* and Z_r remains at 5 percent *C*. Thus, the coordinate Z_r is useful for describing flow variables, e.g., gusts, at locations held fixed with the rotor when the axial spacing varies, which is the case in this paper. From this example, the two coordinates are related by

$$Z_s = Z_g - Z_r \tag{15}$$

where Z_g is the axial gap. Also shown in the enlarged view in Fig. 9 is the location where the normalization of computed disturbances for stator/rotor interaction is taken, which will be described below.

8.0 Normalization of Disturbances

Normalization of vortical and potential disturbances is chosen such that the level of disturbances relative to the rotor for all axial gaps and loadings can be compared on an equal basis. For stator/rotor calculations, the Navier–Stokes calculated time-mean relative velocity, $\bar{W}$, at the location $Z_r/C = 7.5$ percent axially upstream of the rotor leading edge along the extension of the camber line is used to normalize gusts from both the Navier–Stokes and potential calculations (see Fig. 9). The location $Z_r/C = 7.5$ percent is chosed for two reasons: the coordinate Z_r is used, over other choices, since Z_r represents a fixed distance from the rotor for all axial gap cases, and the value of 7.5 percent is mainly due to the constraint imposed by the 10 percent gap case; this leaves only 2.5 percent chord from the stator trailing edge. The justification for using the Navier–Stokes calculated $\bar{W}$ to normalize the potential disturbance is based on the previously stated view that potential calculated gust represents potential disturbance in the Navier–Stokes calculation, Eqs. (7) and (8).

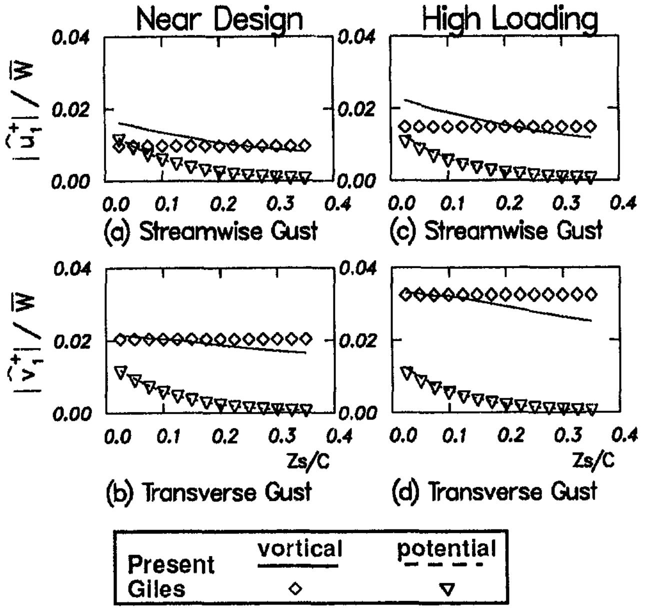

Fig. 8 Comparison of the present vortical and potential disturbance splitting procedure with that of Giles (Manwaring and Wisler, 1993)

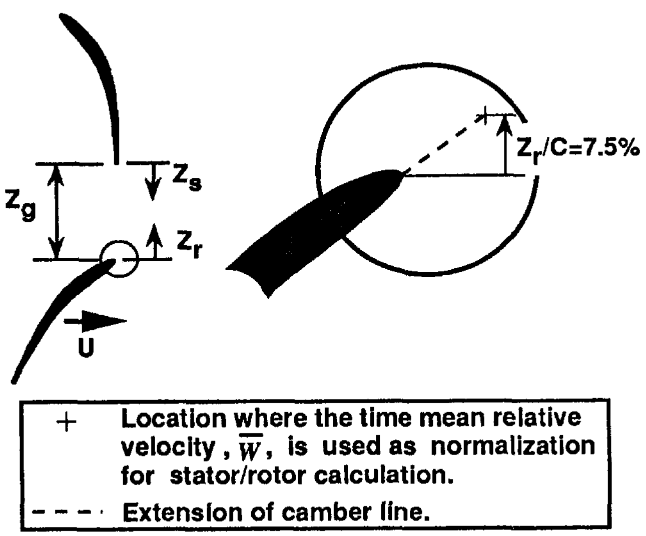

Fig. 9 Sketch showing the relationship between axial gap *Zg* and spatial coordinates *Zs* and *Zr*, *Zs* = *Zg* − *Zr*, and the location for normalization.

For the stator alone calculation, the Navier–Stokes calculated velocity at the exit plane as seen in the relative frame is used for normalization of disturbances.

9.0 Blade Geometries and Stage Characteristics

Table 1 summarizes major blade geometries and flow parameters. The blades are that of a low-speed three repeating stage

Table 1 Blade geometry and flow conditions. The stator exit and the rotor inlet denote the axial location midway between the stator trailing edge and the rotor leading edge for the *Zg*/*C* = 30 percent case.

	Stator	Rotor
Camber	48.00°	35.00°
Stagger	20.67°	-39.50°
Solidity	1.415	1.415
Inlet relative angle, β_1, near design ($\Phi = 0.6$)	45.96°	56.80°
Exit relative angle, β_2, near design ($\Phi = 0.6$)	7.90°	32.34°
Inlet relative angle, β_1, at high loading ($\Phi = 0.5$)	53.55°	61.58°
Exit relative angle, β_2, at high loading ($\Phi = 0.5$)	8.64°	32.87°
Reduced frequency, Ω, near design ($\Phi = 0.6$)	----	4.057
Reduced frequency, Ω, at high loading ($\Phi = 0.5$)	----	4.231

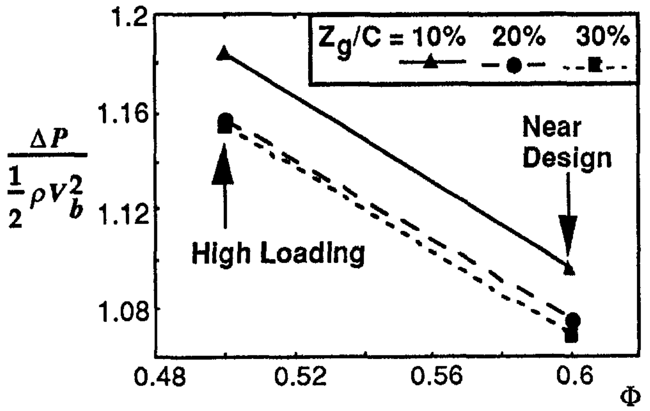

Fig. 10 Stage pressure rise characteristic for three axial spacings computed from Navier–Stokes calculations

axial compressor under construction. The Reynolds number, based on the inlet axial velocity, used in the computations is 1.59×10^5, corresponding to flow coefficient 0.6. The blades are designed using the controlled diffusion concept of Hobbs and Weingold (1984). As can be seen from a reduced scale sketch of Fig. 9, maximum flow diffusion is allowed near the minimum pressure region on the suction surface. Farther downstream, the blade surface is essentially a straight line extending to the trailing edge. The trailing edge thickness is 2 percent chord for both the stator and rotor.

The stage pressure rise characteristic computed by the Navier–Stokes code is shown in Fig. 10 for three axial gaps. It is clearly seen that pressure rise increases as the gap becomes smaller. At the near design point, the pressure rise for the 10 percent gap case is 2.5 percent higher than that of 30 percent case. This increase is consistent with the findings of Smith (1969) and Mikolajczak (1976).

10.0 Stator Alone Calculations

Since the rotor response is due to the forcing function from the stator, it is helpful first to define disturbances due to the stator without the presence of the rotor, as seen in the moving frame. As will be discussed, vortical and potential disturbances from the isolated stator calculation will be compared with those from stator/rotor calculation at the corresponding locations in the gap region. Thus, the degree to which disturbances are distorted due to the downstream rotor can be evaluated. Hence, results presented in this section are calculated with only the stator cascade. This is also conceptually equivalent to infinite axial gap between rows.

The modal amplitudes[2] of vortical and potential disturbances are presented in Fig. 11 for three distances behind the stator trailing edge, Z_s/C = 2.5, 12.5, and 22.5 percent. These three values correspond to a constant 7.5 percent chord axially upstream of the rotor leading edge, if the rotor is present, for gaps of Z_g/C = 10, 20, and 30 percent, respectively. Results show that, first, the vortical disturbance varies with loading but the potential disturbance essentially does not. The increase in vortical disturbance with loading should be related to the increase in the wake momentum thickness, thus leading to an increase in wake width. Results also suggest that the transverse component is larger than the streamwise gust. Since two-dimensional calculations are performed, any increase in vortical disturbance due to three-dimensional effects is not considered. Second, vortical disturbances are all greater than potential disturbances for all cases studied. This fact along with the slow axial decay characteristic of the vortical disturbance (see Fig. 12) suggests that the vortical disturbance plays a larger role in determining the rotor gust response than does the nonnegligible potential disturbance. Third, the vortical disturbance decays nearly linearly with increasing mode, except for mode 1 and 2 at Z_s/C = 2.5 percent, which is very close to the stator trailing edge.

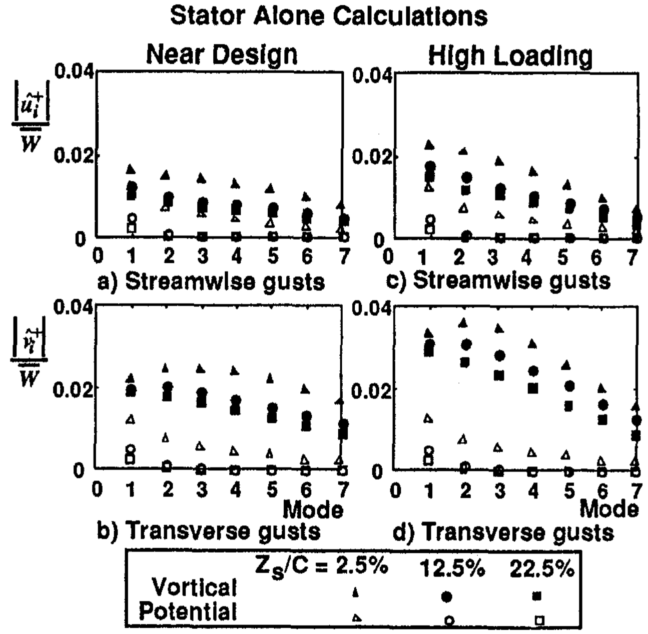

Fig. 11 Modal gust amplitudes as seen in the moving frame at three axial distances (Zs/C = 2.5, 12.5, 22.5 percent) behind the stator trailing edge. Calculations were done with stator alone.

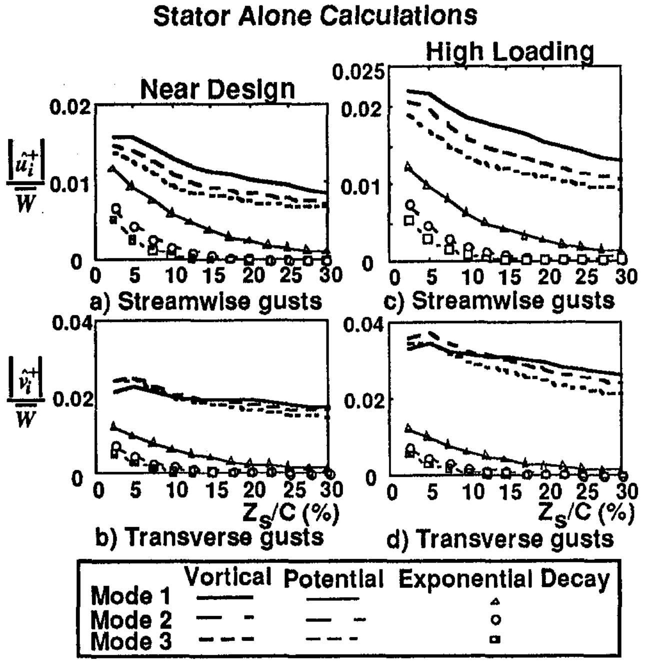

Fig. 12 Axial variation of modal gust amplitudes behind the stator trailing edge. Calculations were done with the stator alone with amplitudes as seen in the moving frame.

---

[2] The time domain output of both the Navier–Stokes and potential calculations are converted to a series of integer multiples of the rotor blade passing frequency using the standard Fast Fourier Transform (FFT), that is, the k^{th} point in the time domain can be written as

$$h_k = \sum_{n=0}^{N-1} H_n e^{-2\pi ikn/N}, \quad k = 1, 2, \ldots, N$$

The amplitude of the n^{th} mode is defined as H_n.

This suggests that several lower-order modes are important for determining the rotor gust response.

The axial variations of vortical and potential disturbances for the first three modes in both the streamwise and transverse directions as seen in the moving frame are presented in Fig. 12. First, the axial decay of vortical disturbance, unlike the potential disturbance, does not vary much with mode for the two loading levels. This again suggests that lower order modes are all important for determining the rotor gust response. Second, at 30 percent chord downstream of the isolated stator trailing edge, the potential disturbance is negligible compared to the vortical disturbance. However, at 10 percent chord, the transverse potential disturbance is about 1/3 that of vortical near design and 1/4 that at high loading. Thus, both disturbances must be considered for small axial gaps. Third, to show that the potential disturbance indeed follows an exponential axial decay, the analytical solution to the Laplace equation for potential flow is also plotted. For the ith mode, the transverse gust component is

$$\frac{\hat{v}_i^+}{W} = \left.\frac{\hat{v}_i^+}{W}\right|_0 \exp\left(-\frac{2\pi i}{S/C}\frac{Z_s}{C}\right), \qquad (16)$$

where the coefficient is the gust at $Z_s/C = 2.5$ percent. An identical exponential form applies for the streamwise gust, with a different value for the coefficient. The results, as plotted in Fig. 12, show that the potential disturbance calculated by the potential code (lines) agrees excellently with the analytical solution (symbols). Thus, the potential disturbance indeed decays exponentially with increasing modes, as opposed to vortical disturbance.

11.0 Stator/Rotor Calculations

Calculations for the stator/rotor configuration with axial gaps Z_g/C = 10, 20, and 30 percent using both Navier–Stokes and potential codes were performed. The focus was on the effect of the axial gap on the vortical and potential disturbances.

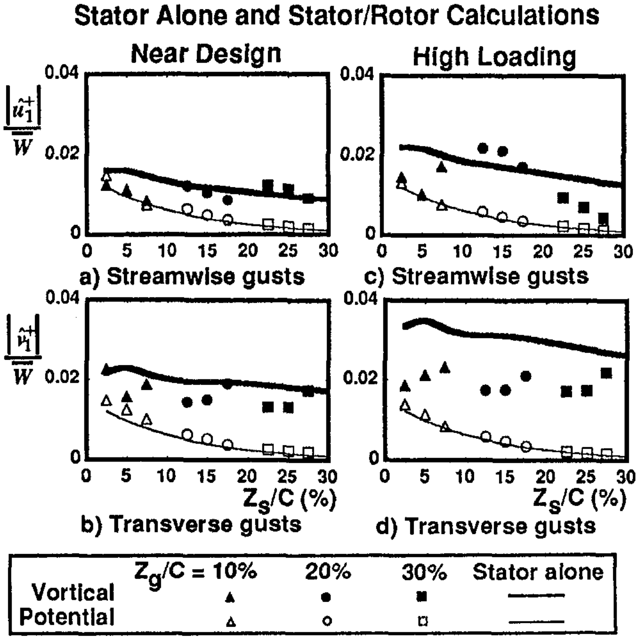

Fig. 13 Comparison of vortical and potential disturbances for the variable axial gap stator/rotor configuration with disturbances due to the stator alone

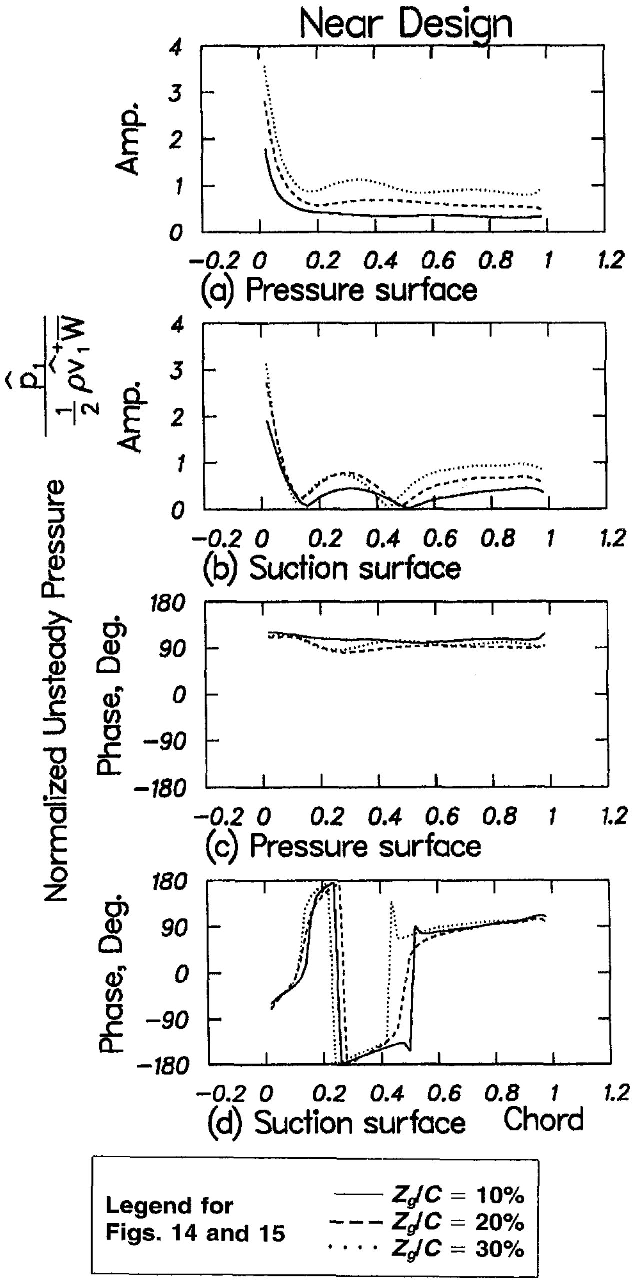

Fig. 14 Rotor surface pressure amplitude and phase (mode 1) for three axial gaps near design loading

Figure 13 presents the vortical and potential disturbance amplitude for the stator/rotor calculation computed at three locations upstream of the rotor leading edge, Z_r/C = 2.5, 5.0, and 7.5 percent. Note that the results are plotted with the abscissa extending from the stator trailing edge (see Fig. 9). Also shown are disturbances for the isolated stator calculation of Fig. 12. The comparison of potential disturbance between the stator alone calculation and the stator/rotor calculation shows that both streamwise and transverse potential disturbances are in good agreement for both loadings. This is perhaps a surprising result, which indicates that the potential disturbance in the relative frame for the stator/rotor configuration can be approximated by that for the isolated stator at the corresponding location in the gap region. One implication of this result is that the potential disturbance due to the rotor is locally uncoupled from that due to the stator; thus the rotor potential field does not interact with the stator potential field under the linear approximation, as suggested by Giles (1994). The comparison of vortical disturbance between the stator/rotor and stator alone configurations is not good as expected, especially at high loading. This suggests that stator/rotor interaction plays an important role in altering the vortical disturbance. The uncoupling/cou-

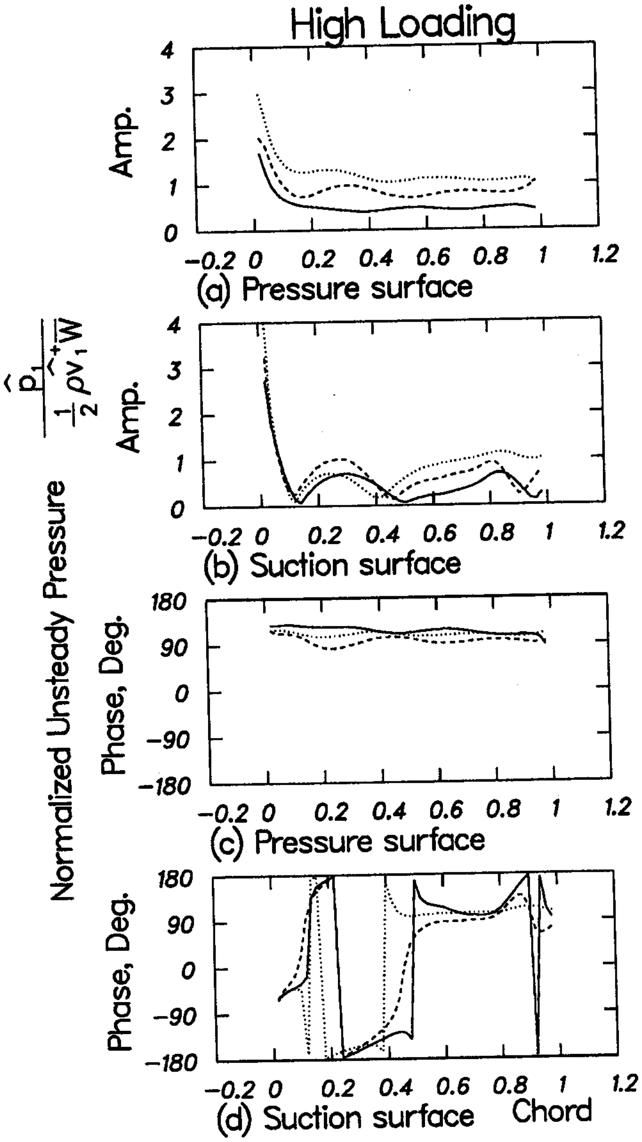

Fig. 15 Rotor surface pressure amplitude and phase (mode 1) for three axial gaps at high loading (see Fig. 14 for legend)

pling nature of the two disturbances is discussed further in Section 12.0.

The unsteady rotor surface pressure amplitude and phase for mode 1, computed by Navier–Stokes, are shown in Figs. 14 and 15, corresponding to near the design point and at high loading, respectively. Note that the normalization is based on the transverse gust, which includes both vortical and potential disturbances, and the time-mean relative velocity, both at Z_r/C = 7.5 percent upstream of the rotor (see Fig. 9). The normalized unsteady pressure on the pressure surface for both loadings, as seen in Figs. 14(*a*) and 15(*a*), appears to increase slightly as the axial gap increases. This is somewhat surprising, since the pressure is already normalized by the transverse gust including both vortical and potential disturbances. The normalized unsteady pressure on the suction surface, as seen in Figs. 14(*b*) and 15(*b*), shows two zero amplitude locations, which vary from about 10 to 15 percent chord and 40 to 50 percent chord with axial gap. The shifting of the upstream region, 10 to 15 percent chord, is smaller than that of the downstream region. The variation of local amplitude with axial gap seems to evolve within these two regions. The phase signatures on the pressure surface for both loadings suggest that essentially constant phase excitation is experienced by the airfoil. On the other hand, the phase signature on the suction surface exhibits a mixture of large phase variation with chord in the forward portion of the airfoil and a region near constant phase aft. This phase variation is also shown to be axial spacing dependent.

12.0 Discussions

The result of Fig. 13 suggests that the potential disturbance is uncoupled at the location calculated. The uncoupling is only local in nature. Numerics for the entire gap region reveal that upstream influence effect near the rotor leading edge contributes to alter the potential disturbance to differ from that for the stator-alone configuration, with the greatest difference near the stator trailing edge at 10 percent gap.

The vortical disturbance is coupled, or dependent on the stator/rotor interaction as shown in Fig. 13, most likely due to contributions from vortices shed into the wake in response to changes in the stator bound circulation. This is inherently a flow interaction resulting from fixed and moving blade rows. The net vortical disturbance as seen in the moving frame is due to the sum of the time-mean and unsteady wake profiles in the stator frame. The time-mean wake profile is mainly due to an isolated stator row as seen in its own frame. (In this case, the wake profile is steady, in the sense that blade row interaction is absent.) This wake profile contributes to the vortical disturbance like an observer fixed to the moving frame sweeping pass the time-mean wake of the isolated stator. This contribution to the vortical disturbance depends on the loading, which is convincingly shown in Fig. 13. The other contribution to the vortical disturbance is due to unsteadiness in the wake profile, which is a direct consequence of stator/rotor interaction.

13.0 Conclusions

The effect of compressor blade row axial spacing on vortical and potential disturbances and gust response for the stator/rotor configuration near the design point and at high loadings has been studied numerically using two-dimensional Navier–Stokes and potential codes. Calculations for axial gaps of 10, 20, and 30 percent chord were performed. Computations for an isolated stator have also been executed, which, by comparison with stator/rotor calculated disturbances, help in evaluating the level of flow interaction due to the presence of the rotor. Results are summarized as follows:

- Vortical and potential disturbances can be extracted from Navier–Stokes and potential codes successfully using the present splitting procedure (see Fig. 7).
- The potential disturbance from the isolated stator configuration is a good approximation for the potential disturbance in the gap region for stator/rotor calculations at the location studied. This suggests that potential disturbances from stator and rotor are locally uncoupled (see Fig. 13).
- The potential disturbance decays exponentially downstream and with increasing mode but does not vary with loading (see Fig. 12).
- The vortical disturbance is coupled, with blade row interaction effects depending on the axial spacing and loadings (see Fig. 14).
- Low-order modes of vortical disturbance are of substantial magnitude and decay much more slowly than do those of potential disturbance downstream (see Figs. 11 and 12).
- Vortical disturbance decays linearly with increasing mode except very close to the stator trailing edge (see Fig. 11).

Acknowledgments

We thank Prof. M. B. Giles, Oxford University, for his insightful discussion on the analysis in Appendix II of Manwaring and Wisler (1993). The authors gratefully acknowledge funding by the National Science Council of the Republic of China (NSC 84-2212-E-002-007). Partial funding of the computing cost by the Institute of Applied Mechanics is also appreciated. The second author acknowledges the help of Jesus Christ throughout the course of this work.

References

AGARD, 1990, "Test cases for computation of internal flows in aero engine components," AGARD Propulsion and Energetics Panel, Working Group 18, AGARD-AR-275.

Basu, B. C., and Hancock, G. J., 1978, "The unsteady motion of a two-dimensional airfoil in incompressible inviscid flow," *Journal of Fluid Mechanics,* Vol. 87, pp. 159–178.

Caruthers, J. E., and Dalton, W. N., 1993, "Unsteady aerodynamic response of a cascade to nonuniform inflow," ASME JOURNAL OF TURBOMACHINERY, Vol. 115, pp. 76–84.

Dring, R. P., Joslyn, H. D., and Hardin, L. W., 1982, "An investigation of axial compressor rotor aerodynamics," ASME *Journal of Engineering for Power,* Vol. 104, pp. 84–96.

Fleeter, S., Jay, R. L., and Bennett, W. A., 1981, "Wake induced time-variant aerodynamics including rotor–stator axial spacing effects," ASME *Journal of Fluids Engineering,* Vol. 103, pp. 59–66.

Gallus, H. E., Grollius, H., and Lambertz, J., 1982, "The influence of blade number ratio and blade row spacing on axial-flow compressor stator blade dynamic load and stage sound pressure level," ASME *Journal of Engineering for Power,* Vol. 104, pp. 633–641.

Giles, M. B., 1994, private communication.

Goldstein, M. E., 1978, "Unsteady vortical and entropic distortions of potential flows round arbitrary obstacles," *Journal of Fluid Mechanics,* Vol. 89, part 3; pp. 433–468.

Gundy-Berlet, K. L., Rai, M. M., Stauter, R. C., and Dring, R. P., 1991, "Temporally and spatially resolved flow in a two-stage axial compressor: Part 2—Computational assessment," ASME JOURNAL OF TURBOMACHINERY, Vol. 113, pp. 227–232.

Hetherington, R., and Moritz, R. R., 1976, "The influence of unsteady flow phenomena on design and operation of aero engines," AGARD-CP-177.

Hobbs, D. E., Wagner, J. H., Dannenhoffer, J. F., and Dring, R. P., 1980, "Supercritical airfoil technology program, wake experiments and modeling for fore and aft-loaded compressor cascades," Final report FR-13514, Pratt & Whitney Aircraft Group, UTC.

Hobbs, D. E., and Weingold, H. D., 1984, "Development of controlled diffusion aerofoils for multistage compressor applications," ASME *Journal of Engineering for Gas Turbine and Power,* Vol. 106, pp. 271–278.

Kielb, R. E., and Chiang, H. D., 1992, "Recent Advancements in Turbomachinery Forced Response Analyses," AIAA Paper 92-0012.

Launder, B. E., and Spalding, D. B., 1974, "The numerical computation of turbulent flow," *Comp. Meth. in Appl. Mech. and Eng.,* Vol. 3, p. 269.

Leonard, B. P., 1979, "A stable and accurate convective modeling procedure based on quadratic upstream interpolation," *Comput. Methods Appl. Mech. Eng.,* Vol. 12, pp. 59–98.

Manwaring, S. R., and Wisler, D. C., 1993, "Unsteady aerodynamics and gust response in compressors and turbines," ASME JOURNAL OF TURBOMACHINERY, Vol. 115, pp. 724–740.

Mikolajczak, A. A., 1976, "The Practical Importance of Unsteady Flow," AGARD-CP-177.

Miller, T. F., and Schmidt, F. W., 1988, "Use of a pressure-weighted interpolation method for the solution of the incompressible Navier–Stokes equations on a nonstaggered grid system," *Numerical Heat Transfer,* Vol. 14, pp. 213–233.

Morse, A. P., 1991, "Application of a low Reynolds number turbulence model to high-speed rotating cavity flows," ASME JOURNAL OF TURBOMACHINERY, Vol. 113, pp. 98–105.

Patankar, S. V., and Spalding, D. B., 1972, "A calculation procedure for heat, mass and momentum transfer in three-dimensional parabolic flows," *Int. J. Heat Mass Transfer,* Vol. 15, p. 1787.

Smith, L. H., 1969, "Casing boundary layers in multistage compressors," *Proc. Symposium on Flow Research on Blading,* Brown Boveri & Co Ltd, Baden, Switzerland 1969. in: Dzung, L. S., ed., *Flow Research on Blading,* Elsevier Publishing Company, 1970.

Sorenson, R. L., 1980, "A computer program to generate two-dimensional grids about airfoils and other shapes by the use of Poisson's equation," NASA-TM-81198.

Verdon, J. M., 1993, "Review of Unsteady Aerodynamic Methods for Turbomachinery Aeroelastic and Aeroacoustic Applications," *AIAA Journal,* Vol. 31, pp. 235–250.

Vortical Gust Response of a Low-Solidity Vane Row Including Steady Loading and Dynamic Stall Effects

G. H. Henderson[1]

S. Fleeter

School of Mechanical Engineering,
Purdue University,
West Lafayette, IN 47906-1288

The effects of high steady loading and separated flow on the unsteady aerodynamic response of turbomachine blade rows are experimentally investigated. This is accomplished utilizing a unique single-stage turbomachine research facility in which the flow is not generated by the blading but rather by an additional fan. Thus, for a particular stator incidence angle, the steady or mean stator aerodynamic performance were determined in a completely steady flow with no rotor and also with unsteady flow generated by a rotor composed of perforated plates at the same mean operating condition, thereby identifying the stator vane row dynamic stall conditions. The unsteady aerodynamic response of the very low-solidity stator vane row is then investigated over a range of incidence angle values, including attached and separated flows with dynamic stall.

Introduction

Bladed disk aerodynamically forced response is a universal problem, with the primary mechanism of blade failure being fatigue caused by vibrations at levels exceeding material endurance limits. These occur when a blade row is subjected to a periodic forcing function with frequency equal to a natural blade resonant frequency. With the resonant airfoil frequencies accurately predicted with finite element structural models, the Campbell diagram is the key design tool in a zeroth-order design system. These display the natural frequency of each blade mode versus rotor speed and, on the same figure, the aerodynamic forcing function frequency versus rotor speed. At each intersection point, an aerodynamic induced vibration problem is possible. Because a blade may have as many critical points of high stress as it has natural modes, the designer must determine which particular modes have the greatest potential for aerodynamic excitation. However, as Campbell diagrams do not consider either the detailed aerodynamic forcing function or the resulting airfoil row unsteady aerodynamics, they provide no measure of the amplitude of the resulting stress at the resonant speeds. Also, it should be noted that the majority of the forced response resonance conditions indicated on Campbell diagrams are at off-design conditions where flow separation may exist.

State-of-the-art linearized unsteady aerodynamic models for predicting blade response are essentially limited to two-dimensional inviscid flows. In all these models, the gust is described in terms of its harmonics, with each harmonic modeled as a gust forcing function boundary condition for the prediction of the corresponding harmonic of the unsteady aerodynamic response. The complete response of a downstream blade row is then the sum of the responses to the individual harmonics. In flat-plate analyses, the steady flow is uniform relative to the responding blade row, with superimposed small perturbations in the streamwise and transverse directions. Advanced inviscid flow analyses are being developed that model thickness and camber in the responding blade row, thereby distorting the perturbation by linearizing about the nonuniform steady flow around the blade rather than the simpler upstream uniform flow, for example Goldstein and Atassi (1976), Scott and Atassi (1990), Hall and Verdon (1989), and Fang (1991).

A number of experiments have been directed toward the verification of such mathematical models and the determination of their applicability and limitations, for example Capece and Fleeter (1989), Kim and Fleeter (1992), Henderson and Fleeter (1993a, b), Manwaring and Wisler (1993), and Feiereisen et al. (1994). As a generalization, it appears that if the assumptions inherent in these analyses are modeled, then the experiments provide data that are in agreement with the predictions. However, if actual compressor operating conditions are experimentally modeled, then the data-prediction correlation is not as good.

To meet performance requirements, advanced blade rows are designed to operate with very high steady loading. As a result, the flow may separate from the suction surface, particularly when the engine is accelerating or operating near the surge line in a high-output situation. In fact, the majority of forced response resonance conditions indicated on Campbell diagrams are at off-design conditions where flow separation may exist. However, the effect of high steady loading and separated flow on the resulting unsteady aerodynamic blade row response is relatively unstudied. Also, dynamic stall, although of prominent research importance for isolated airfoils, i.e., wings, has not been addressed in turbomachines. This is not because dynamic stall may not be significant in turbomachines at high loading conditions, but rather because of the differences between isolated airfoil and turbomachine blade row unsteady flow phenomena and also the experimental facilities utilized for turbomachinery research.

For an isolated airfoil, the steady lift increases with increasing angle of attack. However, when a critical angle of attack is reached, the steady lift drops suddenly because the steady flow over the airfoil is separated. This condition is known as steady airfoil stall, with the critical angle of attack termed the steady stall angle. The term dynamic stall generally refers to the unsteady separation of the flow from the upper surface of an airfoil and the stall phenomena of the airfoil oscillating into and out of stall. Dynamic stall begins at an angle of attack greater than

---

[1] Present address: Advanced Product Development, Cummins Engine Company Columbus, IN.

Contributed by the International Gas Turbine Institute and presented at the 39th International Gas Turbine and Aeroengine Congress and Exposition, The Hague, The Netherlands, June 13–16, 1994. Manuscript received by the International Gas Turbine Institute February 25, 1994. Paper No. 94-GT-295. Associate Technical Editor: E. M. Greitzer.

the static stall angle, i.e., the oscillation of the airfoil and the associated unsteady flow delay the onset of stall. The predominant feature of dynamic stall is the shedding of a strong vortexlike disturbance from the leading edge region, which moves downstream over the upper airfoil surface.

In turbomachines, the airfoil is not oscillating. Rather the inlet flow of the airfoil blade row is unsteady. That is, the wakes from upstream blade and vane rows are the primary source of the unsteady aerodynamics of downstream blade rows. However, this unsteady flow can delay the onset of flow separation at high loading conditions, i.e., dynamic stall occurs in turbomachine blade rows at high incidence angles. Experimentally it is necessary to model the basic unsteady aerodynamic phenomena inherent in this time-variant interaction, including the incidence angle, velocity, and pressure variations, aerodynamic forcing function waveforms, reduced frequency, and blade row interactions. Thus, turbomachine experiments are typically performed in research compressors and turbines, with the steady and unsteady flow generated by the rotor blades and the effect of steady loading considered by varying the operating conditions along a constant speed line.

This paper addresses the effect of high steady loading and separated flow, including dynamic stall effects on turbomachine blading for the first time, on the resulting unsteady aerodynamic blade row response. This is accomplished utilizing a unique single-stage turbomachine research facility in which the flow is not generated by the blading but rather by an additional fan. This provides the ability to quantify the steady or mean performance of the stator row over a range of steady loading levels or incidence angle values both with and without unsteady flow effects. In particular, for a particular stator incidence angle, the steady or mean stator aerodynamic performance are determined in a completely steady flow with no rotor and also with unsteady flow generated by a rotor composed of perforated plates at the same mean operating condition, thereby identifying the stator vane row dynamic stall conditions. The unsteady aerodynamic response of the stator vane row is then investigated over a range of incidence angle values, including attached and separated flows with dynamic stall.

Research Facility

The Purdue Annular Cascade Research Facility is an open-loop draw-through type wind tunnel capable of test section velocities of 70 m/s (220 ft/sec). The inlet flow, conditioned first by a honeycomb section and then a settling chamber, accelerates into the annular test section via a bellmouth inlet. The test section exit flow is diffused into a large plenum. The 224 kW (300 hp) centrifugal fan located downstream of the plenum draws the air through the facility, with guide vanes at the fan inlet allowing flow rate adjustment through the facility. The annular test section, Fig. 1, houses a rotor independently driven by a 7.5 kW (10 hp) A-C motor controlled by a variable frequency drive to create the desired unsteady flow field together with the downstream stator row. For these experiments, the rotor is composed of perforated plates, Fig. 1, fabricated from 56 percent porosity aluminum sheet and mounted on the rotor such that the plate width is normal to the rotor axis. The separate drive motors on the rotor and system fan uncouple the rotor speed from the throughflow velocity. Thus, independent control over unsteady aerodynamic parameters, for example the reduced frequency, is possible since the system flow rate is independent of rotor speed and the rotor configuration.

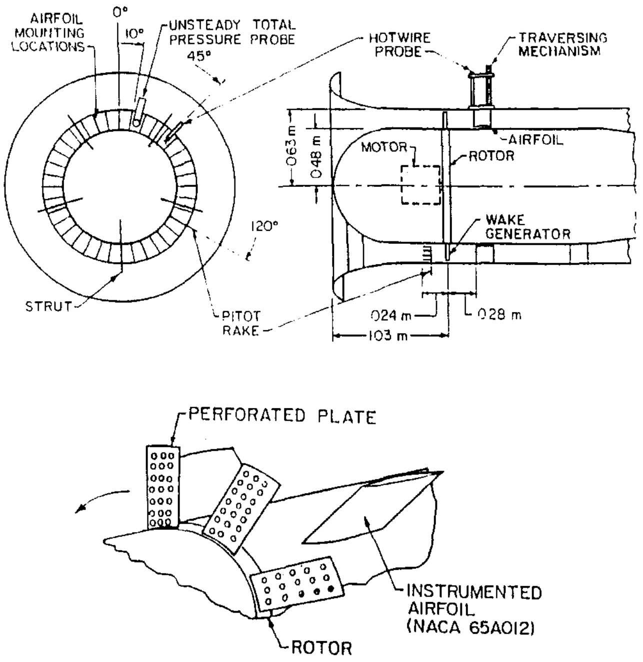

Fig. 1 Annular test section and perforated plate rotor schematic

Basic measurements include the test-section velocity profile upstream of the rotor and the test-section air stagnation temperature and static pressure. The test-section air stagnation temperature is measured using a thermocouple. A pitot tube rake provides the test-section inlet velocity profile. The pitot rake is an assembly of ten total pressure tubes equally spaced across the annular test section and aligned with the annulus axis. Two test-section static taps located on the outer annulus wall are utilized, one near the pitot rake and the other 3.18 cm (1.25 in.) upstream of the leading edge of an optional stator airfoil row. The inlet velocities are calculated from isentropic compressible flow theory using the pitot rake stagnation pressure, the test section air static pressure measurement, and the test section air stagnation temperature measurements as the input parameters.

A low-solidity symmetric airfoil stator cascade is utilized in these experiments. The airfoil chord and span are equal at 0.152 m (6.0 in.), with the profile coordinates obtained from Abbott and von Doenhoff (1959). The twelve midspan chordwise tap locations provide highly detailed spatial resolution of the midspan chordwise pressure distributions, Fig. 2. The stator airfoils are mounted through holes in the outer diameter of the test section by trunnions attached at 35 percent chord. The stator airfoil incidence angle is adjusted by setting the stagger angle, which is adjustable to within ±0.5 deg. The low-solidity stator

Nomenclature

C = airfoil chord
C_L = lift coefficient
C_p = surface pressure coefficient
$C_{m,c/4}$ = quarter chord moment coefficient
$C_{\Delta P}$ = differential pressure coefficient
k_c = reduced frequency based on chord

N_h = number of harmonics
p = perturbation pressure
p_{rms} = pressure scale factor
S = airfoil spacing
$\bar{U}$ = mean absolute velocity
$\hat{v}$ = transverse gust component
w_{rms} = velocity scale factor (velocity fluctuation root-mean-square)

α = angle of attack
ρ = density
overbar = steady component
$\hat{}$ = harmonic component

Subscripts

l = lower surface
u = upper surface

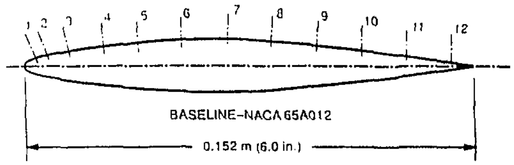

PRESSURE MEASUREMENT LOCATIONS

TAP NO.	1	2	3	4	5	6	7	8	9	10	11	12
% CHORD	2.5	5.0	10.0	17.5	25	35	45	55	65	75	85	95

Fig. 2 Instrumented stator airfoil profile

cascade is comprised of the four instrumented airfoils, two static and two dynamic, resulting in a low solidity value of 0.17. The rotor–stator axial gap is shown in Fig. 1.

Data Acquisition and Analysis

Both steady and unsteady data are required for these experiments. The steady data define the steady or mean flow performance of the stator vane row, including the stator-cascade mean inlet flow field, the static surface pressure distributions, and the lift and moment. The unsteady data define the forcing function or gust generated by the rotating rows of perforated plates defined by the unsteady velocity and static pressure fluctuations downstream of the rotor, as well as the resulting unsteady gust response of the stator vane row, i.e., the detailed stator-airfoil surface periodic aerodynamic loading distribution as specified by the periodic midspan velocity and surface pressure distributions. All experiments were conducted at a Reynolds number of 470,000 based on the stator airfoil chord.

The airfoil unsteady surface pressures are measured with PCB Piezotronics model 103A piezoelectric pressure transducers. The transducers have a nominal sensitivity of 0.22 mV/Pa (1500 mV/psi) and a natural frequency of 13 kHz. Due to space limitations, taps 1, 2, 11, and 12 were connected to the transducers through passages machined in the airfoils. After the transducers were installed in the airfoil, the dynamic response of each airfoil transducer-passage system was experimentally determined to correct the pressure signals for any passage effects. The steady and time-averaged airfoil surface pressures were obtained using a Scanivalve system with a transducer calibrated to within 0.5 percent.

All time-variant signals are digitized over one rotor revolution using approximately 2000 samples. The number of ensemble averages necessary to obtain clean periodic time traces was investigated. Ensemble averaging the hot-wire and pressure transducer signals 150 and 100 times, respectively, produces very clean periodic time traces with the random fluctuations averaged away. The Fourier components of the ensemble-averaged time traces are numerically determined with Fast Fourier Transform software. The sample frequency is set and the number of samples is adjusted to produce time records of exactly one rotor rotation period to eliminate frequency leakage problems in the Fourier Transform analysis. The sample frequency and number of digitizations are set based upon an accurate rotor rotational speed. The rotor rotational speed is measured by digitizing the shaft trigger signal at the maximum sample frequency and counting the number of samples between shaft triggers.

Stator Vane Steady and Unsteady Performance. The stator vane chordwise pressure response data are presented as nondimensional pressure coefficients and are correlated with a steady linear-theory analysis. The unsteady response data are correlated with the compressible flow analysis of Smith (1972) and Whitehead (1984). Both of these analyses account for the cascade stagger angle and the solidity C/S, with the unsteady analysis also considering the reduced frequency k_c and the interblade phase angle.

The steady data are nondimensionalized by calculating a steady surface pressure coefficient:

$$\bar{C}_p(x) = \frac{\bar{p}(x) - p_\infty}{\frac{1}{2}\rho \bar{U}^2} \tag{1}$$

where $\bar{p}$ is the time-averaged airfoil surface pressure and p_∞ is the free-stream pressure measured on the test-section outer diameter just upstream of the stator cascade.

The steady differential pressure coefficient is defined by

$$\bar{C}_{\Delta p} = \bar{C}_{p,l} - \bar{C}_{p,u} \tag{2}$$

where the subscripts l and u refer to the lower and upper airfoil surfaces, respectively.

The unsteady periodic signals are Fourier decomposed and each pressure harmonic nondimensionalized by calculating an unsteady surface pressure coefficient:

$$\hat{C}_p(x) = \frac{\hat{p}(x)}{\rho \bar{U} \hat{v}} \tag{3}$$

where $\hat{p}$ and $\hat{v}$ represent the harmonic surface pressure and transverse gust component, respectively.

The harmonic differential pressure coefficient is defined by

$$\hat{C}_{\Delta p} = \hat{C}_{p,l} - \hat{C}_{p,u} \tag{4}$$

Direct comparison of the experimental and theoretical steady and unsteady lift and quarter-chord moment coefficients is accomplished by integrating the experimental and theoretical chordwise differential pressure coefficients over the airfoil chord:

$$C_L = \frac{1}{C} \int_{0.025C}^{0.95C} C_{\Delta p} dx$$

$$C_{M,c/4} = \frac{1}{C^2} \int_{0.025C}^{0.95C} C_{\Delta p}(x - 0.25) dx \tag{5}$$

The trapezoidal rule is used to evaluate the integral from the discrete differential pressure coefficient data and theoretical predictions. The differential pressure distributions were integrated from the leading edge tap location, $0.025C$, to the trailing edge tap location, $0.95C$.

The complex valued unsteady pressure coefficients, lift coefficients, and moment coefficients contain both amplitude and phase angle information. These quantities are referenced to the transverse gust sinusoid measured by the cross hot-wire in the airfoil leading edge plane. To obtain pressure coefficients for a single equivalent airfoil, the pressure signals are phase corrected to account for the circumferential locations of the instrumented airfoils. The uncertainty of the measured unsteady surface pressure coefficients is estimated at 10 percent where the response is large near the leading edge. The uncertainty of the measured steady surface pressure coefficients is estimated at 5 percent where the value is large near the leading edge.

Rotor Generated Gust Forcing Function. Unsteady data define the forcing function or gust generated by the rotating row of perforated plates. These data are determined by the midspan unsteady velocity and static pressure fluctuations downstream of these rotors. The rotor-exit flow field unsteady total pressure is measured with a hemispherical-nosed total pressure pitot tube fitted with an unsteady pressure transducer. The amplitude of the incident flow angle is a function of the wake generator, with the angle of the pitot tube set to minimize flow angle variations. The criterion presented by Becker and Brown (1974) shows that the errors produced by the incident flow angle fluctuations should be no more than 6 percent. A cross

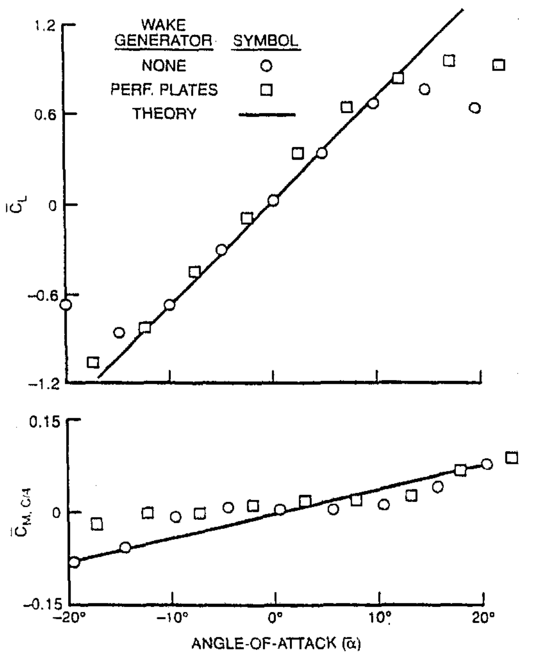

Fig. 3 Time-averaged stator vane lift and moment coefficients

hot-wire anemometer is used to measure the unsteady velocity field. The absolute velocity magnitude and flow angle errors are estimated at 4 percent and 0.5 percent, respectively. The wake velocity deficits are decomposed into streamwise and transverse velocity components. The unsteady static pressure is calculated as the difference between the unsteady total pressure and the unsteady dynamic pressure since the probe dimensions were much smaller than the fluctuation wave lengths.

The unsteady velocity vector and static pressure measurements are scaled so that an unsteady velocity vector of unit length represents a velocity pressure fluctuation equal to a unit pressure fluctuation. The velocity and static pressure scale factors, w_{rms} and p_{rms} for small perturbations, are linearly related by

$$p_{\mathrm{rms}} = \rho \bar{U}_2 w_{\mathrm{rms}} \tag{6}$$

where w_{rms} is the root-mean-square of the velocity fluctuations and p_{rms} is calculated from Eq. (6). Since w_{rms} and p_{rms} are linearly related by the constant $\rho \bar{U}_2$, scaling in this manner allows the direct determination of the relative proportions of the velocity and static pressure fluctuations. The forcing function is measured with no stator vanes installed so that the only unsteady velocity potential fields are those from the wake generators.

Results

A series of experiments was performed to investigate the effect of high steady loading and separated flow, including dynamic stall on the resulting unsteady aerodynamic stator vane row response. For a particular stator incidence angle, the steady or mean stator aerodynamic performance is determined in a completely steady flow with no rotor and also with unsteady flow generated by a rotor at the same mean operating condition, thereby identifying the stator vane row dynamic stall conditions. The rotor is comprised of 20 perforated plate wake generators, resulting in a reduced frequency of approximately 1.35 based on semichord. The unsteady aerodynamic response of the stator vane row is then investigated over a range of incidence angle values, including attached and separated flows with dynamic stall. Note that the pressure data are nondimensionalized by the velocity data obtained with the stator airfoils removed.

Unsteady Flow Effects on Mean Flow

The steady, i.e., time-averaged or mean lift and quarter-chord moment coefficients for the low-solidity stator vane row at various angle of attack are presented in Fig. 3. The effect of unsteady flow on the time-averaged loading is determined by measuring the time-averaged or mean stator-airfoil surface pressure distributions in a steady flow field with no rotor and in the unsteady perforated-plate rotor generated flow. The theoretical predictions were obtained using a two-dimensional incompressible cascade analysis.

The symmetric-airfoil lift coefficients correlate well with the theoretical predictions for angle of attack less than approximately 15 deg. For angle of attack greater than or equal to 15 deg, the steady-flow-field lift coefficients begin to depart from the prediction and show an abrupt decrease in magnitude, indicating stall, for increasing angle of attack. The airfoil stall characteristics for the steady-flow-field, i.e., no wake generators, are similar for large positive and negative angle of attack. That is, the same abrupt decrease in the lift coefficient magnitude seen at the large positive angle of attack is seen at the same angle for negative angle of attack. The stator airfoils exhibit dissimilar stall characteristics in the unsteady perforated-plate-generated flow field. That is, at large positive angle of attack the lift coefficients depart significantly from the theoretical prediction, whereas at large negative angle of attack the measured lift coefficients do not depart nearly as much from the prediction.

There is a delay in airfoil stall onset due to the unsteady flow. At high positive angle of attack, the unsteady flow-field mean lift coefficients increase with increasing angle of attack, although at a much smaller rate than predicted by theory, and they do not exhibit the abrupt decrease found in the steady-flow-field symmetric-airfoil trend. At high negative angle of attack, the airfoil unsteady flow field mean lift coefficients are much closer to the theoretical values than for the same steady-flow-field angle of attack, indicating the delay of stall. The airfoil mean quarter chord moment coefficients correlate well with theory at $\bar{\alpha} = 0$, but exhibit a flat trend where the airfoils are unstalled, whereas the predictions show an increasing trend with angle of attack.

Figure 4 presents the airfoil steady chordwise surface and differential pressure coefficients obtained in a steady flow field for positive and negative angle of attack, respectively. The correlation with linear theory is excellent for angle of attack less than 15 deg. Also the symmetry of the static pressure distributions is excellent for angle of attack less than 15 deg as the surface pressure distributions are reversed for angle of attack of opposite sign. At $\bar{\alpha} = 0$ deg the surface pressures are coincident resulting in zero differential pressure coefficients. For angle of attack greater than 10 deg, stalling is evident. The suction

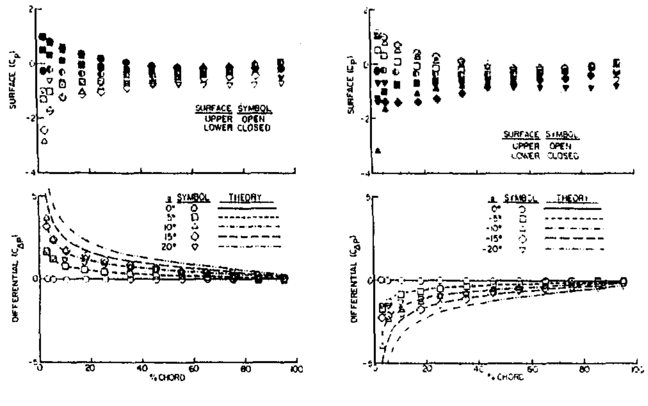

Fig. 4 Steady stator chordwise pressure distributions at positive and negative angles of attack, steady flow

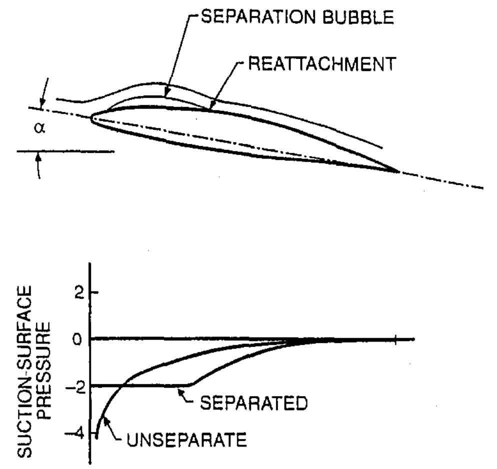

Fig. 5 Airfoil stall characteristics

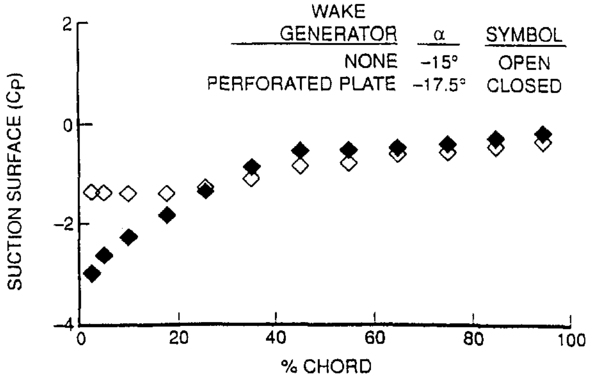

Fig. 7 Unsteady flow field effect on stator vane stall characteristics

surface, i.e., the upper surface for positive angle of attack, pressure coefficients decrease near the leading edge when the angle of attack is increased from +10 to +15 deg. Increasing the angle of attack further to +20 deg results in a constant suction-surface pressure distribution over the entire chord except very near the leading edge, indicating that the suction surface is completely stalled. Increasing the angle of attack from −10 to −15 deg results in a flat pressure distributions near the leading edge on the suction surface. Aft of the constant pressure distribution region, the magnitude of the suction-surface pressure decreases monotonically with chord. At $\bar{\alpha} = -20$ deg the suction surface is again completely stalled.

The constant pressure distribution near the leading edge on the suction surface is explained by the presence of a separation bubble, which appears at high angle of attack, depicted in Fig. 5. Aft of the separation bubble, the flow reattaches as confirmed by the decreasing magnitudes of the suction-surface pressure.

The delay in the steady stall onset in the unsteady flow is clearly seen in the airfoil surface time-averaged chordwise pressure coefficients obtained in the unsteady flow, Fig. 6. The suction surface pressure coefficients resemble unstalled patterns, i.e., monotonically increasing, to higher angle of attack in the unsteady flow fields. For example, as illustrated in Fig. 7, the airfoil suction surface at $\alpha = -15$ deg in the steady flow field depicts more evidence of stall than at $\alpha = -17.5$ deg in the unsteady flow field, even though the steady-flow-field angle of attack is smaller.

Unsteady Flow

The unsteady flow generated by the perforated plate rotor generates the unsteady aerodynamic response of the downstream stator vane row. Thus, it is necessary to first characterize the rotor generated gust forcing function. The resulting unsteady aerodynamic gust response of the downstream stator vane row is then considered.

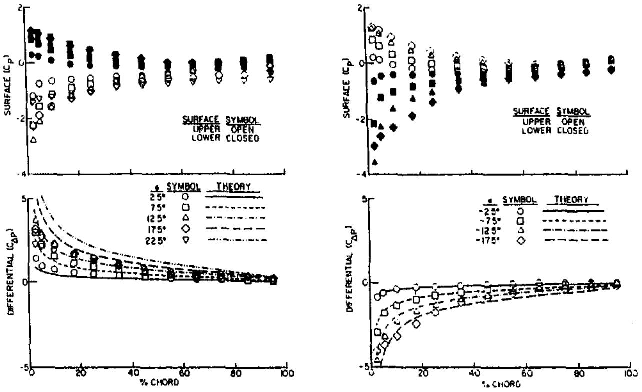

Fig. 6 Time-averaged stator chordwise pressure distributions at positive and negative angles of attack, unsteady flow

Gust Forcing Function. The perforated-plate generated aerodynamic forcing function is presented in Fig. 8. The velocity perturbations are approximately ±25 percent of the mean absolute velocity. No stator vanes were installed for these measurement, so that the only measured unsteady velocity and potential perturbations are those from the wake generators. The periodic velocity vector profile and static pressure distribution define the forcing function. A complete forcing function composed of N_h harmonics is shown, together with the forcing function fundamental harmonic.

The perforated plate wake generators generate a negligible potential field as well as viscous diffusion effects on the small length scale associated with the plate holes. Thus, the viscous effects within the wake diffuse quite rapidly, leaving a large velocity deficit with a negligible static pressure perturbation. Hence, the perforated plate rotor generated forcing function is a dominantly vortical gust, indicated by the minimal unsteady static pressure field. Note that the measured static pressure per-

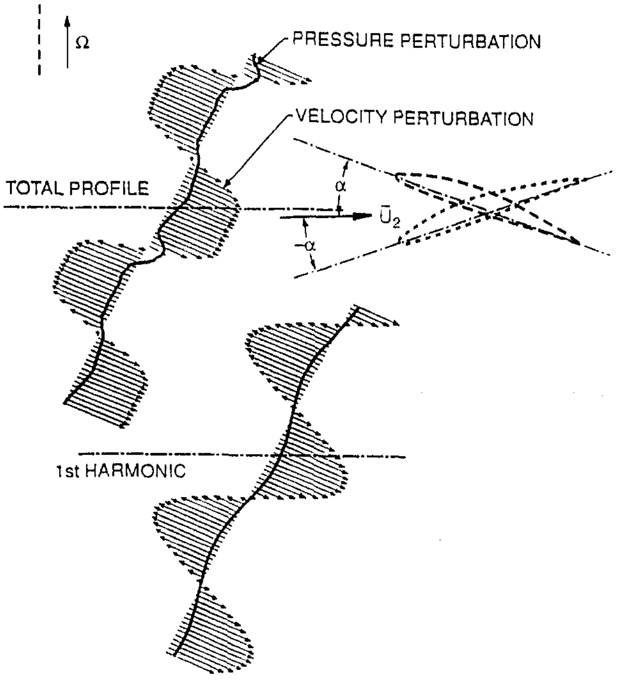

Fig. 8 Perforated plate generated gust forcing functions

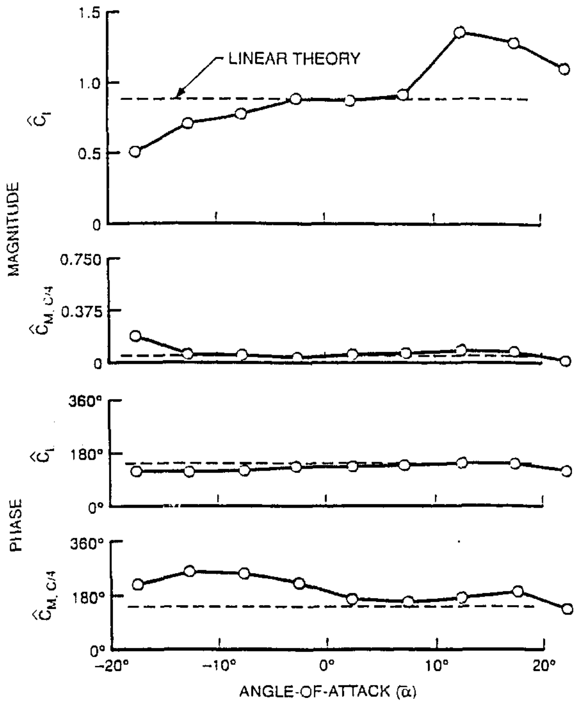

Fig. 9 Steady loading effect on fundamental-harmonic lift and moment coefficients

turbation is nonzero near the edges of each wake. It is believed that this is a measurement artifact due, in part, to the combination of a rapidly changing instantaneous flow angle at the edge of the perforated plate gust and the angular sensitivity of the total pressure probe.

Stator Vane Row Gust Response. The effect of steady loading on the perforated-plate-generated fundamental-harmonic lift and moment coefficients is presented in Fig. 9. The unsteady lift-coefficient magnitudes are in excellent agreement with linear theory for angle of attack between −7 and +7 deg. Between +7 and +12 deg, the unsteady lift-coefficient magnitude increases abruptly, then decreases for increasing angle of attack, with the abrupt increases coinciding roughly with stall inception. Below −7 deg, the unsteady lift coefficient magnitudes decrease with larger negative angle of attack but with no large break in the unsteady lift-coefficient magnitude. The unsteady lift-coefficient phase angles correlate well with the theory. The quarter-chord unsteady moment magnitudes are relatively constant but display an increasing trend as the negative stall angle of attack is approached. No increase in the unsteady moment magnitude is observed for the airfoils stalled at large positive angle of attack. The unsteady moment coefficient phase angle correlation is generally poor.

The fundamental harmonic unsteady chordwise pressure responses are presented in Figs. 10–18. Also included in these figures as a reference are the linear theory vortical gust predictions obtained from Smith (1972).

Positive Incidence Angles. At low steady loading with $\bar{\alpha} = 2.5$ deg, the airfoil surface chordwise unsteady response is presented in Fig. 10. The lower or pressure surface response magnitude decreases monotonically from the leading to trailing edge. The upper or suction surface response magnitude decreases rapidly over the leading quarter chord and has a relative minimum near the quarter chord. The upper-surface response phase angle is nearly constant for the front 15 percent of the chord, then varies smoothly with chord position, first increasing and then decreasing. In contrast, the lower-surface response phase angle is nearly constant with chord position. Near the leading edge, the upper and lower surface responses are 180 deg out-of-phase, becoming in-phase near the trailing edge. The unsteady differential-pressure coefficients are in excellent agreement with the linear-theory magnitude and phase angle vortical gust predictions.

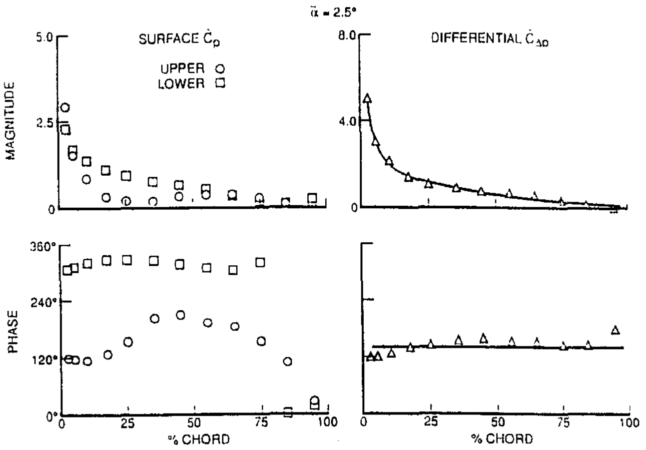

Fig. 10 Unsteady stator chordwise response at $\bar{\alpha} = 2.5$ deg

Increasing the steady loading to $\bar{\alpha} = 7.5$ deg, Fig. 11, causes the lower pressure surface response magnitude to decrease near the leading edge. The lower surface response phase angles also decrease so that the surface responses at the leading edge are now more in-phase. The upper suction surface unsteady response is relatively unaffected by the steady-load increase. Again, the upper-surface response phase angle is nearly constant for the front 15 percent of the chord, then varies smoothly with chord, first increasing and then decreasing, with the lower-surface response phase angle nearly constant with chord. The unsteady differential-pressure-coefficient magnitude correlation is good, but the measured values are slightly greater than the predictions near midchord. The unsteady differential pressure coefficient phase angles become more a function of chord but correlate well with linear vortical gust theory.

Increasing the steady loading to $\bar{\alpha} = 12.5$ deg, Fig. 12, causes a large increase in the upper-suction surface unsteady response magnitude from the 5 percent chord to the 35 percent chord so that the magnitude increases near the leading edge and the dip previously predominant near the quarter chord is absent. The lower-surface unsteady response magnitudes remain relatively unchanged from the lower loading cases. The lower-surface unsteady response phase angle decreases slightly near the leading edge so that the response phase angles are nearly in-phase

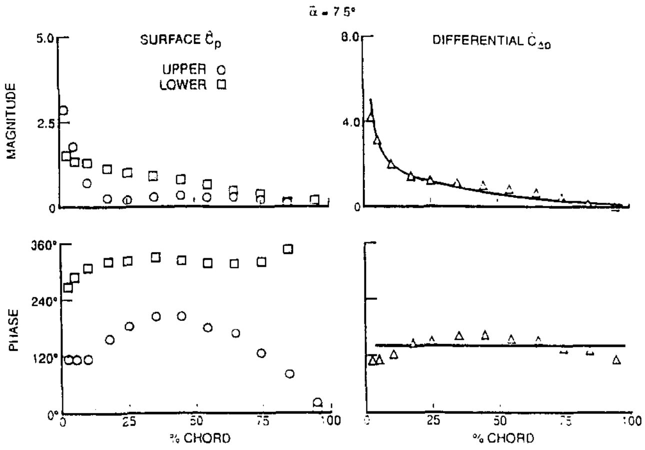

Fig. 11 Unsteady stator chordwise response at $\bar{\alpha} = 7.5$ deg

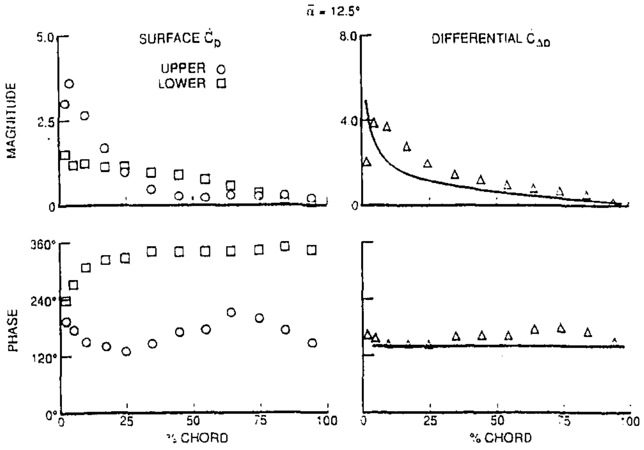

Fig. 12 Unsteady stator chordwise response at $\bar{\alpha}$ = 12.5 deg

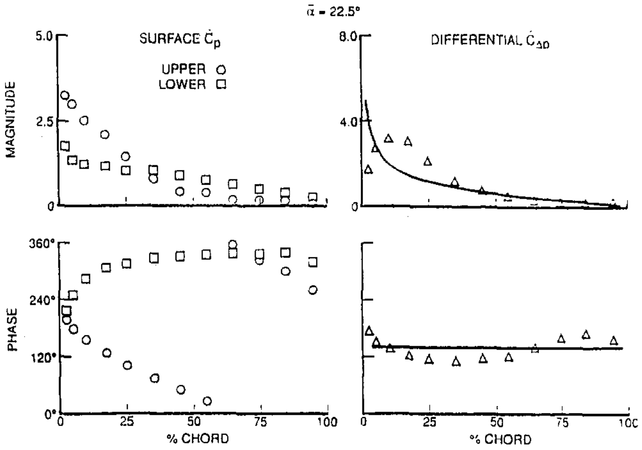

Fig. 14 Unsteady stator chordwise response at $\bar{\alpha}$ = 22.5 deg

at the leading edge. From the quarter-chord to the trailing edge, the lower-surface response phase angle remains unchanged. In contrast, the upper-surface unsteady response phase angle changes as a result of this increased steady loading: increasing greatly from the lower-loading values near the leading edge, no longer being constant over the front 15 percent of the chord, and varying in a different manner over the remainder of the chord. Also, a linear variation of the upper surface phase angle, indicative of a propagating wave on this surface, is apparent over the aft quarter chord. The unsteady differential-pressure-coefficient magnitude deviates from the predicted trend and increases with chord position near the leading edge and exhibits a relative maximum, a peak, near the 5 percent chord position. From the 5 percent chord location to the trailing edge, the unsteady differential-pressure coefficient magnitudes are greater than the predicted values. The unsteady differential-pressure-coefficient phase angles remain relatively constant but display a negative slope near the leading edge instead of the positive slope for the lower-loading $\bar{\alpha}$ = 7.5 deg case.

Increasing the steady loading to $\bar{\alpha}$ = 17.5 deg, Fig. 13, causes the upper or suction surface unsteady response magnitude to increase greatly over the leading quarter chord, whereas the lower-surface unsteady response magnitude remains relatively unaffected. The lower surface unsteady response phase angle is also relatively unaffected by the increased loading. In the leading edge region of the upper surface, the response phase angle is also unaffected by the increased loading. However, from approximately the quarter-chord to the trailing edge, the upper-surface unsteady response phase angle is dominated by an almost linear variation with chord, indicative of a wave propagating down the upper suction surface. Note that an indication of this wave propagation was seen in the $\bar{\alpha}$ = 12.5 deg data in the aft quarter-chord region. Also, this suction surface wave is propagating at approximately 50 percent of the free-stream velocity, a result in agreement with isolated airfoil dynamic stall experimental findings. The peak in the unsteady differential-pressure coefficient magnitude near the 5 percent chord remains predominant and unaffected by the steady loading increase whereas the 2.5 percent chord magnitude increases. The unsteady differential-pressure-coefficient phase angle becomes more of a function of chord and decreases with chord position near the leading edge with a relative minimum near the quarter chord.

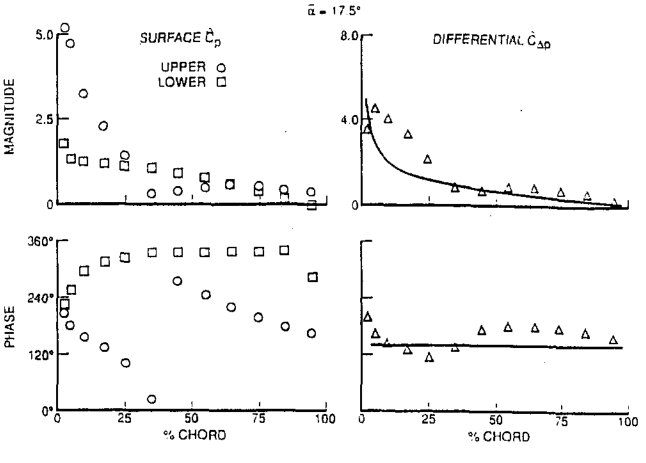

Fig. 13 Unsteady stator chordwise response at $\bar{\alpha}$ = 17.5 deg

Increasing the steady loading to $\bar{\alpha}$ = 22.5 deg, Fig. 14, causes the upper-suction surface unsteady response magnitude to decrease greatly from the $\bar{\alpha}$ = 17.5 deg values near the leading edge. Note the presence of the propagating wave over the entire upper-surface, defined by the linear variation of the upper-surface response phase angles. Again, this wave is propagating at approximately 50 percent of the free-stream velocity. The lower surface unsteady response magnitudes and phase angles are relatively unaffected by the loading increase. The peak in the unsteady differential-pressure-coefficient magnitude decreases and moves aft to the 10 percent chord with increased loading. The unsteady differential pressure coefficient phase angle becomes less of a function of chord position.

Negative Incidence Angles. At low steady loading with $\bar{\alpha}$ = −2.5 deg, Fig. 15, the chordwise unsteady responses are very similar to the $\bar{\alpha}$ = +2.5 deg case. The upper surface corresponds to the suction surface for time-averaged positive angle of attack and the pressure surface for time-averaged negative angle of attack.

Increasing the steady loading to $\bar{\alpha}$ = −7.5 deg, Fig. 16, causes the lower-suction surface unsteady response magnitude to increase greatly from the lower-loading values at the 2.5 percent chord location. However, the remaining lower-surface unsteady response magnitudes, the lower-surface response phase angles, and the upper-surface response magnitudes are unaffected by the increase in steady loading. The upper-pressure surface response phase angles change trends with increased steady loading, now exhibiting a somewhat linear variation with chord. Near the leading edge, the surface-response phase angles remain 180 deg out of phase. The slope of the differential-pressure-coefficient magnitude is greater than the lesser loaded $\bar{\alpha}$ = −2.5 deg case and the prediction curve near the leading edge and the data trend dips below the prediction near midchord. The unsteady differential-pressure-coefficient phase angle is constant over the leading half chord, then shows a slight in-

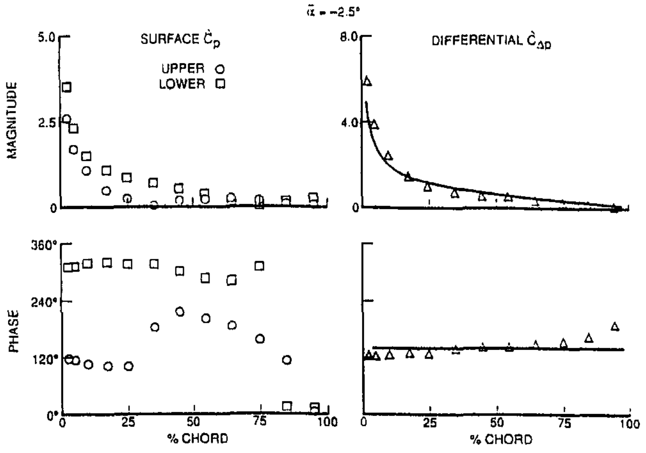

Fig. 15 Unsteady stator chordwise response at $\bar{\alpha}$ = −2.5 deg

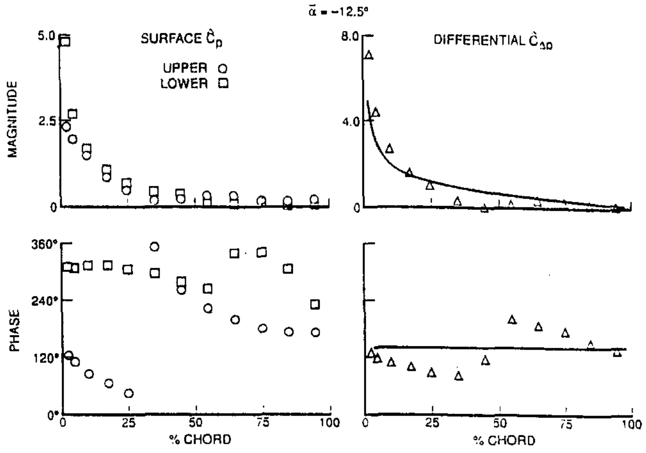

Fig. 17 Unsteady stator chordwise response at $\bar{\alpha}$ = −12.5 deg

crease followed by another constant region not predicted by theory.

Increasing the steady loading to $\bar{\alpha}$ = −12.5 deg, Fig. 17, causes only subtle changes in the surface response magnitudes and phase angles. These result in a slight decrease in the unsteady differential-pressure-coefficient magnitude relative minimum near the midchord and an increase in the variability of the unsteady differential-pressure-coefficient phase angle. Also of note is the linear variation of the lower-suction surface phase angle over the aft quarter-chord, indicative of a convected wave.

Increasing the steady loading to $\bar{\alpha}$ = −17.5 deg, Fig. 18, causes a large increase in the lower-suction surface unsteady response magnitudes from the leading edge to the 17.5 percent chord position. From 25 to 75 percent chord, the lower-surface unsteady response magnitudes are greater than the $\bar{\alpha}$ = −12.5 deg values and show an increasing trend followed by a decreasing trend. The lower-suction surface response phase angles show a dramatic change in trend as they now decrease linearly with chord location, indicating a convected wave. This lower-suction surface wave is propagating at approximately 50 percent of the free-stream velocity, analogous to the positive incidence angle suction surface wave. The upper-surface unsteady response magnitudes and phase angles are unaffected by the steady loading increase. The response phase angles remain 180 deg out of phase near the leading edge. The unsteady differential-pressure-coefficient magnitudes decrease almost linearly over the leading quarter chord, then display a relative minimum near the quarter chord and a relative maximum near midchord. The trend of the unsteady differential-pressure-coefficient phase angle also changes dramatically by decreasing greatly near the leading edge with a lesser decrease from the 35 percent chord position to the trailing edge.

Positive Versus Negative Incidence Angles. Strong asymmetries are found in the unsteady flow generated chordwise responses for increased steady loading, that is the unsteady chordwise responses show markedly different behavior for increasing positive and negative angle of attack. Also, the suction-surface responses were greatly affected by steady loading, with the pressure surface relatively unaffected. When the steady loading is increased to either large positive or large negative angle of attack, a propagating wave is found on the airfoil suction surface, which propagates at approximately 50 percent of the free-stream velocity.

These asymmetries are due to the nature of the unsteady loading cycle. Figure 19 depicts a large axial flow velocity for the free-stream flow. In the wake region, the flow velocity decreases and the absolute flow angle increases to approximately 10 deg, as shown. When the wake region reaches airfoils set at time-averaged positive angle of attack, the instantaneous angle of attack increases as the flow velocity decreases. The increase in angle of attack and the decrease in inlet flow velocity have opposite effects on the instantaneous loading. The increase in angle of attack tends to increase the loading, whereas the decrease in inlet flow velocity tends to decrease the loading. As the flow field changes from wake region back to free-stream region, the decrease in angle of attack and increase in flow velocity have the reverse effect on the instantaneous loading.

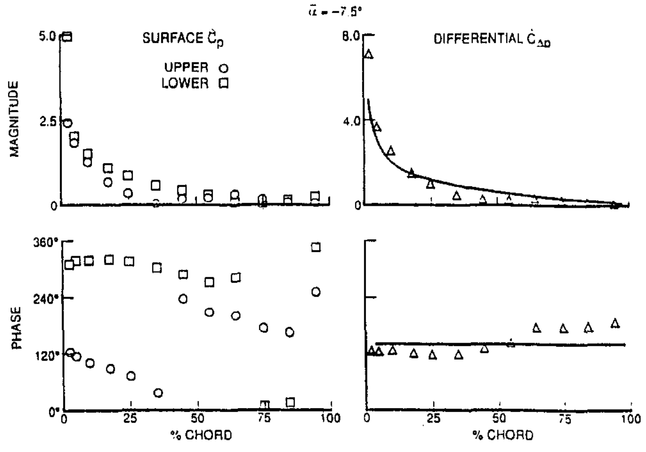

Fig. 16 Unsteady stator chordwise response at $\bar{\alpha}$ = −7.5 deg

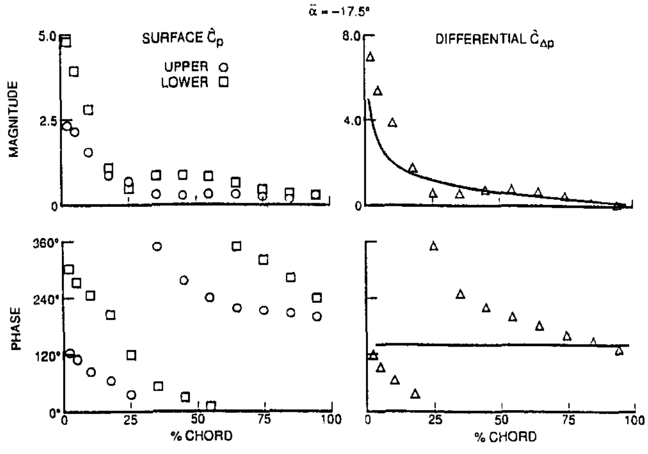

Fig. 18 Unsteady stator chordwise response at $\bar{\alpha}$ = −17.5 deg

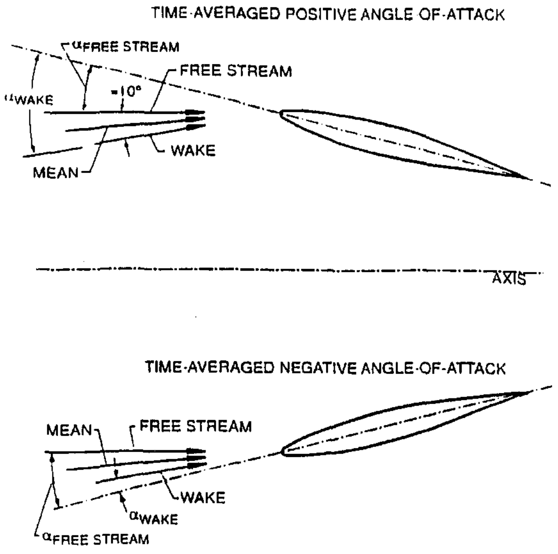

Fig. 19 Airfoil unsteady loading cycle

For airfoils set at time-averaged negative angle of attack, the effects of angle of attack and flow velocity variations are additive. As the flow field changes from free stream to wake region, the instantaneous loading decreases because of the complementary effects of the decreasing angle of attack and flow velocity. The reverse occurs when the flow field changes from the wake region back to the free-stream region. Thus, the loading cycles for airfoils set at time-averaged positive angle of attack are very different from airfoils set at time-averaged negative angle of attack.

From another point of view, the asymmetry in the unsteady response behavior stems from the asymmetry in the unsteady flow field. Figure 8 clearly illustrates the unsteady flow field asymmetry by virtue of the gust propagation direction. Symmetric unsteady response behavior is not expected except for the case where the gust propagation direction and the mean downstream absolute flow velocity vector are aligned producing a pure transverse gust. For a pure transverse vortical gust, opposite airfoil surfaces would experience the same instantaneous loading for the opposite time-averaged angle of attack and the behavior of the unsteady response would not depend upon the sign of the angle of attack.

Summary and Conclusions

The effect of high steady loading and separated flow, including dynamic stall effects, on the resulting unsteady aerodynamic response of turbomachine blade rows was experimentally investigated. This was accomplished utilizing a unique single-stage turbomachine research facility in which the flow is not generated by the blading but rather by an additional fan. Thus, for a particular stator incidence angle, the steady or mean stator aerodynamic performance were determined in a completely steady flow with no rotor and also with unsteady flow generated by a rotor composed of perforated plates at the same mean operating condition, thereby identifying the stator vane row dynamic stall conditions. The unsteady aerodynamic response of the stator vane row was then investigated over a range of incidence angle values, including attached and separated flows with dynamic stall.

The time-averaged loading in the unsteady flow fields was shown to be equal to the steady loading in steady flow fields for unstalled airfoils. The unsteadiness in the flow field delayed the onset of stall.

The unsteady chordwise responses show that the suction surface is greatly affected by steady loading increases, with the pressure surface relatively unaffected. Increasing the steady loading for positive angle of attack results in surface responses that are in-phase near the leading edge and the appearance of a peak in the differential-pressure-coefficient magnitude near the 5 percent chord, which degrades the linear-theory correlation. For increasing negative angle of attack, the surface-responses remained 180 deg out-of-phase near the leading edge. For both positive and negative incidence angles, a propagating wave phenomenon was found on the airfoil suction surface as the steady loading is increased. This wave propagates at approximately 50 percent of the free-stream velocity, a result in agreement with isolated airfoil dynamic stall experimental findings.

The unsteady differential-pressure-coefficient had large increases in magnitude and slope near the leading edge. At high positive angle of attack, the unsteady differential-pressure-coefficient phase angles are much less a function of chord than at the high negative angle of attack. However, when the steady loading increases, the differential-pressure-coefficient phase angle correlation degrades for both positive and negative angle of attack. The chordwise responses for positive and negative angle of attack are asymmetric with respect to angle of attack due to the asymmetry in the unsteady flow field, with propagating found on the suction surfaces at high steady loading.

Acknowledgments

This research was sponsored, in part, by the NASA Lewis Research Center. Both the financial support and the technical interchanges with Dr. Daniel Hoyniak are most gratefully acknowledged.

References

Abbott, I., and Von Doenhoff, A., 1959, *Theory of Wing Sections*, Dover Publications.

Becker, H. A., and Brown, A. P. G., 1974, "Response of Probes in Turbulent Streams," *Journal of Fluid Mechanics*, Vol. 62, Part 1, pp. 85–114.

Capece, V. R., and Fleeter, S., 1989, "Experimental Investigation of Multistage Interaction Gust Aerodynamics," ASME JOURNAL OF TURBOMACHINERY, Vol. 111, pp. 409–417.

Fang, J., 1991, "Compressible Flows With Vortical Disturbances Around Cascades of Airfoils," Ph.D. Thesis, University of Notre Dame, Apr.

Feiereisen, J. M., Montgomery, M. D., and Fleeter, S., 1994, "Unsteady Aerodynamic Forcing Functions: A Comparison Between Linear Theory and Experiment," ASME JOURNAL OF TURBOMACHINERY, Vol. 116, pp. 676–685.

Goldstein, M. E., and Atassi, H., 1976, "A Complete Second-Order Theory for the Unsteady Flow About an Airfoil Due to Periodic Gust," *Journal of Fluid Mechanics*, Vol. 74, part 4, pp. 741–765.

Hall, K. C., and Verdon, J. M., 1989, "Gust Response Analysis for Cascades Operating in Nonuniform Mean Flows," *AGARD Conference—Unsteady Aerodynamic Phenomena in Turbomachines*, AGARD CPP-468.

Henderson, G. H., and Fleeter, S., 1993a, "Forcing Function Effects on Unsteady Aerodynamic Gust Response: Part 1—Forcing Functions," ASME JOURNAL OF TURBOMACHINERY, Vol. 115, pp. 741–750.

Henderson, G. H., and Fleeter, S., 1993b, "Forcing Function Effects on Unsteady Aerodynamic Gust Response: Part 2—Low Solidity Airfoil Row Response," ASME JOURNAL OF TURBOMACHINERY, Vol. 115, pp. 751–761.

Kim, K., and Fleeter, S., 1992, "Compressor Blade Row Unsteady Aerodynamic Response to Attached and Separated Flow Forcing Functions," AIAA Paper No. 92-0147.

Manwaring, S. R., and Wisler, D. C., 1993, "Unsteady Aerodynamics and Gust Response in Compressors and Turbines," ASME JOURNAL OF TURBOMACHINERY, Vol. 115, pp. 724–740.

Scott, J. S., and Atassi, H., 1990, "Numerical Solutions of the Linearized Euler Equations for Unsteady Vortical Flows Around Lifting Airfoils," AIAA Paper No. 90-0694.

Smith, S. N., 1972, "Discrete Frequency Sound Generation in Axial Flow Turbomachines," ARC R & M 3709.

Whitehead, D. S., 1984, "Classical Two-Dimensional Methods," AGARDograph No. 298, *AGARD Manual on Aeroelasticity in Axial Flow Turbomachines, Vol. 1: Unsteady Turbomachinery Aerodynamics*, pp. 3.1–3.30.

Stall Precursor Identification in High-Speed Compressor Stages Using Chaotic Time Series Analysis Methods

M. M. Bright
NASA Lewis Research Center,
Advanced Controls and Dynamics Branch,
Cleveland, OH 44135
email: mbright@limspop.lerc.nasa.gov

H. K. Qammar
Department of Chemical Engineering,
The University of Akron,
Akron, OH 44325

H. J. Weigl

J. D. Paduano

Gas Turbine Laboratory,
Massachusetts Institute of Technology,
Cambridge, MA 02139

This paper presents a new technique for precursor identification in high-speed compressors. The technique is a pseudo-correlation integral method referred to as the correlation method. To provide a basis for comparison, the traveling wave energy technique, which has been used extensively to study prestall data, is also briefly presented and applied. The correlation method has a potential advantage over the traveling wave energy method because it uses a single sensor for detection. It also requires no predisposition about the expected behavior of the data to detect "changes" in the behavior of the compressor. Both methods are used in this study to identify stall precursive events in the pressure fluctuations measured from circumferential pressure transducers located at the front face of the compressor rig. The correlation method successfully identified stall formation or changes in the compressor dynamics from data captured from four different configurations of a NASA Lewis single-stage high-speed compressor while it was transitioned from stable operation into stall. This paper includes an exposition on the use of nonlinear methods to identify stall precursors, a description of the methodologies used for the study, information on the NASA high-speed compressor rig and experimental data acquisition, and results from the four compressor configurations. The experimental results indicate that the correlation method provides ample warning of the onset of rotating stall at high speed, in some tests on the order of 2000 rotor revolutions. Complementary features of the correlation method and the traveling wave energy method are discussed, and suggestions for future developments are made.

Introduction

How to best measure stall inception patterns in aeroengine compressors is currently an active area of research. The existing methods to identify precursors to circumferential flow breakdown (i.e., rotating stall) can be categorized based on whether they are motivated by linear or nonlinear arguments. Tryfonidis et al. (1995), in their study of different compressor configurations, sought precursors to modal instabilities in the pressure measurements prior to stall. This study used an approach motivated by linearized analysis: The energy of traveling waves is measured because stall formation is postulated to stem from instability of small-amplitude waves. Other investigations by Day (1993) showed that short length-scale pressure disturbances often arise prior to rotating stall onset. Presumably some nonlinear event is causing rotating stall inception in such cases. Day (1993) and others have argued that the same compressor can exhibit both types of stall inception pattern.

From this discussion it is clear that stall precursor detection may benefit significantly from analysis techniques that can detect both linear and nonlinear phenomena in the flow. Techniques for detecting long-wavelength, modal type disturbances are relatively well developed. The *traveling wave energy* method is one such technique (see Tryfonidis et al., 1995); it will be presented here primarily to help describe our single-stage compressor data and as a basis for comparison. Techniques for detecting short wavelength and other nonlinear phenomena are much less developed. Thus the primary goal of this paper is to present a new method, named the *correlation integral* method, which borrows ideas from chaos theory to identify changes in the underlying nonlinear dynamics of the fluid flow. A short tutorial on chaotic time series analysis is included to introduce the concepts.

Underlying the mathematical concepts and nonlinear analysis techniques to be presented is the notion that during prestall testing, events may be occurring within the compressor that are quite complex (quasi-periodic or chaotic separation events in the blade passages of a blade row, boundary layer thickening, interaction of flows between stages, etc.). The effects of these events on the sensed variables are often simply interpreted as noise. If, however, the underlying structure of these events can be detected using specialized nonlinear techniques, and if this underlying structure changes significantly as stall is approached, then a basis for nonlinear detection of precursors exists.

Experimental Setup and Preliminary Analysis

Experimental Setup. Four configurations of the NASA rotor/stator pairs 35 and 37 were tested in the High-Speed Compressor Facility (W8) at NASA Lewis. Both stage 35 and 37 are axial-flow, high-speed compressor stages for advanced air-breathing engines. They are inlet stages designed as part of an eight-stage core compressor having an overall pressure ratio of 20:1. The loading per stage is considered high for a research test compressor. The compressor design has a constant mean-line diameter, with an inlet hub–tip ratio of 0.7, and an inlet rotor-tip design speed of 455 meters per second. Additional details on the blading, geometry, and testing of this compressor can be found from Reid and Moore (1978) and Moore and Reid (1980).

Contributed by the International Gas Turbine Institute and presented at the 41st International Gas Turbine and Aeroengine Congress and Exhibition, Birmingham, United Kingdom, June 10–13, 1996. Manuscript received at ASME Headquarters February 1996. Paper No. 96-GT-370. Associate Technical Editor: J. N. Shinn.

All the experiments using the 35 and 37 compressor stages were instrumented with eight circumferentially placed pressure transducers within one chord length upstream of the rotor. These wall static pressure transducers measured the pressure fluctuations during the transition from steady-state operation into stall and surge. Table 1 presents the configurations: The first test was performed on rotor 37 without the stator, the second configuration was with rotor 37 and stator 37 (termed "Stage 37"), the third configuration used rotor 35 only, and the fourth test used rotor 35 with stator 37 (termed "Stage 35/37"). Both stationary throttle and throttle ramp data were acquired during the tests. The pressure data acquired for this paper reflect various sampling rates; for the correlation method all of the throttle ramp data were downsampled to 2 kHz as indicated in Table 1. The data sets shown are for 80 and 100 percent speed. The mixed stage could only be operated at a maximum speed of 80 percent. The 100 and 80 percent speeds correspond to approximately 18,000 rpm and 14,000 rpm, respectively.

Preliminary Analysis Using the Traveling Wave Energy Method. In order to present the basic behavior of the compressor, we rely on spectrograms[1] of the first spatial Fourier coefficient of the pressure traces. This provides a baseline look at the data, and also shows the features that are detectable as long-wavelength disturbances. The "traveling wave energy" method for precursor detection, described in the appendix, is also applied to the data here. This allows us to compare the new method presented below to "state of the art" techniques for stall precursor detection.

The evolution of the first harmonic prestall spectra are shown in Figs. 1(*a*) to 1(*d*) for tests 1, 2, 3, and 4, respectively. The power spectrum magnitude is plotted for up to 2000 rotor revolutions before stall (the amount of available prestall and post-stall data varies from run to run). The frequency axis has been normalized by the rotor frequency in each case.

The main features that we see from the spectrograms are (*a*) spectral peaks at ~40 and 100 percent of the rotor frequency and (*b*) a strong sensitivity of the magnitude of these peaks to throttle position and rotor/stator configurations (these features concur qualitatively with model predictions (see Berndt et al., 1995). Figures 1(*a*) and 1(*b*) show prestall behavior for rotor 37 and stage 37, respectively. In Fig. 1(*a*) there is some distinct traveling near 40 percent speed, but the dominant and most active (i.e., increasing as stall is approached) traveling energy band is at 100 percent speed. In Fig. 1(*b*), the magnitude of the energy at this frequency is comparable to that in Fig. 1(*a*), but in this case there is much more energy at ~40 percent of rotor. The energy at 40 percent is indicative of a low-frequency mode becoming underdamped; the energy at 100 percent rotor speed is postulated to be a higher frequency mode being excited by flowfield disturbances at the rotor frequency. Tryfonidis et al. (1995) observed that in many compressors the mode traveling at 100 percent rotor frequency is the least damped at 100 percent rotor speed—this apparently is not true for all compressors. The spectrum of the third configuration, rotor 35 alone, does not show any distinct bands of traveling energy as shown in Fig. 1(*c*). Even as far back as 8000 revolutions before stall (the spectrum beyond 2000 revolutions is not shown), only a broad range of incoherent traveling is present. Figure 1(*d*) shows yet another form of multimodal stall inception for rotor 35 and stator 37. In this case, there is traveling at 100 percent rotor frequency, which grows steadily, followed by a sharp increase in traveling energy at 40 percent speed just before stall (possibly due to a mode with a rapidly changing damping ratio). Despite the different modal behavior of cases 1, 2, and 4, all have distinct bands of increasing energy as the compressor mass decreases (this is quantified by the integrated traveling wave energy as discussed below).

Table 1 Testing configuration for all compressor stages

Configuration	Rotor	Stator	Sample Rate	Speed
1	37	none	2 Khz	18000 rpm
2	37	37	2 Khz	18000 rpm
3	35	none	2 & 5 Khz	14000 rpm
4	35	37	2 & 20 Khz	14000 rpm

The integrated traveling wave energy (described in the appendix) is included on the right of each of the spectrograms in Fig. 1. Clearly this integral simply picks out the ridges of energy in the spectrogram and allows it to be viewed as a scalar function of time. We briefly discuss the results of stall warning using this signal to provide a backdrop for the discussion of new analysis techniques.

Integrated Traveling Wave Energy for Stall Warning. The traveling wave energy is replotted for the four stall runs in Figs. 2(*a*) through 2(*d*). The integration range for these figures is 0.1 to 1.5 times the rotor frequency. In each case, the magnitude of the first spatial harmonic has been scaled so that perturbations far from stall have unit energy, so that the four compressor configurations can be compared (Fig. 1 plots are scaled in the same manner). Since all of the cases have been scaled in the same way, the same stall warning threshold value can be applied to the four configurations. The time that the traveling wave energy crosses the threshold is the stall warning point. The traveling wave energy has also been plotted beyond stall inception at zero revolutions to show the relative magnitude of the first harmonic perturbations far from stall and for fully developed stall. The energy of rotating stall pressure fluctuations is roughly 60 dB greater than the prestall perturbations in all four cases.

A threshold of 6 dB (well below the energy level of full rotating stall) has been found to be an effective stall indicator for three of the four compressor configurations. The 6 dB threshold gives approximately 900 revolutions warning for stage 37, 200 revolutions for rotor 37, and 1000 revolutions for the rotor 35 and stator 37 configuration. The growth in traveling wave energy for these configurations matches the corresponding prestall spectra. However, the traveling wave energy for rotor 35 does not show any growth over time (as expected from the spectrum in Fig. 2(*c*)). Due to large fluctuations in the traveling wave energy throughout the test, the 6 dB threshold gives a false stall warning even at mass flows well above stall.

It should be noted that the measured development of the prestall traveling modes depends on the way the throttle closes. The stepwise change in the traveling wave energy in Figs. 2(*a*) and 2(*b*) can be attributed to the manual throttle closure technique used during these tests. The data presented in Fig. 2(*d*) was obtained with a constant slow throttle rate, and the development of traveling wave energy is also smoother. Finally, the rotor 35 tests (Fig. 2(*c*)) were performed with a fast throttle closure rate. This rate may have been too high to provide effective results in the prestall spectrum and integrated wave energy method. On the other hand, we will see that the correlation integral method introduced below shows a 2500 rotor revolution warning of stall onset for this data set.

Chaotic Time Series Analysis of Prestall Data

Having seen the data from the perspective of modal decomposition in both time and space, we turn now to methods that attempt to uncover a more general class of structure in the time evolution of the data. The goal here is to investigate the data with no predisposition to a particular type of behavior; new

---

[1] Spectrogram strictly refers to a plot of the time variation of the FFT—here we slightly misuse the term to refer to the time variation of the power spectrum.

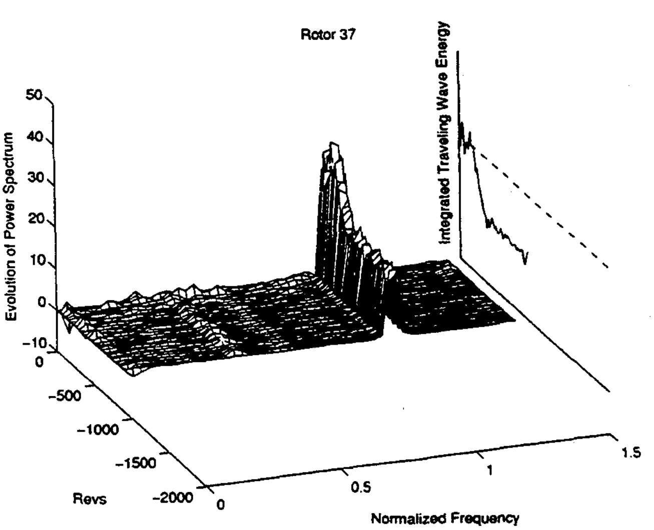

Fig. 1(*a*) First harmonic for Rotor 37

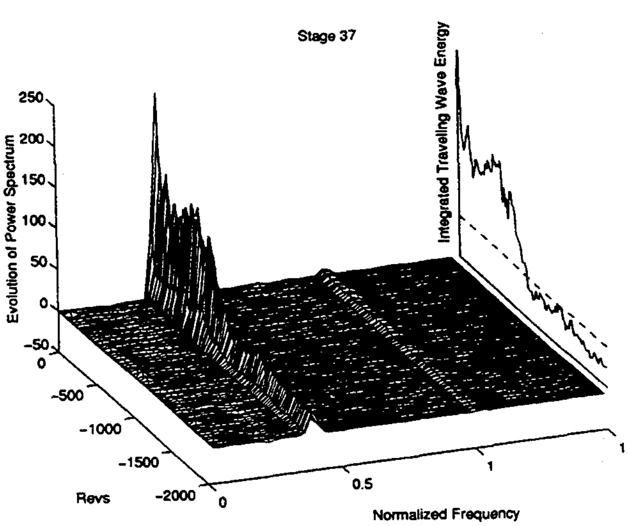

Fig. 1(*b*) First harmonic for Stage 37

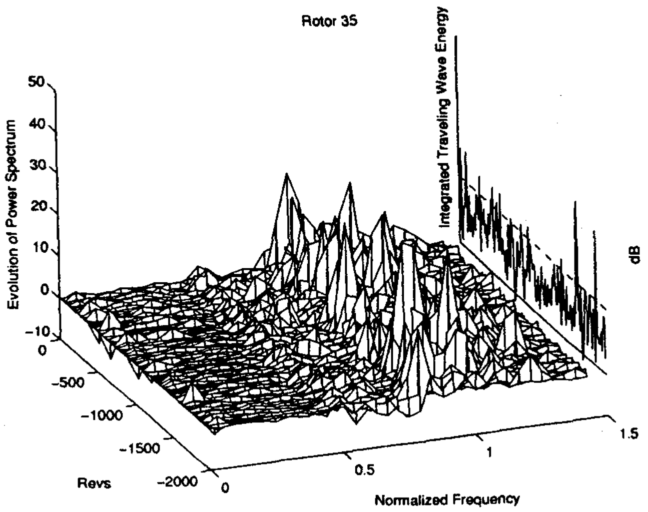

Fig. 1(*c*) First harmonic for Rotor 35

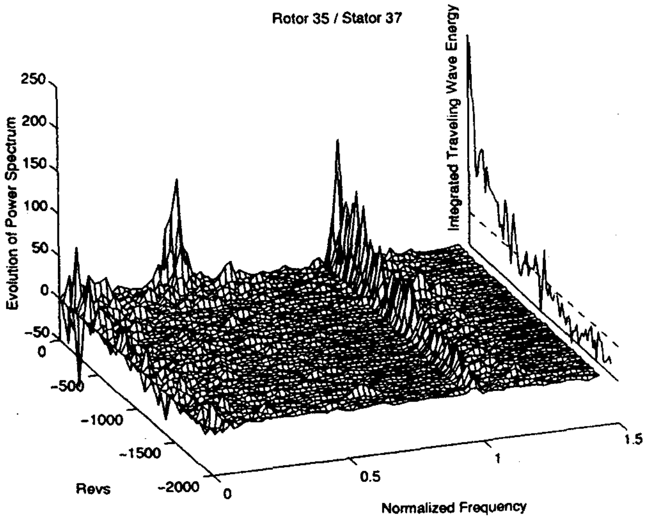

Fig. 1(*d*) First harmonic for mixed Stage 35/37

methods for detecting organized behavior of any kind in the data will be applied, to answer the basic question "what information is available in the data?" The technique that we will discuss has the following potential advantages over traveling wave detection techniques: (1) a single sensor, rather than an array of sensors, is utilized for detection, (2) the technique will detect a variety of "changes" in the behavior of the compressor (no predisposition), and (3) new tools are being applied, with the potential for new insight into compressor prestall dynamic behavior.

Background. In this section we briefly discuss time-series analysis techniques developed by the nonlinear dynamics and chaos community. An excellent comprehensive review of this topic is presented in an article by Abarbanel (1993); which is an update to an earlier review by Eckmann and Ruelle (1992) on the properties of chaotic dynamics. The primary objective of time series analysis is to obtain some quantitative measure of the observed dynamics from a single scalar measurement. Thus, the nonlinear method used in this study reflects data from a *single transducer* instead of all eight transducers.

Since the objective is not to model the infinite-dimensional Navier–Stokes equations, but rather to reconstruct much lower-dimensional flow behavior, we begin with a single pressure data set or scalar time series $P(t)$. Before the dynamics of $P(t)$ can be quantified, it is important to test whether the signal $P(t)$ has significant nonlinearities (which our methods detect) or is best represented as a linear process containing uncorrelated noise. This is done using a *surrogate* test. Theiler (1986) developed a test for detecting nonlinearity in a time series, which uses surrogate data. An excellent discussion on the proper way to obtain a surrogate can be found in Rapp et al. (1994). A surrogate data set has the same Fourier spectra as the original data set. It is generated simply in a three-step manner: (1) compute the Fourier transform of P, (2) randomize the phase of this Fourier transformed data, (3) inverse Fourier transform to obtain the surrogate data set, $S(t)$. The test is then to compare some discriminating statistic of the two data sets to get a measure of nonlinearity. Some example statistics include Kolmogorov entropy, Lyapunov exponents, and correlation dimension. If the statistic for the surrogate and the original are similar, then both the original and the surrogate are stochastic and no significant nonlinearity would be discernible in P. Differences in the statistics are indicative of nonlinear behavior, rather than stochastic behavior, in the original data set $P(t)$.

The next step in the analysis of time series data is to reconstruct the *state space* or the *phase plane* of the observed system from the single time series $P(t)$. An embedding dimension, M, is selected which is sufficient to describe the dynamics of the observed system. For example, if a system behaves periodically on a limit cycle (circle), a two-axis plot could capture this

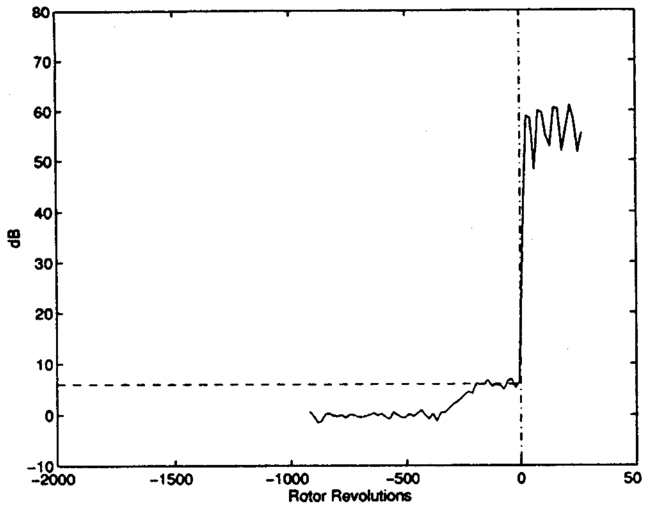

Fig. 2(*a*) Traveling wave energy for Rotor 37

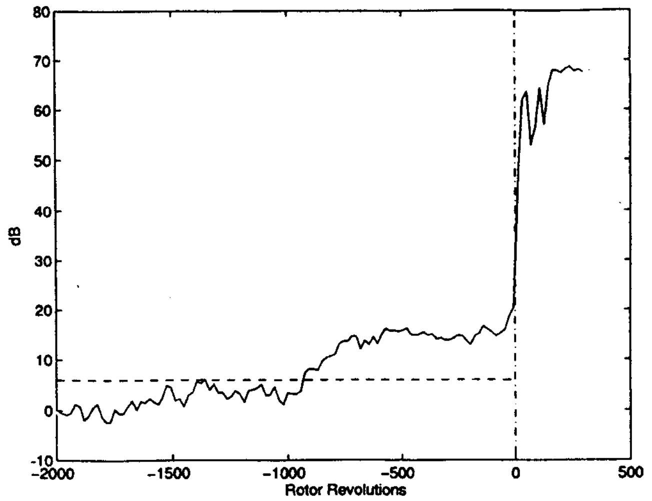

Fig. 2(*b*) Traveling wave energy for Stage 37

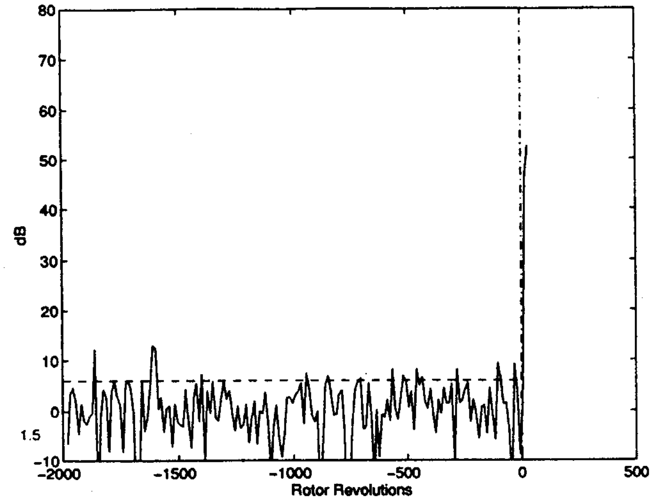

Fig. 2(*c*) Traveling wave energy for Rotor 35

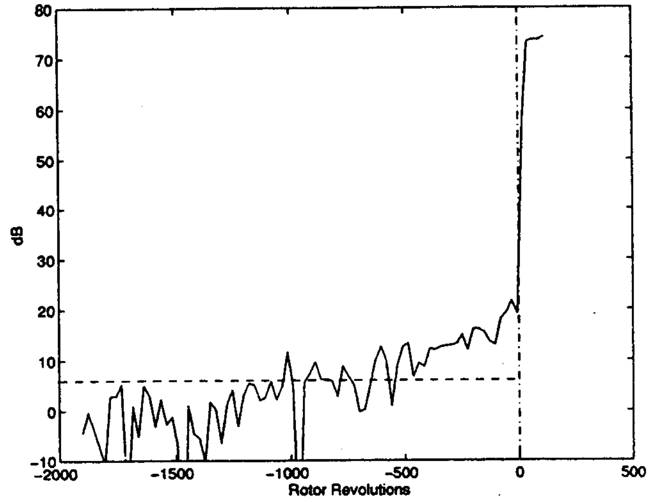

Fig. 2(*d*) Traveling wave energy for mixed Stage 35/37

behavior in state space. Periodic behavior would then require an embedding dimension of $M \geq 2$. If a system had quasi-periodic behavior, this would result in a torus in the phase plane and an embedding dimension of $M \geq 3$ is required. The embedding dimension represents the minimum number of states or the minimum number of differential equations needed to represent the dynamics of the data set. One way to obtain M independent variables from a scalar time-series would be to approximate a sequence of derivatives by finite differences, that is:

$$dP/dt \simeq \frac{P(t + (n + 1)T) - P(t + nT)}{T} \quad (1)$$

Note that the inclusion of each subsequent derivative involves adding another lag. Instead of using derivatives that are sensitive to noise, Packard et al. (1980) chose simply to use a sequence of lagged signals to create an M-dimensional vector, $y(t)$:

$$y(t) = [P(t), P(t + T), P(t + 2T), \dots, P(t + (M - 1)T)] \quad (2)$$

This has become the standard technique to reconstruct multivariate dynamics. The resulting M-dimensional object is called a pseudo-attractor. For a sufficiently large value of M, the reconstructed attractor will have the same topological and geometric properties as the original system (see Sauer et al., 1991).

The last step in the time-series analysis is to quantify the change in the nonlinear behavior of the pseudo-attractors as the compressor approaches stall. One measure is the correlation integral, $C(N, R)$, which computes the fraction of pairs of M-dimensional points that are within a distance R of each other:

$$C(N, R) = \frac{2}{N(N - 1)} \sum_{i,j=1}^{N} H(R - \|y(t_i) - y(t_j)\|) \quad (3)$$

Here, H is the Heaviside function and $\|\cdot\|$ is the Euclidian norm or vectoral distance between two points on the phase plane trajectory. Prior to the onset of rotating stall we expect a change in $C(N, R)$ because the change in the underlying dynamics of the compressor will affect the size and structure of the pseudo-attractor (we will expand on this concept in the following section). Theiler (1991) found that using the correlation integral for some fixed value of R generally provided a more powerful discrimination between the original data and the surrogate data. Albano et al. (1994) in their study of cardiac signals concluded that the correlation integral is less sensitive to perturbations and noise, a property that becomes a virtue when the objective is to classify or diagnose stall precursors in a noisy compressor rig environment.

Application of the Correlation Integral Method. To begin the analysis of these data sets, we use just a single wall static pressure Kulite as input to the surrogate test. The Kolmogorov

Entropy, Ke, is calculated for both the original data set, $P(t)$ and the surrogate data set $S(t)$. The Kolmogorov Entropy is a statistical measure of the randomness of a data set. The Ke for all the original data sets $P(t)$ was found to be an order of magnitude lower than the Ke calculated from the surrogate data sets $S(t)$. This implies that these compressor data are not just noise and a single transducer carries the underlying dynamics of the compressor even in the midst of the noisy rig environment.

The next step in the analysis of the pressure data is to reconstruct the attractor in state space. This exercise is used to determine the dimension required for successful correlation integral analysis; here we will use stationary throttle data from configuration 4 (stage 35/37) to illustrate some basic properties of the attractors (i.e., the compressor dynamics) and the correlation integral itself. In Fig. 3 we show the reconstructed attractor data collected at four throttle positions represented by four points along the 80 percent speedline of the compressor: Fig. 3(*a*) shows the attractor far from stall, 3(*b*) is the attractor near stall, 3(*c*) is the attractor very near stall, and 3(*d*) is the attractor reconstructed while in rotating stall. In each case reconstruction of the attractor is performed using a time delay of 16 samples and an embedding dimension of $M = 2$ (see definition of $y(t)$ above). Also shown in Fig. 3(*e*) are the correlation integral curves for each of these four cases; Fig. 3(*f*) shows the correlation integral as a function of run number for a fixed radius R.

It is immediately clear from the very tangled appearance of the attractors in Figs. 3(*a*) to 3(*c*) that the behavior of the data is more complex than can be represented by embedding the attractor in two dimensions. For the correlation integral curves, then, we use a fourth-order or four-axis reconstruction (i.e., $M = 4$). This allows the correlation integral to distinguish between subtler changes in the behavior of the attractors, as we will now illustrate.

Based on the reconstructed attractor and the more sensitive correlation integral curves, there is no clear evidence of a change in dynamics between Fig. 3(*a*) and Fig. 3(*b*)—both plots look equally uninformative, and the correlation integral is virtually the same in both cases. There is some change in appearance of the attractor from Fig. 3(*b*) to Fig. 3(*c*), but it is very difficult to draw any conclusions from the attractor plots. The correlation integral curves, on the other hand, do detect a difference between these attractors. The most distinct change in the appearance of the attractors is obviously between Fig. 3(*c*) (very near stall) and Fig. 3(*d*) (in stall). This change is a clear indication that the dynamics of the compressor have changed drastically just before stall and during stall. This change is reflected by a very noticeable change in the corresponding correlation integral curves.

The most interesting change in the $C(N, R)$ curves, however, is *not* the obvious jump from the very near stall to the in-stall attractors, since the rotating stall event is well documented and easily detected. Instead we are curious about the differences in the attractors near stall and very near stall. Since these attractors are *not* identical (as quantified by the correlation integral curves) there must be some progressive change in the compressor dynamics between the near stall and very near stall attractors. It is our contention that the detection of changes in these attractors, and hence, changes in the dynamics of the compressor, can be used to identify the formation of dynamics into rotating stall. To detect these changes in attractors, and hence, changes in dynamics, we borrow the method from chaos theory discussed above called the correlation integral method. For this method we simply plot the value of $C(N, R)$, for a fixed value of R, over a sliding window. Thus changes in $C(N, R)$ can be tracked as a function of time, much as changes in traveling wave energy are tracked in the integrated traveling wave energy method.

What we have demonstrated here is that the correlation integral reflects subtle changes in the shape, size, and flow of the attractor. As an attractor becomes more complex and dynamic, the correlation integral increases (more trajectories tend to pass through a given box of size R). As an attractor becomes less complex, with fewer twists and turns, the correlation integral will decrease (indicating a narrower flow of trajectories through a given box). The dynamics of the attractor, and thus, changes in the dynamics of the compressor, are measured as a function of the correlation integral $C(N, R)$. The embedding dimension M, which is the dimension of the vectors $y(t)$, reflects the complexity of behaviors that we are attempting to distinguish with the correlation integral.

Results of the Correlation Method. The throttle ramp data from all four compressor configurations was analyzed using the correlation integral method. Since this is presently an off-line procedure, and the correlation integral algorithm is attempting to detect variations between short sets of pressure data, all the data sets were segmented into 5000 point windows, which are then analyzed by a correlation integral routine, which implements the $C(N, R)$ summation. The window is moved in 500 point steps, that is, 500 new points of data are included into the next calculation of the correlation integral. The correlation integral is recalculated and updated until the stall event. A separate correlation integral calculation was made for each window of data prior to stall. This representation of the data best indicates changes in the attractor as we move into stall and will be similar to our implementation of this method in real time.

Data from configuration 1 were analyzed first using this method. Generally the output of the correlation routine is a plot of correlation integral, $C(N, R)$, versus radius R. Figure 4(*a*) provides a plot of correlation integral versus radius for the test 1 (rotor 37) data. The log of the correlation integral is plotted for each progressive window of data prior to stall. The curves in Fig. 4(*a*) show a trend of movement to the right for each new calculation of the correlation integral. The rightmost curve represents data collected just at the onset of rotating stall. To show this movement (or decrease in correlation integral), we fix the radius at 0.4 and plot the correlation integral decreasing as a function of rotor revolutions prior to stall in Fig. 4(*b*). For this case, a sharp drop in the correlation integral is evident at ~1000 rotor revolutions prior to stall. Figure 5 displays the correlation integral curves for configuration 2, Stage 37 data. Again, this is a cut of data for a fixed radius of 0.4. The radius was chosen near the center of the correlation integral curves. (The radius could be chosen arbitrarily, however a choice of the end points $R = 0$ or $R = 1$ would be statistically inappropriate.) A choice of any radius shows the same trend of correlation integral decreasing prior to stall. Figure 5 also decreases sharply, at ~1500 rotor revolutions prior to stall. Figure 6 shows the results for test 3, rotor 35 data, for a fixed radius. Figure 6 warns of stall approximately 2500 rotor revolutions in advance of stall onset. Figure 7 displays the plot for configuration 4, the mixed stage 35–37. Although the change in correlation integral is more gradual, a decrease is clearly evident 1500–2000 rotor revolutions before the stall event. Thus our contention that changes in the character of the data can be used for rotating stall detection is borne out in all four data sets.

Discussion

Several important features of the correlation integral method can be deduced by comparing the results obtained to those obtained by tracking integrated traveling wave energy. First, by comparing the results for configuration 3 for the two methods (and from the general discussion of the correlation integral), we note that the correlation integral method detects relatively subtle changes in the time series, which may not be detectable as peaks in the spectrum of the data. Thus the method may prove to be complementary to integrated wave energy for stall warning. Second, we note that the distinct jumps in the spectral energy detected in the traveling wave energy curves for three

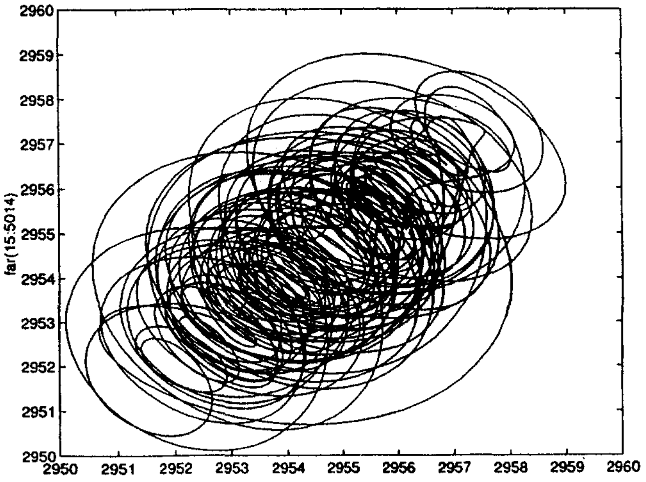

Fig. 3(*a*) Pseudo attractor for data far from stall

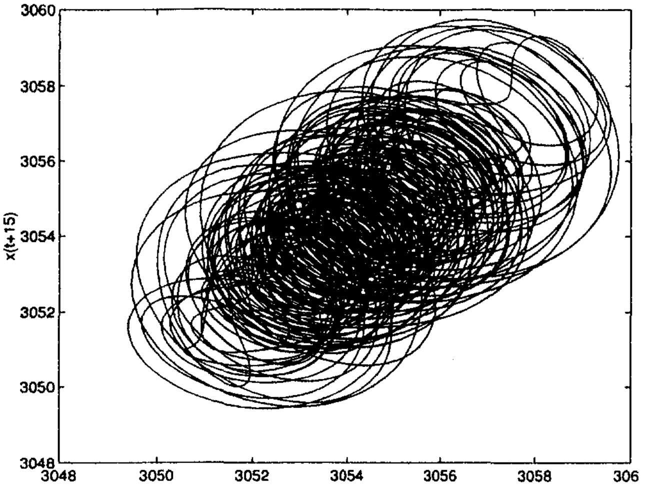

Fig. 3(*b*) Pseudo attractor for data near stall

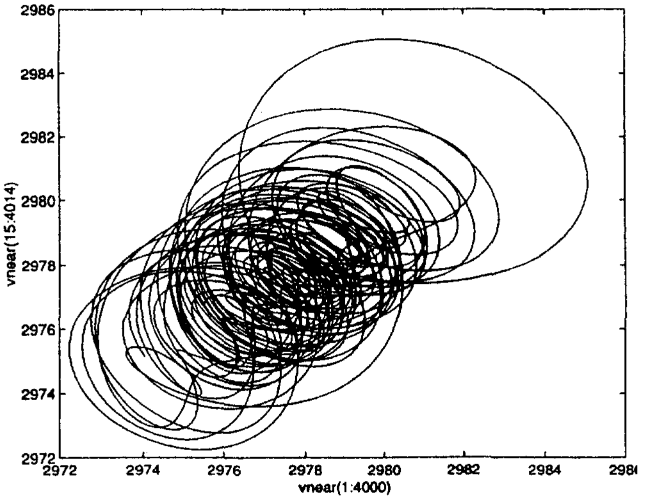

Fig. 3(*c*) Pseudo attractor for data very near stall

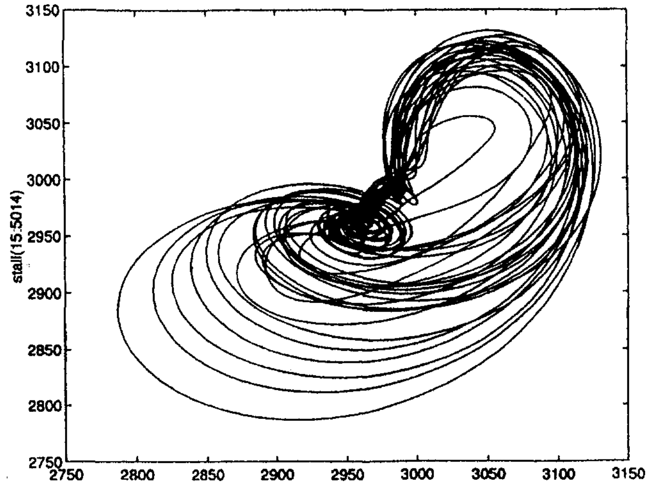

Fig. 3(*d*) Pseudo attractor for data in stall

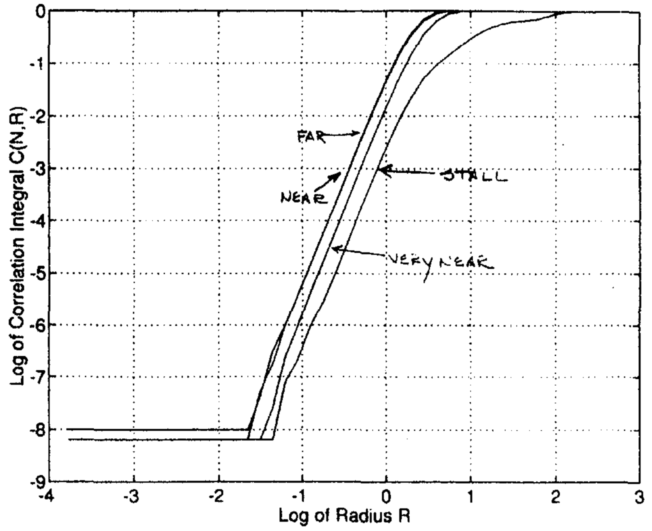

Fig. 3(*e*) Correlation integral curves for all four cases

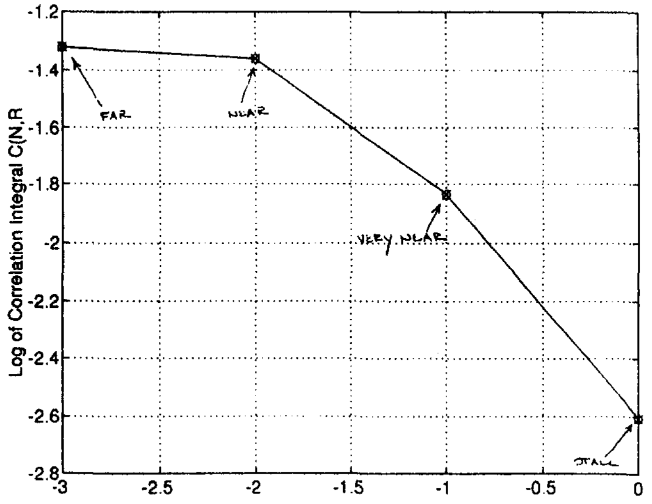

Fig. 3(*f*) Correlation integral changing for fixed radius *R*

of the configurations coincide with a change in slope of the correlation integral curves. Finally, we note that the subtle changes that are detected by the correlation integral tend to result in longer warning times. The operating point on the compressor characteristic at which these changes are detected must also be investigated, to determine the stall margin afforded by the correlation integral method.

The correlation integral method, and other techniques from chaotic time series analysis, offer a completely new way to look at compressor prestall data. These initial results indicate that further study of these new methods is warranted, over a broader range of compressor stall data. Several important issues (beyond those mentioned above) are important to address in this context. For instance, the correlation integral at present has not been tested for enough compressor configurations to determine an

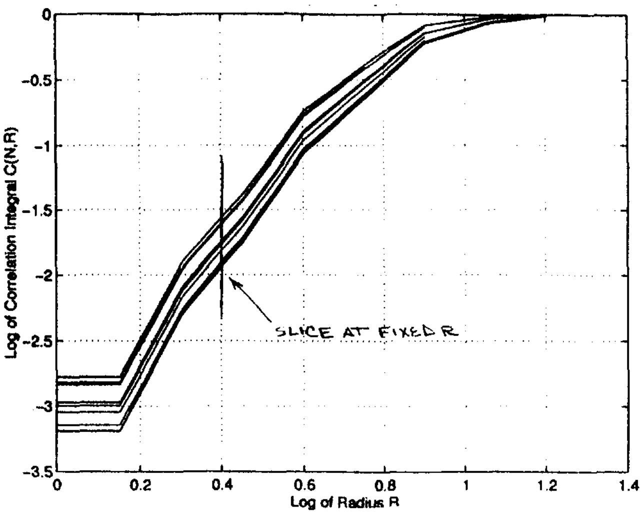

Fig. 4(*a*) Correlation integral versus radius for Rotor 37

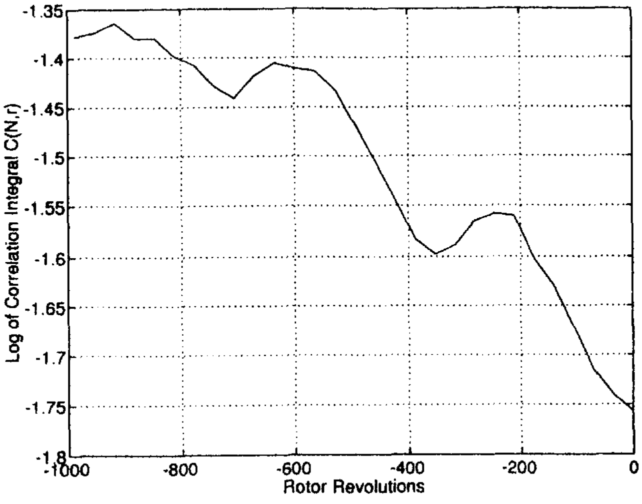

Fig. 4(*b*) Correlation integral changing for Rotor 37

absolute threshold accurately when a compressor is imminently entering stall. This study indicates that combinations of stages 35 and 37 tend to enter stall once the log of $C(N, R)$ goes below -1.6; however, more tests are required to find an absolute threshold for these compressors.

Computing $C(N, R)$ in real time is also an issue that must be addressed (the traveling wave energy method can be implemented essentially as-is in real time). In addition, it is important to correlate changes measured by the approach to physical events in the system to better understand the types of events in the compressor that are best detected using the correlation integral.

In the course of this paper, we have described two methods to identify stall precursors in high-speed compressors. In general, both methods follow the same three steps: (1) obtain representative temporal data, (2) transform the temporal data into a space representation, either Fourier space in the case of the wave energy method, or phase space for the correlation integral method, and (3) classify the changes in the dynamics as we approach stall; for example, sharp peaks in the wave energy spectrum or a decrease in the correlation integral. In showing that both methods detect changes in the compressor dynamics, we hope to minimize a strict preference for either a linear or a nonlinear approach. Rather, our results indicate that any description of the complicated prestall dynamics in the compressor should account for both nonlinear affects and the modal instabilities characteristic of a linearized analysis. Thus a hybrid linear/nonlinear approach to stall detection and modeling may be necessary for high speed compressors. Additionally, both sets of results can assist in the model development and sensor configuration choices necessary for active control of stall at high speed.

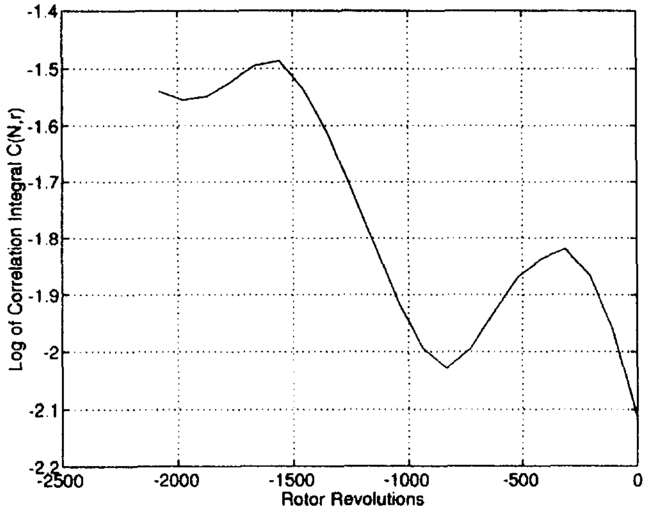

Fig. 5 Correlation integral changing for Stage 37

Conclusion

A new technique for precursor identification in high-speed compressors is described in this paper. The correlation integral is compared with results from the traveling wave energy method for several configurations of a high speed compressor stage. The correlation method has a potential advantage over the traveling wave energy method because it uses a single sensor for detection. The correlation integral method successfully detects changes in the character of the pressure traces for all four high-speed compressor configurations, and did so before the traveling wave energy method diagnosed stall formation. The precise relationship between correlation integral changes and physical flow phenomena must still be established; here we have shown (for the compressors tested) that such a relationship exists and can be exploited for nonlinear detection of stall precursors.

The experimental results indicate that the correlation method provides ample warning of the onset of rotating stall at high

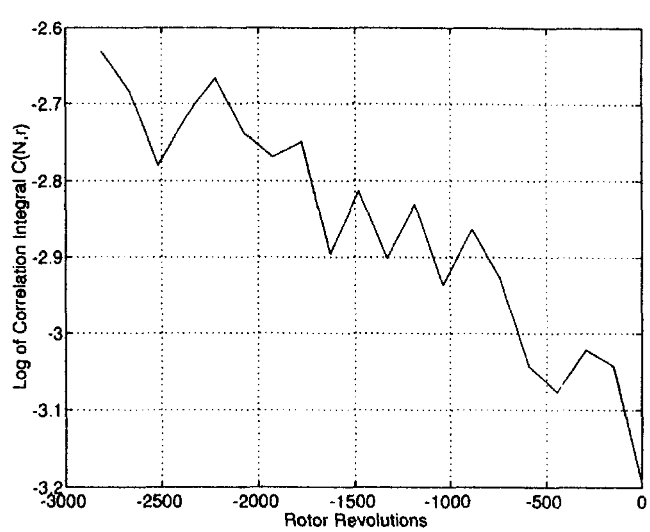

Fig. 6 Correlation integral changing for Rotor 35

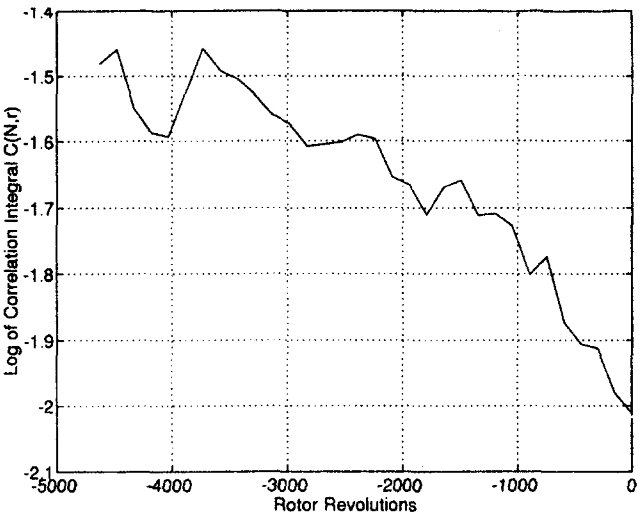

Fig. 7 Correlation integral changing for Stage 35/37

speed, in some tests on the order of 2000–3000 rotor revolutions before stall. Further enhancements will be made to the correlation integral method for application in real time. Additionally, studies are in progress to apply this methodology to a variety of compressors to further verify the use of correlation integral for stall warning.

Acknowledgments

The authors would like to acknowledge funding of this work from an NSF grant CTS-9502327, and NASA Lewis grant #NAG3-1457. Additionally, we would like to thank Stuart Daw of Oakridge National Laboratory and Tony Strazisar of NASA Lewis for their unwavering support.

References

Abarbanel, H. D. I., 1993, "The Analysis of Observed Chaotic Data in Physical Systems," *Rev. Mod. Phys.*, Vol. 65, No. 4, Oct.

Albano, A. M., et al., 1995, *Physical Review E*, Vol. 52, July, p. 196.

Berndt, R. G., Weigl, H. J., Paduano, J. D., and Epstein, A. H., 1995, "Experimental Techniques for Actuation, Sensing, and Measurement of Rotating Stall Dynamics in High-Speed Compressors," presented at the SPIE Aerosense '95 International Symposium, Orlando, FL, Apr.

Bonnaure, L. P., 1991, "Modelling High Speed Multistage Compressor Stability," M.S. Thesis, Department of Aeronautics and Astronautics, Massachusetts Institute of Technology, Sept.

Day, I. J., 1993, "Stall Inception in Axial Flow Compressors," ASME JOURNAL OF TURBOMACHINERY, Vol. 115, pp. 1–9.

Eckmann and Ruelle, 1992, "Fundamental Limitations for Estimating Dimensions and Lyapunov Exponents in Dynamical Systems," *Physica D*, Vol. 56, pp. 185–187.

Etchevers, O., 1992, "Evaluation of Rotating Stall Warning Schemes for Axial Compressors," M. S. Thesis, Dept. of Aeronautics and Astronautics, Massachusetts Institute of Technology, Aug.

Feulner, M. R., Hendricks, G. J., and Paduano, J. D., 1994, "Modeling for Control of Rotating Stall in High Speed Multistage Axial Compressors," ASME Paper No. 94-GT-200; ASME JOURNAL OF TURBOMACHINERY, Vol. 118, No. 1, 1996.

Garnier, V. H., Epstein, A. H., and Greitzer, E. M., 1991, "Rotating Waves as a Stall Inception Indication in Axial Compressors," ASME JOURNAL OF TURBOMACHINERY, Vol. 113, pp. 290–302.

Hendricks, G. J., Bonnaure, L. P., Longley, J. P., Greitzer, E. M., and Epstein, A. H., 1993, "Analysis of Rotating Stall Onset in High-Speed Axial Flow Compressors," AIAA Paper No. 93-2233.

Hoying, D. A., 1993, "Stall Inception in a Multistage High Speed Axial Compressor," presented at the 29th Joint Propulsion Conference, June 28–30, Monterey, CA.

McDougall, N. M., Cumpsty, N. A., and Hynes, T. P., 1989, "Stall Inception in Axial Compressors," ASME Paper No. 89-GT-63; ASME JOURNAL OF TURBOMACHINERY, Vol. 112, pp. 116–125.

Moore and Reid, 1980, "Performance of Single-Stage Axial-Flow Transonic Compressor With Rotor and Stator Aspect Ratios of 1.19 and 1.26, Respectively, and With Design Pressure Ratio of 2.05," NASA Technical Paper 1659, Apr.

Moore, F. K., and Greitzer, E. M., 1986, "A Theory of Post-Stall Transients in Axial Compression Systems, Part I—Development of Equations, and Part II—Application," ASME *Journal of Engineering for Gas Turbines and Power*, Vol. 108, pp. 68–97.

Packard, et al., 1980, "Geometry From a Time Series," *Physical Review Letters*, Vol. 45, pp. 712–716.

Rapp, Albano, Zimmerman, and Jimenez-Montano, 1994, "Phase Randomized Surrogates Can Produce Spurious Identifications of Nonlinear Structure," *Physics Letters A*, Vol. 192, pp. 27–33.

Reid and Moore, 1978, "Design and Overall Performance of Four Highly Loaded, High-Speed Inlet Stages for an Advanced High-Pressure-Ratio Core Compressor," NASA Technical Paper 1337.

Sauer, T., Yorke, J. A., and Casdagli, M., 1991, *J. Stat. Phys.*, Vol. 65, p. 579.

Theiler, J., 1986, "Spurious Dimension From Correlation Algorithms Applied to Limited Time-Series Data," *Physical Review A*, Vol. 34, No. 3, pp. 2427–2432.

Theiler, J., et al., 1991, "Using Surrogate Data to Detect Nonlinearity in Time Series," *Nonlinear Prediction and Modeling*, Addison-Wesley.

Tryfonidis, M., Etchevers, O., Paduano, J. D., Epstein, A. H., and Hendricks, G. J., 1995, "Prestall Behavior of Several High-Speed Compressors," ASME JOURNAL OF TURBOMACHINERY, Vol. 117, p. 62.

APPENDIX

Traveling Wave Energy Analysis

Traveling wave energy analysis is closely coupled to the dynamic modeling of rotating stall inception. Moore and Greitzer (1986) presented a hydrodynamic model of compressor stability applicable to low-speed machines; more recently Bonnaure (1991), Hendricks et al. (1993), and Feulner et al. (1994) extended the analysis to high-speed compressors such as NASA Stage 37 and Stage 35/37. These models can be used to determine whether the compressor will stall at a given operating condition by assessing the stability of small-amplitude flow perturbations that travel around the compressor annulus. As part of this modeling approach, perturbations are decomposed into sinusoidal spatial harmonics. The models predict that these rotating perturbations become underdamped as the mass flow through the compressor is decreased, eventually growing into fully developed rotating stall. The existence and growth of these prestall waves has been verified by researchers for a variety of compressors over the past several years (see for example McDougall et al., 1989; Garnier et al., 1991; and Hoying, 1993). Tryfonidis et al. (1995) presented experiments that indicate that in machines where compressibility is important, the extra degree of freedom of density variations throughout the compressor allows for several lightly damped modes to contribute to the evolution of *each spatial harmonic.* This multimodal behavior has significant implications for both identifying the development of rotating stall and applying stabilizing feedback control.[2]

The purpose of wave energy analysis is to detect the growth of the small-amplitude perturbations as predicted by the stall inception model. If the model is valid, coherent sinusoidal flowfield perturbations are expected to travel at distinct rotation rates and become less damped as the compressor mass flow is decreased. Only an overview of the wave energy analysis procedure is given here; the method is described in detail by Tryfonidis et al. (1995) and applied to nine high-speed compressors.

The spectrogram and subsequent wave energy analysis has been conducted for the Stage 37 and 35 throttle ramp tests in Table 1. In each case, the analysis consists of the following steps:

1 The measured signals from the wall static pressure sensor array are plotted over time as the throttle is closed. The point of large-amplitude stall inception is determined visually from the sensor traces (as described above, the following analysis focuses on the small amplitude prestall perturbations).

---

[2] *A major focus of this ongoing research program is to verify and refine compressible control theoretic modeling through extensive forced response testing on NASA Stage 35, and use the identified stall inception model to design and test stabilizing feedback control schemes (see Berndt, 1995).*

2 The prestall sensor traces are detrended to remove low-frequency variations and normalized to the same rms fluctuations.

3 The sensor traces are decomposed into the first three spatial Fourier harmonics at each point in time. Only results for the first harmonic are presented here since it is expected to be the most lightly damped.

4 The power spectrum of each spatial Fourier coefficient is computed for a short window of data. This calculation is repeated for subsequent slices of data as the compressor transitions into stall to determine the evolution of the spectrum. As discussed by Tryfonidis, a difference in the power spectra between positive and negative frequencies is indicative of traveling energy (a coherent rotating harmonic pressure mode will appear in the corresponding spectrum as a sharp ridge at one frequency).

5 Etchevers (1992) developed a stall inception indicator that can be computed from the evolution of the prestall harmonic spectrum. The traveling energy is computed by integrating the prestall spectrum over a fixed frequency range at each point in time. The traveling energy quantifies the growth of modes that can be seen in the spectrum plots.

Computation of the spectra with a sliding window (Step 5) involves a difficult trade-off. A large enough window of data must be used to provide the necessary resolution to distinguish traveling at distinct frequencies and "average out" noise. However, computation of the spectrum assumes that the underlying statistics of the windowed data do not change in time, i.e., the data are stationary. This assumption is clearly not met if the window length is too long, since the throttle closure during the experiments causes the damping ratios of the prestall modes to change with time. Thus a short enough window must be used to ensure that the underlying dynamics of the measurements do not change significantly. This trade-off must be addressed to detect rapidly changing modal behavior in noisy data.

DISCUSSION

C. Palomba[1]

The work presented surely makes a step toward solving the problem of rotating stall in high-speed axial flow compressors with chaotic times series analysis. However, the proposed application seems to be somehow not in accordance with the basic principles and conditions for chaos theory tools to be applied. The correlation integral of points on a reconstructed attractor leads to the determination of a scaling law that holds over a sufficient range of length scales. The exponent of this scaling law is an estimation of the dimension of the attractor. The correlation integral method proposed by Grassberger and Procaccia (1983) is supposed to be applied to an attractor, i.e., to the asymptotic trajectory after all transients have died out. Only in this condition the points that are temporally correlated by the dynamic are also spatially correlated on the attractor and one may perform the correlation integral evaluation. It is then still to be proved by the authors that such algorithm is applicable to the case of rotating stall transients, and that the results truly reflect the transient dynamics. Has any calculation of steady-state attractors been made to compare with transient portraits at same mass flow? The approach to the embedding procedure and the problem of noise in the data have been not discussed in the paper. The slopes presented look more like subsequent line segments not showing a unique scaling law: At which length scales should the dimension of the attractor be evaluated? This fact makes one wonder whether the embedding procedure is sufficiently accurate. If it is meaningful to evaluate correlation integrals of a phase portrait of a transient, then important parameters like the sampling frequency, the time delay, embedding dimension, and the number of points on the attractor have a big part in the success of the procedure. The number of points equal to 5000 seems quite low for the dimension of the embedding space set equal to 4. This last parameter is especially critical, because the correlation integrals have a slope that is quite steep, meaning an attractor of high dimension. It is understandable that in order to reduce calculation times, the number of points and the dimension of the embedding space must be as low as possible; however, it must be checked first with the several chaos analysis tools that are the minimum values for such parameters. Has any attempt in this direction been made? Could the fact that the correlation integral for a fixed radius decreases be related to the fact that the overall size of the reconstructed phase portrait is reducing? Has this possibility been accounted for?

Phase portrait reconstruction offers a powerful tool in representing system dynamics and the idea of applying nonlinear tools to transient analysis is quite innovative. However, there are also other ways to approach transient phenomena that rely on the inspection of trajectories and patterns identification. A preliminary approach in this direction has already been presented for two low-speed single-stage compressors.

We thank the author for replying. It is interesting to exchange experiences with other researchers working in the same field. Since chaos theory tools are quite new for turbomachinery environment, at this early stage of development it is important that information be shared. Some new insight can be expected from an extensive application of these techniques to different types of machine and stall inception.

References

Breugelmans, F. A. E., Palomba, C., and Funk, T., 1994, "Application of Strange Attractors to the Problem of Rotating Stall," presented at the 7th ISU-AAT, Fukuoka, Japan, Sept. (to be published by Elsevier).

Grassberger, X. X., and Procaccia, X. X., 1983, "Measuring the Strangeness of Strange Attractors," *Physica*, Vol. 9D, pp. 189–208.

Palomba, C., and Breugelmans, F. A. E., 1995, "Phase Portraits From Rotating Stall Time Series," presented at the XII ISABE, Australia, Sept.

Palomba, C., "Un nuovo approccio all'analisi sperimentale dello stallo rotante nei compressori assiali secondo le tecniche della teoria del caos deterministico," *Proc. MIS-MAC III*, Cagliari, Italy, Oct.

Authors' Closure

Our paper presents an innovative approach to detecting stall precursors and we take the opportunity in this discussion to clarify a number of issues in chaotic time series analysis that may be unknown to the turbomachinery community. One issue raised is the description of our data as dynamically "transient." Four of the ramp data sets obtained experimentally in this study were acquired with a slowly increasing throttle using an identical procedure as described in Tryfonidis (1995). As discussed in our appendix, we carefully selected the data window to be large enough to monitor changing statistics but short enough to ensure that the underlying dynamics do not change significantly. This is an identical approach used in the traveling wave energy method and, for that matter, many Fourier analysis techniques. One piece of evidence to suggest that the throttle dynamic is much slower than the fluid physic dynamics of the compressor is the correlation integral for the stationary data sets discussed in the paper follow the same trends as the "pseudo-stationary" ramp data. The use of chaotic time series analysis methods on windowed data is not an innovative application, but rather a standard technique, particularly in medical and physiological

---

[1] Department of Mechanical Engineering, University of Cagliari, Cagliari, Italy.

2 The prestall sensor traces are detrended to remove low-frequency variations and normalized to the same rms fluctuations.

3 The sensor traces are decomposed into the first three spatial Fourier harmonics at each point in time. Only results for the first harmonic are presented here since it is expected to be the most lightly damped.

4 The power spectrum of each spatial Fourier coefficient is computed for a short window of data. This calculation is repeated for subsequent slices of data as the compressor transitions into stall to determine the evolution of the spectrum. As discussed by Tryfonidis, a difference in the power spectra between positive and negative frequencies is indicative of traveling energy (a coherent rotating harmonic pressure mode will appear in the corresponding spectrum as a sharp ridge at one frequency).

5 Etchevers (1992) developed a stall inception indicator that can be computed from the evolution of the prestall harmonic spectrum. The traveling energy is computed by integrating the prestall spectrum over a fixed frequency range at each point in time. The traveling energy quantifies the growth of modes that can be seen in the spectrum plots.

Computation of the spectra with a sliding window (Step 5) involves a difficult trade-off. A large enough window of data must be used to provide the necessary resolution to distinguish traveling at distinct frequencies and "average out" noise. However, computation of the spectrum assumes that the underlying statistics of the windowed data do not change in time, i.e., the data are stationary. This assumption is clearly not met if the window length is too long, since the throttle closure during the experiments causes the damping ratios of the prestall modes to change with time. Thus a short enough window must be used to ensure that the underlying dynamics of the measurements do not change significantly. This trade-off must be addressed to detect rapidly changing modal behavior in noisy data.

DISCUSSION

C. Palomba[1]

The work presented surely makes a step toward solving the problem of rotating stall in high-speed axial flow compressors with chaotic times series analysis. However, the proposed application seems to be somehow not in accordance with the basic principles and conditions for chaos theory tools to be applied. The correlation integral of points on a reconstructed attractor leads to the determination of a scaling law that holds over a sufficient range of length scales. The exponent of this scaling law is an estimation of the dimension of the attractor. The correlation integral method proposed by Grassberger and Procaccia (1983) is supposed to be applied to an attractor, i.e., to the asymptotic trajectory after all transients have died out. Only in this condition the points that are temporally correlated by the dynamic are also spatially correlated on the attractor and one may perform the correlation integral evaluation. It is then still to be proved by the authors that such algorithm is applicable to the case of rotating stall transients, and that the results truly reflect the transient dynamics. Has any calculation of steady-state attractors been made to compare with transient portraits at same mass flow? The approach to the embedding procedure and the problem of noise in the data have been not discussed in the paper. The slopes presented look more like subsequent line segments not showing a unique scaling law: At which length scales should the dimension of the attractor be evaluated? This fact makes one wonder whether the embedding procedure is sufficiently accurate. If it is meaningful to evaluate correlation integrals of a phase portrait of a transient, then important parameters like the sampling frequency, the time delay, embedding dimension, and the number of points on the attractor have a big part in the success of the procedure. The number of points equal to 5000 seems quite low for the dimension of the embedding space set equal to 4. This last parameter is especially critical, because the correlation integrals have a slope that is quite steep, meaning an attractor of high dimension. It is understandable that in order to reduce calculation times, the number of points and the dimension of the embedding space must be as low as possible; however, it must be checked first with the several chaos analysis tools that are the minimum values for such parameters. Has any attempt in this direction been made? Could the fact that the correlation integral for a fixed radius decreases be related to the fact that the overall size of the reconstructed phase portrait is reducing? Has this possibility been accounted for?

Phase portrait reconstruction offers a powerful tool in representing system dynamics and the idea of applying nonlinear tools to transient analysis is quite innovative. However, there are also other ways to approach transient phenomena that rely on the inspection of trajectories and patterns identification. A preliminary approach in this direction has already been presented for two low-speed single-stage compressors.

We thank the author for replying. It is interesting to exchange experiences with other researchers working in the same field. Since chaos theory tools are quite new for turbomachinery environment, at this early stage of development it is important that information be shared. Some new insight can be expected from an extensive application of these techniques to different types of machine and stall inception.

References

Breugelmans, F. A. E., Palomba, C., and Funk, T., 1994, "Application of Strange Attractors to the Problem of Rotating Stall," presented at the 7th ISU-AAT, Fukuoka, Japan, Sept. (to be published by Elsevier).

Grassberger, X. X., and Procaccia, X. X., 1983, "Measuring the Strangeness of Strange Attractors," *Physica*, Vol. 9D, pp. 189–208.

Palomba, C., and Breugelmans, F. A. E., 1995, "Phase Portraits From Rotating Stall Time Series," presented at the XII ISABE, Australia, Sept.

Palomba, C., "Un nuovo approccio all'analisi sperimentale dello stallo rotante nei compressori assiali secondo le tecniche della teoria del caos deterministico," *Proc. MIS-MAC III*, Cagliari, Italy, Oct.

Authors' Closure

Our paper presents an innovative approach to detecting stall precursors and we take the opportunity in this discussion to clarify a number of issues in chaotic time series analysis that may be unknown to the turbomachinery community. One issue raised is the description of our data as dynamically "transient." Four of the ramp data sets obtained experimentally in this study were acquired with a slowly increasing throttle using an identical procedure as described in Tryfonidis (1995). As discussed in our appendix, we carefully selected the data window to be large enough to monitor changing statistics but short enough to ensure that the underlying dynamics do not change significantly. This is an identical approach used in the traveling wave energy method and, for that matter, many Fourier analysis techniques. One piece of evidence to suggest that the throttle dynamic is much slower than the fluid physic dynamics of the compressor is the correlation integral for the stationary data sets discussed in the paper follow the same trends as the "pseudo-stationary" ramp data. The use of chaotic time series analysis methods on windowed data is not an innovative application, but rather a standard technique, particularly in medical and physiological

---

[1] Department of Mechanical Engineering, University of Cagliari, Cagliari, Italy.

Development of a High-Specific-Speed Centrifugal Compressor

C. Rodgers
3010 N Arroyo Drive,
San Diego, CA 92103

This paper describes the development of a subscale single-stage centrifugal compressor with a dimensionless specific speed (Ns) of 1.8, originally designed for full-size application as a high volume flow, low pressure ratio, gas booster compressor. The specific stage is noteworthy in that it provides a benchmark representing the performance potential of very high-specific-speed compressors, of which limited information is found in the open literature. Stage and component test performance characteristics are presented together with traverse results at the impeller exit. Traverse test results were compared with recent CFD computational predictions for an exploratory analytical calibration of a very high-specific-speed impeller geometry. The tested subscale (0.583) compressor essentially satisfied design performance expectations with an overall stage efficiency of 74 percent including, excessive exit casing losses. It was estimated that stage efficiency could be increased to 81 percent with exit casing losses halved.

1 Introduction

The wide diversity of applications for centrifugal compressors and pumps cover impeller designs ranging from dimensional inlet specific speeds as low as 0.3, to as high as 2.0, where

$$\text{specific speed } Ns = \omega(W/\rho)^{0.5}/(gH_{ad})^{0.75}.$$

The classic specific speed charts of Balje [1] for single-stage centrifugal compressors show peak efficiencies close to $Ns = 0.8$, with efficiency diminishing at lower and higher specific speeds. Since the majority of centrifugal compressor designs cluster the optimim efficiency region, limited open literature exists relating to the performance characteristics of the lower efficiency, very low, and very high-specific-speed compressor designs. In a recourse to quantify compressor performance levels of very low specific speeds, the author described the results of experiments with a partial emission centrifugal compressor [2]. The intent of this complementary paper is to quantify the performance characteristics of centrifugal compressors at the opposite end of the *Ns* spectrum, by relating the results of performance calibrations on a single-stage compressor with a design *Ns* of 1.8. The particular ''*F*'' stage to be discussed was an extension of the work described in [3, 4] relating to the component characteristics of a family of compressor stages encompassing an *Ns* range from 0.3 to 1.3, and was conducted using the same compressor test facility. The *F* stage is noteworthy in that it offers to serve as a benchmark representing the performance potential of high-specific-speed centrifugal compressors, of which limited information is found in the literature, with some exceptions, notably [5], besides serving as an intriguing test case for special calibration of the Dawes CFD code. As will be discussed later, the adiabatic efficiency attained for the *F* stage was quite low at 74 percent, yet only 1 percent point below the design test goal, in a *Ns* range best suited by mixed flow compressor designs. The development intent was, however, to extend the flow capability of an existing family of stages using the maximum amount of existing hardware. Recourse to a mixed flow stage would have required almost complete redesign. The ''Achilles Heel'' (or knee, so to speak) of very high *Ns* centrifugal impellers is the high shroud curvature in the knee region, caused by the characteristic geometry with a large inducer eye and large impeller exit tip height, being susceptible to flow separation aft of the inducer throat.

The use of high blade backsweep can assist in delaying the separation susceptibility, in that the stream surface curvatures are relaxed. As a consequence the *F* impeller was designed with 50 deg backsweep (relative to the radial direction). A second problem in the design of high *Ns* stages is the relatively high radial velocity component at the diffuser exit, which can result in a relatively high discharge loss if not recovered in the scroll or discharge collector. As will be discussed later, the exit loss of the *F* stage amounted to several percentage points loss in stage efficiency.

During the initial design of the *F* stage, it was realized that impeller structural constraints could present a limitation in eventual application as a consequence of increased blade and disk stresses, together with high hoop stress for a shrouded impeller option. Preliminary evaluation of the stresses anticipated during developmental air test calibrations with an open shrouded impeller revealed acceptable stress levels commensurate with short time low speed operation. The relationship between specific speed and impeller stresses is addressed later in this paper.

2 Compressor Design Features

The anticipated application of the *F* stage was as a low-pressure-ratio, high-volume flow, gas booster pipeline compressor, in a size 71 percent larger than the air test model stage. Following design of the full-size compressor, hardware compatible for installation and ambient suction testing in an existing subscale compressor rig was designed and procured. The subscale design point air test performance parameters are listed in Table 1. (Note efficiency flange to flange total-to-total, less downstream exit diffuser).

The open face impeller is shown installed in the test rig on Fig. 1, together with the parallel wall diffuser for both vaneless and vaned diffuser testing. Note that the inducer blading was heavily leaned in order to relax the passage curvatures.

3 Test Rig Description

The compressor test rig depicted schematically in Fig. 2 was used to conduct *F* stage performance calibrations at ambient suction conditions. The rig was driven by a 500 hp direct current electric variable speedmotor driving through a speed increaser

---

Contributed by the International Gas Turbine Institute and presented at the 41st International Gas Turbine and Aeroengine Congress and Exhibition, Birmingham, United Kingdom, June 10–13. 1996. Manuscript received at ASME Headquarters February 1996. Paper No. 96-GT-353. Associate Technical Editor: J. N. Shinn.

Table 1 Performance parameters

Pressure ratio	1.21
Corrected airflow, pps	8.3
Adiabatic efficiency, percent	75
Rotational speed, krpm	14
Specific speed, Ns	1.81
Inducer hub diameter, in.	3.5
Inducer tip diameter, in.	8.75
Impeller tip diameter D2 (mean), in.	11.9
Blade exit height, b2, in.	1.63
Impeller backsweep, $\beta 2$, deg	50
Number of blades	14
Inlet flow coefficient, ϕ	0.44
Work factor, q	0.44

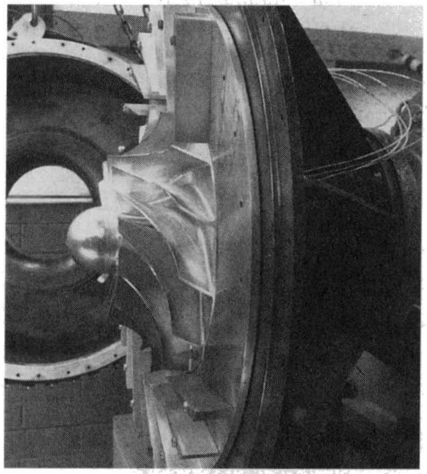

Fig. 1 *F* **stage impeller**

gearbox. The inlet airflow was measured with a bellmouth venturi, and subsequently ducted to the axial inlet gude vanes (IGV's) of the compressor. Airflow regulation was achieved with a butterfly valve at the compressor discharge. The pressure and temperature at the inlet and discharge were measured with Kiel probes and resistance temperature devices. Table 2 lists the test rig instrumentation. Automatic traverse capability with a Cobra probe at 1.29 the impeller tip diameter was provided, together with shroud pressure transducers and thrust transducers to measure axial thrust. Overall compressor efficiency could be determined from both temperature rise and input power measurements.

Analysis of potential measurement errors at the low-speed test conditions revealed that the efficiency uncertainty based on temperature rise was ±1.2 percent points compared to ±1.7 percent points based on torque. Efficiency levels quoted are those based on temperature measurements.

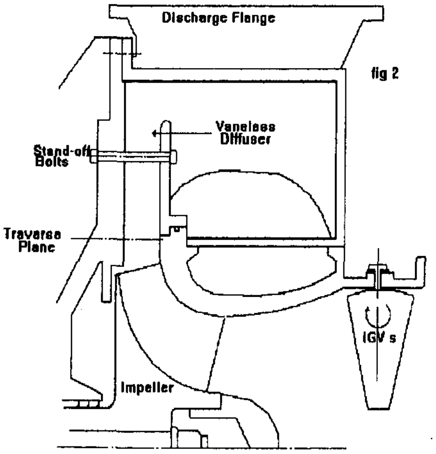

Fig. 2 *F* **stage test rig**

Table 2 List of instrumentation

Station	Temperatures	Pstatic	Ptot
Inlet bellmouth	3	3	1
Inlet flange	3		3
Impeller shroud	—	11	—
Impeller tip	—	5	—
Diffuser exit	—	3	—
Discharge flange	4	3	3

The mixed impeller exit vector conditions were computed using insulated casing discharge total temperature, impeller tip static pressures, and the continuity equation assuming an impeller tip blockage and recirculation plus windage correction according to [3]. Impeller tip traversing with a small cobra probe mounted on an electronically modulated traverse actuator was conducted at several points along a selected constant speed line to determine impeller exit flow profile conditions. The axial inlet (zero camber) IGVs shown on Fig. 3 were manually adjusted to permit calibrations at vane angles of 0, −10, and −25 deg to the axial direction. The impeller was tested at a DeLaval number of Mu = 0.65, and was allowed to stabilize thermally in the insulated casing between all test points. The nominal cold shroud clearance between the impeller and abradable stationary shroud was 0.070 in. (1.8 mm). Very slight shroud rubbing during testing affirmed near zero running clearance.

4 Compressor Test Performances

Prior to performance calibrations of the subscale *F* stage tests were conducted on the impeller with the tip diameter originally machined at 14.0 in. (356 mm), both with a vaned and vaneless

Nomenclature

b = impeller blade height
C = absolute velocity
Cp = diffuser static pressure recovery
D = diameter
g = gravitational acceleration
H = head
IGV = inlet guide vane
k = specific heat ratio
P = total pressure
Mu = Delaval number = $U_2/(gkRT)^{0.5}$
Ns = dimensionless specific speed
q = work factor = $\Delta H/U_2^2$
R = gas constant
T = total temperature
U = tangential velocity
W = massflow
α_2 = impeller tip absolute air angle
β_2 = backsweep angle
Δ = difference
ϕ = inlet flow coefficient = C_1/U_2
η = efficiency
ν = Poisson ratio
ρ = density
σ = stress
ω = angular velocity

Subscripts

1 = impeller inlet
2 = impeller tip
3 = diffuser exit
ad = adiabatic
c = compressor
e = exit

Note: All angles are with respect to the meridional plane.

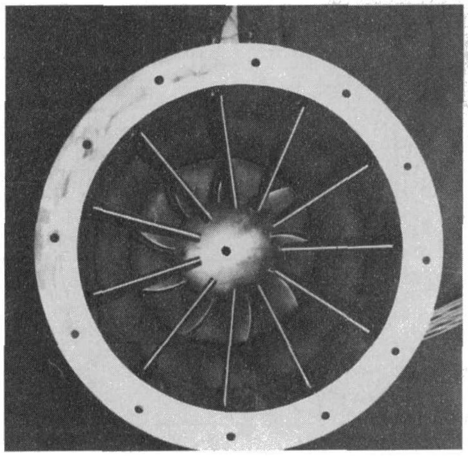

Fig. 3 Inlet guide vanes

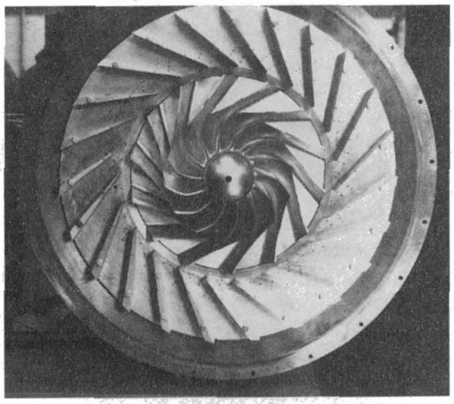

Fig. 4 14.0 tip diameter impeller

diffuser configuration, as shown in Fig. 4. These initial tests indicated essentially the same overall efficiency with either diffuser type as a consequence of high discharge collector losses amounting to complete loss of the diffuser exit dynamic head.

The impeller tip diameter was subsequently machined down to a mean diameter of 11.9 in., and performance calibrations initiated on the design subscale geometric configuration, commencing with tests at zero IGV prewhirl, and Mu = 0.65. Table 3 lists the test sequence followed with IGV settings, and modifications to the vaneless space width and 0.25 in. increased inducer leading edge undercut. Test performances for the various configurations of the subscale *F* stage are shown in Fig. 5 in terms of overall stage efficiency and work factor versus inlet flow coefficient. Test peak efficiencies and corresponding work factors are compared to design goals on Table 4. Decreasing the vaneless space width on Build 10B increased the stage efficiency from 72 to 74.0 percent, basically due to improved diffuser performance. Impeller and diffuser performances for Builds 10A and 10B are shown in Fig. 6, and indicate peak diffuser recovery $Cp_{2\text{-}3}$ increased above 0.6 with the smaller width, while impeller efficiency remained essentially unchanged. Note however that the slip factor also increased slightly as reflected by the change in work factor in Table 4.

Table 3 F stage test sequence

Build No.	Test geometry	Diffuser width	IGV, deg
10 A	Design	1.63	0/−10/25
10 B	Reduced b3	1.42	0
10 C	Modified	1.42	0

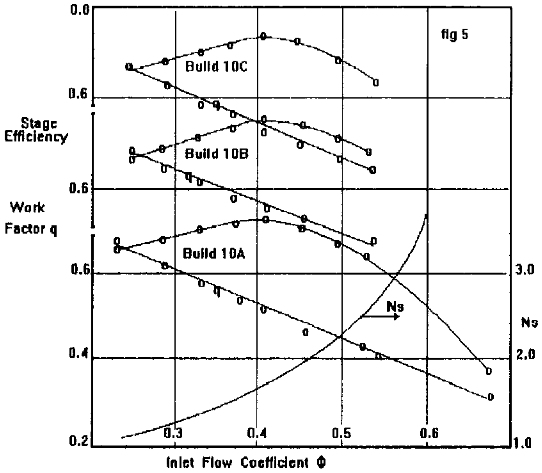

Fig. 5 *F* stage test performances

The casing exit loss coefficient λ defined by total pressure loss from the vaneless diffuser exit to exit flange, divided by the diffuser exit dynamic head is also shown in Fig. 6 and exceeds unity at flow coefficients higher than design.

Adjustment of the IGVs to −10 and 25 deg on Build 10A both decreased the stage efficiency as shown on Fig. 7. Examination of the impeller passage geometry near the inducer throat, at the hub, revealed the possibility of high blockage. It was therefore decided to test the effect of increasing the leading edge sweep angle (negative sweep) from 10 to 35 deg. Subsequent testing on Build 10C showed 1 percent point efficiency loss with the leading edge modification.

Cobra probe traverse results at flow coefficients $\phi = 0.29$, 0.41, and 0.52 are shown in Fig. 8. Near design flow coefficient the flow generally fills the central passage, flipping toward the shroud near stall, while flipping toward the hub as choke is approached. These general patterns of flow migration were recently matched by CFD modeling of the *F* impeller using the Dawes code. Satisfactory agreement of the test flow profiles was obtained with the CFD results, with the exception of the near-stall flow coefficient of $\phi = 0.29$.

The results of performance calibrations on the *F* stage confirmed the design expectations and indicated that further performance improvements would be attainable with enlargement plus additional diffusion in the exit collector. Figure 2 shows the rig collector was of the "folded over" type for ease of fabrication and installation. Such collectors are known to loose a high fraction of the exit dynamic head as discussed in [7]. It was estimated that if the exit loss coefficient was reduced 50 percent, the stage efficiency would increase by 7 percent points, illustrating the importance of the exit casing design on high-specific-speed centrifugal and mixed flow compressors performances.

5 Specific Speed and Impeller Stresses

As mentioned previously, the two major design constraints that limit the application of high-specific-speed centrifugal compressors are excessive impeller stresses and high casing pressure losses.

Table 4 Summary of F stage test performances

Build No.	Peak efficiency	Work factor
Design	0.75	0.44
10 A	0.72	0.48
10 B	0.74	0.50
10 C	0.73	0.50

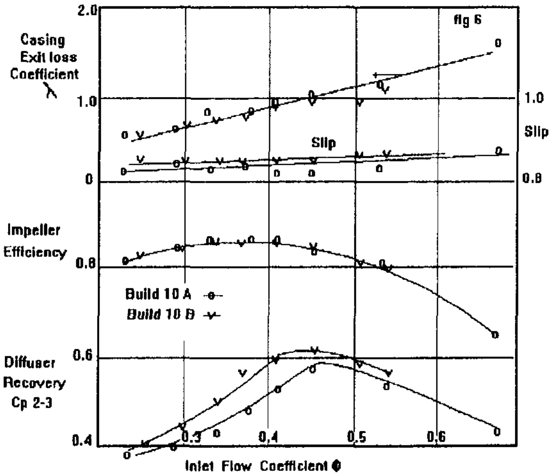

Fig. 6 Builds 10A and 10B performances

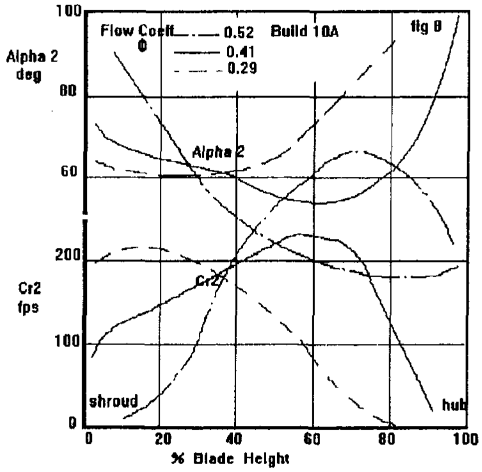

Fig. 8 Traverse results

It can be shown, as [6] extensively describes, that the specific speed concept can be extended beyond impeller aerodynamic characterization, to impeller stresses, inertial, and dynamic properties. For instance, the blade bending stress at the impeller tip can be approximated by the following expression:

Bending Stress

$$\sigma = \rho\omega^2 D_2^2 \sin \beta_2 b_2^2 \frac{(1 + 2x \text{ taper ratio})}{2gh_r} \qquad (2)$$

where h_r = blade root thickness.

This approximate expression ignores the important effect of blade rake, root fillet radius, and load sharing from adjacent blading, but nevertheless provides a useful hand check in preliminary design iterations, and fingerpoints blade features controlling the bending stresses. For example, high *Ns* impellers with intrinsically larger blade height to tip diameter ratios (b_2/D_2), will propagate stresses increasing in proportion to the blade height squared.

The direct relationship between *Ns* and b_2/D_2 is illustrated by the trends shown in Fig. 9 with stage pressure ratio as a parameter. Note that although increasing pressure ratio requires higher tip speed, the impeller tip height diminishes due to the higher density ratio.

The stress relationship can be further simplified by assuming a typical blade taper ratio of 4.0:1, as;

Bending Stress

$$\sigma = \rho U_2^2 \sin \beta_2 (b_2/D_2)(b_2/h_r)/g \qquad (3)$$

Likewise the impeller hub stress is a function of the tip speed, impeller shape (specific speed), and size of the bore.

An approximate expression for the hub stress is given by:

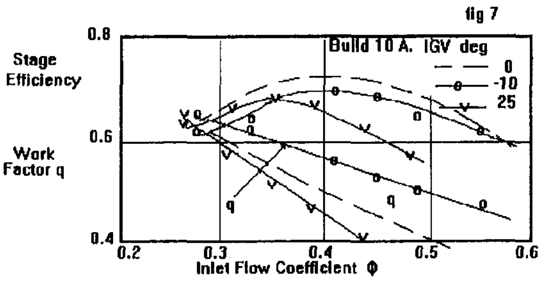

Fig. 7 Performance with IGV = −10 and 25 deg

$$\text{Hub Stress} = \text{Impeller Shape Factor } \rho U_2^2(3 + \nu)/8 \qquad (4)$$

where ν is the Poisson ratio and the impeller shape factor is dependent upon specific speed and shroud configuration, as typified by the data shown in Fig. 10. Since increasing specific speed enlarges the size of the inducer eye, the impeller axial (forward) thrust increases, thus specific speed is also related to the axial thrust characteristics of the impeller. These specific speed relationships are generally only useful in the preliminary design of centrifugal compressors, as their range of application is limited compared to a myriad of impeller geometries that may be possible for any given design case. Nevertheless, the *Ns* connection can provide a rapid sanity check to prepackaged automated computational design programs now popular.

Concluding Remarks

The development of a single-stage high-specific-speed centrifugal compressor has been described to provide a benchmark representing the performance capabilities of high *Ns* stages, and to indicate potential pitfalls in their application. The information also serves to complement an earlier paper by the primary author relating experiments on a very low-specific-speed partial emission centrifugal compressor, thereby completing the "end game." In this respect both low and high *Ns* impeller performance cases are superimposed against the polytropic impeller efficiency correlation of Ref. [8] on Fig. 11, indicating reasonable agreement with the correlation trends. Very high *Ns*, backswept, centrifugal compressors are really only practical at low (air) pressure ratios, as a consequence of relatively high blade

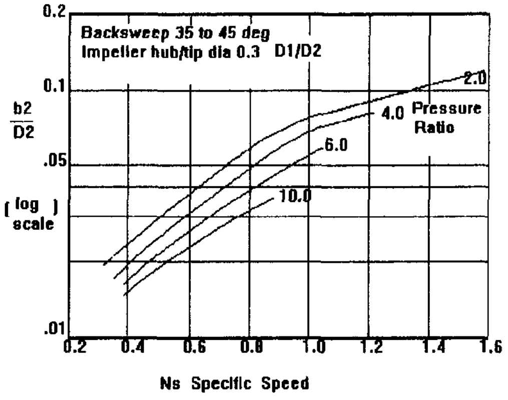

Fig. 9 Impeller *b*2/*D*2 versus specific speed

and disk stresses, and their performance sensitivity to high Mach number operation.

The effects of Mach number and specific speed on higher pressure ratio centrifugal compressors are discussed in [8], where it is disclosed that specific speeds beyond 1.2 with a stage pressure ratio of 4.0 result in low efficiency as a consequence of high inducer shock losses. It was revealed that high flow stages are sensitive to exit diffuser or casing pressure losses, which are moreover, deleterious to either high *Ns* centrifugal or mixed flow impeller geometries.

Although casing enlargement, either in diameter or length, may partially alleviate these exit losses, the solution is self-defeating, to a degree, in that a major motivation for high *Ns* design is stage compactness. Casing enlargement can furthermore prove structurally difficult in high suction pressure gas booster applications. The choice of a high *Ns* compressor design therefore requires a detailed preliminary design life cycle trade study before embarking on a product development program, and it is the hope that this information may prove useful for that purpose.

The adoption of a high *Ns* design is not always an independent design choice, and in fact almost invariably arises as an extension to an existing compressor, turbocharger, or gas turbine product line, as was indeed this particular compressor. One example of this is the practice of impeller tip diameter cropping to match lower head requirements, which intrinsically increases *Ns*. A second example is the continuing demand for increased power in small intermittent operation gas turbines, or expendable turbojets, through higher airflows within the same engine envelope, thereby also increasing compressor specific speeds.

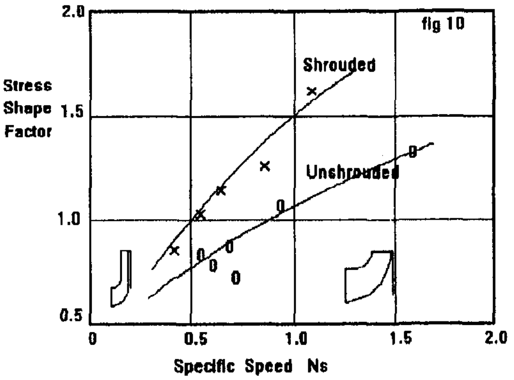

Fig. 10 Impeller shape factor

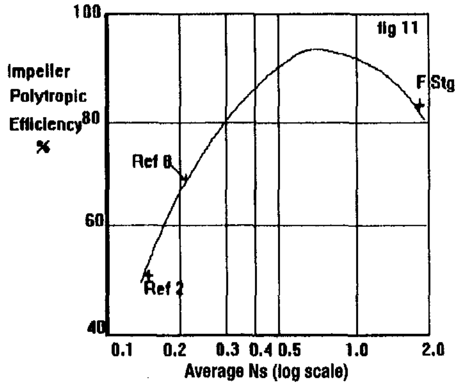

Fig. 11 Impeller efficiency versus average *Ns*

Acknowledgments

The author wishes to acknowledge Solar Turbines Incorporated in approving these results, and the efforts of D. Lucas in conducting the stage testing, and D. Brown in the CFD analysis.

References

1 Balje, O. E., *Turbomachines*, Wiley Interscience, 1981.

2 Rodgers, C., "Experiments With a Low Specific Speed Partial Emission Centrifugal Compressor," ASME JOURNAL OF TURBOMACHINERY, Vol. 112, 1990, pp. 30–37.

3 Rodgers, C., "A Diffusion Factor Correlation for Centrifugal Compressor Stalling," ASME Paper No. 78-GT-61, 1978.

4 Rodgers, C., "The Performance of Centrifugal Compressor Channel Diffusers," ASME Paper No. 82-GT-10, 1982.

5 Yoshinaga, Y., et al., "A Study of Performance Improvements for High Specific Speed Centrifugal Compressors by Using Diffusers With Half Guide Vanes," ASME *Journal of Fluids Engineering*, Vol. 109, No. 4, 1987, pp. 359–367.

6 Wislicenus, G. F., "Preliminary Design of Turbopumps & Related Machinery," NASA Reference Publication 1170, 1986.

7 Mishina, H., and Gyobu, I., "Performance Investigations of Large Capacity Centrifugal Compressors," ASME Paper No. 78-GT-3, 1978.

8 Rodgers, C., "Efficiency of Centrifugal Compressor Impellers," *Performance Prediction of Centrifugal Pumps & Compressors*, ASME, 1980.

Effect of Modification to Tongue and Impeller Geometry on Unsteady Flow, Pressure Fluctuations, and Noise in a Centrifugal Pump

R. Dong

S. Chu

J. Katz

Department of Mechanical Engineering,
The Johns Hopkins University,
Baltimore, MD 21218

Particle Image Velocimetry (PIV), pressure, and noise measurements are used to study the effect of modifications to tongue and impeller geometries on the flow structure and resulting noise in a centrifugal pump. It is demonstrated that the primary sources of noise are associated with interactions of the nonuniform outflux from the impeller (jet/wake phenomenon) with the tongue. Consequently, significant reduction of noise is achieved by increasing the gap between the tongue and the impeller up to about 20 percent of the impeller radius. Further increase in the gap affects the performance adversely with minimal impact on the noise level. When the gap is narrow, the primary sources of noise are impingement of the wake on the tip of the tongue, and tongue oscillations when the pressure difference across it is high. At about 20 percent gap, the entire wake and its associated vorticity trains miss the tongue, and the only (quite weak) effect of nonuniform outflux is the impingement of the jet on the tongue. An attempt is also made to reduce the nonuniformity in outflux from the impeller by inserting short vanes between the blades. They cause reduction in the size of the original wakes, but generate an additional jet/wake phenomenon of their own. Both wakes are weak to a level that their impacts on local pressure fluctuations and noise are insignificant. The only remaining major contributor to noise is tongue oscillations. This effect is shown to be dependent on the stiffness of the tongue.

Introduction and Rationale

Experiments discussed by Chu et al. (1993, 1995a, b) demonstrated that interactions of nonuniform outflux from the impeller with the tongue can be primary contributors to noise generation within the volute of a centrifugal pump. That study included PIV measurements in sufficient spatial and temporal resolutions, which enabled computations of the phase-averaged, unsteady pressure from the velocity distributions (by integrating the Reynolds equations). The results pointed directly at specific sources of noise. Included were effects of the jet/wake phenomenon (introduced and discussed by Dean and Senoo, 1960, and Eckardt, 1975), particularly the wake, and tongue oscillations due to high-pressure differences across it. The present paper continues this effort by focusing on attempts to reduce noise either by modifying the tongue geometry or by reducing the nonuniform outflux from the impeller.

One of the conclusions of prior studies with the same pump (Dong et al., 1992a, b; Chu et al., 1995a, b) was that most unsteady phenomena occur at $r/r_T < 1.2$, in agreement with measurements performed in a different pump by Hamkins and Flack (1987). Thus, an obvious solution to the noise problem is to increase the gap between the tongue and the impeller, thus keeping the tongue out of the region with severe nonuniform flows. Although it is known that the performance of a pump depends on this gap (Hira and Vasandani, 1975), little or next to nothing has been reported about the effect of this gap on the flow structure, and in turn on the mechanisms of noise generation. These issues are some of the objectives of the present paper. It includes measurements of noise, pressure, velocity and vorticity distributions associated with several tongues, ranging in gaps between 7 to 27 percent of impeller radius. These experiments demonstrate how and why even slight increases in the gap alter the flow structure, decrease the noise level, and modify the associated spectrum. The effect of tongue stiffness is also discussed.

Another approach to noise reduction involves tackling the nonuniform outflux from the impeller. Using the original velocity distribution, an attempt is made to reduce the "wake" (region of high circumferential velocity, v_θ, at the exit from the impeller) by inserting short vanes inside the impeller. Unlike typical attempts to install symmetric vanes at the center of a blade passage (Cumpsty, 1989), the location and orientation of the present vanes are selected based on prior data on the flow. As will be shown shortly, this attempt results in partial success. The overall noise level, particularly the noise associated with the wake, is reduced. However, the new vanes cause additional unsteady phenomena.

Setup and Procedures

The test model was a vertical centrifugal pump operating at 890 rpm. The impeller was 9.95 in. in diameter, and had 7 blades, all of them with an exit angle of 20 deg. The configuration of the perimeter (in in.) was $r_v = r_T + 0.34 + 4(\theta/360 \text{ deg})$ where $\theta = 0$ deg was located 3 deg upstream of the tip of the tongue. The volute had constant thickness (0.975 in.), which was equal to the thickness of the impeller. The 4×0.975 in. exit gradually expanded to a 4 in. pipe by using a fiberglass

---

Contributed by the International Gas Turbine Institute and presented at the 40th International Gas Turbine and Aeroengine Congress and Exhibition, Houston, Texas, June 5–8, 1995. Manuscript received by the International Gas Turbine Institute February 11, 1995. Paper No. 95-GT-34. Associate Technical Editor: C. J. Russo.

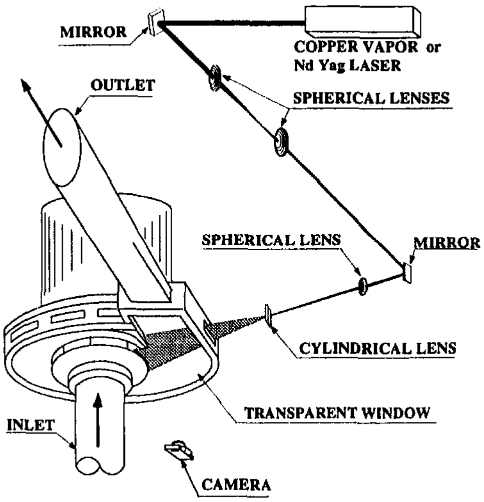

Fig. 1 A schematic description of the optical setup in the pump facility

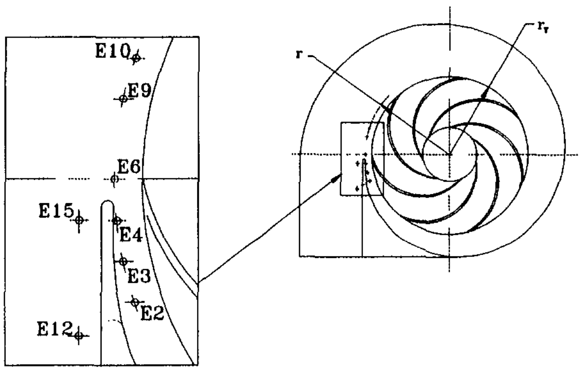

INDEX	E2	E3	E4	E6	E9	E10	E12	E15
r/r_T	1.066	1.066	1.066	1.066	1.066	1.066	1.267	1.187
Θ	18.85°	12.44°	6.18°	360.0°	347.6°	341.2°	21.25°	5.55°

Fig. 2 Location of pressure transducers within the volute

diffuser with maximum expansion angle of 7 deg. The design flux of this volute was 200 gpm, but the maximum efficiency occurred at a slightly lower flux (about 190 gpm). Measurements were performed 35 percent above design flow rate in order to highlight nonuniformities and unsteady phenomena.

Velocity measurements were performed by utilizing PIV (Fig. 1), following procedures described in detail by Dong et al. (1992a, b). Briefly, this method consists of recording multiple exposure images of a flow field illuminated by a 1-mm-thick laser sheet and seeded with microscopic neutrally buoyant particles. The sheet can illuminate any desired section of the volute through the transparent perimeter. Illumination from the bottom in order to study normal planes is also possible. Three 20 ns laser pulses, generated by a frequency-doubled Nd-Yag laser, with a typical delay between pulses of 160 μs, were used for recording a single image. The timing was synchronized with the orientation of the impeller using an encoder attached to the shaft of the pump. The images were recorded by a 35 mm camera and digitized to a 3000 × 2000 pixel array using a slide scanner. The analysis consisted of dividing the image into a large number of small windows (each consisting of 64 × 64 pixels, that correspond to 0.1 in. × 0.1 in. in the volute), and determining the mean shift of all the particles within each window by computing the auto-correlation function of the intensity distribution. Calibration experiments (Dong et al., 1992a) have shown that the uncertainty level can be kept at about 1 percent, provided certain conditions associated with particle density (at least eight particles per window) and magnification (typical displacement between exposures of about 20 pixels) are satisfied. The regions sampled during the present study are outlined in Fig. 3. The data for tongues 2 and 3 were recorded at the center plane of the volute every 10 deg of impeller orientation, namely five per blade passage. While computing the pressure within the original pump (using the PIV results), the data were recorded every 1 deg (Chu et al., 1995a, b). Typically 8–12 images were necessary to obtain phase-averaged distributions. This choice was based on a requirement that the variations caused by adding another distribution should be less than the error level. Vorticity ($\xi_z = \partial v/\partial x - \partial u/\partial y$) was determined by computing $\Delta v/\Delta x - \Delta u/\Delta y$.

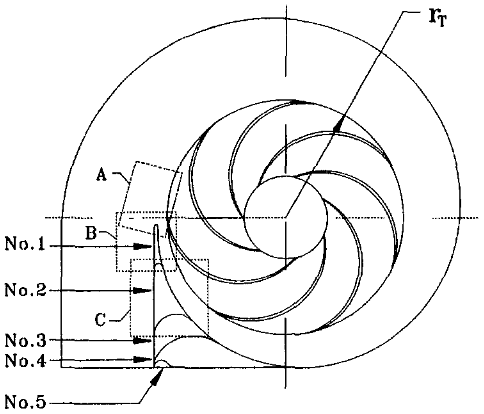

TONGUE	t_c/r_T (%)
1	7
2	11
3	18
4	25
5	27

t_c: the clearance between the impeller and the tongue

r_T : the radius of the impeller

SECTION	SIZE OF SAMPLE SECTION (INCH)
A	2.75 X 2.0
B	2.46 X 2.46
C	3.2 X 3.2

Fig. 3 Sample areas and clearances associated with different tongue geometries

Pressure fluctuation measurements were performed on the upper (hub side) surface, mostly with flush-mounted, 0.1 in. diameter, piezo-electric transducers (PCB model 105B02). The noise was measured with flush-mounted hydrophones (PCB model 106M12) located 3.3 ft upstream and down-

Nomenclature

B_2 = impeller width
D_2 = impeller diameter
p = pressure
Q = overall flow rate
Q_D = design flow rate = 200 gpm
r = radial distance from the center of the impeller
r_T = impeller radius
r_v = outer radius of the volute
T = blade passage period
t = time
U_T = impeller tip speed
v_r, v_θ = absolute radial and circumferential velocities
θ = angular orientation
ξ_z = axial vorticity component

stream of the pump. The signal was amplified and recorded by a PC-based data acquisition system. FFT was used for computing the spectra. Mean pressure measurements were performed using 0.0197 in pressure taps. The transducers were regularly calibrated, and the error level of the absolute pressure (mean + fluctuations) should be about 1 percent. In order to perform both measurements at the same point, part of the upper surface was replaced with an insert that could accommodate either the transducer or the taps. The sites of measurements are indicated in Fig. 2. Only part of the data is included in this paper.

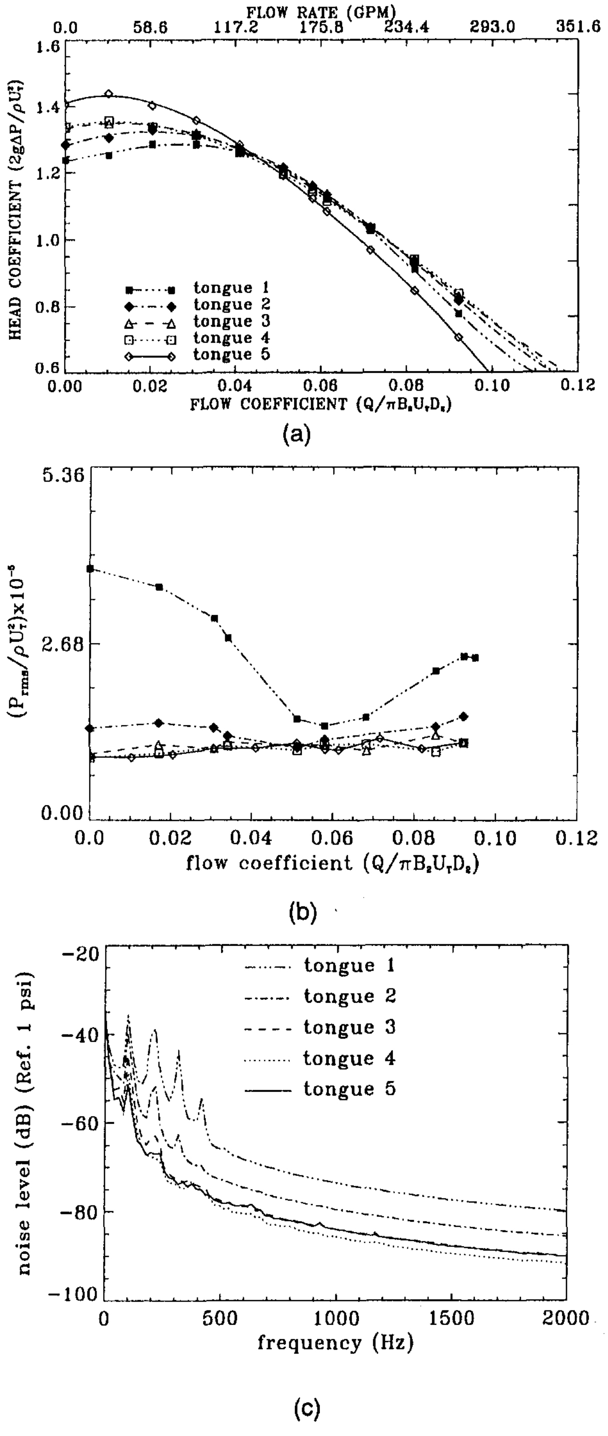

(a)

(b)

(c)

Fig. 4 Effect of the tongue geometry on (*a*) the performance of the pump, (*b*) rms noise, and (*c*) spectra of noise at $Q/Q_D = 1.35$ ($Q_D = 200$ gpm)

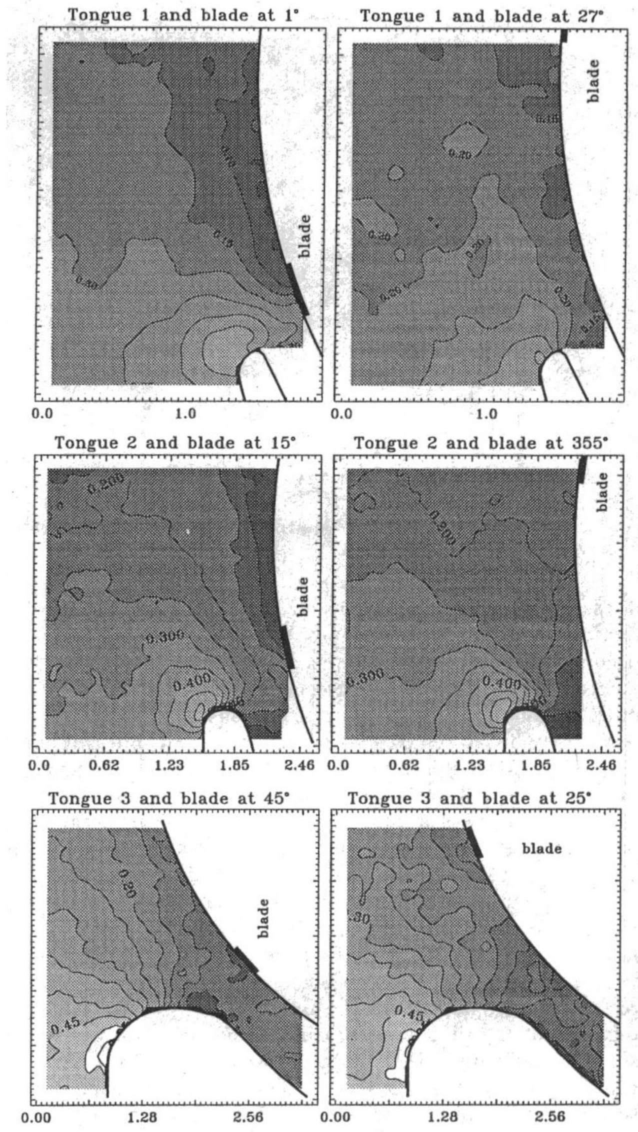

Fig. 5 Effect of modifications to tongue geometry on distributions of v_r/U_T. Increment between adjacent lines is 0.05. Scales are in inches. Flow rate is 270 gpm ($Q/Q_D = 1.35$).

Effect of Tongue Geometry

The five tongue geometries selected for the present study are sketched in Fig. 3. Tongue No. 1 with 7 percent gap is the original geometry studied by Chu et al. (1993, 1995a, b). Variations in pump performance, rms noise levels, and spectra at 270 gpm are presented in Fig. 4(*a–c*). It is evident that increasing the gap up to 23 percent improves the pump performance off-design conditions, and has little effect at design flux, besides a small decrease with tongue No. 4. Further increase in the gap causes a shift of the entire curve toward lower flow rates, with increase in head below design conditions, and substantial reduction above 150 gpm. The conclusions for gaps above 23 percent are consistent with the results of Hira and Vasandani (1975). The impact on reduction of rms noise levels (Fig. 4(*b*)) is particularly noticeable between tongues 1 and 3. Further increase in gap does not seem to have a significant effect. The spectra (Fig. 4(*c*)) show a reduction of the primary harmonics (the blade rate frequency is 105 Hz) when the gap is increased, particularly from 7 to 18 percent. The broad-band noise also decreases significantly with increasing gap, but with diminishing effects between tongues 3 and 4, and a slight increase between 4 and 5.

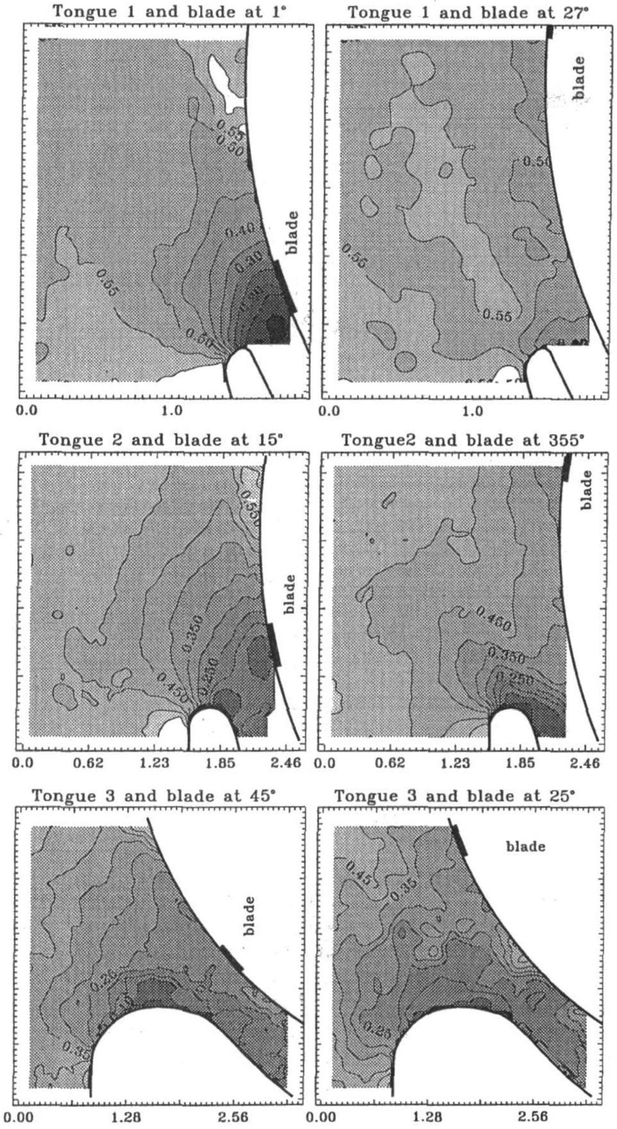

Fig. 6 Effect of modifications to tongue geometry on distributions of v_θ/U_T. Increment between adjacent lines is 0.05. Scales are in inches. Flow rate is 270 gpm (Q/Q_D = 1.35).

The spectral differences suggest that not only the amplitude of noise, but also the flow structure causing it, changes with increasing gap. The impact of changing the gap on the phase-averaged velocity, vorticity, local pressure fluctuations, and noise are illustrated in Figs. 5–9, respectively (unless clearly stated in the caption, all the figures in this paper contain phase-averaged results). Recall that in the original study with tongue 1 (Dong et al., 1992a, b; Chu et al., 1995a, b) we identified that impingement of the wake and its associated vorticity field on the tip of the tongue as well as oscillations of the tongue are primary causes of the main peaks in the noise signal. The existence of a jet (high v_r in Fig. 5) ahead of the blade and a wake (high v_θ in Fig. 6) at about 30 percent of blade passage behind the blade are clearly evident in the velocity distributions, irrespective of tongue geometry. The wake is also clearly marked with a negative vorticity train along its leading edge and positive train behind it (Fig. 7). The jet is also bounded by a pair of vorticity peaks with opposite signs. The negative peak is located in part within the separated region on the tip of the blade, and the positive peak is located ahead of the jet. At the request of reviewers of this paper, Fig. 8 contains two sample vector maps of the velocity distributions that highlight the flow nonuniformity. Note that each map actually shows the magnitude and direction of $v - v_{\text{ref}}$ (the latter is indicated on each map) in order to increase the clarity. The jet is evident in both cases, and impingement of the wake on the tongue is demonstrated in the upper example.

With tongue No. 1 the gap between the tongue and the impeller is small, and since the flow is above design conditions the leakage is also relatively small (Dong et al., 1992a, b). Consequently, as the wake and associated vorticity trains reach the tip of the tongue, they impinge on it and move toward the exit. The impingement causes a peak in both the local pressure fluctuations (e.g. P(E15) at $t/T \sim 0.2$ in Fig. 9(*c*)) and far field noise (signal of tongue 1 at $t/T \sim 0.2$ in Fig. 10(*a*)). Due to the narrow gap, the vorticity peak associated with the jet remains "stuck" in the corner as the blade moves behind the tongue, and coincides with the wake vorticity train when it arrives to the corner. This process is illustrated (in another context) in Figs. 17(*b*) and 19(*b*). Increasing the gap to 11 percent (tongue 2) leaves a larger space for leakage. Consequently, the portion of the wake closest to the impeller leaks to the beginning of the volute, substantially reducing its impact on the tip of the tongue. This phenomenon is demonstrated by

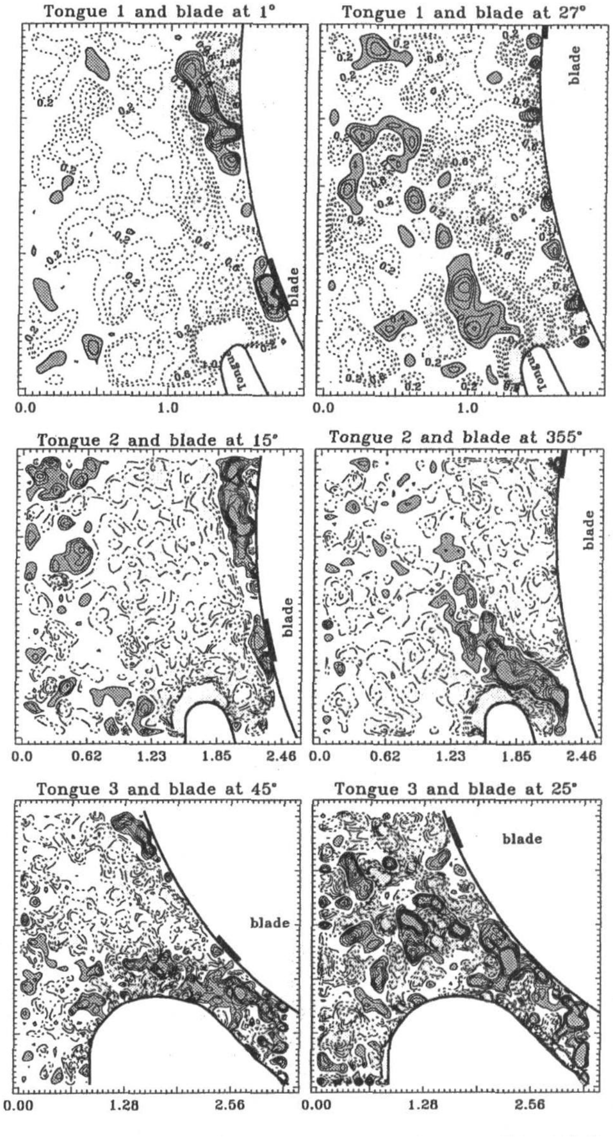

Fig. 7 Effect of modifications to tongue geometry on vorticity distributions. The increment between adjacent lines is 0.2 U_T/r_T. Solid lines represent negative vorticity, and dashed lines are positive vorticity. Scales are in inches. Flow rate is 270 gpm (Q/Q_D = 1.35).

comparing the corresponding circumferential velocity distributions in Fig. 6, and from the vorticity distributions (Fig. 7). With tongue 2, part of the wake vorticity trains and all of the jet vorticity peaks leak to the beginning of the volute. When the gap is increased to 18 percent most of the wake and associated vorticity train miss the tongue.

The impact of these changes on local pressure fluctuations is demonstrated in Figs. 9(*a*) and 9(*b*), which compare corresponding points located upstream of the tongue, as well as in Fig. 9(*c*) for points located at the exit from the volute. Near the impeller and relatively far upstream of the tongue (Fig. 9(*a*)), both signals have two minima during one blade cycle. The first occurs when the blade passes by the transducer (at $t/T = 0.33$) and the second occurs when the negative vorticity train passes by (at $t/T \sim 0.65$). Although the magnitudes are different, both minima are evident for either case. As noted before, impingement of the wake on the tip of tongue 1 causes a pressure pulse, which is sensed throughout the exit region. This peak is significantly smaller with tongue No. 2. It causes a small "bump" in the pressure waveform at $t/T \sim 0.3$ (at E15) and a slight "kink" in the noise signal. Wake impingement does not affect the noise signals of tongues 3–5.

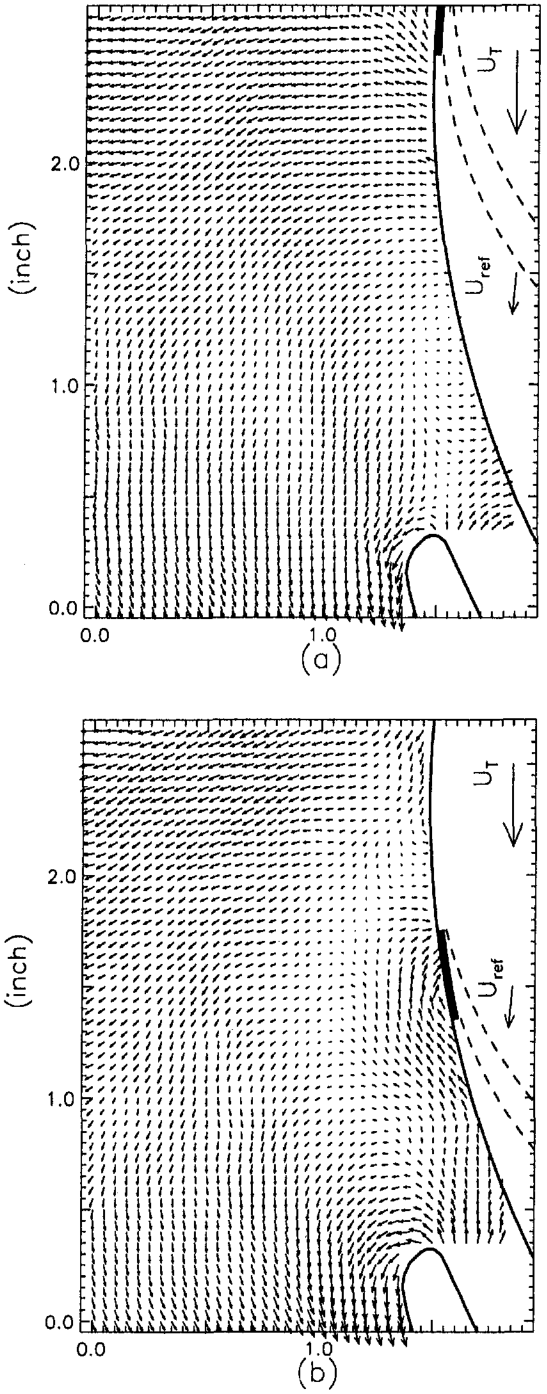

Fig. 8 Sample phase-averaged velocity distributions of tongue 1 data. The impeller is at: (*a*) 337 deg and (*b*) 351 deg. Data are shown as $v - v_{ref}$. The latter is also plotted.

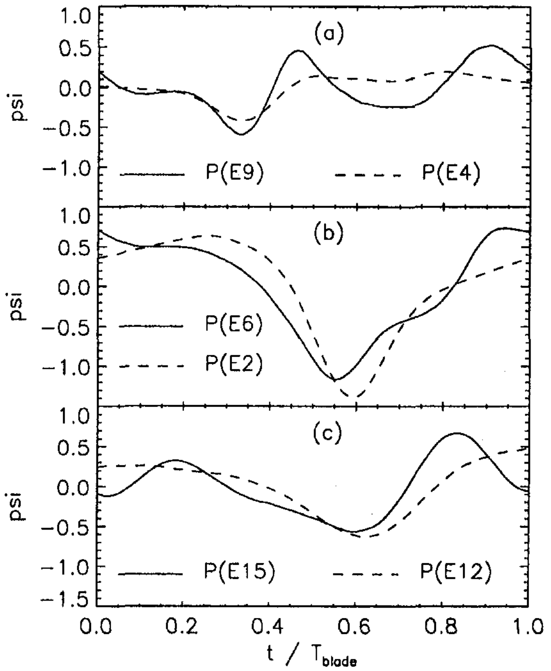

Fig. 9 Phase-averaged pressure waveforms at corresponding points for tongue 1 (solid line) and tongue 2 (dashed line)

Another cause for unsteady phenomena is associated with operation above design conditions and the resulting difference in mean pressure across the tongue. It causes reduction in pressure throughout the exit region (e.g., E15 at $t/T \sim 0.6$) when the gap between the tongue and the impeller is minimal, namely when the blade lines up with the tip of the tongue, and an increase in pressure when the gap is large (the blade is far from the tongue). This phenomenon is responsible in part for the minima at $t/T \sim 0.6$ in Figs. 9(*a*) and 9(*b*). The trend is reversed across the tongue, namely at the beginning of the volute (only one sample is provided for E4 in Fig. 18). Combined, it causes large fluctuations in the pressure difference across the tongue (also shown in Fig. 18 for tongue 1), resulting in tongue oscillations and radiation of noise. This process is responsible for the second peak in the noise signal at $t/T \sim 0.62$ (Fig. 10(*a*)). The same process and resulting noise occur with tongue 2. As the tongue becomes thicker (tongue 3, for example), and the gap becomes larger, this effect disappears.

Close to design conditions (at 170 gpm in Fig. 10(*b*)), when the pressure difference across the tongue is small, the noise peak associated with tongue oscillations disappears. The waveform has only one maximum, which occurs at the same time as the wake impingement peak. In order to clarify the effect of tongue oscillations further, we also replaced the lucite tongue with a steel tongue that had an identical shape (No. 1). The waveforms at E4, E6, and E10 (data not shown) do not change significantly, but there is substantial reduction in the magnitude of the peaks caused by wake impingement and tongue oscillations at the exit region (E15, data not shown) and in the noise signal (Fig. 10(*b*)). Note that the noise of a steel tongue No.

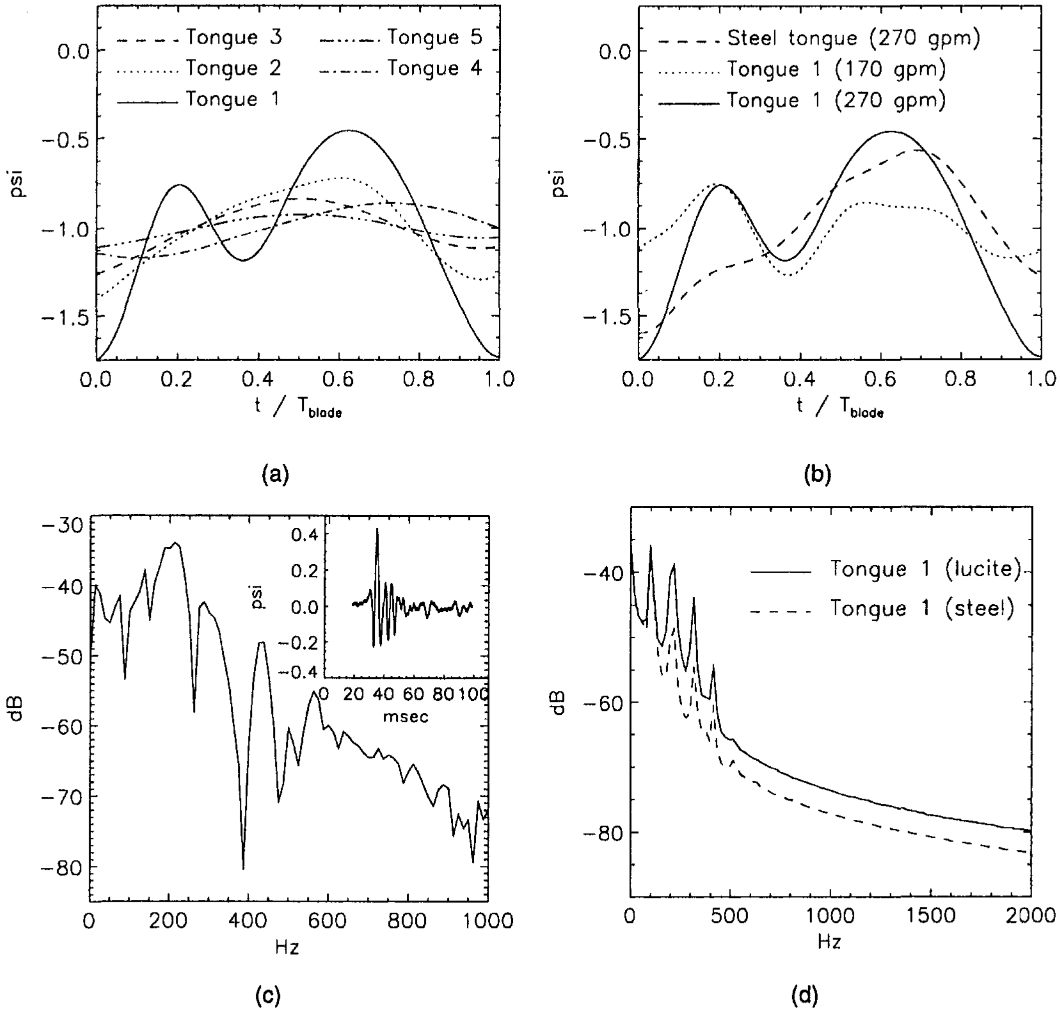

(a) (b)

(c) (d)

Fig. 10 **(*a*) Effect of tongue geometry on the phase-averaged noise. (*b*) Noise signals of a steel tongue 1 at 270 gpm and lucite tongue 1 at 270 and 170 gpm. (c) The pressure signal resulting from bending and releasing the lucite tongue 1 and its spectrum. (*d*) A comparison between the noise spectra of the steel and lucite tongue.**

1 is still considerably higher than that of a lucite tongue No. 2. In order to explore the reasons for the considerable differences between the steel and lucite tongues, we also measured the frequency response of the lucite tongue. This task was performed by bending the tongue and releasing it abruptly in a stationary (impeller at rest), water-filled facility. An extension to one of the blades that pushed the tongue outward and released it as the impeller was manually rotated was used for this purpose. The resulting signals at E15 and the hydrophone (see a sample spectrum at Fig. 10(*c*)) were quite repeatable and had spectral peaks at 84, 136, 208, and 296 Hz. The first two peaks do not match the blade rate frequency (105 Hz), but the third is quite close to the blade's second harmonics. A comparison between the spectra of the steel and lucite tongues (Fig. 10(*d*)) clearly shows that there is little change in the blade rate frequency, but there is substantial difference in the magnitude of the peaks at 210 and 315 Hz. These results suggest that resonant response of the lucite tongue may have contributed to the noise amplitude. However, as noted before, a steel tongue No. 1 is still much noisier than lucite tongues 2–5.

The last unsolved issue involves the sources of noise of tongues 3, 4, and 5. This task is not simple since the noise levels are low and contain a considerably larger broad band component. Thus, the flow phenomena causing them are not as powerful and distinct. Focusing on blade–tongue interactions (tonal noise) of tongue 3 (see data in Figs. 5–7) we examined the velocity distributions carefully. The wake seems to have little effect on the flow around the tongue. The jet (increased v_r ahead of the impeller), on the other hand, impinges on the tip of the tongue when the blade is between 25 and 35 deg and has little effect for the rest of the cycle. The noise peak occurs when the blade is at about 31 deg (at $t/T \sim 0.5$), suggesting that these phenomena are related. The same process occurs with narrower gaps, but there the wake and tongue oscillations are dominant. With tongue 4 the amplitude of the noise signal is even slightly lower. The timing of the peak is consistent with the observations on tongue 3, that is, it occurs when the impeller is located about 10 deg upstream of the tongue (data not shown here—they do not add anything significant). With tongue 5 we cannot identify a clear relationship between flow and noise.

Effect of Modifications to the Impeller

As discussed in the previous section and by Chu et al. (1995a, b), when the tongue is located at $r/r_T < 1.2$, the flow around it and resulting noise are dominated by nonuniformities in the outflux from the impeller. Thus, it is likely that any reduction in the jet/wake phenomenon would have a direct impact on decreasing the noise level. To achieve this goal we inserted short vanes (Fig. 11) within the wake based on the data at 270 gpm, i.e., $Q/Q_D = 1.35$, where $Q_D = 200$ gpm (the corresponding flow coefficient of 0.07), 10 deg behind the origin of the negative vorticity train (Fig. 7). Their exit angles, 18 deg, was set to reduce the magnitude of v_θ within the wake to $v_\theta/U_T \sim$

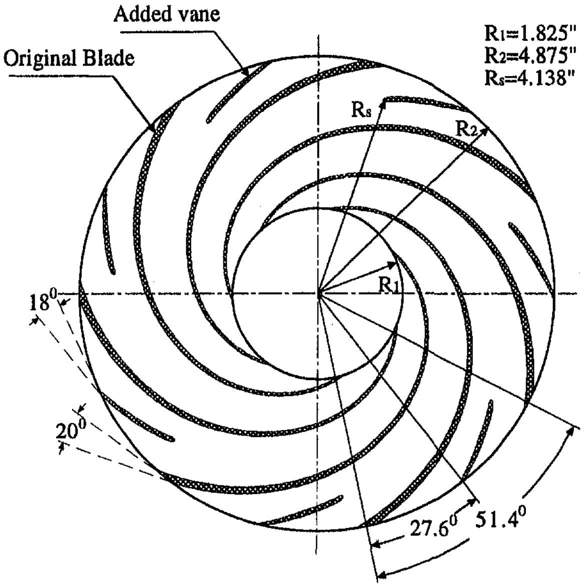

Fig. 11 A sketch of the modified impeller

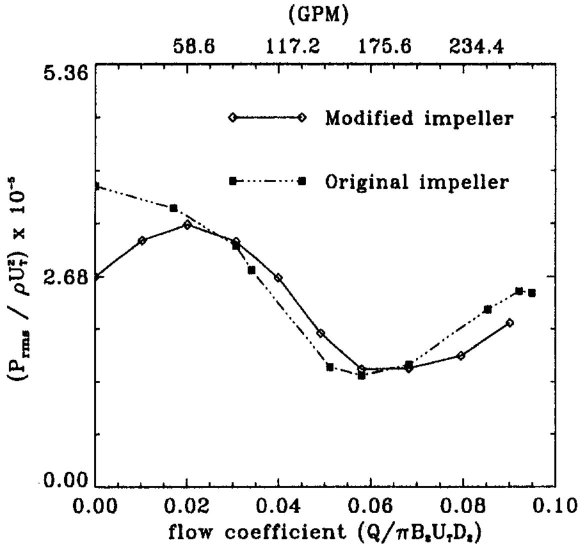

Fig. 13 The Rms noise of the original and modified impellers

0.5, namely to levels comparable to the flow outside of the wake (Fig. 6).

For $0.5 < Q/Q_D < 1.25$, the vanes improved the pump performance slightly (Fig. 12), but reduced it at lower flow rates. The rms noise (Fig. 13) decreased above design conditions (the conditions for which they were designed) and at low flow rates, but increased at $0.4 < Q/Q_D < 1$. Thus, for flows with significant outflux from the impeller near the tongue (above design conditions, according to Dong et al., 1992), the vanes contributed to noise reduction. The spectrum at 270 gpm (Fig. 14) clearly shows a substantial decrease in the magnitude of the primary harmonic (blade rate frequency—105 Hz) and its odd multiples, no change in the second peak, but a slight increase in the fourth harmonics. The latter can be easily explained by the effective doubling of the number of blades. There is also a noticeable decrease in the broadband noise level.

Selected distributions of v_r, v_θ and vorticity within the modified pump are compared to the original data in Figs. 15–17, respectively. They demonstrate that the vanes decrease the original blade jet/wake phenomenon, but create additional similar patterns of nonuniform outflux. For example, in Fig. 16(*a*) the vane significantly reduces, but does not eliminate, the size of the wake region. However, as shown in Fig. 16(*c*), the vane generates an additional wake. Evidence for the formation of an additional vane wake is provided also by the vorticity distributions. In Fig. 17(*a*) the new vorticity train extends from the impeller and in Fig. 17(*c*) it appears on top of the tongue. As expected, Fig. 15(*a*) shows that the vane has little effect on the blade jet (it was not designed for it). Its own jet is much weaker (Fig. 15(*c*)), as long as the vane is located far from the tip of the tongue (a sample for the latter, which will be discussed later, is presented in Fig. 19). Finally, note that traces of wakes generated by the previous blade and vane can be identified on the left sides of Figs. 16(*a*) and 16(*c*), respectively.

The vorticity peak associated with the jet, which in the original pump appears near the blade (Fig. 17(*a*)), does not exist when the impeller is modified. It does form as the blade moves closer to the tongue (data not shown) as the radial velocity at the exit from the impeller increases. This phenomenon is a direct result of increasing blockage to blade passage caused by the tongue, which increases the radial velocity in the unobstructed part. In the original impeller, this vorticity peak "gets

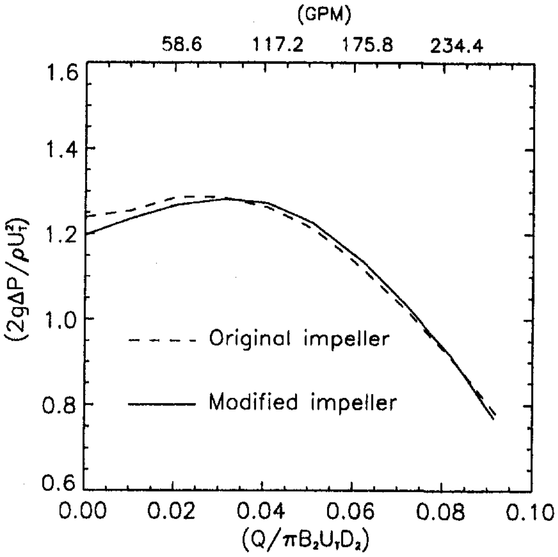

Fig. 12 Performance curves of the original and modified impellers

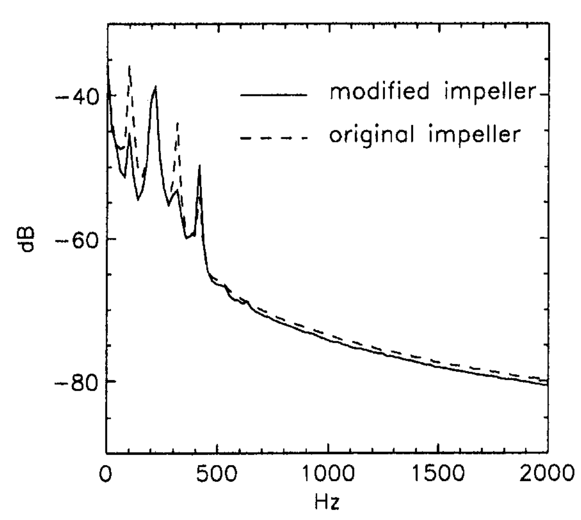

Fig. 14 Noise spectra of the original and modified impellers at $Q = 270$ gpm

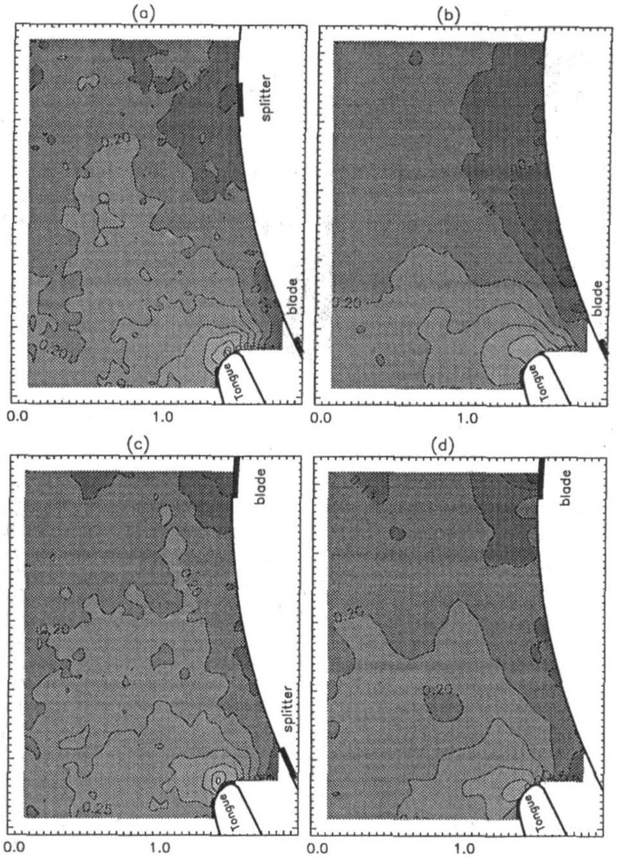

Fig. 15 v_r/U_T **distributions at** Q **= 270 gpm: (*a*) blade is at 8 deg (modified impeller); (*b*) 8 deg (original); (*c*) 338 deg (modified); and (*d*) 338 deg (original); increment between lines 0.05; scales in in.**

stuck'' between the tongue and the impeller as the blade moves behind the tongue (Fig. 17(*b*)) because of the low velocity there. In the modified impeller the new vane increases the radial velocity sufficiently (Fig. 15(*a*)) to push this blade vorticity away.

Comparisons of phase-averaged pressures and noise waveforms are presented in Fig. 18. It is evident that near the tongue (E6) and at the exit (E15) the pressure fluctuations are considerably smaller, whereas somewhat far upstream of the tongue (E10) they are slightly higher. Detailed explanations for the signals of the unmodified impeller, resulting from direct computations of pressure from the PIV data, are presented by Chu et al. (1995a, b). It is demonstrated there that near the impeller (E10 and E6) the pressure minima occur when the blade passes by the transducer, under the negative vorticity train (Figs. 7 and 17), and when the blade lines up with the tip of the tongue. The latter occurs almost simultaneously everywhere and is associated with operation above design conditions. The maxima appear when the transducer is located between the blade and the wake, and everywhere when the blade is located far (35 deg) upstream of the tongue. With the modified impeller, in addition to the pressure minima associated with the original blades (points C and F at E6 and E10, respectively), there are new pressure minima when the vane passes by the transducer (points A and I). Reductions in pressure when the vorticity trains pass by are barely noticed near the modified impeller, mostly since they are overshadowed by simultaneous blade and vane effects. For example, the blade vorticity train reaches E10 (point E) at about the same time that the vane passes by (they are designed that way).

Similar to the impact of the blade, the pressure decreases everywhere in the exit region when the vane lines up with the tip of the tongue (points A and E at E6 and E10, respectively). Pressure maxima occur simultaneously (point D at E6 and J at E10) when the blade is past the tip of the tongue and the vane is still far upstream of it. These peaks occur earlier than the original impeller because of the added vane and the pressure dip near it (point A). Simultaneous pressure maxima occur also when the blade is still about 14 deg upstream of the tongue and the vane is relatively far (10 deg) past it (points B and G). To recapitulate, maxima occur everywhere when the blade and the vane are far from the tip of the tongue, and the minima appear when they are very close to the tongue. Pressure minima occur also when the blade passes by the transducer, but they are barely noticed under the vorticity trains. The latter conclusion is the only result that is inconsistent with the trends observed with the original impeller.

Behind the tongue (E4) the vane impacts the pressure waveform only in its vicinity, causing a new minimum as the vane passes by (point K). Close to the blade, the signal remains quite similar to the original impeller. On the other side of the tongue, near the exit (E15), there are two minima (points L and N), that occur, like anywhere else in the exit region, when the blade and the vane coincide with the tip of the tongue. In the original pump there is a high-pressure peak at E15 (point M) when the wake impinges on the tip of the tongue. Although the impingement still occurs (Fig. 17(*c*)), it has little impact on the pressure at E15. It is possible that weakening of the wake (Fig. 16(*a*)) in the vicinity of the tongue reduces its impact to a level where it is barely noticed. One of the contributing reasons for this weakness is the jet of the vane. As noted before, this jet is fairly small until very close to the tongue, where blockage to blade passage induced by the tongue causes an increase in radial velocity in the unobstructed space (an example of such a process with the main blade is illustrated in Fig. 5). This jet ''blows'' the wake away from the tongue,

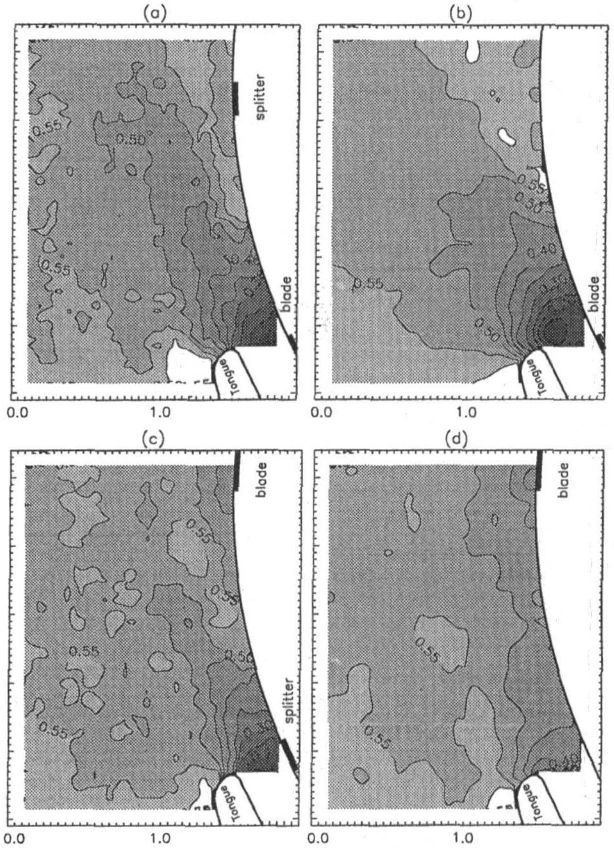

Fig. 16 v_θ/U_T **distributions at** Q **= 270 gpm: (*a*) blade is at 8 deg (modified impeller); (*b*) 8 deg (original); (*c*) 338 deg (modified); and (*d*) 338 deg (original); increment between lines 0.05; scales in in.**

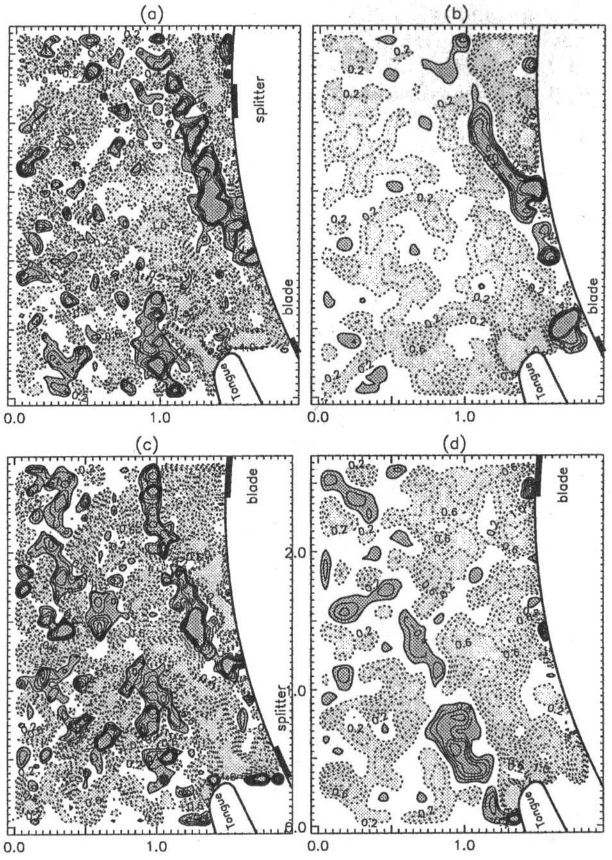

Fig. 17 Vorticity distributions at $Q = 270$ gpm: (*a*) blade is at 8 deg (modified impeller); (*b*) 8 deg (original); (*c*) 338 deg (modified); and (*d*) 338 deg (original). Solid line represents negative vorticity, and dashed line positive. Increment between lines is 0.2 U_T/r_T. Scales are in in.

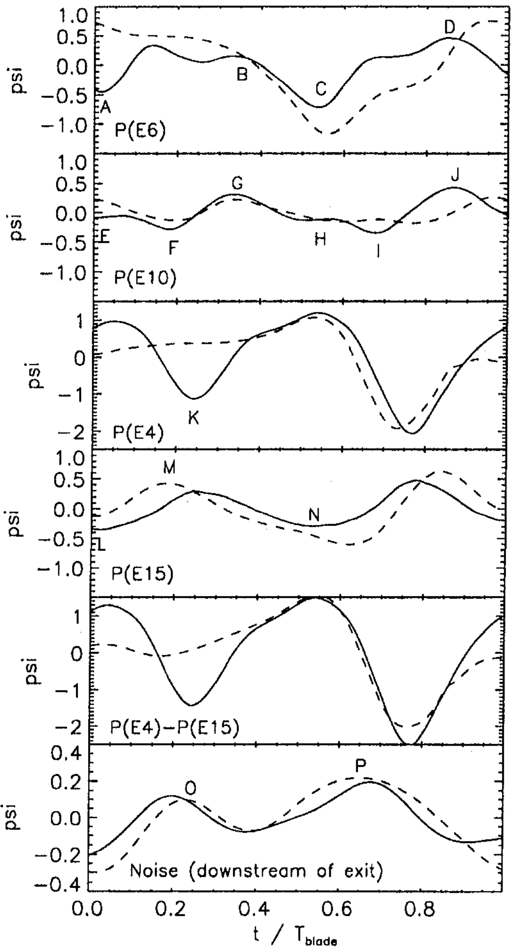

Fig. 18 Phase-averaged pressure and noise waveforms of the original (dashed line) and modified (solid line) impellers (note the differences in scale)

before it has a chance to impinge on it. A clear illustration of this blowing process is provided in Fig. 19. For this reason the vorticity train of the original impeller appears continuous up to the tongue (Fig. 17(*a*)), whereas the train of the modified impeller is much more fragmented. Similar conclusions can be drawn from the distributions of v_θ (Fig. 16(*a*)). Thus, the vane not only reduces the size of the wake, it also prevents impingement on the tip of the tongue. The blade has a similar effect on the wake of the vane (data not shown here).

As discussed and demonstrated Chu et al. (1995a, b), wake impingement also causes a peak in the noise signal (point O) of the original impeller. The delay between points M and O is approximately the time required for the pressure pulse to travel between E15 and the hydrophone. This relationship is obviously not the case with the modified impeller, first since the hydrophone peak occurs before the maximum at E15, and second, since the pressure at E15 in the modified impeller is not affected by the impingement. Thus, it is unlikely that the first peak in the noise signal has anything to do with wake impingement. Furthermore, the data in Fig. 18 suggest that the hydrophone signal has no any clear resemblance or correspondence to the pressure in E15, E6, or E10. The only consistent relationship exists with the pressure at E4, or even more clearly, with the pressure difference across the tongue (P(E4) – P(E15)). Recall that with the original impeller the second noise maximum (point P) is clearly a result of tongue oscillations, induced by the pressure differences across the tongue. There, the delay between maxima in pressure difference and noise signals is about 0.7 ms, approximately the time required for sound to travel between the transducers and the hydrophone (the distance is ~3.3 ft). With the modified impeller, both noise peaks appear only about 1.4 ms after the maxima in pressure difference across the tongue. This delay is about twice the time required for sound to travel between the tongue and the hydrophone. To explain this discrepancy we note that with the original impeller, the pressure maximum behind the tongue occurs almost simultaneously everywhere when the blade lines up with the tip (there are some blade-induced variations). Thus, the maximum force on the tongue should occur almost at the same time as the peak

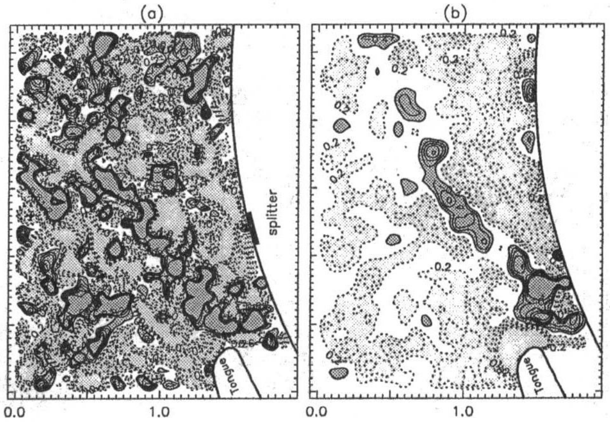

Fig. 19 Vorticity distributions of: (*a*) modified (instantaneous) and (*b*) original (phase-averaged) impellers that demonstrate blowing of the wake by the jet ahead of the vane; increment between lines 0.02 U_T/r_T; scales in in.

at E3. With the modified impeller, the added vane causes a pressure dip 27 deg ahead of the tip (similar to point K at E4). Thus, the maximum force on the tongue does not necessarily coincide with the maximum in P(E4)−P(E15) and a slight delay is quite possible. These results suggest that with the modified impeller tongue oscillations remain the only primary source of noise at the exit from the pump.

Summary and Conclusions

PIV, surface pressure, and noise measurements have been used to study the effects of modifications to tongue and impeller geometries on the flow structure, local pressure fluctuations, and noise. It is demonstrated that increasing the gap between the tongue and the impeller, up to about 20 percent of the impeller radius, reduces the impact of nonuniform outflux from the impeller (mostly the jet/wake phenomenon) on the flow around the tongue and noise. Further increase in the gap affects the performance adversely with minimal impact on the noise level. When the gap is narrow, the primary sources of noise are impingement of the wake on the tip of the tongue, and tongue oscillations when the pressure difference across it is high. At 20 percent gap, the entire wake and its associated vorticity trains miss the tongue, and the only effect of nonuniform outflux from the impeller occurs when the jet impinges on the tongue. This effect is quite small, at least for the present pump.

Based on the available data, we attempted to reduce the nonuniformity in outflux from the impeller by inserting short vanes between the blades. Their location and orientation were selected to reduce the size of the wake and the magnitude of circumferential velocity within it. The experiments were performed only with the narrowest gap between the tongue and the impeller. The results showed that although the original intent was successful, that is, the size of the original wake was reduced, the vanes generated a jet/wake phenomenon of their own. However, both wakes were considerably weaker to a level that their impacts on local pressure fluctuations and far-field noise were insignificant. The jet in front of the vane was an added benefit, since it blew the wake of the blade away from the tongue shortly before impingement, eliminating any direct impact of the wake on noise. The only remaining contributors to noise were tongue oscillations caused by the pressure difference across it. They reach maximum level when either the blade or the vane line up with the tip of the tongue. This effect was particularly noticed with the present fairly narrow lucite tongue. As the experiments with the other tongues have shown, the impact of tongue oscillations decreases with increasing tongue thickness and stiffness.

Acknowledgments

This research has been supported by the Office of Naval Research, under contract No. N00014-89-J-1672.

References

Chu, S., Dong, R., and Katz, J., 1993, "Unsteady Flow, Pressure Fluctuation and Noise Associated With the Blade-Tongue Interaction in a Centrifugal Pump," presented at the Symposium on Flow Noise Modeling, Measurement and Control, ASME Winter Annual Meeting, New Orleans, LA, Nov. 28–Dec. 3.

Chu, S., Dong, R., and Katz, J., 1995a, "Relationship Between Unsteady Flow, Pressure Fluctuations and Noise in a Centrifugal Pump. Part A: Use of PIV Data to Compute the Pressure Field," ASME *Journal of Fluids Engineering*, Vol. 117, No. 1.

Chu, S., Dong, R., and Katz, J., 1995b, "Relationship Between Unsteady Flow, Pressure Fluctuations and Noise in a Centrifugal Pump. Part B: Effect of Blade-Tongue Interaction," ASME *Journal of Fluids Engineering*, Vol. 117, No. 1.

Cumpsty, N. A., 1989, *Compressor Aerodynamics*, Longman Scientific & Technical, England.

Dean, R. C., and Senoo, Y., 1960, "Rotating Wake in Vaneless Diffusers," ASME *Journal of Basic Engineering*, Vol. 82, No. 3, pp. 563–574.

Dong, R., Chu, S., and Katz, J., 1992a, "Quantitative Visualization of the Flow Within the Volute of a Centrifugal Pump. Part A: Technique," ASME *Journal of Fluids Engineering*, Vol. 114, No. 3, pp. 390–395.

Dong, R., Chu, S., and Katz, J., 1992b, "Quantitative Visualization of the Flow Within the Volute of a Centrifugal Pump. Part B: Results," ASME *Journal of Fluids Engineering*, Vol. 114, No. 3, pp. 396–403.

Eckardt, D., 1975, "Instantaneous Measurements in the Jet/Wake Discharge Flow of a Centrifugal Compressor Impeller," ASME *Journal of Engineering for Power*, Vol. 97, No. 3, pp. 337–346.

Hamkins, C. P., and Flack, R. D., 1987, "Laser Velocimeter Measurements in Shrouded and Unshrouded Radial Flow Pump Impeller," ASME JOURNAL OF TURBOMACHINERY, Vol. 109, pp. 70–76.

Hira, D. S., and Vasandani, V. P., 1975, "Influence of Volute Tongue Length and Angle on the Pump Performance," *Journal of Mechanical Engineering (Indian)*, Vol. 56, pp. 55–59.

J. Luo[1]
Graduate Assistant.
Mem. ASME

B. Lakshminarayana
Evan Pugh Professor of
Aerospace Engineering
and Director of Center for
Gas Turbines and Power.
Fellow ASME

Center for Gas Turbine and Power,
The Pennsylvania State University,
University Park, PA 16802

Three-Dimensional Navier–Stokes Computation of Turbine Nozzle Flow With Advanced Turbulence Models

A three-dimensional Navier–Stokes procedure has been used to compute the three-dimensional viscous flow through the turbine nozzle passage of a single-stage turbine. A low-Reynolds-number $k-\epsilon$ model and a zonal k-ϵ/ARSM (algebraic Reynolds stress model) are utilized for turbulence closure. The algebraic Reynolds stress model is used only in the endwall region to represent the anisotropy of turbulence. A four-stage Runge–Kutta scheme is used for time integration of both the mean-flow and the turbulence transport equations. For the turbine nozzle flow, comprehensive comparisons between the predictions and the experimental data obtained at Penn State show that most features of the vortex-dominated endwall flow, as well as nozzle wake structure, have been captured well by the numerical procedure. An assessment of the performance of the turbulence models has been carried out. The two models are found to provide similar predictions for the mean flow parameters, although slight improvement in the prediction of some secondary flow quantities has been obtained by the ARSM model.

Introduction

The three-dimensional flow in a turbine passage is very complex due to the existence of numerous vortical structures, including passage, horseshoe, trailing edge, and corner vortices. Many experiments have been conducted to understand the turbine endwall flows. The data of Langston et al. (1977) provided very useful information on secondary flow patterns in turbine cascades. Sieverding (1985) reviewed the progress in the understanding of basic aspects of secondary flows in turbine blade passages. Moore et al. (1987) found that high levels of turbulence played a significant role in the loss generation process downstream of the cascade. Recently, Gregory-Smith and Cleak (1992) presented detailed measurements of turbulence quantities in the endwall region of a rotor cascade.

Three-dimensional Navier–Stokes computations of turbine endwall flows have also been carried out by many investigators, e.g., Hah (1989), Choi and Knight (1991), Dorney and Davis (1992), Arnone et al. (1993), and Ho and Lakshminarayana (1996). The turbulence models employed range from algebraic eddy-viscosity models to low-Reynolds-number two-equation models. Higher-order anisotropic turbulence models have never been employed for turbine endwall flow computations. Cleak and Gregory Smith (1992) compared three eddy-viscosity models (mixing-length, one-equation, and two-equation models), using their own data for a linear rotor cascade. Their computation was carried out with a coarse grid (about 40,000 points for the entire cascade). Most of the three-dimensional Navier–Stokes computations have been carried out for linear turbine cascades. A comprehensive review of Navier–Stokes techniques for the analysis of turbomachinery flows is given by Lakshminarayana (1991).

The secondary flow patterns in linear turbine cascades may be different from those in actual turbine nozzles and rotors, since the annular design of an actual turbine introduces radial pressure gradient, which may be on the same order of magnitude as the pitchwise pressure gradient. Zaccaria and Lakshminarayana (1995) and Zaccaria et al. (1996) carried out detailed measurements of the three-dimensional flow field inside a nozzle passage of a single-stage turbine (with close stator–rotor spacing) at Penn State. The measured velocities, turning angles, vorticities, and total pressure losses are useful in understanding the entire passage flow, formation, and development of horseshoe and passage vortices.

In this study, three-dimensional Navier–Stokes computations have been carried out for the Penn State turbine nozzle flow. A low-Reynolds-number $k-\epsilon$ model and a zonal $k-\epsilon$/ARSM (algebraic Reynolds stress model) are utilized for turbulence closure. The algebraic Reynolds stress model is used in the endwall secondary flow region, for a better representation of the anisotropy of turbulence, as well as the streamline curvature effects. The computational results are compared with the measurements. The performance of the turbulence models is assessed.

Numerical Technique and Turbulence Models

Governing Equations. The compressible Navier–Stokes equations can be written in conservative form in Cartesian coordinates as

$$\frac{\partial \rho}{\partial t} + \frac{\partial(\rho U_j)}{\partial x_j} = 0 \quad (1)$$

$$\frac{\partial(\rho U_i)}{\partial t} + \frac{\partial(\rho U_i U_j)}{\partial x_j} = -\frac{\partial p}{\partial x_i} + \frac{\partial(\tau_{ij})}{\partial x_j} \quad (2)$$

$$\frac{\partial(\rho e_0)}{\partial t} + \frac{\partial(\rho U_i h_0)}{\partial x_i} = -\frac{\partial(U_j \tau_{ij} - q_i)}{\partial x_i} \quad (3)$$

---

[1] Current address: Solar Turbines, Inc., San Diego, CA.

Contributed by the International Gas Turbine Institute and presented at the 40th International Gas Turbine and Aeroengine Congress and Exhibition, Houston, Texas, June 5–8, 1995. Manuscript received by the International Gas Turbine Institute March 10, 1995. Paper No. 95-GT-302. Associate Technical Editor: C. J. Russo.

where the effective stress tensor τ_{ij} and the effective heat flux vector q_i in the above mean-flow equations are given by (using eddy-viscosity models)

$$\begin{aligned}\tau_{ij} &= \tau_{lij} - \rho\overline{u_iu_j}\\ &= (\mu_l + \mu_t)[(\partial U_i/\partial x_j + \partial U_j/\partial x_i)\\ &\qquad - \tfrac{2}{3}\delta_{ij}\partial U_k/\partial x_k] - \tfrac{2}{3}\delta_{ij}\rho k \qquad (4)\end{aligned}$$

$$q_i = -C_p\left(\frac{\mu_l}{\mathrm{Pr}_l} + \frac{\mu_t}{\mathrm{Pr}_t}\right)\frac{\partial T}{\partial x_i} \qquad (5)$$

where μ_t is the turbulent eddy viscosity, which is computed using the $k-\epsilon$ model. When the algebraic Reynolds stress model is used, the Reynolds stress $\rho\overline{u_iu_j}$ in Eq. (4) is then directly obtained from the algebraic Reynolds stress model, without using the eddy viscosity.

Low-Reynolds-Number $k-\epsilon$ Model. The low-Reynolds-number $k-\epsilon$ model, developed by Chien (1982), is employed in the present computation. In the low-Reynolds-number $k-\epsilon$ model, the eddy viscosity is obtained from the Prandtl–Kolmogorov relation:

$$\mu_t = C_\mu f_\mu \rho\frac{k^2}{\epsilon} \qquad (6)$$

where $C_\mu = 0.09$, f_μ is a near-wall damping function; the turbulent kinetic energy (k) and the dissipation rate of the turbulent kinetic energy (ϵ) are obtained by solving the transport equations for k and ϵ. The low-Reynolds-number $k-\epsilon$ equations can be written as

$$\frac{\partial(\rho k)}{\partial t} + \frac{\partial(\rho U_i k)}{\partial x_i} = \frac{\partial}{\partial x_j}\left[\left(\mu + \frac{\mu_t}{\sigma_k}\right)\frac{\partial k}{\partial x_j}\right] + \rho P_k - \rho(\epsilon + D) \qquad (7)$$

$$\frac{\partial(\rho\epsilon)}{\partial t} + \frac{\partial(\rho U_i\epsilon)}{\partial x_i} = \frac{\partial}{\partial x_j}\left[\left(\mu + \frac{\mu_t}{\sigma_\epsilon}\right)\frac{\partial\epsilon}{\partial x_j}\right] + \rho\frac{\epsilon}{k}[C_{\epsilon1}f_1P_k - C_{\epsilon2}f_2\epsilon] + \rho E \qquad (8)$$

where D, E, f_1, f_2 are near-wall terms, and the production of turbulent kinetic energy is given by

$$P_k = -\overline{u_iu_j}\partial U_i/\partial x_j \qquad (9)$$

The wall proximity length scale y, used in the near-wall terms, is defined as $1/y = 1/y_b + 1/y_w$, where y_b and y_w are

Nomenclature

C = nozzle local axial chord length
C_p = specific heat at constant pressure/static pressure coefficient = $(p - P_{o1})/Q_1$
C_μ, C_1, C_2, $C_{\epsilon1}$, $C_{\epsilon2}$ = turbulence modeling parameters
e = internal energy per unit mass
D, E = near-wall terms in $k-\epsilon$ equation
f_1, f_2, f_μ = near-wall damping functions
h = enthalpy per unit mass
H = nozzle spanwise location = $(R - R_h)/(R_t - R_h)$; duct height
k = turbulent kinetic energy $k = \overline{u_iu_i}/2)$
L_w = semi-wake width
p = static pressure
P_o = total pressure
P_{ij} = production rate of Reynolds stress
P_k = production rate of turbulent kinetic energy
Pr_l, Pr_t = laminar and turbulent Prandtl numbers
PS = pressure surface
q_i = Cartesian components of heat flux vector
Q_1 = inlet dynamic head at midspan = $0.5\rho U_{x1}^2$
R = gas constant/radius
Re = Reynolds number
Re_y = turbulent Reynolds number = $\sqrt{k}y/\nu$
S = percentage pitchwise distance from pressure surface to suction surface
SKE = secondary kinetic energy coefficient = $0.5\rho(U_n^2 + U_r^2)/Q_1$
SS = suction surface
T = temperature
T_u = turbulence intensity $\sqrt{(2/3)k}/U_{x1}$
U = total velocity
U_D = maximum defect in velocity
u_τ = friction velocity
U_i = mean velocity components
U_x, U_θ, U_r = time-averaged velocity components in axial, tangential, and radial directions
u_i = fluctuating velocity component
$\overline{u_iu_j}$, $\langle u_iu_j\rangle$ = Reynolds stress
x = coordinate in axial direction ($x = 0$ at leading edge)
y = coordinate in tangential direction (pitchwise)/normal distance to the wall
y^+ = wall distance variable = yu_τ/ν)
Z = distance from the blade trailing edge in nominal exit flow direction
α = yaw angle (measured from axial direction)
γ = specific heat ratio/underrelaxation factor for ARSM computation
δ_{ij} = Kronecker delta
δ = boundary layer thickness
ϵ = dissipation rate of turbulent kinetic energy
ζ = total pressure loss coefficient = $(P_{o1} - P_o)/Q_1$
θ = tangential position in degree measured from wake center at midspan
μ_l, μ_t = molecular, turbulent viscosity
ν = kinematic viscosity
ρ = density
σ_k, σ_ϵ = Prandtl numbers in k and ϵ equations
τ_{ij} = Cartesian components of stress tensor

Subscripts

h = hub
l = laminar
m = midspan/bulk or mean
n = normal to the primary flow direction
o = stagnation condition
r, θ, x = radial, tangential, axial directions
t = tip/turbulent
w = wall
1 = inlet free stream

Superscripts

$^-$ = time-averaged quantity/pitchwise-mass-averaged quantities

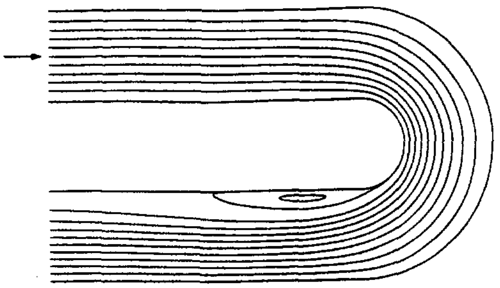

Fig. 1 Computed contour of mean streamlines (by the $k-\epsilon$/ARSM model) of the turn-around-duct flow

absolute distances from the closest blade surface and from the closest endwall surface, respectively. Upstream or downstream of the blade, y_b is approximated by the distance from the leading and trailing edge, respectively. Details of the implementation of this low-Reynolds-number $k-\epsilon$ model can be found from Kunz and Lakshminarayana (1992).

Algebraic Reynolds Stress Model. It is expensive and difficult to solve the "stiff" transport equations of the differential Reynolds stress model (RSM). By assuming the convective and the diffusive transport of individual Reynolds stress components are locally proportional to the transport of turbulent kinetic energy (Rodi, 1976), the differential equations in the RSM can be reduced to nonlinear algebraic equations, resulting in the algebraic Reynolds stress model (ARSM). The RSM and the ARSM models have been tested extensively for two-dimensional flows (and three-dimensional flows with simple geometry), and have been shown to provide better predictions of the streamline curvature effects, rotation effects and separated flows than the isotropic eddy-viscosity models (Launder, 1989).

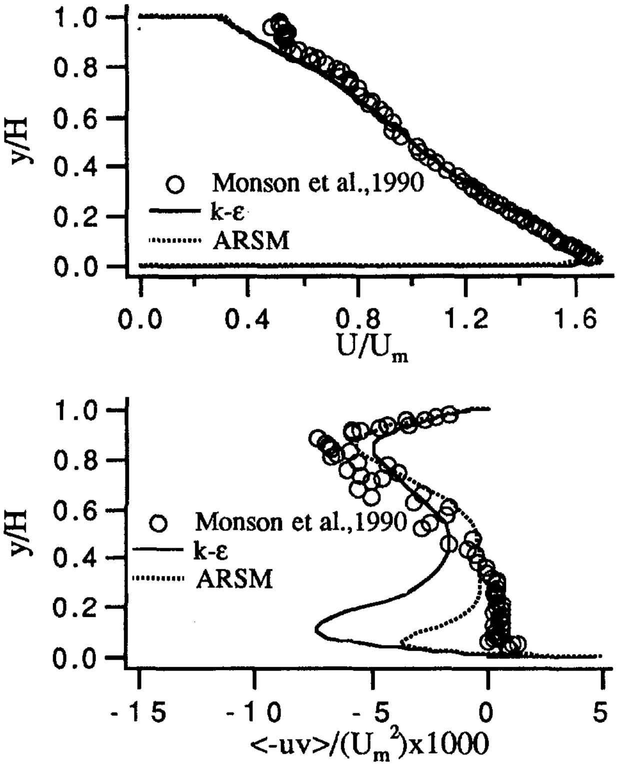

Fig. 2 Profiles of longitudinal mean velocity and turbulent shear stress at $\theta = 60$ deg; $y = 0$ is on inner (convex) wall, $y = H$ is on outer (concave) wall

Table 1 Design features of Penn State turbine facility

Hub tip ratio	0.7269
Tip radius	0.4582 m
Nozzle Guide Vane (tip)	
Number	23
Chord	0.1768 m
Spacing	0.1308 m
Turning angle	70 deg
Vane Re no.	$(3\text{-}4)\times10^5$ (inlet); $(9\text{-}10)\times10^5$ (outlet)
Vane exit design Mach number	0.27
Mass flow rate	11.05 kg/s
Rotor pitchline loading coefficient	1.88
($\Delta h_0/U_b^2$, U_b is blade speed at mid-span)	
Rotor turning angle	95.4 deg (tip), 125.7 deg (hub)
Stator-Rotor spacing	20% nozzle midspan axial chord

In the present study, the system of ARSM equations is derived from the RSM model of Launder et al. (1975). The Reynolds stress components is given by

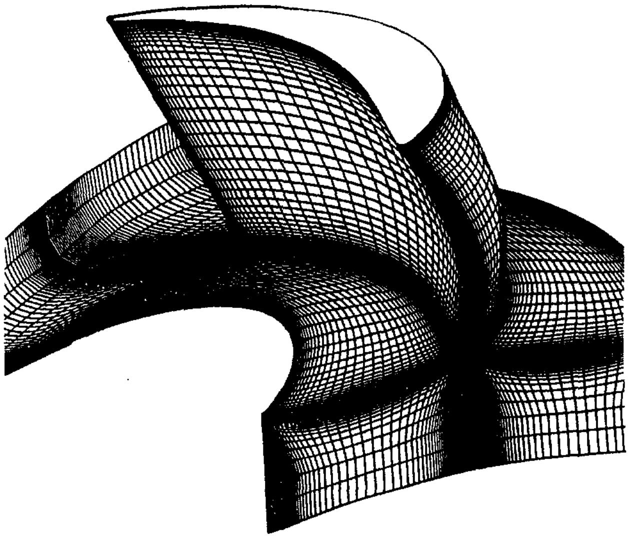

Fig. 3(*a*) Computational grid for the turbine nozzle

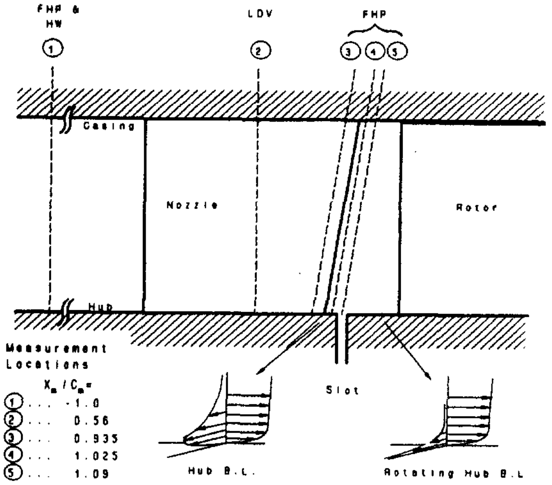

Fig. 3(*b*) Measurement locations for the turbine nozzle (FHP: five-hole probe; LDV: laser-Doppler velocimeter)

$$-\overline{u_iu_j} = -k[(P_{ij} - 2P_k\delta_{ij}/3)(1 - C_2)]/[P_k + \epsilon(C_1 - 1)] - 2/3\delta_{ij}k \quad (10)$$

Since the ARSM model is only valid for fully turbulent flows, the low-Reynolds-number $k-\epsilon$ model is used in the near-wall viscous layer. The matching location of the $k-\epsilon$ model and the ARSM is taken at $\mathrm{Re}_y = 350$ (i.e., $y^+ \approx 200$) where the value of f_μ in Chien's $k-\epsilon$ model is about 0.90, which is quite close to its fully turbulent value of 1.0. Also, for the three-dimensional nozzle flow, the ARSM model is not used in the midspan region (from about $H = 0.25$ to $H = 0.75$), since the viscous flow there is mostly attached two-dimensional boundary layer on both the suction and the pressure surfaces, which can be handled well by the low-Reynolds-number $k-\epsilon$ model. The matching function $f_{k-\epsilon}$ is given by

$$f_{k-\epsilon} = 1 - 0.5\{\tanh[20(\mathrm{Re}_y/350 - 1.0)] + 1\} \quad \text{if } \Delta R \leq 0.2(R_t - R_h) \quad (11a)$$

$$f_{k-\epsilon} = 0.5\left\{\tanh\left[20\left(\frac{\Delta R}{0.25(R_t - R_h)} - 1.0\right)\right] + 1\right\} \quad \text{if } \Delta R > 0.2(R_t - R_h) \quad (11b)$$

where ΔR is the radial distance to the closest endwall. The Reynolds stress tensor $-\overline{u_iu_j}$ in Eq. (4) is thus given by

$$-\overline{u_iu_j} = f_{k-\epsilon}(-\overline{u_iu_j}_{k-\epsilon}) + (1 - f_{k-\epsilon})(-\overline{u_iu_j}_{\mathrm{ARSM}}) \quad (12)$$

where $-\overline{u_iu_j}_{k-\epsilon}$ is obtained using the Boussinesq formulation (Eq. (4)) and $-\overline{u_iu_j}_{\mathrm{ARSM}}$ is obtained from Eq. (10). With these matching functions, the ARSM model is used only in the endwall region where the flow is fully turbulent. The low-Reynolds-number $k-\epsilon$ model is used away from the endwall regions and in the near-wall viscous layers.

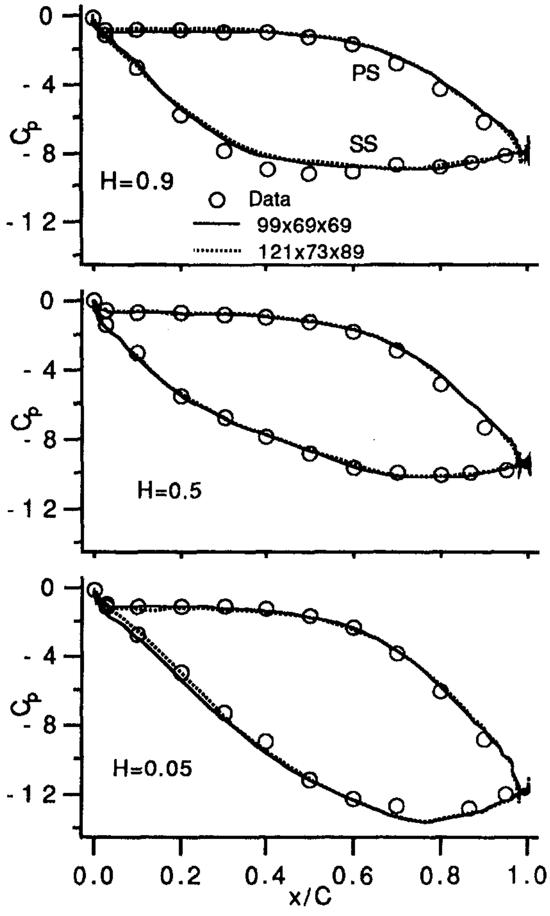

Fig. 4 Blade surface pressure predictions ($k-\epsilon$ model, 99 × 69 × 69 and 121 × 73 × 89 grids) at different radial locations

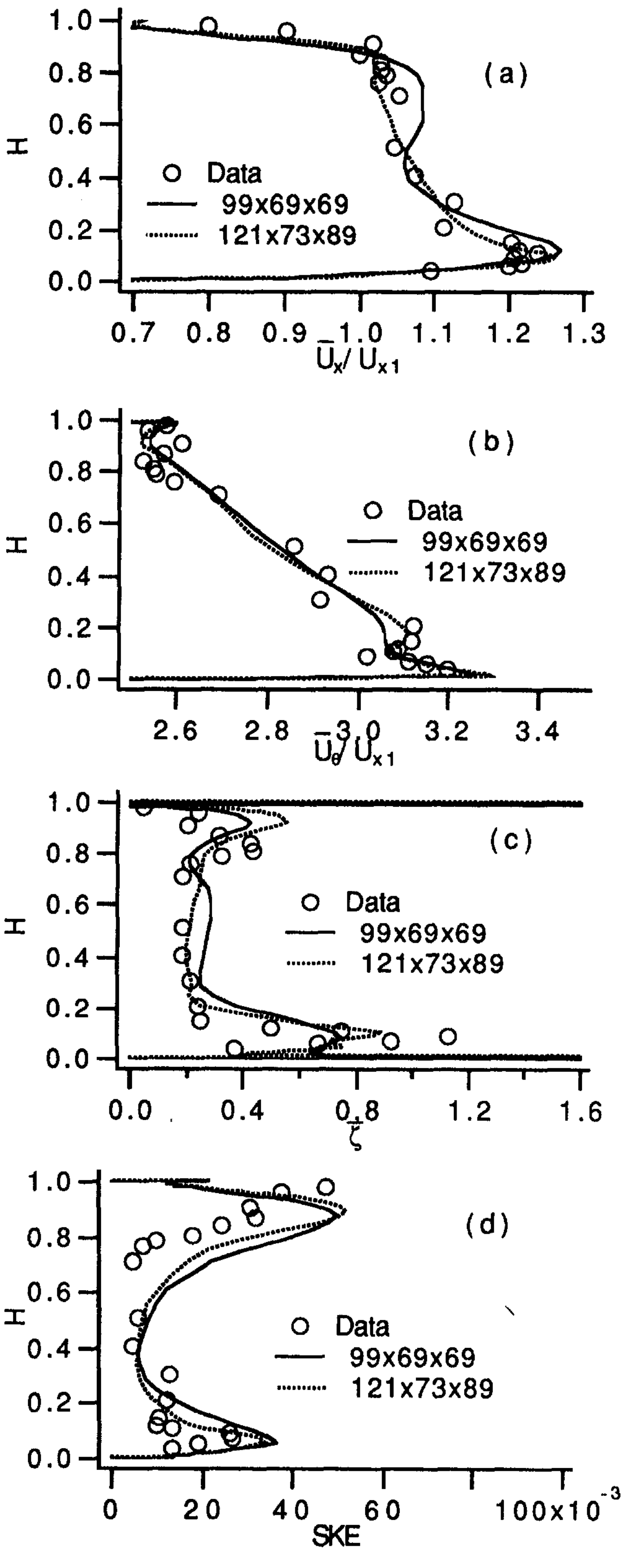

Fig. 5 Pitchwise-mass-averaged parameters (axial velocity, tangential velocity, total pressure loss coefficient and secondary kinetic energy) predicted using 121 × 73 × 89 and 99 × 69 × 69 grids with $k-\epsilon$ model

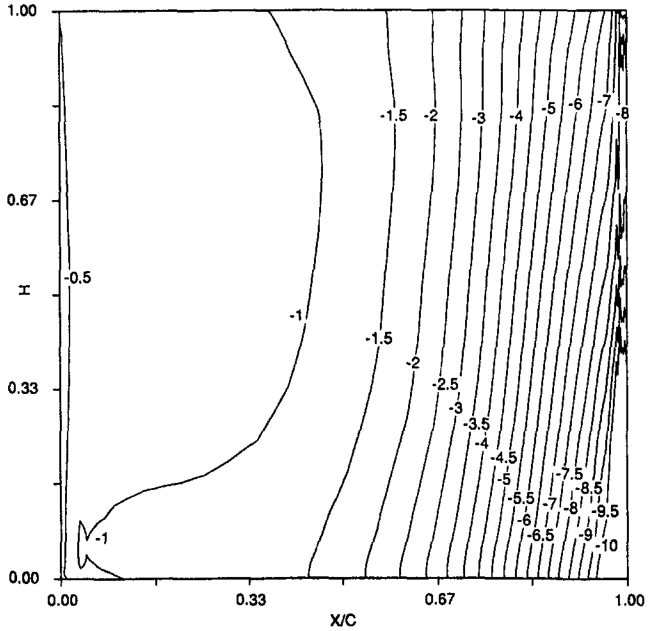

Computation by k-ε model

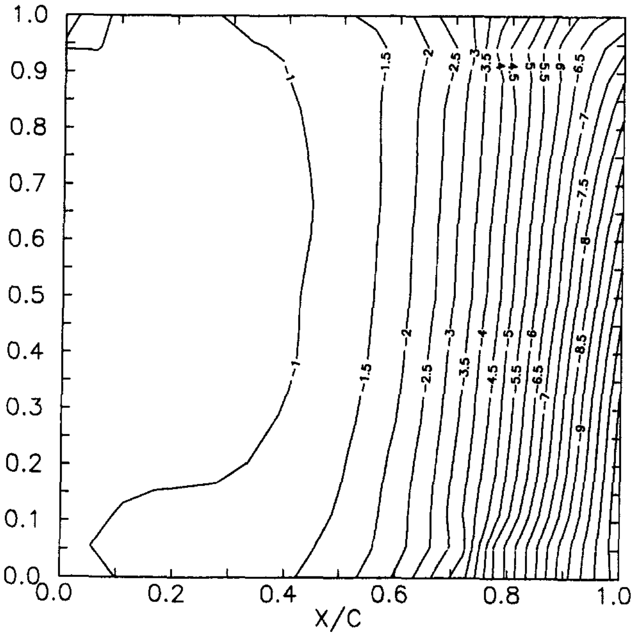

Measurement

Fig. 6(*a*) Nozzle pressure surface static pressure coefficient (C_p)

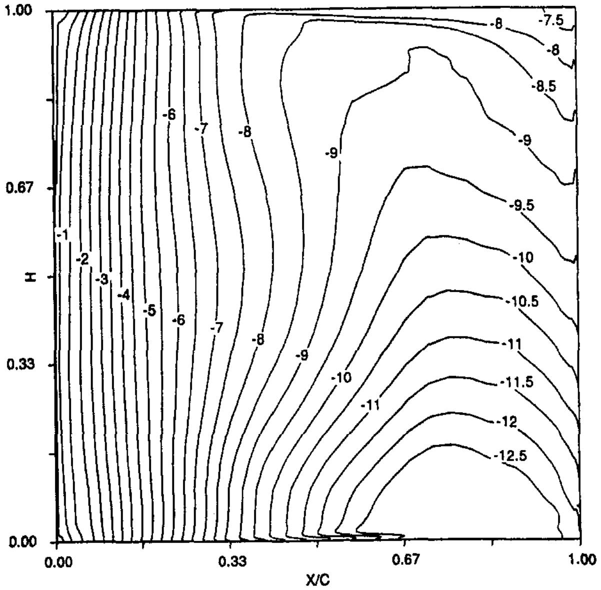

Computation by k-ε model

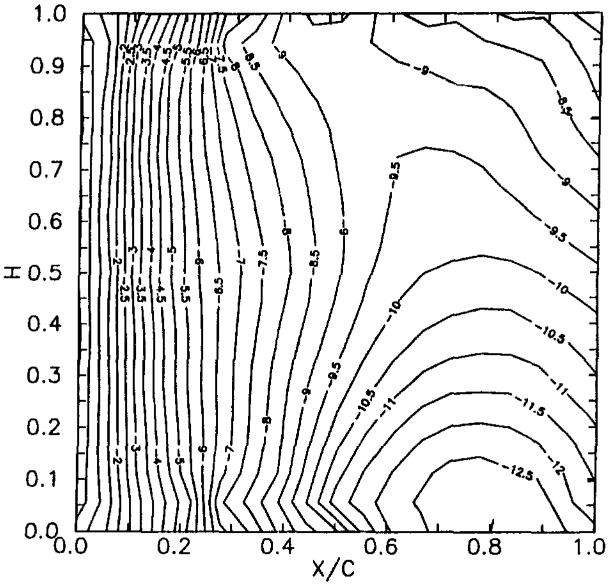

Measurement

Fig. 6(*b*) Nozzle suction surface static pressure coefficient (C_p)

When the ARSM is used, the P_k in Eqs. (7), (8), and (10) are calculated directly with the individual Reynolds stress components from the ARSM equations. Therefore, the turbulent kinetic energy level predicted by the $k-\epsilon$/ARSM model is different from that obtained from the $k-\epsilon$ model. The linear equations for the six Reynolds stress components (details in Kunz, 1991) are solved by Gaussian elimination. During the iteration, the Reynolds stress components are underrelaxed as

$$-\overline{u_i u_j} = (1-\gamma)(-\overline{u_i u_j})_{\text{old}} + \gamma(-\overline{u_i u_j})_{\text{new}} \quad (13)$$

where $\gamma = 0.3$ is used. The convergent $k-\epsilon$ solutions are used to initialize the $k-\epsilon$/ARSM computation.

Numerical Procedure. The three-dimensional Navier–Stokes code (denoted as RKCC, Kunz and Lakshminarayana, 1992) is used in the present research. The RKCC uses a standard four-stage Runge–Kutta scheme (Jameson et al., 1981). Following Jameson et al. (1981), the fourth-order artificial dissipation is included to damp high wave number errors, and the second-order artificial dissipation is used to improve the shock capturing. Since the convection terms in k and ϵ equations are discretized with second-order accurate central differences, artificial dissipation is needed in Eqs. (7) and (8) to prevent odd–even decoupling. It's observed that the inclusion of fourth-order artificial dissipations in Eqs. (7) and (8) does not result in convergent solution. Thus a second-order artificial dissipation term, which has stronger damping effect, is added to Eqs. (7) and (8) to enhance convergence. Anisotropic scaling of artificial dissipation terms is used. Multiplied by the square of the normalized local velocity, $(U/U_1)^2$, the smoothing in the equations is reduced to zero near the wall to avoid contamination of the solution by artificial dissipation. Local variable time-stepping is used to improve convergence.

Validation for a Strongly Curved Duct Flow. The numerical procedure was validated in Kunz and Lakshminarayana (1992). To validate the ability of the turbulence models in capturing the streamline curvature effects, this code is used to compute the flow in a turn-around duct for which detailed turbulence measurements were acquired by Monson et al. (1990). With a curvature parameter δ/R (δ = shear layer thickness, R = curvature radius) = $O(1)$, this flow represents one of the strongest streamline curvatures encountered in aerospace applications, such as in the powerhead of the Space Shuttle Main Engine (SSME). The Reynolds number (based on bulk velocity and duct height) is about one million. The geometry of the duct is shown in Fig. 1, where the contour of the mean streamlines computed by the ARSM model is plotted. The separation bubble downstream of the convex side is captured and is in agreement with the data.

Figure 2 shows the profiles of longitudinal velocity and the turbulent shear stress, i.e., U and $\langle -uv \rangle$ at θ = 60 deg (θ = 0 deg at bend entrance). The turbulent shear stress is almost completely "damped" out by the convex curvature effect and the large acceleration near the inner wall. The ARSM model captures the turbulence damping due to these effects much better than the $k-\epsilon$ model. The amplification of turbulence near the concave wall is also captured by the ARSM model. This comparison suggests the need for higher order turbulence models when curvature and anisotropic effects are present.

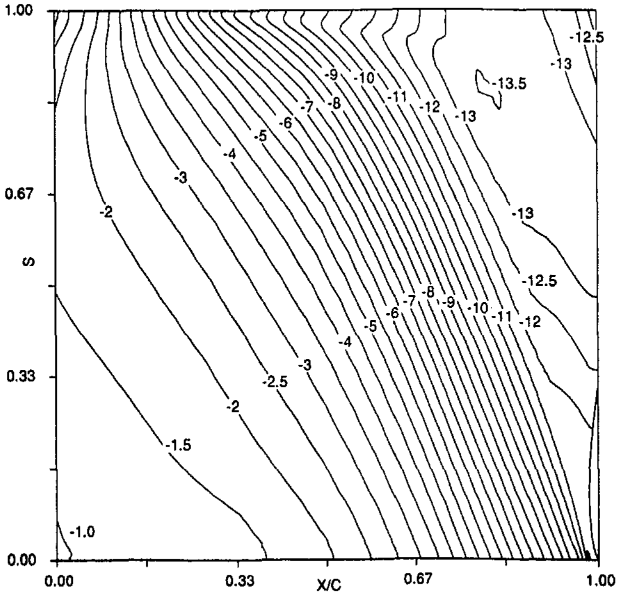

Computation by k-ε/ARSM model

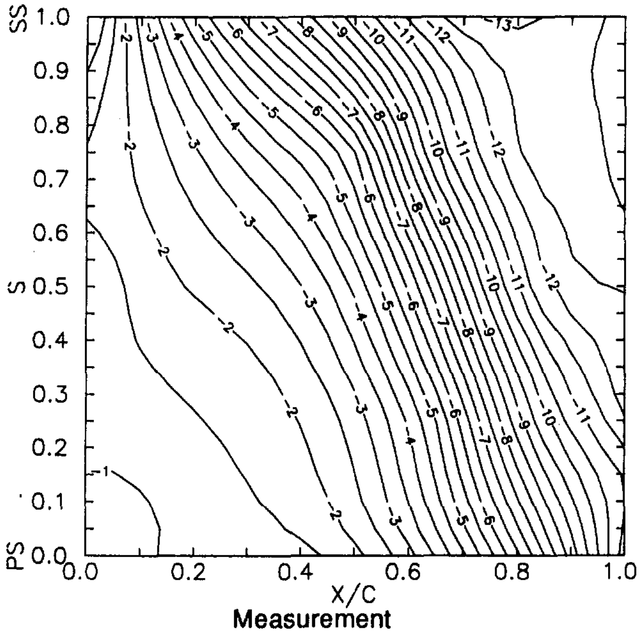

Measurement

Fig. 7 Nozzle hub wall static pressure coefficient (C_p)

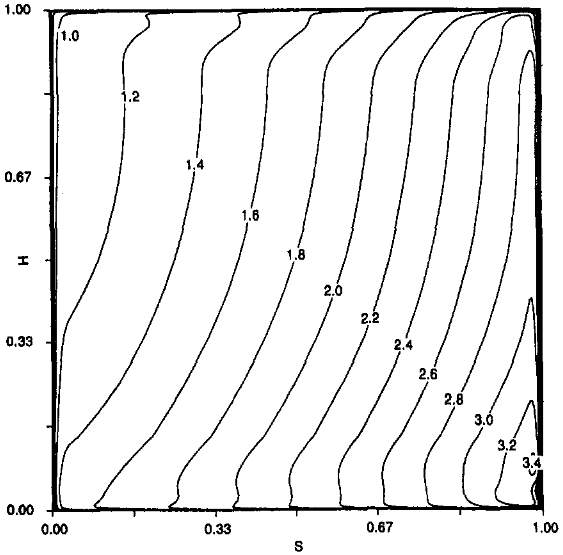

Computation by k-ε/ARSM model

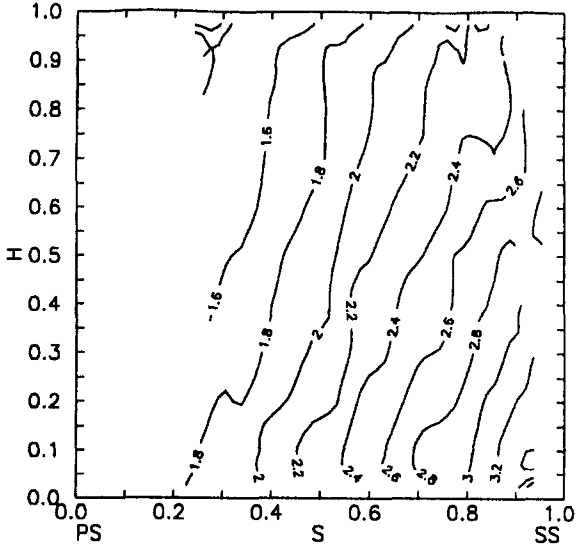

Measurement

Fig. 8(a) Total velocity (U/U_{x1}) contour at x_m/C_m = 0.56

Computation of Three-Dimensional Viscous Flow in a Turbine Nozzle

Brief Description of the Penn State Axial Turbine Nozzle. Zaccaria and Lakshminarayana (1995) and Zaccaria et al. (1996) carried out detailed measurements of the three-dimensional flow field through the nozzle passage of a single-stage turbine with an advanced axial turbine blading configuration designed by GE Aircraft Engine engineers. A brief summary of the nozzle and blade parameters is given in Table 1.

Grid-Sensitivity Study. Two sets of three-dimensional H mesh, with 99 × 69 × 69 and 121 × 73 × 89 (axial *pitchwise* spanwise) grid points, were generated by using IGB (the grid-generation software developed by Beach, 1990). The grid closely represents the actual geometry, including the "radial bowed" leading edge as shown in Fig. 3(a). Figure 3(b) (Zaccaria et al., 1993) shows the axial locations where comparisons

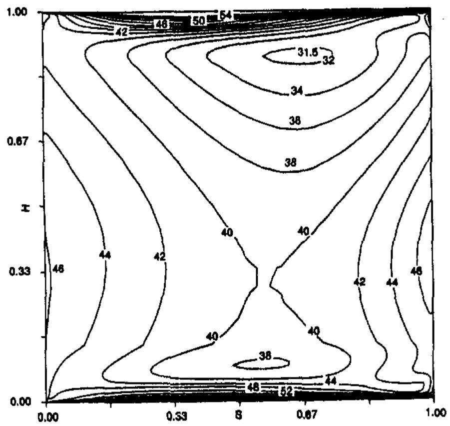

Computation by k-ε/ARSM model

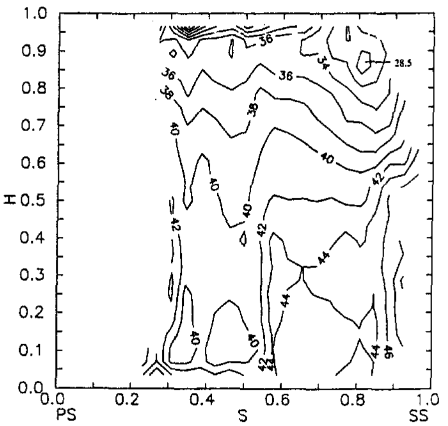

Measurement

Fig. 8(*b*) Yaw angle (α, in deg) contour at $x_m/C_m = 0.56$

will be made between predictions and measurements. The experiment was carried out in the nozzle passage of a single stage turbine with close nozzle–rotor spacing. In the computation, the nozzle is taken as an isolated nozzle passage without the downstream rotor. The computational inlet boundary is located at $x_m = -0.7C_m$ upstream of the nozzle leading edge. The outlet boundary is at $x_m = 1.7C_m$ downstream of the trailing edge.

The first grid spacing at both the hub and the casing for the 121 × 73 × 89 (fine) and 99 × 69 × 69 (medium) mesh is specified as 5×10^{-5} and 1×10^{-4} of the midspan chord length, which yields converged values of y^+ ranging from 1 to 2 and 2 to 4 along endwalls, respectively. The first grid spacing at the blade surface is specified as 8×10^{-5} and 1.5×10^{-4} of the midspan chord length for these two grids, respectively. In the axial direction, the fine mesh has 19 points upstream, 60 points inside, and 42 points downstream of the blade passage, respectively. The medium mesh (99 × 69 × 69) has 14 points upstream, 60 points inside, and 25 points downstream of the blade passage, respectively. The fine mesh has almost double the number of grids located in the secondary flow region compared to the medium mesh. The pitchwise resolution is almost the same for both grids.

Three sets of computational results will be presented below, obtained using the 99 × 69 × 69 grid with the $k-\epsilon$ model, and the 121 × 73 × 89 grid with the $k-\epsilon$ model and the $k-\epsilon$/ARSM, respectively. The computations in each case, by the two models, have been carried out with identical grids, boundary conditions, artificial dissipation rates, and convergence criteria. Three orders of magnitude drop in the rms density residual and two to two-and-a-half orders of magnitude drop in the rms turbulent kinetic energy residual are specified as convergence criteria. The error in mass flow rates at the inlet and the outlet is less than 0.15 percent of the inlet mass flow rate. The CPU time with the $k-\epsilon$/ARSM is about 50 percent more than that with the $k-\epsilon$ model.

The predicted blade static pressure coefficients (C_p) on suction and pressure surfaces at various radial locations, are shown in Fig. 4, for both the fine and medium grids using the $k-\epsilon$ model. The agreement with the data is very good at all locations, including that at 5 percent blade height ($H = 0.05$). The variation in C_p distribution at different radial sections is due to the spanwise differences in the aerodynamic loading, the three-dimensional blade geometry, and secondary flow effects near the hub and casing endwall regions. Figure 4 shows small discrepancy between the data and the predictions at about x/C =

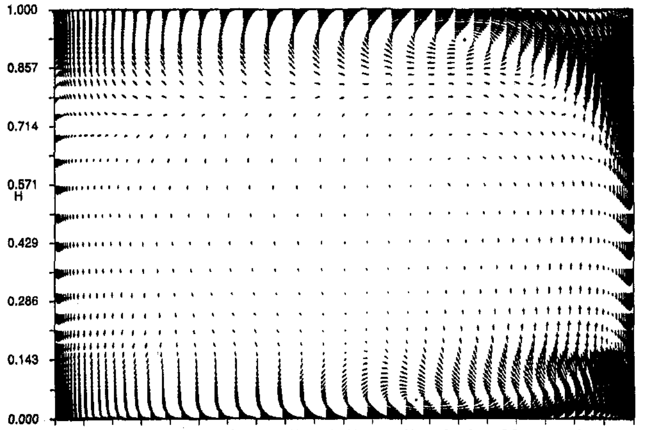

(a) Computation by k-ε model

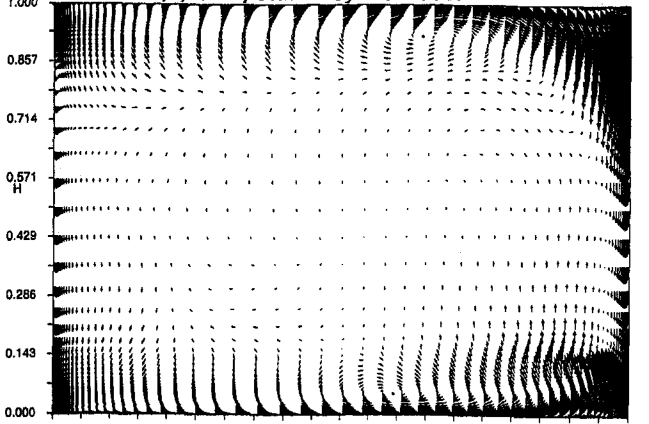

(b) Computation by k-ε/ARSM model

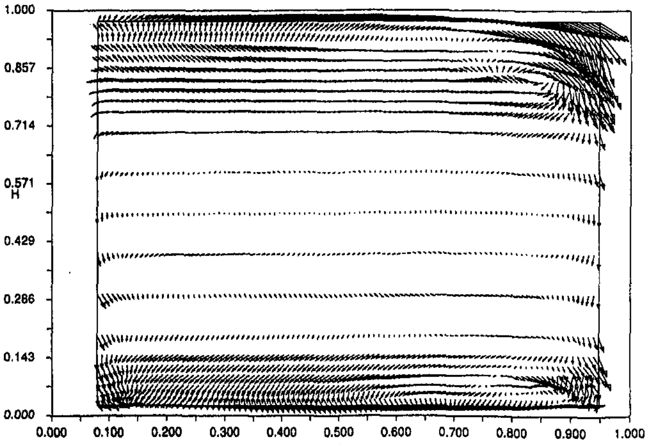

(c) Measurement

Fig. 9 Secondary velocity vectors at $x_m/C_m = 0.935$

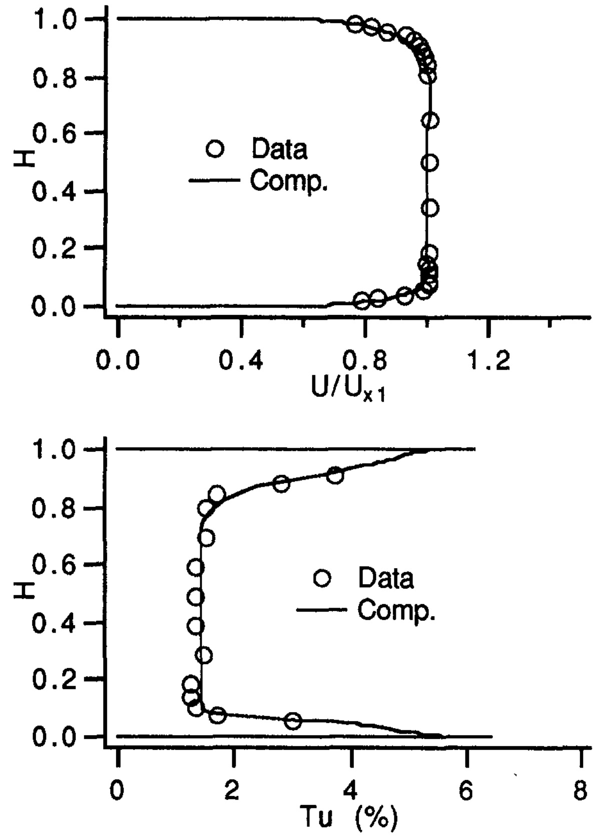

Fig. 10 Total velocity and turbulence intensity profile at x_m/C_m = −1

0.40 near the casing (H = 0.90), this may be attributed to the insufficient resolution of the suction-side leg of the horseshoe vortex and the secondary vortex. Zaccaria et al. (1996) also noted that the suction peak occurred earlier than the design, which was probably caused by the secondary flow effects.

The passage-mass-averaged properties (at x_m/C_m = 1.025) predicted with the $k-\epsilon$ model, using both the fine and medium grid, are presented in Fig. 5. The passage-averaged axial velocity (U_x) profile predicted by the $k-\epsilon$ model with the fine grid is in excellent agreement with the data. It is significantly better than the prediction with the medium grid. It can be seen from Fig. 5(b) that the large velocity gradient inside the secondary flow region is captured better by the fine grid, which has almost twice the resolution of the medium grid in that region, as noted above. The predicted total pressure loss (ζ) and secondary kinetic energy (SKE) obtained with the fine grid also show better agreement with the data (Figs. 5(c) and 5(d)). It is observed that, for almost all the properties, the fine grid predictions are in closer agreement with the data. Thus, only the predictions with the fine grid will be presented below.

Surface Static Pressure Distribution. The contours of static pressure coefficient on the blade pressure and suction surfaces are presented in Figs. 6(a) and 6(b), respectively. The flow is approximately two dimensional over the entire pressure surface as is demonstrated by nearly constant values of C_p in the spanwise direction. It is also clear that the flow accelerates mainly from the midchord to the trailing edge. On the suction surface, the flow remains two dimensional from the leading edge to about x/C = 0.45, with large flow acceleration. From x/C = 0.45 to the trailing edge, the flow is highly three dimensional with the radial pressure gradient on the same order of magnitude as the streamwise pressure gradient. The predictions using the $k-\epsilon$ model are in good agreement with the experiment. The blade surface C_p predictions using the $k-\epsilon$/ARSM model (not shown for brevity) are very close to those plotted in Fig. 6, since the turbine surface pressure distributions are largely determined by invicid mechanisms and are not sensitive to the turbulence models employed.

Calculated and measured contours of the hub wall static pressure coefficient are presented in Fig. 7. The C_p distribution on the hub computed by the $k-\epsilon$/ARSM model is generally in good agreement with the data. However, one significant difference is that the computation indicates that the minimum static pressure region on the hub endwall extends from the suction surface to about 20 percent blade spacing, while the experiment seems to suggest that the minimum static pressure region is confined to the area near the suction surface. The static pressure distributions on the casing (not shown) calculated by both models also show similar features. The present computation is consistent with the observation made by Langston et al. (1977) in a linear turbine cascade. They observed that the minimum static pressure is associated with separation of the endwall boundary layer. The $k-\epsilon$ solution (not shown) is close to the $k-\epsilon$/ARSM solution due to the reasons mentioned above.

Flow Field Inside the Passage (X_m/C_m = 0.56 and 0.935). Contours of total velocity and yaw angles at x_m/C_m = 0.56 are shown in Figs. 8(a) and 8(b), respectively. The experimental data was acquired with a laser–Doppler velocimeter (Zaccaria

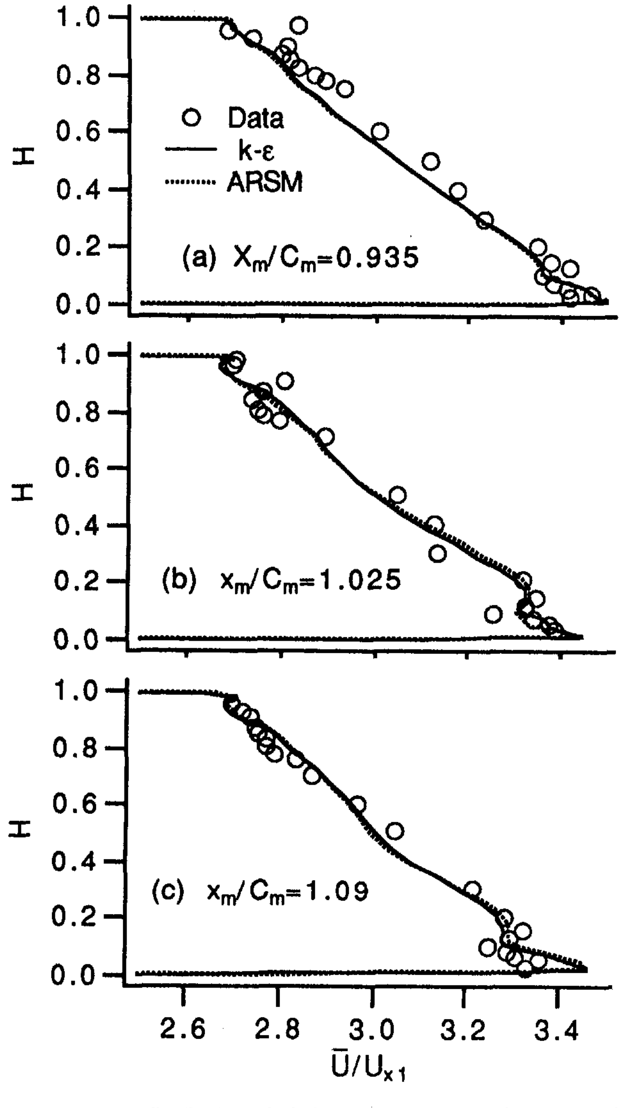

Fig. 11 Radial distribution of pitchwise-mass-averaged total velocity profile

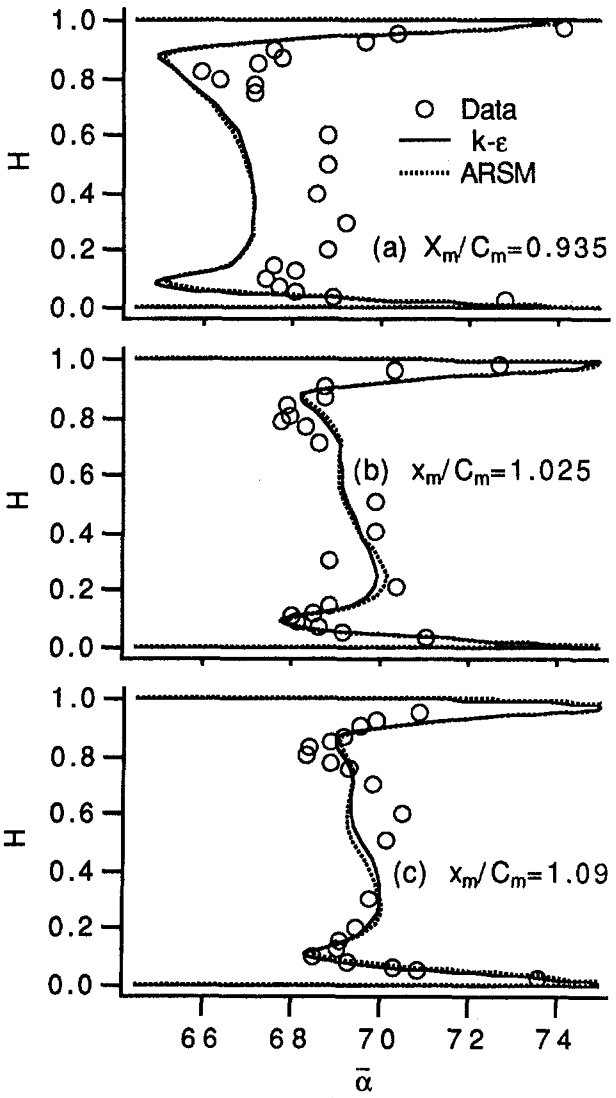

Fig. 12 Radial distribution of pitchwise-mass-averaged yaw angle ($\bar{\alpha}$, in deg) profiles

et al., 1996). Due to limitations caused by the shadow region, no data are available near the endwalls and blade surfaces. The computation (Fig. 8(*a*), contour levels from 0.2 to 3.6) by the zonal $k-\epsilon$/ARSM model shows very thin boundary layers near the hub and casing walls, but appreciable growth of the suction surface boundary layer. The velocity gradients are large in the blade-to-blade direction. It should be noted that the boundary layer thicknesses are about 8 percent blade height near the hub and 12 percent blade height near the casing at the computational inlet ($x_m/C_m = -0.70$). The endwall boundary layer thicknesses decrease inside the passage due to the large flow acceleration and the sweeping of the boundary layer fluid off the endwall into the secondary vortices. The computed turbulent kinetic energy level within endwall boundary layers is observed to decrease inside the passage, indicating a relaminarizing process predicted by the low-Reynolds-number $k-\epsilon$ model near the endwalls. The predictions of the velocity field are in very good agreement with the data, as shown in Fig. 8(*a*).

The data shown in Fig. 8(*b*) indicate that the flow angle near the midspan is close to the design turning angle (40 deg), and this is in agreement with the computation. The computation closely agrees with the measured data everywhere, except in the passage vortex core region near the corner formed by the casing and the suction surface. The computation seems to predict a turning angle about three degrees higher than the measurement near the secondary vortex core. It should be noted that the flow is undergoing rapid turning at this location; thus a small shift in the axial location (in measurement or computation) will result in large variation in the turning angle.

At the plane close to the trailing edge (x_m/C_m = 0.935), comparisons are made between the measured and computed secondary flow vectors. The secondary velocity is defined as,

$$\underline{U}_{\mathrm{sec}} = (\underline{U})_{\mathrm{actual}} - (\underline{U})_{\mathrm{design}} = \underline{r}U_r + \underline{n}U_n \tag{14}$$

where U_n is the velocity normal to the design flow direction ($\underline{U}_{\mathrm{design}}$) and only its projection on the axial plane is plotted. The $\underline{U}_{\mathrm{design}}$ is either the computed or the measured velocity vector. The flow angle of the design velocity $\underline{U}_{\mathrm{design}}$ at x_m/C_m = 0.935 is the flow angle at the midspan at the respective tangential position. The design flow angle is 70.0 deg for the downstream locations (x_m/C_m = 1.025 and 1.09).

The secondary vortices with clockwise rotation near the casing and anticlockwise rotation near the hub, respectively, are captured by both models (Figs. 9(*a*) and 9(*b*)). In the experiment (Fig. 9(*c*)), the secondary vortex near the casing is very strong, while the secondary vortex near the hub is much weaker and its core region is not easy to identify. The secondary flow patterns predicted by the $k-\epsilon$ model and the ARSM model are in

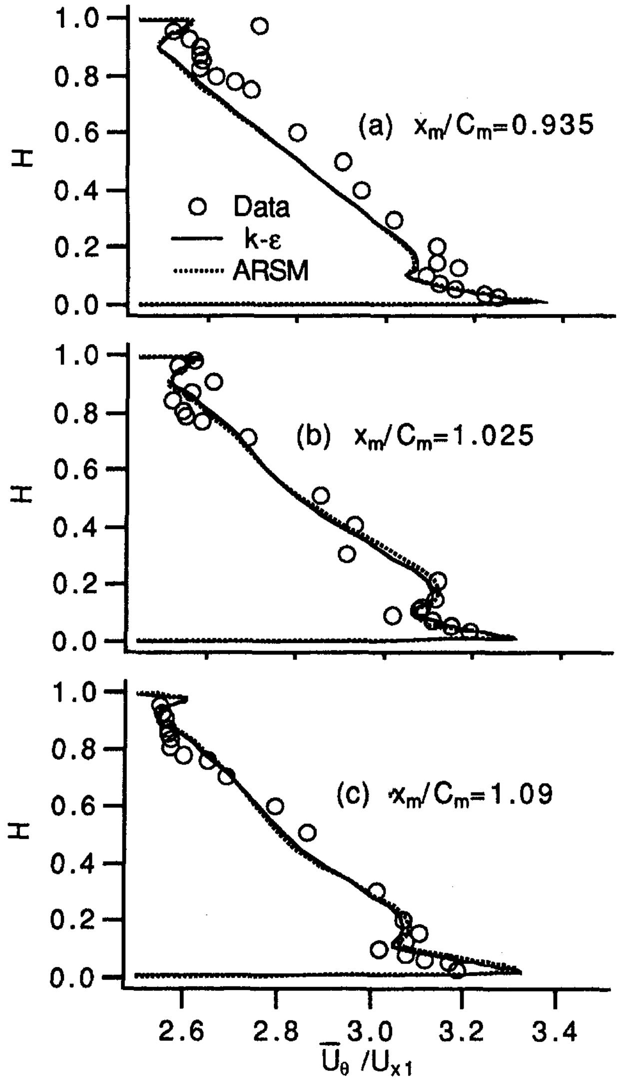

Fig. 13 Radial distribution of pitchwise-mass-averaged tangential velocity profile

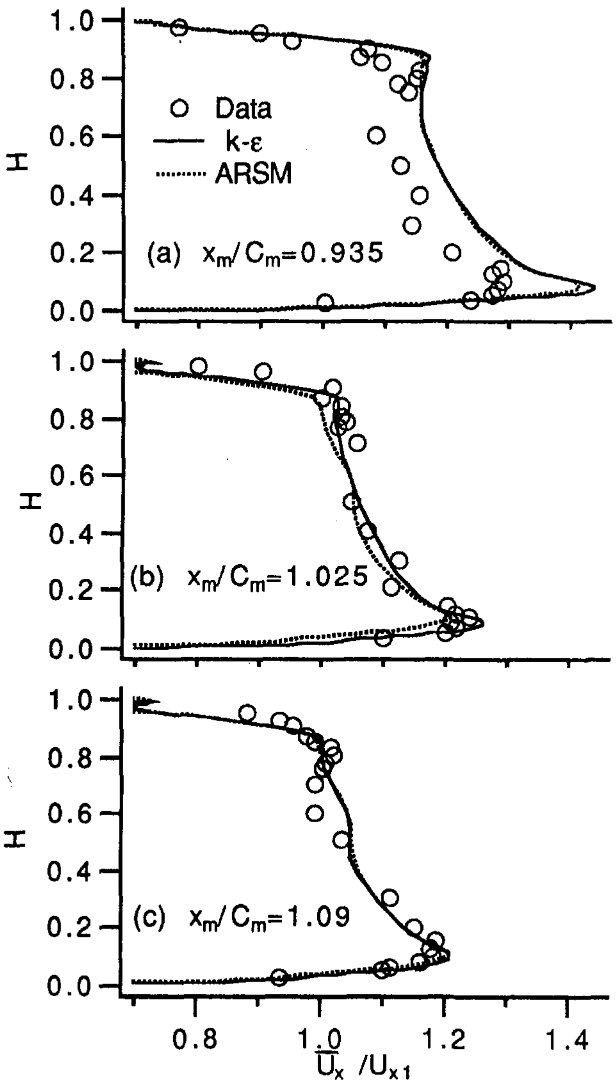

Fig. 14 Radial distribution of pitchwise-mass-averaged axial velocity profiles

general agreement with the data. Near the casing, the secondary vortices predicted by the two models have some difference. The secondary flow predicted by the $k-\epsilon$ model appears to be stronger than that predicted by the ARSM model. Neither the data nor the predictions indicate that the secondary flow has rolled up into a discrete, strong vortex, usually observed in cascades. The magnitudes of secondary flow velocities are captured reasonably well. One reason for the discrepancy between the data and predictions may be the downstream rotor influence, which is present in the experiment but absent from the computation. The discrepancy may also be due to the insufficient grid resolution (in axial, radial, and pitchwise directions) for the endwall boundary layer and secondary flow development. The prediction for the secondary flows near both walls might be improved further if finer grids could be used, as suggested by Fig. 5(*d*). The present grid does capture most features of the endwall flow quite well, as shown more clearly in the radial distribution of mass-averaged quantities presented later.

Near the hub, computations reveal more distinct secondary velocity vectors than the measurement. Again, the secondary flow predicted by the $k-\epsilon$ model appears to be stronger and closer to the suction side than that predicted by the ARSM model. The agreement between the computation and the experiment is qualitative in this region.

Radial Distribution of Pitchwise-Mass-Averaged Properties. Zaccaria et al. (1996) provided circumferentially mass-averaged profiles of mean flow variables (U, U_x, U_θ, α, ζ) at several axial locations from upstream of the nozzle to downstream of the nozzle. The computed values are compared with the data in this section. At about one chord length upstream of the nozzle, the measured endwall boundary layer thicknesses are about 8 percent blade height at the hub and 12 percent blade height at the casing. To match the inlet mean flow and turbulence quantities in the experiment, a two-dimensional channel flow is computed to provide the profiles for U_x, k, and ϵ, which are specified at the inlet in the three-dimensional computation. As can be seen from Fig. 10, the computational inlet velocity profile is in close agreement with the measurement, as is the turbulence intensity profile. During the computation, it is found that an accurate specification of inlet profiles for k and ϵ (i.e., profiles for k and ϵ in turbulent boundary layers on upper and lower walls, and the uniform profiles for k and ϵ in free-stream turbulence) is quite important. This is better than the common practice of specifying uniform k and ϵ profiles across the entire passage at the inlet. Accurate prediction of secondary flows depends on the accurate prediction of endwall boundary layer velocity profiles.

All the velocities shown here have been nondimensionalized by the midspan inlet axial velocity (U_{x1}). Pitchwise mass-aver-

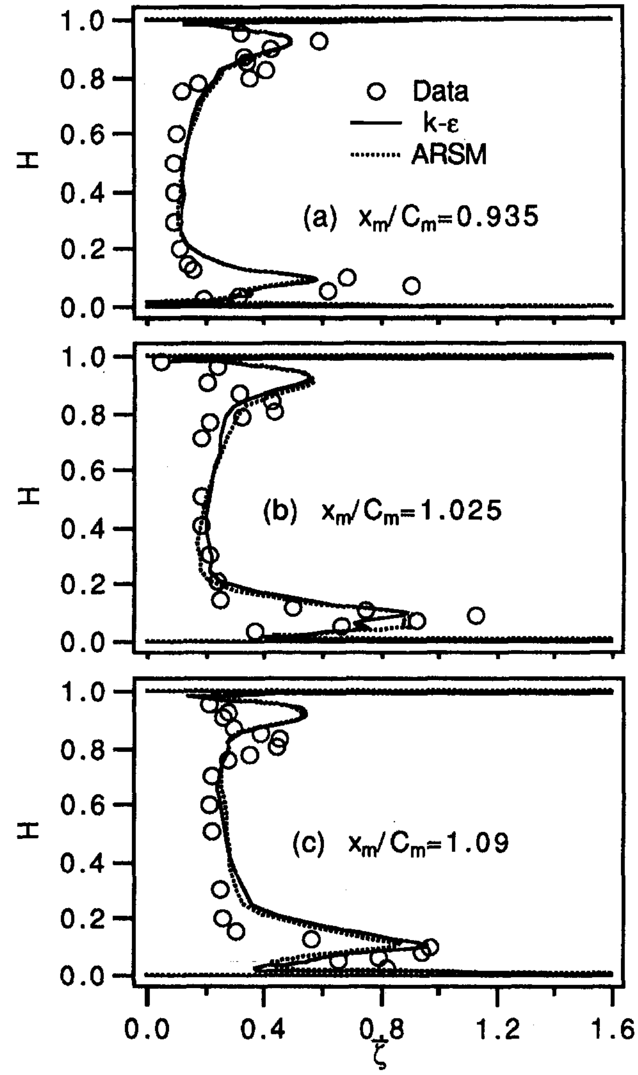

Fig. 15 Radial distribution of pitchwise-mass-averaged total pressure loss coefficient ($\bar{\zeta}$)

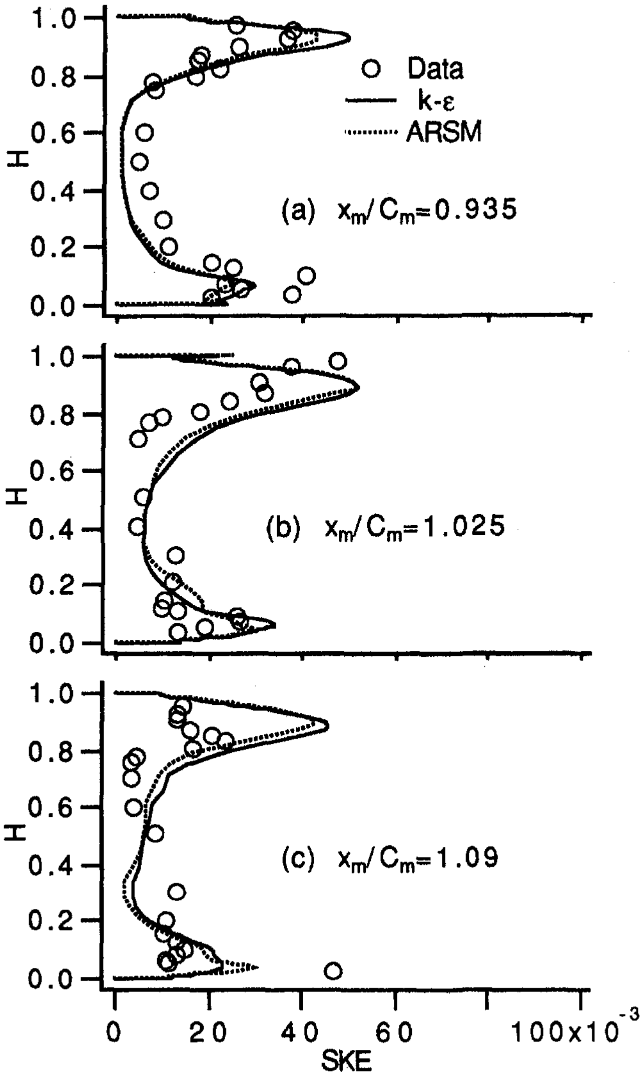

Fig. 16 Radial distribution of pitchwise-mass-averaged secondary kinetic energy coefficient (SKE)

aged total velocities (U) at three axial locations $x_m/C_m = 0.935$, $x_m/C_m = 1.025$, and $x_m/C_m = 1.09$ are plotted in Fig. 11. The velocity profile across the entire passage, including the endwall regions, is captured very well by both the turbulence models. The $k-\epsilon$ solution and the ARSM solution are very similar except for some slight difference in the secondary vortex region (Figs. 11).

At $x_m/C_m = 0.935$, the predicted value of flow angle (α) is about 67 degs, while the measured turning angle near the midspan (Fig. 12(a)) is about 69 deg. Near both endwalls, the predictions agree well with the data. The overturning and underturning angles caused by secondary vortices are captured well. Immediately downstream of the trailing edge (Fig. 12(b), $x_m/C_m = 1.025$), both the measurement and computations indicate highly three-dimensional character of the flow field, in which the design turning angle (70 deg) is observed only in a small region near $H = 0.3$. Once again, the predictions of the overturning and underturning from hub-to-tip agree very well with the data. The yaw angle profiles further downstream ($x_m/C_m = 1.09$), are plotted in Fig. 12(c). Near the hub, the calculations agree very well with the measurement, the prediction from the ARSM being similar to that from the $k-\epsilon$ model. However, from the midspan to the tip, there is some discrepancy between the predictions and the data. Specifically, the turning angle at $H = 0.6$ is underpredicted by about 1.5 deg, although the overturning near the casing has been captured well. As can be seen from Fig. 3(b), the downstream rotor is actually very close to the measurement plane at $x_m/C_m = 1.09$ near the tip. Thus, the discrepancy in this region may be attributed to the potential interaction between the stator and the rotor. The secondary flow and the wake will decay faster in the presence of favorable pressure gradient and unsteadiness caused by the downstream rotor. It is unlikely that the computation of an isolated nozzle passage, such as the present one, can capture the influence of the downstream rotor.

The passage-mass-averaged tangential velocity (U_θ) profiles at all three axial locations are shown in Fig. 13. Figure 14 shows the corresponding pitchwise-mass-averaged axial velocity (U_x) profiles. The U_θ profiles are similar to the U profiles shown in Fig. 11, but the U_x profiles are significantly different. As observed earlier, the difference in predictions by the two turbulence models is small. The difference between the predictions and data for U_θ and U_x at $x_m/C_m = 0.935$ is mainly due to the difference in the yaw angle, since the predicted total velocity is quite close to the measured value (Fig. 11(a)).

The pitchwise-mass-averaged total pressure loss coefficient (ζ) is presented in Fig. 15. At $x_m/C_m = 0.935$, the location of peak loss coefficient, near both the hub and the casing walls due to secondary flows, are captured well by the computation. However, the value of peak loss has been underpredicted. The

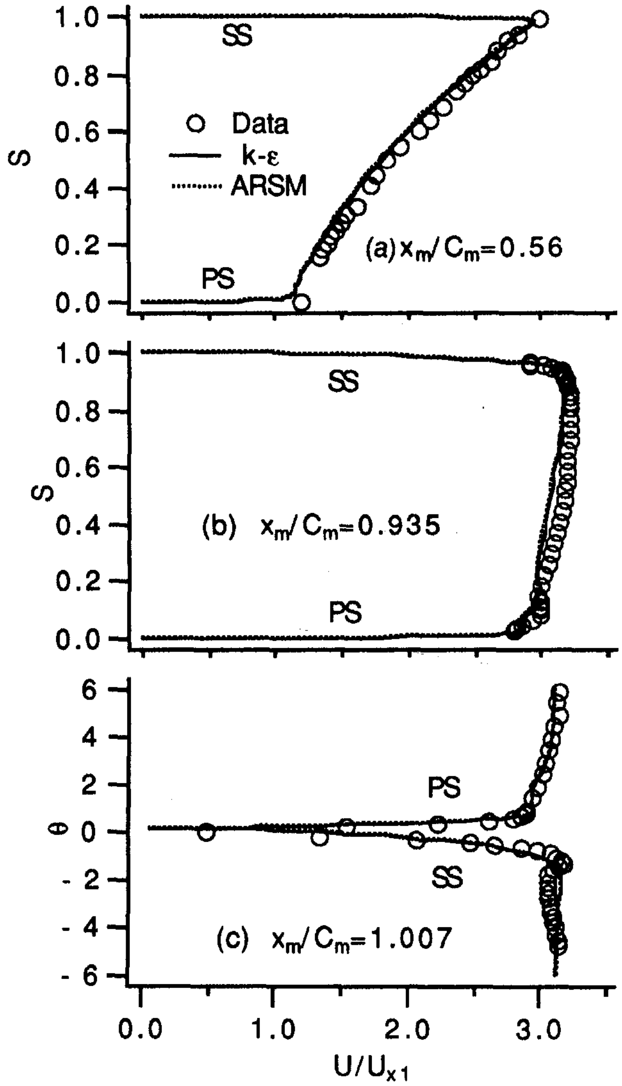

Fig. 17 Midspan total velocity profile

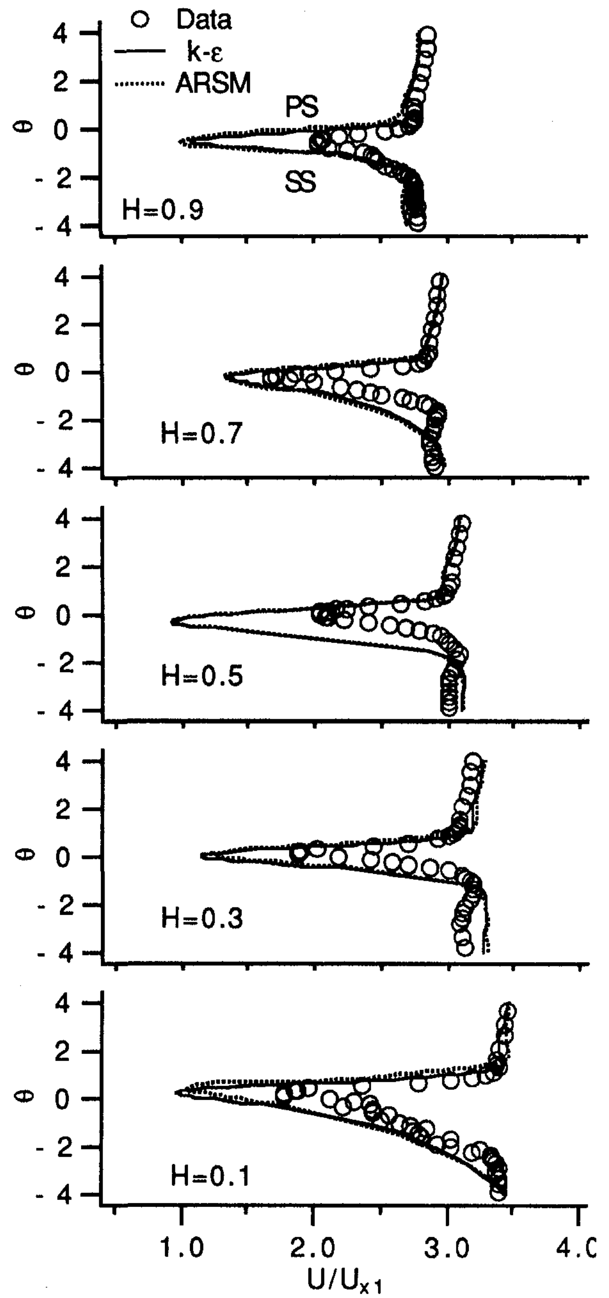

Fig. 18(*a*) Total velocity profile at $x_m/C_m = 1.025$ (pitchwise position θ is in deg, blade spacing is 15.65 deg)

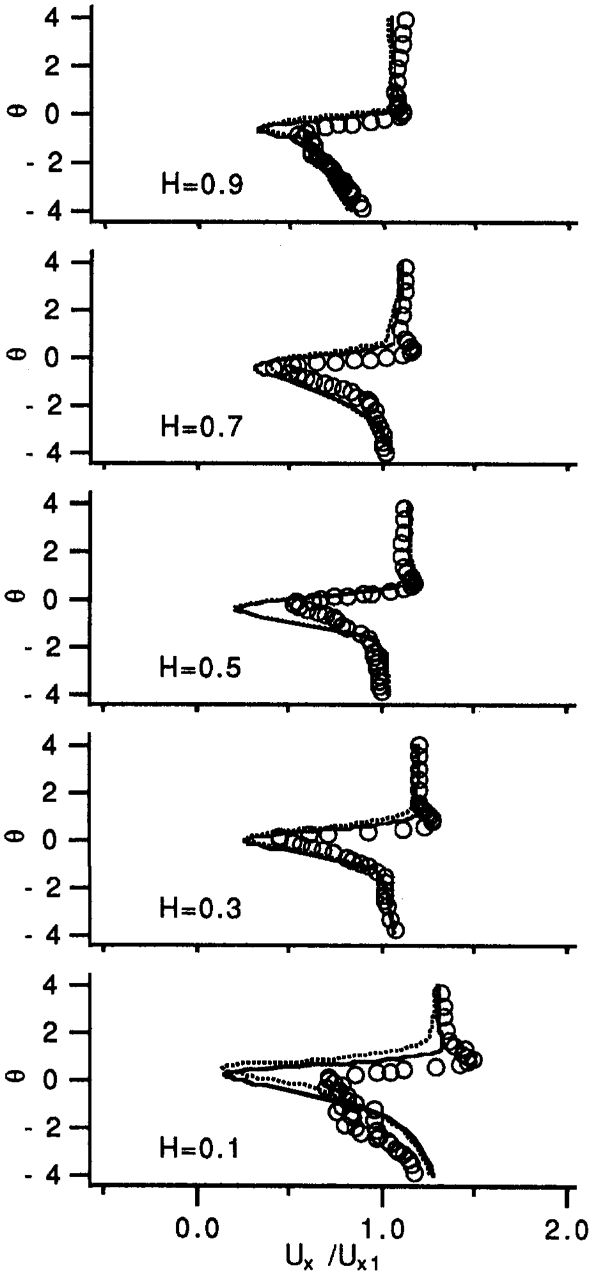

Fig. 18(*b*) Axial velocity profile at $x_m/C_m = 1.025$

predictions by the two models are very close. At $x_m/C_m = 1.025$, the total pressure loss at the midspan region is significantly higher than that at $x_m/C_m = 0.935$, due to the mixing loss associated with the wake. It is captured well by the computation. Farther downstream at $x_m/C_m = 1.09$ (Fig. 15(*c*)), the computations show an increase in losses across the entire passage and the profile loss near the midspan is slightly overpredicted. In both the measurement and the computation, the peak value of total pressure loss near the hub wall is higher than that near the casing wall. This is due to the large radial inward transport of the surface (particularly the suction surface) boundary layers (as seen in the secondary velocity vectors in Fig. 9) and the nozzle blade wake toward the hub.

The magnitude of secondary flow velocities and vortex strength can be assessed quantitatively through pitchwise-mass-averaged secondary kinetic energy coefficient (SKE), which is defined in the Nomenclature. As seen in Fig. 16(*a*), the predictions agree well with the data at $x_m/C_m = 0.935$. The ARSM model predicts a lower level of secondary kinetic energy than the $k-\epsilon$ model in both the hub and casing secondary flow regions (being consistent with the observation made in Fig. 9). This trend continues immediately downstream of the trailing edge ($x_m/C_m = 1.025$, Fig. 16(*b*)). However, it is found that both turbulence models predict larger inward radial velocity in the wake than the measurement, which result in overpredictions of the secondary kinetic energy near the casing. Further downstream at $x_m/C_m = 1.09$ (Fig. 16(*c*)), the trend is similar to those observed earlier. This may also be partially attributed to the influence of the downstream rotor in the experiment, which is absent in the computation.

As stated earlier, the ARSM model has been shown to capture the effects of streamline curvature (e.g., Fig. 2), rotation, and separation better than the $k-\epsilon$ model (Launder, 1989). It is well known that the isotropic $k-\epsilon$ model cannot predict any turbuence-driven secondary flow, which is caused by the differ-

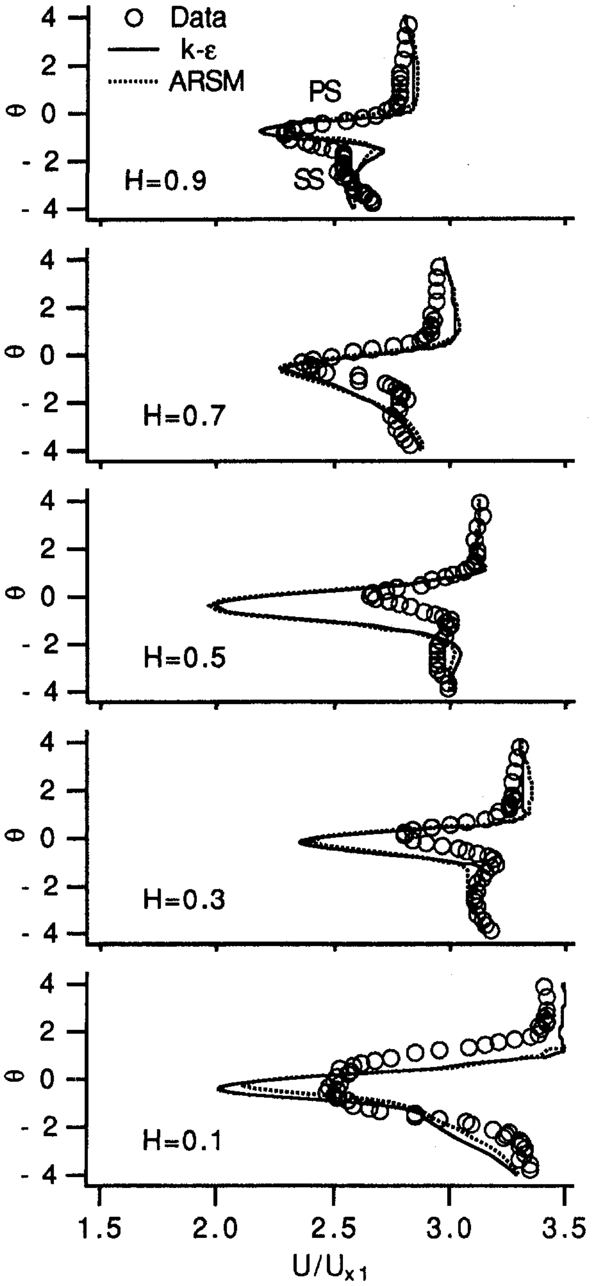

Fig. 19(*a*) Total velocity profile at $x_m/C_m = 1.09$

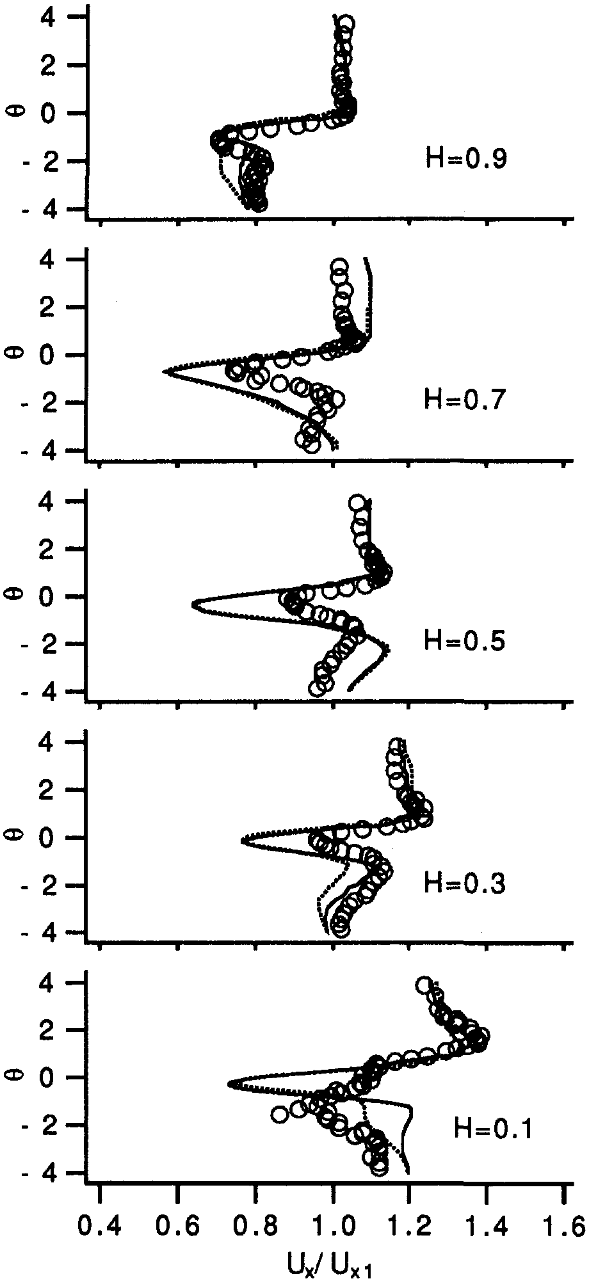

Fig. 19(*b*) Axial velocity profile at $x_m/C_m = 1.09$

ence in normal Reynolds stress, such as the secondary flow in a straight duct flow. The anisotropic ARSM model has been applied successfully (e.g., Demuren and Rodi, 1984) to compute turbulence-driven secondary motion in noncircular ducts. In the present investigation, the ARSM predictions are found to be close to those obtained by the $k-\epsilon$ model, although slight improvement has been observed for some secondary flow quantities, such as the secondary kinetic energy (Fig. 16). This is probably due to the fact that the secondary flow in turbine endwall regions are primarily driven by pressure gradients.

Midspan Velocity Profile and Radial Variation in Wake Profiles. The blade-to-blade distribution of the total velocity at midspan at $x_m/C_m = 0.56$ is shown in Fig. 17(*a*). The viscous effect is seen to be confined to the boundary layers on the suction and pressure surfaces and the mainstream velocity profile follows the usual inviscid trend. The prediction is in good agreement with the measurement. The two predictions are almost identical since the ARSM model is not used near the midspan, thus the turbulence model used there is the same (i.e., $k-\epsilon$ model). Figure 17(*b*) shows the midspan total velocity profile at $x_m/C_m = 0.935$. There is a slight discrepancy between the prediction and the data in the mainstream. The predicted velocity profile seems to follow the inviscid trend as observed at $x_m/C_m = 0.56$. The computed and measured midspan velocity profiles at $x_m/C_m = 1.007$ are plotted in Fig. 17(*c*). An excellent agreement has been observed for both sides of the wake, which indicates that surface boundary layers have been captured well by the computation. The slight overshoot in the measured velocity on the suction side boundary layer is not predicted.

The total and the axial velocity (U, U_x) profiles in the wake at five radial locations at $x_m/C_m = 1.025$ are plotted in Figs. 18(*a*) and 18(*b*), respectively. The tangential distance (θ) is in deg, and $\theta = 0$ is the wake center at the midspan. The positive values of θ are on the pressure side of the wake and the negative values of θ are on the suction side (blade spacing is 15.65 deg).

The wake profiles at $H = 0.1, 0.3, 0.5, 0.7$, and 0.9 have differing velocity defect and width. The wake width is largest near the hub due to the radial inward flows inside the wake. The predictions from the $k-\epsilon$ model and $k-\epsilon$/ARSM are quite close for all the locations. At midspan ($H = 0.50$), the two predictions are almost identical due to the reason mentioned above. It is seen that the predicted axial velocity profiles are in closer agreement with the data than the predicted total velocity profile.

The discrepancy between the prediction and the data is largest at the midspan region, where the wake width and depth are overpredicted. As observed at $x_m/C_m = 1.007$ (Fig. 17(c)), the $k-\epsilon$ model predicted an earlier transition on the suction side, resulting in an overprediction of the boundary layer thickness, which leads to an overprediction of the wake width, and also an overprediction of the total pressure loss as observed in Figs. 15(b) and 15(c). The flow is predicted to be laminar over the entire pressure surface, and this is in agreement with the data, hence the pressure side velocity profile is captured very well. Near the hub and the casing, the blade boundary layers are turbulent from the leading edge due to the existance of upstream endwall turbulent flows. Thus, unlike the midspan wake profiles, the wake profiles in the endwall regions are not influenced by transition. Indeed, the predictions of the wake profiles near both endwalls are in closer agreement with the data than those near the midspan.

The predictions of the wake profiles further downstream at $x_m/C_m = 1.09$ are presented in Fig. 19. The predictions are in reasonable agreement with the data. The wake profiles at midspan show the largest discrepancy due to the reason discussed above. The discrepancy may also be due to the following reasons:

1 The influence of the downstream rotor. As discussed earlier, the presence of the downstream rotor results in favorable pressure gradients and unsteadiness, which tend to cause faster decay of the wake. Indeed, as seen in Fig. 20(a), the predicted wake decay is in closer agreement with the data for an annular cascade due to Goldman and Seasholtz (1992) and the data for a nozzle with much larger rotor-stator spacing due to Dring et al. (1987). The wake correlation due to Raj and Lakshminarayana (1973) is also included in Fig. 20(a) for reference.

2 The error in measuring the wake profile with a five-hole probe. The measurement tends to underestimate (due to the spatial averaging procedure) the maximum velocity defect. As can be seen in Fig. 17(c), the measured value of the minimum velocity is about $0.5U_{x1}$, while the predicted value is very close to zero. The prediction is more feasible, as the velocity should be close to zero in this region. The error in measuring the width of the wake should be smaller than the error in measuring the maximum velocity defect. This is supported by the plot shown in Fig. 20(b), where the predicted wake width is in much better agreement with the data than the predicted maximum velocity defect (Fig. 20(a)).

The discrepancy between the predictions and the data may also be due to insufficient numerical resolution in the near wake region. However, a computation of the midspan flow with a very fine grid (161×99), using the two-dimensional version of the present code, did not result in improved prediction for the near wake profile. As a matter of fact, periodic vortex shedding at the blunt trailing edge is observed in the fine-grid two-dimensional solution. This is in contrast to the present solution in which two steady (or quasi-steady) vortices (with counterrotations) are formed in the near wake. Further research is needed to resolve this issue. The difference in the prediction may be due to different levels of numerical diffusion associated with the two grids. It is also possible that the flow is unsteady in the near-wake region and hence a time-accurate computation may be needed to capture the near wake accurately.

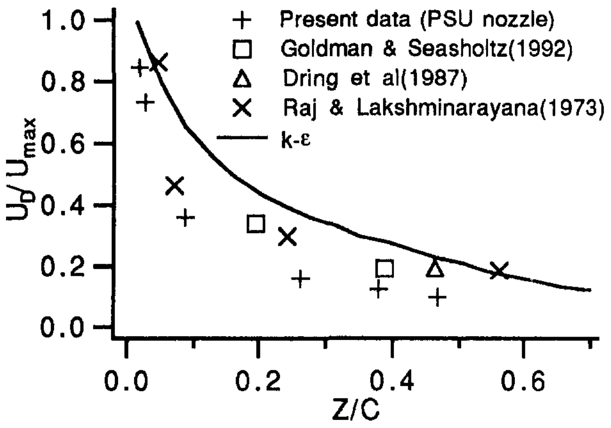

a) Decay of midspan total velocity defect with streamwise distance

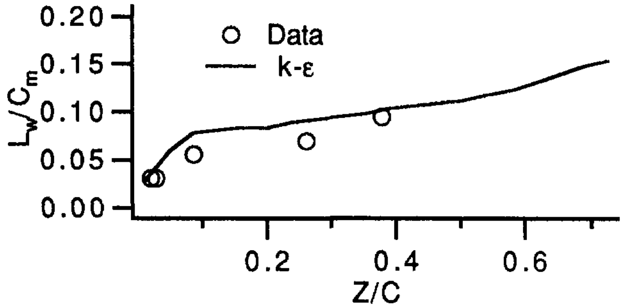

b) Variation of semi-wake width

Fig. 20 Predicted and measured midspan wake decay

Concluding Remarks

The Navier–Stokes prediction of the three-dimensional viscous flow through an annular turbine nozzle passage is presented in this paper. Comparison between the computation and the experimental data shows that most features of the vortex-dominated endwall flow in the annular turbine nozzle have been captured accurately by the numerical procedure. The passage-mass-averaged properties, particularly the yaw angle and velocity profiles, are captured very well by the present numerical computation. It is observed that the predictions by the anisotropic ARSM model are close to those by the isotropic $k-\epsilon$ model for the mean flow properties, although slight improvement in the prediction of some secondary flow quantities (e.g., the secondary kinetic energy) has been obtained by the ARSM model. The turbine secondary flows are primarily driven by pressure gradients and the effects of the anisotropy of turbulence appear to be insignificant. This becomes important when the secondary flow rolls up into a distinct vortex. Its dissipation and diffusion may only be captured by the ARSM and other anisotropic turbulence models (e.g., Fig. 1, Lakshminarayana, 1991).

The wake profiles inside the endwall boundary layers are predicted better than those near the midspan. The width and depth of the wake at the midspan are overpredicted due to a premature transition predicted by the $k-\epsilon$ model on the blade suction surface in the presence of low free-stream turbulence. The discrepancy in the wake profile is also due to the downstream rotor influence and the possible error in experimental measurements.

Acknowledgments

This work was supported by the U.S. National Aeronautics and Space Administration through contract NAS 8-38867 monitored by Lisa Griffin of Marshall Space Flight Center (MSFC). The authors wish to acknowledge NASA for providing supercomputing resources at NASA MSFC and NASA Ames Research Center. The authors wish to thank the National Science Foundation for travel grant (NSF Grant INT 90-15984), which enabled interaction with the turbulence group at Ecole Centrale de Lyon (France).

References

Arnone, A., Liou, M.-S., and Povinelli, L. A., 1993, "Multigrid Calculation of Three-Dimensional Viscous Cascade Flows," *Journal of Propulsion and Power,* Vol. 9, No. 4, pp. 605–614.

Beach, T. A., 1990, "An Interactive Grid Generation Procedure for Axial and Radial Flow Turbomachinery," AIAA Paper No. 90-0344.

Chien, K. Y., 1982, "Prediction of Channel and Boundary-Layer Flows With a Low-Reynolds-Number Turbulence Model," *AIAA Journal,* Vol. 20, No. 1.

Choi, D., and Knight, C. J., 1991, "Aerodynamic and Heat Transfer Analysis for a Low Aspect Ratio Turbine Using a 3D Navier–Stokes Code," AIAA Paper No. 91-2240.

Cleak, J. G. E., and Gregory-Smith, D. G., 1992, "Turbulence Modeling for Secondary Flow Prediction in a Turbine Cascade," ASME JOURNAL OF TURBOMACHINERY, Vol. 114, pp. 590–598.

Demuren, A. O., and Rodi, W., 1984, "Calculation of Turbulence-Driven Secondary Motion in Non-circular Ducts," *J. Fluid Mech.,* Vol. 140, pp. 189–222.

Dorney, D. J., and Davis, R. L., 1992, "Navier–Stokes Analysis of Turbine Blade Heat Transfer and Performance," ASME JOURNAL OF TURBOMACHINERY, Vol. 114, pp. 479–485.

Dring, R. P., Joslyn, H. D., and Blair, M. F., 1987, "The Effects of Inlet Turbulence and Rotor/Stator Interactions on the Aerodynamics and Heat Transfer of a Large-Scale Rotating Turbine Model," NASA-CR-179469, Vol. 4.

Goldman, L. J., and Seasholtz, R. G., 1992, "Laser Anemometer Measurements and Computations in an Annular Cascade of High Turning Core Turbine Vanes," NASA TP 3252.

Gregory-Smith, D. G., and Cleak, J. G. E., 1992, "Secondary Flow Measurements in a Turbine Cascade With High Inlet Turbulence," ASME JOURNAL OF TURBOMACHINERY, Vol. 114, pp. 173–183.

Hah, C., 1989, "Numerical Study of Three-Dimensional Flow and Heat Transfer Near the Endwall of a Turbine Blade Row," AIAA Paper No. 89-1689.

Ho, Y.-H., and Lakshminarayana, B., 1996, "Computational Modeling of Three-Dimensional Endwall Flow Through a Turbine Rotor Cascade With Strong Secondary Flows," ASME JOURNAL OF TURBOMACHINERY, Vol. 118, pp. 250–261.

Jameson, A., Schmidt, W., and Turkel, E., 1981, "Numerical Solutions of Euler Equations by Finite Volume Methods Using Runge–Kutta Time-Stepping Schemes," AIAA Paper No. 81-1259.

Kunz, R. F., 1991, "Explicit Navier–Stokes Computation of Turbomachinery Flows," Ph.D. thesis, Penn State University.

Kunz, R. F., and Lakshminarayana, B., 1992, "Three-Dimensional Navier–Stokes Computation of Turbomachinery Flows Using an Explicit Numerical Procudure and a Coupled $k-\epsilon$ Turbulence Model," ASME JOURNAL OF TURBOMACHINERY, Vol. 114, p. 627.

Lakshminarayana, B., 1991, "An Assessment of Computational Fluid Dynamic Techniques in the Analysis and Design of Turbomachinery—The 1990 Freeman Scholar Lecture," ASME *Journal of Fluids Engineering,* Vol. 113, p. 315.

Langston, L. S., Nice, M. L., and Hooper, R. M., 1977, "Three-Dimensional Flow Within a Turbine Cascade Passage," ASME *Journal of Engineering for Power,* Vol. 99, No. 1, pp. 21–28.

Launder, B. E., 1989, "Second Moment Closure: Present . . . and Future?" *International Journal of Heat and Fluid Flow,* Vol. 10, No. 4, pp. 282–299.

Launder, B. E., Reece, G. J., and Rodi, W., 1975, "Progress in the Development of a Reynolds-Stress Turbulence Closure," *J. Fluid Mech.,* Vol. 68, p. 537.

Monson, D. J., Seegmiller, H. L., McConnaughey, P. K., and Chen, Y. S., 1990, "Comparison of Experiment With Calculations Using Curvature-Corrected Zero and Two Equation Turbulence Models for a Two-Dimensional U-Duct," AIAA Paper No. 90-1484.

Moore, J., Shaffer, D. M., and Moore, J. G., 1987, "Reynolds Stresses and Dissipation Mechanisms Downstream of a Turbine Cascade," ASME JOURNAL OF TURBOMACHINERY, Vol. 109, pp. 258–267.

Rodi, W., 1976, "A New Algebraic Relation for Calculating Reynolds Stress," *ZAMM,* Vol. 56, p. 219.

Raj, R., and Lakshminarayana, B., 1973, "Characteristics of the Wake Behind a Cascade of Airfoils," *J. Fluid Mech.,* Vol. 61, pp. 707–730.

Sieverding, C. H., 1985, "Recent Progress in the Understanding of Basic Aspects of Secondary Flows in Turbine Blade Passages," ASME *Journal of Engineering for Gas Turbines and Power,* Vol. 107, pp. 248–257.

Zaccaria, M., Ristic, D., and Lakshminarayana, B., 1996, "Three-Dimensional Flow Field in a Turbine Nozzle Passage," *J. of Propulsion and Power,* Vol. 12, pp. 974–983.

Zaccaria, M., and Lakshminarayana, B., 1995, "Investigation of Three-Dimensional Turbine Flow Field at the Exit of the Nozzle," *J. of Propulsion and Power,* Vol. 11, No. 1, p. 55.

Development of Blade Profiles for Low-Pressure Turbine Applications

E. M. Curtis

H. P. Hodson

M. R. Banieghbal

J. D. Denton

R. J. Howell

Whittle Laboratory,
University of Cambridge,
Cambridge, United Kingdom

N. W. Harvey

Rolls-Royce plc,
Derby, United Kingdom

This paper describes a program of work, largely experimental, which was undertaken with the objective of developing an improved blade profile for the low-pressure turbine in aero-engine applications. Preliminary experiments were conducted using a novel technique. An existing cascade of datum blades was modified to enable the pressure distribution on the suction surface of one of the blades to be altered. Various means, such as shaped inserts, an adjustable flap at the trailing edge, and changing stagger were employed to change the geometry of the passage. These experiments provided boundary layer and lift data for a wide range of suction surface pressure distributions. The data were then used as a guide for the development of new blade profiles. The new blade profiles were then investigated in a low-speed cascade that included a set of moving bars upstream of the cascade of blades to simulate the effect of the incoming wakes from the previous blade row in a multistage turbine environment. Results are presented for two improved profiles that are compared with a datum representative of current practice. The experimental results include loss measurements by wake traverse, surface pressure distributions, and boundary layer measurements. The cascades were operated over a Reynolds number range from 0.7×10^5 to 4.0×10^5. The first profile is a "laminar flow" design that was intended to improve the efficiency at the same loading as the datum. The other is a more highly loaded blade profile intended to permit a reduction in blade numbers. The more highly loaded profile is the most promising candidate for inclusion in future designs. It enables blade numbers to be reduced by 20 percent, without incurring any efficiency penalty. The results also indicate that unsteady effects must be taken into consideration when selecting a blade profile for the low-pressure turbine.

Introduction

The low-pressure turbine of a large, high-bypass ratio fan engine provides the power to drive the fan, and often some compressor stages as well. It is constrained to operate at a low rotational speed equal to the fan rpm (unless a gearbox is provided) and this requires several stages, typically about five, and a large diameter. The resulting turbine is heavy, perhaps around one-third of total engine weight, and expensive. The goal of the research program, part of which is the subject of this paper, was to attempt to improve on the blading currently used in the low-pressure turbine.

There are three factors to take into account in assessing different blade profiles in this context. These are the loss, the weight, and the cost.

In general, the "best" blade will represent the optimum balance between these factors. In this paper, the "cost" of each choice is expressed in terms of bladerow efficiency. To simplify the design problem, all the blade profiles in this program were designed for the same inlet and outlet flow angles. In other words, they would all have the same stage loading if used in a turbine. Under these circumstances, the blade loading coefficient is directly proportional to the pitch/chord ratio of the bladerow.

The profile for which improvements were sought was a "thin-solid" profile, and the other blades developed in the program were also designed as thin profiles. All profiles were to have the same cross-sectional area as the datum profile and so have the same weight per blade, ignoring any differences in the weight of the shrouds.

The blading in the low-pressure turbine has a large aspect ratio, typically about 5:1. Secondary flows are therefore not a very important feature of the flow. For this reason, the search for improvements concentrated on the blade-to-blade flow and all the experiments were conducted using a rectilinear cascade.

Figure 1 shows an estimated breakdown of the loss for the datum blade. The data is taken from Banieghbal et al. (1995). The two-dimensional loss is subdivided into four components using the control volume analysis described by Denton (1993). It is evident from Fig. 1 that the largest loss arises from the suction side boundary layer. Consequently, the main thrust of the present work was directed at attempting to improve the suction surface flow. The trailing edge is also a significant source of loss and would be improved if trailing edge thickness were reduced or if the shape of the trailing edge were altered. In the work presented here, each profile had the same trailing edge thickness ($\frac{1}{75}$ chord) and shape (semicircular). Mechanical integrity prevents the use of very thin trailing edges but an alternative shape such as an elliptical trailing edge may reduce the loss (Sutton, 1990).

At the Reynolds numbers involved in low-pressure turbines, the flow on the suction surface is likely to remain laminar over a significant fraction of the surface and to undergo transition via a laminar separation bubble shortly after peak suction. Unsteady effects arising from upstream wakes are likely to affect the transition process and the losses. In general the increased turbulence from wakes might be expected to increase losses. A simple theoretical treatment (Hodson et al., 1993) provides a prediction method based on evaluating the increase in boundary layer momentum thickness due to wake-induced transition in attached boundary layers. More recent experimental investigations

---

Contributed by the International Gas Turbine Institute and presented at the 41st International Gas Turbine and Aeroengine Congress and Exhibition, Birmingham, United Kingdom, June 10–13, 1996. Manuscript received at ASME Headquarters February 1996. Paper No. 96-GT-358. Associate Technical Editor: J. N. Shinn.

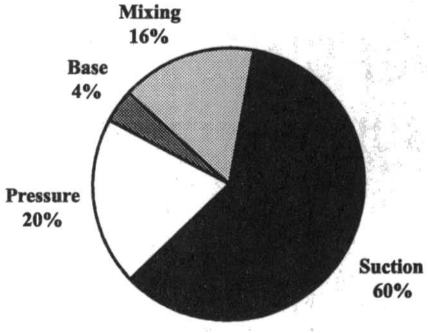

Fig. 1 Estimated loss breakdown for datum blade

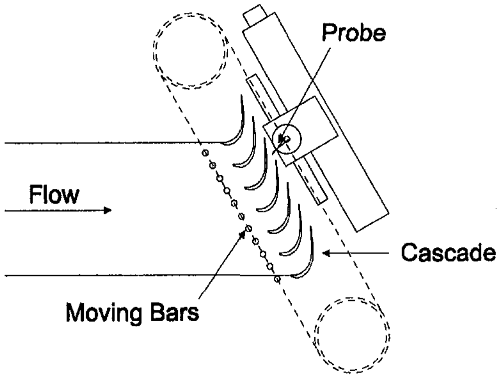

Fig. 2 Schematic arrangement of cascade wind tunnel

(Schulte and Hodson, 1994; Banieghbal et al., 1995; Halstead et al., 1997a, b) carried out using hot-film gages, have indicated that wake effects may be beneficial. This is because they may cause attached laminarlike flow to persist downstream of the nominal separation point, possibly as far back as the trailing edge. Earlier work by Ladwig and Fottner (1993) had shown that stationary wakes could also be beneficial. The results presented here show that the effect of incoming wakes is sometimes to reduce loss, particularly at low Reynolds number. Schulte and Hodson (1996), who build on the work of Halstead et al. (1997a, b), describe the mechanisms responsible for these observations. The aim of the present paper is to describe a successful strategy for the development of LP profiles with a higher lift than that described by Banieghbal et al. (1995). Hourmouziadis (1989) presented a review of LP turbine aerodynamics that provides a detailed description of the then state of the art.

Experimental Details

Datum Cascade. Figure 2 shows the cascade wind tunnel that was used as the basis for the present investigation. The datum cascade has been described by Banieghbal et al. (1995). It consists of seven blades, with a chord of approximately 150 mm. The profile of the datum cascade was chosen such that its nondimensional velocity distribution and exit flow angle matched the normalized Mach number distribution and exit flow angle of the cold-flow turbine investigated by Hodson et al. (1994). Consequently, the air inlet angle is slightly different from that in the cold-flow turbine. Table 1 provides further details of the datum cascade.

To simulate the presence of upstream wakes, and so study the effects of wake-induced transition, the cascade was fitted with a moving bar system (see Fig. 2) for some of the later experiments. The bars were driven by a variable-speed DC motor and their speed is continuously monitored during the experiment. The bar speed was set to correspond to a flow coefficient of 0.75. In the actual turbine, the stator blades outnumber the rotor blades. The diameter of the bars (1 mm) and their relative spacing was chosen so as to provide representative wakes during a simulation of the interaction of stator wakes with a downstream rotor. The bars moved in a plane 0.5 axial chords upstream of the cascade. When the cascade was operated without bars, the inlet turbulence was low, approximately 0.5 percent. Banieghbal et al. (1995) and Schulte and Hodson (1996) provide further details of the facility.

The inlet stagnation temperature was measured using a thermocouple that was placed within the inlet plenum. A Pitot probe placed downstream of the moving bars provided the reference cascade inlet stagnation pressure. By traversing the Pitot in the axial direction in the absence of the cascade, it was shown that the effects of unsteadiness on the readings from this Pitot probe were not significant at the selected measurement location (Schulte and Hodson, 1996).

This cascade had previously been used to measure the losses of the datum blade both with and without the upstream wakes. In the present work it was initially adapted for the ''flap tests'' as described in the next section, and later used to measure the losses of the new profiles developed, Blades *L* and *H*.

Flap Tests. Experiments were undertaken at the start of the current program to obtain an overview of the potential for designing a blade with an improved suction surface flow, either by reducing the loss or by increasing the loading.

In these experiments only the suction side of the test blade was being investigated. Consequently, there was no requirement to have a periodic cascade. The objective was to determine the suction side loss for a wide range of surface pressure distributions. The variations in surface pressure were achieved by fitting an adjustable flap to the trailing edge of the airfoil adjacent to the one under investigation in the datum cascade. The flap was hinged at the trailing edge of the adjacent blade. Further changes in pressure distribution were made by altering the stagger of the adjacent blade. Figure 3 shows the arrangement. The hinged flap had a perforated surface and suction could be applied to it using an auxiliary fan in order to prevent the flow separating from the flap at the highest loadings. Inserts to alter the shape of the pressure side of the passage, and splitter vanes, were also used.

Blade surface static pressures were determined using pressure tappings located along the midspan section. Boundary layer data

Nomenclature

C_p = pressure coefficient (Eq. (1))
C_{pb} = base pressure coefficient = $\{(p_2 - p_b)/(p_{01} - p_2)\}$
D = diffusion factor (Eq. (2))
o = throat width
p = pressure on surface
p_{01} = stagnation pressure at inlet
p_2 = pressure on surface at trailing edge
$p_{\min}$ = minimum pressure on suction surface
R_s = relative pitch
s = pitch or surface length
s_{bar} = bar spacing
t = trailing edge thickness
V = isentropic velocity on surface
V_2 = isentropic velocity on surface at trailing edge
α_2 = outlet flow angle
δ^* = boundary layer displacement thickness
ζ = loss coefficient (Eq. (6))
θ = boundary layer momentum thickness
ρ = density

Table 1 Low-speed cascade geometry for datum blade

Chord	150 mm
Axial Chord	126.7 mm
Pitch-Chord Ratio	0.68
Aspect Ratio	2.5
Air Inlet Angle (from axial)	30.4°
Design Exit Angle (from axial)	-62.8°
Bar Pitch/Cascade Pitch (1mm bars)	0.667
Bar Passing Frequency (1mm bars)	200 Hz
Axial Distance: Bars-Cascade L.E.	0.5 C_X
Lift Coefficient	0.819
Inlet Free-stream turbulence intensity.	0.5%
Suction Surface Length	193 mm

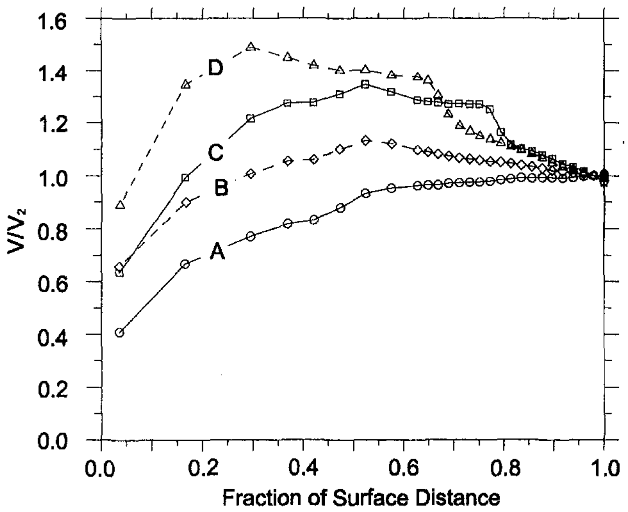

Fig. 4 Typical flap test velocity distributions

were obtained by traversing a flattened Pitot tube, 0.2 mm thick, at a location 1.5 percent of surface length (3 mm) upstream of the trailing edge, adjacent to the final tapping on the suction surface. As the flow is not periodic, data from this final pressure tapping are deemed to be representative of the exit static pressure from the equivalent periodic cascade. For a periodic cascade with Blade *H* profiles, our tests indicated a far-downstream mixed-out velocity head about 3 percent higher than the dynamic head based on the pressure at the final static tapping. Our definition of diffusion factor is based on the suction surface isentropic velocity since in the flap tests there is no proper cascade outlet condition because the flow is not periodic.

All the data reported here were obtained at a Reynolds number of 2×10^5, based on true chord and exit conditions. The inlet flow was steady with no simulation of incoming wakes for the flap tests conducted using the datum cascade as a basis.

Results and Discussion

Flap Tests

Velocity Distributions. Blade surface static pressure measurements and their associated boundary layer measurements were made for 42 test cases. The static pressure data are presented in terms of a normalized suction side velocity coefficient defined as

$$\frac{V}{V_2} = \sqrt{C_p} = \sqrt{\frac{P_{01} - p}{P_{01} - p_2}} \qquad (1)$$

Representative velocity distributions are shown in Fig. 4. They are identified by the letters A through D. Test cases C and D show that a separation bubble is present, with the bubble occupying approximately 20 percent of the surface length for case C and slightly more for case D. Though not evident in Fig. 4, it is likely that the suction side boundary layer will separate in case B. The presence of laminar separation bubbles in at least some of the tests confirms the observations made by Banieghbal et al. (1995) that substantial regions of laminar flow exist under steady flow conditions.

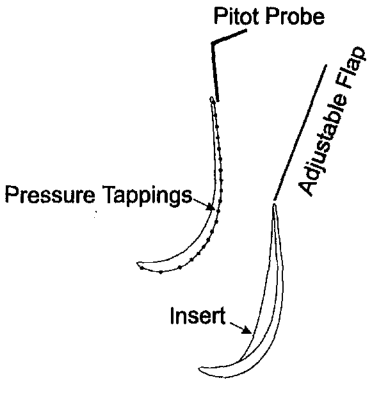

Fig. 3 Typical arrangement of flap in cascade

Two parameters that may be significant in defining the velocity distribution are the amount of deceleration from the peak suction point and the location of the peak suction point. The local diffusion factor is defined here as:

$$D = \frac{V_{\max}}{V_2} - 1 \qquad (2)$$

The experiments covered a wide range of diffusion factors, from 0.0 to beyond 0.8, and with peak suction position varying from 30 to 85 percent of surface length. The importance of these parameters is discussed below.

In the flap tests, a pressure distribution is established around a representative airfoil shape. Nevertheless, the actual shape of an airfoil having the same pressure distribution in a periodic cascade would differ. For this reason, it is not possible to determine the suction side loading by integration of the pressure distribution in the axial direction.

In the present paper, the blade loading is evaluated using the concept of circulation, where

$$\text{Lift} \propto \oint V ds \qquad (3)$$

The flap test experiments give information only about the suction surfaces of alternative designs. To evaluate the circulation and therefore the lift, the contribution of the pressure side is also required. This was assumed to be equal to the value of the integral for the datum blade, as evaluated from the pressure distribution in a periodic cascade experiment. The loading thus evaluated was nondimensionalized as:

$$\text{Relative Pitch} = R_s = \frac{\int_{\text{Suction}} V ds - \left(\int_{\text{Pressure}} V ds\right)_{\text{Datum}}}{\left(\int_{\text{Suction}} V ds - \int_{\text{Pressure}} V ds\right)_{\text{Datum}}} \qquad (4)$$

The blade numbers corresponding to a particular distribution are inversely proportional to the relative pitch.

Losses. The momentum thickness is plotted against the relative pitch in fig. 5. The maximum value is approximately six times greater than the minimum value, whereas the momentum thickness increases tenfold for the same conditions. Figure 5 shows that increasing the blade loading will inevitably lead to an increase in the suction side boundary layer thickness and that the rate of increase is greater at higher loadings.

From the viewpoint of blading design, the loss data must be set in context. It is to be expected that high suction surface diffusion coefficients will lead to increases in suction surface boundary layer loss. However, in a good design, more diffusion is likely to imply higher loading and therefore a larger pitch. The increased pitch counteracts the increase in boundary layer thickness to some extent. These effects must be taken into consideration when evaluating the suction side loss.

To a first order, the boundary layer momentum thickness at the trailing edge of the suction surface may be represented in the form of a loss coefficient as

$$\frac{2\theta}{R_s(s \cos \alpha_2)_{\text{Datum}}} \qquad (5)$$

The overall profile loss of any new cascade must include contributions from the pressure side and from the base region of the trailing edge, in addition to the suction side. To relate the momentum thickness measured in the flap tests to the loss for an equivalent blade, a model is required. Here, the expression derived by Denton (1993) for the stagnation pressure loss coefficient using a control volume analysis

$$\zeta = \frac{\Delta P_0}{0.5\rho V_2^2} = \frac{C_{pb}t}{o} + \frac{2\theta}{o} + \left(\frac{\delta^* + t}{o}\right)^2 \qquad (6)$$

where

$$o = R_s(s \cos \alpha_2)_{\text{Datum}}$$

is employed to evaluate the overall stagnation pressure loss. The values of boundary layer momentum thickness and displacement thickness are given by the flap tests only for the suction surface and for the pressure surface they are taken as equal to those for the datum blade. In general the pressure surface contribution to the loss is relatively small. The base pressure coefficient is difficult to determine. In this case it is assumed to be constant, with a value of 0.1. This is consistent with the application of Eq. (6) to the datum blade if the loss coefficient ζ is equated to the experimentally determined loss of the datum blade.

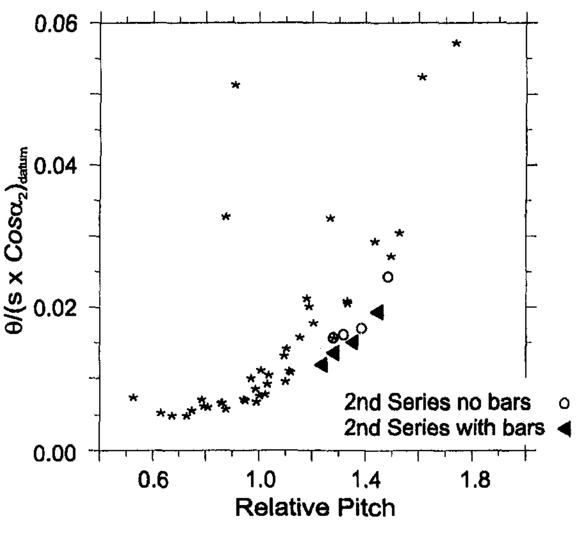

Fig. 5 Flap tests: momentum thickness versus relative pitch

Using the assumptions described above and Eq. (6), it is possible to derive the data plotted in Fig. 6. This plot is possibly the most useful for design assessment purposes. The lower edge of the field of points is demarcated by the so-called optimum line. It indicates the best performance that is to be expected as the loading is varied. The scatter of points above this line is due to the wide range of pressure distributions investigated. Nonoptimum distributions would not normally be used for blade design.

Figure 6 shows how, by increasing the pitch (i.e., the loading), the effect of the pressure side and base region losses are diluted. Nevertheless, an important feature of Fig. 6 is that the datum blade, with relative pitch of unity, appears to have about the lowest loss. This makes the task of developing a better profile more difficult. Test case B (see Fig. 4) lies close to the optimum. It has relatively little suction surface diffusion ($D \approx 0.1$).

Test case A has no suction side diffusion. As a consequence, the boundary layer at the trailing edge of the suction surface is laminar. However, the loading is also reduced and the net effect is an increase in profile loss. Thus it would appear that designing for a lower lift than the datum is unattractive since the loss increases and more blades are required.

Test cases C and D have relatively more suction surface diffusion ($D \approx 0.35$ and 0.5, respectively) than the datum profile and consequently greater loss. However, the optimum curve is fairly flat around the minimum and a modest increase in lift of, say, 20 percent, does not result in a large loss increase. Increasing the lift is attractive since, although the loss is likely to increase, weight and cost savings may be achieved.

Figure 6 gives an optimum based on the flap tests, plus the assumptions on base pressure and pressure side loss. It has the advantage of enabling promising directions for development to be identified. It does not replace the subsequent need to get accurate cascade loss measurements for particular profiles, preferably over a Reynolds number range and with a simulation of incoming wakes.

Additional Flap Tests. Some additional flap tests were performed recently in order to obtain more complete information relating to the suction surface boundary layer at loadings in the region of 20 to 40 percent above the datum loading. These used a similar variable geometry arrangement to the original flap tests on a cascade of Blade H profiles. Steady flow and unsteady flow effects were investigated in these additional tests.

The unsteady effects were simulated in these flap tests using moving bars located 90 mm upstream of the leading edge. Relative to the datum cascade, the bar diameter was increased to 2 mm and the spacing of the bars was doubled, in anticipation of operating at higher lift coefficients with higher losses. Schulte and Hodson (1996) report measurements on the Blade H cascade using the same bars. The boundary layer traverses were obtained with a hot wire probe.

The results from these tests are plotted on Fig. 6 along with the original results. The open circles refer to the steady data, the closed triangles to the unsteady data. The results of the additional flap tests, using Blade H, are similar to those of the first series, which used the datum blades. It appears, therefore, that the flap test results are not significantly dependent on the precise geometry used to set up the flow. It also shows that the loss is almost the same for the steady and unsteady cases at a Reynolds number of 2×10^5 and realistic blade loadings. The latter conclusion is in accordance with the cascade measurements on Blade H described in the next section and is consistent with the view that the unsteady effects due to wakes affect the suction surface loss component and not the trailing edge or pressure side components. It also suggests that the blades of somewhat higher loading than Blade H may have similar suction side boundary layer features.

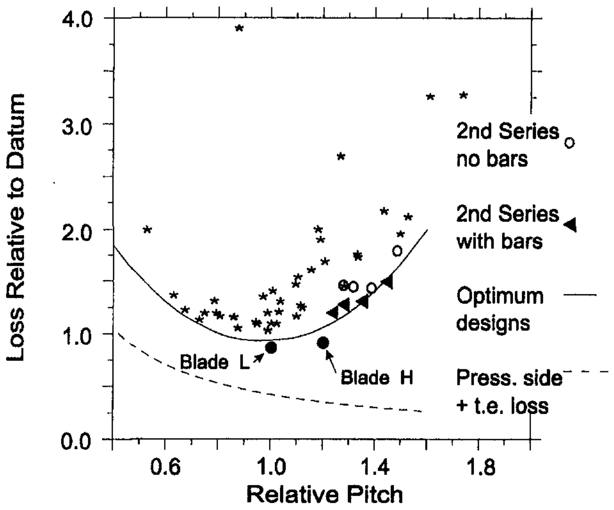

Fig. 6 Flap tests: loss versus relative pitch

Diffusion Factors and Loading Distribution. It is often stated that the two parameters that are significant in defining the velocity distribution on the suction surface are the amount of deceleration and the location of the maximum velocity. Lieblein (1956) showed that in the case of compressor airfoils, the loss of a cascade depended only weakly on the (local) diffusion factor as defined by Eq. (2) until a value of $D \approx 0.4-0.5$ was exceeded. Figure 7 presents selected data from the current flap tests in a form that is similar to that presented by Lieblein. Only those data points that lie closest to the optimum line are shown. Figure 7 shows that the loss of an "optimum" cascade is essentially constant for diffusion factors below $D = 0.2$. The data also show that the loss then begins to increase relatively slowly with diffusion factor until $D \approx 0.4-0.5$ is exceeded. It is also noted here that a diffusion factor of 0.8 was about the maximum that could be achieved before the flow failed to reattach by the trailing edge. Of course, a different operating Reynolds number might yield different results.

Following these observations, the authors attempted to determine whether an aft-loaded or a forward-loaded profile gave the lower loss. No clear correlation was found, either by correlating against center of pressure, or against the location of the point of peak velocity. Previous investigations (Hashimoto and Kimura, 1984; Hoheisel et al., 1987) have concluded that aft-loading is preferable, although at similar conditions to the flap tests (low inlet turbulence, low Mach number) there was not much difference. For our additional flap tests (described later), where inlet wakes were present, aft-loading did appear to give less loss. It may also be preferable from the viewpoint of secondary flow.

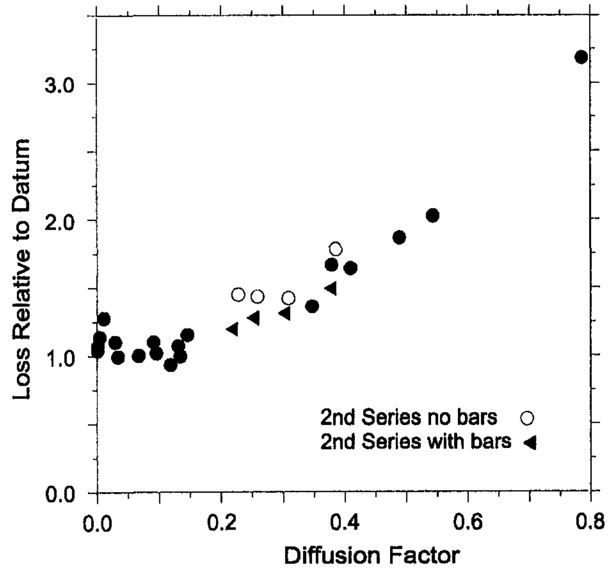

Fig. 7 Flap tests: loss versus diffusion factor

Cost Optimization. Increasing the blade loading reduces the number of blades and, if the weight of an individual blade is not increased, it reduces the overall weight of the engine.

The potential for achieving a benefit in terms of overall costs is illustrated in Fig. 8. This is developed from the loss data plotted in Fig. 6 and incorporates the cost savings that arise from increasing the pitch and hence reducing the number of blades. This cost saving is due to two factors: the direct saving in manufacturing cost of having fewer blades and the saving on other costs of the associated weight reduction. The cost saving is assumed to be linearly proportional to the pitch.

The parameter Z

$$Z = \frac{\text{Cost saving for 1 percent increase in pitch}}{\text{Cost for 1 percent point increase in profile loss}} \tag{7}$$

can be used to denote the exchange rate in terms of cost between a change in pitch and a change in blading loss. It represents the ratio of the cost benefit of a 1 percent increase in pitch to the cost resulting from a 1 percent point reduction in low-pressure turbine efficiency.

The larger the relative cost benefit of having fewer blades, the larger the value of Z. The curves in Fig. 8 show that higher values of pitch are optimum as Z increases. The value of Z to use in a particular case can only be determined by considering all the factors that are relevant. These include the thermodynamic analysis of the cycle, the manufacturing costs, and the application. Figure 8 is based on losses corresponding to the line drawn on Fig. 6 for optimum designs, and as the datum blade is somewhat above this line, then the minimum of the $Z = 0$ curve in Fig. 8 is not located exactly at unity relative pitch or at zero cost difference.

Cascade Tests. The situation shown in Fig. 8 is a useful guide, but the underlying assumptions and the limitations of the flap tests mean that some further investigation was required to confirm the performance of particular blade designs. On the basis of the original flap tests, it was decided to proceed with the development of two new blade designs and to evaluate their performance in cascade tests. The tests were to be conducted with and without a simulation of incoming wakes. The results were to be compared with the datum blade reported by Baniegh-

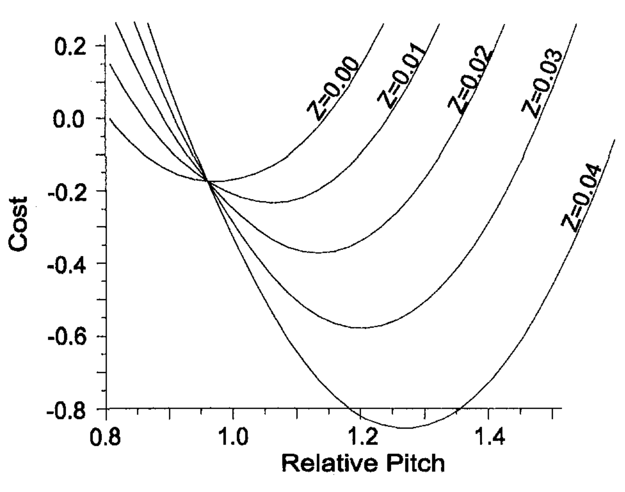

Fig. 8 Flap tests: cost versus relative pitch

bal et al. (1995). Each cascade consisted of seven blades with a nominal chord of 150 mm. Each was tested over a range of Reynolds numbers from 0.7×10^5 up to 4×10^5. The results presented here are for zero incidence.

Pitchwise traverses were performed at midspan to measure the profile loss of the three blades at the center of the cascade. The traverse was performed at a distance 0.25 axial chords downstream of the trailing edge plane of the cascade. A fixed-direction four-hole Neptune probe was used for these midspan traverses. The local mean flow angle, static pressure, and total pressure were determined from the calibration. Integration of these local values was then carried out using a constant-area mixing calculation to provide the required mixed-out values.

A Laminar Flow Design (Blade L). On the basis of the flap tests, the datum blade appears to have a loading close to the optimum for best efficiency. The scope for improving the datum design thus appears limited. However, for the datum design, the suction side boundary layer undergoes transition via a separation bubble and it seemed there was therefore some possibility of a new design in which suction surface transition was avoided altogether while maintaining the same blade loading as the datum blade. Thus the objective for the first of the new designs described here was to have laminar flow on the whole of the suction surface. On the basis that the largest component of loss for the datum blade arises from the momentum thickness of the suction side boundary layer, the likely reduction in loss by achieving laminar flow appeared substantial.

The main difficulty with the laminar flow design concept was to achieve sufficient loading when the diffusion had to be limited to a low value to prevent transition from occurring. The curves in Figs. 6 and 8 show that the design would be uncompetitive if the loading were reduced much below the datum. For the laminar design, therefore, it was decided to keep the loading at the datum value. The pitch would therefore be the same as for the datum blade and the improvement, if any, would be solely due to a reduction in aerodynamic loss. This blade is referred to in this Paper as Blade L.

An Increased Lift Design (Blade H). The second new design was intended to have a loading 20 percent higher than the datum. It was anticipated that it would have a higher loss than the datum blade and would only be competitive if the saving in blade numbers was worth more than the expected reduction in efficiency. The higher loading inevitably involves transition to turbulent flow on the suction surface. The design objectives for this blade were to have a maximum diffusion factor of 0.2 while locating the point of maximum velocity as far back as was possible while ensuring reattachment of the laminar separation before the trailing edge. It was intended that the extent of the surface covered by turbulent flow would thus be minimized, even though there was no strong evidence to support such a loading distribution from the flap tests. This blade is referred to as Blade H.

Velocity Distributions. Plots of isentropic surface velocity distributions are given in Fig. 9 for the datum profile, and for the high-lift blade (Blade H). All the data shown here were obtained at a Reynolds number of 2×10^5.

For the datum cascade, Fig. 9 shows maximum velocity occurs at 56 percent surface length, with local diffusion factor $D = 0.15$. Laminar separation is known to occur near 62 percent surface length. On the pressure surface, a separation bubble is again present, the scatter in the data being believed to be associated with unsteadiness in the separation bubble, or with errors in measurement of the low velocities in this region.

The laminar blade (not plotted), has a small amount of diffusion ($D \approx 0.05$) and as a consequence, the suction side boundary layer remained attached (shape factor 2.5, see Table 2) at the trailing edge. As compared with the datum blade, the loading over the forward part of the blade had to be increased to maintain the loading.

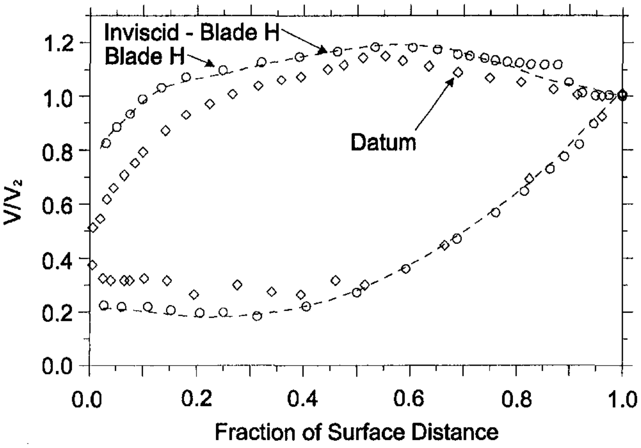

Fig. 9 Velocity distributions for datum blade and Blade *H*

A comparison of the predicted (inviscid) and measured distribution for the high lift blade (Fig. 9) reveals a perturbation to the measured distribution that is caused by a laminar separation bubble. Laminar separation occurs at approximately 70 percent surface length and reattachment at about 90 percent of surface length at the design Reynolds number (2×10^5). At the lower Reynolds number of 1×10^5, the pressure distributions showed that reattachment occurs close to the trailing edge. Boundary layer measurements also indicate that the flow remains attached above $Re = 1 \times 10^5$. When the incoming wakes are present, the observed perturbation of surface pressure by the bubble is reduced and the trailing edge suction surface boundary layers are more turbulent (lower shape factors).

Blade H has a diffusion factor of $D = 0.20$. This is 0.05 greater than the datum cascade and this change, together with an increased loading over the forward part of the blade accounts for the majority of the increase in lift.

The pressure distributions for both Blade L and Blade H are consistent with the design intent for each.

Profile Losses. Table 2 provides a summary of the state and thickness of the trailing edge boundary layers on the three profiles.

Under steady flow conditions, the datum blade has an intermittent attached boundary layer at the trailing edge. For this reason, the shape factor is higher than that of an attached turbulent boundary layer. Under the same circumstances, Blade L has an attached laminar boundary layer at the trailing edge while that for Blade H is attached and turbulent. The loss (i.e., momentum thickness) of the Blade L boundary layer is much reduced by comparison with the datum blade while that for Blade H is much larger. These changes are in line with the design predictions.

With wake-generated unsteadiness at inlet, the datum blade has an almost fully turbulent boundary layer at the trailing edge (Banieghbal et al., 1995). Under the same circumstances, Blade L has an attached transitional boundary layer and Blade H has one that is attached and turbulent. An examination of the momentum thicknesses shows that on the datum blade and Blade L, the losses are increased by the wakes. In both cases, this change is due wake-induced transition. Blade H does not appear to be affected.

Schulte and Hodson (1996) show that the boundary layer on Blade H is also affected by the wakes. While wakes promote transition as they pass over the surface and this serves to increase the loss, the calmed regions that follow these events contain attached laminar flow that persists to the trailing edge.

Table 2 Measured suction surface boundary layer parameters (Reynolds number 2×10^5, measured 3 mm upstream of trailing edge)

	Without Bars		With Bars	
	Momentum Thickness (mm)	Shape Factor	Momentum Thickness (mm)	Shape Factor
Datum	0.30	2.4	0.49	1.7
Blade H	0.56	1.6	0.56	1.6
Blade L	0.20	2.5	0.33	2.1

These latter regions produce less loss than would arise in steady flow and so there is little change in the time-averaged loss.

The variations of loss with Reynolds number, for tests without incoming wake disturbances, are plotted in Fig. 10. It can be seen that blades L and H both have a lower loss than the datum blade over most of the Reynolds number range. This is to be expected for Blade L because this has laminar flow over the whole suction surface, but was a surprising result for Blade *H*.

Table 3 provides a breakdown of the losses in the manner of Eq. (6) with and without the wakes. Measured values of boundary layer parameters and of trailing edge pressures are used to derive the tabulated data. Under steady flow conditions, it can be seen that the changes in the boundary layer losses were in line with expectations. Unfortunately, the base pressure loss appears to be higher than that of the datum (attached, intermittent) for Blade L (attached, laminar), and lower than that of the datum for Blade H (attached, turbulent). This suggests that the changes indicated by the changes in boundary layer loss are partially offset by the changes in base pressure. However, it should be noted that estimates of the effect using base pressures from measurements on the cascades showed an effect significantly less than the measured differences in loss as determined from the wake traverses.

The measured cascade losses (steady) for Blades L and H have been superimposed on the predictions of Fig. 6. Blade L is not directly comparable with flap test predictions because it achieved laminar flow over the entire suction surface whereas the flap tests, at the same loading, did not have laminar flow at the trailing edge, although they did achieve laminar flow at lower loadings. Blade L was expected to have a loss about 75 percent of the datum loss. The measured loss for Blade L was higher at 88 percent of datum loss due to the base pressure effect. In contrast the high lift profile, Blade H, benefits from a higher base pressure and so has a lower loss than predicted.

Table 3 Breakdown of cascade losses relative to datum at Re = 2.0×10^5

Blade	With Bars	Base Pressure Loss	Boundary Layer Loss	Trailing Edge Blockage	Sum of Previous Columns	Measured Loss
		$\frac{-C_{pb}t}{s\cos\alpha_2}$	$\frac{2\theta}{s\cos\alpha_2}$	$\left(\frac{\delta^*+t}{s\cos\alpha_2}\right)^2$	$\frac{\Delta P_0}{P_{02}-p_2}$	$\frac{\Delta P_0}{P_{02}-p_2}$
Datum		0.041	0.878	0.190	1.109	1.0
Datum	√	0.041	1.267	0.190	1.357	1.493
L		0.104	0.557	0.163	0.824	0.878
L	√	0.104	0.787	0.163	1.054	1.109
H		-0.045	1.059	0.154	1.167	0.932
H	√	-0.036	1.077	0.136	1.177	1.054

The loss results for the tests with the moving bars at cascade inlet are plotted in Fig. 11. As is the case for the tests with no wakes, Blades L and H have lower losses than the datum. For both blades L and H, the gain over the datum is somewhat greater with bars than without. It is also noteworthy that at the lowest Reynolds numbers, the loss with the bars is smaller than the loss without bars. This is thought to be due to the suppression of separation for the datum blade. In the case of the high lift profile, Blade H, the balance between the increased loss due to wake-induced transition and the reduced loss due to the calmed regions alters. This change is responsible for the improvement (see Schulte and Hodson, 1996).

In summary, it has been shown that the cascade results show that two effects that were not included in the original flap tests are important. These are the effect of the base pressure and the effect of the wakes. Even though the flap test results differ from the cascade results in detail, they were invaluable in providing wide-ranging data at the start of the profile development process. Finally, it is noted that the profile with the highest efficiency of the three is Blade H. Since this also has the highest loading it is the best. The anticipated trade-off between efficiency and loading is not relevant in this particular case.

Conclusions

1 There is scope for improving LP blade designs by adopting higher loadings than the datum blade.
2 Lower blade loadings than the datum are not attractive.
3 Unsteady effects are important for low-pressure turbine blading and should be simulated in cascade experiments.

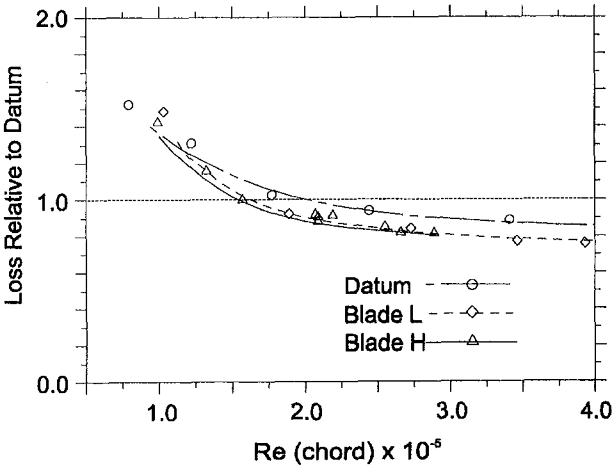

Fig. 10 Cascade tests: losses without bars

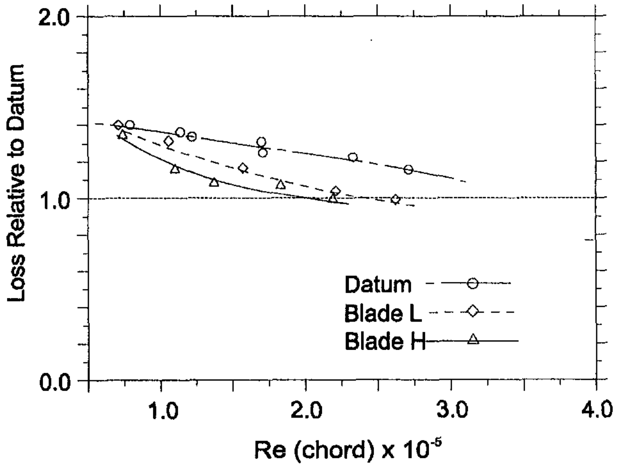

Fig. 11 Cascade tests: losses with bars

4 The unsteady flow features, particularly where transition is involved, mean that CFD cannot yet be relied on for predicting the losses.
5 The loss occurring at the trailing edge is important when comparing different profiles but is difficult to predict.
6 The benefit of a laminar suction surface boundary layer was offset by a high trailing edge loss whereas a more turbulent boundary layer reduced the trailing edge loss.

Acknowledgments

The authors wish to thank Rolls-Royce plc, and the Defence Research Agency, Pyestock, for their support of the project and their permission to publish this paper.

References

Banieghbal, M. R., Curtis, E. M., Denton, J. D., Hodson, H. P., Huntsman, I., and Schulte, V. S., 1995, "Wake Passing in LP Turbines," Paper No. 23, AGARD Conf. Loss Mechanisms and Unsteady Flows in Turbomachines, Derby, May.

Denton, J. D., 1993, "Loss Mechanisms in Turbomachines," ASME JOURNAL OF TURBOMACHINERY, Vol. 115, pp. 621–656.

Halstead, D. E., Wisler, D. C., Okiishi, T. H., Walker, G. J., Hodson, H. P., and Shin, H.-W., 1997a, "Boundary Layer Development in Axial Compressors and Turbines: Part 1 of 4—Composite Picture," ASME JOURNAL OF TURBOMACHINERY, Vol. 119, pp. 114–127.

Halstead, D. E., Wisler, D. C., Okiishi, T. H., Walker, G. J., Hodson, H. P., and Shin, H.-W., 1997b, "Boundary Layer Development in Axial Compressors and Turbines: Part 3 of 4—Turbines," ASME JOURNAL OF TURBOMACHINERY, Vol. 119, pp. 232–244.

Hashimoto, K., and Kimura, T., 1984, "Preliminary Study of Forward Loaded Cascades Designed With Inverse Method for Low Pressure Turbine," ASME Paper No. 84-GT-65.

Hodson, H. P., Banieghbal, M. R., and Dailey, G. M., 1993, "The Analysis and Prediction of the Effects of Bladerow Interactions in Axial Flow Turbines," presented at the I Mech. E Conf., Turbomachinery, London, Oct. 1994.

Hodson, H. P., Huntsman, I., and Steele, A. B., 1994, "An Investigation of Boundary Layer Development in a Multistage LP Turbine," ASME JOURNAL OF TURBOMACHINERY, Vol. 116, pp. 375–383.

Hoheisel, H., Kiock, R., Lichtfuss, H. J., and Fottner, L., 1987, "Influence of Free-Stream Turbulence and Blade Pressure Gradient on Boundary Layer and Loss Behavior of Turbine Cascades," ASME JOURNAL OF TURBOMACHINERY, Vol. 109, pp. 210–219.

Hourmouziadis, J., 1989, "Aerodynamic Design of Low Pressure Turbines," AGARD Lecture Series LS-167, June.

Ladwig, M., and Fottner, L., 1993, "Experimental Investigations of the Influence of Incoming Wakes on the Losses of a Linear Turbine Cascade," ASME Paper No. 93-GT-394.

Lieblein, S., 1956, "Experimental Flow in 2D Cascades," Chap. VI of *The Aerodynamic Design of the Axial Flow Compressor,* NACA RME 56B03, reprinted as NASA SP36, 1965.

Schulte, V., and Hodson, H. P., 1994, "Wake-Separation Bubble Interaction in Low Pressure Turbines," Paper No. AIAA-94-2931.

Schulte, V., and Hodson, H. P., 1996, "Unsteady Wake-Induced Boundary Layer Transition in Highly Loaded LP Turbines," ASME Paper No. 96-GT-486; accepted for publication in the ASME JOURNAL OF TURBOMACHINERY.

Sutton, A. J., 1990, "The Trailing Edge Loss of Subsonic Turbine Blades," Msc Thesis, Univ. Cambridge.

Design Method for Turbomachine Blades With Finite Thickness by the Circulation Method

J. Jiang

T. Dang

Department of Mechanical, Aerospace
and Manufacturing Engineering,
Syracuse University,
Syracuse, NY 12344

This paper presents a procedure to extend a recently developed three-dimensional inverse method for infinitely thin blades to handle blades with finite thickness. In this inverse method, the prescribed quantities are the blade pressure loading and the blade thickness distributions, and the calculated quantity is the blade mean camber line. The method is formulated in the fully inverse mode whereby the blade shape is determined iteratively using the flow-tangency condition along the blade surfaces. Design calculations are presented for an inlet guide vane, an impulse turbine blade, and a compressor blade in the two-dimensional inviscid- and incompressible-flow limit. Consistency checks are carried out for these design calculations using a panel analysis method and the analytical solution for the Gostelow profile.

1 Introduction

Several authors have used the circulation method to design infinitely thin blades in three dimensions (Tan et al., 1984). The method has been successfully demonstrated in three dimensions for rotational flows (Dang and McCune, 1984a), transonic flows (Dang, 1993), and viscous flows (Zangeneh, 1994). A design study using this inverse method was performed for a radial inflow turbine, and the results were validated using both Euler and Navier–Stokes analysis codes (Yang et al., 1993). An experimental verification study was also carried out for a low-speed radial inflow turbine to illustrate the usefulness of this inverse method (Borges, 1990).

Compared to existing inverse methods, which are at most quasi-three-dimensional (Novak and Haymann-Haber, 1983; Sanz, 1984; Giles and Drela, 1987), the strength of the circulation method is its ability to treat the flow three dimensionally. The primary limitation of the current theory is the assumption of infinitely thin blade, although Dang and McCune (1984b) did demonstrate with limited success that the circulation method can be formulated for blades with finite thickness. This paper presents a new approach to tackle the thickness problem using the circulation method. The theory has been developed here in the first instance for two-dimensional inviscid and incompressible flows, but the theory is formulated so that it can readily be extended to three-dimensional compressible flows.

In the inverse method proposed here, the prescribed quantities are the pressure loading and the blade thickness distributions, and the calculated quantity is the blade mean camber line. The theory is formulated in a fully inverse mode whereby the blade geometry is determined iteratively from the blade boundary conditions. The method is illustrated for the design of compressor and turbine blades.

The paper is arranged as follows: In section 2, a description of the theory for handling blades with finite thickness is given. In section 3, the numerical techniques employed to solve the resulting equations are summarized. Design examples are presented in section 4, and concluding remarks are given in section 5.

2 Theory

The early theory of the circulation method for infinitely thin blades can be generalized to handle blades with finite thickness by representing the blade upper and lower surfaces using two bound-vortex sheets (Hawthorne, 1988). Assuming that the approaching flow is steady and irrotational, the absolute vorticity can be expressed as

$$\vec{\Omega} = \delta_p(\alpha^+)\nabla\Gamma^+ \times \nabla\alpha^+ + \delta_p(\alpha^-)\nabla\Gamma^- \times \nabla\alpha^- \quad (1)$$

In Eq. (1), δ_p is the periodic Delta function, and $\Gamma^\pm = \Gamma^\pm(x)$ are the circulation functions. The blade upper (+) and lower (−) surfaces are defined as

$$\alpha^\pm = y - (f \pm T) = \pm ns \quad (2)$$

where $f = f(x)$ is the unknown mean camber line, $T = T(x)$ is the prescribed blade half thickness distribution, s is the prescribed blade spacing to chord ratio, and n is an integer (Fig. 1). The Clebsch construction of the bound vorticity given in Eq. (1) ensures that it is divergence free and lies on the blade surfaces.

Following closely the early work for infinitely thin blades, a pitch-averaged tangential velocity $\bar{V}_y = \bar{V}_y(x)$ is defined

$$\bar{V}_y(x) = \frac{1}{s}\int_{f+T}^{f+T+s} V_y(x, y)dy \quad (3)$$

Note that the integral given in Eq. (3) is evaluated from the upper surface of an arbitrary blade to the upper surface of the adjacent blade. Consequently, it includes the region "inside" the blade.

Following the previous studies for infinitely thin blades, the pitch-averaged tangential velocity is treated as a prescribed quantity, and the velocity vector is divided into a pitch-averaged part and a periodic part. On using Eq. (1), a Clebsch representation of the velocity field is

$$\vec{V}(x, y) = \bar{\vec{V}}(x) + [\nabla\tilde{\Phi} - S(\alpha^+)\nabla\Gamma^+ - S(\alpha^-)\nabla\Gamma^-] \quad (4)$$

where S is the periodic Sawtooth function. In Eq. (4), the term in the bracket on the right-hand side is the periodic part of the velocity vector. It consists of a potential part denoted by $\tilde{\Phi} = \tilde{\Phi}(x, y)$, and the remaining terms constitute the rotational part of the periodic velocity vector. Taking the curl of Eq. (4) and

---

Contributed by the International Gas Turbine Institute and based on a paper presented at the 39th International Gas Turbine and Aeroengine Congress and Exposition, The Hague, The Netherlands, June 13–16, 1994. Manuscript received by the International Gas Turbine Institute March 4, 1994. Paper No. 94-GT-368. Associate Technical Editor: E. M. Greitzer.

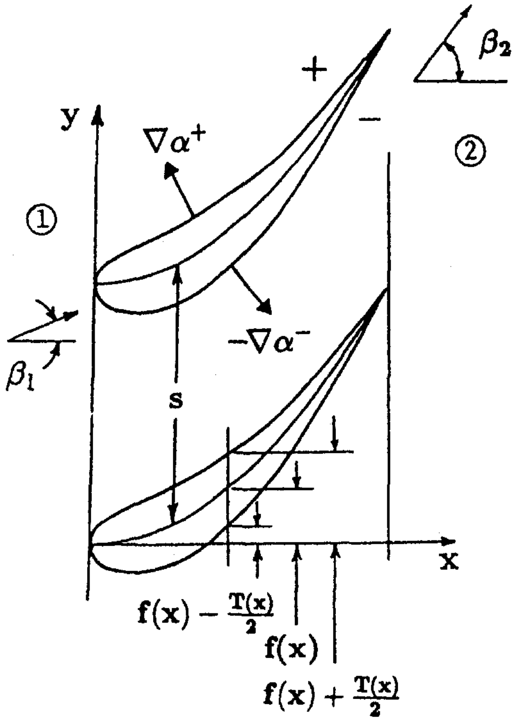

Fig. 1 Cascade notation

comparing it with Eq. (1), it can be shown that the pitch-averaged velocity vector must satisfy the following condition:

$$\nabla \times \bar{\vec{V}} = \nabla\Gamma^+ \times \nabla\alpha^+ + \nabla\Gamma^- \times \nabla\alpha^- \tag{5}$$

In the two-dimensional case, Eq. (5) imposes the following constraint between the pitch-averaged tangential velocity and the sum of the circulation functions

$$\bar{V}_y = \Gamma^+ + \Gamma^- \tag{6}$$

For incompressible flow, the pitch-averaged flow is chosen to be divergence free. In this case, the pitch-averaged axial velocity takes on the form

$$\bar{V}_x = \cos\beta_1 \tag{7}$$

where β_1 is the inlet flow angle.

In the inverse problem, treating the pitch-averaged tangential velocity as a prescribed quantity, the pitch-averaged velocity vector is fully determined. Using the definitions for the blade surfaces given in Eqs. (2), the four unknowns appearing in Eq. (4) are the potential function $\tilde{\Phi}$, the blade mean camber line f, and the circulation functions $\Gamma^{\pm}$. The four available equations are the continuity equation, the constraint given in Eq. (6), and the following boundary conditions along the blade upper and lower surfaces:

$$\vec{V}^{\pm} \cdot \nabla\alpha^{\pm} = 0 \tag{8}$$

In the following subsections, the governing equations for the potential part $\{\tilde{\Phi}\}$ and the rotational parts $\{f, \Gamma^{\pm}\}$ of the velocity vector are derived. In addition, a strategy to update the pitch-averaged tangential velocity from the prescribed blade pressure loading is presented. This step is necessary in order to satisfy the constraint set by the Kutta condition on $\bar{V}_y$.

2.1 Potential Function. The potential function $\tilde{\Phi}$ is determined from the continuity equation. For incompressible flow, the continuity equation takes on the form

$$\nabla \cdot \bar{\vec{V}} = 0 \tag{9}$$

Formally, on substituting Eq. (4) into Eq. (9), along with the use of the divegence-free condition of the pitch-averaged flow, the potential function must satisfy the following elliptic equation:

$$\nabla^2\tilde{\Phi} = \nabla \cdot [S(\alpha^+)\nabla\Gamma^+ + S(\alpha^-)\nabla\Gamma^-] \tag{10}$$

In order to solve Eq. (10), boundary conditions for $\tilde{\Phi}$ must be prescribed at the inflow and outflow boundaries, and along the upper and lower (or periodic) boundaries. In the inverse problem, the computational domain in the bladed region extends from the upper surface of one blade to the upper surface of the adjacent blade, including the region "inside" the blade (Fig. 2).

The boundary conditions for $\tilde{\Phi}$ at the inflow and outflow boundaries are assigned in a similar fashion as in a standard analysis method. At the inflow boundary, the potential function is set to zero. At the outflow boundary, the axial gradient of the potential function is set to zero. Along the periodic boundaries, which include the bladed region, the potential function satisfies the following periodic condition:

$$\tilde{\Phi}(x, y = f + T) = \tilde{\Phi}(x, y = f + T + s) \tag{11}$$

Implementation of the inverse problem using the "conventional" computational domain (i.e., without the region "inside" the blade) can also be formulated and can be found in Jiang and Dang (1994).

2.2 Mean Camber Line. The equation used to update the mean camber line is obtained from the blade boundary conditions. Adding the blade boundary conditions given in Eq. (8) yields

$$(V_x)_{bl}\frac{df}{dx} = (V_y)_{bl} - \Delta(V_x)\frac{dT}{dx} \tag{12}$$

In Eq. (12), $\vec{V}_{bl}$ denotes the sum of the upper- and lower-surface velocities. Given the velocity field from the previous iteration, Eq. (12) can be solved for the mean camber line from the blade leading edge to the blade trailing edge.

2.3 Circulation Functions. Earlier, the sum of the circulation functions $(\Gamma^+ + \Gamma^-)$ was shown to be subjected to the constraint given in Eq. (6). In order to evaluate Γ^+ and Γ^- individually, the difference in the circulation functions $\Delta\Gamma = (\Gamma^+ - \Gamma^-)$ must be calculated. From the blade kinematic conditions derived earlier for the case of infinitely thin blades (Tan et al., 1984), along with the fact that the velocity in the region "inside" the blade must vanish, the blade upper- and lower-surface velocities take on the forms

$$\vec{V}^{\pm} = \pm s\,\frac{(\nabla\Gamma^{\pm} \times \nabla\alpha^{\pm}) \times \nabla\alpha^{\pm}}{|\nabla\alpha^{\pm}|^2} \tag{13}$$

Nomenclature

f = mean camber line
p = static pressure
s = blade spacing to chord ratio
S = periodic Sawtooth function
T = blade axial thickness distribution
V = velocity
α = blade surface
Γ = circulation function
δ_p = periodic delta function
Φ = potential function
Ω = absolute vorticity

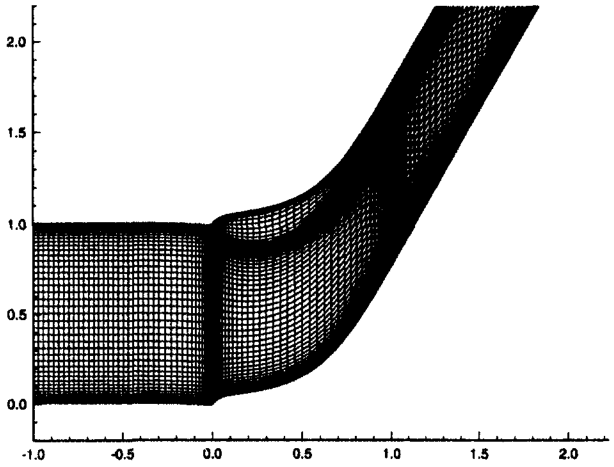

Fig. 2 Computational mesh for inlet guide vane

Dotting Eq. (13) with $\vec{V}^+$ and $\vec{V}^-$, respectively, and adding the two resulting equations, the governing equation for $\Delta\Gamma$ is obtained:

$$(V_x)_{bl}\frac{d(\Delta\Gamma)}{dx} = -\frac{|\vec{V}^+|^2 + |\vec{V}^-|^2}{s/2} - \Delta(V_x)\frac{d\bar{V}_y}{dx} \qquad (14)$$

Given the velocity field from the previous iteration, Eq. (14) can readily be solved to obtain $\Delta\Gamma$. One boundary condition on $\Delta\Gamma$ is required for this initial-value problem. The quantity $\Delta\Gamma$ is set to zero in the region upstream of the blade leading edge. The quantity $\Delta\Gamma$ in the bladed region is calculated by solving Eq. (14) from the blade leading edge to the blade trailing edge. In the region behind the blades, $\Delta\Gamma$ is set to the value at the blade trailing edge given by the solution of Eq. (14). The conditions imposed on $\Delta\Gamma$ in the regions upstream and downstream of the blades ensure that the vorticity vanishes in these regions.

2.4 Pitch-Averaged Tangential Velocity. In the theory for infinitely thin blades, the primary prescribed flow quantity is the pitch-averaged tangential velocity (or swirl) in the bladed region. This quantity was shown to be subjected to a constraint set by the Kutta condition. In the case of infinitely thin blade in two-dimensional irrotational flows, the Kutta condition requires $d\bar{V}_y/dx = 0$ at the blade trailing edge (Hawthorne et al., 1984). In the case of blades having finite thickness, the constraint set by the Kutta condition on $\bar{V}_y$ at the blade trailing edge can no longer be set explicitly at the start of the calculation.

In the present study, to eliminate the need to modify the value of $\bar{V}_y$ at the blade trailing edge during the iteration process for the camber line in order to satisfy the Kutta condition, the following alternative choice of prescribed flow quantities are used: (1) the "shape" of the pressure loading distribution, and (2) the inlet and outlet pitch-averaged tangential velocities. The pitch-averaged tangential velocity distribution in the bladed region is iterated during the calculation based on the prescribed pressure loading shape.

The strategy for updating the pitch-averaged tangential velocity distribution in the bladed region is as follows. For incompressible and irrotational flows, Bernoulli's equation reads

$$\frac{\Delta p}{\rho} = \frac{1}{2}(|\vec{V}^-|^2 - |\vec{V}^+|^2) \qquad (15)$$

Replacing the right-hand side of Eq. (15) with the relations for the blade-surface velocities given in Eq. (13), a relation between $\bar{V}_y$ and $\Delta p/\rho$ is obtained

$$(V_x)_{bl}\frac{d\bar{V}_y}{dx} = \frac{2}{s}\frac{\Delta p}{\rho} + V_x^-\frac{d\Gamma^+}{dx} + V_x^+\frac{d\Gamma^-}{dx} \qquad (16)$$

Given the velocity field from the previous iteration, the pitch-averaged tangential velocity can be determined by solving Eq. (16) from the blade leading edge to the blade trailing edge. In solving Eq. (16), the value of $\bar{V}_y$ at the inlet is used as the initial data for this initial-value problem, where as the magnitude of the pressure loading shape Δp is adjusted so that the blade produces the prescribed value of $\bar{V}_y$ at the outlet. The specification of the "shape" of the pressure loading distribution must satisfy the Kutta condition, which simply requires $\Delta p = 0$ at the blade trailing edge.

3 Numerical Techniques

In this section, the numerical technique used to solve the relevant equations described in section 2 are presented, and the overall iterative precedure for the mean camber line is summarized. The iterative scheme for the blade mean camber line consists of solving Eq. (10) for the potential function $\tilde{\Phi}$, Eq. (12) for the blade mean camber line f, Eq. (14) for the difference in the circulation functions $\Delta\Gamma$, and Eq. (16) for the distribution of the pitch-averaged tangential velocity $\bar{V}_y$ in the bladed region.

3.1 Solver for Potential Part. The governing equation for the potential part $\tilde{\Phi}$ is of the elliptic type. Equation (10) is solved by first transforming it from the physical domain to a rectangular computational domain, then central-differencing the transformed equation using a Line-Successive-Over-Relaxation (LSOR) scheme in conjunction with a cell-centered finite-volume formulation. In this numerical scheme, the discretized form of the potential equation utilized for formulating the relaxation scheme is

$$L\{\tilde{\Phi}^{n+1}_{i,j} - \tilde{\Phi}^{n}_{i,j}\} = \frac{1}{A}\sum_{m=1}^{4}(V_x\Delta y - V_y\Delta x)_m \qquad (17)$$

where A is the cell area, and the summation is taken over the four sides forming the cell. In Eq. (17), the operator L is the Laplacian operator written in the computational space, and n is the iterative level in the relaxation loop for the potential function. To accelerate convergence, the V-cycle multigrid technique has been employed in the relaxation scheme (Brandt, 1977).

3.2 Solver for Rotational Parts. The governing equations for the blade mean camber line f (Eq. (12)), the difference in the circulation functions $\Delta\Gamma$ (Eq. (14)), and the pitch-averaged tangential velocity $\bar{V}_y$ (Eq. 16)) are initial-value problems. These equations are solved numerically by integrating along the axial direction using the trapezoid rule.

3.3 Overall Iteration Procedure for Blade Profile. The blade mean camber line f is determined by an iterative procedure. After guessing an initial flowfield and the blade profile, the following iterative scheme is utilized:

1 Update the potential function $\tilde{\Phi}$ using Eq. (17).
2 Update the pitch-averaged tangential velocity $\bar{V}_y$ using Eq. (16).
3 Update the circulation functions Γ^+ and Γ^- using Eq. (6) and Eq. (14).
4 Update the mean camber line f using Eq. (12).
5 Repeat steps [1] to [4] until convergence in the camber line f is achieved.

In the iteration process for the blade profile outlined above, most of the computational time is consumed in step (1) where

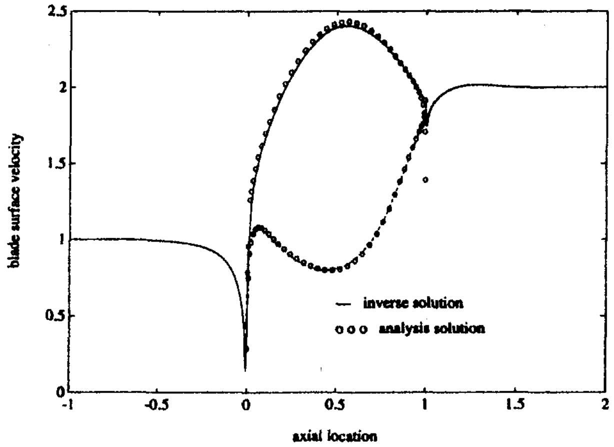

Fig. 3 Surface velocity distribution for inlet guide vane

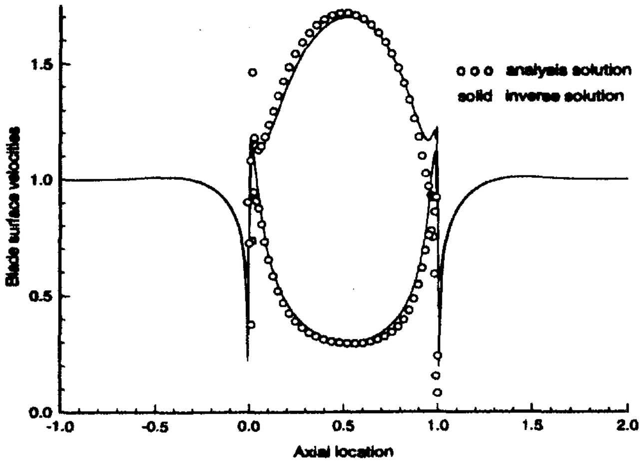

Fig. 5 Surface velocity distribution for impulse turbine

a two-dimensional elliptic equation is solved. The calculations performed in steps (2) to (4) are small since they simply involve performing one integration in each step. To reduce the overall computational time, it was found that during the iterative procedure for the blade camber line, only one multigrid relaxation cycle for the potential function is necessary in step (1) before going to steps (2) to (4).

Finally, as the blade geometry is constantly updated during the iteration process for the blade profile, the geometry of the computational domain changes at every iteration. To alleviate the grid-generation task, the sheared *H*-grid is employed (Fig. 2). This choice of mesh reduces to the shifting of the mesh points along a given constant axial location in the *y* direction, with the amount of shifting being equalled to the local change in **f** between iterations.

4 Results and Discussions

To illustrate the method, the design of an inlet guide vane, an impulse turbine, and a compressor blade are presented. A typical computational mesh employed in these calculations comprises 120 cells in the axial direction, 40 cells in the pitchwise direction for the gap region, and 12 cells in the pitchwise direction for the region "inside" the blade. A converged solution with six orders of magnitude reduction in the maximum residual is typically obtained after 200 multigrid cycles.

Figure 2 shows the design of an inlet guide vane with inflow and outflow angles of 0 and 60 deg, respectively. The maximum blade thickness used in this design calculation is 20 percent of the axial chord, and the blade solidity is 1. In this example, the "shape" of the pressure loading is chosen to be a parabolic distribution

$$\Delta p \propto x(1 - x)$$

and the blade thickness distribution is chosen to produce a rounded leading edge and a sharp trailing edge

$$T \propto \sqrt{x}(1 - x)$$

A consistency study was carried out using an analysis code to check the accuracy of the results given by this inverse method. The analysis code employed in this consistency study is the McFarland panel code developed at NASA Lewis Research Center (McFarland, 1982). In the consistency study, the blade profile designed by the inverse method is analyzed by the panel method, and the results of the blade surface velocity distributions are compared. Figure 3 illustrates the comparison of the blade-surface velocity distribution for the inlet guide vane shown in Fig. 2. Excellent agreement is obtained between the solutions given by the inverse and the analysis methods.

Figure 4 illustrates the design of an impulse turbine blade with a maximum thickness-to-chord ratio of 20 percent and an overall turning of 100 deg. The blade solidity is taken to be 1. In this example, the pressure loading is taken to be a parabolic profile

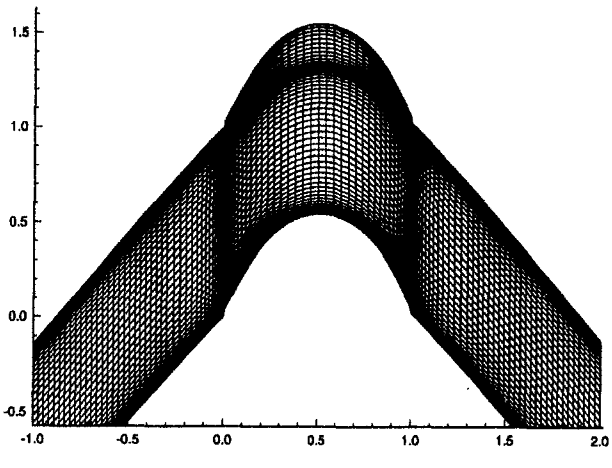

Fig. 4 Computational mesh for impulse turbine

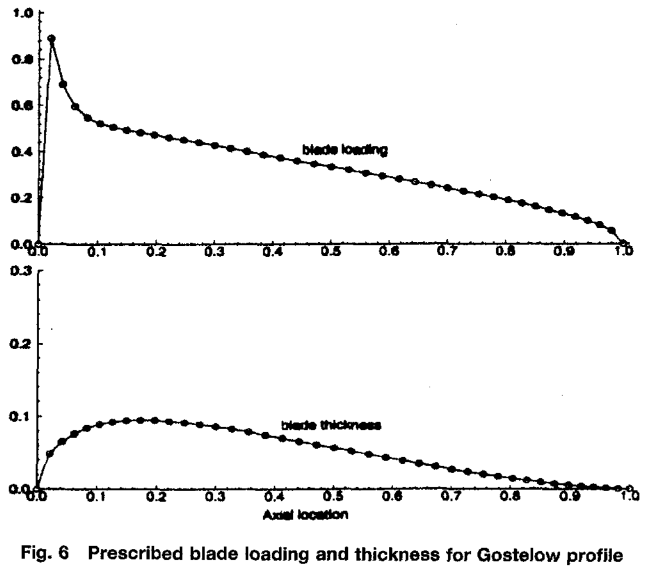

Fig. 6 Prescribed blade loading and thickness for Gostelow profile

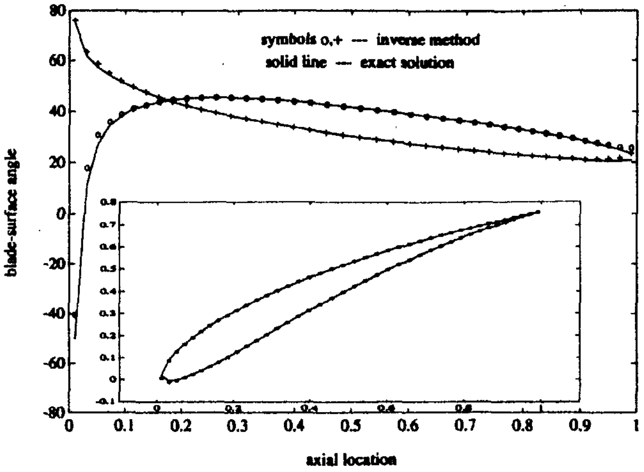

Fig. 7 Comparison of blade geometry for Gostelow-profile test case

$$\Delta p \propto x(1-x)$$

The blade thickness distribution is taken to be of the form

$$T \propto \sqrt{x}\sqrt{1-x}$$

The above prescribed thickness distribution corresponds to a symmetrical blade profile with rounded leading and trailing edges (Fig. 4). Figure 5 shows the comparison of the blade surface velocities given by this inverse method and the analysis method of McFarland. The overall agreement between these two solutions is very good, with some errors occuring near the leading- and trailing-edge regions.

Finally, the analytical solution of the Gostelow profile is used to verify the present method. In this consistency study, an attempt is made to reproduce the Gostelow profile with the present inverse method. Figure 6 shows the axial distributions of the pressure loading and blade thickness employed as inputs to the present inverse method. The prescribed values of the inflow and outflow pitch-averaged tangential velocities are computed from the known inflow and outflow angles of 53.5 and 30.02 deg, respectively. The blade spacing-to-chord ratio is 1.2392, and the maximum blade thickness-to-chord ratio is 0.0946. These quantities, along with the prescribed shapes for Δp and T shown in Fig. 6, are computed directly from the known analytical solutions of the Gostelow profile (Gostelow, 1984).

Figure 7 illustrates the comparisons of the blade profile and the blade-surface angle distributions between the results given by the present inverse method (symbols) and the exact analytical solutions (solid line). This figure shows excellent agreement between the exact Gostelow blade profile and the blade profile given by the inverse method.

5 Conclusions

The inverse method for infinitely thin blades based on the circulation method has been successfully extended to handle blades with finite thickness in the two-dimensional limit. In this inverse method, the primary prescribed quantities are: (1) the inflow and outflow pitch-averaged tangential velocities, (2) the "shape" of the pressure loading distribution, and (3) the blade thickness distribution. The calculated geometric quantity is the blade mean camber line. In the present study, the flow is assumed to be incompressible and inviscid, and the incoming flow is assumed to be uniform.

The method has been demonstrated for the design of an inlet guide vane and an impulse turbine having leading/trailing-edge roundness and maximum blade thickness typically found in turbine applications. The blade shapes given by the inverse method were checked against a panel analysis code, and very good agreement in the two solutions was obtained.

The method has also been verified against the analytical solution of the Gostelow profile. In this consistency check, the prescribed blade pressure loading and thickness distributions for the present inverse method are obtained from the analytical solutions, and the resulting blade geometry is sought. The blade profile computed by the present inverse method compares very well with the exact Gostelow profile. Finally, the method is being implemented in three dimensions.

Acknowledgments

This project was sponsored by the NASA Lewis Research Center under grant No. NAG3-1468 (J. Veres, Technical Monitor), and the CASE Center at Syracuse University. The authors would like to thank Sir William Hawthorne at Cambridge University and Dr. Jeffery Yokota at the NASA Lewis Research Center for their helpful discussions.

References

Borges, J. E., 1990, "A Three-Dimensional Inverse Method in Turbomachinery: Part 2—Experimental Verification," ASME JOURNAL OF TURBOMACHINERY, Vol. 112, pp. 355–361.

Brandt, A., 1977, "Multi-level Adaptive Solutions to Boundary-Value Problems," *Mathematics of Computation*, Vol. 31, No. 138, pp. 333–390.

Dang, T. Q., 1993, "A Fully Three-Dimensional Inverse Method for Turbomachinery Blading in Transonic Flows," ASME JOURNAL OF TURBOMACHINERY, Vol. 115, pp. 354–361.

Dang, T. Q., and McCune, J. E., 1984a, "A Three-Dimensional Design Method in Rotational Flow," *Proc. International Conference on Inverse Design Concepts in Engineering Science*, G. S. Dulikravich, ed., University of Texas, Austin, pp. 397–417.

Dang, T. Q., and McCune, J. E., 1984b, "Design Method for High-Loaded Blades With Blockage in Cascade," *Proc. ASME Conference on Computational of Internal Flows: Methods and Applications*, P. M. Sockol and K. N. Ghia, eds., New Orleans, pp. 129–136.

Giles, M., and Drela, M., 1987, "Two-Dimensional Aerodynamic Design Method," *AIAA Journal*, Vol. 25, pp. 1199–1205.

Gostelow, J. P., 1984, *Cascade Aerodynamics*, Pergamon Press.

Hawthorne, W. R., Wang, C., Tan, C. S., and McCune, J. E., 1984, "Theory of Blade Design for Large Deflections: Part 1—2D Cascade," ASME *Journal of Engineering for Gas Turbines and Power*, Vol. 106, pp. 346–353.

Hawthorne, W. R., 1988, private communication.

Jiang, J., and Dang, T., "Design Method for Turbomachine Blades With Finite Thickness by the Circulation Method," ASME Paper No. 94-GT-368.

McFarland, E. R., 1982, "Solution of Plane Cascade Flow Using Improved Surface Singularity Methods," ASME *Journal of Engineering for Power*, Vol. 104, pp. 668–674.

Novak, R. A., and Haymann-Haber, 1983, "A Mixed-Flow Cascade Passage Design Procedure Based on a Power Series Expansion," ASME *Journal of Engineering for Power*, Vol. 105, pp. 231–242.

Sanz, J. M., 1984, "Improved Design of Subcritical and Supercritical Cascades Using Complex Characteristics and Boundary-Layer Correction," *AIAA Journal*, Vol. 22, no. 7, pp. 950–956.

Tan, C. S., Hawthorne, W. R., McCune, J. E., and Wang, C., 1984, "Theory of Blade Design for Large Deflections: Part 2—Annular Cascades," ASME *Journal of Engineering for Gas Turbines and Power*, Vol. 106, pp. 354–365.

Yang, Y. L., Tan, C. S., and Hawthorne, W. R., 1993, "Aerodynamic Design of Turbomachinery Blading in Three-Dimensional Flow: An Application to Radial Inflow Turbines," ASME *Journal of Engineering for Gas Turbines and Power*, Vol. 115, pp. 602–613.

Zangeneh, M., 1994, "Inviscid–Viscous Interaction Method for Three-Dimensional Inverse Design of Centrifugal Impellers," ASME JOURNAL OF TURBOMACHINERY, Vol. 116, pp. 280–290.

Analysis of Hot Streak Effects on Turbine Rotor Heat Load

T. Shang
Pratt & Whitney,
400 Main St.,
East Hartford, CT 06108

A. H. Epstein
Gas Turbine Laboratory,
Massachusetts Institute of Technology,
Cambridge, MA 02139

The influence of inlet hot streak temperature distortion on turbine blade heat load was explored on a transonic axial flow turbine stage test article using a three-dimensional, multiblade row unsteady Euler code. The turbine geometry was the same as that used for a recently reported testing of hot streak influence. Emphasis was placed on elucidating the physical mechanisms by which hot streaks affect turbine durability. It was found that temperature distortion significantly increases both blade surface heat load nonuniformity and total blade heat load by as much as 10–30 percent (mainly on the pressure surface), and that the severity of this influence is a strong function of turbine geometry and flow conditions. Three physical mechanisms were identified that drive the heat load nonuniformity: buoyancy, wake convection (the Kerrebrock–Mikolajczak effect), and rotor–stator interactions. The latter can generate significant nonuniformity of the time-averaged relative frame rotor inlet temperature distribution. Dependence of these effects on turbine design variables was investigated to shed light on the design space, which minimizes the adverse effects of hot streaks.

Introduction

Modern gas turbine engines can be designed with high turbine inlet temperatures because of the availability of improved alloys and efficient airfoil cooling arrangements. Detailed, accurate airfoil heat load determination is a critical step for realizing the long component lives demanded of modern turbines, so that painstaking efforts are made to advance the state of the art of turbine heat transfer prediction methods. Currently, numerical codes can do a good job at predicting the turbine heat flux data taken in cascades or even rotating rigs (Abhari et al., 1992). Heat transfer levels in engines, however, are often much higher than these predictions. The fact that predictions agree with subscale rig and cascade data but not engine experience implies that not all flow characteristics important in an engine are modeled by test rigs and computational models.

One flow phenomenon absent (intentionally) in most test facilities is the spatial and temporal gas temperature nonuniformities generated by the combustor. These temperature distortions add additional dimensionality to turbine flows, complicating the heat transfer processes. In the past ten years, significant effort has led to progress in understanding temperature distortion's influence in turbine heat transfer. One of the earliest experimental efforts was that by Butler et al. (1986) in a large-scale low-speed rotating rig. In this experiment, one circular hot streak (seeded with CO_2) was injected upstream of the stator blade row. Rotor surface temperatures were then inferred from gas concentration measurements. Test results revealed that temperature distortion increased blade pressure surface temperature. Hot/cold gas segregation and secondary flows were identified as the main drivers. It was later shown by Sharma et al. (1994) that the magnitude of hot/cold gas segregation scales with flow coefficient (i.e., the ratio of axial velocity to wheel speed).

Several investigators subsequently performed numerical analyses based on this experimental data, using a variety of two-dimensional and three-dimensional, Euler and *N–S* CFD codes, for example Rai and Dring (1987), Krouthen and Giles (1988), Dorney et al. (1990), and Takahashi and Ni (1990). Most authors predicted trends similar to those observed in the experimental data, with varying degrees of quantitative agreement. Other investigators, including Harasgama (1990) and Saxer and Giles (1993), analyzed the influence of axisymmetric radial temperature distortions on rotor heat transfer.

More recently, heat transfer data were taken with inlet temperature distortions in a fully scaled transient test rig on a transonic turbine stage (Shang et al., 1995). Enginelike radial and circumferential temperature distortions were introduced at the turbine inlet, and their effects on rotor heat transfer were directly measured using surface-bonded heat flux gages. The inlet temperature distortions were shown to alter the spatial heat flux distribution significantly. Local heat transfer increases of as much as 50 percent were observed. These data suggest that heat flux changes correlate with local gas temperature (or more accurately, the gas-to-wall temperature difference). They also imposed velocity turbulence at the turbine inlet with intensity and length scales comparable to modern combustor exit flows. No change in rotor heat transfer was measured due to these inlet turbulence variations.

This paper presents a computational analysis of turbine flows with hot streak inlet temperature distortions. It is based on the geometry and flow conditions tested by Shang. In the following sections, the numerical procedure and computational setup will be briefly described. The bulk of this paper, however, concentrates on observations of the fluid dynamic phenomena that govern the behavior of hot streaks and set rotor blade heat load.

Numerical Procedure and Approach

The main tool in this analysis is a three-dimensional, multiblade row unsteady Euler solver written by Saxer (1992). The full nonlinear Euler equations are solved on an **H**-type grid using the Ni–Lax–Wendroff time marching scheme, with nonreflective boundary conditions implemented at flow inlet and exit to avoid nonphysical reflections. The computational grid is shown in Fig. 1. For this investigation, each nozzle guide vane (NGV) passage has a grid block of 56 axial, 36 circumferential, and 21 radial grid points, while each rotor passage has 56 axial, 22 tangential, and 21 radial grid points.

The test article studied here is a 4:1 pressure ratio, transonic turbine, for which heat transfer data with inlet distortion were previously reported by Shang et al. (1995). At design conditions, both the NGV and rotor blade rows are choked. Design parameters of this turbine are given in Table 1. The computa-

---

Contributed by the International Gas Turbine Institute and presented at the 41st International Gas Turbine and Aeroengine Congress and Exhibition, Birmingham, United Kingdom, June 10–13, 1996. Manuscript received at ASME Headquarters February 1996. Paper No. 96-GT-118. Associate Technical Editor: J. N. Shinn.

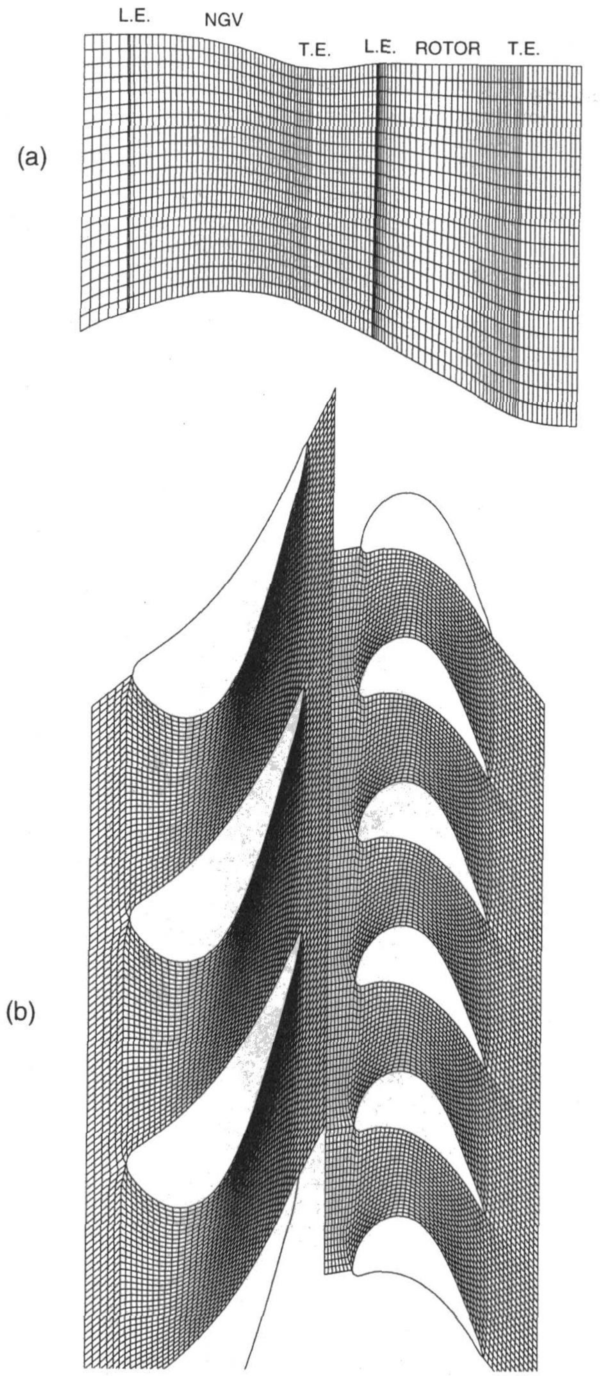

Fig. 1 **Computational grid for the transonic turbine stage: (*a*) side view, (*b*) midspan blade–blade grid of the 3 NGV–5 rotor blade domain calculated here**

Table 1 **Design parameters of turbine stage**

Turbine Load, $\Delta H/U^2$	2.3
Total Pressure Ratio	4.0
Flow Coefficient, C_x/U	0.63
NGV Exit Mach Number	1.22
Gap/Rotor Chord	0.4
Rotor Inlet & Outlet Angles*	57°, 65°
NGV Inlet & Outlet Angles*	0°, 74°

* Angles defined from axial

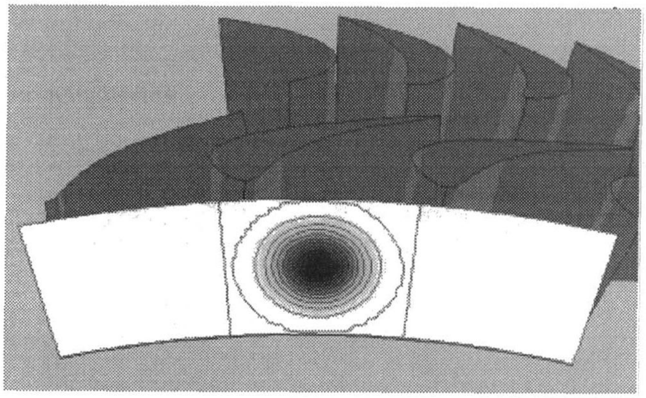

Fig. 2 **NGV inlet temperature distortion in the form of a circular hot streak; contours are of total temperature**

tional domain is shown in Fig. 1 and consists of 3 NGV and 5 rotor passages, closely simulating the 36 NGV-to-61 rotor airfoil count ratio of the test turbine.

To examine effects of temperature distortion on turbine heat load, a circular Gaussian temperature distortion (hot streak) was superposed on an otherwise uniform temperature field at the NGV inlet plane (total pressure kept uniform). The hot streak is positioned midway between NGV leading edges at 50 percent span into the center of the three stator passages, Fig. 2. This is equivalent to 12 hot streaks around the 36 vane annulus, typical of engine fuel injector placement. A Gaussian temperature profile is used with a half-height width of 40 percent of the NGV pitch. This length scale is comparable to that tested by Butler et al. (1986) and allows sufficient grid resolution to avoid numerical dissipation of the temperature gradient. Two levels of temperature distortion were examined, with peak to free-stream temperature ratios of 1.4 and 1.8. (These will later be referenced as hot streak ''magnitudes'' of 1.4 and 1.8.) Flow with uniform inlet temperature was also calculated as a baseline for comparison. To accentuate the phenomena, most of the results that follow will be based on calculations with a hot streak magnitude of 1.8. Comparisons between hot streak levels of 1.4 and 1.8 are then used to show scaling.

All results reported herein are obtained from time-accurate unsteady flow simulations. In other words, the flow field is converged to a periodic solution simulating the relative motion between the NGV and rotor. Time-averaged blade surface gas temperatures are used as a measure of blade heat load. It should be emphasized that the ''time-averaged'' temperature fields shown here were obtained by directly averaging the instantaneous temperature values through a complete flow cycle (hot streak passing period), not derived from time-averaged pressure and density values by using the state equation.

The use of an Euler code implies that there is no modeling of viscous effects, such as secondary flows caused by the endwall boundary layer and tip clearance flows. Given this limitation, our objective is to examine trends and parametric scaling that can be captured by inviscid calculations rather than to seek absolute values. As will be evident in the following sections, many of the governing flow phenomena are inviscid, so that useful physical insight can be obtained.

Results and Discussion

Before proceeding to the rotor flow field, it is worthwhile to discuss flow conditions in the NGV passage. Because NGV inlet total pressure is specified as uniform here, flow patterns in the NGV are not altered by the introduction of temperature distortion, as stipulated by the Munk and Prim substitution principle (Munk and Prim, 1947). Rather, the hot streaks introduced at the NGV inlet shown in Fig. 2 stay in midpassage, and

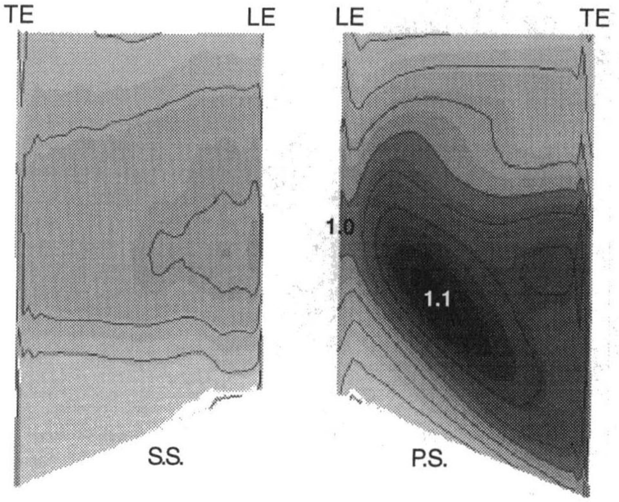

Fig. 3 Time-averaged total temperature distribution on the rotor's pressure and suction surfaces with a hot streak magnitude of 1.8. Temperature is normalized by midspan leading edge value with contour intervals of 0.02.

NGV surface temperatures are not affected by the temperature distortion. On the other hand, flow conditions in the rotor are substantially altered.

Our primary objective is to investigate turbine blade heat loading. The distribution of time-averaged gas temperature at the rotor blade surface is shown in Fig. 3. (With uniform inlet conditions, gas temperatures at the blade surface have little spatial variation, less than one of the contours used in Fig. 3.) The hot streak clearly generates a considerable nonuniform temperature on the pressure surface. In addition to the radial temperature gradients, which are caused in part by the hot streak radial profile, there are large chordwise temperature variations. The maximum surface temperature on the pressure side is higher than the averaged gas temperature at rotor leading edge. The flow phenomenon generating this nonuniformity was first linked by Butler et al. (1986) to the Kerrebrock and Mikolajczak effect (Kerrebrock and Mikolajczak, 1970), and can be explained with simple velocity triangle arguments. The hot streak exits the stator at roughly the same Mach number and flow angles as the main flow, but with higher fluid temperature and so at a larger velocity in the absolute frame. In the rotor relative frame upon subtraction of wheel speed, the hot fluid has a slip velocity toward the pressure surface as compared to the cooler main flow surrounding the hot streak. This segregates the hotter fluid and transports it toward the pressure surface. The net result is that pressure side has a higher time-averaged surface temperature than does the suction side. To illustrate this phenomenon, one snapshot of the unsteady flowfield is shown in Fig. 4. The location of the hot streak (fluid with temperatures above half height) is shown using entropy as a marker. (One NGV airfoil was deleted for a clearer view of the hot streak.) The hot streak is periodically chopped by the rotor and convected downstream within the rotor passage. Because there are five rotor blades for each hot streak, flow conditions in successive rotor passages can also be viewed as events at different times of the passage flow cycle. The accumulation of high-temperature fluid on the pressure surface can be seen by comparing the two rotor passages that have a hot streak within them (blades #4 and #5 in Fig. 4(*a*)). Although the hot streak diameter as marked is about half the blade height entering the rotor, it has spread over most of the span of the pressure surface of blade #5, leading to hot/cold fluid segregation, and higher time-averaged temperatures on the pressure surface.

Given that the hot/cold fluid segregation process results in temperature nonuniformities on the blade surface, do these gas temperature changes translate into significant heat transfer variations? Here we consider a two-dimensional blade-to-blade section across the maximum temperature point along the span shown in Fig. 3. The surface gas temperature around the airfoil perimeter is shown in Fig. 5, for two hot streak magnitudes and for uniform NGV inlet temperature. For the turbine under study, the ratio between mean rotor inlet relative total temperature and the mean metal temperature is about 1.35. The surface temperature variation from leading edge values was converted into heat flux changes by comparison with the mean gas-to-metal temperature difference. For a hot streak magnitude of 1.4, the peak local heat flux change on the pressure surface is about 10 percent. However, as the distortion level is doubled, the change in heat flux rises to 40 percent. This nonlinear influence is qualitatively explainable using the velocity triangle arguments presented earlier. The increase in averaged surface temperature is proportional to the temperature of the accumulated fluid, and the accumulation rate of this hot fluid, as caused by the velocity difference, scales with hot streak temperature as well.

Another observation from Fig. 4 is that the hot streak tends to move radially toward the hub. This radially inward displacement is most distinctive in Fig. 4(*b*), where the hot streak is

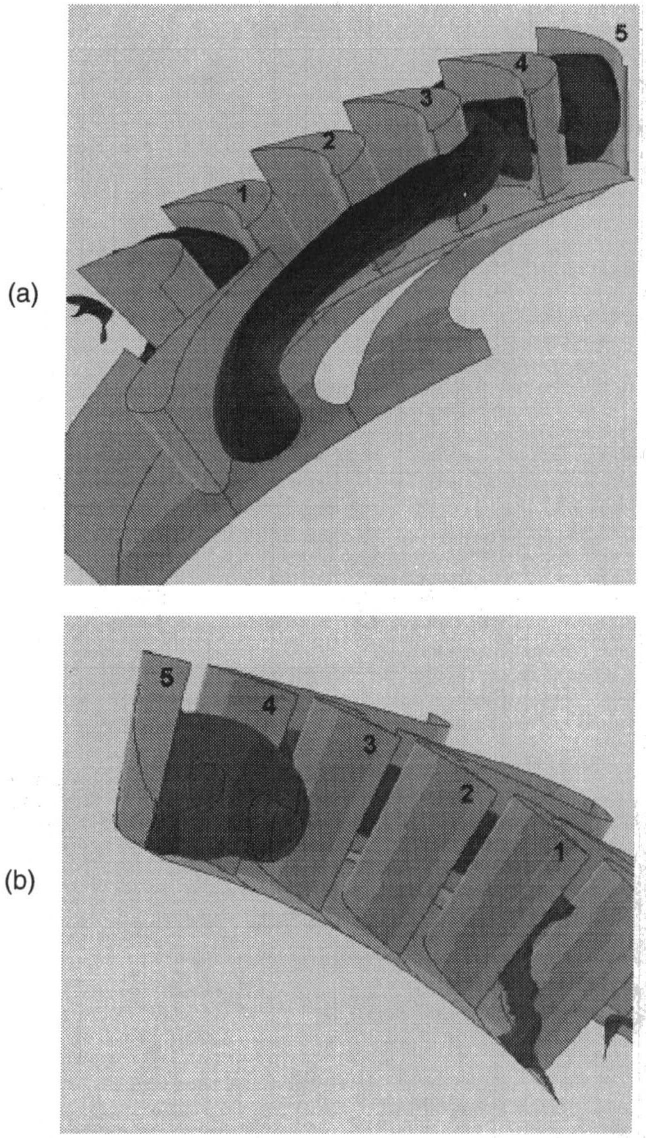

Fig. 4 Snapshot of flowfield showing convection of hot streak through turbine stage: (*a*) view from upstream of stage inlet; (*b*) view from downstream of rotor exit

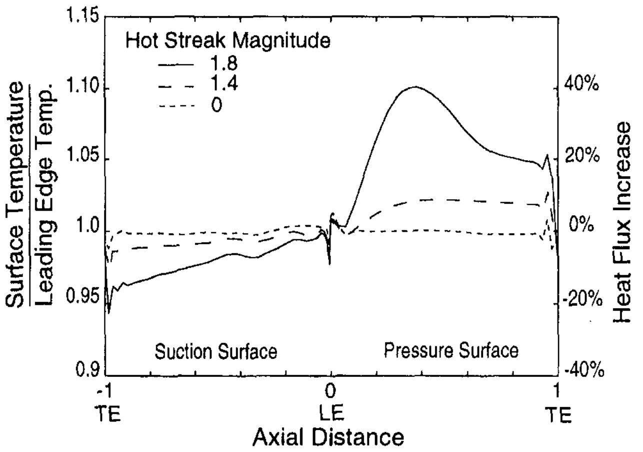

Fig. 5 Surface gas temperature distribution and resultant heat flux change along a two-dimensional blade-to-blade surface

seen at the exit of rotor passage #4. A simple analysis using radial equilibrium equations will now be used to show that this motion is due primarily to buoyancy and to estimate the scaling of this effect.

Buoyancy Effects. The radial displacement of hot streak fluid can be estimated using radial equilibrium equations in the rotor relative frame. For simplicity, a force balance on a fluid element from the core of the hot streak (at peak temperature) as it is transported along the pressure surface will be performed. The radial pressure gradient is established by the background flow, as denoted by subscript "0";

$$\frac{\partial p_0}{\partial r} = \rho_0 \Omega^2 R + 2\rho_0 W_{\theta,0}\Omega + \rho_0 \frac{W_{\theta,0}^2}{R} \qquad (1)$$

where W_θ is tangential velocity in the rotor relative frame and Ω is the rotational speed, P_0 and ρ_0 the fluid static pressure and density, and R the radius. The terms on the right-hand side of Eq. (1) represent centrifugal force due to rotation, Coriolis force, and relative swirl. For this rotor, the tangential velocity is much smaller than wheel speed over a large portion of the blade pressure surface. Therefore Eq. (1) can be reduced to

$$\frac{\partial p_0}{\partial r} = \rho_0 \Omega^2 R \qquad (2)$$

Denoting the radial displacement of hot streak element toward the hub by δ and assuming that the static pressure field is approximately that established by the uniform flow, a force balance on the hot streak core fluid yields

$$-\frac{\partial p_0}{\partial r} + \rho_{hs}\Omega^2 R = -\rho_{hs}\frac{D^2\delta}{Dt^2} \qquad (3)$$

where D^2/Dt^2 stands for the Lagrangian derivative and the subscript "hs" denotes the hot streak. Combining Eqs. (2) and (3) and recognizing that $Dt = dx/W_x$, $\rho_0/\rho_{hs} \sim T_{hs}/T_0$, and $W_x/\Omega R = \phi$, we have

$$\frac{d^2\delta}{dx^2} = \frac{1}{R}\left(\frac{T_{hs}}{T_0} - 1\right)\frac{(\Omega R)^2}{W_x^2(x)} = \frac{1}{R}\left(\frac{T_{hs}}{T_0} - 1\right)\frac{1}{\phi^2} \qquad (4)$$

We can now estimate the radial displacement of the hot streak core fluid on the pressure surface by integrating Eq. (4) in the streamwise direction using the axial velocity W_x on the blade pressure surface. The hot streak core trajectory can also be interrogated from the CFD solution. A comparison between the two is shown in Fig. 6. The close agreement indicates that the simple analysis outlined above captures the essential physics responsible for the hot streak migration toward the hub.

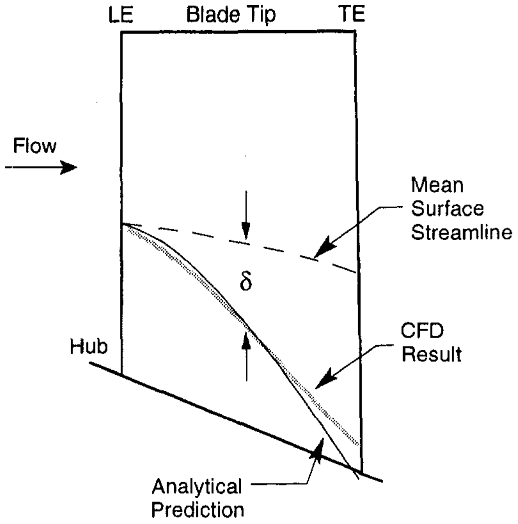

Fig. 6 Simple model predicted (Eq. (4)) and CFD calculated hot streak core trajectory along the rotor pressure surface. The mean surface streamline position was extracted from a uniform inflow calculation.

Examination of Eq. (4) provides some insight on the scaling of buoyancy. First, the effect scales linearly with hot streak temperature. Second, the dependence on rotational speed (centrifugal force) and flow through time (axial velocity) lumps into the familiar nondimensional flow coefficient ϕ. Therefore, the effect of buoyancy is more pronounced at low versus high flow coefficients.

This buoyancy influence, combined with the Kerrebrock and Mikolajczak effect, tends to push the hot streak toward the blade root platform. The time-averaged rotor relative total temperature on the rotor platform is shown in Fig. 7. The local temperature at the corner between the pressure surface trailing edge and the hub wall is about 5 percent higher than rotor inlet values for a hot streak magnitude of 1.8. This temperature variation would lead to a 20 percent increase in heat flux for this turbine.

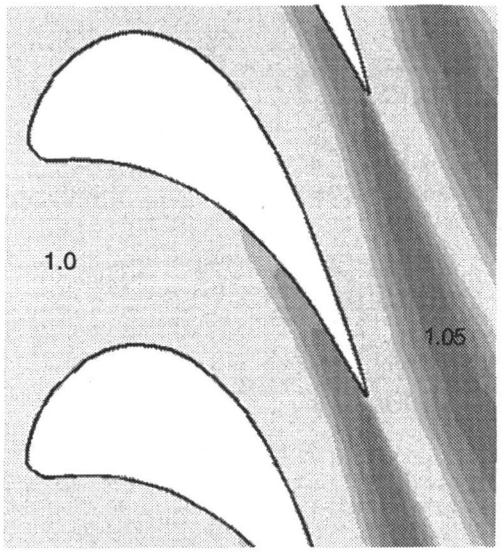

Fig. 7 Time-averaged rotor relative total temperature distribution on rotor hub platform. The temperatures are normalized by the average value at the hub inlet.

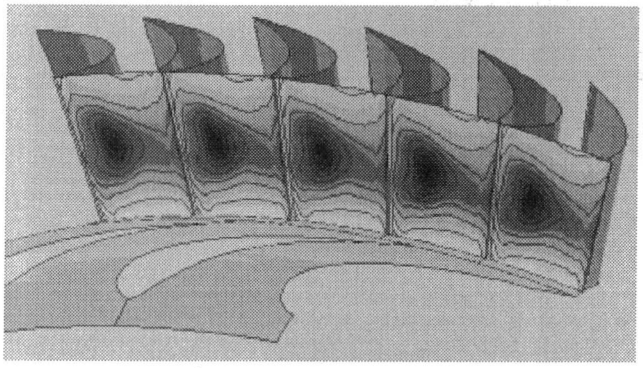

Fig. 8 Time-averaged rotor relative total temperature at rotor leading edge plane. Contour intervals are 2 percent of averaged rotor inlet relative temperature. (Hot streak magnitude of 1.8.) The hot spot at the center is 3 percent higher than the midspan average.

Unsteady Blade Row Interaction Effects. The flow field illustration of Fig. 4 suggests the unsteady time and length scales associated with hot streak/rotor interaction. At its leading edge, a rotor blade periodically sees a temperature peak as it passes through each hot streak, imposing an unsteady heat load on the airfoil. However, it is the time-averaged gas temperature that has the most bearing on turbine durability. It is commonly believed that the relative motion between the hot streak and rotor ''smears out'' the pitchwise temperature gradient, so that the time-averaged total temperature relative to the rotor is circumferentially uniform at the rotor inlet, with only the radial temperature gradient retained. We will show here that circumferential variations do occur in the *time-averaged* rotor relative total temperature at the rotor inlet. This can be seen in the time-averaged flowfields at two axial planes upstream of the rotor (leading edge and 20 percent chord upstream) shown in Figs. 8 and 9(a). It is clear from these figures that the rotor blades are subject to azimuthal as well as radial variations in the time-averaged temperature. The radial variation is readily understandable because of the radial gradient of the hot streak. The cause of pitchwise variation, present even 20 percent chord upstream of rotor leading edge, is less obvious and implies a flow phenomenon that is not widely appreciated at this time. The circumferential time-averaged temperature variation at midspan as shown in Fig. 9(b) is about 5 percent of the averaged rotor inlet stagnation temperature, or 100 K for a modern turbine with inlet gas temperatures of about 1920 K (3000°F). (Note that the perspective of Fig. 9(a) is misleading and that the hottest spot is at midpassage, as indicated in Fig. 9(b).) A temperature variation of this magnitude can certainly be significant in terms of rotor life. We will now address the causes of this temperature variation.

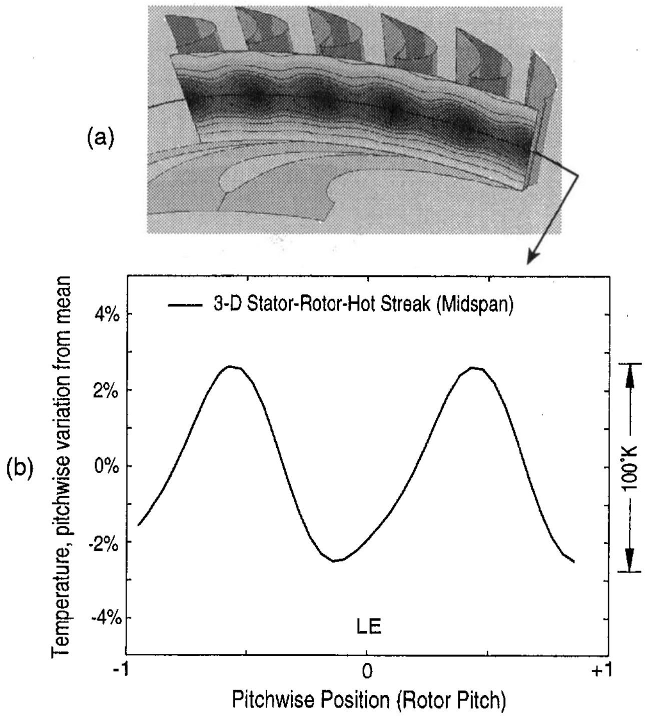

Fig. 9 (a) Time-averaged rotor relative total temperature at an axial station 20 percent rotor chord upstream of leading edge; (b) pitchwise variation from (a) at midspan (hot streak magnitude 1.8)

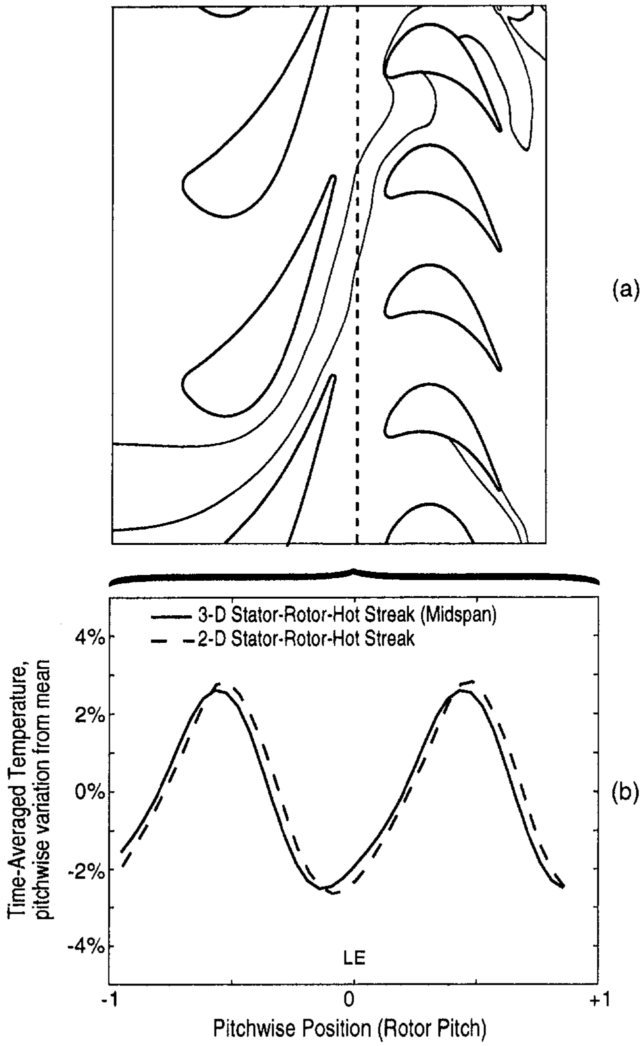

Fig. 10 (a) Hot streak calculation using a two-dimensional Euler solver based on midspan flow conditions of the three-dimensional calculation; (b) comparison of pitchwise variation of time-averaged rotor relative total temperatures at 20 percent rotor chord upstream of leading edge

A two-dimensional CFD procedure, chosen to expedite the research, was used to explore these circumferential variations further. A two-dimensional unsteady Euler solver, UNSFLO (Giles, 1988), was adapted to simulate the stator–rotor flowfield with a hot streak, Fig. 10(a). The blade geometry and boundary conditions were all based on midspan results of the three-dimensional calculation. The first question addressed was whether a two-dimensional approach produces the same circumferential variations seen in the three-dimensional calculation. Figure 10(b) compares the results of three-dimensional and two-dimensional calculations. The agreement between the two

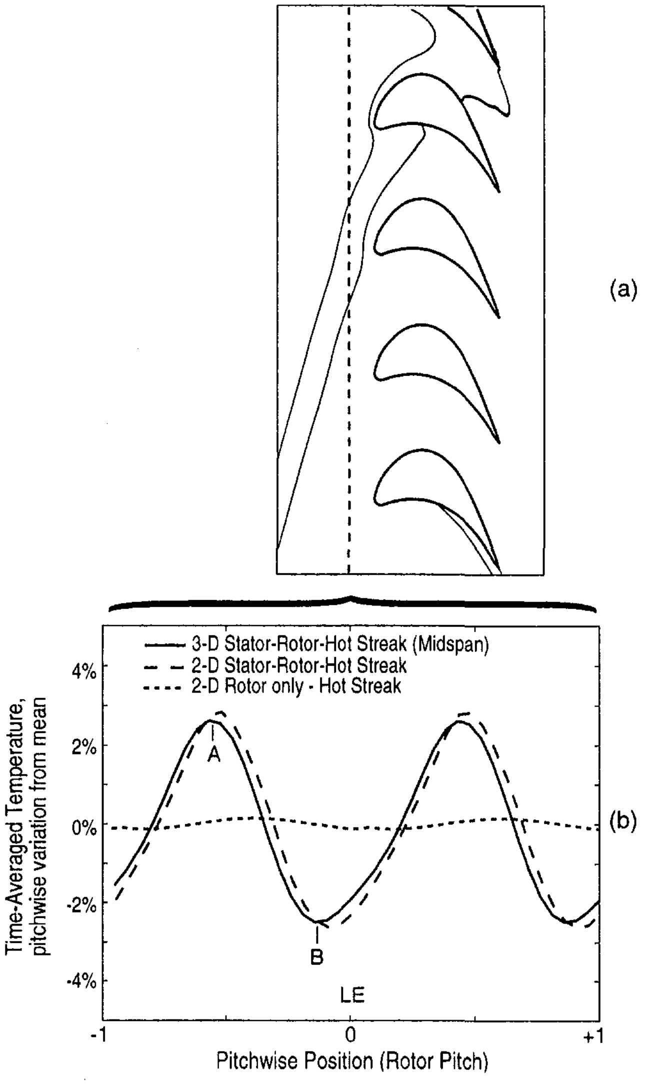

Fig. 11 **(*a*) Rotor hot streak-only calculation: inlet conditions based on two-dimensional stator–rotor calculation; (*b*) pitchwise variation of time-averaged rotor relative total temperature at 20 percent rotor chord upstream of leading edge**

is excellent, both in phase and magnitude. This agreement implies that the time-averaged circumferential temperature variation is physically a result of two-dimensional flow phenomena.

As the hot streak approaches the rotor blade, it responds to the upstream potential field of the rotor, twisting and deforming as it reaches the blade leading edge. If the potential interaction between the hot streak and rotor contributes to the time-averaged azimuthal temperature variation, the interaction would attenuate as the upstream distance to the rotor was increased, since the potential influence of the rotor decays exponentially with axial distance. This was investigated with a rotor-only UNSFLO calculation, in which a hot streak is specified at the rotor inlet flow boundary (as illustrated in Fig. 11(*a*)). Inflow conditions were specified to match the stator exit flows from the two-dimensional calculation. The hot streak temperature profile is the same as that used in the two-dimensional stator–rotor calculation. Time-averaged rotor relative total temperature as a function of pitchwise position is shown in Fig. 11(*b*), together with two-dimensional and three-dimensional stator–rotor–hot streak results. Although a small pitchwise variation does exist in the hot streak–rotor result, it is less than 10 percent of the magnitude of the stator–rotor calculations. This implies that the dominant driving mechanism is not a hot streak–rotor potential interaction.

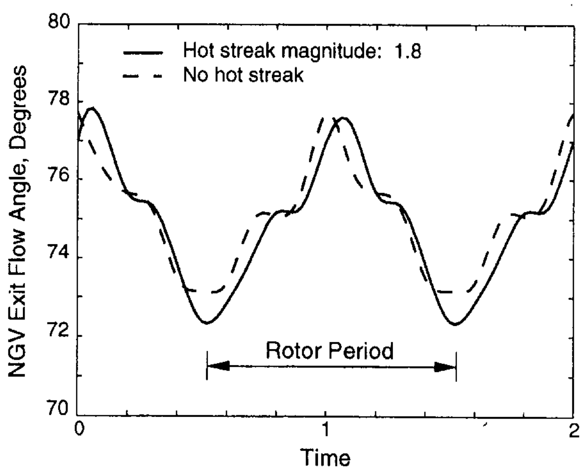

Fig. 12 **NGV exit flow angle (from axial) history at midpassage**

A comparison between Figs. 10 and 11 implies that the unsteady potential interaction between the NGV and rotor may be the driver of the pitchwise variation of time-averaged rotor relative total temperature at the rotor inlet. The NGV and rotor both see unsteadiness at NGV/blade passing frequency. After thorough examination of the CFD flow field solutions, including animation using flow visualization tools, the unsteady fluctuation of NGV exit flow angle as the rotor passes by was identified as the mechanism driving the variation in time-averaged rotor relative temperature.

The time history of the NGV exit tangential flow angle at midpassage is plotted in Fig. 12. The flow angle with uniform inlet conditions is shown for comparison. Figure 12 shows that NGV exit flow angle changes by about 6 deg as the rotor passes by. The presence of the hot streak does not significantly alter this flow angle variation, suggesting that the NGV loading variation due to blade row interaction is not strongly affected by the temperature distortion. This change in flow angle causes the hot streak to "wobble" in the tangential direction, at rotor blade passing frequency. The two extreme positions of the hot streak from the three-dimensional calculation are illustrated in Fig. 13 at midspan. The angular wobble of the hot streak means that the period of interaction between the hot streak and rotor varies.

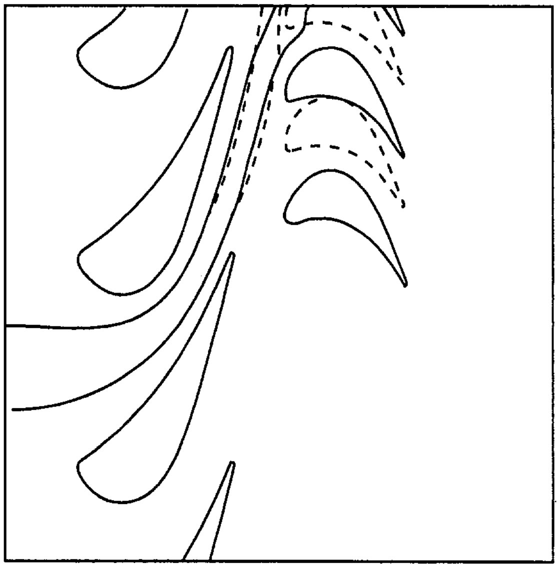

Fig. 13 **Two extreme positions of the hot streak showing hot streak wobble due to stator-rotor interaction. Entropy is used as a flow marker.**

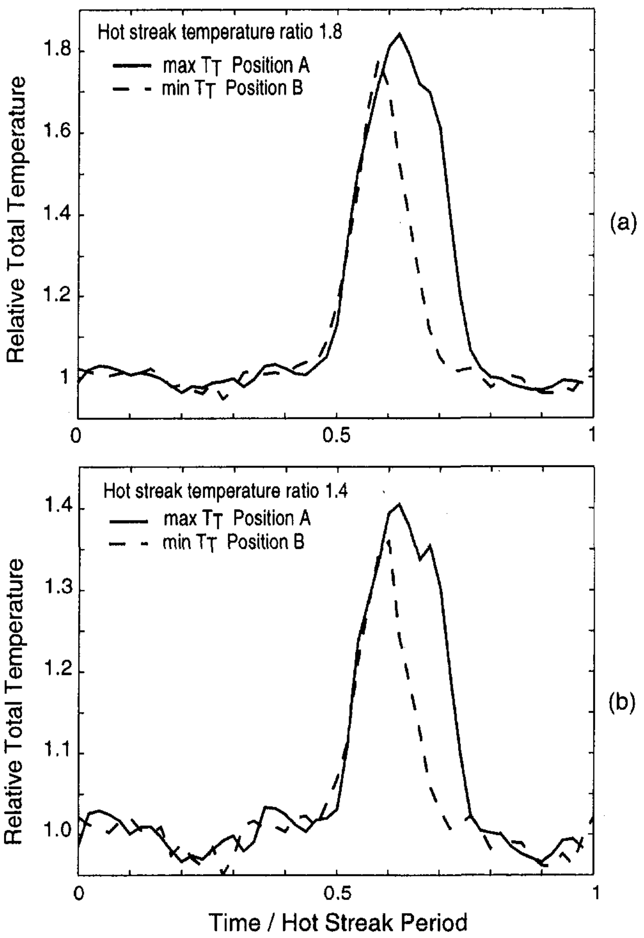

Fig. 14 Time history of rotor relative total temperature at two pitchwise positions with maximum (Position *A* in Fig. 11) and minimum (Position *B* in Fig. 11) time-averaged values. Temperature normalized by free-stream value. [Note the vertical axis scale change between (*a*) and (*b*).]

As the NGV exit flow swings toward the maximum angle, the hot streak is moving at a lower tangential speed relative to the rotor (solid lines in Fig. 13) so that the time-averaged temperature at this position is higher because of the longer hot streak residence time. On the other hand, at the minimum flow angle (dotted lines in Fig. 13), the hot streak is moving faster relative to the rotor, so that less time is spent in the hot fluid, which results in a lower time-averaged gas temperature. The time history of the instantaneous relative total temperatures at two points, corresponding to midspan maximum and minimum averaged temperatures (Points *A* and *B* in Fig. 11), is shown in Fig. 14, for two hot streak magnitudes. The left edges of the hot streak profile are aligned to allow "width" comparison. The change in hot streak width is a clear manifestation of the hot streak wobbling just described. Because the flow angle change is caused by the interaction of stator and rotor and is at the most a weak function of temperature distortion, the width of the hot streak wobbling should be independent of the hot streak temperature. Indeed, this is confirmed in Figs. 14(*a*) and 14(*b*), in that the width change is nearly identical for two hot streak magnitudes. This suggests that the pitchwise variation in relative gas temperature upstream of the rotor leading edge should be linearly proportional to hot streak strength. The magnitude of pitchwise variation is a fixed proportion of the excess thermal energy contained in the hot streak. This linear proportionality with hot streak magnitude is shown in Fig. 15, where the maximum-to-minimum difference in averaged temperature at midspan is plotted against hot streak temperature. A second axis is included to show the corresponding dimensional temperature variation by assuming a turbine inlet gas temperature of 1920 K (3000°F). For a hot streak temperature magnitude of 1.4, the variation is about 50 K, which can be significant to turbine life.

The nonuniformity in time-averaged total temperature upstream of the rotor implies that the rotor leading edge can operate at temperatures different from the circumferential mean. For the flow conditions examined here, the blade leading edge temperature is lower than the circumferential average, Fig. 8, lowering turbine heat load there and is thus advantageous.

Many design parameters can influence the unsteady blade row interaction process, and thus modify the time-averaged rotor inflow temperature distribution. We have explored one such parameter, the stator–rotor pitch ratio (or relative airfoil count ratio). Calculations with NGV to blade count ratios of 3:4 and 3:6 were carried out in addition to the 3:5 design configuration. The rotor blade chord was scaled (by a factor of 5/4 or 5/6 accordingly) to maintain the rotor blade row solidity as originally designed. The NGV–rotor gap was kept constant and the stator geometry and inlet hot streak pattern were the same for all calculations.

The time-averaged rotor relative total temperature distributions at the rotor leading edge plane are shown in Fig. 16 for the three different pitch ratios. To facilitate comparison, the rotor relative temperatures were normalized by NGV inlet gas temperature, which is identical for all three calculations. Figure 16 shows that the magnitude of the pitchwise temperature variation differs among three calculations. For the 3:4 configuration, the pitchwise variation is slightly larger than for the 3:5 case. For blade count ratios of 3:6, however, the circumferential temperature distribution is more uniform. This trend of decreasing variation with increasing number of rotor blades can be readily explained since, as the number of rotor blade count increases, the circumferential nonuniformity is reduced. (As the rotor blade count approaches infinity, the influence of rotor unsteadiness vanishes.)

Another observation that can be made from Fig. 16 is that the position of peak temperature point relative to the blade leading edge varies with the NGV–rotor pitch ratio. For the 3:5 ratio, the blade leading is positioned in a region where temperature is lower than average, while for the 3:4 blade count ratio, the blade leading edge is in a region with higher than average gas temperatures. For the 3:6 configuration, the circumferential variation is small so that the blade leading edge temperature is close to the average value. Notice that the time-averaged gas temperatures at the hub and tip radii are close to the same for all three cases. This suggests that the 3:4 configuration has the highest leading edge gas temperature with the strongest radial temperature gradient, while the 3:5 configuration has the

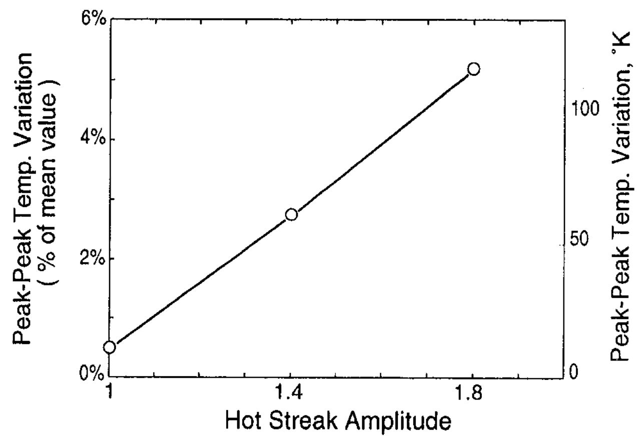

Fig. 15 Peak-to-peak magnitude of pitchwise variation of time-averaged rotor relative total temperature at midspan for hot streak magnitudes of 0, 1.4, and 1.8. The dimensional temperature variation is for a mean inlet temperature of 1920 K [3000°F].

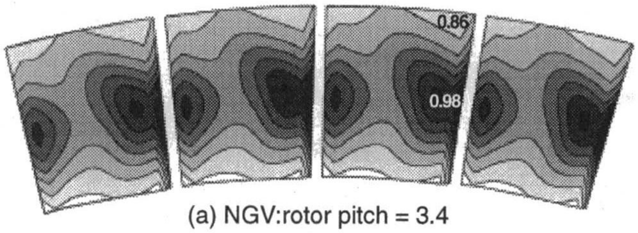

(a) NGV:rotor pitch = 3.4

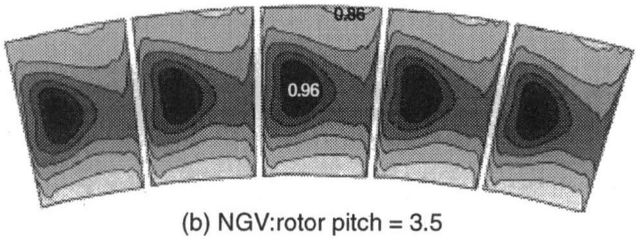

(b) NGV:rotor pitch = 3.5

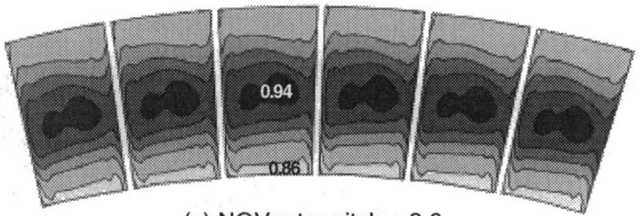

(c) NGV:rotor pitch = 3.6

Fig. 16 The rotor relative time-averaged total temperature at the rotor leading edge plane showing the influence of NGV-rotor pitch ratio (hot streak magnitude 1.8)

lowest leading edge gas temperature, with the 3:6 configuration being somewhere in between the other two cases. The differing conditions at blade leading edge result in different blade surface temperature distributions, as can be seen in Fig. 17. All three cases showed strong surface nonuniformity due to the hot/cold gas segregation. The 3:4 pitch ratio has higher pressure surface temperature and strongest radial variation, and the 3:5 ratio has lowest pressure surface temperature and weakest radial temperature gradient. The blade suction surfaces demonstrate similar behavior.

The data in Fig. 17 are also presented as three-dimensional surfaces in Fig. 18, which shows heat transfer to both sides of the blades. Here, the height is the gas-to-wall temperature difference normalized by the average NGV inlet temperature, and is thus a measure of heat transfer. The shape of the figure illustrates the heat transfer distribution while the volume represents the total heat load to the blade. The design 3 NGV to 5 blade count shows a nearly uniform heat transfer around the blade (Fig. 18(*a*)). This changes dramatically with the addition of a hot streak (Fig. 18(*b*)). Now, the total heat load has increased and is very nonuniform. Increased nonuniformity is apparent for the 3:4 (Fig. 18(*c*)) and 3:6 (Fig. 18(*d*)) NGV to blade count ratios.

Since most of the adverse effects due to the hot streak are on the pressure surface, we compare pressure side surface area-averaged gas temperatures (essentially a measure of the total pressure side heat load) for the three airfoil count ratios as a function of hot streak magnitude in Fig. 19. Without distortion, all three airfoil counts produced about the same surface temperature.

As the hot streak magnitude increases, the 3:4 pitch ratio case shows the strongest influence and the 3:5 ratio the least, in keeping with the observations in Figs. 16 and 17. To help in judging the importance of these unsteady effects to turbine life, we have labeled the right-hand vertical axis of Fig. 19 as the increase in total pressure surface heat transfer due to the hot streaks. (Parameters typical of a modern turbine design were chosen, NGV inlet temperature of 1920 K [3000°F] and blade metal temperature of 1310 K [1900°F].) For a hot streak magnitude of 1.4, the pressure side heat load increased by 13 percent compared to uniform inflow for the 3:5 case, and by 27 percent for the 3:4 case. (Since there is little change on the suction surface, this is about the total heat load increase on the blade.) There are two factors at work here, the degree of temperature nonuniformity and the position of the peak temperature in the passage relative to the blade surface. Examination of the calculation solutions shows that the 3:5 ratio has the lowest heat load because of favorable positioning of the hot spot relative to the blade rather than to lower circumferential gradients at the rotor inlet plane.

There are several inferences that can be drawn from this analysis. The first is that there may be an optimal vane/blade count that minimizes the rotor heat load and maximizes turbine life. To the detail examined here, it would be 3:5 for this turbine. This optimum may be a function of operating condition, but turbine life is set mainly by the peak temperature operating

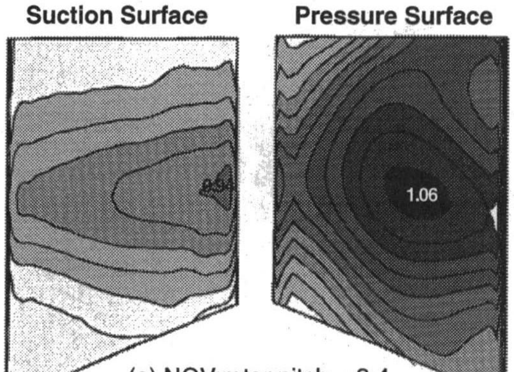

(a) NGV:rotor pitch = 3.4

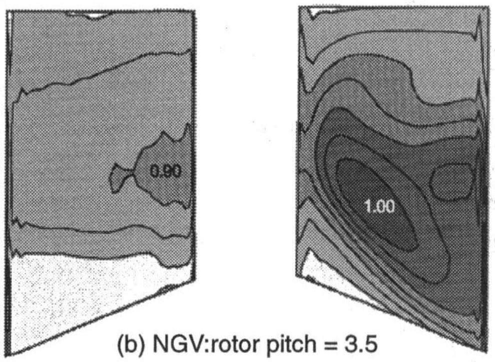

(b) NGV:rotor pitch = 3.5

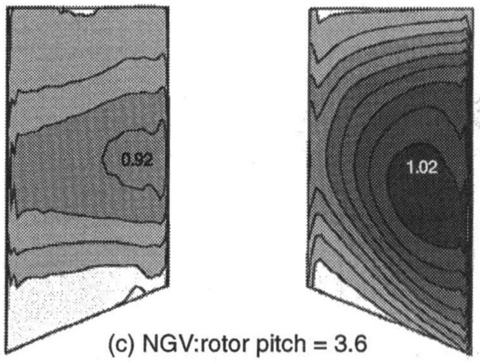

(c) NGV:rotor pitch = 3.6

Fig. 17 Time-averaged blade surface temperature distribution for three blade count ratios (temperatures normalized by NGV inlet temperature contour levels of 0.02)

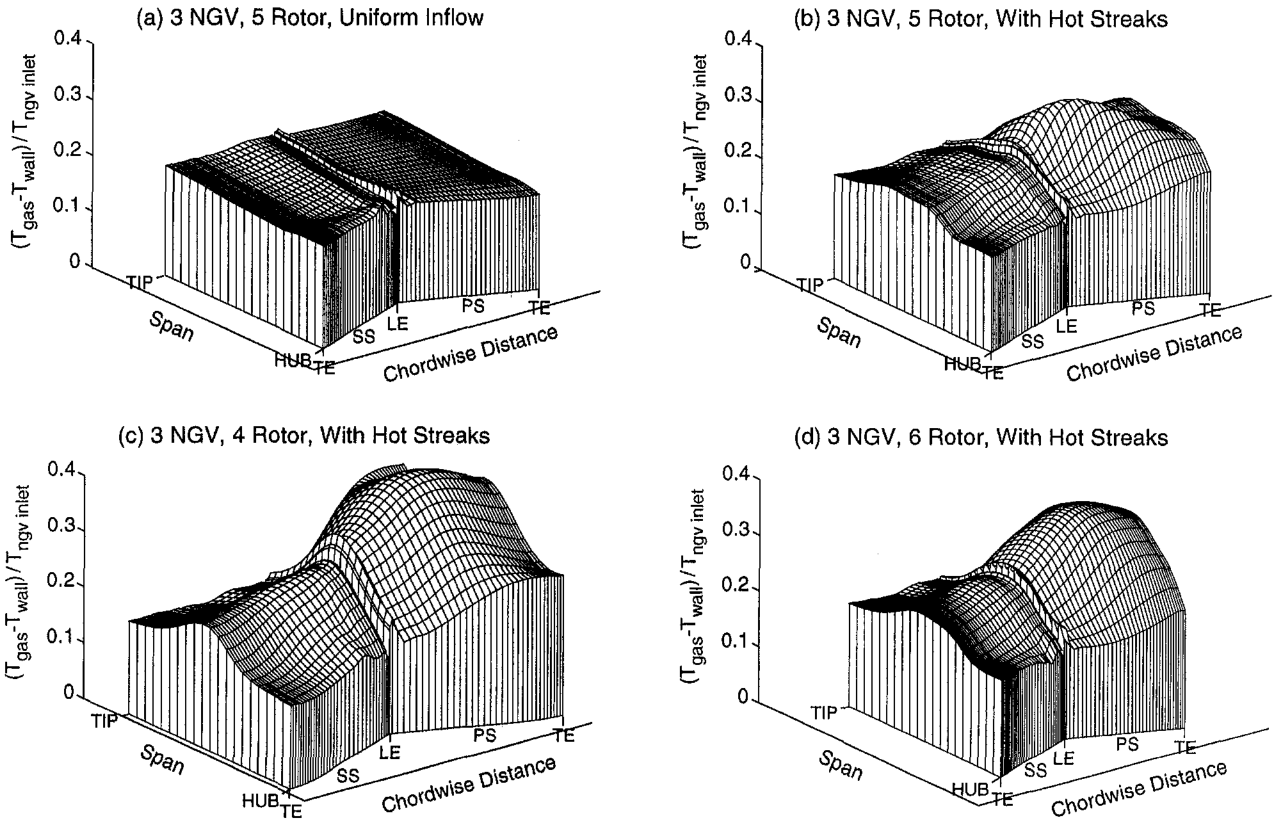

Fig. 18 Nondimensional heat load distribution into rotor blade

condition (i.e., full engine power, the case examined here), so that shifts in the relative heat loads at lower powers will not be as large a concern.

The second point is that vane/blade count is important and must be accurately simulated. Ratios of one vane to one blade, often used in CFD simulations to save computer time, can give misleading results.

Third, there is an industry trend toward the use of smaller numbers of longer chord turbine blades in order to reduce turbine parts count and cost. The results reported herein suggest that this trend can have an implicit cost of increased heat load given the presence of hot streaks. This would increase the cooling required as well as attendant cycle penalties. Also, the increased nonuniformity of the heat load makes the cooling design more challenging in that efficient use of coolant demands accurate determination of the distorted flowfield and resultant heat transfer. The combustor design could be considered more difficult as well since the low blade count turbine has a greater sensitivity to combustor hot streaks.

Last, we point out that this nonuniformity in the time-averaged rotor relative inflow results from the interplay between two quite different unsteady phenomena—rotor influence on an upstream vane row and wake/streak influence on a downstream rotor—and as such can be considered a second-order interaction. It is surprising to us that such a second-order phenomenon has a first-order influence on rotor heat load, as has been shown here.

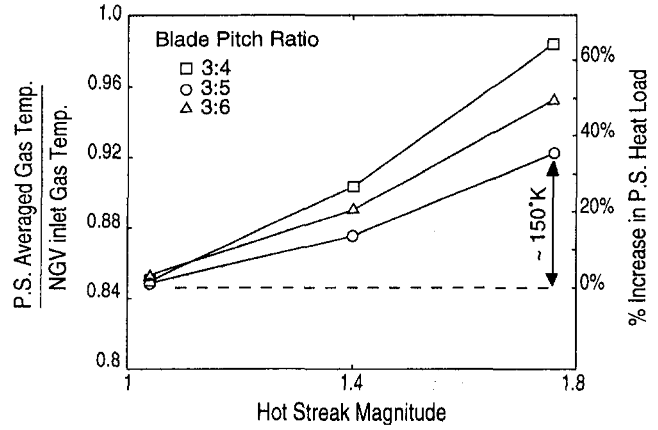

Fig. 19 Pressure surface area-averaged gas temperatures as functions of NGV-blade pitch ratio and hot streak magnitude. (Temperature is normalized by the NGV inlet gas temperature.) The percent increase in pressure side heat load is for a turbine with a 1920 K (3000°F) NGV inlet temperature and a 1310 K (1900°F) blade metal temperature.

Concluding Remarks

The complicated flow phenomena in an axial flow turbine with inlet temperature distortion have been rigorously examined and the detrimental effects due to inlet hot streaks elucidated. Three separate physical mechanisms have been identified that influence rotor blade surface gas temperatures of turbines subjected to a hot streak type of inlet distortion. Parametric scaling of these effects with turbine design variables was also studied. To summarize briefly the lessons learned in this study, the following mechanisms are key to assessing hot streak influence on turbine rotor heat transfer:

1 Preferential migration of hot fluid onto the pressure surface increases the time-averaged local surface temperatures and temperature nonuniformity. The resultant increase in surface temperature depends nonlinearly on the level of inlet temperature distortion.

2 Buoyancy forces drive high-temperature fluid toward the hub and increase local platform surface temperature. The magnitude of the displacement is linearly proportional to hot streak

temperature and inversely proportional to the square of the flow coefficient.

3 Unsteady blade row interaction and a resultant NGV exit flow angle fluctuation cause the hot streak to wobble at the rotor blade passing frequency. This generates nonuniformity in the *time-averaged* relative total temperature at the rotor inlet. As a result, rotor leading edge temperature is different from the local circumferential mean. The degree of pitchwise variation is linearly proportional to the magnitude of temperature distortion. Because this unsteady interaction is a strong function of NGV–rotor blade count ratio, an optimum NGV–rotor blade count may exist that minimizes the influence of hot streaks on rotor blade life.

The linkage of unsteady blade row interaction to hot streak wobble and the resultant effect on turbine blade heat load is a novel flow phenomenon not previously reported in the literature. These results are somewhat surprising in that a relatively small flow interaction (±3 deg swing in NGV exit angle) generates flow features of considerable engineering significance (100 K temperature variations). It would be interesting to examine other situations in which strong blade row interactions occur for similar effects, NGV coolant wakes, endwall vortices, and tip leakage flows, for example.

Acknowledgments

This work was supported by the USAF Office of Scientific Research, NASA LeRC, SNECMA, and ABB.

References

Abhari, R. S., Guenette, G. R., Epstein, A. H., and Giles, M. B., 1992, "Comparison of Time-Resolved Turbine Rotor Heat Transfer Measurements and Numerical Calculations," ASME JOURNAL OF TURBOMACHINERY, Vol. 114, pp. 818–827.

Butler, T. L., Sharma, O. P., Joslyn, H. D., and Dring, R. P., 1986, "Redistribution of an Inlet Temperature Distortion in an Axial Flow Turbine Stage," Paper No. AIAA-86-1468.

Dorney, D. J., Davis, R. L., Edwards, D. E., and Madavan, N. K., 1990, "Unsteady Analysis of Hot Streak Migration in a Turbine Stage," Paper No. AIAA-90-2354.

Giles, M. B., 1988, "UNSFLO: A Numerical Method for Unsteady Inviscid Flow in Turbomachinery," MIT Gas Turbine Laboratory Report #195.

Harasgama, S. P., 1990, "Combustor Exit Temperature Distortion Effects on Heat Transfer and Aerodynamics Within a Rotating Turbine Blade Passage," ASME Paper 90-GT-174.

Kerrebrock, J. L., and Mikolajczak, A. A., 1970, "Intra Stator Transport of Rotor Wakes and Its Effect on Compressor Performance," ASME *Journal of Engineering for Power,* Vol. 92, pp. 000–000.

Krouthen, B., and Giles, M. B., 1988, "Numerical Investigation of Hot Streaks in Turbines," Paper No. AIAA-88-3015.

Munk, M., and Prim, R., 1947, "On the Multiplicity of Steady Gas Flows Having the Same Streamline Pattern," *Proc. National Academy of Sciences,* U.S., Vol. 33.

Rai, M. M., and Dring, R. P., 1987, "Navier–Stokes Analyses of the Redistribution of Inlet Temperature Distributions in a Turbine," Paper No. AIAA-87-2146.

Saxer, A. P., 1992, "A Numerical Analysis of 3-D Inviscid Stator Rotor Interactions Using Non-reflecting Boundary Conditions," Ph.D. Thesis, Dept. of Aeronautics and Astronautics, MIT, Cambridge, MA.

Saxer, A. P., and Giles, M. B., 1993, "Predictions of 3-D Steady and Unsteady Inviscid Transonic Stator/Rotor Interaction With Inlet Radial Temperature Non-Uniformity," ASME Paper No. 93-GT-10; ASME JOURNAL OF TURBOMACHINERY, Vol. 116, pp. 347–357.

Shang, T., 1995, "Influence of Inlet Temperature Distortion on Turbine Heat Transfer," Ph.D. Thesis, Dept. of Aeronautics and Astronautics, MIT, Cambridge, MA.

Shang, T., Guenette, G. R., Epstein, A. H., and Saxer, A. P., 1995, "The Influence of Inlet Temperature Distortion on Rotor Heat Transfer in a Transonic Turbine," Paper No. AIAA-95-3042.

Sharma, O. P., Ni, R. H., and Tanrikut, S., 1994, "Unsteady Flows in Turbines—Impact on Design Procedure," *Turbomachinery Design Using CFD,* AGARD lecture series 195.

Takahashi, R. K., and Ni, R. H., 1990, "Unsteady Euler Analysis of the Redistribution of an Inlet Temperature Distortion in a Turbine," Paper No. AIAA-90-2262.

High-Temperature Reactive Flow of Combustion Gases in an Expansion Turbine

T. Godin

S. Harvey

P. Stouffs

Laboratoire d'Energétique,
Ecole des Mines de Nantes—Isitem,
Rue C. Pauc BP 90604
F-44306 Nantes Cedex 03, France

The analysis of the chemical behavior of the working fluid in gas turbines is usually restricted to the combustion chamber sections. However, the current trend toward higher Turbine Inlet Temperatures (TIT), in order to achieve improved thermal efficiency, will invalidate the assumption of frozen composition of the gases in the first stages of the expansion process. It will become necessary to consider the recombination reactions of the dissociated species, resulting in heat release during expansion. In order to quantify the influence of this reactivity on the performance of high TIT gas turbines, a one-dimensional model of the reactive flow has been developed. Preliminary results were reported in a previous paper. The authors concluded that, in the case of expansion of combustion gases in a subsonic static uncurved distributor nozzle, the residual reactivity must be taken into account above a temperature threshold of around 2000 K. The present study extends these results by investigating the reactive flow in a complete multistage turbine set, including a transonic first-stage nozzle. A key result of this study is that heat release during the expansion process itself will be considerable in future high-temperature gas turbines, and this will have significant implications for turbine design techniques. Furthermore, we show that, at the turbine exit, the fractions of NO and CO are very different from the values computed at the combustor outlet. In particular, NO production in the early part of the expansion process is very high. Finally, the effects of temperature fluctuations at the turbine inlet are considered. We show that residual chemical reactivity affects the expansion characteristics in gas turbines with TITs comparable to those attained by modern high-performance machines.

Introduction

In order to improve thermal efficiency, gas turbines have developed considerably in recent years with respect to their maximum working fluid temperatures and pressures. Ambitious research programs forecast gas turbine operation with TIT close to the stoichiometric flame temperature (around 2600 K for natural gas fuel) within the foreseeable future.

The analysis of the chemical evolution of the working fluid in gas turbines is usually restricted to the combustion system sections. However, the current trend toward higher TITs could invalidate the assumption of frozen chemical composition of the gases downstream from the combustion system. When the TIT exceeds 2000 K, the gas mixture at the combustor outlet contains dissociated chemical species. As the gas expands, these species recombine, and supplementary heat is released. Given the extremely quickly changing aerothermodynamic conditions during the expansion, the above-mentioned chemical reactions are assumed to be far from equilibrium and, thus, governed by kinetics. A coupled analysis with respect to both aerodynamics and thermochemistry becomes necessary when one aims to understand the impact of a chemically reactive working fluid on the flow characteristics in this part of the engine. However, an extensive literature review indicated only one existing study in the field of reactive expansion nozzle flow in gas turbines (Mencherini, 1993).

In a previous study (Leide and Stouffs, 1996), the authors presented a one-dimensional model of reactive flow through a first-stage turbine nozzle. The results indicated that for hot combustion gases in a subsonic static uncurved distributor nozzle, it is imperative to account for chemical reactivity for nozzle inlet temperatures exceeding 2000 K. However, in view of the current trend toward increased velocities at the exit of the first-stage turbine nozzle, it is necessary to extend the preliminary results by investigating the case of transonic nozzles. Furthermore, the preliminary study indicated that the residual reactivity of the high-velocity hot gases is still considerable at the nozzle exit, and therefore in this paper, we extend the previous results by modeling the reactive flow in the first-stage turbine rotor wheel and beyond. Finally, detailed measurements of the temperature field at the exit of a combustion chamber reveal considerable fluctuations of the local temperature. In this paper we will present results that attempt to account for such fluctuations at the nozzle inlet.

Description of the One-Dimensional Flow Model

The reader is referred to a previous paper (Leide and Stouffs, 1994) for a more complete description of the proposed model. The main features of the model are outlined below.

Working Fluid Composition. The gas mixture at the exit of the combustion system can be characterized by the following two hypotheses:

1 The gas mixture entering the nozzle is free of hydrocarbon molecules.
2 The mixture is assumed to be at chemical equilibrium, with the exception of the NO species.

The following 11 species are retained for the present study: CO_2, CO, H_2O, H_2, H, OH, O_2, O, N_2, N, and NO.

Chemical Reaction Kinetics. The fluid undergoes rapidly changing temperature and pressure conditions while expanding through the turbine. To account correctly for the resulting fluid

---

Contributed by the International Gas Turbine Institute and presented at Cogen-Turbo Power, Vienna, Austria, August 23–25, 1995. Manuscript received by the International Gas Turbine Institute May 15, 1995. ASME Paper No. 95-CTP-7. Associate Technical Editor: C. J. Russo.

composition variations, a detailed chemical reaction scheme must be considered, together with the appropriate reaction kinetics. In this study, the reaction scheme is described by the second step of the *Quasi-Global Approach* proposed by Edelman and Fortune (1969).

The retained reactions are listed below:

Elementary Reaction Mechanism	
No.	Reaction
1	$CO + OH \rightleftharpoons CO_2 + H$
2	$OH + H_2 \rightleftharpoons H + H_2O$
3	$OH + OH \rightleftharpoons H_2O + O$
4	$O + H_2 \rightleftharpoons OH + H$
5	$H + O_2 \rightleftharpoons OH + O$
6	$O + H + M \rightleftharpoons OH + M$
7	$O + O + M \rightleftharpoons O_2 + M$
8	$H + H + M \rightleftharpoons H_2 + M$
9	$H + OH + M \rightleftharpoons H_2O + M$

In order to analyze pollutant formation history throughout the nozzle, this reaction mechanism was extended by incorporating the following Zeldovich mechanism for nitrogen oxide formation:

10	$O + N_2 \rightleftharpoons N + NO$
11	$N + O_2 \rightleftharpoons NO + O$
12	$N + OH \rightleftharpoons NO + H$

The resulting mechanism of 12 reactions is sufficiently detailed to enable the analysis of the high-temperature dissociation/recombination phenomena, including production of major pollutants such as CO and NO.

The reaction kinetics for the forward reactions are described using Arrhenius expressions for the reaction rates. The forward reaction rate constants were taken from Miller and Bowman (1989). The reverse reaction rates were calculated from the reaction equilibrium constants. Finally, the reacting gas mixture is assumed to behave like an ideal gas.

Flow Equations. Real flow fields in turbomachinery applications present nonuniformities due to clearance effects, wake phenomena, and secondary flows. Furthermore, unsteady pressure fluctuations, due to compressor operation and flame oscillations, occur in real operation at the expansion turbine intake. Since the intent of the present work is to provide basic information about the interaction between the working fluid chemical reactivity and its other flow characteristics, the current model considers one-dimensional stationary flow, the spatial dimension considered being the nozzle axis z. The model is further simplified by assuming adiabatic and frictionless flow.

In this section, we summarize the flow equations for the stator nozzles. In the following section, we show how these equations must be modified to describe the flow in the rotor wheels.

The chemically reactive, adiabatic, frictionless one-dimensional stationary stator nozzle flow is described by the following equations expressing conservation of mass, momentum, and energy, and chemical species balances (one equation per chemical species), respectively:

$$d\dot{m} = d(\rho A v) = 0 \tag{1}$$

$$\rho v \frac{dv}{dz} + \frac{dp}{dz} = 0 \tag{2}$$

$$\frac{dh}{dz} + v \frac{dv}{dz} = 0 \tag{3}$$

$$\rho v \frac{dy_i}{dz} = \dot{\omega}_i M_i \tag{4}$$

$\dot{\omega}_i$ represents the chemical species production rate, computed from the reaction rate expressions. Note also that the reference state for enthalpy calculations is that of the constituent elements of the compound at standard state and pressure.

The flow between blades in the rotating turbine wheels may be described by a similar set of equations. The equations expressing conservation of mass and chemical species balances remain unchanged. The momentum and energy equations may be modified as follows (note that, as before, v denotes the absolute gas velocity):

$$\rho v \frac{dv}{dz} + \frac{dp}{dz} = \rho \frac{dW}{dz} \tag{5}$$

$$\frac{dh}{dz} + v \frac{dv}{dz} = \frac{dW}{dz} \tag{6}$$

where W refers to the specific work produced by one unit mass of fluid as it expands in the rotor wheel. In order to evaluate the right-hand side terms in Eqs. (5) and (6), we introduce the assumption that the local *degree of reaction* Λ is constant throughout the rotor wheel. This leads to:

$$\frac{dW}{dz} = \frac{1}{\Lambda} \frac{dh}{dz} \tag{7}$$

Flow through the nozzle followed by the rotor wheel may now be modeled by coupling Eqs. (1)–(7) with appropriate equations describing the chemical reactions. The resulting set of ordinary differential equations is solved using Allan/Neptunix (CISI, 1989) ODE solver software. Note finally that, as announced previously, we consider the case where the first turbine stage is transonic, and care must be taken when computing flow characteristics in the region where the Mach number is close to 1.0. As we will discuss later, the simulation proceeds by imposing a pressure profile on the fluid, and flow in the throat region can therefore be easily treated using the "specified pres-

Nomenclature

A = nozzle section, m^2
c = absolute gas velocity in rotor, m/s
h = specific mass enthalpy, J/kg
$\Delta\bar{h}_f^o$ = molar formation enthalpy, J/mol
$\Delta H^o_{r,\mathrm{CH}_4}$ = reaction heat of methane, J/mol
$\dot{m}$ = mass flux, kg/s
M = molecular mass, kg/mol
n = volumetric products/dry air ratio
p = pressure, Pa
S = molecular species
$[S]$ = species concentration, mol/m^3
T = temperature, K
v = velocity, m/s
w = relative gas velocity in rotor, m/s
W = specific work, J/kg
x = molar fraction, mol/mol
y = mass fraction, kg/kg
z = nozzle axis, m
α_1 = velocity angle at stator outlet
ϵ = stoichiometric fuel/air ratio
Λ = degree of reaction
η_{HR} = chemical heat release efficiency
ρ = density, kg/m^3
ϕ = fuel richness
$\dot{\omega}$ = chemical production rate, mol/(m^3 s)

Table 1 Inlet conditions

	TIT	P	NO	ϕ	$T_{Cmp.Dis}$
case	[K]	[bar]	[ppm]	[−]	[K]
1	1600	30.0	25	0.37	788
2	2000	35.0	50	0.57	823
3	2300	40.0	75	0.75	855
4	2600	45.0	100	0.99	884

sure method,'' as discussed by Zucrow and Hoffman (1977). Subsequent turbine stages are assumed to be subsonic.

Overview of Main Model Parameters

Turbine Inlet Conditions. A zero-dimensional model generates a burned-gas mixture composition as it is discharged from a methane/air gas turbine combustion system. Two operating conditions are required, namely the combustion chamber exit pressure and temperature (TIT). The inlet Mach number is set equal to 0.2. As discussed previously, the gas mixture leaving the combustion chamber is assumed to be completely free of hydrocarbon molecules and also to be at chemical equilibrium, with the exception of the NO species. The combustor outlet conditions are computed assuming adiabatic reactor behavior. The pressure drop is neglected. The fuel is assumed to enter the combustor at the operating pressure and the ambient temperature. The air is first compressed from ambient pressure up to the operating pressure. Table 1 lists the corresponding compressor discharge temperatures ($T_{\mathrm{Cmp.Dis}}$). The compressed air enters the combustor uncooled. The molar composition is easily computed using equilibrium data from the Janaf tables (Chase et al., 1985). The combustion equation is written as follows:

$$\frac{\phi\epsilon}{n}\mathrm{CH_4} + \frac{1}{n}(0.21\mathrm{O_2} + 0.79\mathrm{N_2}) \rightarrow x_{\mathrm{CO_2}}\mathrm{CO_2} + x_{\mathrm{CO}}\mathrm{CO} + x_{\mathrm{O_2}}\mathrm{O_2} + x_{\mathrm{O}}\mathrm{O} + x_{\mathrm{H_2O}}\mathrm{H_2O} + x_{\mathrm{OH}}\mathrm{OH} + x_{\mathrm{H_2}}\mathrm{H_2} + x_{\mathrm{H}}\mathrm{H} + x_{\mathrm{N_2}}\mathrm{N_2} + x_{\mathrm{N}}\mathrm{N} + x_{\mathrm{NO}}\mathrm{NO} \quad (8)$$

with the fuel richness ϕ, the stoichiometric fuel/air ratio $\epsilon = 0.105$, the volumetric products/dry air ratio $n = 1.58/(2x_{\mathrm{N_2}} + x_{\mathrm{NO}} + x_{\mathrm{N}})$.

In practice, NO concentrations at the combustion chamber outlet are considerably lower than those indicated by the equilibrium calculations. Thus, the NO concentrations at the nozzle inlet are set at nonequilibrium values, which appear reasonable compared to levels attained by current technology burners. We will consider values ranging from 25 ppm to 100 ppm according to the TIT value.

Table 1 lists the turbine inlet conditions that have been chosen for the present study. Case 1 is representative of current advanced gas turbine machinery. Case 4 is the limiting case of quasi-stoichiometric combustion of natural gas fuel. Note that the high TIT calculated in this case is due in part to the high temperature of the air discharged from the compressor, due in turn to the high compression ratio. Cases 2 and 3 are representative of future development of combustion chamber and gas turbine technology.

Nozzle and Rotor Operating Conditions. The turbine inlet conditions considered were discussed in the previous section. Flow through the first-stage nozzle and rotor may now be simulated by imposing a pressure profile on the flow together with the given inlet conditions (we also recall that the inlet Mach number is set equal to 0.2). The outlet pressure is chosen such that the outlet Mach number attains a given value. In this study we consider a transonic nozzle with outlet Mach number equal to 1.1 for all cases. This fixes the nozzle outlet pressure, and we consider a half period sinusoidal variation of the pressure between the inlet and the outlet.

To discuss the choice of the rotor outlet pressure, we refer to Fig. 1, which shows the fluid velocity triangles at the inlet and outlet of the rotor. As discussed above, the hot gases leave the nozzle at Mach = 1.1, and a corresponding absolute velocity c_1. The c_1 vector is defined by setting the angle α_1 to 60 deg. Subtracting the rotor speed u yields the relative rotor inlet velocity ω_1. We then assume that the axial velocity components are equal at rotor inlet and outlet, and that the absolute velocity at the rotor exit is purely axial, which fixes c_2. Note that the outlet velocity c_2 is greater than the nozzle inlet velocity c_0, indicating that the first turbine stage does not have the normal characteristics of a ''repeating stage.'' This is current practice in modern high-performance gas turbine design. The rotor outlet pressure is selected such that the velocity is equal to the specified value c_2, and as before the pressure variation between the outlet and the inlet is sinusoidal. Finally, we obtain the relative velocity w_2 by subtracting velocity u from c_2. The degree of reaction Λ may then be computed according to:

$$\Lambda = \frac{w_1^2 - w_2^2}{(w_1^2 - w_2^2) + (c_2^2 - c_1^2)} \quad (9)$$

The rotor velocity u is set in each case such that Λ is equal to the chosen value 0.25, with u chosen within the range 400 to 600 m/s, in accordance with current machine design practice.

This discussion is valid for the first stage of the turbine. For the case of stoichiometric inlet conditions, we will present results for several stages. The first stage is modeled as described above. Subsequent stages are modeled with equal velocities at the stator inlet and the rotor outlet. Furthermore, the blade velocity u is assumed equal to the value chosen during first-stage calculations. The angle α_1 remains equal to 60 deg in each stage. The pressure levels are set such that Mach = 0.9 at the nozzle outlet and $c_2 = c_0$ at the rotor outlet. The degree of reaction can no longer be chosen. The Λ values resulting from these assumptions are $\Lambda = 0.42$ in the second stage, 0.46 in stage 3, and 0.48 in stage 4, i.e., close to the expected value of 0.5 for a repeating stage.

Temperature Fluctuations at Combustor Outlet. In this paper we also discuss the effect of temperature fluctuations at the inlet of the first stage nozzle. Figure 2 shows typical time fluctuations of the temperature measured along the axis of the combustor exit ducting, measured by SNECMA and ONERA (Magre et al., 1991). The corresponding average temperature

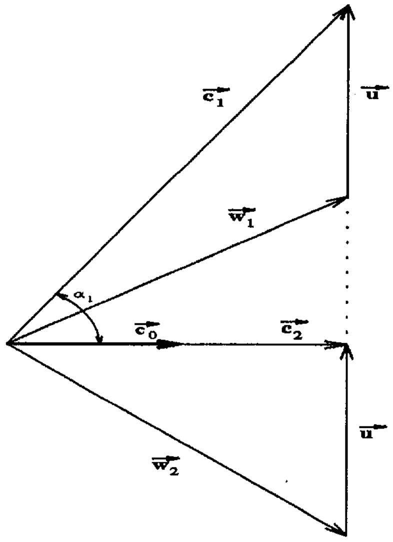

Fig. 1 Velocity vector diagram for first turbine stage

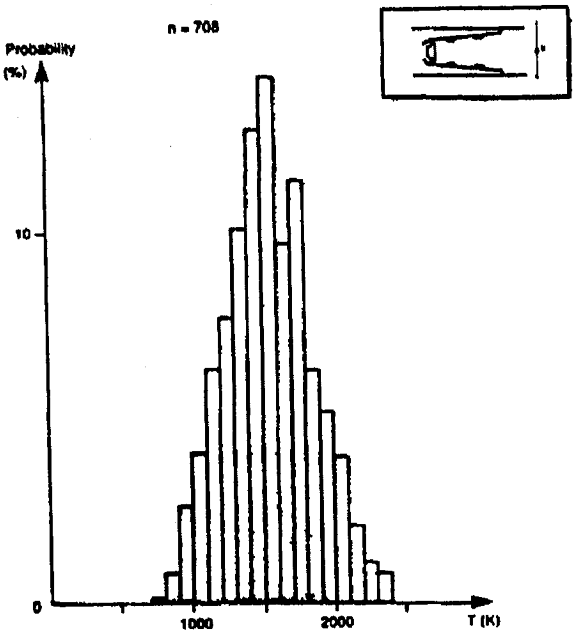

Fig. 2 Measured temperature fluctuations at combustor outlet

is 1544 K, but the instantaneous measurements fluctuate considerably around this value. In order to quantify the effect of these fluctuations, simulations were run with the different inlet temperatures represented in the figure, and identical pressure conditions at the inlet and outlet. The results presented correspond to a weighted average of the individual results. The weighting is proportional to the probability of occurrence of the corresponding temperature. This procedure is equivalent to assuming that the different temperature gas streams expand independently with no mixing or heat exchange between the streams. The results are then compared with those corresponding to a uniform temperature distribution at the nozzle inlet, with the uniform temperature equal to the average value of the measured distribution. The two sets of results are limiting cases. In reality, a certain degree of mixing and heat exchange between different temperature streams occurs during the expansion, and the expansion characteristics will lie between the two presented.

In this paper, we also attempt to study the effects of temperature fluctuations for higher inlet temperatures. In such cases, experimental data are not available. The results presented correspond to the turbine inlet conditions of Case 3 in Table 1. Since the temperature distribution for TIT_{mean} = 1544 K is clearly Gaussian, a similar distribution type was chosen for TIT_{mean} = 2300 K. The standard deviation is lower, since the instantaneous temperature cannot exceed the adiabatic stoichiometric combustion temperature. The chosen standard deviation value is 80 K. It is important to note that higher temperatures are attained with considerably reduced excess air. The problems associated with defective air–fuel mixing are thus reduced, which in turn reduces the temperature fluctuations. This justifies the choice of a lower standard deviation.

Note finally that for these simulations, we only consider nonuniform inlet temperature conditions. The other inlet variables defining the problem are maintained constant at the values indicated in Table 1, i.e., the pressure and NO fraction are assumed to be equal to the value representative of the average temperature of the flow. For TIT_{mean} = 1544 K, the inlet pressure and NO composition values are taken equal to those corresponding to TIT = 1600 K in Table 1.

Results

In this section, we present results for the different cases discussed above. We first present results for uniform inlet conditions, as presented in Table 1. In particular, we show plots of the evolution of temperature, NO and CO composition, and chemical heat release efficiency. The latter is a measure of the fraction of the fuel heating value that has not been released due to the presence of dissociated and partially oxidized species. We define this efficiency as follows:

$$\eta_{HR} = \frac{\sum_i (x_i \Delta\bar{h}^o_{f,i}) - \frac{\phi\epsilon}{n}\Delta\bar{h}^o_{f,\mathrm{CH_4}}}{\frac{\phi\epsilon}{n}\Delta H^o_{r,\mathrm{CH_4}}} \quad (10)$$

For all cases considered we show the results obtained assuming that the fluid composition corresponds throughout the turbine to that measured at the combustor exit (frozen composition), which we compare to the results obtained assuming the chemical reaction mechanisms discussed previously (kinetic results).

Results With Uniform Temperature at Nozzle Inlet. Figure 3 shows the evolution of the temperature in the first turbine stage for the different inlet conditions considered. With the two lower temperature cases considered, the two assumptions (kinetic and frozen) lead to identical results, as expected. As the inlet temperature is increased, the effect of the chemical reactivity becomes clear. At stoichiometric inlet conditions (2600 K) for example, the temperature difference between the two calculation methods is considerable: 29 K at the first nozzle outlet and 46 K at the first rotor outlet. The heat release by chemical reactivity within the turbine stage is therefore substantial. This is further illustrated in Fig. 4, in which the chemical heat release efficiency is shown as a function of axis distance. For stoichiometric inlet conditions, only 94 percent of the fuel heating value is released in the combustor, and a further 3 percent is released during the expansion, which explains the considerable difference between the temperature profiles calculated assuming kinetic and frozen behavior. Furthermore, at the rotor outlet, 3 percent of the heating value remains unreleased. Clearly, it is of interest for the high inlet temperature case to consider further stages, and later in this section we will show how the expansion characteristics evolve if we consider a further three stages.

Figure 5 shows the NO composition profiles. Again, we note that the temperature threshold for chemical reactivity to have a noticeable effect on the expansion characteristics is located at around 2000 K. For inlet temperatures of 2300 K and 2600 K we note a considerable production of thermal NO within the stator nozzle as a result of the chemical reactions. Little production occurs in the rotor because the residence time is low and

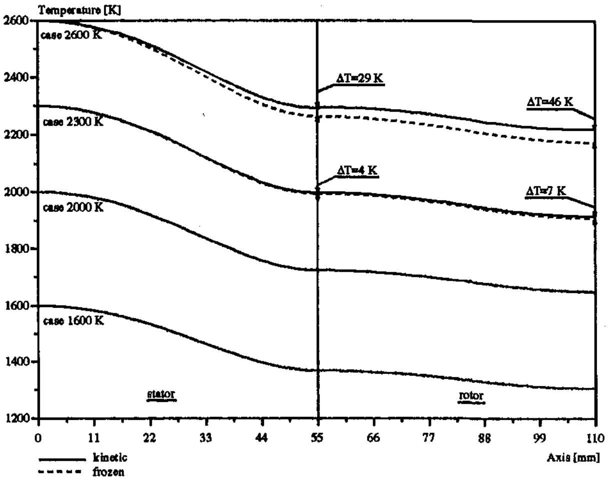

Fig. 3 Temperature profiles in first turbine stage

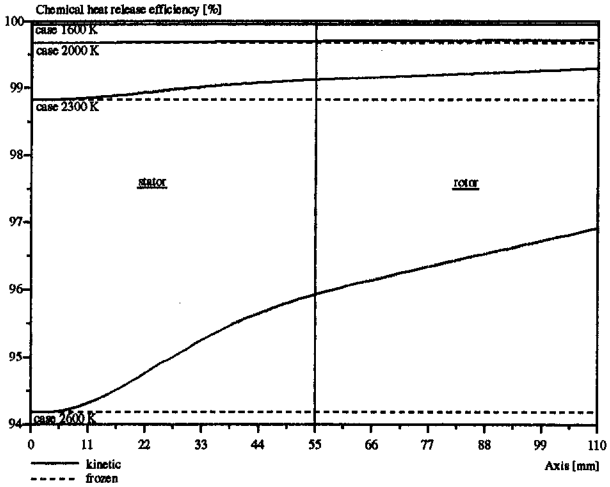

Fig. 4 Chemical heat release efficiency in first turbine stage

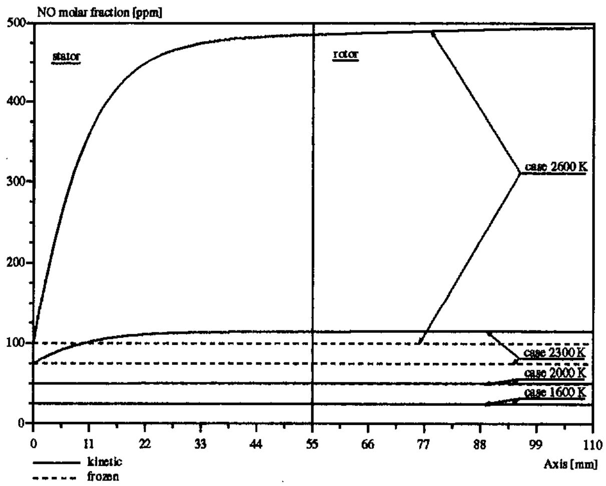

Fig. 5 NO composition profiles in first turbine stage

the temperature drop in the stator nozzle is sufficient to reduce the NO production rate. With such considerable NO production rates within the expansion turbine itself at high temperatures, it appears clear that in order to meet strict future emission standards, gas turbine manufacturers will most probably have to resort to catalytic exhaust gas clean-up, whereas present-day NO_x reduction effort is mostly centered on combustor design innovation.

Figure 6 shows CO mole fraction profiles. Note that the CO recombination reaction is the major internal heat source for the expanding gas stream, and this reaction is therefore responsible for most of the temperature increase compared to the frozen expansion case, as shown in Fig. 3. Note the different scales used for the four different cases shown. At 1600 K, the CO composition is negligible, but increases rapidly as the inlet temperature increases. At 2600 K TIT, the stator inlet CO mole fraction is 10,000 ppm. As the gas expands (and the temperature decreases), the CO recombines to form CO_2. Heat is released, and the temperature decreases less rapidly than if a frozen composition is assumed. Note finally that the CO levels in the first-stage rotor in the high temperature cases is still considerable, and the corresponding heat release efficiency is thus far from 100 percent.

For the stoichiometric inlet conditions (i.e., 2600 K), we have shown that at the outlet of the first-stage rotor, we still have a high level of dissociation: CO mole fraction = 5200 ppm, combustion efficiency $\eta_{HR} = 97.0$ percent. Figures 7 and 8 present results for a four-stage expansion (i.e., four nozzles and four rotors). The pressure level at the exit of the fourth rotor is 2.3 bar. The temperature profiles are not shown. The temperature differences (i.e., the difference between temperature profiles computed according to kinetic and frozen assumptions) at the outlet of the first, second, third, and fourth-stage rotors are 47, 58, 57, and 55 K, respectively. This indicates that the heat release by chemical recombination reactions occurs essentially in the first two stages. This is confirmed in Fig. 7, which shows the chemical heat release efficiency. We note that in the fourth stage the efficiency is clearly "frozen" well below 100 percent, indicating that the heating value of the fuel is not fully recovered in the turbine. Figure 8 shows the corresponding evolution of the CO mole fraction. The CO recombination reaction occurs throughout the four stages, but slows down considerably in the third and fourth stages. At the outlet of the third rotor, the CO fraction is 2935 ppm, and drops to 2534 ppm at the outlet of the fourth stage. These levels were compared to levels corresponding to a shifting equilibrium of the gas mixture throughout the expansion, yielding equilibrium CO fractions of 155 and 8 ppm at the third and fourth rotor outlets, respectively. These results indicate that at the end of the expansion, the CO level is effectively frozen at a level three orders of magnitude higher than the corresponding equilibrium value, which explains that 100 percent heat release efficiency is not attained. Furthermore, we underline the significant difference in CO outlet composition according to whether shifting equilibrium, reaction kinetics, or frozen composition are assumed. Future high-temperature gas turbine design methods must clearly model the chemical reactivity of the expanding flow accurately if they wish to predict the CO emission levels generated by the combustion turbine system. Finally, the multistage analysis confirms the frozen NO composition as already suggested in Fig. 5, and the NO profile throughout the four turbine stages is therefore not shown.

Thus, at this stage we may draw a very important conclusion: The chemical reactivity of the expanding gas mixture can have a strong effect on the overall energy performance of the system, since for stoichiometric inlet conditions, two percent of the fuel heating value remains unreleased as thermal energy. Furthermore, the effect on the production of environmental pollutants is considerable, as is the modification of the temperature profile of the expanding gas stream. For both these reasons, and given the current trend toward very high TITs, it is imperative for state-of-the-art gas turbine manufacturers to integrate chemical reactivity into their design procedures within the near future.

Results With Fluctuating Nozzle Inlet Temperatures. If we re-examine Fig. 6, we note that for the low-temperature case (1600 K TIT), the CO fraction predicted by the equilibrium combustion model is very low (0.38 ppm). This value is much lower than the levels measured in practice. One of the key reasons for the higher measured values is that the range of temperature fluctuations at the combustor outlet is considerable, and the high-temperature "pockets" contribute significantly to the overall CO composition. In practice therefore, temperature fluctuations around a mean value at the combustor outlet are considerable, and in this section we attempt to take such effects into account. In this section we present results for combustor outlet temperature fluctuations around a mean value of 1544 K (based on experimental results) and 2300 K (Gaussian distribution). Clearly, these temperature fluctuations disappear with time during the expansion as a result of mixing and internal heat exchange. In order to assess the impact of the temperature fluctuations on the fluid expansion characteristics, we examine two limiting cases. First of all, we assume no mixing and no internal heat exchange. We consider isolated gas pockets with different initial temperatures and compositions that expand individually. The results presented show the averaged results of these individual expansions. In the second limiting case, we

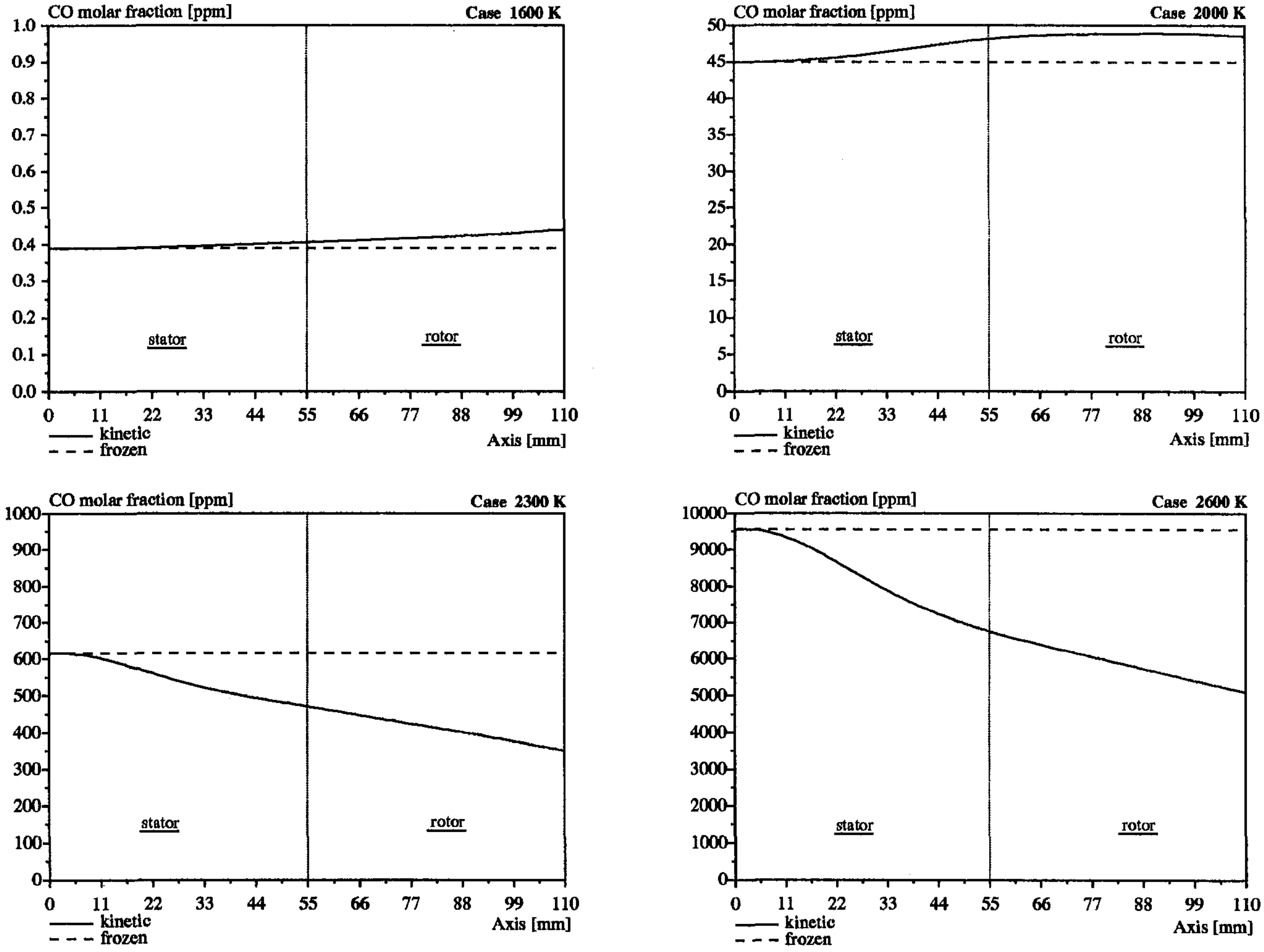

Fig. 6 CO composition profiles in first turbine stage

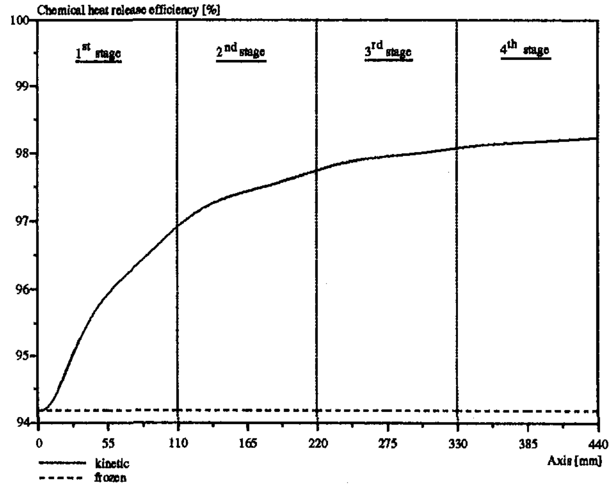

Fig. 7 Chemical heat release efficiency profile in multistage turbine

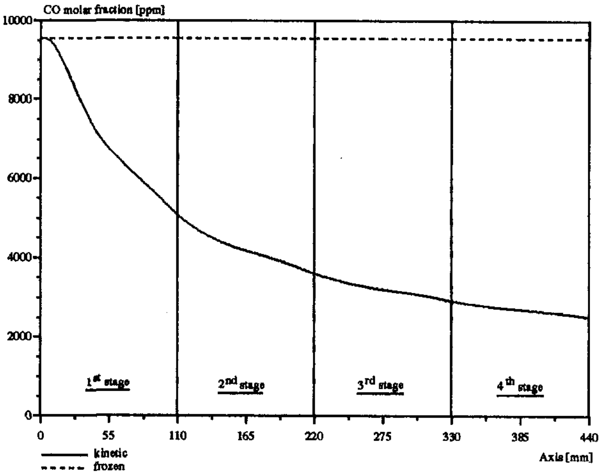

Fig. 8 CO composition profile in multistage turbine

assume complete mixing at the inlet of the stator nozzle, and we model the expansion of the uniform fluid through the stator and the rotor. A third intermediate case, which is not presented, is the case where mixing is assumed to occur at the rotor inlet. A rapid analysis of the results for the two cases considered indicates that little stands to be gained from considering this intermediate case. This analysis is limited to the first stage of the turbine, since mixing inevitably occurs in the first-stage rotor and it is unreasonable to assume unmixed expansion beyond this point.

Figure 9 shows the chemical heat release efficiency as a function of axis length. For both temperature levels considered, if we account for inlet temperature fluctuations, we observe a significant drop in the chemical heat release efficiency. This is due to the poor chemical heat release efficiency of the high-

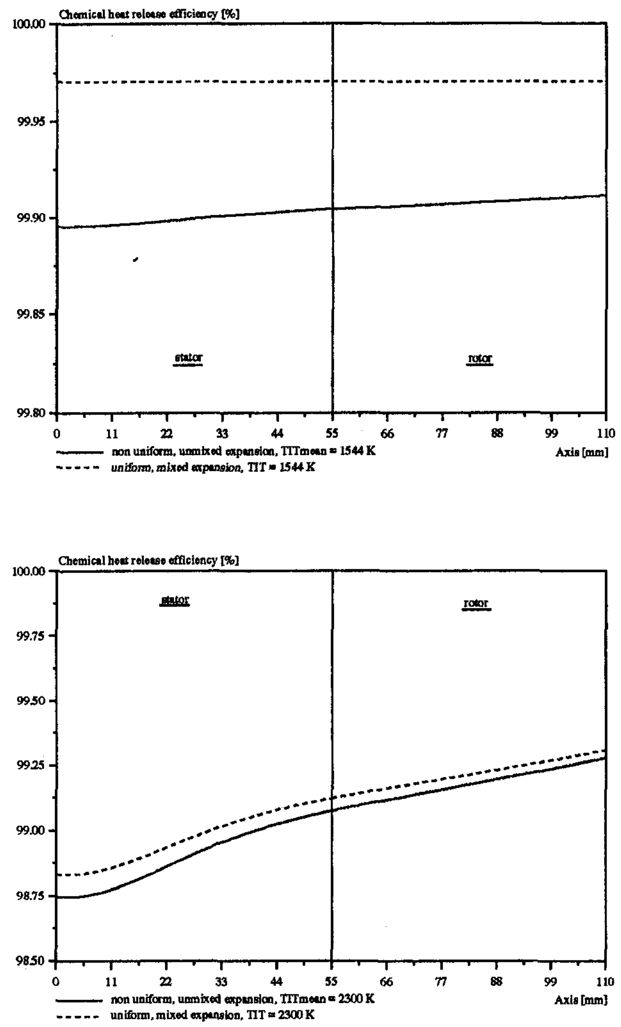

Fig. 9 Chemical heat release efficiency profiles in first turbine stage. Effect of fluctuating inlet temperature.

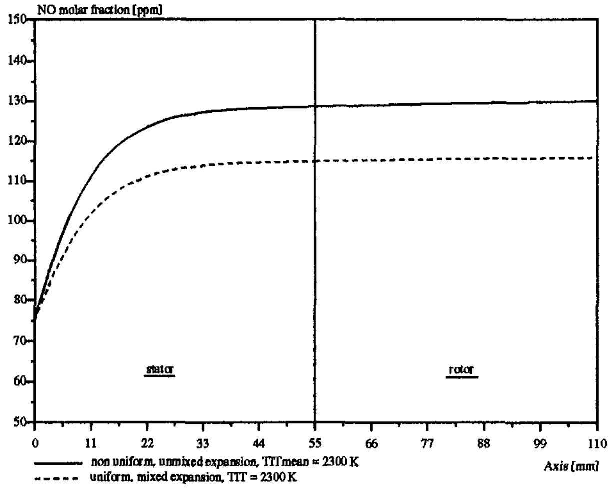

Fig. 10 NO composition profiles in first turbine stage. Effect of fluctuating inlet temperature

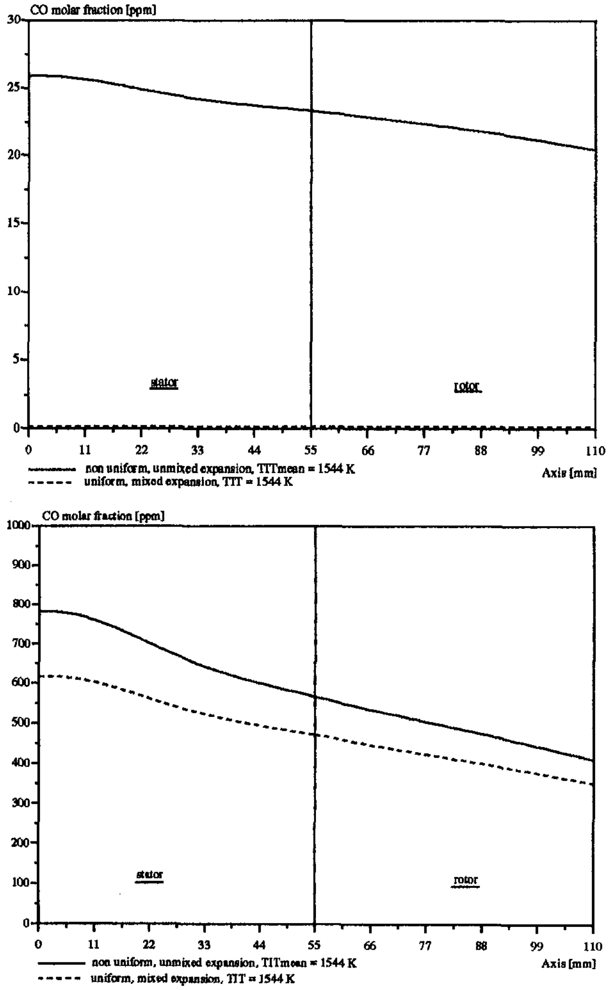

Fig. 11 CO composition profiles in first turbine stage. Effect of fluctuating inlet temperature.

temperature fractions of the gas stream, i.e., the high level of dissociation of CO_2 in the high-temperature gas pockets. The difference is less noticeable for the high-temperature case. This is due to a less pronounced temperature distribution, since the range of temperature fluctuations is limited by the stoichiometric flame temperature. Figure 10 shows the evolution of the NO fractions for TIT_{mean} equal to 2300 K. Little difference (i.e., less than 1 ppm) was observed between the two mixing scenarios for TIT_{mean} equal to 1544 K. The high-temperature case shows a significant difference in NO composition at the stator exit, and a frozen composition in the rotor, due to the increased gas velocities (i.e., short residence times) and the reduced production rate. Figure 11 shows the results attained with both mean TIT values for the CO species. It is interesting to note the high CO composition at the stator inlet for the nonmixed case with $TIT_{mean} = 1544$ K, i.e., 26 ppm, as compared to a very low value for the mixed case. 26 ppm is close to values measured in practice at the combustor exit for similar temperature levels, and it is well known that this value is to be attributed to considerable temperature variations within the gas mixture, the high-temperature regions contributing to the high CO composition. Both temperature cases considered show similar results, with a much higher CO composition for the nonmixed scenario. Finally, as before, the major evolution occurs within the stator.

Conclusions

1 At high temperature levels, the chemical combustion efficiency is well below 100 percent at the combustor outlet. As the expansion proceeds, the incompletely oxidized species (mainly CO and H_2 recombine with oxygen, forming CO_2 and H_2O, and further heat is released. However, for the high-temperature cases, the expansion characteristics are such that a nonnegligible portion of the heating value is not released as thermal energy.

2 For TIT values above 2000 K, the flow and thermochemical characteristics of the expanding fluid are very different according to whether the frozen or kinetic assumptions are made. Particular attention is drawn to the differing temperature profiles and exit pollutant levels, with clear important implications for future gas turbine design work.

3 In practice, the hot gases at the turbine inlet show significant temperature fluctuations, and we have shown in this study that this has important implications for the formation of major air pollutants (namely CO and NO).

4 The present one-dimensional analysis allowed a preliminary understanding of the effects of chemical reactivity of high-temperature expanding flow, and justifies further work in this field. Thus, the authors are currently working on a two-dimensional analysis of chemically reactive flow through a first-stage nozzle. It is hoped that such an analysis will allow the exact locations of intense heat release to be located, with possible implications for future blade cooling design.

Acknowledgments

This work was undertaken in collaboration with the Catholic University of Louvain (Prof. P. Wauters and Prof. J. Martin) at Louvain-La-Neuve/Belgium and the University of Florence/Italy (Prof. B. Facchini). The authors acknowledge the continued interest and support of these institutes. They also extend their special thanks towards Mr. F. Hirsinger at ONERA (Châtillon, France) for a number of helpful suggestions.

References

Chase, M. W., Davies, C. A., Downey, J. R., Frurip, D. J., McDonald, R. A., and Syverud, A. N., 1985, *Janaf Thermo-Chemical Tables,* 3rd ed., Am. Chem. Soc., Am. Inst. of Physics, Nat. Bureau of Standards.

CISI-Ingenierie, 1989, "Neptunix—ODE Solver and Model Description," Division Génie Logiciel et Application, 3 rue Lecorbusier, SILIC 232, F-94528 Rungis.

Cohen, H., Rogers, G. F. C., and Saravanamuttoo, H. I. H., 1987, *Gas Turbine Theory,* 3rd ed., Longman Scientific & Technical.

de Piolenc, M., 1992, "Latest Jet Engine Technology Could Radically Change Industrial Designs," *Gas Turbine World.*

Edelman, R. B., and Fortune, O. F., 1969, "A Quasi-Global Chemical Kinetic Model for the Finite Rate Combustion of Hydrocarbon Fuels With Application to Turbulent Burning and Mixing in Hyper-sonic Engines and Nozzles," presented at the AIAA 7th Aerospace Sciences Meeting, New York.

Goldman, L. J., and Seasholtz, R. G., 1982, "Laser Anemometer Measurements in an Annular Cascade of Core Turbine Vanes and Comparison With Theory," NASA Technical Paper 2018.

Gras, J. M., 1992, "Matériaux de Turbines à Combustion—Evolution des Tendances," EDF-DER, Service IPN, Dép. SID, F-92141 Clamart.

Leide, B., and Stouffs, P., 1996, "Residual Reactivity of Burned Gases in the Early Expansion Process of Future Gas Turbines," ASME *Journal of Engineering for Gas Turbines and Power,* Vol. 118, pp. 54–60.

Magre, P., Collin, G., Ansart, D., Baudouin, C., and Bouchie, Y., 1991, "Mesures de Température par DASC et Validation d'un Code de Calcul sur Foyer de Turboréacteur," Technical report, ONERA (Châtillon, France) and SNECMA (Villaroche, France). Third European Forum on Aeronautic Propulsion Systems EPF 91, Nov., Paris, France.

Mencherini, A., 1993, "Alcuni Aspetti nella Simulazione della Combustione/Espansione nelle Turbine a Gas," Tesi di Laurea, Università di Firenze, Italy.

Miller, J. A., and Bowman, C. T., 1989, "Mechanism and Modelling of Nitrogen Chemistry in Combustion," *Prog. Energy Combust. Sci.,* Vol. 15, pp. 287–338.

Schuetz, H., and Muehleck, P., 1991, "Influence of the Flight Trajectory on the Exhaust Gas Composition of a H_2-Fueled Air-Breathing Ramjet Engine," *Orbital Transports: Meteorological, Technical and Chemical Aspects,* Springer Verlag, H. Oertl and H. Körner, eds., 3rd Aerospace Symposium Braunschweig, Aug. 26–28.

Szanca, E. M., Schum, H. J., and Hotz, G. M., 1974, "Research Turbine for High-Temperature Core Engine Application," NASA Technical Note d-7557, Washington DC.

Zucrow, M. J., and Hoffman, J. D., 1977, *Gas Dynamics—Multidimensional Flow,* Wiley, New York.

P. M. Ligrani
Professor,
Convective Heat Transfer Laboratory,
Department of Mechanical Engineering,
University of Utah,
Salt Lake City, UT 84112
Mem. ASME

A. E. Ramsey
Graduate Student,
Department of Mechanical Engineering,
Naval Postgraduate School,
Monterey, CA 93943

Film Cooling From Spanwise-Oriented Holes in Two Staggered Rows

Adiabatic effectiveness and iso-energetic heat transfer coefficients are presented from measurements downstream of film-cooling holes inclined at 30 deg. with respect to the test surface in spanwise/normal planes. With this configuration, holes are spaced 3d apart in the spanwise direction and 4d in the streamwise direction in two staggered rows. Results are presented for an injectant to free-stream density ratio near 1.0, and injection blowing ratios from 0.5 to 1.5. Spanwise-averaged adiabatic effectiveness values downstream of the spanwise/normal plane holes are significantly higher than values measured downstream of simple angle holes for $x/d < 25-70$ (depending on blowing ratio) when compared for the same normalized streamwise location, blowing ratio, and spanwise and streamwise hole spacings. Spanwise-averaged iso-energetic Stanton number ratios range between 1.0 and 1.41, increase with blowing ratio at each streamwise station, and show little variation with streamwise location for each value of blowing ratio tested.

Introduction

Two factors are most important in influencing the protection provided by a layer of cooling film. These are the locations of the film, and the ability to absorb and store thermal energy. Film hole geometry, especially orientations of different compound angle hole arrangements, is particularly important regarding film cooling performance through its connection to these characteristics. Investigations of film cooling from compound angle holes are described by Mayle and Camarata (1975), Kim et al. (1978), Ligrani et al. (1992, 1994a, b, 1995, 1997), Sen et al. (1996), and Schmidt et al. (1996). Work conducted with lateral injection from holes in *spanwise/normal* planes is described by Goldstein et al. (1970), Honami and Fukagawa (1987), Sathyamurthy and Patankar (1990), and Honami et al. (1994).

The present study also investigates the behavior of boundary layers film cooled with holes oriented in spanwise/normal planes. Results from this configuration are compared to ones with the same spanwise and streamwise hole spacings both from a different compound angle arrangement and from a simple angle arrangement. As such, the present investigation is part of a larger comprehensive study of the effects of hole orientation on film cooling performance (Ligrani et al., 1992, 1994a, b, 1995, 1997).

Experimental Approach

The open-circuit, subsonic wind tunnel is the same one used in the experiments of Ligrani et al. (1992, 1994a, b, 1995, 1997). For the present investigation, a zero pressure gradient is set along the length of the test section (without the film cooling) to within 0.01 in. of water differential pressure. The free-stream velocity is 10 m/s and the free-stream turbulence intensity is approximately 0.13 percent based on the same velocity.

A schematic showing the test section and coordinate system is presented in Fig. 1. Dimensional values of distances labeled in Fig. 1 are given in Table 1 for configuration 4. Ligrani et al. (1994a) present values for configurations 1, 2, and 3. The total boundary layer thickness just downstream of the injection holes ($x/d = 2.75$) is 0.973 cm, giving a thickness-to-hole diameter ratio of 1.05. The ratio of displacement thickness to hole diameter at this location is 0.23. Respective values at the upstream edges of the holes are approximately 0.99, and 0.22.

The *injection system* is described by Ramsey (1992) and Ligrani et al. (1994a, 1995). The ratio of injectant to free-stream density ρ_c/ρ_∞ is from 0.94 to 1.00. Each injection tube is about 7.6 cm long, giving a length-to-diameter ratio of about 8.

The *heat transfer surface,* also described by Ramsey (1992) and Ligrani et al. (1994a, 1995), provides a constant heat flux over its area. Surface temperatures are measured using 126 thermocouples after their outputs are corrected for contact resistance and conduction through a sheet of foil located next to the air stream. To determine the heat loss by conduction, an energy balance is performed. Radiation losses from the top of the test surface are analytically estimated. Corrections to account for streamwise and spanwise conduction along the test surface are employed using procedures developed and described by Wigle (1991). Radiation and conduction typically account for 2–3 and 6–8 percent of the heater power, respectively.

Adiabatic film cooling effectiveness values are determined using linear superposition theory applied to Stanton number ratios measured at different injection temperatures. Additional details of this approach are described by Ligrani et al. (1994a), including a test to check the procedure using a direct η measurement with a near adiabatic condition on the test plate. η differences from the two techniques were always less than experimental uncertainties, ranging from 0.01 to 0.02 effectiveness units (Ligrani et al., 1994a).

Additional experimental details are given by Ligrani et al. (1994a, b, 1995) including discussion of temperature measurements, data acquisition components, and baseline measurements.

Experimental uncertainty estimates are based upon 95 percent confidence levels, and determined following procedures described by Kline and McClintock (1953) and Moffat (1982). Typical nominal values of free-stream recovery temperature and wall temperature are 18.0 and 40.0°C, with respective uncertainties of 0.13 and 0.21°C. The free-stream density, free-stream velocity, and specific heat uncertainties are 0.009 kg/m^3 (1.23

Contributed by the International Gas Turbine Institute and based on a paper presented at the 40th International Gas Turbine and Aeroengine Congress and Exhibition, Houston, Texas, June 5–8, 1995. Manuscript received by the International Gas Turbine Institute February 4, 1995. Paper No. 95-GT-39. Associate Technical Editor: M. Dunn.

kg/m^3), 0.15 m/s (10.0 m/s), and 1 J/kgK (1006 J/kgK), where typical nominal values are given in parentheses. For convective heat transfer, heat transfer coefficient, and heat transfer area, 10.5 W (270 W), 1.03 W/m^2 K (24.2 W/m^{2}K), and 0.0065 m^2 (0.558 m^2) are typical uncertainties. The uncertainties of St, St/St$_o$, m, and x/d are 0.000086 (0.00196), 0.058 (1.05), 0.025 (0.50), and 0.36 (41.9). Uncertainties of $\bar{\eta}$ and $\overline{St}_f/St_o$ are dependent upon the linear superposition technique employed. The uncertainty of $\overline{St}_f/St_o$ is the same as for St/St$_o$. The uncertainty of $\bar{\eta}$ varies between 0.02 and 0.04 effectiveness units where higher values in this range apply when $\bar{\eta}$ is less than about 0.15.

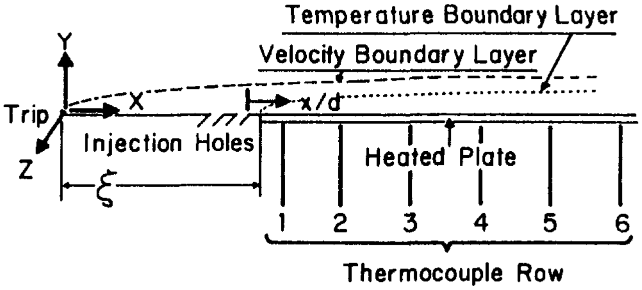

Fig. 1 Coordinate system and schematic of wind tunnel test section

Injection Configurations

Figure 2 shows a schematic of the film hole geometry for configuration 4. Nominal hole diameter d is 0.925 cm, and holes are oriented such that $\Omega = 90$ deg and $\beta = 30$ deg (see Table 2). Within the plane of each hole, individual centerlines are then oriented at an angle of 30 deg from the plane of the test surface such that $\alpha = 90$ deg and $\theta = 30$ deg. Here, comparisons are made between configuration 4 and simple angle configuration 2, and between configuration 4 and compound angle configuration 3, as spanwise and streamwise hole spacings (a and b, respectively) are maintained constant at 3.0d and 4.0d, respectively. Hole geometries of configurations 1, 2, 3, and 4 are summarized in Table 2.

Local Adiabatic Effectiveness, and Injectant Distributions

Effects of Blowing Ratio, Configuration 4. Figure 3 shows that the highest local adiabatic effectiveness magnitudes across the span of the measurement plane occur at m of 0.5 and 1.0 for $x/d = 6.8$. Of the three effectiveness distributions, these two also show the greatest spanwise periodicity, which evidences periodic injectant concentrations and deficits across the span of the test surface. Small variations from one concentration to another occur for $m = 0.5$ because of small variations in the ways adjacent injectant accumulations coalesce. Locally higher η values in Fig. 3 correspond to locations with abundant amounts of injectant near the test surface, and lower values correspond to locations where the injectant coverage is more sparse. Exceptions occur for $Z/d > 10$, where all three distributions decrease because they are measured at locations slightly away from the spanwise edge of the injectant. At $Z/d < 10$, the spanwise periodicity of the η distributions decreases as blowing ratio becomes greater than 1.0. Local η minima are about the same magnitude for all three m.

Additional explanation of the trends seen in Fig. 3 is obtained from the local injectant distributions in Fig. 4. These are obtained using procedures described by Ligrani et al. (1994a) in which the injectant is the only source of thermal energy relative to the free-stream flow, an arrangement produced by heating the injectant without providing any heat to the test plate. With this approach, $\rho_c/\rho_\infty = .91$. Distributions of $(T - T_{r,\infty})/(T_{r,c} - T_{r,\infty})$ such as the ones in Figs. 4 and 6 thus show injectant distributions in spanwise/normal planes, where $T_{r,c}$ is measured at the centerlines of the injection hole exits. These then illustrate how the injectant accumulates and is rearranged by diffusion and advection (including secondary flow effects) between the hole and the measurement station. Measurement points are spaced 0.508 cm apart in vertical and spanwise directions. Near the wall, $(T - T_{r,\infty})/(T_{r,c} - T_{r,\infty})$ distributions match η values and show that no important features are missed in the η distributions even though spatial resolution is slightly less. Values of Y and Z of 4 cm and 8 cm correspond to Y/d and Z/d of 4.32 and 8.65 in Figs. 4 and 6.

Like the η distributions in Fig. 3, the injectant distributions in Fig. 4 for $x/d = 7.4$ are spanwise periodic. For all three blowing ratios, the spanwise length scale of this periodicity is about 6d, the spanwise spacing between holes in the downstream row, rather than 3d, the spacing between the holes in both rows. For configuration 4, this behavior results from the coalescence of injectant concentrations from individual holes in the upstream row with concentrations from adjacent individual holes in the downstream row.

At $m = 0.5$ and $m = 1.0$, Fig. 4 shows that injectant accumulations from the downstream row of holes cover larger portions

Nomenclature

a = spanwise film hole spacing
b = streamwise film hole spacing
d = injection hole diameter
m = blowing ratio = $\rho_c U_c / \rho_\infty U_\infty$
Re$_d$ = injection Reynolds number = $d U_c / \nu$
Re$_x$ = Reynolds number based on streamwise distance = $X U_\infty / \nu$
St = Stanton number with film injection
St$_o$ = baseline Stanton number, no film injection
St$_f$ = iso-energetic Stanton number with film injection
$\overline{St}_f$ = spanwise-averaged iso-energetic Stanton number with film injection
T = static temperature
U = mean (time-averaged) velocity
X, x = streamwise distance
Y, y = distance normal to the surface
Z, z = spanwise distance from test surface centerline
α = angle of orientation, angle of the plane of the film holes from the streamwise/normal plane
β = injection hole angle with respect to the test surface as projected into the spanwise/normal plane
η = adiabatic film cooling effectiveness = $(T_{aw} - T_{r,\infty})/(T_{r,c} - T_{r,\infty})$
$\bar{\eta}$ = spanwise-averaged adiabatic film cooling effectiveness
θ = nondimensional injection temperature = $(T_{r,c} - T_{r,\infty})/(T_w - T_{r,\infty})$
θ = angle of inclination, angle of the film holes from the streamwise/spanwise plane of the test surface
ν = kinematic viscosity
ξ = unheated starting length
ρ = density
Ω = injection hole angle with respect to the test surface as projected into the streamwise/normal plane

Subscripts

aw = adiabatic wall
c = injectant at exits of injection holes
o = stagnation condition or baseline data
r = recovery condition
w = wall
∞ = free stream

Superscripts

$\bar{\ }$ = spanwise average

Table 1 Test section geometry characteristics for injection configuration 4

	Compound Angle Configuration 4		
	X(m)	x/d	x(m)
Downstream Edge of Injection Holes	1.059	0.00	0.000
Unheated Starting Length, ξ	1.072	1.41	0.013
Row 1*	1.122	6.81	0.063
Row 2*	1.222	17.62	0.163
Row 3*	1.372	33.83	0.313
Row 4*	1.572	55.46	0.513
Row 5*	1.772	77.08	0.713
Row 6*	1.972	98.70	0.913

*Refers to thermocouple row locations

Table 2 Hole angles and spanwise hole spacing of injection configurations

	α	θ	Ω	β	a, b
1+	50.5°	24°	35°	30°	3.9d, 5.2d
2+	0°	35°	35°	90°	3.0d, 4.0d
3+	50.5°	24°	35°	30°	3.0d, 4.0d
4+	90°	30°	90°	30°	3.0d, 4.0d

+ Refers to configuration.

of the measurement plane than accumulations from the upstream row of holes. Clear indications of secondary concentrations of injectant from the upstream row of holes are particularly evident near the wall for $m = 0.5$. In Fig. 4, these are located at Z of -9.0 cm, -3.5 cm, 2.0 cm, and 7.5 cm in close proximity and just to the right of the large concentrations from the downstream row. Each pair of concentrations is so close and so intermingled that no deficits of injectant are apparent between and no η minima are apparent at corresponding locations in Fig. 3. Similar secondary accumulations near the wall are less apparent in Fig. 4 for $m = 1.0$, and practically nonexistent for $m = 1.5$. The same spanwise spacings of η distributions and injectant concentrations at $x/d = 6.8-7.4$ is also apparent at locations farther downstream, especially for $m = 1.0$ and $m = 1.5$.

The injectant distribution for $m = 0.5$ is also different from the distributions at higher m because the film is located over a thinner layer near the wall, and because injectant accumulations are convected away from the holes a smaller distance in the spanwise direction. The high momentum flux ratio ($I = 2.25$) at $m = 1.5$ causes large injectant concentrations to lift off of the test surface just downstream of the holes. By the time the film reaches $x/d = 7.4$, Fig. 4 shows that the largest accumulations are located 1.0 to 2.0 cm from the surface. The high concentrations of injectant at these locations also result because injectant from an individual hole in the upstream row is then convected downstream away from the wall until it coalesces with injectant from the closest hole in the downstream row. This coalescence seems to become more severe as the blowing ratio increases, and as such, plays a factor in injectant lift-off. Together, lift-off and coalescence produce localized regions where less injectant covers the test surface resulting in spanwise periodic regions of lower protection. For $m = 1.0$, near-wall deficits of injectant are located in Fig. 4 at Z of -10 cm, -4.5 cm, 1 cm, and 6.5 cm. Corresponding locations of η minima in Fig. 3 at Z/d of -11, -5, 0.0, and 6. Thus, both spanwise-averaged $\bar{\eta}$, and local η minima decrease in magnitude as the blowing ratio increases and increasing amounts of injectant are located away from the test surface.

Comparison of Configurations 2, 3, and 4. Local adiabatic film cooling effectiveness distributions for $x/d = 6.7-6.8$ from configurations 2, 3, and 4 are presented and compared in Fig. 5 for m of 0.5, 1.0, and 1.5. Surveys of injectant distributions from configurations 2, 3, and 4 are compared in Fig. 6 for m of 1.0 and $x/d = 7.4-9.9$.

For all three blowing ratios, Fig. 5 shows η values for compound angle configurations 3 and 4, which are higher with significantly greater spanwise periodicity than the ones for simple angle configuration 2. The spanwise periodicity results because injectant from individual holes in the upstream row coalesces with injectant from adjacent individual holes in the downstream row. As this occurs, injectant concentrations either lift off of the wall at spanwise intervals at lower blowing ratios ($m < 1$) or lift off continuously across almost all of the measurement plane span at higher blowing ratios ($m > 1$). Injectant trajectories from simple angle configuration 2 tend to produce spanwise uniform η (Fig. 7, Ligrani et al., 1994a), however, because of the way in which they are distributed along the surface, the spanwise-averaged effectiveness at $x/d = 6.8$, $\bar{\eta}$,

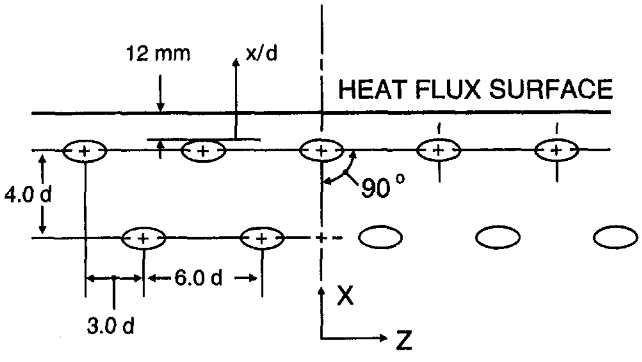

Fig. 2 Test surface geometry for configuration 4

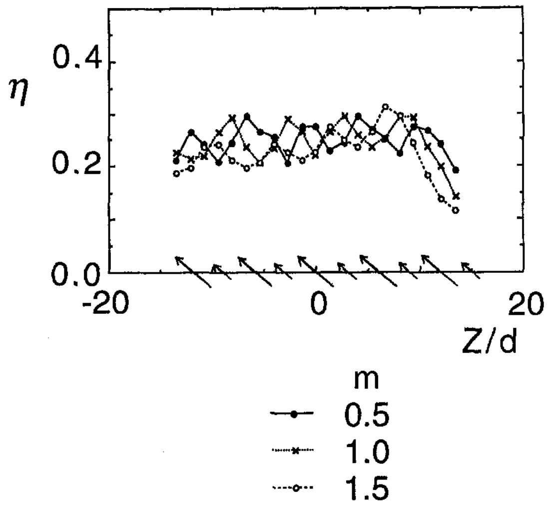

Fig. 3 Adiabatic film cooling effectiveness downstream of configuration 4 at $x/d = 6.8$. Spanwise locations of holes in the downstream row and upstream row are denoted by large and small arrows along the abscissa, respectively.

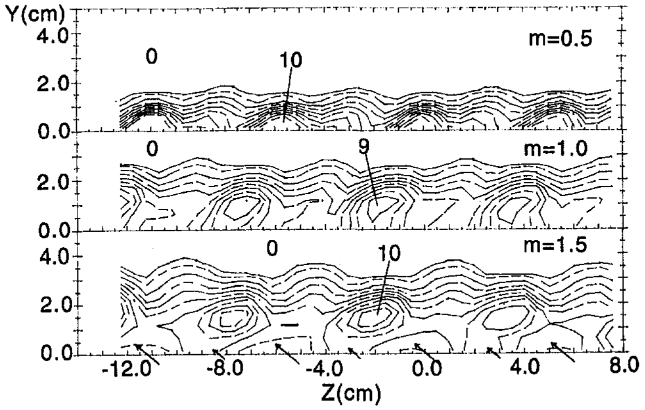

$T-T_{r,\infty}$ (°C) RANGES			
0	<0.5	6	5.0-6.0
1	0.5-1.0	7	6.0-7.0
2	1.0-2.0	8	7.0-8.0
3	2.0-3.0	9	8.0-9.0
4	3.0-4.0	10	>9.0
5	4.0-5.0		

Fig. 4 Mean temperature fields showing distributions of film injectant downstream of configuration 4 at x/d = 7.4 and ρ_c/ρ_∞ = 0.91. Hole location indicators are the same as for Fig. 3.

is lower than for the compound angle configurations 3 and 4. More of the injectant from these two configurations remains in close proximity to the wall downstream of individual compound angle holes (Figs. 4, 6). Consequently, the wall is exposed to a wider range of temperatures (and overall temperature levels that give improved protection) across the span of the test surface. For simple angle holes, Fig. 6 shows that the largest concentrations of injectant barely touch the surface, which results in a nearly constant distribution of η with Z/d.

The η distributions in Fig. 5 for configuration 2 should be ignored for $Z/d < -10$ and for $Z/d > 10$ for configurations 3 and 4 because these locations lie away from the regions of injectant coverage along the test surface.

The injectant distributions from configurations 2, 3, and 4 in Fig. 6 are significantly different from each other even though they are compared for the same spanwise hole spacing ($3.0d$), approximate streamwise location ($x/d = 7.4$–9.9), and blowing ratio (m = 1.0). Differences are apparent regarding distributions of injectant, amounts of merging and coalescence, and lift-off and proximity of concentrations to the wall.

The spanwise spacings between adjacent accumulations is twice as much for configuration 4 compared to configurations 2 and 3, which indicates merging of injectant concentrations from holes in the upstream row of configuration 4 with injectant that originated in holes located in the downstream row. Although some merging is occurring with configuration 3 holes, injectant accumulations spanwise spaced about $3d$ apart are clearly apparent. The configuration 2 distributions in Fig. 6 represent large circular concentrations of injectant also spaced about $3d$ apart. Every other accumulation for this configuration as well as for configuration 3 is qualitatively similar. Adjacent distributions are different since injectant from the downstream row of holes is located slightly closer to the wall than injectant from the upstream row of holes.

Variations of injectant accumulations with Y in Fig. 6 indicate different susceptibilities for lift off. Lift-off is most likely with configuration 2, followed by configuration 4 and then 3, although the lift-off dependence on I is about the same for these last two configurations.

Spanwise-Averaged Adiabatic Film Cooling Effectiveness Values and Stanton Number Ratios

Spanwise-averaged magnitudes of effectiveness and iso-energetic Stanton number ratio downstream of configurations 2, 3, and 4 are determined from local measurements of these quantities for each thermocouple row (Fig. 1 and Table 1) by averaging the first 13 data points from each row over $Z/d = -13.7$ to $+2.7$. The middle 15 points are used for configuration 2, which corresponds to $Z/d = -9.4$ to $+9.4$ (Ligrani et al., 1992, 1994a, b). The iso-energetic Stanton number is based on a heat transfer coefficient determined when $T_{r,c} = T_{r,\infty}$.

Effects of Hole Orientation, Configurations 2 and 4. Referring first to configuration 4 data in Fig. 7, $\bar{\eta}$ values at $x/d < 20$ decrease for $m > 1$ because of the coalescence and lift-off of injectant from the test surface discussed earlier in reference to Figs. 3–6. However, as the boundary layers advect farther downstream, $\bar{\eta}$ values decrease with m as successfully smaller amounts of film are located near the test surface. These differences also result partially because of the different ways in which the injectant spreads along the test surface discussed earlier.

The trends of the present simple angle (configuration 2) data in Fig. 7 are fairly complex, especially for $x/d < 40$. The reader is referred to Ligrani et al. (1994a) for discussion of the details.

Comparing effectiveness values for configurations 2 and 4 in Fig. 7, it is evident that the simple angle data lie below the compound angle data for $x/d < 25$ for $m = 0.5$, and for $x/d < 70$ when m = 1.0 and 1.5. Thus, at smaller x/d, configuration 4 provides significantly improved protection for the same spanwise hole spacing, x/d, and blowing ratio m. Changes in effectiveness are significant for all three blowing ratios, especially at $x/d = 6.8$. At x/d larger than 25–70 (depending on m), the compound angle data generally cover about the same range as the simple angle data if the data at individual blowing ratios are examined.

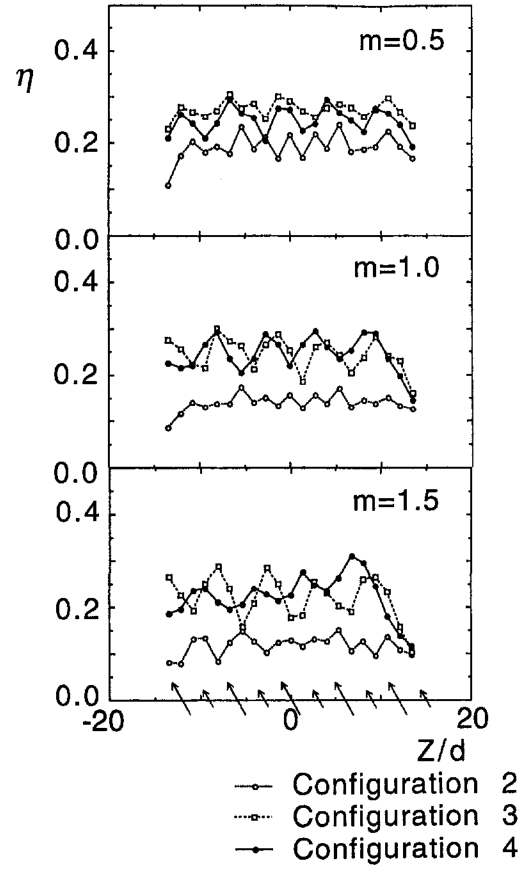

Fig. 5 Adiabatic film cooling effectiveness at x/d = 6.7–6.8. Hole location indicators are the same as for Fig. 3.

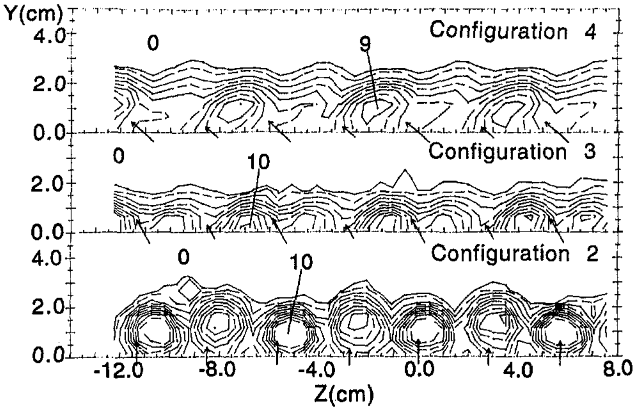

To-T∞(°C) RANGES

0	<0.5	6	5.0-6.0
1	0.5-1.0	7	6.0-7.0
2	1.0-2.0	8	7.0-8.0
3	2.0-3.0	9	8.0-9.0
4	3.0-4.0	10	>9.0
5	4.0-5.0		

Fig. 6 Mean temperature fields showing distributions of film injectant at x/d = 7.4–9.9 for m = 1.0 and ρ_c/ρ_∞ = 0.91. Hole location indicators are the same as for Fig. 3. $(T - T_{r,\infty})/(T_{r,c} - T_{r,\infty})$ values are given with Fig. 4.

Spanwise-averaged iso-energetic Stanton number ratios in Fig. 7 for configurations 2 and 4 show trends consistent with Ligrani et al. (1994a). First, little $\overline{\mathrm{St}_f/\mathrm{St}_o}$ variation with x/d is evident for each value of m. Second, compound angle data cover approximately the same range of values as the simple angle data, especially when the two sets of results are compared at the same blowing ratio. The only exception occurs for m = 1.5 when the configuration 4 results are somewhat higher. Third, for each x/d, $\overline{\mathrm{St}_f/\mathrm{St}_o}$ values generally increase with m.

Effects of Hole Orientation, Configurations 3 and 4. The configuration 3 $\bar{\eta}$ data in Fig. 8 show smaller variations with blowing ratio when compared to configuration 4 data at each x/d. Ligrani et al. (1994a) indicate that these configuration 3 variations are due to spanwise nonuniform accumulations of injectant for m = 1.0 and 1.5, especially at $x/d > 40$. Similar qualitative variations are not present at m = 0.5 when injectant distributions are fairly spanwise uniform. For m = 1.0 and 1.5, the injectant accumulation from each upstream hole merges with the injectant from the adjacent downstream hole. Because of this, the spanwise periodicity of effectiveness distributions downstream of configuration 3 is half as frequent as the holes themselves, and important spanwise deficits of injectant occur across the span of the measurement plane. This causes the effectiveness to show a weak dependence on blowing ratio since increasing the blowing ratio does not put proportionally more injectant near the test surface.

$\bar{\eta}$ values for configurations 3 and 4 in Fig. 8 cover the same range of values for m = 1.0 at all x/d. At m = 0.5, configuration 4 values are consistently less than configuration 3 values. With m = 1.5, configuration 4 $\bar{\eta}$ values are significantly higher than ones from configuration 3 for all $x/d > 6.8$.

Spanwise-averaged iso-energetic Stanton number ratios in Fig. 8 for configurations 3 and 4 are also consistent with results presented by Ligrani et al. (1994a). The only interesting exception again occurs for m = 1.5 where the configuration 4 values are higher than the ones produced by configuration 3.

Summary and Conclusions

Experimental results are presented that describe the development and structure of flow downstream of two staggered rows

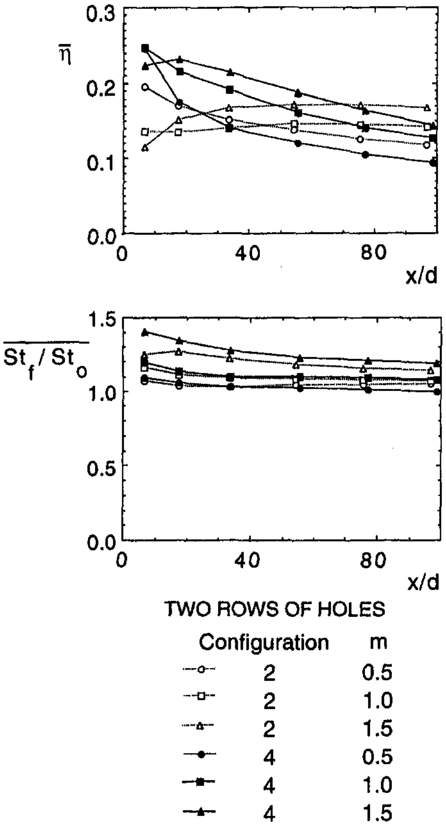

Fig. 7 Spanwise-averaged adiabatic film cooling effectiveness and iso-energetic Stanton number ratio downstream of configurations 2 and 4

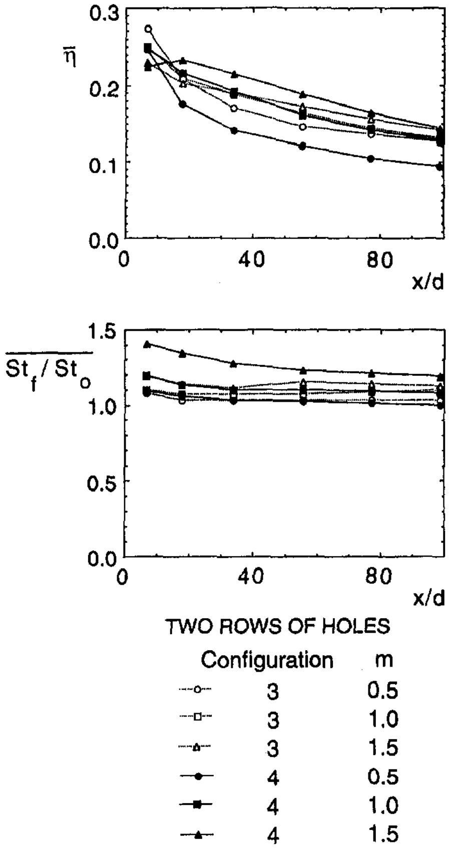

Fig. 8 Spanwise-averaged adiabatic film cooling effectiveness and iso-energetic Stanton number ratio downstream of configurations 3 and 4

of film-cooling holes, denoted configuration 4, which are oriented in spanwise/normal planes.

Configuration 4 provides significantly higher film effectiveness values compared to simple angle configuration 2 for the same a, b, x/d, and m, for $x/d < 25$ when $m = 0.5$, and for $x/d < 70$ when $m = 1.0$ and 1.5. Local adiabatic effectiveness values downstream of the configuration 4 holes at all x/d investigated (especially for $x/d = 6.7$–6.8 when $m = 1.0$ and 1.5) also show spanwise periodic regions of lower protection, and thus, greater spanwise periodicity than ones downstream of configuration 2. This is because of different dependence of injectant lift-off on injectant momentum flux ratio, and because injectant from individual holes in the upstream row of configuration 4 merges and coalesces with injectant from adjacent holes the downstream row.

Comparing configurations 3 and 4 shows that the one providing the highest film effectiveness values depends on blowing ratio if the comparison is made at the same a, b, x/d, and m. The most significant advantage of the spanwise/normal plane injection holes occurs for $m = 1.5$ at $x/d = 6.8$. Local measurements of effectiveness and injectant distributions indicate that merging and coalescence of injectant from the two rows of holes is more extensive with configuration 4 than configuration 3.

Spanwise-averaged iso-energetic Stanton number ratios downstream of configuration 4 range between 1.0 and 1.41 and show quantitative and qualitative trends similar to Ligrani et al. (1994a).

Acknowledgments

This study was supported by: (1) the Naval Sea Systems Command, Job Order Numbers N622711-RGPLG and N622712-RTBPL (Dr. Dan Groghan and Dr. Sam Shepard were program monitors), and (2) the Aero-Propulsion Laboratory of Wright Patterson Air Force Base, MIPR Numbers FY 1455-89-N0670 and FY 1455-92-N0641 (Dr. Bill Troha was program monitor).

References

Goldstein, R. J., Eckert, E. R. G., Eriksen, V. L., and Ramsey, J. W., 1970, "Film Cooling Following Injection Through Inclined Circular Tubes," *Israel Journal of Technology,* Vol. 8, pp. 145–154.

Honami, S., and Fukagawa, M., 1987, "A Study on Film Cooling Behavior of a Cooling Jet Over a Concave Surface," Paper No. 87-Tokyo IGTC-72, *Proc. 1987 Tokyo International Gas Turbine Congress,* Vol. 3, pp. 209–216.

Honami, S., Shizawa, T., and Uchiyama, A., 1994, "Behavior of the Laterally Injected Jet in Film Cooling: Measurements of Surface Temperature and Velocity/Temperature Field Within the Jet," ASME JOURNAL OF TURBOMACHINERY, Vol. 116, pp. 106–112.

Kim, H. K., Moffat, R. J., and Kays, W. M., 1978, "Heat Transfer to a Full-Coverage, Film-Cooled Surface With Compound-Angle (30° and 45°) Hole Injection," Report No. HMT-28, Thermosciences Division, Department of Mechanical Engineering, Stanford University, Stanford, CA.

Kline, S. J., and McClintock, F. A., 1953, "Describing Uncertainties in Single-Sample Experiments," *Mechanical Engineering,* Jan., pp. 3–8.

Ligrani, P. M., Ciriello, S., and Bishop, D. T., 1992, "Heat Transfer, Adiabatic Effectiveness, and Injectant Distributions Downstream of a Single Row and Two Staggered Rows of Compound Angle Film-Cooling Holes," ASME JOURNAL OF TURBOMACHINERY, Vol. 114, pp. 687–700.

Ligrani, P. M., Wigle, J. M., Ciriello, S., and Jackson, S. W., 1994a, "Film-Cooling From Holes With Compound Angle Orientations: Part 1—Results Downstream of Two Staggered Rows of Holes With 3d Spanwise Spacing," ASME *Journal of Heat Transfer,* Vol. 116, pp. 341–352.

Ligrani, P. M., Wigle, J. M., and Jackson, S. W., 1994b, "Film-Cooling From Holes With Compound Angle Orientations: Part 2—Results Downstream of a Single Row of Holes With 6d Spanwise Spacing," ASME *Journal of Heat Transfer,* Vol. 116, pp. 353–362.

Ligrani, P. M., and Ramsey, A. E., 1995, "Film Cooling From Spanwise Oriented Holes in Two Staggered Rows," ASME Paper No. 95-GT-39.

Ligrani, P. M., and Ramsey, A. E., 1997, "Film Cooling From a Single Row of Holes Oriented in Spanwise/Normal Planes," ASME JOURNAL OF TURBOMACHINERY, to appear.

Mayle, R. E., and Camarata, F. J., 1975, "Multihole Cooling Film Effectiveness and Heat Transfer," ASME *Journal of Heat Transfer,* Vol. 97, pp. 534–538.

Moffat, R. J., 1982, "Contributions to the Theory of Single-Sample Uncertainty Analysis," ASME *Journal of Fluids Engineering,* Vol. 104, pp. 250–260.

Ramsey, A. E., 1992, "A Study of Film Cooling Downstream of One and Two Rows of Holes Oriented in Spanwise/Normal Planes," M. S. Thesis, Department of Mechanical Engineering, Naval Postgraduate School, Monterey, CA.

Sathyamurthy, P., and Patankar, S. V., 1990, "Prediction of Film Cooling With Lateral Injection," *Heat Transfer in Turbulent Flows,* ASME-HTD Vol. 138, pp. 61–70.

Schmidt, D. L., Sen, B., and Bogard, D. G., 1996, "Film Cooling With Compound Angle Holes: Adiabatic Effectiveness," ASME JOURNAL OF TURBOMACHINERY, Vol. 118, pp. 807–813.

Sen, B., Schmidt, D. L., and Bogard, D. G., 1996, "Film Cooling With Compound Angle Holes: Heat Transfer," ASME JOURNAL OF TURBOMACHINERY, Vol. 118, pp. 800–806.

Wigle, J. M., 1991, "Heat Transfer, Adiabatic Effectiveness and Injectant Distributions Downstream of Single and Double Rows of Film Cooling Holes With Compound Angles," M. S. Thesis, Department of Mechanical Engineering, Naval Postgraduate School, Monterey, CA.

Bulk Flow Pulsations and Film Cooling: Flow Structure Just Downstream of the Holes

P. M. Ligrani
Professor.
Mem. ASME

R. Gong
Graduate Student.

J. M. Cuthrell
Graduate Student.

Convective Heat Transfer Laboratory,
Department of Mechanical Engineering,
University of Utah,
Salt Lake City, UT 84112

Experimental results are presented that describe the effects of bulk flow pulsations on film cooling from a single row of simple angle film cooling holes. The pulsations are in the form of sinusoidal variations of static pressure and streamwise velocity. Such pulsations are important in turbine studies because: (i) Static pressure pulsations result in significant periodic variations of film cooling flow rates, coverage, and trajectories, and (ii) static pressure pulsations occur near blade surfaces in operating engines from potential flow interactions between moving blade rows and from families of passing shock waves. Distributions of ensemble-averaged and time-averaged Reynolds stress tensor components are investigated just downstream of the holes along with distributions of all three mean velocity components. Important changes are evident in all measured quantities. In particular, maximum Reynolds shear stresses $-2\overline{u'v'}/\overline{u}_\infty^2$ *are lower in regions containing the largest film concentrations because the strong shear layer produced by the injectant is more three dimensional, larger in extent, and oscillates its position from the wall with time.*

Introduction

Turbine unsteadiness develops from four different sources: potential flow disturbances, wake passage, shock waves, and random free-stream turbulence from the combustion chamber.

Of these, the two having the most dramatic effect on film cooling are potential flow disturbances and passing shock waves. This is because both result in important variations of the *static* pressure near cooling hole exits as blade rows move relative to each other. Amplitudes of static pressure pulsations far exceed amplitudes of total pressure pulsations for the ranges of shock wave Mach numbers encountered in first turbine stages ($\leq 1.2-1.3$). Periodically unsteady static pressure fields at the exits of the injection holes result in pulsating coolant flow rates. In addition, passing potential flow disturbances and shock waves produce pulsating static pressure and velocity fields in the boundary layer just downstream from the injection holes. These result in complex variations with time of the trajectories, distributions, as well as the coverage of the film along surfaces. In some cases, reversal of the coolant flow over part of the unsteadiness cycle can occur if the pressure difference between the coolant plenum and the wall static pressure at hole exits is periodically negative (Abhari and Epstein, 1994).

In contrast, different qualitative and quantitative consequences result from the periodic *total* pressure pulsations and increased turbulence levels associated with passing wakes. The perturbations to a film by fluctuating diffusion rates from passing wakes cause the film to spread laterally and to become somewhat less concentrated as it is advected away from the holes. In addition, lower momentum levels in the wakes are also sometimes associated with an increased probability of lift-off of protective films. However, because static pressure variations in wakes are minimal, the changes to film protection are significantly less than ones pertaining to shock waves and potential flow disturbances. In fact, Ou et al. (1993), Mehendale et al. (1994), and Ou and Han (1993) point out that high free-stream unsteadiness is often more important than passing wakes, and passing wake effects on film cooling and heat transfer are equivalent to mild increases in freestream turbulence intensity.

Dring et al. (1980), Takeishi et al. (1992), Mehendale et al. (1994), Ou et al. (1993), and Ou and Han (1993) address the effects of wake flows on film cooling. Norton et al. (1990), Rigby et al. (1990), and Abhari and Epstein (1994) address the influences of passing shock waves and wakes on film cooling. Of important studies of shock waves on turbine heat transfer with no film cooling, Ashworth et al. (1985), Johnson et al. (1989), Rigby et al. (1990), and Abhari et al. (1992) all measured or predicted large pulses of surface heat transfer from shock passage relative to heat transfer variations from all other events, including wakes.

The present study is designed to examine the effects on film cooling of bulk flow pulsations in the form of periodic variations of static pressure and streamwise velocity. Changes to the three mean velocity components and turbulence structure (i.e., Reynolds stress tensor components) measured just downstream of the holes at $x/d = 4.5$ are presented and discussed. These data are of interest because they show the dramatic effects of imposed bulk flow static pressure (and velocity) pulsations on boundary layer film cooling. New understanding of the physical interactions between pulsations and film cooling is thus provided, thereby enabling the development of improved numerical models and design methods to account for these effects. In doing so, insight is also provided into the important changes to surface heat transfer that occur on blade surfaces during the passage of static pressure pulsations from potential flow interactions and passing shock waves. No similar study on detailed flow structure with pulsations and film cooling is presently known to the authors.

Experimental Apparatus and Procedures

The experiment is conducted on a large scale to allow detailed probing of flow features. Low speeds, flat-plate test sections, and constant-property flows are used to isolate the interactions between the film cooling, imposed bulk flow pulsations, and boundary layer.

Wind Tunnel. The wind tunnel is open-circuit, subsonic, and located in the Convective Heat Transfer Laboratory of the Department of Mechanical Engineering of the University of

---

Contributed by the International Gas Turbine Institute and based on a paper presented at the 40th International Gas Turbine and Aeroengine Congress and Exhibition; Houston, Texas, June 5–8, 1995. Manuscript received by the International Gas Turbine Institute February 3, 1995. Paper No. 95-GT-44. Associate Technical Editor: M. G. Dunn.

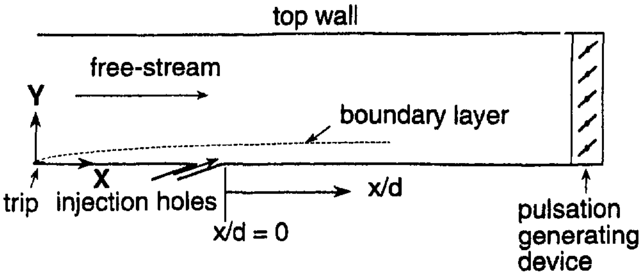

Fig. 1 Schematic of test section and coordinate system

Utah. The test section is a rectangular duct 3.05 m long and 0.61 m wide. The zero pressure gradient employed here is set to within 0.001 inches of water differential pressure along the length of the test section, both with and without pulsations. Flow at the test section inlet shows excellent spatial uniformity and a free-stream turbulence level less than 0.1 percent at a free-stream velocity of 10.7 m/s.

A schematic of the test section, including the coordinate system, is shown in Fig. 1. A boundary layer trip is located on the test plate just downstream of the nozzle exit. The downstream edge of the injection holes is then 1.050 m downstream of the trip, and measuring stations are subsequently located at x/d of 4.5. Corresponding Reynolds numbers, based on streamwise distance (from the trip) and a free-stream velocity of 10.7 m/s, range from 790,000 to 1,090,000.

Film Cooling Configuration and Air Supply. The film cooling holes are placed in a single row with spanwise spacing of 3 hole diameters. Each of five holes is oriented in a streamwise/normal plane (i.e., with a simple angle orientation) at a 35 deg angle from the test surface. Hole diameter is 2.22 cm, giving an l/d ratio of 4.0, and a ratio of boundary layer thickness to hole diameter of 1.23 (measured with no pulsations 0.237 m or $10.7d$ upstream of $x = 0$). Ratios of displacement thickness to hole diameter, and momentum thickness to hole diameter are 0.191, and 0.136, respectively. The test section and injectant air supply are maintained isothermal at ambient temperature (about 19°C) for all tests so that minimal temperature variations are present in the test section as surveys are made with the hot-wire probes. Blowing ratio m, momentum flux ratio, and ratio of injectant to free-stream density are all 1.0 for all tests. Injection Reynolds number $d\overline{u_c}/\nu$ is then about 15,000.

Mean Velocity and Turbulence Structural Details, and Data Acquisition System. Boundary layer mean velocity components and Reynolds stress tensor components are measured using hot-wire anemometry probes. A Dantec 55P05 hot-wire probe with sensor length of 1.25 mm is used to measure the instantaneous longitudinal velocity. A Dantec 55P51 crossed hot-wire probe, with sensors having the same approximate sensor lengths, is used to measure simultaneously either u and v, or u and w. Disa 55M10 constant-temperature bridges are used to operate all of the sensors at an overheat ratio of 1.6. Each hot wire is calibrated in the free-stream potential flow of the wind tunnel. During calibrations and measurements, the voltage signal from each hot-wire bridge is processed using a Dantec Model 56N20 signal conditioner system set with an amplifier gain of 1, a low-pass filter of 3 kHz, and no high-pass filter.

Signals from the signal conditioners connected to the hot-wire anemometry bridges are acquired using a Hewlett-Packard data acquisition system, controlled and programmed using a Hewlett-Packard Model 9836S mainframe computer. The system is capable of acquiring up to 24 channels of data at a total rate up to 100 kHz (for all channels).

Additional details are provided by Ligrani et al. (1995).

Generation of Bulk Flow Pulsations

Static pressure pulsations are produced in the test section using an array of rotating shutters located at the exit of the test section and driven by a system of gears and an electric motor (Karlsson, 1959). This approach is used because: (1) The shutters oscillate the static pressure without significant total pressure variations (Karlsson, 1959; Al-Asmi and Castro, 1993), (2) static pressure pulsations produce the most important disruptions to the flow rates, trajectories, and distributions of the film coolant, (3) much higher frequencies of pulsation can be produced than with many other methods (Al-Asmi and Castro, 1993), and (4) deterministic sinusoidal variations of static pressure can be produced at selected frequencies (Karlsson, 1959).

In producing these bulk flow pulsations, two different time scales are important to consider. The first pertains to the time required for the boundary layer to recover fully after the passing of each different type of disturbance (Doorly and Oldfield, 1985). This is characterized by free-stream Strouhal number St_∞, which equals 0.031 in the present study. The second important time scale pertains to the adjustment of coolant flow rates. According to Abhari and Epstein (1994), temporal pressure variations will influence the mass flow rate of the coolant when the disturbance passing frequency is low compared with the propagation time of disturbances through the coolant holes. This occurs if the product of coolant flow Mach number M_c and coolant Strouhal number St_c is about 1 or less ($M_c St_c \leq 1$). Typical values for operating turbines range from 0.2 to 0.6, which gives St_c from 0.2 to 6.0. To insure that the pulsations affect the film in the present experiment, $St_c = 0.11$. This is expected to give quasi-steady film behavior (Ligrani et al., 1995).

Phase-Averaging and Data Processing

For each measurement location, a total of 14,000 data points are acquired for each of two channels at a rate of 4 kHz per channel, giving a total sampling time of 3.5 s. Each spanwise/

Nomenclature

d = injection hole diameter
l = injection hole length
m = blowing ratio = $\rho_c \overline{u_c}/\rho_\infty \overline{u_\infty}$
n = pulsation frequency in Hz
St_c = coolant Strouhal number = $2\pi n l/\overline{u_c}$
St_∞ = free-stream Strouhal number = $2\pi n \delta/\overline{u_\infty}$
u = velocity
$\overline{u_\tau}$ = friction velocity
v = normal velocity
w = spanwise velocity
x = streamwise distance measured from downstream edge of injection holes
X = streamwise distance measured from trip
Y, y = distance normal to the surface
$y^+ = Y\overline{u_\tau}/\nu$
Z, z = spanwise distance from test surface centerline
δ = boundary layer thickness
ν = kinematic viscosity
ρ = density

Subscripts

c = injectant at exit plane of injection holes
∞ = free-stream

Superscripts

$'$ = fluctuating component
$\overline{\ }$ = time-averaged component
$\hat{\ }$ = phase-averaged component
$\tilde{\ }$ = periodic component

normal plane survey covers a grid of 15 by 12 locations spaced 0.508 cm apart.

With imposed periodic flow, instantaneous velocities u can be considered to be the sum of three components such that $u = \bar{u} + \tilde{u} + u'$, where $\bar{u}$ is the time-averaged velocity, $\tilde{u}$ is the periodic velocity, and u' is the fluctuating component (Hussain and Reynolds, 1970). In the present study, $\bar{u}$ and $\tilde{u}$ are combined as the phase-averaged velocity $\hat{u}$, such that $u = \hat{u} + u'$ following Ramaprian and Tu (1980). $\hat{u}$ is then determined from phase-averaging instantaneous velocity results using the equation given by

$$\hat{u}(n)|_{n=1}^{2000} = \frac{1}{\text{npulse}} \sum_{m=1}^{\text{npulse}} u(m, n)|_{n=1}^{2000}$$

where m and n correspond to the number of pulsations and to the number of locations across each phase where data are sampled, respectively, and npulse denotes total number of pulsations.

Phase-averaging is accomplished here using procedures developed exclusively for this study. After the velocities u, u and v, or u and w are determined at a particular probe location, $\bar{u}$, the time-averaged magnitude of the longitudinal velocity, is calculated. Pulsation time periods are then determined using least-squares curve fits to locate mean value crossings near the end of each pulsation. All individual periods are then averaged to compute the overall pulsation time period and frequency. Phase-averaged velocities ($\hat{u}$, $\hat{v}$, $\hat{w}$), and time-averaged Reynolds stress component magnitudes ($\overline{u'^2}$, $\overline{v'^2}$, $\overline{w'^2}$, $-\overline{u'v'}$, $\overline{u'w'}$) are then determined along with maximum and minimum magnitudes of $\hat{u}$.

The pulsating generating device produces near-sinusoidal velocity (and static pressure) wave forms at a frequency of 2 Hz at peak-to-peak amplitudes from 37–40 percent of $\bar{u}$ in the free stream to 125 percent of $\bar{u}$ near the wall (Ligrani et al., 1995). The pulsations propagate throughout the wind tunnel test section including all locations within the boundary layer developing along the test surface. With an average free-stream velocity of 10.75 m/s, the pulsating free stream ranges from 8.75 to 12.75 m/s. This results in a ±9 percent change to the instantaneous blowing ratio, which then varies from 0.91 to 1.09 (average injectant mass flux is 11.1 kg/m^2 s). The reader is referred to Ligrani et al. (1995) for additional details.

Uncertainty Estimates

Uncertainty estimates are based on 95 percent confidence levels, and determined using the methods described by Kline and McClintock (1953) and by Moffat (1988). The uncertainty of the phase-averaged velocity $\hat{u}$ is about 2.5 percent, and the uncertainty of $\bar{u}$ is about 1.5 percent. Uncertainty of $\overline{u'^2}$ is typically 4 percent. Uncertainties of $\overline{v'^2}$, $\overline{w'^2}$, $-\overline{u'v'}$, and $\overline{u'w'}$ are each about 10 percent.

Baseline Test Results

Three types of baseline tests were conducted: (a) no film cooling and no pulsations, (b) with film cooling and no pulsations, and (c) with bulk flow pulsations and no film cooling. The first two types of baseline tests show expected behavior. With no pulsations and no film cooling, normalized profiles of $\overline{u'^2}$, $\overline{v'^2}$, $\overline{w'^2}$, and $-\overline{u'v'}$ show behavior characteristic of turbulent boundary layers with two-dimensional mean flow fields, and excellent agreement with the measurements of Green (1989) and Klebanoff (1954), after accounting for a different free-stream turbulence level in the latter case. Profiles of $\sqrt{\overline{u'^2}}/\bar{u}_\infty$ and $\sqrt{\overline{v'^2}}/\bar{u}_\infty$ obtained in turbulent boundary layers both with and without pulsations and no film cooling show reasonable agreement with measurements from Menendez and Ramaprian (1989). Additional details are provided by Ligrani et al. (1995).

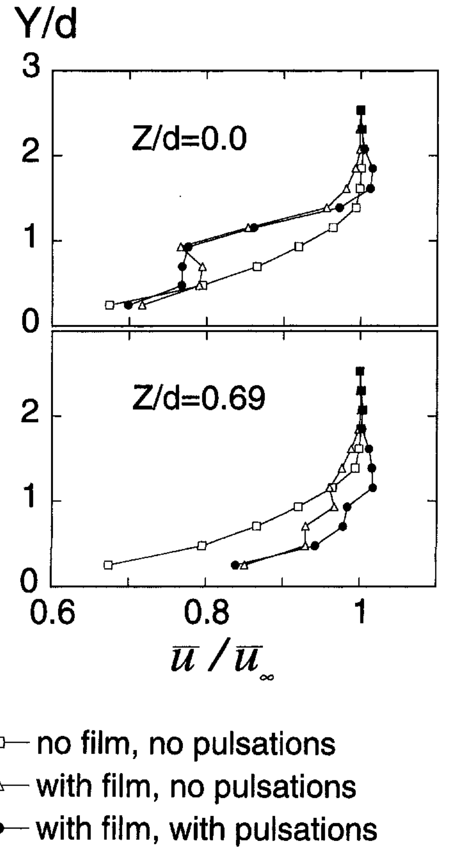

Fig. 2 Profiles of normalized time-averaged streamwise velocity $\bar{u}$ at x/d = 4.5 and Z/d = 0.00, 0.69

Mean Velocity Component Results

Flow Structure With No Pulsations. Considering results with film cooling and no pulsations, positive magnitudes of $\bar{v}/\bar{u}_\infty$ in Fig. 3 correspond to the most important injectant concentration from the center hole. The oval-shaped distribution (Ligrani et al., 1994), extends from the wall to about Y/d = 1.6, and from $Z/d = -0.50$ to $Z/d = +0.50$. The region is characterized by positive magnitudes of normal velocity $\bar{v}$ from $0.00\bar{u}_\infty$ to $0.18\bar{u}_\infty$ resulting from the upward trajectory of the film as it moves away from the holes.

Streamwise velocities shown in Fig. 2 for the boundary layer with film cooling and no pulsations at $Z/d = 0$ are significantly less than ones present with no film cooling for Y/d locations up to 1.8–2.0. The gradient of $\bar{u}$ thus becomes significant at Y/d from 0.90 to 1.6, which corresponds to the outer portion of the film concentration. The gradient evidences a shear layer developing at the interface between fluid with low streamwise momentum (below) and fluid with high streamwise momentum (above).

Outside of the region with the most important film accumulations at $Z/d > 0.50$ and $Z/d < -0.50$, $\bar{v}$ in Fig. 3 are negative, and $\bar{v}/\bar{u}_\infty$ ranges from 0.0 to −0.09 indicating significant normal velocities toward the wall. Profiles of $\bar{u}/\bar{u}_\infty$ in Fig. 2 at Z/d of 0.69 show values significantly greater than ones measured with no film cooling, especially for $Y/d < 1.10$.

Effects of Pulsations on Flow Structure. Significant changes to the flow structure occur when the pulsations are present. In particular, Figs. 3 and 4 show that maximum values of $\bar{v}/\bar{u}_\infty$ and $\bar{w}/\bar{u}_\infty$ are lower, and the region of positive $\bar{v}/\bar{u}_\infty$ is more spread out and located farther from the wall. Magnitudes of positive $\bar{w}/\bar{u}_\infty$ with pulsations are also lower at a particular measurement location compared to results with no pulsations.

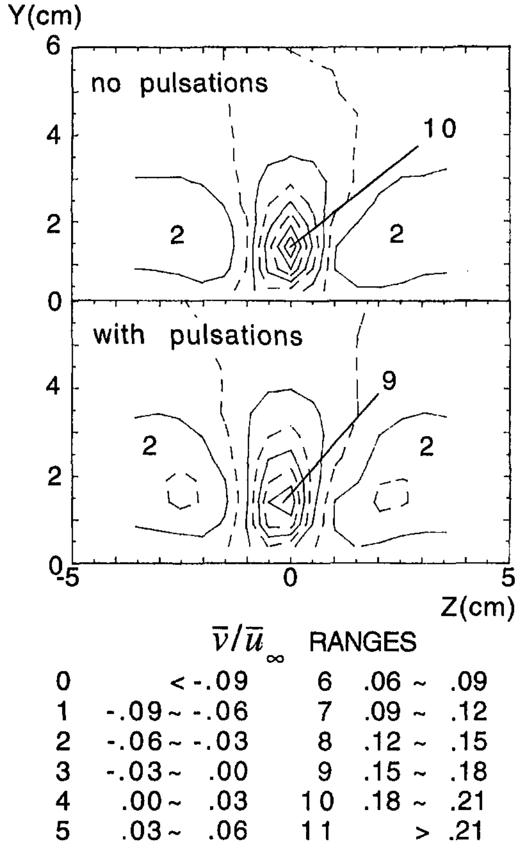

Fig. 3 Surveys of normalized time-averaged normal velocity $\bar{v}$ at x/d = 4.5

Together, these observations evidence lower secondary flow velocities, lower circulation magnitudes, and lower vorticity levels in each vortex leg located on either side of the injectant concentration. This is partially because of small alterations to vortex structure that occur from the imposed unsteadiness (i.e., from different levels of vorticity diffusion), but mostly because the results in Figs. 3 and 4 represent time-averaged distributions of structures, which are changing position with time (Ligrani et al., 1995).

Distributions of $\bar{u}/\bar{u}_\infty$ in Fig. 2 show even more significant alterations from the presence of the pulsations. The most important change in the film-cooled boundary layer at Z/d of 0.69 are higher $\bar{u}/\bar{u}_\infty$ with pulsations over most of the boundary layer thickness. Different behavior occurs at $Z/d = 0.0$, where values with pulsations are lower than ones with no pulsations for $Y/d = 0.50$–0.90, about the same for $Y/d = 0.90$–1.35, and higher than the ones with no pulsations at Y/d from 1.35–2.0. Thus, the same $\bar{u}/\bar{u}_\infty$ shear layer gradient is present in the film-cooled boundary layer both with and without pulsations, but it extends over a larger vertical portion of the boundary layer when the pulsations are imposed. At $Z/d = 0.0$, this leads one to conclude that the pulsations augment both the motion of low streamwise momentum fluid away from the wall at $Y/d = 0.50$–0.90, and the motion of fluid with high streamwise momentum to $Y/d = 1.35$–2.0 (compared to the film-cooled boundary layer with no pulsations). As this occurs in the outer portion of the boundary layer, the effect is so dramatic that streamwise velocities are locally higher than the free-stream velocity. Similar behavior is also observed at Z/d of 0.23, 0.46, and 0.69 (Ligrani et al., 1995).

This behavior results because the periodically unsteady static pressure fields at the exits of the injection holes produced by the imposed pulsations result in pulsating coolant flow rates. In addition, the pulsating static pressure and velocity fields in the boundary layer just downstream from the injection holes result in complex variations with time of the trajectories, distributions, as well as the coverage of the injectant along the surface. The film thus instantaneously changes its momentum and position in the boundary layer when bulk flow pulsations are imposed. The mean injectant trajectory with pulsations is also somewhat different, and the same amount of injectant is spread over a larger volume compared to nonpulsating flow. The local streamwise velocities higher than the free-stream velocity in Fig. 2 are then due to the behavior of the injectant when its momentum is highest during each pulsation cycle. During each of these intervals, the injectant is lifted farther away from the wall than the trajectory produced with m constant at 1.0. The result is augmented $\bar{u}/\bar{u}_\infty$ at $Y/d = 1.35$–2.0.

Reynolds Shear Stress Results

Flow Structure With No Pulsations. The film cooled $-2\overline{u'v'}/\bar{u}_\infty^2$ distributions in Fig. 5 and the film-cooled $\overline{u'w'}/\bar{u}_\infty^2$ distributions in Fig. 6 (with no pulsations) are significantly different from ones with no film cooling (and no pulsations).

At Z/d of 0.00, the profile in Fig. 5 shows an important local maximum in $-2\overline{u'v'}/\bar{u}_\infty^2$ located from $0.9d$ to $1.1d$ from the wall. The shear layer at the interface between fluid with low streamwise momentum below and fluid with much higher streamwise momentum above is responsible. This region of high $-2\overline{u'v'}/\bar{u}_\infty^2$ is bounded by Y/d regions where the normalized Reynolds shear stress is sometimes negative and significantly lower than measured in the baseline boundary layer.

Values of normalized three-dimensional shear stress $\overline{u'w'}/\bar{u}_\infty^2$ in Fig. 6 at $Z/d = 0.0$ from the film-cooled boundary layer are generally negative and significantly less than in the baseline boundary layer.

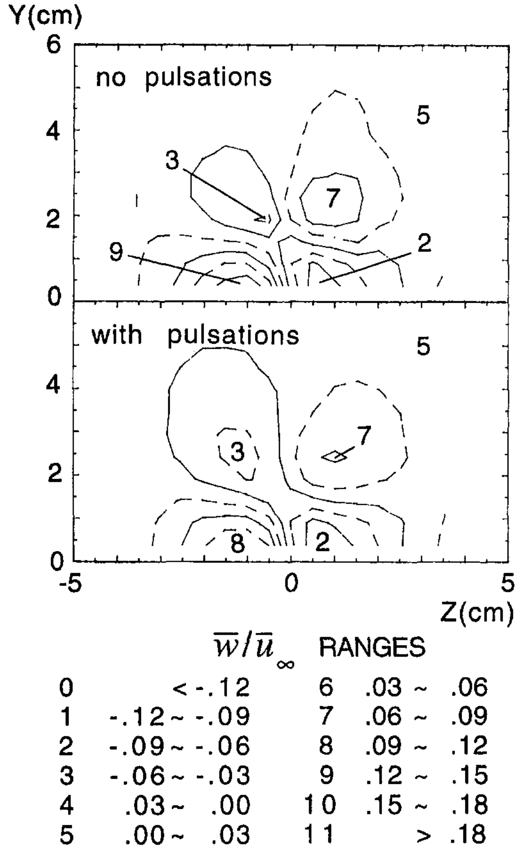

Fig. 4 Surveys of normalized time-averaged spanwise velocity $\bar{w}$ at x/d = 4.5

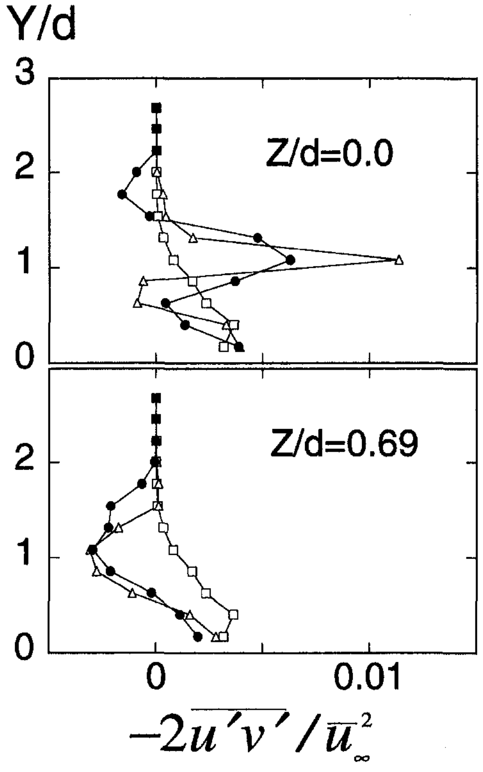

Fig. 5 Profiles of normalized $-\overline{u'v'}$ Reynolds shear stress at $x/d = 4.5$ and $Z/d = 0.00, 0.69$

At Z/d equal to 0.69, magnitudes of film-cooled $-2\overline{u'v'}/\overline{u}_\infty^2$ in Fig. 5 are less than ones measured with no pulsations and no film cooling over the entire boundary layer thickness. In addition $-2\overline{u'v'}/\overline{u}_\infty^2$ values are negative at Y/d greater than 0.5 to 0.7. Profiles of $\overline{u'w'}/\overline{u}_\infty^2$ with film cooling and no pulsations in Fig. 6 at $Z/d = 0.69$ are generally greater than baseline values and positive at all Y/d less than 1.1 to 1.2. At the same Z/d, streamwise mean velocities are higher than ones in the baseline boundary layer over much of the boundary layer thickness, and the normal component of mean velocity $\overline{v}$ is negative.

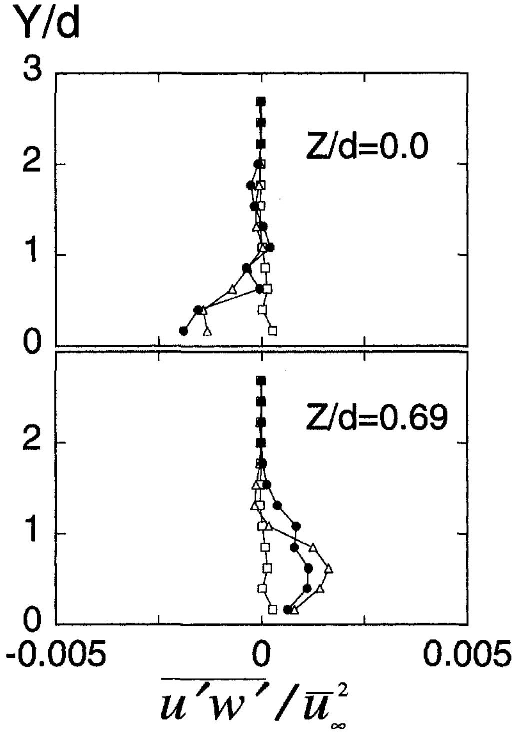

Fig. 6 Profiles of normalized $\overline{u'w'}$ Reynolds shear stress at $x/d = 4.5$ and $Z/d = 0.00, 0.69$

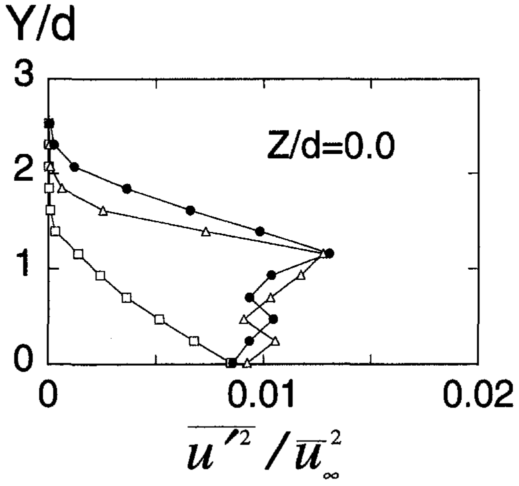

Fig. 7 Profiles of normalized $\overline{u'^2}$ longitudinal Reynolds normal stress at $x/d = 4.5$ and $Z/d = 0$

Effects of Pulsations on Flow Structure. As for the mean velocity components, significant changes to the Reynolds shear stresses occur when the pulsations are present. One of the most important effects is alteration of the positions of different flow structures with time.

At $Z/d = 0.0$ in Fig. 5, the highest measured $-\overline{u'v'}$ are contained in the shear layer described earlier. As this shear layer oscillates to and from the wall at $Z/d = 0.00$, the fluid containing the largest Reynolds stresses (i.e., the highest values of $-\overline{u'v'}$) changes its vertical position with time. Distributions are thus more spatially spread out, which gives lower time-averaged magnitudes of maximum Reynolds shear stress $-2\overline{u'v'}/\overline{u}_\infty^2$ in Fig. 5. This figure also shows that the Y/d locations of these *time-averaged* maxima in the pulsating flow do not change at $Z/d = 0.00$ when compared to the flow with no pulsations.

Profiles of $\overline{u'w'}/\overline{u}_\infty^2$, at Z/d equal to 0.00, show fairly complicated behavior relative to the film-cooled boundary layer with no pulsations in the first region. Figure 6 shows that values from the pulsating flow are both higher or lower than in the nonpulsating flow depending upon the spanwise and normal locations.

At Z/d equal to 0.69, the pulsations act to decrease $-2\overline{u'v'}/\overline{u}_\infty^2$ at $Y/d > 1.1$ in Fig. 5, giving values that are more negative over larger portions of the overall boundary layer thickness relative to the boundary layer with no pulsations. In Fig. 6, three-dimensional stresses $\overline{u'w'}$ increase in the boundary layer at $Y/d = 0.90-1.80$, and decrease at $Y/d < 0.90$ relative to the film-cooled boundary layer with no pulsations.

Normal Reynolds Stress Results

Flow Structure With No Pulsations. Figures 7 and 8 show that film-cooled $\overline{u'^2}/\overline{u}_\infty^2$ and $\overline{v'^2}/\overline{u}_\infty^2$ profiles with no pulsations are all significantly higher than the baseline profiles over most of the boundary layer thickness at Z/d of 0.00. Results at $Z/d = 0.69$ are qualitatively similar. Magnitudes of $\overline{u'^2}/\overline{u}_\infty^2$ and $\overline{v'^2}/\overline{u}_\infty^2$ are especially large at Y/d from 0.5 to 1.35, which correspond to locations within and below the shear layer.

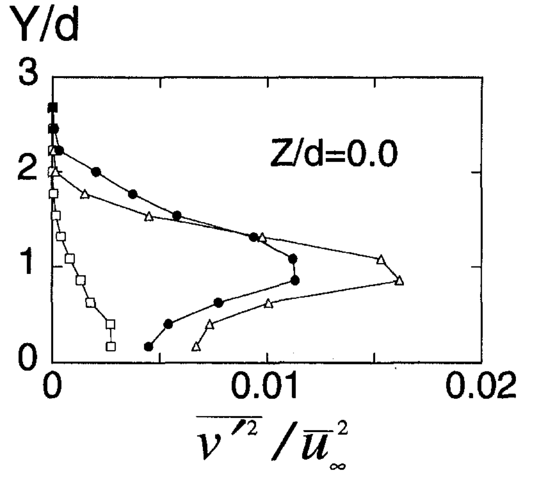

Fig. 8 Profiles of normalized $\overline{v'^2}$ normal Reynolds normal stress at $x/d = 4.5$ and $Z/d = 0$

Effects of Pulsations on Flow Structure. Figure 8 illustrates typical $\overline{v'^2}/\overline{u}_\infty^2$ values at $Z/d = 0.0$ that are higher than profiles with film cooling and no pulsations at Y/d greater than 0.90–1.35, and lower at Y/d less than 0.90–1.35. Figure 7 shows a profile of $\overline{u'^2}/\overline{u}_\infty^2$ from the pulsating film cooled boundary layer at $Z/d = 0.0$, which is about the same as the film-cooled boundary layer with no pulsations for $Y/d < 1.1$. Values in the pulsating flow then become relatively higher as Y/d increases to values larger than 1.1.

Summary and Conclusions

Experimental results are presented that describe the effects of bulk flow pulsations on film cooling. Sinusoidal velocity (and static pressure) wave forms at a frequency of 2 Hz are produced using an array of rotating shutters placed at the downstream end of the wind tunnel test section. The pulsations produce important changes to the flow structure, especially because the imposed pulsations produce periodically unsteady static pressure fields at the exits of the injection holes, which result in pulsating coolant flow rates. In addition, the pulsating static pressure and velocity fields in the boundary layer just downstream from the injection holes result in complex variations with time of the trajectories, distributions, as well as the coverage of the injectant along the surface (Ligrani et al., 1995). Film concentrations move to and from the wall with each flow oscillation, which often gives a different mean injectant trajectory, and acts to spread the same amount of injectant over a larger volume.

Profiles of time-averaged Reynolds stress tensor components and all three mean velocity components measured at $x/d = 4.5$ indicate that the pulsations produce important changes at locations where injectant is present and very small alterations otherwise. With pulsations, the position of the shear layer present in the outer portions of the film concentration at $Y/d = 0.90$–1.35 is believed to oscillate with respect to the wall. As this occurs at spanwise locations near the holes, the fluid containing the largest Reynolds stresses (i.e., the highest values of $-\overline{u'v'}$) changes its vertical position. The spatial extent of the shear layer increases significantly, and fluid with high $-\overline{u'v'}$ is more spread out spatially, which gives lower time-averaged magnitudes of maximum normalized Reynolds shear stress $-2\overline{u'v'}/\overline{u}_\infty^2$. This is believed to occur because the bulk flow pulsations cause the film trajectory and momentum to change with time. As this occurs in the outer portion of the boundary layer, the effect is so dramatic that streamwise velocities are locally higher than the free-stream velocity at Z/d from 0.00 to 0.69.

The pulsations also produce significant changes to profiles of $\overline{u}/\overline{u}_\infty$, $\overline{u'w'}/\overline{u}_\infty^2$, $\overline{u'^2}/\overline{u}_\infty^2$, and $\overline{v'^2}/\overline{u}_\infty^2$ in the film-cooled boundary layer over most of the boundary layer thickness.

References

Abhari, R. S., and Epstein, A. H., 1994, "An Experimental Study of Film Cooling in a Rotating Transonic Turbine," ASME Journal of Turbomachinery, Vol. 116, No. 1, pp. 63–70.

Abhari, R. S., Guenette, G. R., Epstein, A. H., and Giles, M. B., 1992, "Comparison of Time-Resolved Turbine Rotor Blade Heat Transfer Measurements and Numerical Calculations," ASME Journal of Turbomachinery, Vol. 114, pp. 818–827.

Al-Asmi, K., and Castro, I. P., 1993, "Production of Oscillatory Flow in Wind Tunnels," *Experiments in Fluids*, Vol. 15, pp. 33–41.

Ashworth, D. A., LaGraff, J. E., Schultz, D. L., and Grindrod, K. J., 1985, "Unsteady Aerodynamics and Heat Transfer Processes in a Transonic Turbine Stage," ASME *Journal of Engineering for Gas Turbines and Power*, Vol. 107, pp. 1022–1030.

Doorly, D. J., and Oldfield, M. L. J., 1985, "Simulation of the Effects of Shock Wave Passing on a Turbine Rotor Blade," ASME Journal of Engineering for Gas Turbines and Power, Vol. 107, pp. 998–1006.

Dring, R. P., Blair, M. F., and Joslyn, H. D., 1980, "An Experimental Investigation of Film Cooling on a Turbine Rotor Blade," ASME *Journal of Engineering for Power*, Vol. 102, pp. 81–87.

Green, J. G., 1989, "Turbulence Structure Resulting From Interactions Between an Embedded Vortex and Wall Jet," Master of Science Thesis, Department of Mechanical Engineering, U.S. Naval Postgraduate School, Monterey, CA.

Hussain, A. K. M. F., and Reynolds, W. C., 1970, "The Mechanics of an Organized Wave in Turbulent Shear Flow," *Journal of Fluid Mechanics*, Vol. 41, No. 2, pp. 241–258.

Johnson, A. B., Rigby, M. J., Oldfield, M. L. G., Ainsworth, R. W., and Oliver, M. J., 1989, "Surface Heat Transfer Fluctuations on a Turbine Rotor Blade Due to Upstream Shock Wave Passing," ASME Journal of Turbomachinery, Vol. 111, pp. 105–115.

Karlsson, S. K., 1959, "An Unsteady Turbulent Boundary Layer," *Journal of Fluid Mechanics*, Vol. 14, pp. 622–636.

Klebanoff, P. S., 1954, "Characteristics of Turbulence in a Boundary Layer With Zero Pressure Gradient," NACA Technical Note 3178.

Kline, S. J., and McClintock, F. A., 1953, "Describing Uncertainties in Single-Sample Experiments," *Mechanical Engineering*, Jan., pp. 3–8.

Ligrani, P. M., Wigle, J. M., and Jackson, S. W., 1994, "Film Cooling From Holes With Compound Angle Orientations: Part 2—Results Downstream of a Single Row of Holes With 6*d* Spanwise Spacing," ASME *Journal of Heat Transfer*, Vol. 116, pp. 353–362.

Ligrani, P. M., Cuthrell, J. M., and Gong, R., 1995, "Bulk Flow Pulsations and Film Cooling: Flow Structure Just Downstream of the Holes," ASME Paper No. 95-GT-44.

Mehendale, A. B., Han, J.-C., Ou, S., and Lee, C. P., 1994, "Unsteady Wake Over a Linear Turbine Cascade Blade With Air and CO_2 Film Injection: Part II—Effect on Film Effectiveness and Heat Transfer Distributions," ASME Journal of Turbomachinery, Vol. 116, pp. 730–737.

Menendez, A. N., and Ramaprian, B. R., 1989, "Experimental Study of a Periodic Turbulent Boundary Layer in Zero Mean Pressure Gradient," *Aeronautical Journal*, Vol. 93, pp. 195–206.

Moffat, R. J., 1988, "Describing the Uncertainties in Experimental Results," *Experimental Thermal and Fluid Science*, Vol. 1, No. 1, pp. 3–17.

Norton, R. J. G., Forest, A. E., White, A. J., Henshaw, D. G., Epstein, A. H., Schultz, D. L., and Oldfield, M. L. G., 1990, "Turbine Cooling System Design, Volume I—Technical Report," Report WRDC-TR-89-2109, Aero Propulsion and Power Laboratory, Wright Research Development Center, Air Force System Command, Wright-Patterson Air Force Base, OH.

Ou, S., and Han, J.-C., 1993, "Unsteady Wake Effect on Film Effectiveness and Heat Transfer Coefficient From a Turbine Blade With One Row of Air and CO_2 Film Injection," submitted to ASME *Journal of Heat Transfer*.

Ou, S., Han, J.-C., Mehendale, A. B., and Lee, C. P., 1993, "Unsteady Wake Over a Linear Turbine Cascade With Air and CO_2 Film Injection: Part I—Effect on Heat Transfer Coefficients," to appear ASME Journal of Turbomachinery.

Ramaprian, B. R., and Tu, S. W., 1980, "An Experimental Study of Oscillatory Pipe Flow at Transitional Reynolds Numbers," *Journal of Fluid Mechanics*, Vol. 100, pp. 513–544.

Rigby, M. J., Johnson, A. B., and Oldfield, M. L. G., 1990, "Gas Turbine Rotor Blade Film Cooling With and Without Simulated Shock Waves and Wakes," ASME Paper No. 90-GT-78.

Takeishi, K., Aoki, S., Sato, T., and Tsukagoshi, K., 1992, "Film Cooling on a Gas Turbine Rotor Blade," ASME Journal of Turbomachinery, Vol. 114, pp. 828–834.

R. J. Goldstein

L. D. Stone

Heat Transfer Laboratory,
Mechanical Engineering Department,
University of Minnesota,
111 Church Street SE,
Minneapolis, MN 55455

Row-of-Holes Film Cooling of Curved Walls at Low Injection Angles

Film cooling effectiveness data are presented against a backdrop of ammonia-diazo flow visualizations for row-of-holes injection along a convex wall and a concave wall at angles of 15, 25, and 45 deg to the mainstream and at density ratios of approximately one and two. Injection angle effects vary with the rate of injection: At low blowing rates the injection angle is unimportant, at moderate blowing rates the shallower angles provide better effectiveness, and at high blowing rates a steeper injection angle sometimes provides better effectiveness. The condition of the local boundary layer, the severity of jet lift-off, and the strength of vortex interactions among the bound vortices of neighboring jets are key considerations in interpreting the data.

Introduction

Film cooling is used to protect solid surfaces exposed to hot gas flows. A secondary, cold fluid is injected into the boundary layer, usually from discrete holes in the surface. This method of cooling finds extensive application in gas turbines, where thermodynamic considerations provide a great incentive to push the combustion temperatures to the limit that the gas turbine components and associated cooling systems can withstand.

Ramsey and Goldstein (1971) measured wall temperatures along a flat plate for heated injection from a single hole inclined 35 and 90 deg to the mainstream. A significant injection-angle effect was found only at high blowing rates. Since a 35-deg jet follows a trajectory closer to the wall, the centerline effectiveness downstream of injection is much higher for 35-deg injection than for normal injection. Considerably less lateral and vertical spreading is associated with the 35-deg jet, however, so variations in area-averaged effectiveness with the injection angle may not be well indicated by the observed differences in centerline effectiveness.

Foster and Lampard (1980) measured the flow field and film cooling effectiveness distribution for row-of-holes film cooling along a flat plate at a density ratio of two; injection at 35, 55, and 90 deg to the mainstream was used. Shallower injection angles performed better at low blowing rates, since jet lift-off was less severe. At high blowing rates, however, the 90-deg jets actually performed best. Lateral profiles of film cooling effectiveness at high blowing rates (when liftoff apparently occurred for all three injection angles) showed that while the centerline effectiveness was about the same for all three angles, the midline (between holes) effectiveness was significantly higher for steeper injection. They explained that at high blowing rates the steeper jets spread more quickly in the lateral direction than the shallower jets (as found for a single jet by Ramsey and Goldstein, 1971), merging closer to injection than did the shallower jets.

Kruse (1985) measured film cooling effectiveness and heat transfer coefficients for injection from a row of holes along convex, flat, and concave walls, the injection point being just upstream of the onset to curvature (for $\alpha = 10$, 45, and 90 deg; $1.5 < S/D < 5$; $0.5 < M < 2.0$; $\rho_2/\rho_\infty \approx 1.24$). At this lower density ratio Kruse found that lower injection angles provide better film cooling.

Kruse did find a strong hole-spacing effect. Like Foster and Lampard, he found that a smaller hole spacing works better. Temperature measurements in the boundary layer for injection along a flat plate at 45 deg to the mainstream and a blowing rate of two indicated that at close spacing the jets spread more laterally and coalesced a shorter distance from injection, and that in between the jets coolant migrated toward the wall. Significantly, he also found that jets that influence one another in this way do not penetrate as far into the mainflow as jets that do not interact in this way. Putting these pieces together, Kruse suggests that ''the secondary [bound] vortices of neighboring jets form counterrotating systems of vortices . . . which may intensify the tendency to reattach to the wall.'' A reproduction of Fig. 6 of Kruse is given as Fig. 1.

Experimental Method

The temperature along an adiabatic wall under film cooling is expressed in dimensionless form as the film cooling effectiveness,

$$\eta = \frac{T_{aw} - T_\infty}{T_2 - T_\infty}, \qquad (1)$$

for low-speed flow. The film cooling effectiveness is zero if the wall is at the mainstream temperature and one or 100 percent if the wall is at the coolant temperature.

In the present experiment, the thermal flow conditions including the adiabatic bounding wall required for measuring film cooling effectiveness are modeled by using a mass transfer analogy. To model density ratios of about one and two, a 5 percent by volume mixture of helium in air and a 25 percent by volume mixture of sulfur hexafluoride in air, respectively, are injected into a mainflow of air; film cooling effectiveness is then determined from measurements of impermeable-wall concentrations downstream of injection. Since $C_\infty = 0$, the analog to Eq. (1) is:

$$\eta = \frac{C_{iw}}{C_2} \qquad (2)$$

Figure 2 is a plan view of the test section, incorporated into the suction tunnel described at length by Schwarz (1986). A developing mainstream of air with a core velocity of about 40 m/s approaches from the 102 mm wide by 489 mm high

---

Contributed by the Heat Transfer Division and presented at the International Mechanical Engineering Congress and Exposition, Chicago, Illinois, November 6–11, 1994. Manuscript received by the Heat Transfer Division January 8, 1996. Associate Technical Editor: M. G. Dunn.

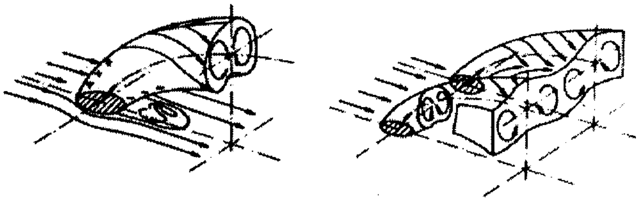

Fig. 1 Sketch of bound vortices for an isolated jet and for a row of jets (reproduction of Fig. 6 in Kruse (1985))

development section, where three 1.2-mm-dia tripwires are positioned, as shown, to produce thin, turbulent boundary layers ($\delta_{99} \approx 10$ mm) at the onset to curvature. The flow turns through a 135-deg bend at constant radius and cross section ($r_{cvx} \approx 101$ mm). The "coolant" flow is injected through a single row of holes with three-diameter spacing on either the concave wall, where the nine active holes are 4.70 mm diameter and located 40 deg from the onset of curvature, or on the convex wall, where the 15 active holes are 2.18 mm diameter and located 45 deg from the onset of curvature (the inactive row would be taped over). Note that the relative curvature, $2r/D$, is the same on the concave and convex walls. The injection angle could be 15, 25, or 45 deg according to a choice of injection plates; for all plates the length of the injection holes is about ten diameters, matching that of Schwarz et al. (1991).

When measuring film cooling effectiveness, gas samples are slowly drawn through small taps located on the injection plenums and along the wall downstream of injection. The samples are stored in glass tubes for later analysis, using an HP-5570B gas chromatograph. The flow rate and density of injectant are determined from measurements of the injected air flow rate (using a sharp-edged orifice meter) and the mass concentration of foreign gas in the injection plenum (using the chromatograph). The potential wall velocity (used in the blowing rate) is determined from measurements of total pressure (using an impact probe) and static pressure (at an endwall tap) using the potential-vortex relationship:

$$u_{pw} = \frac{r_{\mathrm{ref}}\, u_{\mathrm{ref}}}{r_w} \qquad (3)$$

Boundary-layer measurements near the injection locations are taken with a gooseneck impact tube. Key test parameters are summarized in Table 1. Note that the blowing rates listed are nominal.

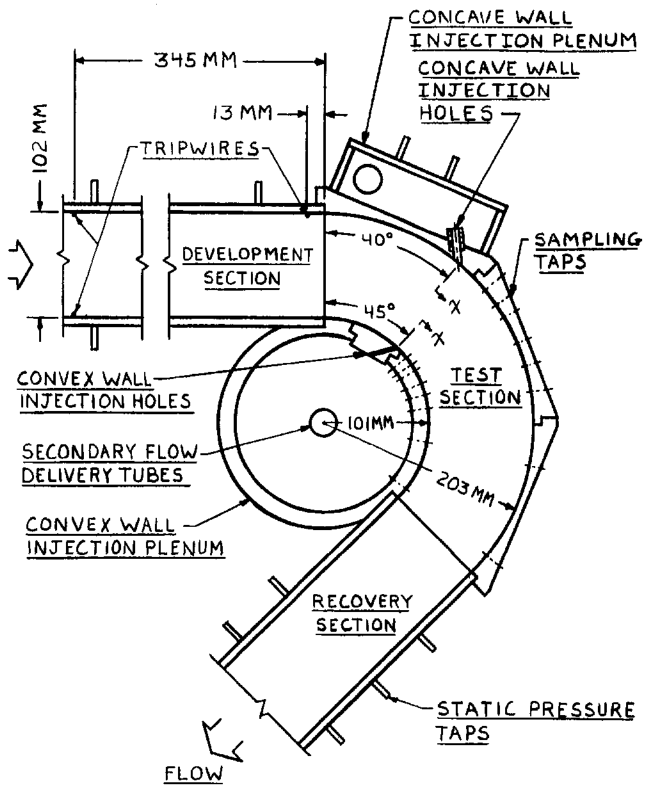

Fig. 2 Plan view of test section for study of row-of-holes film cooling of curved surfaces

Uncertainties in the density ratio and blowing rate are estimated at 0.1 and 2.5 percent, respectively, following the recommendations of Moffat (1982) for the evaluation of 95 percent confidence intervals and those of Kline and McClintock (1953) for the propagation of uncertainties (as recommended by Kim et al., 1993). These estimates are valid for all runs. Based on extensive, long-term repeatability trials, the uncertainty in laterally averaged effectiveness can be as high as ±0.010 absolute for convex-wall measurements near injection at high blow-

Nomenclature

C_{iw} = mass concentration of foreign gas at an impermeable wall
C_2 = mass concentration of foreign gas in injectant
C_∞ = mass concentration of foreign gas in the mainstream
D = diameter of injection hole
H = shape factor = δ_0^*/θ
h = convective heat transfer coefficient
I = momentum flux ratio = $\rho_2 u_2^2/\rho_\infty u_\infty^2$
M = blowing rate = $\rho_2 u_2/\rho_\infty u_\infty$
q'' = wall heat flux
r = radius of wall, approximately $45D$ for both walls
r_{cvx} = radius of convex wall
r_w = radius of wall
r_{ref} = radial position within potential core where u_{ref} is measured
$\mathrm{Re}_{2,D}$ = injection Reynolds number = $\rho_2 u_2 D/\mu_2$
$\mathrm{Re}_{2,s}$ = injection Reynolds number = $\rho_2 u_2 s/\mu_2$
Re_D = free-stream Reynolds number = $\rho_\infty u_\infty D/\mu_\infty$
S = hole spacing, approximately $3D$ on both walls
s = equivalent slot width of injection holes
T_{aw} = temperature of an adiabatic wall
T_w = wall temperature
T_2 = temperature of injectant
T_∞ = temperature of free stream
u_{pw} = potential-flow velocity at wall, extrapolated from the core flow
u_{ref} = velocity at reference location within potential core
u_2 = average velocity of injection
u_∞ = free-stream velocity
x = streamwise coordinate (from point of injection)
Z = spanwise coordinate (from center of injection hole)
α = injection angle
δ_{99} = 99 percent boundary layer thickness
δ_0^* = displacement thickness
θ = momentum thickness
μ_2 = dynamic viscosity of injectant
μ_∞ = dynamic viscosity of free stream
η = film cooling effectiveness, equation (1)
$\bar{\eta}$ = laterally averaged film cooling effectiveness
ρ_2 = density of injected fluid
ρ_∞ = density of free stream fluid

Table 1 Ranges of experimental parameters in present study

PARAMETER		CONVEX WALL	CONCAVE WALL
GEOMETRICAL	$\frac{2r}{D}$	+92.5	-86.5
	$\frac{S}{D}$	2.965	2.920
	α	15°, 25°, 45°	
COOLANT FLOW	$\frac{\rho_2}{\rho_\infty}$	0.95, 2.0	
	M	$0.25^*, 0.50, 0.75, 1.00, 1.50, 2.00, 2.50^*$	
	$Re_{2,D}$	1,900 - 24,800	
	$Re_{2,s}$	500 - 6,500	
UNDISTURBED MAINFLOW (Measured at injection, $x/D = 0$)	u_{pw}	64 m/sec	32 m/sec
	$\frac{\delta_{99}}{D}$	4.6	5.1
	$\frac{\delta_0^*}{D}$	0.50	1.19
	$\frac{\theta}{D}$	0.32	0.85
	H	1.6	1.4
	Re_D	9,000	

* For $\rho_2/\rho_\infty = 0.95$ only

ing rates; under any other conditions the repeatability was at least twice as good (±0.005 or better).

An ammonia vapor injection system is used for flow visualization. Parallel to the normal flow path into the injection plenum, a second line passes through an evaporation chamber fabricated by modifying a 22-quart pressure cooker. Typically a one-liter charge of 30 percent solution ammonium hydroxide in water is placed in the evaporation chamber and a piece of speed-5 or speed-10 diazo paper mounted downstream of injection in the test section. After the wind tunnel is brought up to operating conditions, the valve to the evaporation chamber is opened. The surface flow visualization pattern appears on the diazo paper within about thirty seconds. Flow continues for one to four minutes to let the pattern darken.

Results

Flow Visualization. Figures 3 and 4 present the ammonia-diazo visualizations for injection at a density ratio near unity along the convex and concave walls, respectively. At very low blowing rate ($M = 0.25$, Figs. 3(a, e, i), and 4(a, e, i)) the ammonia traces are similar on both walls and for all injection angles; they are quite wide and straight. The coolant gently flows out of the holes and is carried directly downstream by the approach flow; the coolant-mainstream interactions are too mild for the injection angle to have any appreciable influence on the time-mean "coolant" traces. A wall-curvature effect is detected, however: on the convex wall the coolant traces remain quite dark far downstream, whereas on the concave wall a rapid streamwise-fading of the ammonia traces occurs. The "jets" also seem to remain distinct much farther downstream in the convex-wall boundary layer than in the concave-wall boundary layer.

These differences are due to the cross-stream pressure gradient, as discussed by Schwarz et al. (1991) and Ito et al. (1978). In curved flows a cross-stream pressure gradient exists that holds low-momentum fluid particles against a convex wall but pulls low-momentum fluid particles away from a concave wall. The effects on the mainstream boundary layers themselves is to enhance mixing and entrainment in a concave-wall boundary layer but to suppress mixing and entrainment in a convex-wall boundary layer (see also Meroney and Bradshaw, 1975). On the convex wall, then, coolant injected at low blowing rate stays close to the wall and in line with the injection holes, whereas on the concave wall the coolant is mixed out into the boundary layer over a comparatively short distance downstream of injection. (In separate trials where low-blowing jets were fully marked with smoke, the convex jets seemed to flow straight and smoothly, whereas the concave jets appeared to flicker back and forth spanwise, shedding lumps of coolant into the boundary layer.) Further experimental support of this interpretation is given by Mayle et al. (1976) for slot injection over curved walls.

As the blowing rate is increased to 0.75 (Figs. 3(b, f, j), and 4(b, f, j)) the traces become narrower, indicating that the jets are lifting away from the wall. Judging from the relative narrowness of the ammonia traces, lift-off seems to be stronger for 25-deg and 45-deg injection than for 15-deg injection. This seems intuitive.

The traces do not simply continue to grow narrower as the blowing rate is increased further, however. Thus, at the highest blowing rate studied, 2.25 (Figs. 3(d, h, l) and 4(d, h, l)), an interesting injection-angle effect is observed. For 25-deg injection along the convex wall and 45-deg injection along both the convex wall (Fig. 3(h, l)) and the concave wall (Fig. 4(h, l)), lift-off is nearly complete immediately downstream of injection, but is soon followed (at about $x/D \approx 5$ on the concave wall and $x/D \approx 8$ on the convex wall) by a return of injectant to the wall. These regions were the first to turn blue after the ammonia vapor was turned on; this fact, and the rather steep color gradients (white to blue in the originals), encourage the authors to label these as regions of "coolant touchdown." Similar effects have also been observed at high blowing rate on a flat surface (Cho, 1994).

Kruse posits that bound-vortex interactions help serve to deliver coolant to the wall. Vortex interactions should be stronger for steep injection at high blowing rate, since the bound vortices of the jets are stronger under these conditions, and since the centers of the vortices would also be closer. Coolant touchdown would also be expected to occur off-centerline first. The lines of coolant touchdown are, indeed, found to occur earliest for the steepest injection angles and highest blowing rates studied (Figs. 3(l), 4(l)), and coolant touchdown does first occur midway between the holes. Vortex interactions among the bound vortices of neighboring jets is believed to be an important characteristic of the flow field.

Effectiveness Measurements. Lateral profiles of effectiveness are shown in Goldstein and Stone (1994) but are not repeated here due to space limitations. Generally they show either flat profiles (especially on the concave wall) or peaks along the centerlines of injection. Under conditions where bound-vortex interactions are expected to play a role, effectiveness is shown to be higher midway between the holes than along the centerlines.

Representative streamwise profiles of laterally averaged effectiveness are shown in Fig. 5; these are for a density ratio of 0.95 along the concave wall. At low blowing rate, $M \approx 0.50$, there is almost no effect of injection angle. The picture is approximately one of coolant "calmly" and evenly filling the boundary layer; the impact of the "jets" on the approach boundary layer is too mild for the hole inclination to matter.

At moderate blowing rate, $M \approx 1.00$, the lower injection angles provide better effectiveness on the concave surface (Fig. 5(b)). Jets have begun to lift away from the wall; since jets injected more tangentially are more easily turned by the approach flow, they follow trajectories closer to the wall, thus providing better film cooling coverage than steeper jets. The improvement is moderate but definite.

This trend does not continue indefinitely, however, as shown in Fig. 5(c). At high blowing rate, $M \approx 2.00$, the 15-deg jets still perform best for these operating conditions but near injec-

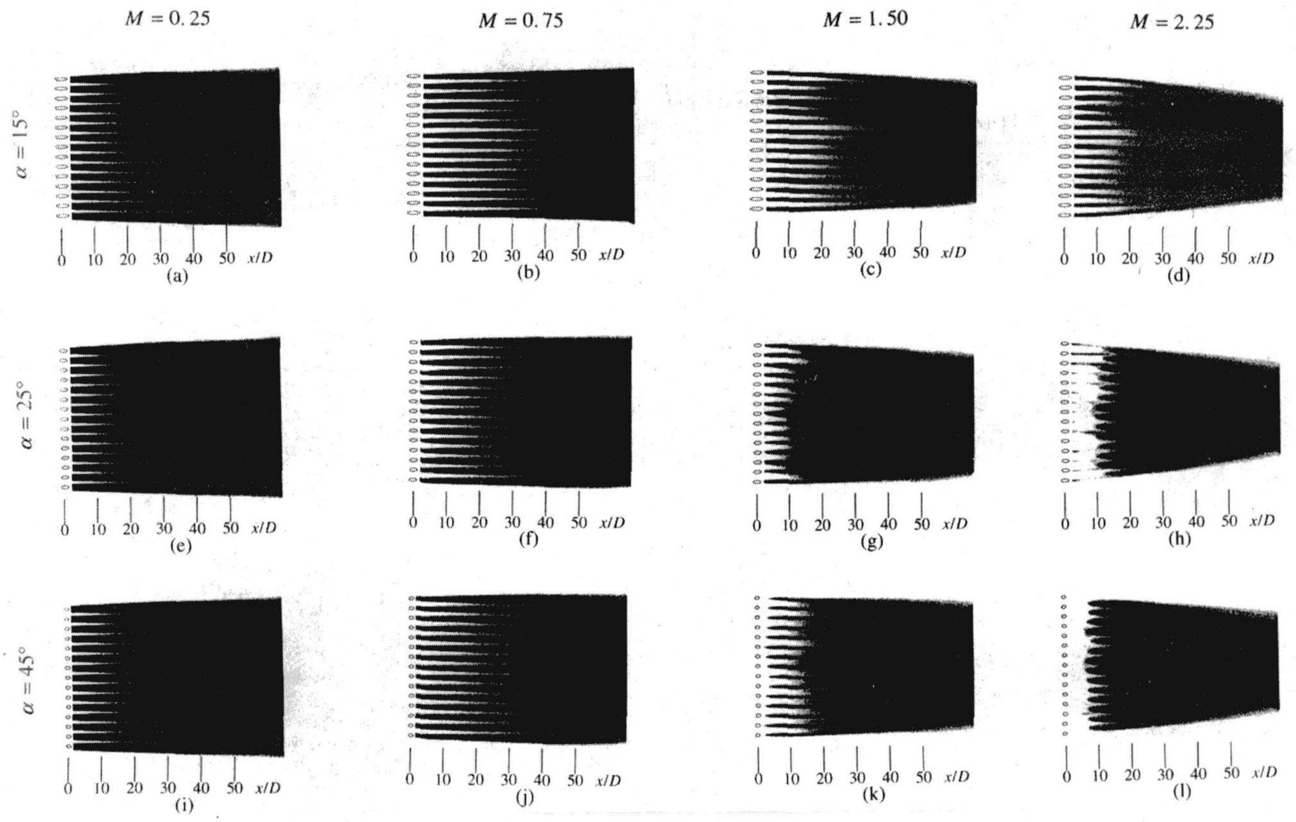

Fig. 3 Ammonia-diazo visualizations of film cooling along a convex wall

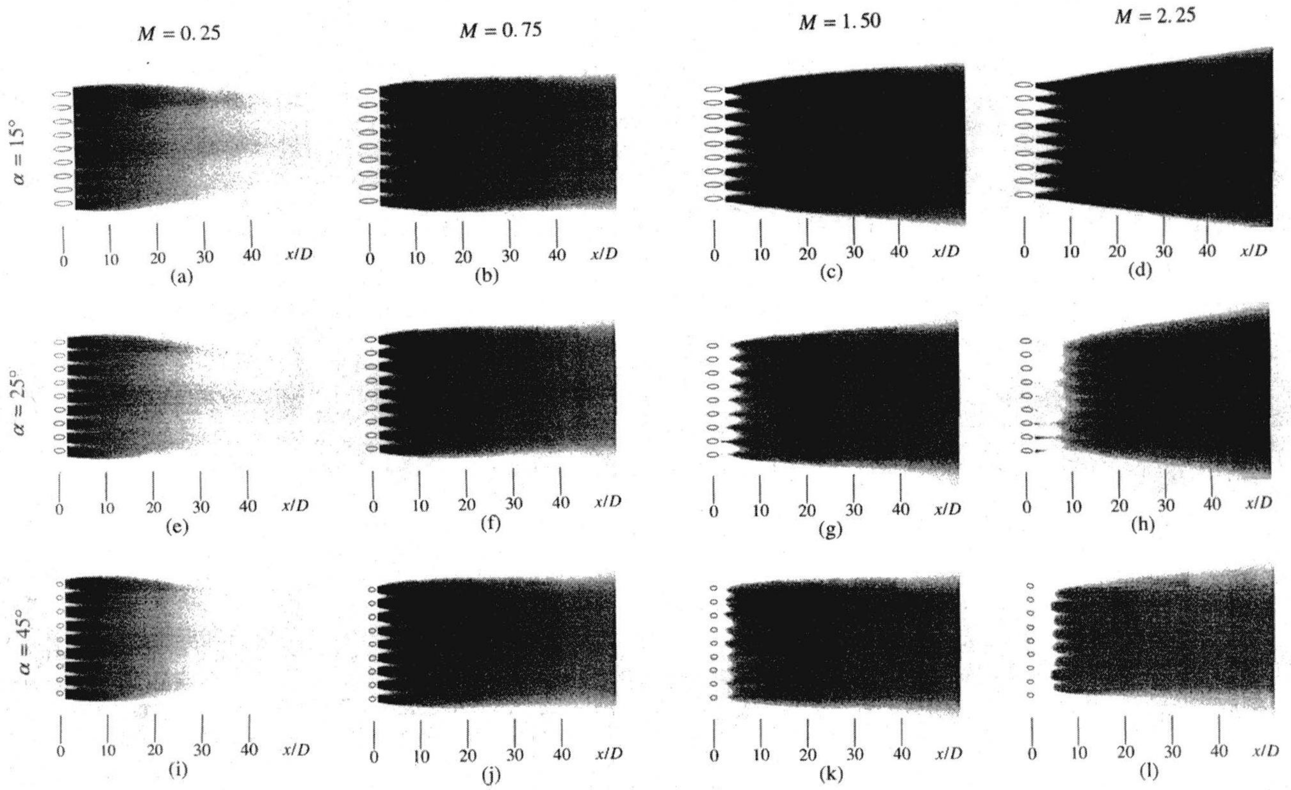

Fig. 4 Ammonia-diazo visualizations of film cooling along a concave wall

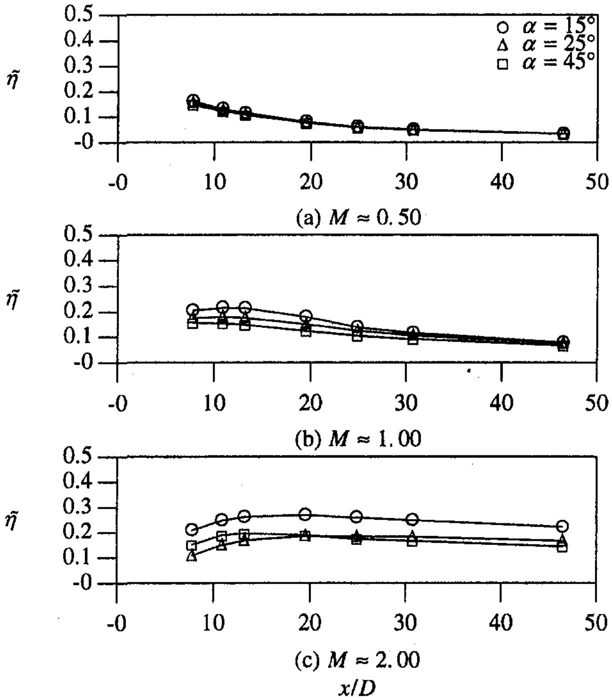

(a) $M \approx 0.50$

(b) $M \approx 1.00$

(c) $M \approx 2.00$

x/D

Fig. 5 Streamwise profiles of effectiveness on the concave wall ($\rho_2/\rho_\infty \approx 0.95$)

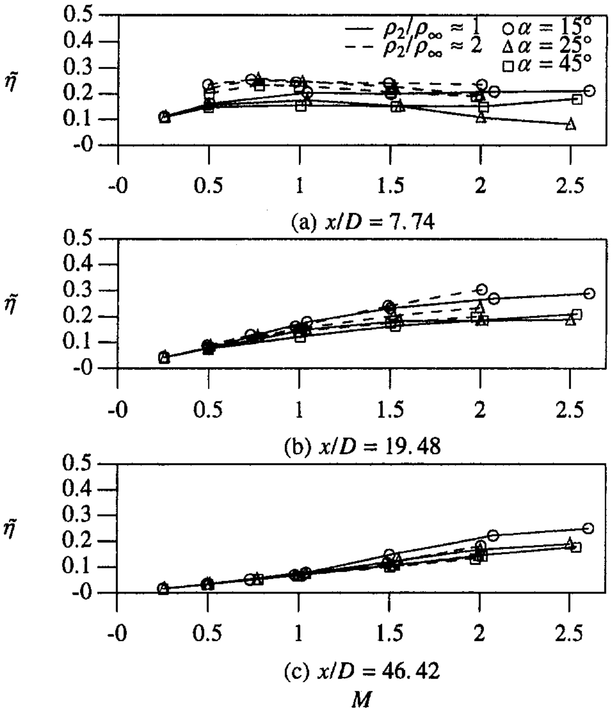

(a) $x/D = 7.74$

(b) $x/D = 19.48$

(c) $x/D = 46.42$

M

Fig. 7 Film cooling effectiveness on the concave wall: effects of density ratio, injection angle, and blowing rate

tion the 45-deg jets are seen to yield higher laterally averaged film cooling effectiveness than the 25-deg jets. As described earlier, such injection-angle role reversals have been reported by Foster and Lampard (1980) for injection over a flat plate as well, and are believed to be caused by vortex interaction between bound vortices of neighboring jets (cf. Kruse, 1985).

Figure 6 shows the corresponding profiles for the convex wall. Even at a blowing rate of about 0.50, the shallow injection angles have already begun to provide better effectiveness. Figure 6(c) shows the effect of jet lift-off near injection on the convex wall, but it also shows how farther downstream, jets that have presumably lifted off the convex wall can come back to coat the wall more effectively than near-tangential (15-deg) jets. Both lift-off and vortex interaction play important, counteracting roles in convex-wall injection at high blowing rates. Avoiding jet lift-off requires shallow injection whereas strengthening the bound-vortex interactions requires steeper injection angles.

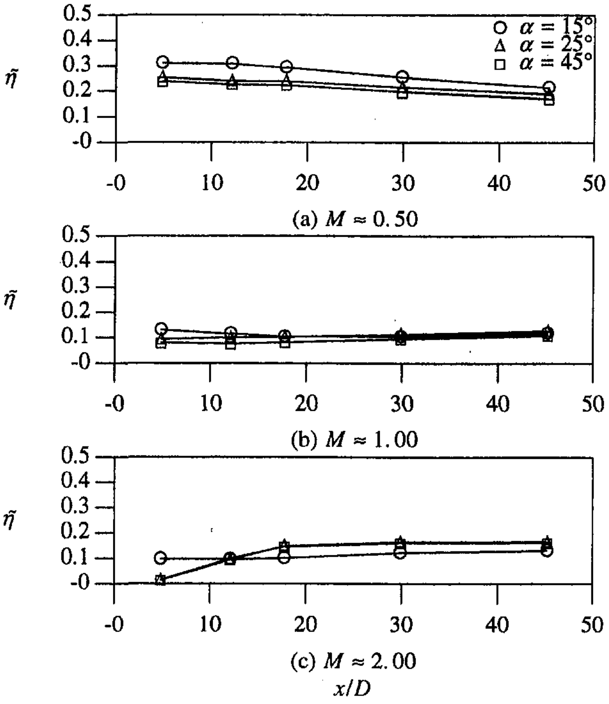

(a) $M \approx 0.50$

(b) $M \approx 1.00$

(c) $M \approx 2.00$

x/D

Fig. 6 Streamwise profiles of effectiveness on the convex wall ($\rho_2/\rho_\infty \approx 0.95$)

This contrasts with concave-wall injection where the maximum degree of jet lift-off is geometrically limited. Since at high blowing rate the 15-deg jets never really leave the wall, near-tangential injection always produces the highest levels of laterally averaged effectiveness on the concave wall, everywhere downstream and at all blowing rates (Fig. 5(c)). Still, Fig. 5(c) does show that even on the concave wall vortex interactions can be strong enough for the 45-deg jets that they slightly outperform the 25-deg jets under certain conditions.

Figures 7 and 8 summarize the variations of laterally averaged effectiveness with injection angle, density ratio, and blowing rate on the concave and the convex wall, respectively. Note that on the convex wall the data for different injection angles cluster according to density ratio, and on the concave wall the film cooling effectiveness is primarily a function of blowing rate, secondarily of injection angle (especially downstream).

At low blowing rate (in the absence of lift-off) a monotonic increase in effectiveness with increasing blowing rate occurs, since under such mildly disturbed conditions it is simply the mass (enthalpy) flux of coolant available for mixing within the boundary layer, which determines the effectiveness level. Within the unstable concave-wall boundary layer, the view of a boundary layer accumulating coolant holds rather well (Fig. 7) for blowing rates as high as two, beyond a certain distance downstream of injection. Why do the 15-deg jets begin to perform better at high injection rates? It is suggested that the more tangential jets disturb the approach boundary less severely than the steeper jets, resulting in a thinner cooling film, hence less dilution of coolant with mainstream fluid.

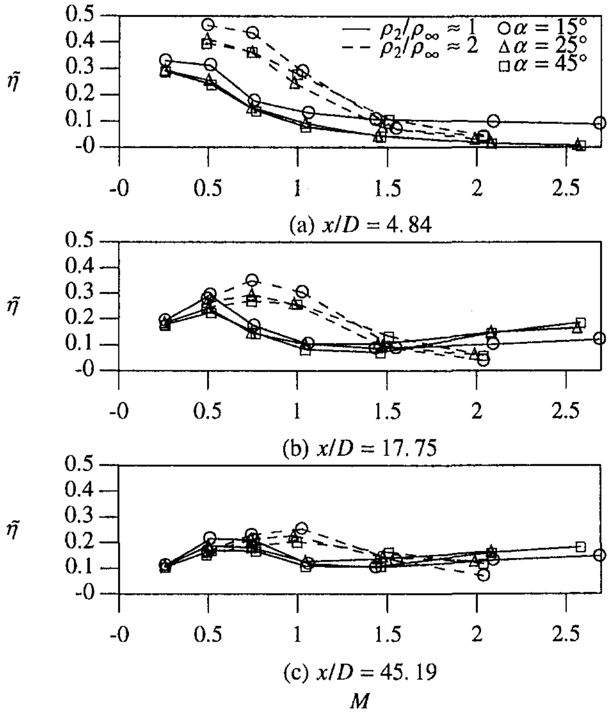

Fig. 8 Film cooling effectiveness on the convex wall: effects of density ratio, injection angle, and blowing rate

On the convex wall (Fig. 8), on the other hand, as the blowing rate is increased the jets soon begin to lift away from the wall, the effectiveness dropping considerably. The precise value of this critical, lift-off blowing rate depends upon the streamwise position and the density ratio, but as a rule of thumb the film cooling effectiveness is seen to be optimized at a blowing rate of about 0.50 for a density ratio of 0.95 and at a blowing rate of about 0.75 for a density ratio of two. Note that the momentum flux ratio, I, is approximately 0.25 in both cases, thus suggesting a general rule for optimum film cooling coverage for row-of-holes injection along a convex wall, for three-diameter hole spacing. It is also apparent from Fig. 8 that injection at a higher density ratio and a lower injection angle improves film cooling effectiveness when $I \approx 0.25$.

Conclusions

On both concave and convex walls, whether a shallower or a steeper injection angle yields higher film cooling effectiveness depends on the rate of injection. At very low blowing rates the coolant gently flows into the boundary layer and the film cooling effectiveness increases with blowing rate, independently of injection angle; it is the condition of the mainflow itself that largely determines the resulting effectiveness levels at low blowing rates. As the blowing rate is increased past the lift-off blowing rate (the blowing rate at which the jets lift away from the wall and the effectiveness begins to drop—about 0.50 for near-uniform-density injection on the convex surface), the shallower angles begin to perform better, the trajectories of shallower jets being somewhat closer to the walls than those of steeper jets. At high blowing rates, however, the tendency of steeper jets to lift farther from the wall is counteracted to some extent by vortex interaction in which counterrotating vortex pairs can translate toward the wall. Ammonia-diazo visualizations provide evidence of this effect, which is strong on the convex wall but also present on the concave wall. At high blowing rates, therefore, a row of steeper film cooling jets can actually protect a wall better than a row of shallower jets.

Even so, film cooling effectiveness was found to be optimized at lower injection angles. On the concave wall, injection at 15 deg or lower and at high blowing rates is preferred. Use of a higher density ratio often brings some improvement but has almost no affect on the effectiveness far downstream at low blowing rates. On the convex wall, injection at a momentum flux ratio of 0.25, a high density ratio, and a shallow injection angle provides the best effectiveness for this hole spacing.

Acknowledgments

Support provided by the U.S. Air Force Office of Scientific Research, and more recently Advanced Gas Turbine System Research of the Department of Energy, is greatly appreciated, with special thanks to Dan Fant.

References

Cho, H. H., 1994, personal communication.

Eckert, E. R. G., 1983, "Analysis of Film Cooling and Full-Coverage Film Cooling of Gas Turbine Blades," ASME Paper No. 83-GTJ-2.

Eckert, E. R. G., 1976, "Analogies to Heat Transfer Processes," *Measurements in Heat Transfer,* 2nd ed., Ernst R. G. Eckert and Richard J. Goldstein, eds., Hemisphere Publishing Corp., Washington, DC.

Foster, N. W., and Lampard, D., 1980, "The Flow and Film Cooling Effectiveness Following Injection Through a Row of Holes," ASME *Journal of Engineering for Power,* Vol. 102, pp. 584–588.

Goldstein, R. J., Eckert, E. R. G., Eriksen, V. L., and Ramsey, J. W., 1970, "Film Cooling Following Injection Through Inclined Circular Tubes," *Israel J. Technology,* Vol. 108, pp. 145–154.

Goldstein, R. J., and Taylor, J. R., 1982, "Mass Transfer in the Neighborhood of Jets Entering a Crossflow," ASME *Journal of Heat Transfer,* Vol. 104, pp. 715–721.

Goldstein, R. J., and Stone, L. D., 1994, "Row-of-Holes Film Cooling of a Convex and a Concave Wall at Low Injection Angles," ASME HTD-Vol. 300, pp. 15–29.

Ito, S., Goldstein, R. J., and Eckert, E. R. G., 1978, "Film Cooling of a Gas Turbine Blade," ASME *Journal of Engineering for Power,* Vol. 100, pp. 476–481.

Kim, J. H., Simon, T. W., and Viskanta, R., 1993, "Journal of Heat Transfer Policy on Reporting Uncertainties in Experimental Measurements and Results," ASME *Journal of Heat Transfer,* Vol. 115, pp. 5–6.

Kline, S. J., and McClintock, F. A., 1953, "Describing Uncertainties in Single-Sample Experiments," *Mechanical Engineering,* Vol. 75, Jan., pp. 3–8.

Kruse, H., 1985, "Effects of Hole Geometry, Wall Curvature and Pressure Gradient on Film Cooling Downstream of a Single Row," *Heat Transfer and Cooling in Gas Turbines,* AGARD-CP-390.

Mayle, R. E., Kopper, F. C., Blair, M. F., and Bailey, D. A., 1976, "Effect of Streamline Curvature on Film Cooling," ASME Paper No. 76-GT-90.

Meroney, R. N., and Bradshaw, P., 1975, "Turbulent Boundary-Layer Growth Over a Longitudinally Curved Surface," *AIAA J.,* Vol. 13, pp. 1448–1453.

Moffat, R. J., 1982, "Contributions to the Theory of Single-Sample Uncertainty Analysis," ASME *Journal of Fluids Engineering,* Vol. 104, pp. 250–260.

Pedersen, D. R., Eckert, E. R. G., and Goldstein, R. J., 1977, "Film Cooling With Large Density Differences Between the Mainstream and Secondary Fluid Measured by the Heat—Mass Transfer Analogy," ASME *Journal of Heat Transfer,* Vol. 99, pp. 620–627.

Ramsey, J. W., and Goldstein, R. J., 1971, "Interaction of a Heated Jet With a Deflecting Stream," ASME *Journal of Heat Transfer,* Vol. 93, pp. 365–372.

Schwarz, S. G., 1986, "Film Cooling of Curved Surfaces," Ph.D. Thesis, University of Minnesota, Minneapolis, MN.

Schwarz, S. G., and Goldstein, R. J., 1989, "The Two-Dimensional Behavior of Film Cooling Jets on Concave Surfaces," ASME JOURNAL OF TURBOMACHINERY, Vol. 111, pp. 124–130.

Schwarz, S. G., Goldstein, R. J., and Eckert, E. R. G., 1990, "The Influence of Curvature on Film Cooling Performance," ASME JOURNAL OF TURBOMACHINERY, Vol. 100, pp. 472–478.

Stone, L. D., 1992, "Film Cooling of Curved Surfaces at Low Injection Angles," M.S. Thesis, University of Minnesota, Minneapolis, MN.

Stone, L. D., and Goldstein, R. J., 1994, "Film Cooling Effectiveness Data for Simple Injection Geometries: A Collection of Three-Axis Plots," *Int. J. of Rotating Machinery,* Vol. 1(1), pp. 73–81.

Heat Transfer Coefficients Over a Flat Surface With Air and CO_2 Injection Through Compound Angle Holes Using a Transient Liquid Crystal Image Method

S. V. Ekkad[1]

D. Zapata

J. C. Han

Turbine Heat Transfer Laboratory,
Department of Mechanical Engineering,
Texas A&M University,
College Station, TX 77843-3123

This paper presents the detailed heat transfer coefficients over a flat surface with one row of injection holes inclined streamwise at 35 deg for three blowing ratios ($M = 0.5$–2.0). Three compound angles of 0, 45, and 90 deg with air ($D.R. = 0.98$) and CO_2 ($D.R. = 1.46$) as coolants were tested at an elevated free-stream turbulence condition ($Tu \approx 8.5$ percent). The experimental technique involves a liquid crystal coating on the test surface. Two related transient tests obtained detailed heat transfer coefficients and film effectiveness distributions. Heat transfer coefficients increase with increasing blowing ratio for a constant density ratio, but decrease with increasing density ratio for a constant blowing ratio. Heat transfer coefficients increase for both coolants over the test surface as the compound angle increases from 0 to 90 deg. The detailed heat transfer coefficients obtained using the transient liquid crystal technique, particularly in the near-hole region, will provide a better understanding of the film cooling process in gas turbine components.

Introduction

Advanced gas turbine engines operate at high gas temperatures (1200–1400°C) to improve thermal efficiency and power output. As these temperatures are far above the permissible metal temperatures, gas turbine blades must be cooled to operate without failure. In film cooled turbine blades, relatively cool air injected from inside the blade to the outside surface forms a protective layer between the blade surface and high-temperature gases. Film cooling depends mostly on the amount of coolant used, density of the coolant, and the type of film cooling hole geometry on the blade surface. The amount of coolant to be injected depends upon the blowing ratio of injection. Blowing ratio is the ratio of coolant-to-mainstream mass flux ratio. The effect of coolant-to-mainstream density ratio is another important parameter. There exists a large difference in the temperature of coolant and mainstream in gas turbine engines that causes variations in density of coolant compared to mainstream.

Compound angle holes are holes oriented about both the surface and the flow direction, and should provide more uniform protection and higher effectiveness over simple angle holes. Past film cooling studies have focused on film cooling effectiveness and heat transfer coefficient on turbine blades, leading edge models, and flat surfaces. However, this paper focuses only on the flat surface heat transfer coefficients with coolant injection through inclined circular holes.

Several studies have concentrated on film cooling heat transfer coefficients on flat surfaces for low free-stream turbulence. Eriksen and Goldstein (1974), Liess (1975), Goldstein and Yoshida (1982), Hay et al. (1985), Teekaram et al. (1989) and Ammari et al. (1990) studied the effects of blowing ratio, density ratio, and film hole geometries on flat surfaces. They measured heat transfer coefficients for several blowing ratios and low free-stream turbulence ($Tu < 1$ percent) with air as a coolant ($D.R. \approx 1.0$) through a single row of holes inclined streamwise at 35 deg on a flat plate. Most of the studies reported increases in heat transfer coefficients with film injection for blowing ratios higher than 0.5. Teekaram et al. (1989) and Ammari et al. (1990) studied the effect of density ratio on film cooling heat transfer. They concluded that heat transfer coefficient at a fixed blowing ratio decreases as the coolant-to-mainstream density ratio increases for streamwise 35 deg injection through a single row of holes.

Few studies have concentrated on the effect of compound angle injection on film cooling. Ligrani et al. (1992) measured heat transfer and film cooling effectiveness downstream of one row and downstream of two staggered rows of film cooling holes with compound angle orientations. Ligrani et al. (1994a, b) presented heat transfer and film cooling measurements for compound angle orientations. Ligrani et al. (1994b) measured the heat transfer coefficient downstream of injection from a single row of holes inclined at $\alpha = 35$ deg and $\beta = 30$ and 50.5 deg with 6-d spanwise spacing. They reported that jet liftoff is less likely to occur with compound angle injection because the lateral component of the momentum of the injectant from the compound angle holes causes the injectant to spread out more in the lateral direction as it is convected downstream. This keeps larger concentrations of the injectant close to the test surface. Sen et al. (1996) investigated the effect of compound angle injection on heat transfer coefficients. They studied a single row of compound angle holes with $\alpha = 35$ deg and $\beta = 0$ and 60 deg. They reported that the compound angle holes did not affect heat transfer rates at low momentum flux ratios. However, the heat transfer levels increased significantly at high momentum flux ratios. The studies described above presented results for film cooling with air as the coolant and low oncoming free-stream turbulence.

Ireland and Jones (1986) were the first to present a transient liquid crystal technique for measuring local heat transfer coefficients for a non-film cooling hole surface. Camci et al. (1993)

---

[1] Present address: Allison Engine Company, Indianapolis, IN.

Contributed by the International Gas Turbine Institute and presented at the 40th International Gas Turbine and Aeroengine Congress and Exhibition, Houston, Texas, June 5–8, 1995. Manuscript received by the International Gas Turbine Institute February 4, 1995. Paper No. 95-GT-10. Associate Technical Editor: C. J. Russo.

presented a hue capturing based transient liquid crystal technique for measuring heat transfer coefficients on a curved surface without film holes. Martinez-Botas et al. (1995) presented heat transfer coefficients on transonic gas turbine blades without film holes using a similar improved transient liquid crystal technique. Vedula and Metzger (1991) extended Ireland and Jones' (1986) technique and developed a method to measure local heat transfer coefficient and film cooling effectiveness. They used a thin thermochromic liquid crystal coating on a flat surface with a thermal transient test. They presented heat transfer coefficients and film effectiveness results for simple injection holes (α = 35 deg, β = 0 deg). Ekkad (1991) used Vedula and Metzger's (1991) technique to measure local heat transfer coefficient and film effectiveness on film cooled turbine blade tip models. Kim et al. (1995) presented an improved transient liquid crystal technique to measure local heat transfer coefficient and film effectiveness on cooled turbine blade tip models. They used two different color change temperatures to obtain the heat transfer coefficient and film effectiveness from a single test. The present study uses two similar tests and a single color change temperature to obtain heat transfer coefficient and film effectiveness. Ekkad and Han (1995) presented detailed heat transfer coefficients and film effectiveness on a flat surface using the transient liquid crystal technique described by Vedula and Metzger (1991). They used air as a coolant with one row of simple injection holes.

Local heat transfer coefficients were measured for three blowing ratios ($M = 0.5, 1.0, 2.0$) with air ($D.R. = 0.98$) and CO_2 ($D.R. = 1.46$) as coolants. Three compound angle orientations with $\alpha = 35$ deg and $\beta = 0$, 45, and 90 deg were studied. This study provides detailed heat transfer coefficients, particularly near the film hole region, for these parameters at an elevated mainstream turbulence condition ($Tu \approx 8.5$ percent). The high resolution of the liquid crystal transient technique will provide a better understanding of the film cooling process. This paper presents the heat transfer coefficient results. Film effectiveness results for the same conditions are presented in the companion paper by Ekkad et al. (1997).

Theory

The local heat transfer coefficient (h) over a surface coated with liquid crystals without film injection can be obtained by using a one-dimensional semi-infinite solid assumption for the test surface. The one-dimensional transient conduction equation, the initial condition, and the convective boundary condition on the liquid crystal coated surface are:

$$k \frac{\partial^2 T}{\partial x^2} = \rho c_p \frac{\partial T}{\partial t} \tag{1}$$

$$\text{at} \quad t = 0, \quad T = T_i \tag{2}$$

$$\text{at } x = 0, \; -k \frac{\partial T}{\partial x} = h(T_w - T_m); \; \text{as } x \to \infty, \; T = T_i \tag{3}$$

Solving Eq. (1) with prescribed initial and boundary conditions, one obtains the dimensionless temperature at the convective boundary surface (at $x = 0$):

$$\frac{T_w - T_i}{T_m - T_i} = 1 - \exp\left(\frac{h^2 \alpha t}{k^2}\right) \operatorname{erfc}\left(\frac{h\sqrt{\alpha t}}{k}\right) \tag{4}$$

By knowing the initial temperature (T_i) of the test surface and the mainstream temperature (T_m) and measuring the color change temperature from the liquid crystal coated surface (T_w) at time (t), the local heat transfer coefficient (h) can be calculated from Eq. (4).

Film cooling over a surface is a three-temperature problem involving the mainstream temperature (T_m), the coolant temperature (T_c), and the wall temperature (T_w). In film cooling situations, the mainstream temperature (T_m) in Eq. (4) must be replaced by a film temperature (T_f), which is a mixed temperature between the mainstream and coolant temperatures that governs the convection from the liquid crystal coated surface. To find the unknown T_f in terms of known quantities T_m and T_c, a nondimensional temperature is defined as the film cooling effectiveness (η):

$$\eta = \frac{T_f - T_m}{T_c - T_m};$$

$$\text{or} \quad T_f = \eta(T_c - T_m) + T_m = \eta T_c + (1 - \eta) T_m \tag{5}$$

Replacing T_m in Eq. (4) by T_f from Eq. (5), we get the following equation with two unknowns, h and η:

$$T_w - T_i = \left[1 - \exp\left(\frac{h^2 \alpha t}{k^2}\right) \operatorname{erfc}\left(\frac{h\sqrt{\alpha t}}{k}\right)\right] \times [\eta T_c + (1 - \eta) T_m - T_i] \tag{6}$$

To obtain both the heat transfer coefficient (h) and film effectiveness (η), it is necessary to obtain two equations with two unknowns (h and η) and solve for h and η. Therefore, two similar transient tests are run to obtain two different sets of conditions. In the first test, the mainstream is heated to a desired temperature and the coolant and surface are at room temperature. In the second test, the mainstream and coolant are both heated to a desired temperature and the surface is at room temperature. In the first test (represented by 1), the heated mainstream temperature varies as a function of time. In the second test (represented by 2), both heated mainstream and heated coolant temperatures vary with time. The gradual changes in temperatures with time are recorded on a strip chart recorder. The temperatures are represented as a series of time step changes (τ_j, $j = 1, \ldots, N$). Using superposition, both transient test solutions can be obtained from Eq. (6) and represented as:

Nomenclature

c_p = specific heat of test surface
d = injection hole diameter
$D.R.$ = coolant-to-mainstream density ratio = ρ_c/ρ_m
h = local convection heat transfer coefficient, W/m^2-K
I = coolant-to-mainstream momentum flux ratio = $(\rho U^2)_c/(\rho U^2)_m$
k = thermal conductivity of test surface
L = length of injection hole
M = blowing ratio (coolant-to-mainstream mass flux ratio) = $(\rho U)_c/(\rho U)_m$
Re_d = mainstream Reynolds number = $\rho U d/\mu$
S = hole spacing
t = time of color change
T = temperature
Tu = mainstream turbulence intensity
U = mainstream velocity
X = axial distance from downstream edge of the film hole
Z = spanwise distance
α = thermal diffusivity of the test surface; streamwise angle
β = angle with respect to the mainstream flow
μ = fluid dynamic viscosity
ρ = fluid density
τ = time step

$$T_w - T_{i_1} = \sum_{j=1}^{N} \left[1 - \exp\left(\frac{h^2 \alpha (t_1 - \tau_j)}{k^2} \right) \operatorname{erfc} \left(\frac{h\sqrt{\alpha (t_1 - \tau_j)}}{k} \right) \right] \times [\eta T_{c_1} + (1 - \eta) \Delta T_{m_1} - T_{i_1}] \quad (7)$$

$$T_w - T_{i_2} = \sum_{j=1}^{N} \left[1 - \exp\left(\frac{h^2 \alpha (t_2 - \tau_j)}{k^2} \right) \operatorname{erfc} \left(\frac{h\sqrt{\alpha (t_2 - \tau_j)}}{k} \right) \right] \times [\eta \Delta T_{c_2} + (1 - \eta) \Delta T_{m_2} - T_{i_2}] \quad (8)$$

where ΔT_m and ΔT_c are step changes in mainstream and coolant temperatures, respectively. Equations (7) and (8) are iteratively solved using a standard mathematical subroutine. The h values are calculated for a small tolerance of 1.e-6. The h obtained is used to calculate η in Eq. (8).

Test Setup and Procedure

Figure 1 shows the schematic of the test setup. The test setup consists of an image processing unit and the test section. The image processing unit consists of an RGB camera, a PC, a monitor, and a frame grabber. The composite signal from the camera is split into red, green, and blue components before passing on to the color Frame Grabber board inside the PC. The live image can be adjusted using the monitor as reference. The frame-to-frame color change analysis is done using an image processing software. The time of color change to green at each point on the test surface is the measured quantity.

The compressor-based air supply is routed through a filter and an in-line air heater. A temperature controller controls the heater and the air is routed away from the test section during heating. The routing is through a three-way ball diverter valve. The air enters the test section if the valve is flipped. A diffuser expands the air, which then passes through a straight section. The straight section is followed by a two-dimensional converging nozzle followed by a 9.16 × 15.24 cm rectangular plexiglass duct. One side of the duct holds the test plate. A turbulence grid is placed right after the nozzle before the flow enters the rectangular test duct. The coolant flow circuit is similar. The coolant flow, when being heated, is also diverted away from the test surface. The coolant expands into a cavity behind the test plate when the valve is flipped. A porous plate placed inside the cavity ensures proper mixing of the coolant. The coolant is ejected out through the injection holes on the test plate. A chart recorder measures the mainstream and coolant temperatures during the transient tests.

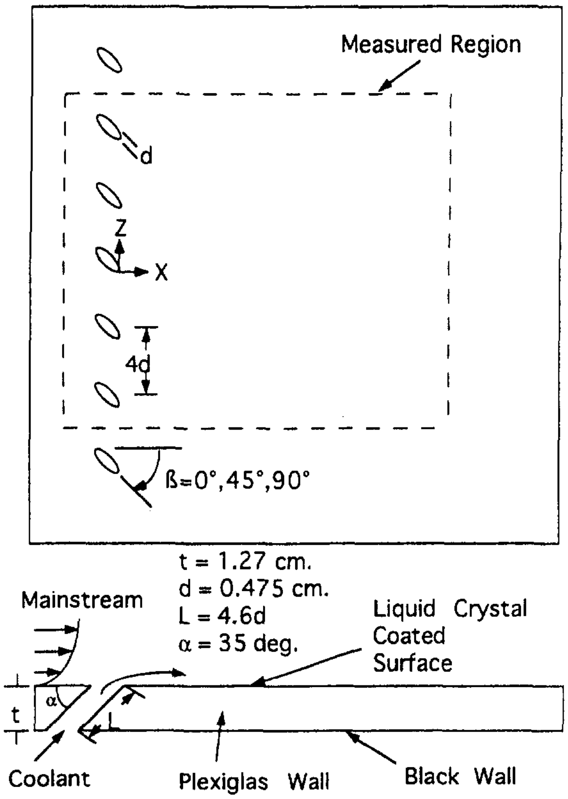

M	I for Air D.R.=0.98	I for CO_2 D.R.=1.46
0.5	0.255	0.172
1.0	1.02	0.685
2.0	4.08	2.74

Fig. 2 Test surface configuration and film cooling parameters

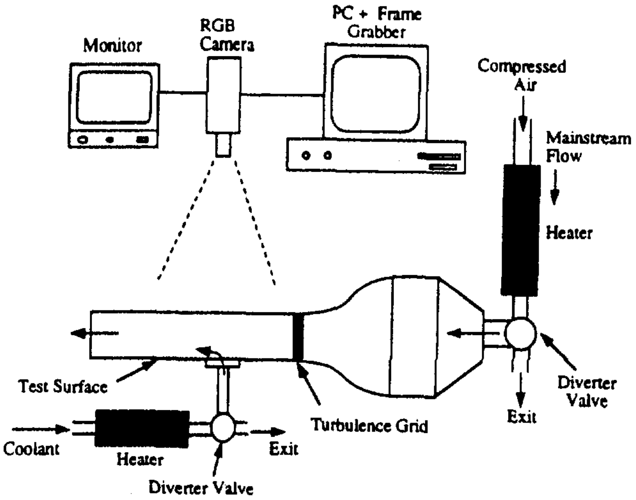

Fig. 1 Schematic of the experimental setup

The test surface is sprayed with a thin layer of commercially available encapsulated liquid crystal coating (Hallcrest, Type BM/R32C5W/C17-10). Color to temperature calibration is done on a copper bar coated with liquid crystals as suggested by Vedula and Metzger (1991). The primary color display of liquid crystals is from an initial colorless stage to red then green, blue, and then colorless again. The color change temperatures to red, green, and blue are 31.6°C, 32.7°C, and 37.2°C, respectively. The coating is a light spray 1 μm thick. Ireland and Jones (1987) showed that the response time for the liquid crystals to be only a few milliseconds. The duration of the transient test is much larger than the response time of the liquid crystals. The liquid crystals are sprayed once for a series of tests with the intensity level checked after 20 tests.

Figure 2 shows the test plate configuration with one row of inclined compound angle holes. The mainstream velocity was maintained at 8.35 m/s for all tests. The mainstream Reynolds number based on film hole diameter (Re_d) was 2.5 × 10^3. The biplanar square-bar grid (0.32 × 0.32 cm) with 50 percent porosity was placed 40 hole diameters upstream of the injection holes. The turbulence intensity was measured to be 8.5 percent at one hole diameter upstream of injection location using a calibrated single hot wire probe. The corresponding streamwise integral length scale was estimated to be 0.5 cm. The boundary layer velocity was measured to be very close to the $\frac{1}{7}$th fully turbulent boundary layer profile. The momentum thickness Reynolds number (Re_θ) was obtained as 505, the boundary layer thickness (δ) was obtained to be 1.02 cm, and the ratio of displacement thickness to hole diameter (δ_1/d) was obtained to be 0.267. Figure 2 also lists the coolant-to-mainstream blowing ratios (M), density ratios ($D.R.$), and momentum flux ratios (I).

The test section is assembled after spraying the liquid crystals. The camera is set and focused on the test surface. The mainstream and coolant flows are set using orifice meters and heated using in-line air heaters. A temperature controller controls the heater power. When steady temperatures are achieved, the software is started and the color threshold is set. Both the mainstream and coolant valves are switched on simultaneously. The temperature does not undergo a true step change. The chart recorder records the gradual change in the mainstream and coolant temperature profiles during the transient tests. The region of interest on the test surface is divided into 3850 pixels (55 × 70) (see Fig. 2). The color change time is measured at each pixel location. The mainstream and coolant temperatures are heated to temperatures so that the color change times on the test surface are between 20–80 seconds. This short transition time helps maintain the assumption that the surface is semi-infinite. The recorded temperature and time data are uploaded into the mainframe computer and the heat transfer and film effectiveness values are obtained from Eqs. (7) and (8). The advantage of this method is using a single liquid crystal coating to map the entire test surface. High heat transfer regions record less time compared to low heat transfer regions.

The biggest contribution to uncertainty is in measuring time on the test surface. The expected maximum error in time for color change measured is ±0.5 s. The calibration error for color change temperature is ±0.2°C. Other uncertainty contributions

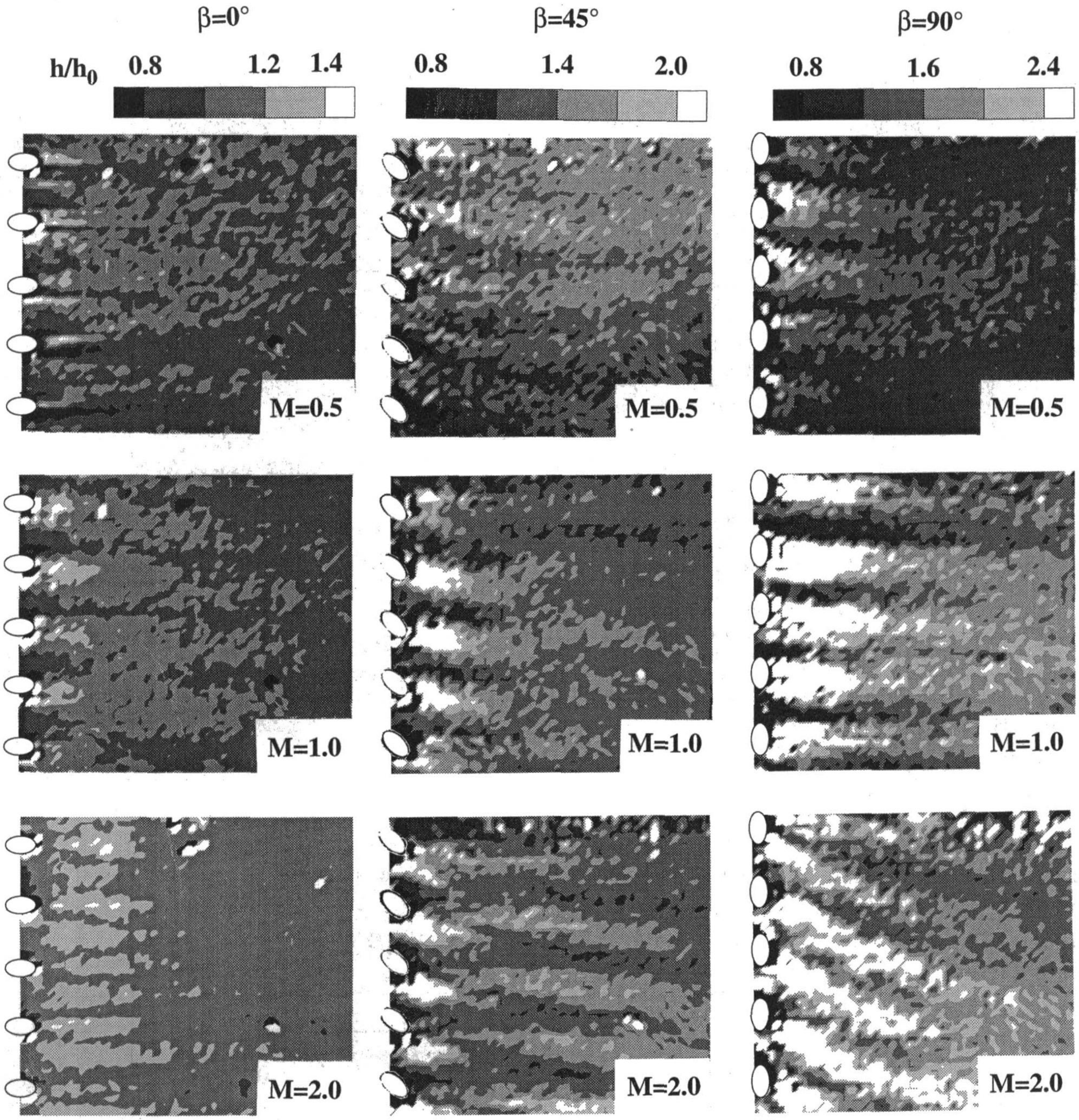

Fig. 3 Detailed heat transfer coefficient ratio distributions for air injection

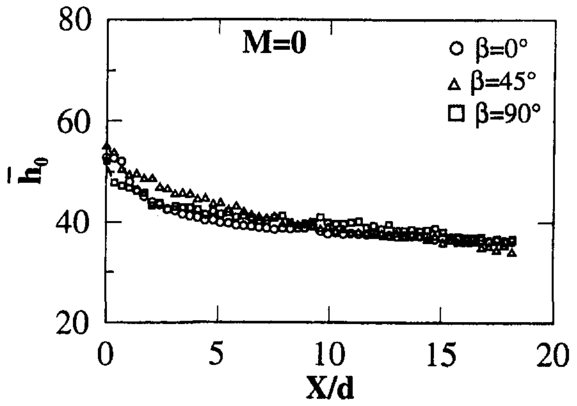

Fig. 4 Laterally averaged heat transfer coefficient distributions for no-injection case ($M = 0$)

include thermocouple measurements for mainstream and coolant temperatures, flow measurements, and test surface properties. Combining these uncertainties will give an uncertainty in the heat transfer coefficient h of 6.5 percent. Due to simultaneous calculation of η from Eqs. (7) and (8), uncertainty in η also involves uncertainty in h and is obtained at 8.5 percent. Kline and McClintock (1953) explain in detail the methodology to obtain uncertainty. Repetition of experiments has consistently provided nearly the same results. Radiation losses are assumed to be minimal because the entire walls of the test duct are heated by mainstream at fairly uniform temperatures. Conduction losses are also small because the transient test time is short and the test surfaces are made of insulating material.

Results and Discussion

Results are presented for three blowing ratios (M) of 0.5, 1.0, and 2.0: two density ratios ($D.R.$) of 0.98 (air) and 1.46 (CO_2): and three compound angle orientations (β) of 0, 45, and 90 deg.

The results are presented as heat transfer coefficient ratios (h/h_0) to reduce the effect of mainstream Reynolds number. Heat transfer coefficient ratio at a particular location is obtained by normalizing the heat transfer coefficient with injection (h) by heat transfer coefficient without injection (h_0, $M = 0$) at the same location.

Figure 3 presents the local h/h_0 distributions for air injection. The detailed distributions of local heat transfer coefficient ratio (h/h_0) are presented for all blowing ratios and hole angle configurations. The heat transfer coefficient ratio increases with an increase in blowing ratio for simple angle injection ($\beta = 0$ deg). Compound angle injection ($\beta = 45$ deg, 90 deg) produces higher h/h_0 values for a medium blowing ratio of $M = 1.0$ near the injection hole region ($X/d < 5$). The h/h_0 values increase with increase in blowing ratio for larger X/d. At low blowing ratios, the presence of a counterrotating vortex pair (CRVP) could cause high heat transfer coefficients near the injection hole. The presence of a CRVP for high blowing ratios could cause recirculation of coolant fluid further downstream of injection and increase h/h_0 values to greater than 1.0.

Compound angle injection provides higher h/h_0 values than simple angle injection, particularly for higher M ($M > 1.0$). Simple injection produces limited interaction between coolant and mainstream flows, whereas compound angle injection increases lateral interaction. This increased lateral spreading of the jets for compound angle injection could be the cause of higher heat transfer coefficients on the surface. The heat transfer coefficients are higher immediately downstream of injection and the enhancement is along the direction of the hole angle β.

Figure 4 presents the effect of compound angle hole orientation on laterally averaged heat transfer coefficient ($\bar{h}_0$) for the case without injection ($M = 0$). Local heat transfer coefficients are averaged over the entire span and plotted against normalized axial distance, X/d, for each of the three spanwise angles. Heat transfer coefficient values are highest immediately downstream of the injection hole and decrease downstream. Laterally averaged $\bar{h}_0$ for all three compound angles shows a similar trend except that $\beta = 45$ deg has higher $\bar{h}_0$ values for X/d less than 7.

Figures 5(a–c) present the effect of blowing ratio on laterally averaged heat transfer coefficient ratio ($\bar{h}/h_0$) for both coolants for a $\beta = 0$, 45, and 90 deg, respectively. In general, heat transfer enhancement ($\bar{h}/h_0$) increases and reaches a maximum at $X/d \approx 1$, and then decreases as X/d increases. The $\bar{h}/h_0$ values are fairly constant for $X/d > 5$ for all blowing ratios. Higher density injectant (CO_2) produces a much lower $\bar{h}/h_0$ for a high M of 2.0 and lower density injectant (air) produces a slightly lower $\bar{h}/h_0$ for a low M of 0.5. The higher density coolant (CO_2) possesses lower momentum and is expected to stay closer to the surface. The lower density coolant (air) at the same blowing ratio possesses higher momentum. This will cause more interaction between the mainstream and high-momentum coolant jets, thus increasing heat transfer coefficients on the surface.

The $\bar{h}/h_0$ values increase with increasing blowing ratio for both coolants with simple angle injection. Compound angle injection produces higher $\bar{h}/h_0$ near injection ($X/d < 5$) for a blowing ratio of $M = 1.0$. However, the $\bar{h}/h_0$ values increase monotonically downstream ($X/d > 5$) with increasing blowing ratio.

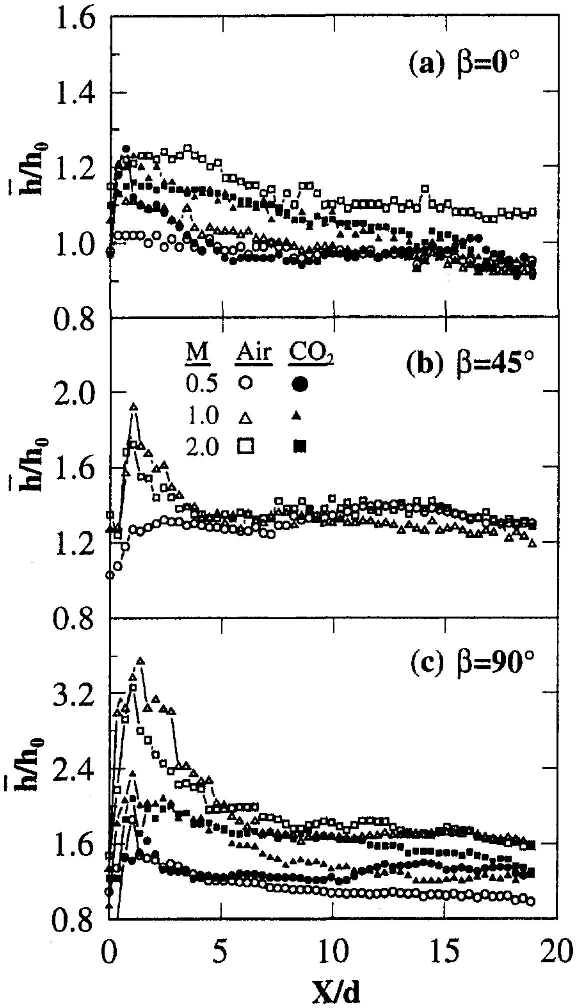

Fig. 5 Effect of blowing ratio and density ratio on laterally averaged heat transfer coefficient ratio

Figures 6(*a*–*c*) present the effect of compound angle and density ratio on $\bar{h}/h_0$ for each blowing ratio. For a low blowing ratio of 0.5, the $\bar{h}/h_0$ values are fairly uniform for both coolants. Compound angle injection produces higher $\bar{h}/h_0$ values than simple injection. The $\bar{h}/h_0$ values increase with an increase in β from 0 to 90 deg for blowing ratios of 1.0 and 2.0. For a high blowing ratio of 2.0, the $\bar{h}/h_0$ values are much higher for air injection than CO_2 injection with β = 90 deg, but the effect is very small for simple angle injection (β = 0 deg).

Figure 7 compares the present results for simple injection (β = 0 deg) to published results from Eriksen and Goldstein (1974), Hay et al. (1985), Ligrani et al. (1994a), and Sen et al. (1996). All these studies used discrete thermocouples to make local measurements and all except Ligrani et al. (1994a) had a 3-d spacing between holes. Ligrani et al. (1994a) presented results for two rows of staggered holes with a 3-d spacing between holes. The streamwise angle (α) in these studies is the same as the present study. For a blowing ratio of 0.5, the present results are in agreement with previous results. The present results match well with the results of Sen et al. (1996) for M = 1.0. The other studies have slightly higher results.

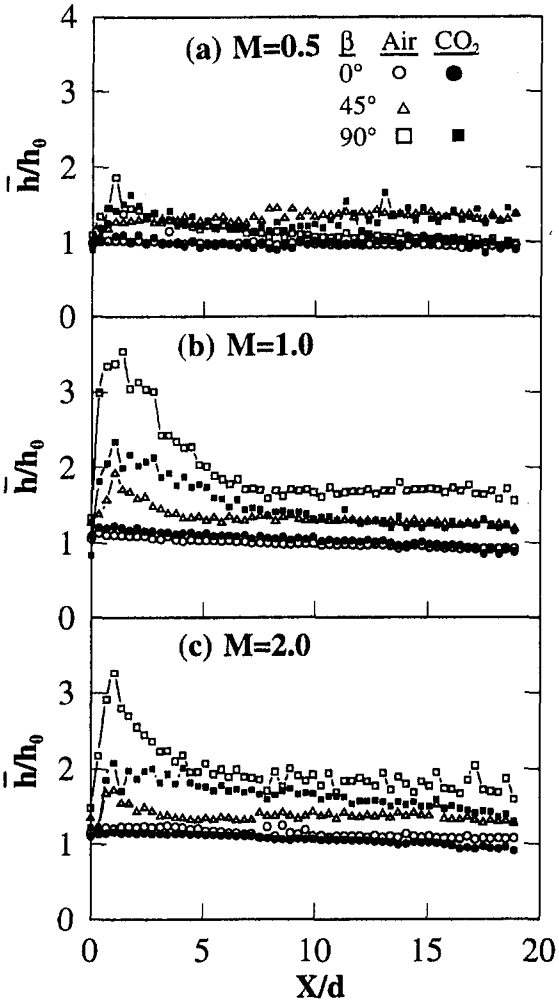

Fig. 6 Effect of compound angle and density ratio on laterally averaged heat transfer coefficient ratio

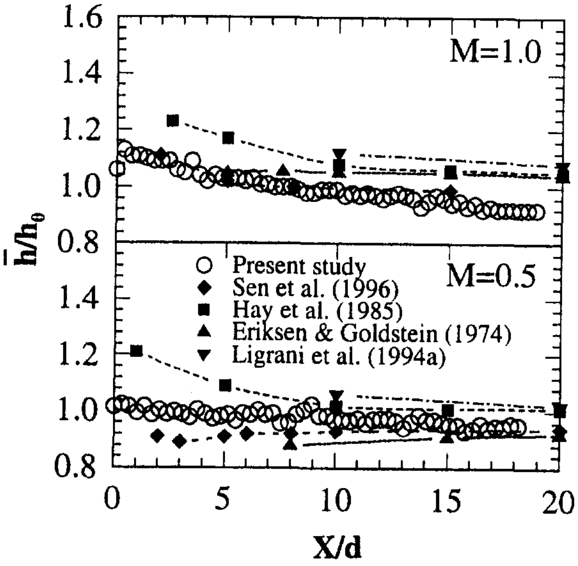

Fig. 7 Comparison of results from present study with previous studies for simple injection case

Local heat transfer coefficient ratios (h/h_0) downstream of injection over the entire surface ($0 < X/d < 19$) are averaged to produce a single spatially averaged heat transfer coefficient for each blowing ratio for each coolant. These spatially averaged values $\bar{\bar{h}}/h_0$) are plotted against the momentum flux ratio (I) in Fig. 8. Air and CO_2 results are plotted on separate lines for each compound angle. The $\bar{\bar{h}}/h_0$ values increase with increasing I (or M) for both coolants and all injection angles. The compound angle produces higher $\bar{\bar{h}}/h_0$ values than simple injection for both coolants. Air injection with β = 0 deg holes produces similar results as CO_2 injection. This indicates that the density ratio effect is not significant for simple injection holes. However, the effect of density ratio is significant on $\bar{\bar{h}}/h_0$ values for β = 90 deg and large I.

Figure 8 also includes results from Sen et al. (1996) for simple injection (β = 0 deg) and compound angle injection (β = 60 deg) with air as coolant. They measured heat transfer coefficient using discrete thermocouples and a constant heat flux surface. Present results for simple injection (β = 0 deg) are in good agreement, while the results for β = 45 deg are slightly higher than those for β = 60 deg from Sen et al. (1996) for small I.

Conclusions

Detailed heat transfer coefficient distributions for three compound angle orientations for three blowing ratios with two cool-

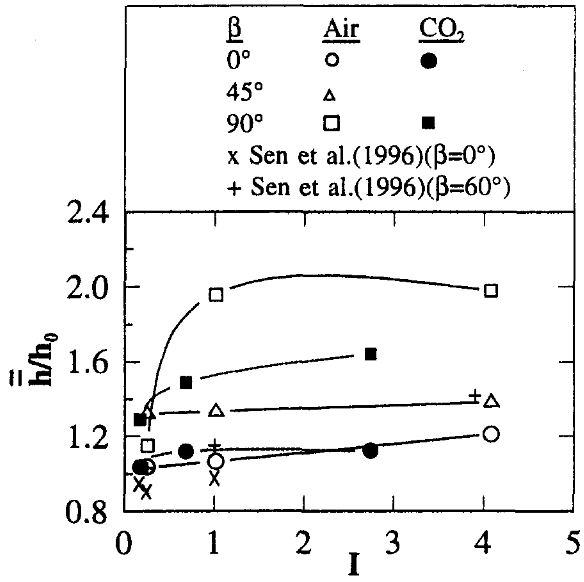

Fig. 8 Variation of spatially averaged heat transfer ratio with momentum flux ratio

ants have been presented. Tests were performed for a mainstream Re_d of 2500, momentum thickness Reynolds number of 505, and free-stream turbulence intensity of 8.5 percent for three compound angle orientations ($\alpha = 35$, $\beta = 0, 45, 90$ deg).

1 In general, an increase in blowing ratio increases heat transfer coefficient for both coolants for all three hole configurations. The heat transfer coefficients downstream of injection were much higher than 1.0 for higher blowing ratios.

2 The heat transfer coefficient with compound angle injection was found to be higher than simple injection for all cases. An increase in angle β produces slight increases in the heat transfer coefficient at a low blowing ratio of $M = 0.5$. However, for higher M, the increase in angle β produces larger increases in local heat transfer coefficient values.

3 The density ratio effect on heat transfer coefficient values is small for simple angle injection but air injection produces much higher heat transfer coefficient values than CO_2 injection for large I with compound angle injection ($\beta = 90°$).

Acknowledgments

This project was sponsored in part by the Texas Higher Education Coordinating Board Advanced Technology Program under grant number 999903-104. The first author (S. V. Ekkad) completed his M.S. degree from Arizona State University in December of 1991 under the guidance of the late Prof. D. E. Metzger. Acknowledgments also go to Meyer Instruments for help in developing the software for analyzing the color transients for the Texas A&M University Turbine Heat Transfer Laboratory between June 1992 and August 1993.

References

Ammari, H. D., Hay, N., and Lampard, D., 1990, "The Effect of Density Ratio on the Heat Transfer Coefficient From a Film Cooled Flat Plate," ASME JOURNAL OF TURBOMACHINERY, Vol. 112, pp. 444–450.

Camci, C., Kim, K., Hippensteele, S. A., and Poinsatte, P. E., 1993, "Evaluation of a Hue Capturing Based Transient Liquid Crystal Method for High-Resolution Mapping of Convective Heat Transfer on Curved Surfaces," ASME *Journal of Heat Transfer,* Vol. 115, pp. 311–318.

Ekkad, S. V., 1991, "Local Heat Transfer and Film Effectiveness Measurements on Film Cooled Turbine Blade Tip Models," M.S. Thesis, Arizona State University, Tempe, AZ.

Ekkad, S. V., and Han, J. C., 1995, "Flat Plate Film Cooling and Heat Transfer Using a Transient Liquid Crystal Technique," presented at the 4th ASME/JSME Thermal Engineering Joint Conference, Maui, Hawaii, Mar.

Ekkad, S. V., Zapata, D., and Han, J. C., 1997, "Film Effectiveness Over a Flat Surface With Air and CO_2 Injection Through Compound Angle Holes Using a Transient Liquid Crystal Image Method," ASME JOURNAL OF TURBOMACHINERY, Vol. 119, this issue, pp. 587–592.

Eriksen, V. L., and Goldstein, R. J., 1974, "Heat Transfer and Film Cooling Following Injection Through Inclined Circular Tubes," ASME *Journal of Heat Transfer,* Vol. 96, pp. 239–245.

Goldstein, R. J., and Yoshida, T., 1982, "The Influence of Laminar Boundary Layer and Laminar Injection on Film Cooling Performance," ASME *Journal of Heat Transfer,* Vol. 104, pp. 355–362.

Hay, N., Lampard, D., and Saluja, C. L., 1985, "Effect of Cooling Films on the Heat Transfer Coefficient on a Flat Plate With Zero Mainstream Pressure Gradient," ASME *Journal of Engineering for Gas Turbines and Power,* Vol. 107, pp. 105–110.

Ireland, P. T., and Jones, T. V., 1986, "The Measurement of Local Heat Transfer Coefficients in Blade Cooling Geometries," AGARD CP 390, Paper No. 28.

Ireland, P. T., and Jones, T. V., 1987, "The Response Time of a Surface Thermometer Employing Encapsulated Thermochromic Liquid Crystals," *Journal of Physics E,* Vol. 20, pp. 1195–1199.

Kim, Y. W., Downs, J. P., Soechting, F. O., Abdel-Messeh, W., Steuber, G. D., and Tanrikut, S., 1995, "A Summary of the Cooled Turbine Blade Tip Heat Transfer and Film Effectiveness Investigations Performed by Dr. D. E. Metzger," ASME JOURNAL OF TURBOMACHINERY, Vol. 117, pp. 1–11.

Kline, S. J., and McClintock, F. A., 1953, "Describing Uncertainties in Single Sample Experiments," *Mechanical Engineering,* Vol. 75, pp. 3–8.

Liess, C., 1975, "Experimental Investigation of Film Cooling With Injection From a Row of Holes for the Application to Gas Turbine Blades," ASME *Journal of Engineering for Power,* Vol. 97, pp. 21–27.

Ligrani, P. M., Ciriello, S., and Bishop, D. T., 1992, "Heat Transfer, Adiabatic Effectiveness, and Injectant Distributions Downstream of a Single Row and Two Staggered Rows of Compound Angle Film-Cooled Holes," ASME JOURNAL OF TURBOMACHINERY, Vol. 114, pp. 687–700.

Ligrani, P. M., Wigle, J. M., Ciriello, S., and Jackson, S. W., 1994a, "Film-Cooling From Holes With Compound Angle Orientations: Part 1—Results Downstream of a Two Staggered Rows of Holes with 3d Spanwise Spacing," ASME *Journal of Heat Transfer,* Vol. 116, pp. 341–352.

Ligrani, P. M., Wigle, J. M., and Jackson, S. W., 1994b, "Film-Cooling From Holes With Compound Angle Orientations: Part 2—Results Downstream of a Single Row of Holes With 6d Spanwise Spacing," ASME *Journal of Heat Transfer,* Vol. 116, pp. 353–362.

Martinez-Botas, R. F., Lock, G. D., and Jones, T. V., 1995, "Heat Transfer Measurements in an Annular Cascade of Transonic Gas Turbine Blades Using the Transient Liquid Crystal Technique," ASME JOURNAL OF TURBOMACHINERY, Vol. 117, pp. 425–431.

Sen, B., Schmidt, D. L., and Bogard, D. G., 1996, "Film Cooling With Compound Angle Holes: Heat Transfer," ASME JOURNAL OF TURBOMACHINERY, Vol. 118, pp. 800–806.

Teekaram, A. J. H., Forth, C. J. P., and Jones, T. V., 1989, "The Use of Foreign Gas to Simulate the Effect of Density Ratios in Film Cooling," ASME JOURNAL OF TURBOMACHINERY, Vol. 111, pp. 57–62.

Vedula, R. J., and Metzger, D. E., 1991, "A Method for the Simultaneous Determination of Local Effectiveness and Heat Transfer Distributions in Three-Temperature Convection Situations," ASME Paper No. 91-GT-345.

Film Effectiveness Over a Flat Surface With Air and CO_2 Injection Through Compound Angle Holes Using a Transient Liquid Crystal Image Method

S. V. Ekkad[1]

D. Zapata

J. C. Han

Turbine Heat Transfer Laboratory,
Department of Mechanical Engineering,
Texas A&M University,
College Station, TX 77843-3123

This paper presents detailed film effectiveness distributions over a flat surface with one row of injection holes inclined streamwise at 35 deg for three blowing ratios ($M = 0.5, 1.0, 2.0$). Three compound angles of 0, 45, and 90 deg with air (D.R. = 0.98) and CO_2 (D. R. = 1.46) as coolants are tested at an elevated free-stream turbulence condition ($Tu \approx 8.5$ percent). A transient liquid crystal technique is used to measure local heat transfer coefficients and film effectiveness. Detailed film effectiveness results are presented near and around film injection holes. Compound angle injection provides higher film effectiveness than simple angle injection for both coolants. Higher density injectant produces higher effectiveness for simple injection. However, lower density coolant produces higher effectiveness for a large compound angle of 90 deg. The detailed film effectiveness obtained using the transient liquid crystal technique, particularly in the near-hole region, provided a better understanding of the film cooling process in gas turbine components.

Introduction

Gas turbine engines use film cooling to protect the surfaces coming in contact with high gas temperatures. Recent film cooling studies have investigated the effect of compound angle injection of film effectiveness. Many film cooling papers have presented film effectiveness studies for turbine blades, leading edge models, and flat plates. This paper is limited to flat surface film effectiveness studies.

Pederson et al. (1977), Foster and Lampard (1980), Goldstein and Yoshida (1982), Han and Mehendale (1986), and Sinha et al. (1991) studied the effects of coolant-to-mainstream blowing ratio and density ratio on film effectiveness. Pedersen et al. (1977) measured the adiabatic wall effectiveness by injecting foreign gases to simulate the effect of coolant-to-mainstream density ratio. They studied a wide range of density ratios and blowing ratios. Han and Mehendale (1986) studied the effect of blowing ratio with air and steam injection. Sinha et al. (1991) used cooler air as an injectant to study the effect of density ratio on film effectiveness. They found that an increase in coolant-to-mainstream density ratio (for constant blowing ratio) leads to an increase in film effectiveness. All these studies used simple injection holes ($\beta = 0$ deg) at low free-stream turbulence condition ($Tu < 1$ percent).

Compound angle holes are oriented with respect to both the surface and the flow direction. Better protection and higher effectiveness are expected for compound angle injection due to orientation in two directions. Few studies have focused on the effect of compound angle injection on film cooling effectiveness. Ligrani et al. (1992) made film cooling effectiveness measurements downstream of both one row and two staggered rows of film cooling holes with compound angle orientations. Ligrani et al. (1994a) measured film effectiveness downstream of two staggered rows of holes with 3d spanwise hole spacing. Ligrani et al. (1994b) measured film effectiveness downstream of injection from a single row of holes inclined at $\alpha = 35$ deg and $\beta = 30$ and 50.5 deg with 6-d spanwise spacing. Schmidt et al. (1996) presented the effect of film injection through one row of holes with $\alpha = 35$ deg and $\beta = 0$ and 60 deg. They reported that compound angle injection for momentum flux ratios up to 4.0 gives higher film effectiveness and higher heat transfer coefficients over simple injection. These studies presented results with air as a coolant and at low free-stream turbulence condition.

Many studies have focused on the effect of mainstream turbulence on film cooling on turbine blades and leading edge models but very few on the flat plate. Kadotani and Goldstein (1979a, b), Jumper et al. (1991), and Bons et al. (1996) studied the effect of mainstream turbulence on flat surface film effectiveness through simple injection holes with air as a coolant. Kadotani and Goldstein studied the effect of varying free-stream turbulence intensities up to 20 percent on film effectiveness. They concluded that the turbulence intensity, blowing ratio, and ratios of length scale to hole diameter and length scale to mainstream boundary layer thickness at hole location appeared to alter the mixing rate between the mainstream and the film coolant. Jumper et al. (1991) studied several Reynolds numbers and turbulence levels. They reported that the optimum blowing ratios for the high turbulence levels were found to be much broader and higher than those reported for the low turbulence studies. Bons et al. (1996) studied free-stream turbulence levels up to 17.4 percent. They reported that free-stream turbulence decreases film effectiveness directly downstream of the injection hole and increases film effectiveness between injection holes due to enhanced mixing.

This study presents detailed film effectiveness distributions with the use of liquid crystal coatings. Vedula and Metzger (1991) were the first to use a transient liquid crystal technique to determine local heat transfer coefficients and film effectiveness. Vedula and Metzger presented both heat transfer coefficients

---

[1] Present address: Allison Engine Company, Indianapolis, IN.

Contributed by the International Gas Turbine Institute and presented at the 40th International Gas Turbine and Aeroengine Congress and Exhibition, Houston, Texas, June 5–8, 1995. Manuscript received by the International Gas Turbine Institute February 14, 1995. Paper No. 95-GT-11. Associate Technical Editor: C. J. Russo.

and film effectiveness downstream of one row of simple injection holes ($\alpha = 35$ deg, $\beta = 0$ deg) with air as a coolant at low free-stream turbulence condition. Kim et al. (1995) used an improved transient liquid crystal technique to measure local heat transfer coefficients and film effectiveness on film cooled turbine blade tip models. They used two different color change temperatures to obtain heat transfer coefficients and film effectiveness from a single test. The present study uses two similar tests with a single color change temperature to obtain heat transfer coefficient and film effectiveness. Ekkad and Han (1995) presented film effectiveness over a flat surface with only air as a coolant through simple injection holes using the transient liquid crystal technique. The present study uses a transient liquid crystal technique similar to that of Vedula and Metzger (1991).

Local film effectiveness results for three blowing ratios of 0.5, 1.0, and 2.0 with air ($D.R. = 0.98$) and CO_2 ($D.R. = 1.46$) injection are presented. Three compound hole orientations with $\alpha = 35$ deg and $\beta = 0$, 45, and 90 deg are studied at an elevated free-stream turbulence condition ($Tu \approx 8.5$ percent). This paper presents detailed film effectiveness results. Heat transfer coefficient results are presented for the same conditions in the companion paper by Ekkad et al. (1997).

Theory

The local heat transfer coefficient (h) over a surface coated with liquid crystals without film injection can be obtained by using a one-dimensional semi-infinite solid assumption for the test surface. The one-dimensional transient conduction equation, the initial condition, and the convective boundary condition on the liquid crystal coated surface are:

$$k \frac{\partial^2 T}{\partial x^2} = \rho c_p \frac{\partial T}{\partial t} \tag{1}$$

$$\text{at} \quad t = 0, \quad T = T_i \tag{2}$$

$$\text{at} \quad x = 0, \quad -k \frac{\partial T}{\partial x} = h(T_w - T_m);$$

$$\text{as} \quad x \to \infty, \quad T = T_i \tag{3}$$

Solving Eq. (1) with prescribed initial and boundary conditions, one obtains the dimensionless temperature at the convective boundary surface (at $x = 0$):

$$\frac{T_w - T_i}{T_m - T_i} = 1 - \exp\left(\frac{h^2 \alpha t}{k^2}\right) \operatorname{erfc}\left(\frac{h\sqrt{\alpha t}}{k}\right) \tag{4}$$

By knowing the initial temperature (T_i) of the test surface and the mainstream temperature (T_m) and measuring the color change temperature from the liquid crystal coated surface (T_w) at time (t), the local heat transfer coefficient (h) can be calculated from Eq. (4).

Film cooling over a surface is a three-temperature problem involving the mainstream temperature (T_m), the coolant temperature (T_c), and the wall temperature (T_w). In film cooling situations, the mainstream temperature (T_m) in Eq. (4) must be replaced by a film temperature (T_f), which is a mixed temperature between the mainstream and coolant temperatures that governs the convection from the liquid crystal coated surface. To find the unknown T_f in terms of known quantities T_m and T_c, a nondimensional temperature is defined as the film cooling effectiveness (η):

$$\eta = \frac{T_f - T_m}{T_c - T_m};$$

$$\text{or} \quad T_f = \eta(T_c - T_m) + T_m = \eta T_c + (1 - \eta) T_m \tag{5}$$

Replacing T_m in Eq. (4) by T_f from Eq. (5), we get the following equation with two unknowns, h and η:

$$T_w - T_i = \left[1 - \exp\left(\frac{h^2 \alpha t}{k^2}\right) \operatorname{erfc}\left(\frac{h\sqrt{\alpha t}}{k}\right)\right] \times [\eta T_c + (1 - \eta) T_m - T_i] \tag{6}$$

To obtain both the heat transfer coefficient (h) and film effectiveness (η), it is necessary to obtain two equations with two unknowns (h and η) and solve for h and η. Therefore, two similar transient tests are run to obtain two different sets of conditions. The two different conditions are obtained by running the two tests at two different coolant temperatures, one with heated coolant and another with coolant at room temperature. In both cases, the mainstream is heated. The gradual changes of the temperatures with time are recorded on the strip chart recorder. The temperatures are represented as a series of time step changes (τ_j, $j = 1, \ldots, N$). Using superposition, both transient test solutions can be obtained from Eq. (6) and represented as:

$$T_w - T_{i_1} = \sum_{j=1}^{N} \left[1 - \exp\left(\frac{h^2 \alpha (t_1 - \tau_j)}{k^2}\right) \operatorname{erfc}\left(\frac{h\sqrt{\alpha (t_1 - \tau_j)}}{k}\right)\right] \times [\eta T_{c_1} + (1 - \eta) \Delta T_{m_1} - T_{i_1}] \tag{7}$$

$$T_w - T_{i_2} = \sum_{j=1}^{N} \left[1 - \exp\left(\frac{h^2 \alpha (t_2 - \tau_j)}{k^2}\right) \operatorname{erfc}\left(\frac{h\sqrt{\alpha (t_2 - \tau_j)}}{k}\right)\right] \times [\eta \Delta T_{c_2} + (1 - \eta) \Delta T_{m_2} - T_{i_2}] \tag{8}$$

where ΔT_m and ΔT_c are step changes in mainstream and coolant temperatures, respectively. Equations (7) and (8) are iteratively

Nomenclature

c_p = specific heat of test surface
d = injection hole diameter
$D.R.$ = coolant-to-mainstream density ratio = ρ_c/ρ_m
h = local convection heat transfer coefficient, W/m^2-K
I = coolant-to-mainstream momentum flux ratio = $(\rho U^2)_c/(\rho U^2)_m$
k = thermal conductivity of test surface
L = length of injection hole
M = blowing ratio (coolant-to-mainstream mass flux ratio) = $(\rho U)_c/(\rho U)_m$
q'' = forced convective heat flux
Re_d = mainstream Reynolds number = $\rho U d/\mu$
S = hole spacing
t = time of color change
T = temperature
Tu = mainstream turbulence intensity
U = mainstream velocity
X = axial distance from downstream edge of the film hole
Z = spanwise distance
α = thermal diffusivity of test surface; streamwise angle
β = angle with respect to mainstream flow
η = local film cooling effectiveness
μ = fluid dynamic viscosity
ρ = fluid density
Φ = overall cooling effectiveness = $(T_w - T_m)/(T_c - T_m)$

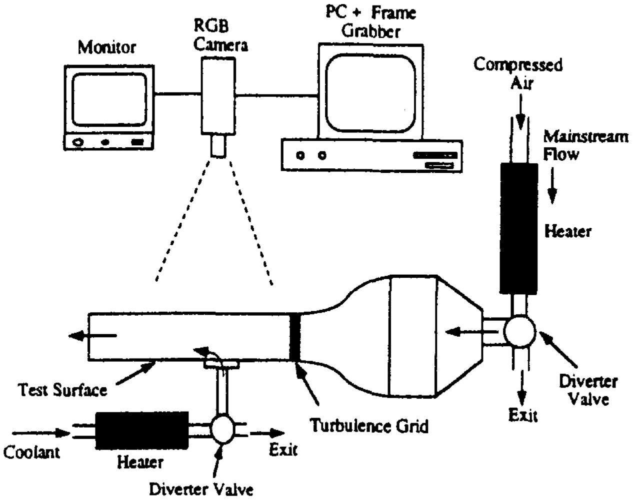

Fig. 1 Schematic of experimental setup

solved using a standard mathematical subroutine. The h values are calculated for a tolerance of 1.e-6. The h obtained is used to calculate η in Eq. (8).

Test Setup and Procedure

Figure 1 shows the schematic of the test setup. The test setup consists of an image processing unit and the test section. The image processing unit consists of an RGB camera, a PC, a monitor, and a frame grabber. The composite signal from the camera is split into red, green, and blue components before passing on to the color Frame Grabber board inside the PC. The live image can be adjusted using the monitor as reference. The frame-to-frame color change is analyzed using an image processing software. The time of color change to green at each point on the test surface is the measured quantity.

The compressor-based air supply is routed through a filter and an in-line air heater. A temperature controller controls the heater and the air is routed away from the section during heating. The routing is through a three-way ball diverter valve. The air enters the test section if the valve is flipped. A diffuser expands the air, which then passes through a straight section. The straight section is followed by a two-dimensional converging nozzle followed by a 9.16 × 15.24 cm rectangular plexiglass duct. One side of the duct holds the test plate. A turbulence grid is placed right after the nozzle before the flow enters the rectangular test duct. The coolant flow circuit is similar. The coolant flow, when being heated, is also diverted away from the test surface. The coolant expands into a cavity behind the test plate when the valve is flipped. A porous plate placed inside the cavity ensures proper mixing of the coolant. The coolant is ejected out through the injection holes on the test plate. A chart recorder measures the mainstream and coolant temperatures during the transient tests.

The test surface is sprayed with a thin layer of commercially available encapsulated liquid crystal coating (Hallcrest, Type BM/R32C5W/C17-10). Color to temperature calibration is done on a copper bar coated with liquid crystals as suggested by Vedula and Metzger (1991). The primary color display of liquid crystals is from an initial colorless stage to red then green, blue, and then colorless again. The color change temperatures to red, green, and blue are 31.6°C, 32.7°C, and 37.2°C, respectively. The coating is a light spray of approximately 1 μm thickness. Ireland and Jones (1987) showed that the response time for the liquid crystals to be only a few milliseconds. The duration of the transient test is much larger than the response time of the liquid crystals. The liquid crystals are sprayed for a series of tests with the intensity level checked after 20 tests.

Figure 2 shows the test plate configuration with one row of inclined compound angle holes. The mainstream velocity was maintained at 8.35 m/s for all tests. The mainstream Reynolds number based on film hole diameter (Re_d) was 2.5×10^3. The bi-planar square-bar grid (0.32 × 0.32 cm) with 50 percent porosity was placed 40 hole diameters upstream of the injection holes. The turbulence intensity was measured to be 8.5 percent at one hole diameter upstream of injection location using a calibrated single hot wire probe. The corresponding streamwise integral length scale was estimated to be 0.5 cm. The boundary layer velocity was measured to be very close to the $\frac{1}{7}$th fully turbulent boundary layer profile. The momentum thickness Reynolds number (Re_θ) was obtained as 505, the boundary layer thickness (δ) was obtained to be 1.02 cm, and the ratio of displacement thickness to hole diameter (δ_1/d) was obtained to be 0.267. Figure 2 also lists the coolant-to-mainstream blowing ratios (M), density ratios ($D.R.$), and momentum flux ratios (I).

The test section is assembled after spraying the liquid crystals. The camera is set and focused on the test surface. The mainstream and coolant flows are set using orifice meters and heated using in-line air heaters. When steady temperatures are achieved, the software is started and the color threshold is set. Both the mainstream and coolant valves are switched on simultaneously. The temperature does not undergo a true step change. The chart recorder records the gradual change in the mainstream and coolant temperature profiles during the transient tests. The region of interest on the test surface is divided into 3850 pixels (55 × 70) (see Fig. 2). The color change time at each pixel

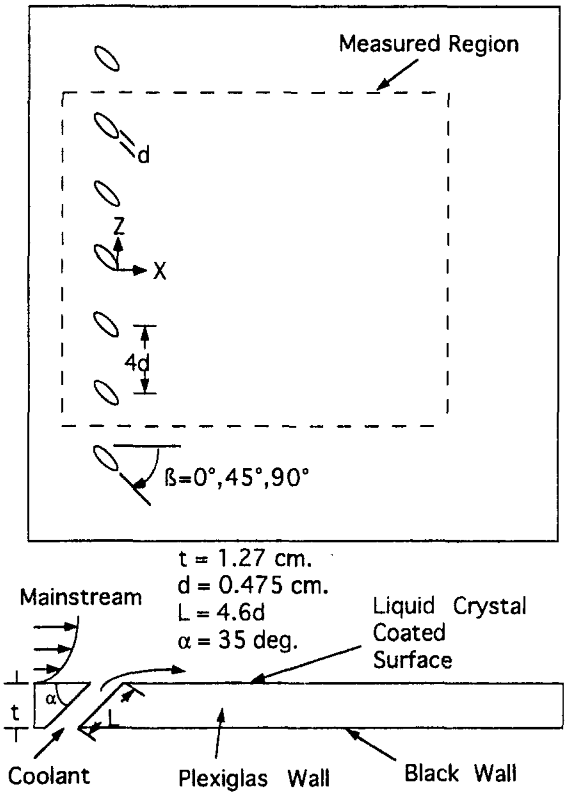

M	I for Air D.R.=0.98	I for CO_2 D.R.=1.46
0.5	0.255	0.172
1.0	1.02	0.685
2.0	4.08	2.74

Fig. 2 Test surface configuration and film cooling parameters

location is measured. The mainstream and coolant temperatures are heated to temperatures so that the color change times on the test surface are between 20–80 seconds. This short transition time helps maintain the assumption that the surface is semi-infinite. The recorded temperature and times data are uploaded into the mainframe computer and the heat transfer and film effectiveness values are obtained from Eqs. (7) and (8). The advantage of this method is using a single liquid crystal coating to map the entire test surface. High heat transfer regions record less time compared to low heat transfer regions.

The biggest contribution to uncertainty is in measuring time on the test surface. The expected maximum error in time for color change measured is ±0.5 s. The calibration error for color change temperature is ±0.2°C. Other uncertainty contributions include thermocouple measurements for mainstream and coolant temperatures, flow measurements, and test surface properties. Combining these uncertainties will give an uncertainty in the heat transfer coefficient h of 6.5 percent. Due to simultaneous calculation of η from Eqs. (7) and (8), uncertainty in η also involves uncertainty in h and is obtained at 8.5 percent. Kline and McClintock (1953) explain in detail the methodology to obtain uncertainty. Repetition of experiments has consistently provided nearly the same results. The results are explained based on the observations during the tests. Radiation losses are assumed to be minimal because the entire walls of the test duct are heated by mainstream at fairly uniform temperatures. Conduction losses are small because the transient test time is short and the test surfaces are made of insulating material.

Results and Discussion

Film Effectiveness. Film effectiveness results are presented for three blowing ratios of 0.5, 1.0, and 2.0, two density

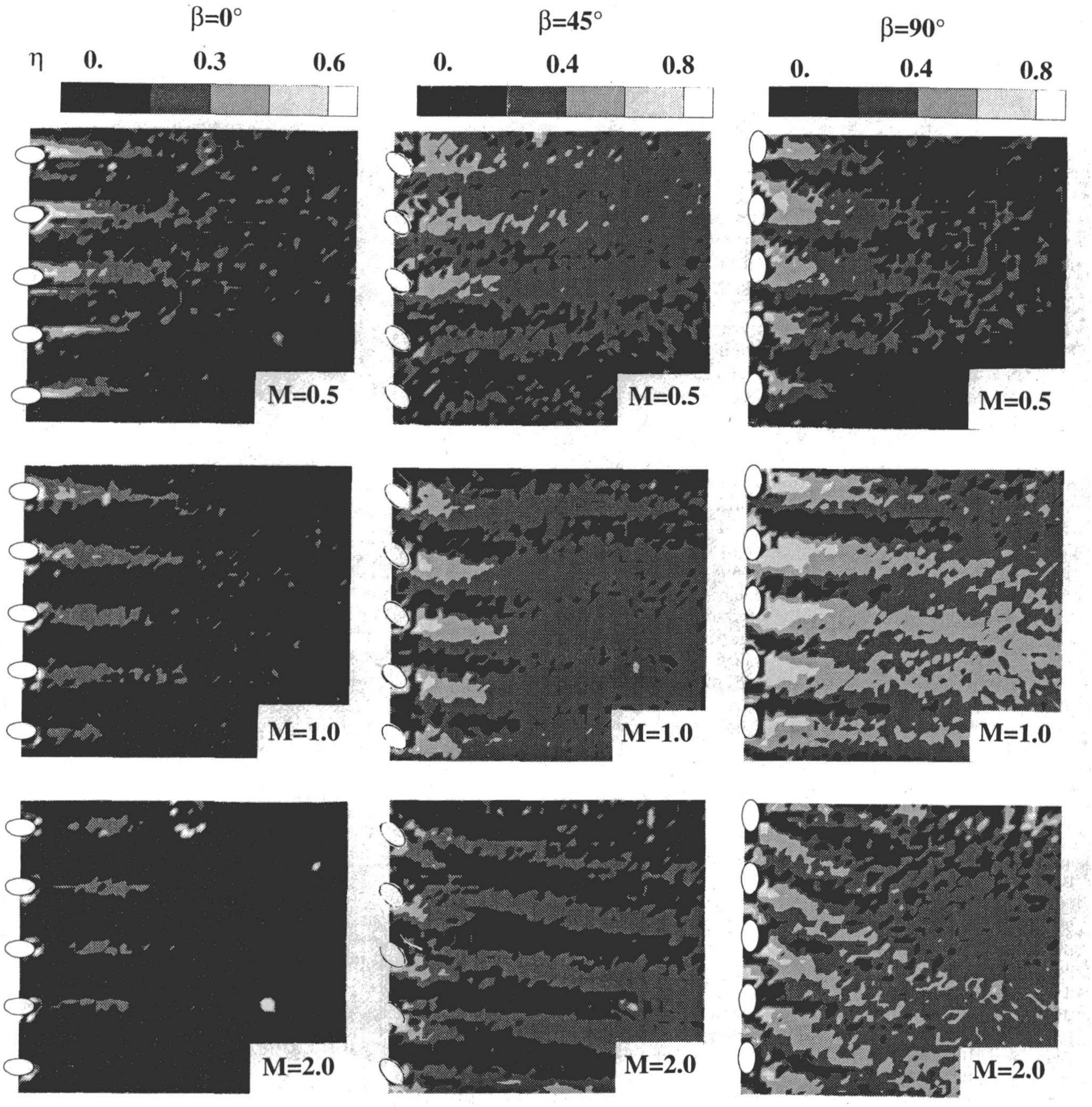

Fig. 3 Detailed film effectiveness distributions for air injection

ratios of 0.98 (air) and 1.46 (CO_2), and three compound angles of 0, 45, and 90 deg.

Figure 3 presents the local film effectiveness (η) distributions for air injection. The effectiveness distributions for all blowing ratios and hole configurations are presented. Film effectiveness decreases with an increase in blowing ratio for simple angle injection. The highest effectiveness values are obtained for a blowing ratio of $M = 1.0$ with compound angle injection (β = 45 and 90 deg). The presence of a counterrotating vortex pair (CRVP) associated with a jet in a crossflow could be attributed to higher effectiveness near the injection hole ($X/d < 5$) for a low blowing ratio of 0.5. Downstream ($X/d > 5$), higher blowing ratios produce slightly higher effectiveness caused by recirculation of coolant fluid from the counter rotating vortex pair.

In general, compound angle injection provides more coverage and effectiveness than simple angle injection. Effectiveness increases with an increase of angle β from 0 to 90 deg near injection ($X/d < 5$) for a low blowing ratio of 0.5. Higher blowing ratios ($M = 1.0$ and 2.0) produce higher effectiveness with an increase in angle β. The effectiveness for higher blowing ratio is higher along the direction of the angle β. A compound angle creates more uniform effectiveness on the entire surface compared to the effectiveness provided by simple angle injection. The lateral interaction of the jets with the mainstream for compound angle injection could be attributed to the higher and more uniform effectiveness on the surface.

The local film effectiveness values are averaged over the entire span of the measured test surface. Laterally averaged film effectiveness ($\bar{\eta}$) values are plotted against the normalized axial distance X/d. Figures 4(a–c) present the effect of blowing ratio on laterally averaged film effectiveness ($\bar{\eta}$) for both coolants for β = 0, 45, and 90 deg, respectively. In general, the highest $\bar{\eta}$ is obtained at $X/d \approx 1$ and then decreases as X/d increases. The laterally averaged effectiveness values decrease as the blowing ratio increases for air with simple angle injection. Compound angle injection (β = 45 and 90 deg) with air as the coolant produces higher effectiveness at a blowing ratio of 1.0. At a higher blowing ratio of 2.0, the coolant mass is blowing into the mainstream and very little coolant remains on the surface for protection. For a low blowing ratio of 0.5, the coolant jets are weaker, thus producing lower effectiveness farther downstream.

Effectiveness is highest at a blowing ratio of 1.0 for CO_2 injection with both simple angle injection (β = 0 deg) and compound angle injection (β = 90 deg). CO_2 produces much higher effectiveness than air as coolant for simple injection. The higher density coolant (CO_2) has a lower momentum, which could cause the coolant to stay closer and protect the surface better for simple angle injection. However, for compound angle injection (β = 90 deg) the high lateral momentum of the jets could be producing the same amount of spreading over the surface for both coolants and thus diminishing the density ratio effect on film effectiveness.

Figures 5(a–c) present the effect of compound angle and density ratio for each blowing ratio. A compound angle produces higher effectiveness than simple angle injection for both coolants. Air as coolant produces the highest effectiveness for a low blowing ratio of 0.5 with compound angle injection (β = 45 deg). For higher blowing ratios, laterally averaged effectiveness increases with an increase in angle β from 0 to 90 deg for both coolants.

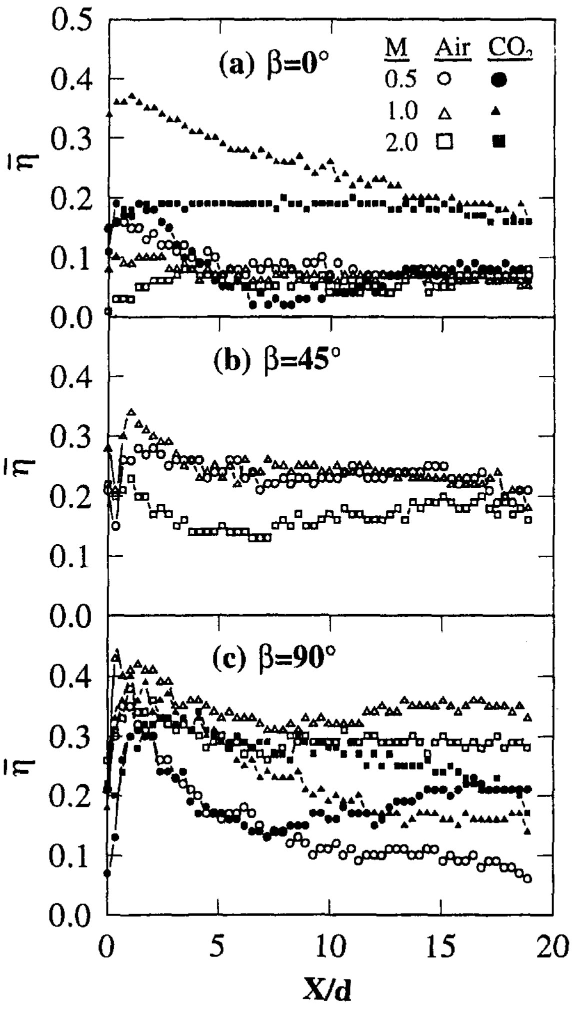

Fig. 4 Effect of blowing ratio and density ratio on laterally averaged film effectiveness

Comparisons. Figure 6(a) compares the centerline film effectiveness (η_c) for $I = 1.02$ from the present study to previous investigators. Pedersen et al. (1977), Han and Mehendale (1986), and Sinha et al. (1991) measured film effectiveness with a single row of simple angle holes (α = 35 deg, β = 0 deg) at low free-stream turbulence ($Tu < 1$ percent). Bons et al. (1996) studied the effect of free-stream turbulence on film effectiveness for a single row of simple angle holes with air injection. The present results at an elevated free-stream turbulence condition are lower than the previous studies at low free-stream turbulence except for Sinha et al. (1991). This may be because the elevated free-stream turbulence creates greater interaction between the mainstream and film layers and reduces the film effectiveness. Results from the present study ($Tu \approx$ 8.5 percent) and Bons et al. (1996) ($Tu \approx 11.5$ percent) agree reasonably well for X/d smaller than 2 and larger than 10.

Figure 6(b) compares laterally averaged film effectiveness ($\bar{\eta}$) for compound angle injection from the present study for a blowing ratio of 0.5 to previous results. The present results for β = 45 deg and β = 90 deg are compared to data for a compound angle of 50.5 deg from Ligrani et al. (1994b) for a blowing ratio of 0.5 with 6d spacing and Schmidt et al. (1996) with β = 60 deg for a blowing ratio of 0.6 with 3d spacing and 6d spacing. This comparison is to show that the present results are closer to the results obtained by other studies with different hole geometries. Note that values for β = 60 deg and 3d spacing from Schmidt et al. (1996) are closer to values for 45 deg angle and 4d spacing from the present study. The present study provides more detailed results near the injection hole ($X/d < 3$).

Local film effectiveness (η) downstream of injection over the test surface ($0 < X/d < 19$) are averaged to produce a single spatially averaged film effectiveness ($\bar{\bar{\eta}}$) value for each blowing ratio for each coolant. The spatially averaged effectiveness ($\bar{\bar{\eta}}$) is plotted against momentum flux ratio (I) in Fig. 7. Compound angle injection (β > 0 deg) provides higher effectiveness than simple injection (β = 0 deg) for both coolants. CO_2 injection provides higher $\bar{\bar{\eta}}$ than air for

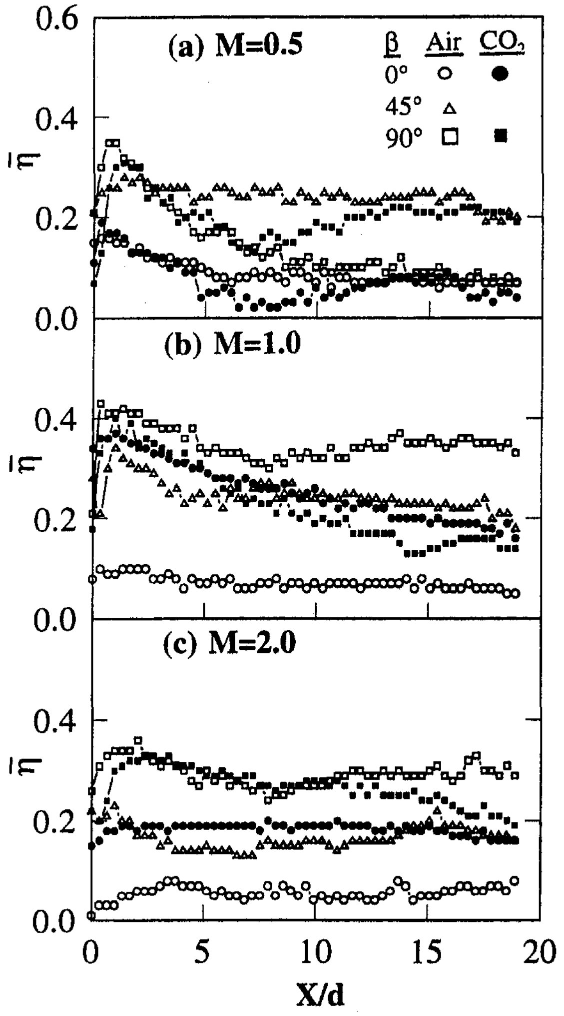

Fig. 5 Effect of compound angle and density ratio on laterally averaged film effectiveness

simple injection. However, air provides higher $\bar{\bar{\eta}}$ for $\beta = 90$ deg. The present results at an elevated free-stream turbulence are lower than those of Schmidt et al. (1996) for simple injection ($\beta = 0$ deg) at low free-stream turbulence condition. Higher free-stream turbulence is expected to break down film protection and reduce film effectiveness. Results from the present study for $\beta = 45$ deg with air injection are closer to results for $\beta = 60$ deg injection from Schmidt et al. (1996). The free-stream turbulence may not have a significant effect on the film effectiveness for compound angles ($\beta > 0$ deg) due to increased lateral interaction between coolant and mainstream flows. Schmidt et al. (1996) measured adiabatic wall temperatures using discrete thermocouples and used cooler air as the coolant ($D.R. = 1.6$).

Heat Transfer. Since both h/h_0 (Ekkad et al., 1997) and η increase for compound angle injection, it is necessary to compare their overall film cooling performance. According to Mehendale et al. (1994), the local heat flux ratio (q''/q''_0), the ratio of heat flux with film injection to that without film injection, can be expressed as

$$\frac{q''}{q''_0} = \frac{h}{h_0}\frac{(T_w - T_f)}{(T_w - T_m)} = \frac{h}{h_0}\left(1 - \frac{\eta}{\Phi}\right) \qquad (9)$$

where η is the local film effectiveness and Φ is the overall cooling effectiveness given by $\Phi = (T_w - T_m)/(T_c - T_m)$. The values of Φ range from 0.5 to 0.7 for gas turbine blades. A heat flux ratio of less than unity indicates that film injection reduces the surface heat load over the no film injection case. Local heat transfer coefficient enhancement, h/h_0 (Ekkad et al., 1997), and film effectiveness, are spatially averaged downstream of injection over the entire

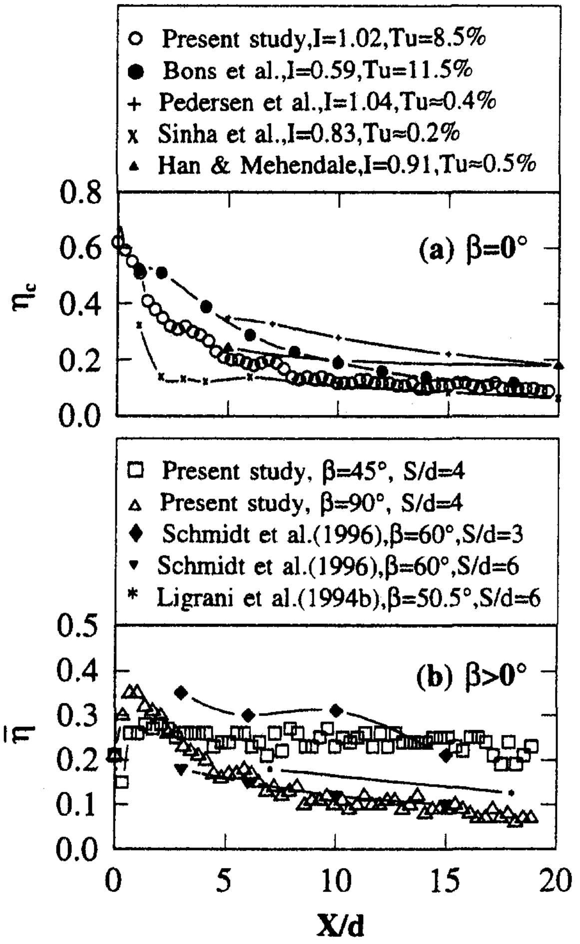

Fig. 6 Comparison of film effectiveness results with previous studies

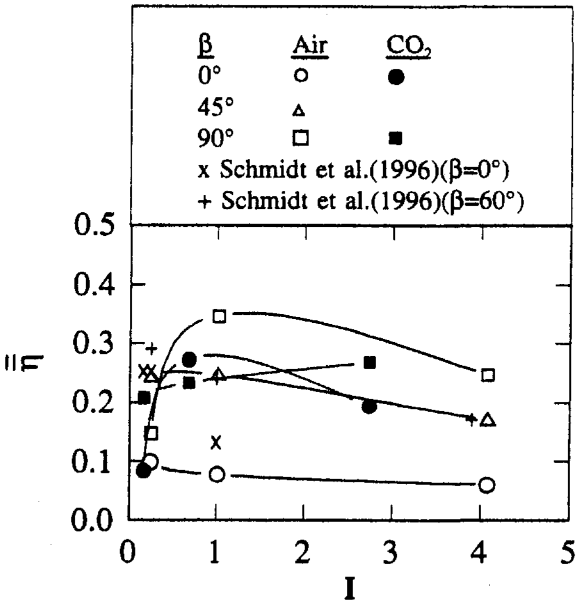

Fig. 7 Variation of spatially averaged film effectiveness with momentum flux ratio

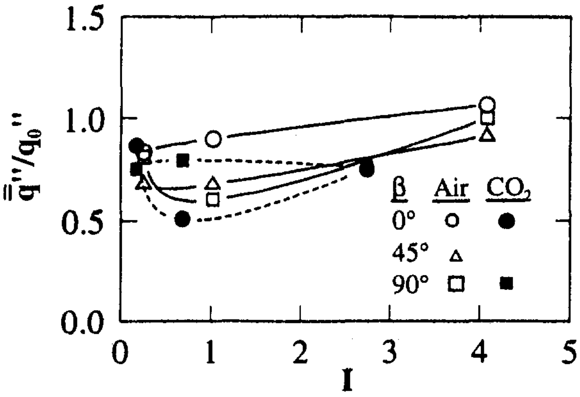

Fig. 8 Variation of spatially averaged heat flux ratio with momentum flux ratio

test surface (X/d up to 19) to obtain spatially averaged heat flux ratio. Figure 8 shows these spatially averaged heat flux ratios plotted against coolant-to-mainstream momentum flux ratio (I) for an overall cooling effectiveness value of $\Phi = 0.5$. Film injection reduces overall heat flux for both coolants. A compound angle provides lower heat flux ratios for air injection compared to a simple angle. However, for CO_2 injection, the compound angle produces lower heat flux ratios only at low momentum flux ratios. In general, CO_2 injection produces lower heat flux ratios than air injection for large I (or M).

Note

The effect of property difference between CO_2 and air as coolants to simulate difference in density is noted. Ou et al. (1994) and Mehendale et al. (1994) reminded researchers of the differences in kinematic viscosity and local Reynolds number, and thermal conductivity. Due to inherent differences in the properties of air and CO_2, researchers should be cautious in applying the results obtained by using CO_2 to simulate higher coolant-to-mainstream density air to real engines.

Conclusions

Detailed film effectiveness distributions for three blowing ratios with two coolants have been presented. Tests were performed for a mainstream Re_d of 2500, momentum thickness Reynolds number of 505, and free-stream turbulence intensity of 8.5 percent for three compound angle orientations ($\alpha = 35$ deg, $\beta = 0, 45, 90$ deg).

1 In general, highest effectiveness was obtained at a blowing ratio of 1.0 for both coolants for simple and compound angle injection except air with simple angle injection in which case the film effectiveness decreases with an increase in blowing ratio.

2 Compound angle injection produces higher effectiveness than simple angle injection for the same blowing ratio for both coolants.

3 Higher density coolant (CO_2) produces higher effectiveness for simple angle injection. However, lower density coolant (air) produces higher effectiveness for compound angle injection ($\beta > 0$ deg) at large momentum flux ratios ($I > 1$).

4 Film injection reduces the overall surface heat flux for both coolants. In general, CO_2 produces lower heat flux ratio than air injection for higher momentum flux ratios.

Acknowledgments

This project was sponsored in part by the Texas Higher Education Coordinating Board Advanced Technology Program under grant number 999903-104. The first author (S. V. Ekkad) completed his M.S. degree from Arizona State University in December of 1991 under the guidance of the late Prof. D. E. Metzger. Acknowledgments also go to Meyer Instruments for help in developing the software for analyzing the color transients for the Texas A&M University Turbine Heat Transfer Laboratory between June 1992 and August 1993.

References

Bons, J. P., MacArthur, C. D., and Rivir, R. B., 1996, "The Effect of High Free-Stream Turbulence on Film Cooling Effectiveness," ASME JOURNAL OF TURBOMACHINERY, Vol. 118, pp. 814–825.

Ekkad, S. V., and Han, J. C., 1995, "Flat Plate Film Cooling and Heat Transfer Using a Transient Liquid Crystal Technique," presented at the 4th ASME/JSME Thermal Engineering Joint Conference, Maui, HI, Mar.

Ekkad, S. V., Zapata, D., and Han, J. C., 1997, "Heat Transfer Coefficients Over a Flat Surface With Air and CO_2 Injection Through Compound Angle Holes Using a Transient Liquid Crystal Image Method," ASME JOURNAL OF TURBOMACHINERY, Vol. 119, this issue, pp. 580–586.

Foster, N. W., and Lampard, D., 1980, "The Flow and Film Cooling Effectiveness Following Injection Through a Row of Holes," ASME *Journal of Engineering for Power,* Vol. 102, pp. 584–588.

Goldstein, R. J., and Yoshida, T., 1982, "The Influence of Laminar Boundary Layer and Laminar Injection on Film Cooling Performance," ASME *Journal of Heat Transfer,* Vol. 104, pp. 355–362.

Han, J. C., and Mehendale, A. B., 1986, "Flat-Plate Film Cooling With Steam Injection Through One Row and Two Rows of Inclined Holes," ASME JOURNAL OF TURBOMACHINERY, Vol. 108, pp. 137–144.

Ireland, P. T., and Jones, T. V., 1987, "The Response Time of a Surface Thermometer Employing Encapsulated Thermochromic Liquid Crystals," *Journal of Physics E,* Vol. 20, pp. 1195–1199.

Jumper, G. W., Elrod, W. C., and Rivir, R. B., 1991, "Film Cooling Effectiveness in High-Turbulence Flow," ASME JOURNAL OF TURBOMACHINERY, Vol. 113, pp. 479–483.

Kadotani, K., and Goldstein, R. J., 1979a, "On the Nature of Jets Entering a Turbulent Flow Part A—Jet Mainstream Interaction," ASME *Journal of Engineering for Power,* Vol. 101, pp. 459–465.

Kadotani, K., and Goldstein, R. J., 1979b, "On the Nature of Jets Entering a Turbulent Flow, Part B—Film Cooling Performance," ASME *Journal of Engineering for Power,* Vol. 101, pp. 466–470.

Kim, Y. W., Abdel-Messeh, W., Downs, J. P., Soechting, F. O., Steuber, G. D., and Tanrikut, S., 1995, "A Summary of the Cooled Turbine Blade Tip Heat Transfer and Film Effectiveness Investigations Performed by Dr. D. E. Metzger," ASME JOURNAL OF TURBOMACHINERY, Vol. 117, pp. 1–11.

Kline, S. J., and McClintock, F. A., 1953, "Describing Uncertainties in Single Sample Experiments," *Mechanical Engineering,* Vol. 75, pp. 3–8.

Ligrani, P. M., Ciriello, S., and Bishop, D. T., 1992, "Heat Transfer, Adiabatic Effectiveness, and Injectant Distributions Downstream of a Single Row and Two Staggered Rows of Compound Angle Film-Cooled Holes," ASME JOURNAL OF TURBOMACHINERY, Vol. 114, pp. 687–700.

Ligrani, P. M., Wigle, J. M., Ciriello, S., and Jackson, S. W., 1994a, "Film-Cooling From Holes With Compound Angle Orientations: Part 1—Results Downstream of Two Staggered Rows of Holes With 3d Spanwise Spacing," ASME *Journal of Heat Transfer,* Vol. 116, pp. 341–352.

Ligrani, P. M., Wigle, J. M., and Jackson, S. W., 1994b, "Film-Cooling From Holes With Compound Angle Orientations: Part 2—Results Downstream of a Single Row of Holes With 6d Spanwise Spacing," ASME *Journal of Heat Transfer,* Vol. 116, pp. 353–362.

Mehendale, A. B., Han, J. C., Ou, S., and Lee, C. P., 1994, "Unsteady Wake Over a Linear Turbine Blade Cascade With Air and CO_2 Film Injection: Part II—Effect on Film Effectiveness and Heat Transfer Distributions," ASME JOURNAL OF TURBOMACHINERY, Vol. 116, pp. 730–737.

Ou, S., Han, J. C., Mehendale, A. B., and Lee, C. P., 1994, "Unsteady Wake Over a Linear Turbine Blade Cascade With Air and CO_2 Film Injection: Part I—Effect on Heat Transfer Coefficients," ASME JOURNAL OF TURBOMACHINERY, Vol. 116, pp. 721–729.

Pedersen, D. R., Eckert, E. R. G., and Goldstein, R. J., 1977, "Film Cooling With Large Density Differences Between the Mainstream and the Secondary Fluid Measured by the Heat-Mass Transfer Analogy," ASME *Journal of Heat Transfer,* Vol. 99, pp. 620–627.

Schmidt, D. L., Sen, B., and Bogard, D. G., 1996, "Film Cooling With Compound Angle Holes: Adiabatic Effectiveness," ASME JOURNAL OF TURBOMACHINERY, Vol. 118, pp. 807–813.

Sinha, A. K., Bogard, D. G., and Crawford, M. E., 1991, "Film Cooling Effectiveness Downstream of a Single Row of Holes With Variable Density Ratio," ASME JOURNAL OF TURBOMACHINERY, Vol. 113, pp. 442–449.

Vedula, R. J., and Metzger, D. E., 1991, "A Method for the Simultaneous Determination of Local Effectiveness and Heat Transfer Distributions in Three-Temperature Convection Situations," ASME Paper No. 91-GT-345.

Combined Effect of Grid Turbulence and Unsteady Wake on Film Effectiveness and Heat Transfer Coefficient of a Gas Turbine Blade With Air and CO_2 Film Injection

S. V. Ekkad[1]

A. B. Mehendale[2]

J. C. Han

Turbine Heat Transfer Laboratory,
Department of Mechanical Engineering,
Texas A&M University,
College Station, TX 77843

C. P. Lee

General Electric—Aircraft Engines,
Cincinnati, OH 45215

Experiments were performed to study the combined effect of grid turbulence and unsteady wake on film effectiveness and heat transfer coefficient of a turbine blade model. Tests were done on a five-blade linear cascade at the chord Reynolds number of 3.0×10^5 at cascade inlet. Several combinations of turbulence grids, their locations, and unsteady wake strengths were used to generate various upstream turbulence conditions. The test blade had three rows of film holes in the leading edge region and two rows each on the pressure and suction surfaces. Air and CO_2 were used as injectants. Results show that Nusselt numbers for a blade with film injection are much higher than that without film holes. An increase in mainstream turbulence level causes an increase in Nusselt numbers and a decrease in film effectiveness over most of the blade surface, for both density injectants, and at all blowing ratios. A free-stream turbulence superimposed on an unsteady wake significantly affects Nusselt numbers and film effectiveness compared with only an unsteady wake condition.

Introduction

Many studies have investigated the effect of upstream unsteady wake and free-stream turbulence on heat transfer coefficients from a turbine blade without film cooling. Dunn (1986), Dunn et al. (1986, 1989, 1994), Blair et al. (1989a, b), Abhari et al. (1992), and Blair (1994) conducted experiments in rotor–stator blade rows. However, Pfeil et al. (1983), Ashworth et al. (1985), Doorly and Oldfield (1985), Wittig et al. (1987), Doorly (1988), O'Brien and Capp (1989), Dullenkopf et al. (1991), Han et al. (1993), and Zhang and Han (1995) did laboratory simulations of upstream unsteady wake conditions. They reported significant increases in heat transfer due to unsteady wake plus an earlier and longer transition region on the suction surface.

Nirmalan and Hylton (1990), Camci and Arts (1990), and Abhari and Epstein (1994) studied heat transfer coefficients on a film-cooled turbine blade, whereas Takeishi et al. (1992) compared the film effectiveness values for a stationary cascade under 4 percent mainstream turbulence intensity and a rotor blade using the heat-mass transfer analogy. Ito et al. (1978) and Haas et al. (1992) studied the effect of injectant density on the film effectiveness of a gas turbine blade under low mainstream turbulence and no wake conditions. Ou and Han (1994), Ou et al. (1994), and Mehendale et al. (1994) studied the effects of incident unsteady wake conditions and injectant density on the blade heat transfer coefficient and film effectiveness from a linear turbine blade cascade. They reported that an increase in unsteady wake strength causes an increase in the heat transfer coefficient and a decrease in film effectiveness. They also reported that a higher density injectant provides better film effectiveness at higher blowing ratios.

This study is a continuation of Ou and Han (1994), Ou et al. (1994), and Mehendale et al. (1994), who studied only the effect of unsteady wake. This investigation focuses on the effect of incident grid turbulence with an unsteady wake (to simulate combustor turbulence and stator-generated unsteady wake interaction, experienced by first-stage rotor blades). The objectives of this study are to find: (1) the effect of grid turbulence strength on blade heat transfer coefficients and film effectiveness for a given unsteady wake condition; (2) the effect of an unsteady wake on blade heat transfer coefficients and film effectiveness for a given grid turbulence strength; and (3) the effect of injectant density on blade heat transfer coefficients and film effectiveness under the combined effect of an unsteady wake and grid turbulence strength.

Test Apparatus and Instrumentation

Figure 1 shows the low-speed, open-loop wind tunnel designed for this study. See Ou et al. (1994) for a detailed description. The center part of Fig. 1 shows the linear cascade, which accommodates the low-speed wind tunnel facility with an inlet velocity of 21 m/s. The flow has a 107 deg turn in the cascade and the mean velocity increases 2.5 times from inlet to the outlet. The airfoil configuration, scaled up by a factor of 5, produces a velocity distribution similar to that of a typical advanced high-pressure turbine blade row. The blade, made of high quality model wood, has a chord length C of 22.68 cm, a radial span of 25.4 cm, and a blade spacing of 17.01 cm at inlet. The middle blade is the instrumented heat transfer blade. A schematic of the top view of the test blade is shown in Fig. 2. The first cavity supplied three rows of film holes, one near the leading edge, and one each on the pressure and suction surfaces. The second cavity supplied one row each on the pressure and suction surfaces. The third and fourth cavities supplied

---

[1] Present address: Allison Engine Company, Indianapolis, IN.

[2] Present address: General Electric—Aircraft Engines, Cincinnati, OH.

Contributed by the Heat Transfer Division for publication in the JOURNAL OF TURBOMACHINERY. Manuscript received by the Heat Transfer Division February 1994; revision received November 1995. Associate Technical Editor: M. G. Dunn.

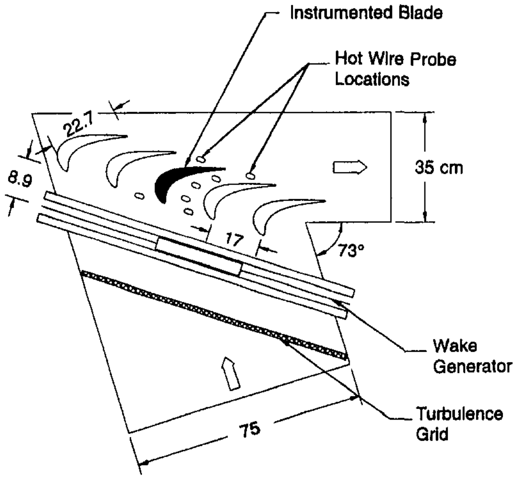

Fig. 1 Schematic of test geometry

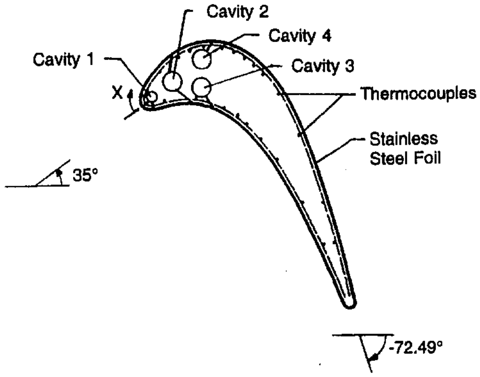

Film Hole Row Location	P/D	Axial Angle	Radial Angle	Tangential Angle
Cavity 1: All Three	7.31	90°	27°	-
Cavity 2: Pressure Side	6.79	-	32°	55°
Cavity 2: Suction Side	4.13	-	90°	45°
Cavity 3: Pressure Side	5.00	-	35°	50°
Cavity 4: Suction Side	5.71	-	90°	30°

Fig. 2 Schematic of the test blade with film holes

one row of film holes on pressure and suction surfaces, respectively. Details of the blade film hole configurations are presented by Ou et al. (1994).

The heat transfer instrumented turbine blade is the same as that used by Ou et al. (1994) and Mehendale et al. (1994). Eighty-eight calibrated, 36-gage, copper constantan thermocouples, on the midspan of the blade, measured the time-averaged temperatures on the blade surface. Thermocouples mounted in the injection cavities measured the secondary flow temperatures just before injection. All thermocouples were connected to a 100-channel FLUKE 2280A datalogger interfaced with the 386SX machine. A FLUKE multimeter and a current clamp measured the input voltage and line current for both test blades.

Two turbulence grids were used in this study. Grid 1 was of 1.3 cm square tubes spaced 4.8 cm apart in both the horizontal and vertical directions. Grid 1 was placed at location 1, which is 21 cm upstream of the cascade leading edge, to obtain the strong grid turbulence strength. This corresponds to 16.5 tube widths for grid 1. Grid 2 was of 0.5 cm square bars spaced 1.9 cm apart in both the horizontal and vertical directions. Grid 2 was placed at location 2, which is 30 cm upstream of the cascade leading edge, to obtain the medium grid turbulence strength. This corresponds to 63.0 tube widths for grid 2.

A rotating spoked-wheel type generator, similar to the one used by Ou et al. (1994), simulated the unsteady moving wake. The spoked wheel type wake generator had 32 rods, each 0.63 cm in diameter to simulate the trailing edge of an upstream blade. Its shaft was 20 cm below the bottom wall of the wind tunnel. The wake Strouhal number was adjusted by controlling motor speed and measuring the wake generator rotation speed with a Pioneer DT-36M digital photo tachometer. The error caused by using nonlinear rotating rods with a linear blade cascade was small and is discussed by Ou et al. (1994).

Test Conditions and Data Analysis

All tests were done at the chord Reynolds number (Re) of 3×10^5 at cascade inlet (or Re = 7.5×10^5 at the cascade exit). The corresponding cascade inlet and outlet velocities were 21 and 52 m/s, respectively. Unsteady wake strength is given by wake Strouhal number $S = 2\pi Ndn/(60V_1)$. Six turbulence conditions at the cascade inlet were studied as shown in Table 1: Case (1): the "no grid, no wake" condition where all rods from the wake generator were removed ($\overline{Tu} = 0.75$ percent); Case (2): the "wake only" ($S = 0.3$) condition ($\overline{Tu} = 13.9$ percent); Case (3): the "medium grid turbulence" condition ($\overline{Tu} = 5.7$ percent); Case (4): the "medium grid turbulence and wake" condition ($\overline{Tu} = 16.4$ percent); Case (5): the "strong grid turbulence" condition ($\overline{Tu} = 17$ percent); and Case (6): the "strong grid turbulence and wake" condition ($\overline{Tu} = 21.2$ percent). The integral length scales at the cascade inlet

Nomenclature

C = blade chord length, straight distance between leading and trailing edge
d = wake generator rod diameter
D = film hole diameter
D.R. = density ratio (secondary to mainstream) = ρ_s/ρ_∞
h = local heat transfer coefficient
k = local air thermal conductivity
M = blowing ratio (secondary to mainstream mass flux ratio) = $(\rho V)_s/(\rho V)_\infty$
n = number of rods in the wake generator
N = wake generator rotation speed, rpm
Nu = local Nusselt number based on blade chord = hC/k
$\overline{\text{Nu}}$ = spanwise-averaged Nusselt number
P = film hole pitch
q'' = heat flux
r_m = distance between the wake generator shaft center and the cascade midspan
Re = Reynolds number based on the blade chord = V_1C/ν
S = wake Strouhal number = $2\pi Ndn/(60V_1)$
T = temperature
$\overline{Tu}$ = mean turbulence intensity
U_r = rotational velocity at the cascade midspan
V = local mainstream velocity
V_1 = mean mainstream velocity at cascade inlet
V_2 = mean mainstream velocity at the cascade exit
X = streamwise distance from stagnation along blade surface
η = local film effectiveness
$\overline{\eta}$ = spanwise averaged film effectiveness
ν = kinematic viscosity

Table 1 Six turbulence conditions at the cascade inlet presented in this study

Case	Grid and Location	Wake	$\overline{Tu}$ %
1	No Grid	No Wake	0.75
2	No Grid	Wake (S=0.3)	13.9
3	Grid 2 at Location 2 (medium grid)	No Wake	5.7
4	Grid 2 at Location 2 (medium grid)	Wake (S=0.3)	16.4
5	Grid 1 at Location 1 (strong grid)	No Wake	17
6	Grid 1 at Location 1 (strong grid)	Wake (S=0.3)	21.2

for a strong grid turbulence and medium grid turbulence were estimated to be about 1.3 cm and 1.1 cm, respectively. A wake Strouhal number of S = 0.3 was achieved by setting $N = 287$ rpm on the wake generator hub, which corresponds to a flow coefficient $V_1/U_r = dn/(r_m S)$ of 1.9.

A single hot wire is used to measure the instantaneous velocity profile under the effect of the passing wake and grid-generated turbulence at the entrance of the blade cascade. The hot-wire sensor is located at 8.82 cm downstream of the rotating rod. The velocity and turbulence intensity are time dependent and periodic and, because of the periodic nature of the wake passing and shedding, the analysis of the unsteady random signal indicates that its behavior cannot be characterized by time averaging only. The phase-averaged (or ensemble-averaged) method was used to obtain the time-dependent periodic velocity and the time-dependent turbulence intensity. For this study, a mean turbulence intensity ($\overline{Tu}$) is used to find the turbulence level of the combined grid turbulence and unsteady wake flow. The mean turbulence intensity is the mean value of the phase-averaged turbulence intensity over one period of unsteady flow, described in detail by Zhang and Han (1995).

The secondary (injectant) mass flux rate for a given row of injection holes was based on the time-averaged local mainstream velocity at that location (measured with a pressure tap instrumented blade, Han et al., 1993) and the desired blowing ratio. Tests were conducted at the blowing ratios of 0.4, 0.8, and 1.2. During the heat transfer coefficient tests, the stainless steel foils were electrically heated and the injectant (air or CO_2) temperature was maintained the same as the ambient mainstream temperature. However, no foil heat was applied and the injectant was heated during the film effectiveness tests.

As in Ou et al. (1994), the local heat transfer coefficient with or without film injection was calculated from

$$h = \frac{q''_{\text{gen}} - (q''_{\text{cond}} + q''_{\text{rad}})}{T_w - T_\infty} = \frac{q''_{\text{gen}} - (q''_{\text{cond}} + q''_{\text{rad}})}{T_w - T_{aw}} . \quad (1)$$

Since Mach number $\ll 1$, $T_{aw} = T_\infty$, heat loss tests estimated the total heat loss.

During the heat transfer coefficient tests, T_w was in the 40–50°C range and T_{aw} was about 25°C. The measured total heat loss was about 10 percent of the foil-generated heat. On an average, the conduction and radiation heat losses were 4 and 6 percent, respectively, of the heat generated. Heat loss through the tiny thermocouple wires was estimated to be small (less than 0.1 percent), and axial and lateral conduction through the thin foil was also negligible. Local Nusselt number (Nu) was calculated from Nu = hC/k. Local Nusselt numbers at a given streamwise location were averaged to obtain the spanwise averaged Nusselt number ($\overline{\text{Nu}}$) at that location.

As in Ou and Han (1994) and Mehendale et al. (1994), local film effectiveness was calculated from

$$\eta = \frac{T_w - T_\infty}{T_s - T_\infty} + \frac{(q''_{\text{cond}} + q''_{\text{rad}}) - q''_{\text{cond},g}}{h(T_s - T_\infty)} . \quad (2)$$

During the film effectiveness tests, T_s was maintained at 50°C. Local film effectiveness values at a given streamwise location were averaged to obtain the spanwise-averaged film effectiveness ($\overline{\eta}$) at that location.

The above-mentioned thin foil-thermocouple technique and the related data analysis method to calculate heat transfer coefficient and film effectiveness are the same as in Ou et al. (1994), Mehendale et al. (1994), and Ou and Han (1994). Five sets of data were recorded at steady state at each location and averaged to reduce random errors. Similarly, five sets of data were recorded for the hot-wire measurements. Measurement and estimation accuracies in voltage, current, wall temperature, and heat losses contributed to uncertainty in Nusselt number and film effectiveness. An uncertainty analysis as in Kline and McClintock (1953) showed the uncertainty in Nusselt number and film effectiveness to be about ±5 percent.

Results and Discussion

Velocity profiles in the radial direction at the inlet and outlet of the passages adjacent to the instrumented blade are shown in Ou et al. (1994). Results show that the inlet and outlet velocity profiles in the flow paths are essentially uniform in the midspan region. Also, the flow direction at the inlet and outlet of both flow paths was uniform. Thus, the Nusselt numbers are free from the top and bottom wall boundary layer effects. An identical profile blade with static pressure taps measured local mainstream velocity around the blade (Han et al., 1993). The local-to-exit velocity ratio (V/V_2) distribution for various upstream turbulence conditions is shown in Zhang and Han (1995).

Effect of Film Injection. Figure 3 shows the effect of blowing ratio and injectant density on spanwise-averaged Nusselt number distribution at a representative mean turbulence intensity of $\overline{Tu}$ = 16.4 percent (Case 4). Also shown for comparison are the results from a no film holes test model at $\overline{Tu}$ = 0.75 percent (Case 1) and $\overline{Tu}$ = 16.4 percent (Case 4). Results from the no film holes test model at a "no grid no wake" base condition show that Nusselt numbers on the suction surface decrease gradually with increasing streamwise distance from stagnation due to a laminar boundary layer growth. Past X/C = 0.85, however, Nusselt numbers increase sharply due to

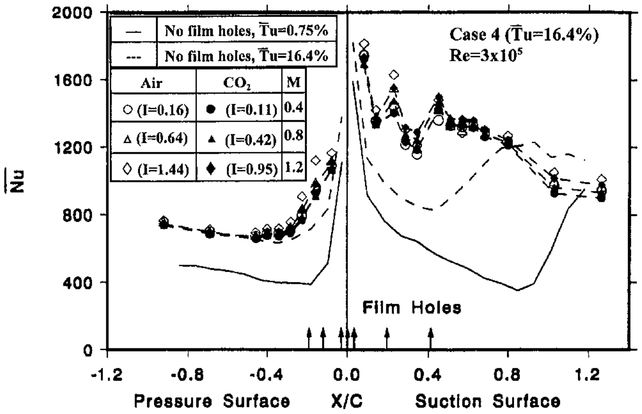

Fig. 3 Effect of air or CO_2 injection on Nu distributions for Case 4

boundary layer transition. For the same "no grid no wake" condition, Nusselt numbers on the pressure surface decrease sharply with increasing X/C (due to a much lower flow velocity and therefore a faster boundary layer growth), but increase beyond $X/C = -0.2$ due to strong acceleration. Results for the no film holes test model at $\overline{Tu} = 16.4$ percent show that an increased flow unsteadiness disturbs the boundary layer and causes an increase in heat transfer coefficient distribution over the entire blade surface. This effect is more severe on the suction surface than on the pressure surface. Upstream unsteady flow conditions cause an earlier laminar to turbulent boundary layer transition on suction surfaces (at only half the distance of the no grid no wake case) and an increase in transition length (since strong acceleration in the midchord region delays production of turbulence spots).

With film injection, sharp increases in heat transfer coefficients are observed immediately downstream of the film hole row locations on the suction surface as seen in Fig. 3. They are caused by the highly disturbed boundary layer due to the injection. Following such peaks, boundary layer growth and dilution of injectant jets cause the heat transfer coefficients to decrease. Since a lower mainstream velocity produces a thicker boundary layer on the pressure surface, increases in heat transfer coefficients by flow disturbances due to film injection are less prominent on the pressure surface. An increase in blowing ratio causes an increase in the interaction between the mainstream and injection jets and results in an increase in heat transfer coefficients near film holes for both injectants (air and CO_2). The effect of blowing ratio is not as significant as it would be at lower mainstream turbulence levels (Ou et al., 1994) since the boundary layer is already highly disturbed due to high turbulence levels in the mainstream. The blowing ratio effect decreases farther downstream of the last row of film holes due to the decreasing effect of the injectant jets and stronger mainstream.

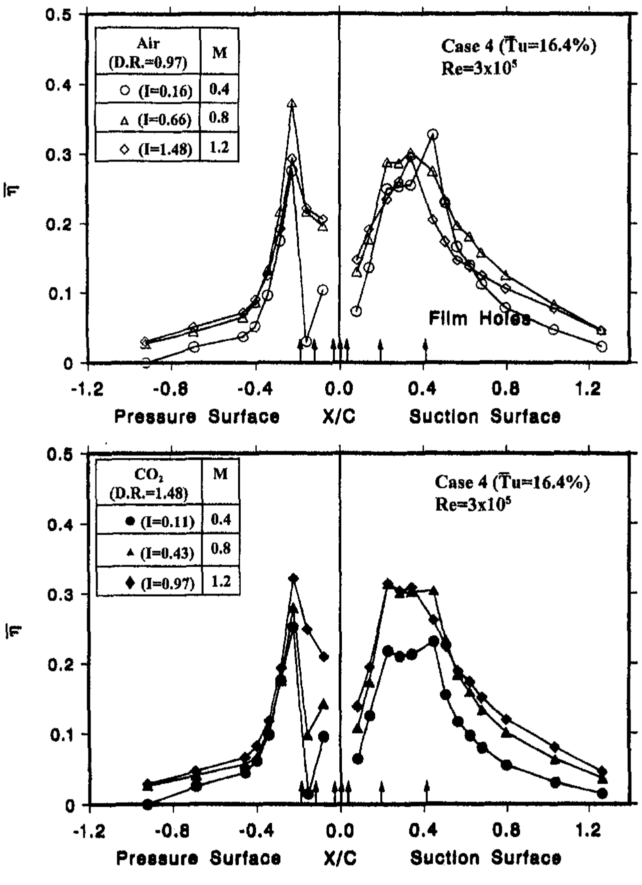

Fig. 4 Effect of air or CO_2 injection on η distributions for Case 4

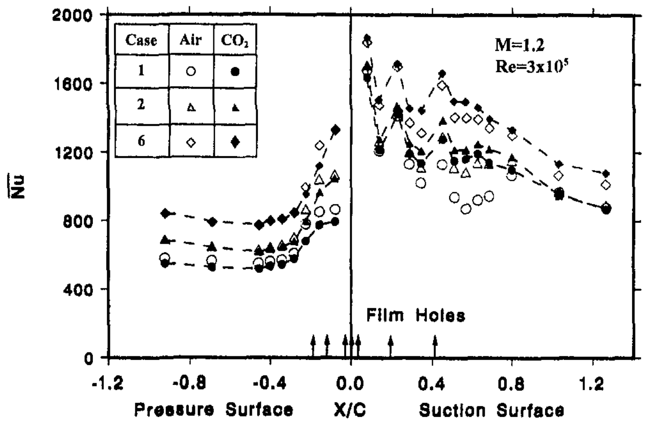

Fig. 5 Effect of an unsteady wake with and without strong grid turbulence on Nu distributions for air or CO_2 injection at $M = 1.2$

For a given blowing ratio, as the injectant density increases the momentum flux ratio decreases. So, at a given blowing ratio, the lower density injectant jet (air, D.R. ≈ 1.0) penetrates farther than the higher density injectant jet (CO_2, D.R. ≈ 1.5). This increase in turbulent mixing between the mainstream and injectant jets for the lower density injectant results in higher heat transfer coefficients. The effect of injectant density is seen just downstream of most of the film holes where heat transfer coefficients for air injection are higher than for CO_2 injection. This effect is reduced downstream of the second row of film holes on the suction surface. The effect of injectant density is not as significant as it would be at lower mainstream turbulence levels (Ou et al., 1994).

Figure 4 shows the effect of film injection on spanwise-averaged film effectiveness distribution for air or CO_2 injection at mainstream mean turbulence intensity of $\overline{Tu} = 16.4$ percent (Case 4). Overall, film effectiveness increases downstream of film holes for both air and CO_2 injections. The peaks in film effectiveness are due to better film coverage downstream of the film holes. Following such peaks, film effectiveness decreases due to injectant dilution and the effectiveness values are very small far downstream of the film holes. For air injection, the blowing ratio of 0.8 (with a medium momentum flux ratio and a medium mass flow rate) provides optimum film coverage and therefore the best film effectiveness over most of the blade surface. At a higher blowing ratio of 1.2 for air, a much higher momentum flux ratio causes more injectant jet penetration into the mainstream, which results in lower film effectiveness. At the lower blowing ratio of 0.4 for air, the mass flow rate of the injectant is very low and provides limited film coverage that results in lower film effectiveness. For the CO_2 injection, a blowing ratio of 1.2 provides the best film effectiveness over most of the blade surface. Since CO_2 is about 1.5 times as dense as air, its momentum flux ratio at the blowing ratio of 1.2 is only 66 percent that of air injection at the same blowing ratio, which results in lower jet penetration. This lower jet penetration combined with the highest injectant mass flow rate at this blowing ratio results in the best film coverage.

Mehendale et al. (1994) have shown that higher density injectant at higher blowing ratios provide the best heat load reduction. Since density and blowing ratios in a gas turbine engine are on the high side, combined turbulence effect on heat transfer coefficient and film effectiveness is presented only at the highest blowing ratio of $M = 1.2$.

Nusselt Number Results. Figure 5 shows the enhancement in spanwise averaged Nusselt number distribution from "Case 2" (Ou et al., 1994) to "Case 6" for air or CO_2 injection at the blowing ratio of 1.2. Here, Case 6 ($\overline{Tu} = 21.2$ percent) is compared with Case 2 ($\overline{Tu} = 13.9$ percent). Results at $\overline{Tu}$

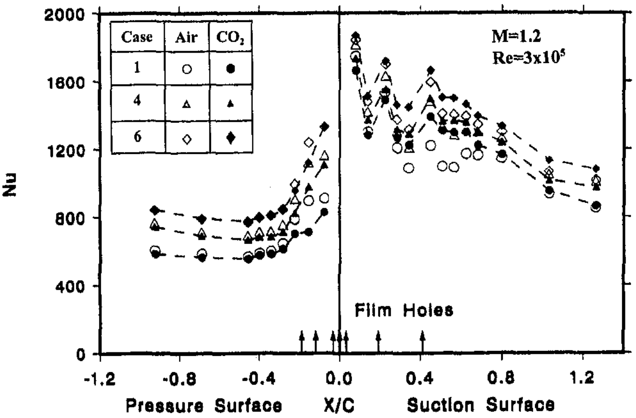

Fig. 6 Effect of an unsteady wake with medium or strong grid turbulence on Nu distributions for air or CO_2 injection at $M = 1.2$

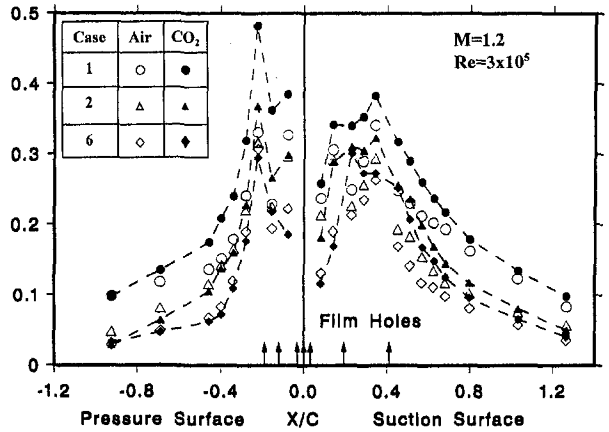

Fig. 8 Effect of an unsteady wake with and without strong grid turbulence on $\bar{\eta}$ distributions for air or CO_2 injection at $M = 1.2$

= 0.75 percent (Case 1, Ou et al., 1994) are also shown for comparison. As mainstream turbulence increases, unsteady flow fluctuations disturb the boundary layer and cause higher heat transfer coefficients at all locations for both injectants (Case 1 to Case 2). It is clear from the figure that the combination of a strong grid turbulence with an unsteady wake ($\overline{Tu}$ = 21.2 percent) enhances the heat transfer coefficients significantly when compared with the unsteady wake case ($\overline{Tu}$ = 13.9 percent).

Figure 6 shows the enhancement in spanwise averaged Nusselt number distribution from "Case 4" to "Case 6" for air or CO_2 injection at the blowing ratio of 1.2. Here, the effects of adding a strong or medium grid turbulence ($\overline{Tu}$ = 17 or 5.7 percent) to an unsteady wake ($\overline{Tu}$ = 13.9 percent) are compared. Results at $\overline{Tu}$ = 0.75 percent (Case 1) are also shown for comparison. An increase in mainstream turbulence causes higher heat transfer coefficients at all locations for both injectants (Case 1 to Case 4). Note that even at such elevated combined turbulence levels, a strong grid turbulence with wake ($\overline{Tu}$ = 21.2 percent) still creates higher heat transfer coefficients than the medium grid turbulence with wake ($\overline{Tu}$ = 16.4 percent). The increase in Nusselt numbers for the increase of mean turbulence levels from 16.4 (Case 4) to 21.2 percent (Case 6) is not as significant as that for an increase from 13.9 (Case 2) to 21.2 percent (Case 6).

Figure 7 shows the enhancement in spanwise averaged Nusselt number distribution from "Case 5" to "Case 6" for air or CO_2 injection at the blowing ratio of 1.2. Here, the effect of adding an unsteady wake to a strong grid turbulence is studied. Results at $\overline{Tu}$ = 0.75 percent are also shown for comparison. An increase in mainstream turbulence causes higher heat transfer coefficients at all locations for both injectants (Case 1 to Case 5). Compared with the strong grid turbulence case ($\overline{Tu}$ = 17 percent), the combination of an unsteady wake with a strong grid turbulence ($\overline{Tu}$ = 21.2 percent) does not produce a significant change in the heat transfer coefficients on either the pressure or suction sides of the blade.

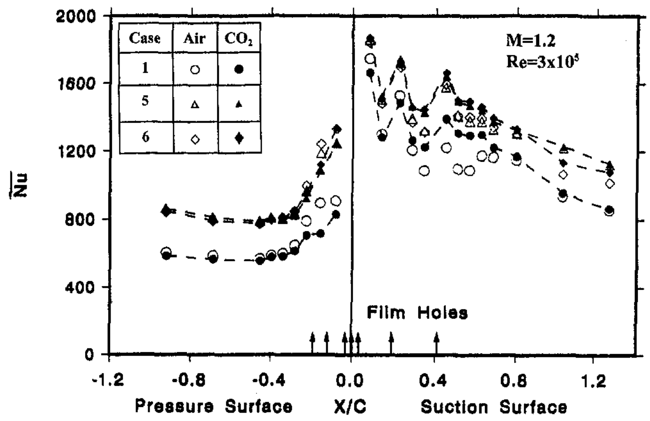

Fig. 7 Effect of a strong grid turbulence with and without an unsteady wake on Nu distributions for air or CO_2 injection at $M = 1.2$

Three key conclusions can be made based on observations from Figs. 5, 6, and 7. Superimposition of a strong grid turbulence on an unsteady wake enhances heat transfer coefficients significantly over an unsteady wake condition. Superimposition of an unsteady wake on a strong grid turbulence does not enhance heat transfer coefficients over a strong grid turbulence condition. For a given unsteady wake condition, an increase in grid turbulence level from a medium grid turbulence ($\overline{Tu}$ = 5.7 percent) to strong grid turbulence ($\overline{Tu}$ = 17 percent) significantly increases the heat transfer coefficient. Thus, a strong grid turbulence ($\overline{Tu}$ = 17 percent) plays a more dominant role than an unsteady wake (S = 0.3, $\overline{Tu}$ = 13.9 percent).

Film Effectiveness Results. Figure 8 shows the reduction in spanwise-averaged film effectiveness distribution from "Case 2" (Mehendale et al., 1994) to "Case 6" for air or CO_2 injection at the blowing ratio of 1.2. The results for Case 6 ($\overline{Tu}$ = 21.2 percent) are compared with those for Case 2 ($\overline{Tu}$ = 13.9 percent). Results at $\overline{Tu}$ = 0.75 percent (Mehendale et al., 1994) are also shown for comparison. As mainstream turbulence increases, flow fluctuations disrupt film coverage, resulting in lower film effectiveness values (Case 2 to Case 1). On the suction surface, CO_2 injection provides higher film effectiveness than air injection because CO_2 injection provides optimum film coverage at the blowing ratio of 1.2, and because air injection has a very high momentum flux ratio at that blowing ratio. This behavior is also observed on the pressure surface at low mainstream turbulence ($\overline{Tu}$ = 0.75 percent), but the differences are reduced for higher mainstream turbulence cases. Note that the film effectiveness distribution for a combined strong grid turbulence and unsteady wake (Case 6) is lower than for unsteady wake only (Case 2).

Figure 9 shows the reduction in spanwise-averaged film effectiveness distribution from "Case 4" to "Case 6" for air or CO_2 injection at the blowing ratio of 1.2. Here, the effect of adding a strong or medium grid turbulence ($\overline{Tu}$ = 17 or 5.7 percent) to an unsteady wake ($\overline{Tu}$ = 13.9 percent) are compared. Results at $\overline{Tu}$ = 0.75 percent are also shown for comparison. An increase in mainstream turbulence reduces film effectiveness at all locations for both injectants (Case 4 to Case 1). For the lower density injectant (air) with much a higher momentum ratio, superimposing unsteady wake with either strong or medium grid turbulence seems to produce similar film effectiveness distributions (Case 6 to Case 4). Case 6 will reduce film effectiveness more than Case 4 for the higher density injectant (CO_2) at such elevated combined mainstream turbulence levels, but the decreases on the pressure surface are not as significant as the suction surface. This behavior is not similar to the corresponding heat transfer coefficient distributions discussed earlier. Higher density injectant (CO_2) produces higher film effectiveness on the suction surface.

Figure 10 shows the reduction in spanwise-averaged film effectiveness distribution from "Case 5" to "Case 6" for air or CO_2 injection at the blowing ratio of 1.2. Here, the effect of adding an unsteady wake to a strong grid turbulence is studied. Results at $\overline{Tu} = 0.75$ percent are also shown for comparison. An increase in mainstream turbulence produces lower film effectiveness at all locations for both injectants (Case 5 to Case 1). As in Fig. 9, both high turbulence conditions (Cases 5 and 6) seem to produce similar effects on film effectiveness distribution for the lower density injectant (air). Case 5 produces a lower film effectiveness than that for the Case 6 for higher density injectant (CO_2), particularly on the pressure surface of the blade. This behavior is not similar to the corresponding heat transfer coefficient distributions discussed earlier. Higher density injectant (CO_2) produces higher film effectiveness on the suction surface but not on the pressure surface.

Similar trends were observed at the two lower blowing ratios of $M = 0.4$ and 0.8, but increases in the heat transfer coefficient and decreases in film effectiveness, due to mainstream turbulence, were more prominent at the lowest blowing ratio studied of $M = 0.4$.

Concluding Remarks

The effect of combined grid turbulence and unsteady wake on film effectiveness and heat transfer coefficient distributions of a model turbine blade, with air (D.R. ≈ 1.0) or CO_2 (D.R. ≈ 1.5) film injection, in a linear cascade was investigated. Tests were done at the chord Reynolds number of 3×10^5 at the cascade inlet ($Re = 7.5 \times 10^5$ at the cascade exit), at the mainstream mean turbulence intensities of 0.75, 13.9, 16.4, 17, and 21.2 percent at the cascade inlet, and at blowing ratios of 0.4, 0.8, and 1.2. The main findings are:

1 As blowing ratio increases, heat transfer coefficients over most of the blade surface increase. Blowing ratios of 1.2 and 0.8 provide the best film effectiveness over most of the blade surface for CO_2 and air injections, respectively.

2 Superimposing a medium grid turbulence on an unsteady wake (Case 4, $\overline{Tu} = 16.4$ percent) produced higher heat transfer coefficients and lower film effectiveness compared with a very low free-stream turbulence condition (Case 1, $\overline{Tu} = 0.75$ percent).

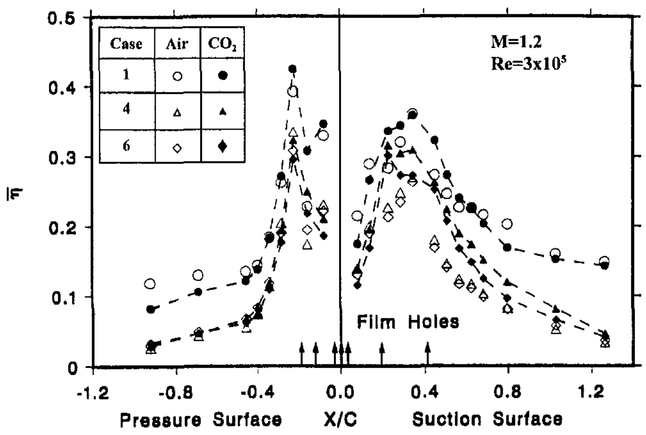

Fig. 9 **Effect of an unsteady wake with medium or strong grid turbulence on $\bar{\eta}$ distributions for air or CO_2 injection at $M = 1.2$**

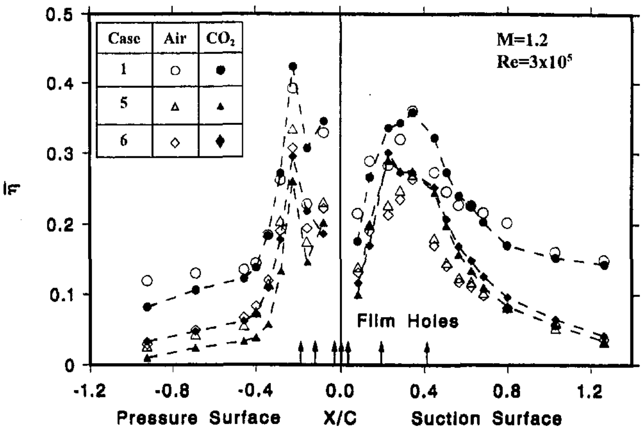

Fig. 10 **Effect of a strong grid turbulence with and without an unsteady wake on $\bar{\eta}$ distributions for air or CO_2 injection at $M = 1.2$**

3 Superimposing a medium or strong free-stream turbulence on an unsteady wake (Case 4, $\overline{Tu} = 16.4$ percent and Case 6, $\overline{Tu} = 21.2$ percent) produced higher heat transfer coefficients and lower film effectiveness compared to only an unsteady wake condition (Case 3, $\overline{Tu} = 13.9$ percent).

4 Superimposing an unsteady wake on a strong grid turbulence (Case 6, $\overline{Tu} = 21.2$ percent) provides almost the same heat transfer coefficients and film effectiveness as the strong grid turbulence itself (Case 5, $\overline{Tu} = 17$ percent). This suggests that in the presence of a strong grid turbulence, adding an unsteady wake may have no further effect;

5 Mainstream turbulence produces very similar trends in heat transfer coefficient distributions for both injectants. Overall, higher density injectant (D.R. ≈ 1.5) produces higher heat transfer coefficients and higher film effectiveness on a suction surface. Lower density injectant (D.R. ≈ 1.0) produces higher heat transfer coefficients on the pressure side. The effectiveness distribution does not follow any trend on the pressure side.

Acknowledgments

The project was sponsored by the Texas Higher Education Coordinating Board—Advanced Technology Program, under grant number 999903-104 and by the U.S. Naval Air Warfare Center through General Electric Aircraft Engines.

References

Abhari, R. S., Guenette, G. R., Epstein, A. H., and Giles, M. B., 1992, "Comparison of Time-Resolved Measurements and Numerical Calculations," ASME JOURNAL OF TURBOMACHINERY, Vol. 114, pp. 818–827.

Abhari, R. S., and Epstein, A. H., 1994, "An Experimental Study of Film Cooling in a Rotating Transonic Turbine," ASME JOURNAL OF TURBOMACHINERY, Vol. 116, pp. 63–70.

Ashworth, D. A., LaGraff, J. E., Schultz, D. L., and Grindrod, K. J., 1985, "Unsteady Aerodynamics and Heat Transfer in a Transonic Turbine Stage," ASME *Journal of Engineering for Gas Turbines and Power*, Vol. 107, pp. 1022–1030.

Blair, M. F., Dring, R. P., and Joslyn, H. D., 1989a, "The Effects of Turbulence and Stator/Rotor Interactions on Turbine Heat Transfer: Part I—Design Operating Conditions," ASME JOURNAL OF TURBOMACHINERY, Vol. 111, pp. 87–96.

Blair, M. F., Dring, R. P., and Joslyn, H. D., 1989b, "The Effects of Turbulence and Stator/Rotor Interactions on Turbine Heat Transfer: Part II—Effects of Reynolds Number and Incidence," ASME JOURNAL OF TURBOMACHINERY, Vol. 111, pp. 97–103.

Blair, M. F., 1994, "An Experimental Study of Heat Transfer in a Large-Scale Turbine Rotor Passage," ASME JOURNAL OF TURBOMACHINERY, Vol. 116, pp. 1–3.

Camci, C., and Arts, T., 1990, "An Experimental Convective Heat Transfer Investigation Around a Film-Cooled Gas Turbine Blade," ASME JOURNAL OF TURBOMACHINERY, Vol. 112, pp. 497–503.

Doorly, D. J., and Oldfield, M. L. G., 1985, "Simulation of the Effect of Shock-Waves Passing on a Turbine Rotor Blade," ASME *Journal of Engineering for Gas Turbines and Power*, Vol. 107, pp. 998–1006.

Doorly, D. J., 1988, "Modeling the Unsteady Flow in a Turbine Rotor Passage," ASME JOURNAL OF TURBOMACHINERY, Vol. 110, pp. 27–37.

Dullenkopf, K., Schulz, A., and Wittig, S., 1991, "The Effect of Incident Wake Conditions on the Mean Heat Transfer of an Airfoil," ASME JOURNAL OF TURBOMACHINERY, Vol. 113, pp. 412–418.

Dunn, M. G., 1986, "Heat Flux Measurements for the Rotor of a Full-Stage Turbine: Part I—Time Averaged Results," ASME JOURNAL OF TURBOMACHINERY, Vol. 108, pp. 90–97.

Dunn, M. G., George, W. K., Rae, W. J., Woodward, S. H., Moller, J. C., and Seymour, J. P., 1986, "Heat Flux Measurements for the Rotor of a Full-Stage Turbine: Part II—Description of Analysis Technique and Typical Time-Resolved Measurements," ASME JOURNAL OF TURBOMACHINERY, Vol. 108, pp. 98–107.

Dunn, M. G., Seymour, P. J., Woodward, S. H., George, W. K., and Chupp, R. E., 1989, "Phase-Resolved Heat Flux Measurements on the Blade of a Full-Scale Rotating Turbine," ASME JOURNAL OF TURBOMACHINERY, Vol. 111, pp. 8–19.

Dunn, M. G., Kim, J., Civinskas, K. C., and Boyle, R. J., 1994, "Time Averaged Heat Transfer and Pressure Measurements and Comparison With Prediction for a Two-Stage Turbine," ASME JOURNAL OF TURBOMACHINERY, Vol. 116, pp. 14–22.

Haas, W., Rodi, W., and Schönung, B., 1992, "The Influence of Density Difference Between Hot and Coolant Gas on Film Cooling by a Row of Holes: Predictions and Experiments," ASME JOURNAL OF TURBOMACHINERY, Vol. 114, pp. 747–755.

Han, J. C., Zhang, L., and Ou, S., 1993, "Influence of Unsteady Wake on Heat Transfer Coefficient From a Gas Turbine Blade," ASME *Journal of Heat Transfer,* Vol. 115, pp. 904–911.

Ito, S., Goldstein, R. J., and Eckert, E. R. G., 1978, "Film Cooling of a Gas Turbine Blade," ASME *Journal of Engineering for Power,* Vol. 100, pp. 476–481.

Kline, S. J., and McClintock, F. A., 1953, "Describing Uncertainties in Single-Sample Experiments," *Mechanical Engineering,* Vol. 75, Jan., pp. 3–8.

Mehendale, A. B., Han, J. C., Ou, S., and Lee, C. P., 1994, "Unsteady Wake Over a Linear Turbine Blade Cascade With Air and CO_2 Film Injection: Part II—Effect on Film Effectiveness and Heat Transfer Distributions," ASME JOURNAL OF TURBOMACHINERY, Vol. 116, No. 4, pp. 730–737.

Nirmalan, V., and Hylton, L. O., 1990, "An Experimental Study of Turbine Vane Heat Transfer With Leading Edge and Downstream Film Cooling," ASME JOURNAL OF TURBOMACHINERY, Vol. 112, pp. 477–487.

O'Brien, J. E., and Capp, S. P., 1989, "Two-Component Phase-Averaged Turbulence Statistics Downstream of a Rotating Spoked-Wheel Wake Generator," ASME JOURNAL OF TURBOMACHINERY, Vol. 111, pp. 475–482.

Ou, S., and Han, J. C., 1994, "Unsteady Wake Effect on Film Effectiveness and Heat Transfer Coefficient From a Turbine Blade With One Row of Air and CO_2 Film Injection," ASME *Journal of Heat Transfer,* Vol. 116, pp. 921–928.

Ou, S., Han, J. C., Mehendale, A. B., and Lee, C. P., 1994, "Unsteady Wake Over a Linear Turbine Blade Cascade With Air and CO_2 Film Injection: Part I—Effect on Heat Transfer Coefficients," ASME JOURNAL OF TURBOMACHINERY, Vol. 116, pp. 721–729.

Pfeil, H., Herbst, R., and Schroeder, T., 1983, "Investigation of the Laminar–Turbulent Transition of Boundary Layers Disturbed by Wakes," ASME *Journal of Engineering for Gas Turbines and Power,* Vol. 105, pp. 130–137.

Takeishi, K., Aoki, S., Sato, T., and Tsukagoshi, K., 1992, "Film Cooling on a Gas Turbine Rotor Blade," ASME JOURNAL OF TURBOMACHINERY, Vol. 114, pp. 828–834.

Wittig, S., Dullenkopf, K., Schulz, A., and Hestermann, R., 1987, "Laser-Doppler Studies of the Wake-Effected Flow Field in a Turbine Cascade," ASME JOURNAL OF TURBOMACHINERY, Vol. 109, pp. 170–176.

Zhang, L., and Han, J. C., 1995, "Combined Effect of Free-Stream Turbulence and Unsteady Wake on Heat Transfer Coefficients From a Gas Turbine Blade," ASME *Journal of Heat Transfer,* Vol. 117, pp. 296–302.

Measurements of Heat Transfer Coefficients and Friction Factors in Rib-Roughened Channels Simulating Leading-Edge Cavities of a Modern Turbine Blade

M. E. Taslim

T. Li

Department of Mechanical Engineering,
Northeastern University,
Boston, MA 02115

S. D. Spring

GE Aircraft Engines,
Lynn, MA 02190

Leading edge cooling cavities in modern gas turbine blades play an important role in maintaining the leading edge temperature at levels consistent with airfoil design life. These cavities often have a complex cross-sectional shape to be compatible with the external contour of the blade at the leading edge. A survey of many existing geometries shows that, for analytical as well as experimental analyses, such cavities can be simplified in shape by a four-sided polygon with one curved side similar to the leading edge curvature, a rectangle with one semicircular side (often the smaller side) or a trapezoid, the smaller base of which is replaced by a semicircle. Furthermore, to enhance the heat transfer coefficient in these cavities, they are mostly roughened on three sides with ribs of different geometries. Experimental data on friction factors and heat transfer coefficients in such cavities are rare if not nonexistent. A liquid crystal technique was used in this experimental investigation to measure heat transfer coefficients in six test sections representing the leading-edge cooling cavities. Both straight and tapered ribs were configured on the two opposite sidewalls in a staggered arrangement with angles of attack to the mainstream flow, α, of 60 and 90 deg. The ribs on the curved surface were of constant cross section with an angle of attack 90 deg to the flow. Heat transfer measurements were performed on the straight sidewalls, as well as on the round surface adjacent to the blade leading edge. Effects such as rib angle of attack to the mainstream flow and constant versus tapered rib cross-sectional areas were also investigated. Nusselt numbers, friction factors, and thermal performances are reported for nine rib geometries in six test sections.

Introduction

Various methods have been developed over the years to keep turbine blade temperatures below critical levels. A main objective in turbine blade cooling design is to achieve maximum heat transfer coefficients while minimizing the coolant flow rate. One such method is to route coolant air through rib-roughened serpentine passages within the airfoil and convectively remove heat from the blade. The coolant is then ejected either at the tip of the blade, through the cooling slots along the trailing edge, or via cooling holes on the airfoil surface.

Geometric parameters such as passage aspect ratio (AR), rib height to passage hydraulic diameter or blockage ratio (e/D_h), rib angle of attack (α), the manner in which the ribs are positioned relative to one another (in-line, staggered, criss-cross, etc.), rib pitch-to-height ratio (S/e) and rib shape (round versus sharp corners, fillets, rib aspect ratio (AR_r), and skewness toward the flow direction) have pronounced effects on both local and overall heat transfer coefficients. Some of these effects were studied by different investigators, such as Burggraf (1970), Chandra (1988), Chandra and Han (1989), Han (1984), Han et al. (1978, 1992), Metzger et al. (1983), Taslim and Spring (1988a, b, 1991), Taslim et al. (1991), Webb et al. (1971), and Zhang et al. (1994). The available data in the open literature, however, are mostly for circular, square or rectangular channels roughened with ribs of uniform cross-sectional area.

As dictated by the external shape of blade leading edge, leading-edge cooling cavities in modern engines often have a complex shape that for analytical as well as experimental analyses can be simplified to a triangular or rectangular channel with at least one curved wall representing the leading side. Furthermore, the shape of the cavity often necessitates the use of horseshoe-shaped ribs on the curved surface and tapered ribs on the two walls adjacent to the blade suction and pressure sides. This complex geometry creates a complex flow field with spanwise as well as longitudinal variations in heat transfer coefficient. Experimental or theoretical work in this area encompassing all the above-mentioned effects is rare if not nonexistent. The relatively few experimental or numerical studies in rib-roughened channels simulating the leading-edge cooling cavities of turbine blades are as follows. Metzger et al. (1987) reported on the measured heat transfer coefficient in a rib-roughened triangular duct. Using a transient technique, they investigated long and short ribs at 30, 60, and 90 deg angles to the axial flow direction. Ribs with a blockage ratio of 0.0866 and a pitch-to-height ratio of 10 were mounted on two walls of an equilateral triangle in a staggered arrangement. They concluded,

---

Contributed by the International Gas Turbine Institute and presented at the 40th International Gas Turbine and Aeroengine Congress and Exhibition, Houston, Texas, June 5–8, 1995. Manuscript received by the International Gas Turbine Institute February 4, 1995. Paper No. 95-GT-40. Associate Technical Editor: C. J. Russo.

among others, that the 60 deg ribs were superior to others due to the streamwise growing secondary flows induced by these ribs, and a 25 percent cut in rib length in the corner region did not improve the heat transfer characteristics.

Metzger and Vedula (1987) measured heat transfer coefficients in smooth and rib-roughened triangular ducts. Again, using a transient technique, they investigated 30, 60, and 90 deg rib angles to the axial flow direction. Test section geometry and rib blockage were the same as in their previous work mentioned above. Major conclusions from this work were that the 60 deg ribs produced higher heat transfer coefficients than 30 deg ribs, a pitch-to-height ratio of 7.5 showed the best performance, angled ribs produced higher heat transfer coefficients than 90 deg ribs due to the presence of secondary flows, and, for angled ribs, there existed an oscillatory variation in heat transfer coefficient along the duct.

Dutta and Han (1994) studied the effect of model orientation on local heat transfer in an orthogonally rotating two-pass smooth triangular duct. A right angle triangular smooth channel was tested for 0, ±45, and 90 deg tilt angles with respect to the direction of rotation. They concluded that: (*a*) The Nusselt number for the radially outward flow increased with rotation on the trailing wall and decreased on the leading wall, (*b*) the reverse trend in Nusselt number was observed for radially inward flows, (*c*) a −45 deg tilt angle produced one dominant secondary vortex while the 0, 45, and 90 deg tilt angles produced two vortices of comparable strengths.

The above-mentioned studies did not deal with rounded-wall channels roughened with horseshoe-shaped ribs simulating the leading edge cooling cavity of many turbine blades, nor did they investigate high-blockage ratio ribs presently used in modern small gas turbines. This investigation deals with some unique features of channel and rib geometries associated with the blade leading edge cooling cavity.

Figures 1–6 show schematically the layout, cross-sectional area, and the rib geometry for the six test sections investigated in this report. Since some test sections were roughened with more than one set of ribs, Table 1 contains the specifications of all geometries tested in this investigation. A liquid crystal technique was employed to measure the heat transfer coefficients in these test sections (see Moffat, 1990). In this technique, the most temperature-sensitive color displayed by the liquid crystals is chosen as the reference color corresponding to a known temperature. By proper adjustment of the Ohmic power to a very thin foil heater immediately underneath the liquid crystals, the reference color is moved from one location to another so that the entire area of interest is eventually covered with the reference color at one time or another. This process results in a series of photographs, which correspond to a certain location of the reference color. Among the advantages of liquid crystal thermography is to depict the flow "footprints"

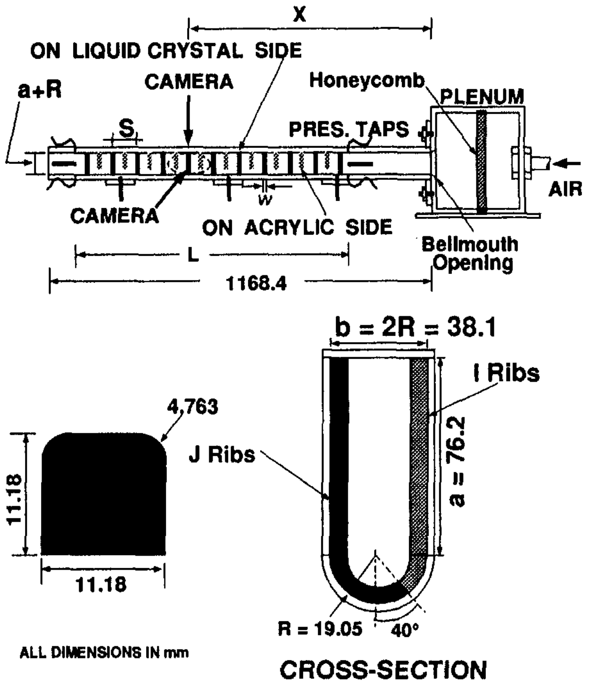

Fig. 1 Schematic geometry of test section 1

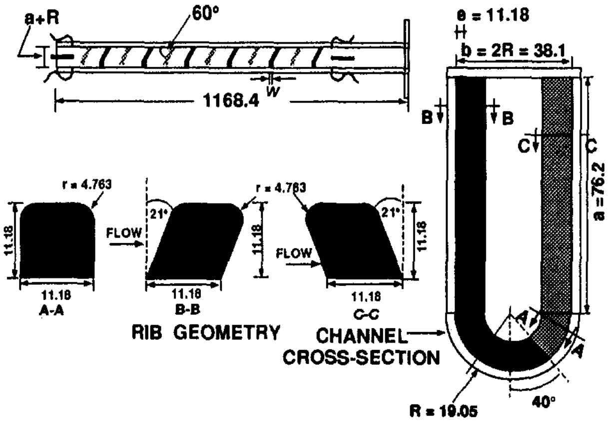

Fig. 2 Schematic geometry of test section 2

Nomenclature

a = channel straight sidewall (Figs. 1–6)
b = channel width (Figs. 1–6)
A = cross-sectional area without ribs
AR_t = rib aspect ratio = e/w
D_h = hydraulic diameter based on the cross-sectional area without ribs = $4A/P$
e = rib height
$\bar{f}$ = Darcy friction factor = $\Delta P(D_h/L)/(\frac{1}{2}\rho U_m^2)$
$\bar{f}_s$ = Darcy friction factor in an all-smooth-wall channel
h_t = average heat transfer coefficient between a pair of ribs
k = air thermal conductivity
L = length of the roughened portion of the test section
$\overline{\text{Nu}}$ = average Nusselt number between a pair of ribs = $h_t D_h/k$
$\overline{\text{Nu}}_s$ = Nusselt number in a smooth passage
P = channel perimeter without ribs
R = channel radius at the leading edge
R' = horseshoe rib inner radius (Fig. 5)
r = rib rounded corner radius
r_1 = rib inner radius on the leading-edge wall (Fig. 4)
Re = Reynolds number = $\rho U_m D_h/\mu$
S = rib pitch (center-to-center)
T_f = film temperature (0.5 $(T_s + T_m)$)
T_m = air mixed mean temperature
T_s = surface temperature
U_m = air mean velocity
w = rib width
w_1 = tapered ribs minimum width
w_2 = tapered ribs maximum width
X = distance between camera and test section entrance
α = angle of attack
ΔP = pressure differential across the roughened portion of the test section
μ = air dynamic viscosity
ρ = air density

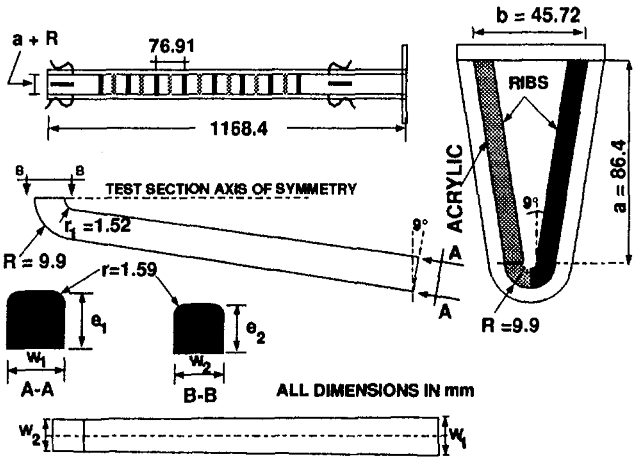

Fig. 3 Schematic geometry of test section 3

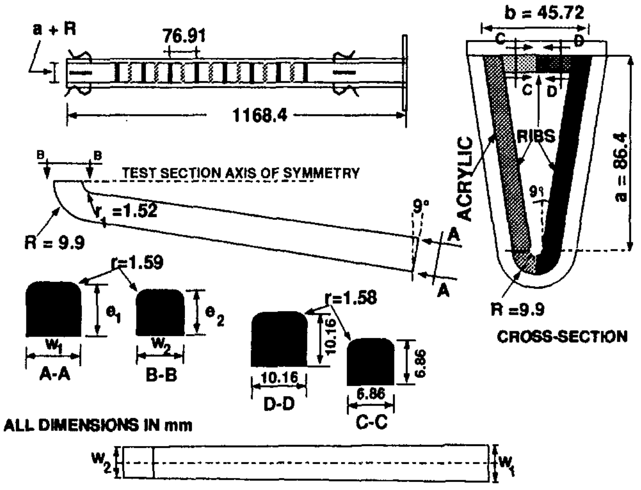

Fig. 4 Schematic geometry of test section 4

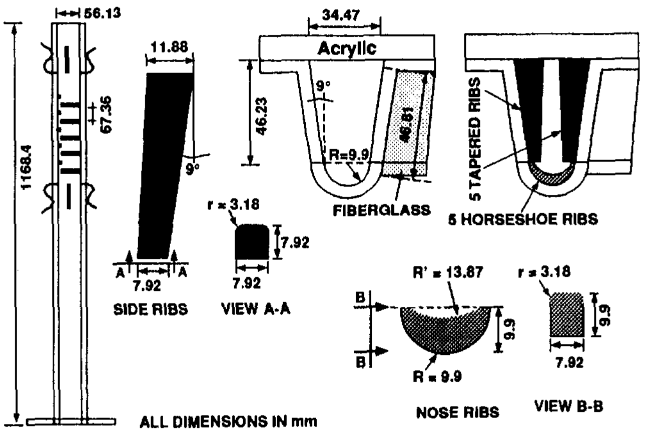

Fig. 5 Schematic geometry of test section 5

and local values of heat transfer coefficient on the surface under investigation. This simultaneous "flow visualization" enhances the understanding of the underlying physics and helps the investigator in interpretation of the results. Furthermore, unexpected asymmetries in flow are revealed as well as the slightest heat and flow leaks, nonuniformities in surface heat flux, imperfections associated with the attachment of the heater to the test section surface and nonuniformities in wall material thermal conductivity.

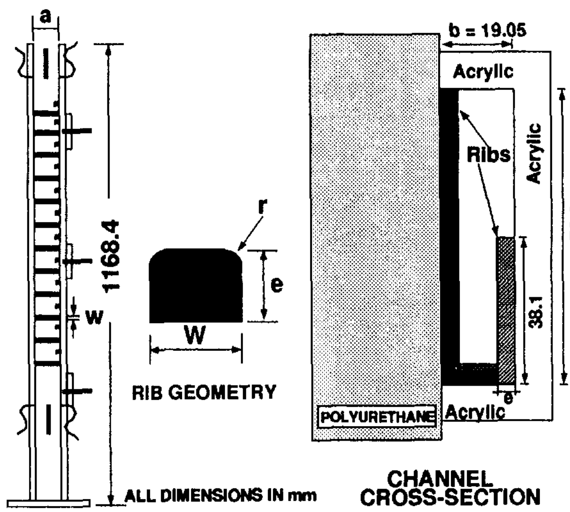

Fig. 6 Schematic geometry of test section 6

All test sections were 116.8 cm long. The two side walls and the top wall, making up the straight walls of tests sections 1–5, were made of 1.27-cm-thick clear acrylic plastic. The semicylindrical curved walls in those test sections, representing the cooling cavity wall adjacent to the blade leading edge, were made of molded fiberglass. Custom-made etched-foil heaters with a thickness of 0.1524 mm were placed on the walls where measurements were taken. Each heater, had a nominal resistance of 40Ω and was 27.94 cm long. The width of each heater was determined by the width of the area it covered. For example, in test section 1, heaters covering the semicylindrical leading edge area were 3.81 cm wide, while those covering the side walls were 3 in. wide. On both the leading edge and the sidewalls, there were four heaters with a total coverage of 111.76 cm in the axial direction of the channel. Leading-edge and sidewall heaters met at the junction of the two walls. Electrical AC power was supplied to the individual heaters. The typical amperage and voltage levels for each heat heater ranged from 0.1–0.8 amps and 10–80 volts. The encapsulated liquid crystals, sandwiched between a protective mylar sheet and a black background paint layer to form a total thickness of 0.325 mm, were then laid on the heaters. Ribs, also made of clear acrylic, were glued onto the surface of the liquid crystal layer. Test section 6 had a flat leading-edge wall and, as shown in Fig. 6, three walls were made of clear acrylic plastic and the fourth wall, on which the heaters and liquid crystal sheets were attached and all measurements were taken, was made of a 5-cm-thick machinable polyurethane slab. The entrance region of all test sections was left unturbulated to simulate the cooling passage in the dovetail region of an airfoil. Heat transfer measurements were performed for an area between a pair of ribs in the middle of the roughened zone.

The heaters covered the entire test section length including the smooth entry length. However, they did not extend over the rib surfaces. Thus the reported heat transfer coefficients are those averaged over the wall surface area between a pair of ribs. The heat transfer coefficients on the rib surfaces, an important issue in blade cooling technology (especially for high blockage ribs), are reported by investigators such as Metzger et al. (1988) and Taslim and Wadsworth (1997). It is noted that an experimental investigation by El-Husayni et al. (1994) on heat transfer in a roughened channel with one, two, and four heated walls showed that, in a stationary channel, the heat transfer coefficient is not sensitive to the number of heated walls. Static pressure taps were mounted on all three acrylic walls of each test section to measure the pressure drop across the turbulated portion of the test section. The reported friction factor is the overall passage average, $\bar{f}$.

Except for a small window at the location where the pictures were taken, the test sections were covered on all sides by 5-cm-

Table 1 Specifications

TESTS	a	b	R	D_h	e	w	AR_t	α (deg)	e/D_h	S/e	Footnote
1	76.2	38.1	19.05	55.5	11.18	11.18	1	90 Stag	0.2	10	1
2	76.2	38.1	19.05	55.5	11.18	11.18	1	60 90 Stag	0.2	10	2
3a	82.3	45.72	9.9	46.66	8.53 - 8.89	8.53 - 8.89	1 1	90 Stag	0.183- 0.191	9- 8.65	3
3b	82.3	45.72	9.9	46.66	7.87 - 8.18	9.27 - 9.65	0.85 0.85	90 Stag	0.169- 0.175	9.77- 9.4	3
4	82.3	45.72	9.9	46.66	8.53 - 8.89	8.53 - 8.89	1 1	90 Stag	0.183- 0.191	9- 8.65	4
5	34.47	46.81	9.9	35.38	7.92 - 11.88	7.925	1- 1.5	90 In-Li Stag	0.224- 0.336	8.5- 5.67	5
6a	76.2	19.05	0.	30.48	2.946	5.918	0.5	90 In-Li Stag	0.097	11.1	6
6b	76.2	19.05	0.	30.48	3.937	4.928	0.8	90 In-Li Stag	0.129	8.33	6
6c	76.2	19.05	0.	30.48	4.928	5.918	0.83	90 In-Li Stag	0.161	6.65	6

ALL DIMENSIONS IN mm

1) i and j ribs
2) i and j ribs, $\alpha = 60^{o}$ on the sidewalls, $\alpha = 90^{o}$ on the leading-edge side, i-ribs 21^{o} tilted towards flow on the sidewall, j-ribs 21^{o} tilted away from flow on the sidewall
3) Tapered, staggered, symmetric ribs on side and leading-edge walls. Values in pair represent the minimum and maximum for tapered ribs.
4) Tapered, staggered, symmetric ribs on side and leading-edge walls, half-length ribs on the top wall
5) Tapered, in-line ribs on the sidewalls, staggered horseshoe-shaped ribs on the leading-edge wall
6) full-length ribs on one sidewall and on the leading-edge wall, half-length ribs on the other sidewall, in-line ribs on opposite sidewalls, staggered on the leading-edge wall

thick styrofoam sheets to minimize heat losses to the environment. The radiational heat loss from the heated wall to the unheated walls as well as losses to ambient air were taken into consideration when heat transfer coefficients were calculated. A 35 mm programmable SLR camera, in conjunction with proper filters and background lighting to simulate daylight conditions was used to take photographs of the isochrome patterns formed on the liquid crystal sheet. Surface heat flux in the test section was generated by the heaters through a custom-designed power supply unit. Each heater was individually controlled by a variable transformer.

Procedure

Before testing, the liquid crystal sheets were calibrated as follows. A water bath was used to attain uniform isochromes on a small sample piece of the liquid crystal sheet used throughout this investigation. The temperature corresponding to each color was measured using a precision thermocouple and photographs were taken at laboratory conditions simultaneously so as to simulate closely the actual testing environment. A reference color along with its measured temperature of 36.9°C was then chosen to be used throughout the experiments. It should be noted that all possible shades of the selected reference color showed a temperature difference of no more than 0.3°C. All tests were run at atmospheric pressure. A contact micromanometer with an accuracy of 0.025 mm of water column measured the pressure differences between the static pressure taps mounted before and after the rib-roughened section of each channel. The static pressure at each location was assumed to

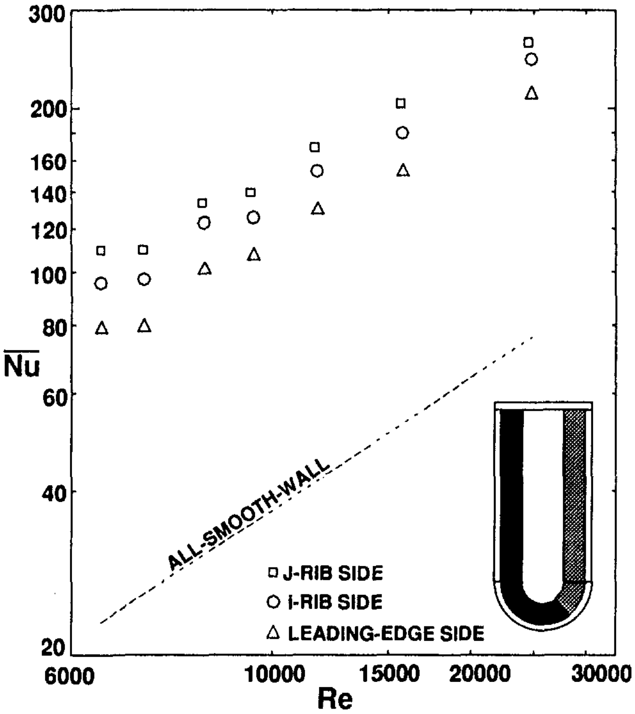

Fig. 7 Nusselt number comparisons for different sides of test section 1 (90 deg ribs)

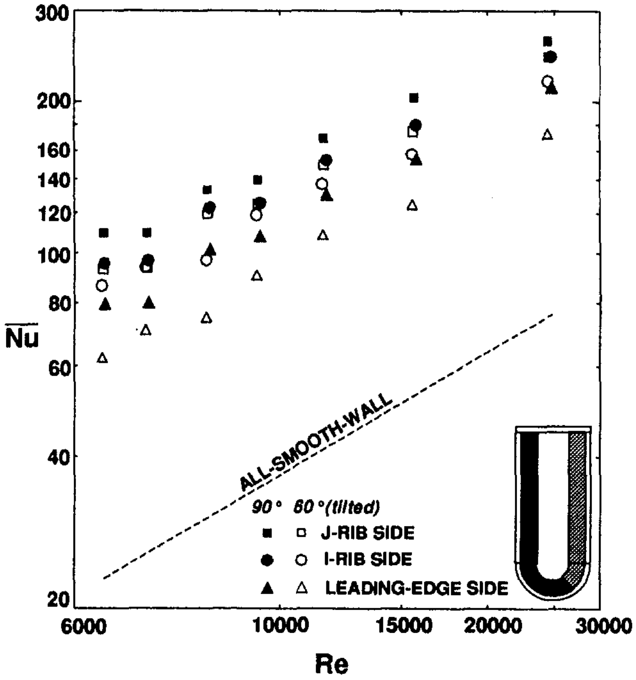

Fig. 8 Comparison of Nusselt numbers for 90 and 60 deg ribs

be the same for the entire cross section at that location. This was based on the readings of the two sets of three pressure taps mounted on three walls of the test section before the first and after the last rib (see Figs. 1–6). For all cases tested, a critical venturimeter was used to measure the total mass flow rate entering the test section. The air mixed mean temperature at the point where heat transfer coefficient was measured was calculated via energy balance starting from the test section inlet to the camera location using the known surface heat flux along the test section and the air temperature at the test section inlet. Typical air temperature increase from the inlet to the point of measurement was about 6°C. In this analysis, the small heat losses through the test section walls to the ambient environment, as well as the heat transfer through the acrylic ribs, were taken into account.

For a typical test run, the Reynolds number was set by precisely fixing the mass flow rate. The heat flux was then induced by turning on the main power supply and adjusting heater power until the first band of reference color was observed on the liquid crystal sheet in the area of interest. Each heater was adjusted individually so that uniform heat flux was accomplished over the entire tested surface. Enough time was allowed so that the system came to thermal equilibrium when a photograph was taken and data recorded. The power to the heaters was then increased so that the reference color was moved to a location next to the previous one and another picture was taken. This procedure was continued until the entire surface between a pair of ribs was covered by the reference color at one time or another. The process was repeated for all Reynolds numbers. Each photograph was digitized in order to measure the area covered by the reference color. This was done by using a magnetic tablet and a commercial software package installed on a PC. Once the areas were measured, an area-weighted average heat transfer coefficient was calculated. For verification of the liquid crystal technique accuracy, an all-smooth-wall channel was tested with heaters on one wall. The results, which were within ±5 percent of the well-known Dittus–Boelter (1930) correlation, are reported in Taslim (1990). Furthermore, these authors' previous results (Taslim et al., 1991) of turbulated channels of various geometries using the same technique compared favorably with those of Metzger et al. (1990).

Maximum experimental uncertainties, following the method of Kline and McClintock (1953), were determined to be ±7 and ±8 percent for the heat transfer coefficient and friction factor, respectively.

Results and Discussion

Local average heat transfer coefficient results for an area between a pair of ribs corresponding to $X/D_h = 9.5 - 11.6$ for

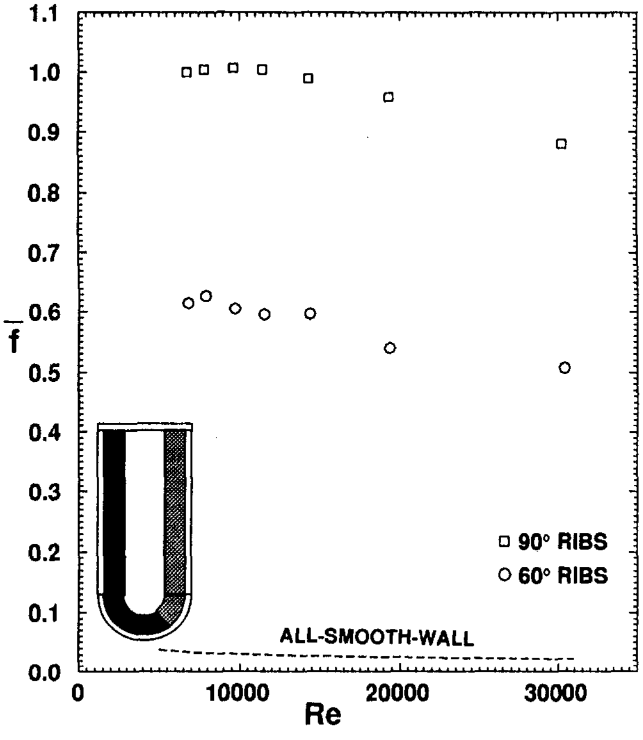

Fig. 9 Channel average friction factors for test sections 1 and 2

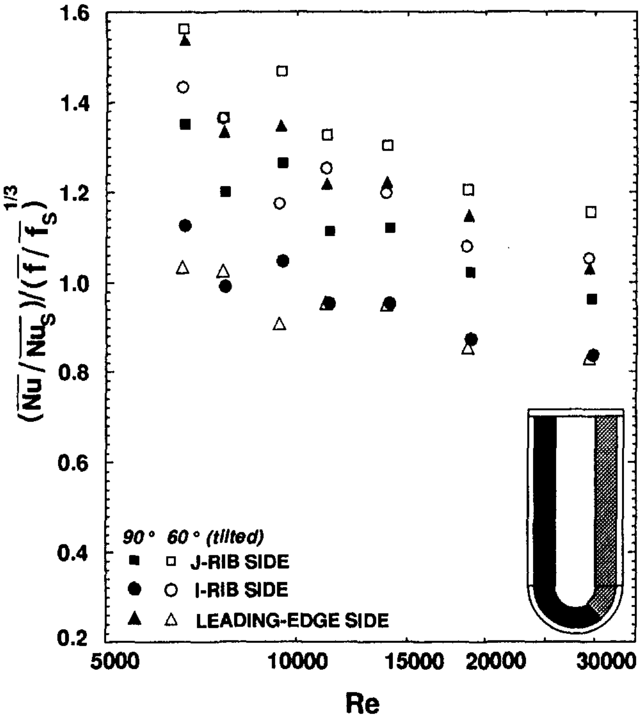

Fig. 10 Thermal performance comparisons for 90 and 60 deg ribs

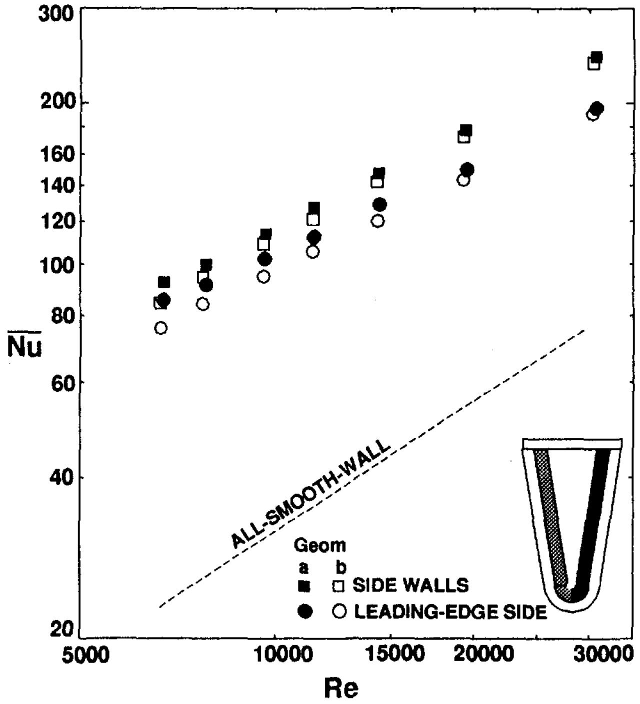

Fig. 11 Nusselt number comparisons for two rib geometries in test section 3

nine rib geometries in six channels are compared with the all-smooth-wall channel Dittus–Boelter (1930) correlation:

$$\mathrm{Nu}_s = 0.023\ \mathrm{Re}^{0.8}\ \mathrm{Pr}^{0.4}$$

With this correlation, the enhancement in rib-roughened heat transfer coefficients can be readily evaluated. The thermal performance, based on the same pumping power, is given by:

$$(\overline{\mathrm{Nu}}/\overline{\mathrm{Nu}}_s)/(\bar f/\bar f_s)^{1/3}$$

(Han et al., 1985), where $\bar f_s$ is the *all-smooth-wall* friction factor from Moody (1944). Air properties for Nusselt and Reynolds number calculations are based on the local film temperature, T_f for all cases.

Test Sections 1 and 2. These test sections, as shown in Figs. 1 and 2, are identical in all aspects except that rib angles with flow direction are different. Test section 1 was roughened with i- and j-shaped ribs positioned at 90 deg with flow direction in a staggered arrangement. This particular shape of ribs, in contrast to symmetric ribs, occurs often as a result of the casting process. Nusselt number variation with Reynolds number on sidewalls, as well as the leading-edge wall, are shown in Fig. 7. The high rib blockage ratio, e/D_h, of 0.2 created a large enhancement in heat transfer coefficient when compared with that in all-smooth-wall channels. The sidewall on which the j-ribs are mounted exhibits a higher heat transfer coefficient than the other two walls. This is somewhat expected since the j-ribs extend farther on the leading-edge wall (Fig. 1) creating a more effective blockage against the flow. The lower enhancement on the leading-edge wall can be explained by the velocity profile in a small aspect ratio channel where flow is biased toward the center of the passage. This behavior is even more pronounced with the presence of the ribs in the nose region.

To investigate the effects of rib angle with flow direction on heat transfer and friction factor, test section 2 was roughened with angled ribs as shown in Fig. 2. Two aspects of the rib geometry need to be clarified here. First, only the lengths of the ribs on the side walls were angled and the small portion of the rib length covering the leading-edge wall remained at a 90 deg angle with the flow direction as was the case in test section 1. Second, the rib cross section on the sidewalls was tilted 21 deg away from the flow on the j-rib wall and 21 deg toward the flow on the i-rib wall, simulating the need to accommodate necessary draft angles associated with the small turbine blade casting processes. Nusselt number variations with Reynolds number on all ribbed walls are shown in Fig. 8. The pattern of heat transfer enhancement on different walls is the same as in test section 1. However, 90 deg ribs produced higher enhance-

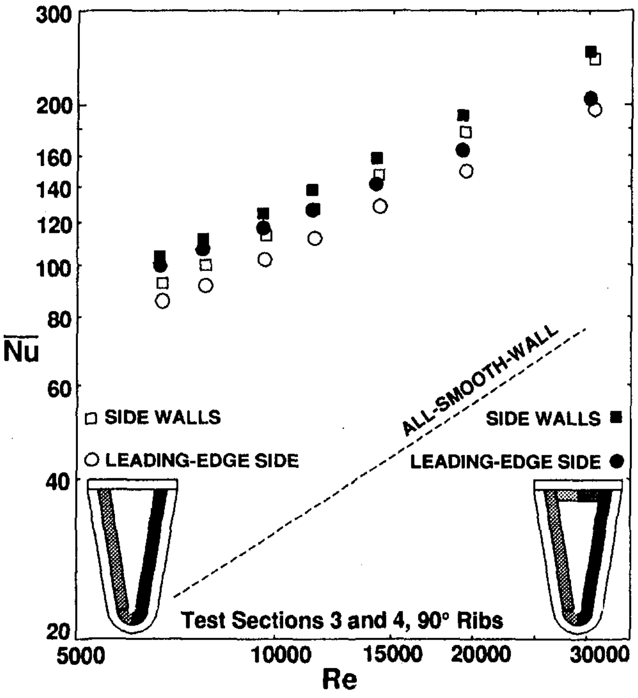

Fig. 12 Effects of top wall ribs on side and leading-edge wall Nusselt numbers

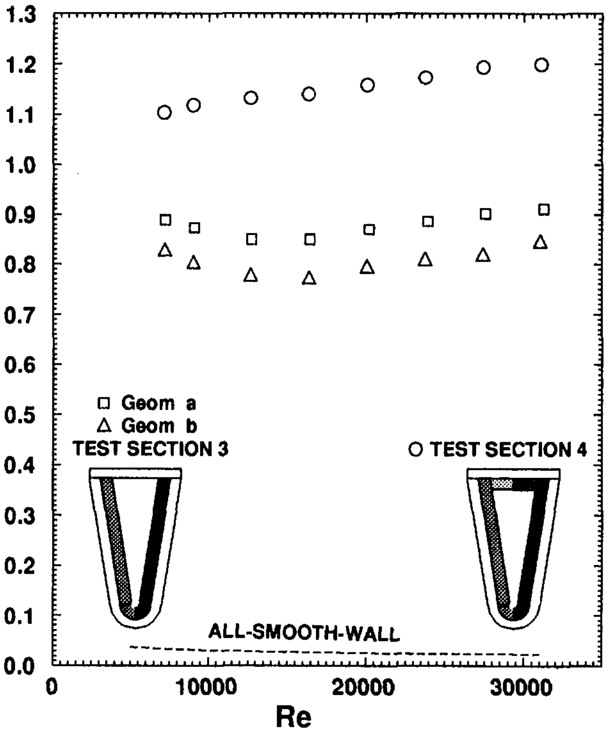

Fig. 13 Channel average friction factors for test sections 3 and 4

ments, at the expense of higher friction factors, as shown in Fig. 9. This is consistent with the Colburn analogy between heat transfer and fiction. A combination of rib angle of attack and the rib tilt in the flow direction (Fig. 2) contributed to a lower friction factor for the 60 deg ribs. A comparison between the thermal performance of these two rib geometries is made in Fig. 10. It is seen that the thermal performance for 60 deg ribs is higher than that for 90 deg ribs on the *i*-rib and *j*-rib walls and is lower on the leading-edge side.

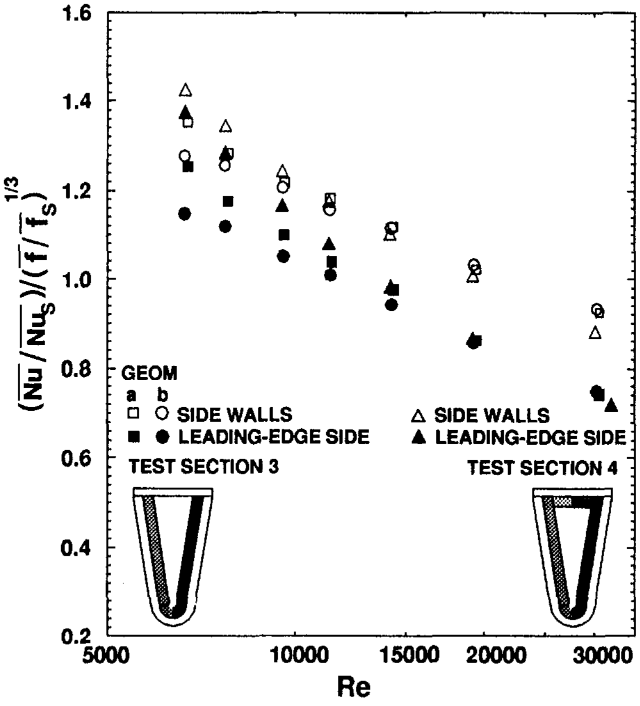

Fig. 14 Thermal performance comparisons for test sections 3 and 4

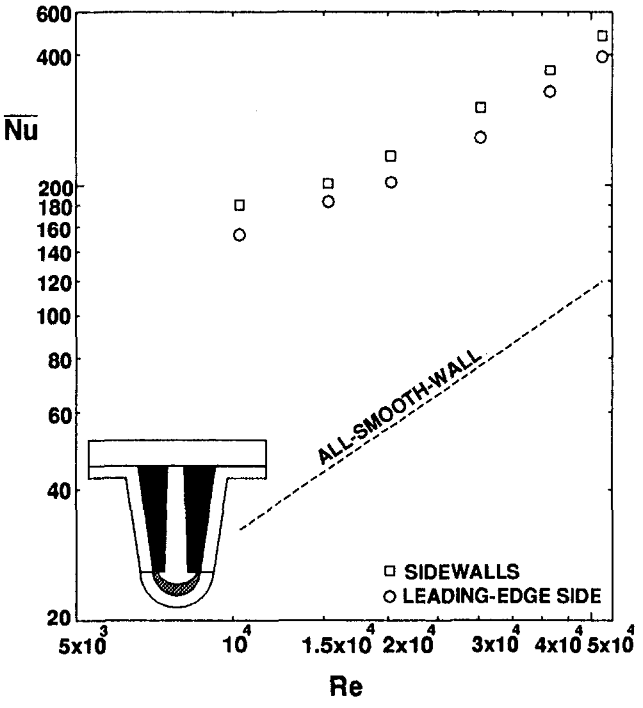

Fig. 15 Nusselt numbers for the side and leading-edge walls in test section 5

Test Section 3. Test section 3 represents a geometry of common occurrence for turbine leading-edge cooling cavity. Two rib blockage ratios (geometries *a* and *b*) were tested in this test section. These two rib geometries could represent the nominal and minimum allowable geometries in a given design, thus providing the design engineer with maximum deviation from the nominal heat transfer coefficient. A decrease in heat transfer coefficient (Fig. 11) for the smaller ribs due to their lower blockage and higher pitch-to-height ratios is in line with

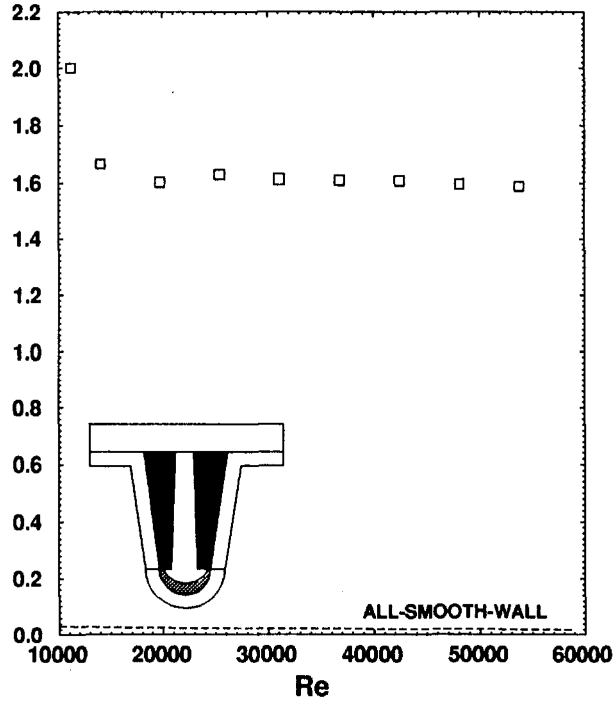

Fig. 16 Channel average friction factors for test section 5

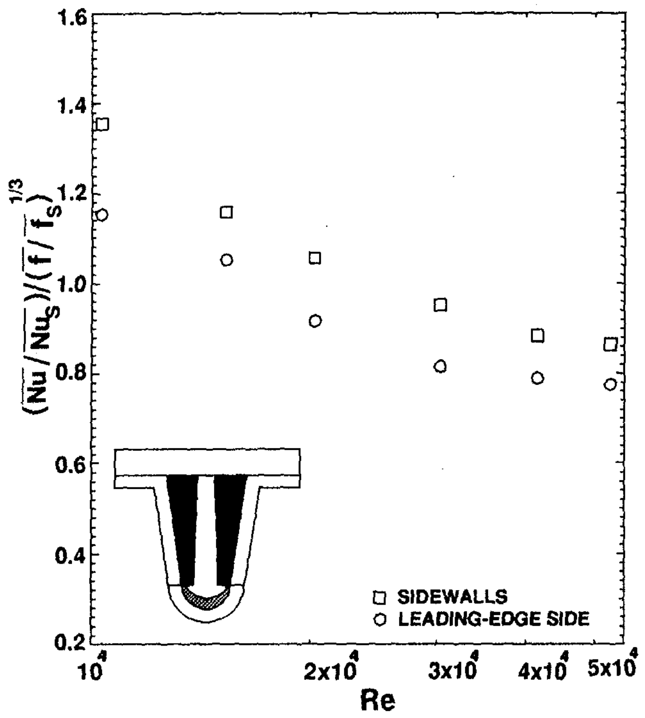

Fig. 17 Thermal performance for side and leading-edge walls in test section 5

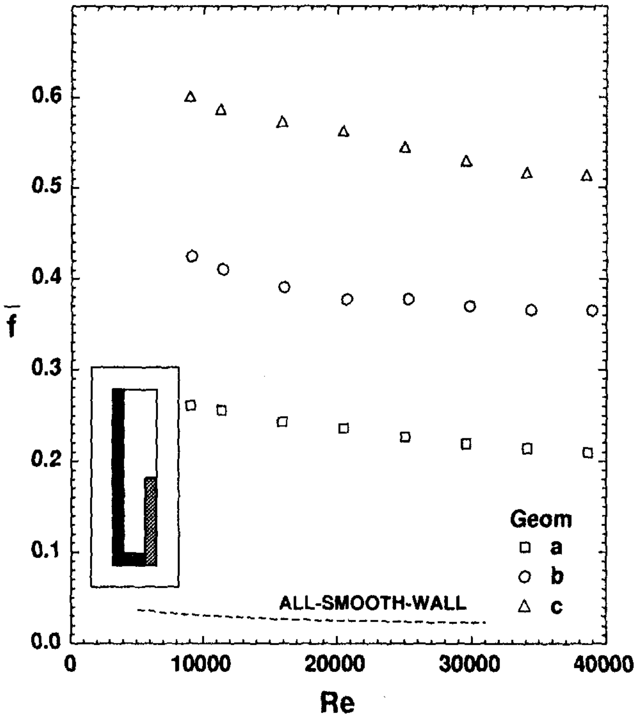

Fig. 19 Channel average friction factors for test section 6

the same behavior observed in square and rectangular channels by these and other investigators. Similarly as for test sections 1 and 2, Nusselt numbers are lower in the nose region than for the sidewalls. Friction factors for geometries *a* and *b* as well as that for test section 4 are compared in Fig. 13. In line with Colburn analogy, higher friction factors correspond to higher heat transfer coefficients.

Test Section 4. In an effort to enhance the heat transfer coefficient further on the side and leading-edge walls of test section 3 without changing the existing rib geometry, section 4 was tested next. This test section was identical to test section 3 (geometry *a*) in all aspects except that the top wall was roughened with half-length ($b/2$) ribs mounted at the same axial locations as the sidewall ribs extending from the opposite wall to the center of top wall in a staggered arrangement as shown in Fig. 4. Figure 12 compares the heat transfer coefficients for test sections 3 (geometry *a*) and 4. In this comparison it is seen that the presence of the top ribs has altered the flow pattern enough to increase the heat transfer coefficient on the sidewalls as well as the leading-edge wall. This increase, as expected, is in conjunction with an increase in the

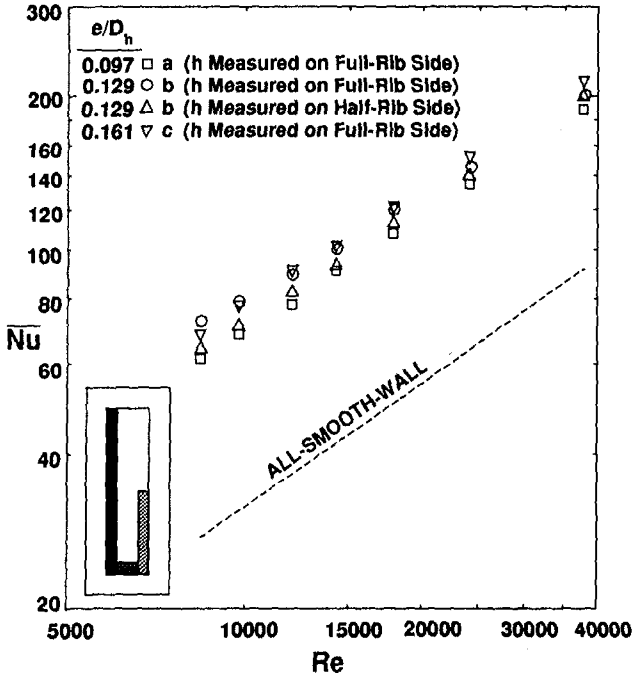

Fig. 18 Nusselt number comparisons for three rib geometries in test section 6

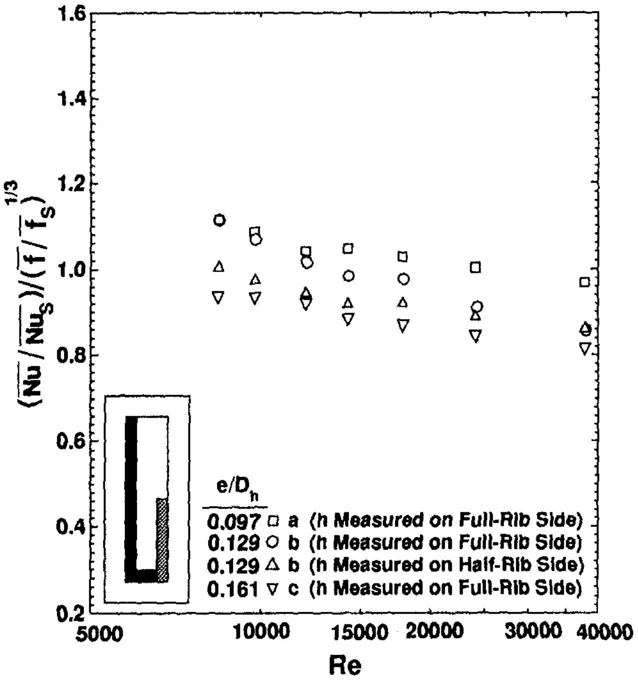

Fig. 20 Thermal performance comparisons for test section 6

friction factor, which is evidenced by Fig. 13. The heat transfer coefficient on the top wall itself was not measured in this investigation since the opposite surface was not a see-through wall to allow the recording of liquid crystal isochromes. Thermal performances of test sections 3 and 4 are shown in Fig. 14. Sidewalls in both test sections have a higher thermal performance than the leading-edge walls. This is expected since, in each test section, for the same channel friction factor, Nusselt number on the sidewalls was higher than that on the leading-edge wall. It is also noted that thermal performance of all walls in test section 4 is higher than those in test section 3 at the lower Reynolds number range. At the higher range of Reynolds number, the thermal performances of the leading-edge walls come very close to each other but the sidewall thermal performance in test section 4 begins to fall below that in test section 3. Therefore, the half-length ribs on the top wall present a double bonus, i.e., higher Nusselt numbers as well as thermal performance in the lower range of Reynolds number.

Test Section 5. Test section 5 represents another possible geometry for leading-edge cooling cavities. It is roughened with identical, in-line, tapered ribs on the sidewalls and horseshoe-shaped ribs, staggered with respect to the sidewall ribs, on the leading-edge side. The very high rib blockage is the cause of high heat transfer coefficients on sidewalls and on the leading-edge wall as shown in Fig. 15. The friction factor is also very high, as shown in Fig. 16. The combined effects of high heat transfer coefficients and friction factors is shown in Fig. 17, which indicates a lower thermal performance compared with the geometries presented so far.

Test Section 6. Test section 6 represents a simplified geometry of a leading-edge cooling cavity in which the ribbed sidewalls (adjacent to blade suction and pressure sides) are much different in width. Three rib geometries (*a*, *b*, and *c*) representing a typical casting process variation in blockage ratio are tested in the same test section. Figures 18 and 19 show the Nusselt numbers and friction factors for these rib geometries. Heat transfer results for the geometry *b* are shown for both full-rib and half-rib walls. First, it is seen that as rib blockage ratio increases from minimum to maximum, both Nusselt numbers and friction factors increase accordingly, and second, the half-rib wall produces a lower heat transfer coefficient than the full-rib wall. This is expected since a big portion of the cooling air passes over that surface without any interactions with the ribs. Thermal performances of these ribs are compared in Fig. 20. As was the case in other test sections, low blockage ratio ribs have a higher thermal performance. Also it should be noticed that this set of ribs represented a lower range of blockage ratios and consequently produced lower levels of heat transfer enhancement, friction factor, and thermal performance than the other test sections.

Conclusions

Six test sections roughened with nine rib geometries, simulating the leading-edge cooling cavities of turbine blades, were tested for heat transfer and pressure drop variations. From this study, it is concluded that for these geometries:

1 The effect of pertinent geometric parameters (e/D_h, S/e, AR_t, etc. . . .) on heat transfer behavior is consistent with previously reported results obtained from circular or rectangular test sections when surface average values are compared.

2 Roughening of nonparticipating walls in a cooling cavity improves the heat transfer enhancement on other participating walls and the overall heat transfer behavior of that cavity. This occurs at the expense of higher friction factors.

3 Heat transfer coefficient on the leading-edge wall, for all geometries tested here, was less than that on the sidewalls.

References

Burggraf, F., 1970, "Experimental Heat Transfer and Pressure Drop With Two Dimensional Turbulence Promoters Applied to Two Opposite Walls of a Square Tube," *Augmentation of Convective Heat and Mass Transfer*, A. E. Bergles and R. L. Webb, eds., ASME, New York, pp. 70–79.

Chandra, P. R., Han, J. C., and Lau, S. C., 1988, "Effect of Rib Angle on Local Heat/Mass Transfer Distribution in a Two-Pass Rib-Roughened Channel," ASME JOURNAL OF TURBOMACHINERY, Vol. 110, pp. 233–241.

Chandra, P. R., and Han, J. C., 1989, "Pressure Drop and Mass Transfer in Two-Pass Ribbed Channels," *Journal of Thermophysics*, Vol. 3, No. 3, pp. 315–319.

Dittus, F. W., and Boelter, L. M. K., 1930, *Publications in Engineering*, Vol. 2, No. 13, University of California, Berkeley, CA, pp. 443–461.

Dutta, S., and Han, J. C., 1994, "Effect of Model Orientation on Local Heat Transfer in a Rotating Two-Pass Smooth Triangular Duct," presented at the ASME Winter Annual Meeting.

El-Husayni, H. A., Taslim, M. E., and Kercher, D. M., 1994, "An Experimental Investigation of Heat Transfer Coefficients in a Spanwise Rotating Channel With Two Opposite Rib-Roughened Walls," ASME JOURNAL OF TURBOMACHINERY, Vol. 113, pp. 75–82.

Han, J. C., Glicksman, L. R., and Rohsenow, W. M., 1978, "An Investigation of Heat Transfer and Friction for Rib Roughened Surfaces," *International Journal of Heat and Mass Transfer*, Vol. 21, pp. 1143–1156.

Han, J. C., 1984, "Heat Transfer and Friction in Channels With Two Opposite Rib-Roughened Walls," ASME *Journal of Heat Transfer*, Vol. 106, No. 4, pp. 774–781.

Han, J. C., Park, J. S., and Lei, C. K., 1985, "Heat Transfer Enhancement in Channels With Turbulence Promoters," ASME *Journal of Engineering for Gas Turbines and Power*, Vol. 107, pp. 628–635.

Han, J. C., Zhang, Y. M., and Lee, C. P., 1992, "Influence of Surface Heat Flux Ratio on Heat Transfer Augmentation in Square Channels with Parallel, Crossed, and V-Shaped Angled Ribs," ASME JOURNAL OF TURBOMACHINERY, Vol. 114, pp. 872–880.

Kline, S. J., and McClintock, F. A., 1953, "Describing Uncertainty in Single-Sample Experiments," *Mechanical Engineering*, Vol. 75, Jan., pp. 3–8.

Metzger, D. E., Fan, C. S., and Pennington, J. W., 1983, "Heat Transfer and Flow Friction Characteristics of Very Rough Transverse Ribbed Surfaces With and Without Pin Fins," *Proc. ASME–JSME Thermal Engineering Joint Conference*, Vol. 1, pp. 429–436.

Metzger, D. E., Vedula, R. P., and Breen, D. D., 1987, "The Effect of Rib Angle and Length on Convection Heat Transfer in Rib-Roughened Triangular Ducts," *Proc. ASME–JSME Thermal Engineering Joint Conference*, Vol. 3, pp. 327–333.

Metzger, D. E., and Vedula, R. P., 1987, "Heat Transfer in Triangular Channels With Angled Roughness Ribs on Two Walls," *Experimental Heat Transfer*, Vol. 1, pp. 31–44.

Metzger, D. E., Chyu, M. K., and Bunker, R. S., 1988, "The Contribution of On-Rib Heat Transfer Coefficients to Total Heat Transfer From Rib-Roughened Surfaces," *Transport Phenomena in Rotating Machinery*, J. H. Kim, ed., Hemisphere Publishing Co.

Metzger, D. E., Fan, C. S., and Yu, Y., 1990, "Effects of Rib Angle and Orientation on Local Heat Transfer in Square Channels With Angled Roughness Ribs," *Compact Heat Exchangers: A Festschrift for A. L. London*, Hemisphere Publishing Co., pp. 151–167.

Moffat, R. J., 1990, "Experimental Heat Transfer," *Proc. 9th Int. Heat Transfer Conf.*, Vol. 1, pp. 187–204.

Moody, L. F., 1944, "Friction Factors for Pipe Flow," *Transactions of ASME*, Vol. 66, p. 671.

Taslim, M. E., and Spring, S. D., 1988a, "An Experimental Investigation of Heat Transfer Coefficients and Friction Factors in Passages of Different Aspect Ratios Roughened With 45° Turbulators," *Proc. ASME National Heat Conference*, Houston, TX.

Taslim, M. E., and Spring, S. D., 1988b, "Experimental Heat Transfer and Friction Factors in Turbulated Cooling Passages of Different Aspect Ratios, Where Turbulators are Staggered," Paper No. AIAA-88-3014.

Taslim, M. E., 1990, "Application of Liquid Crystals in Heat Transfer Coefficient Measurement," *Proc. IEEE ELECTROR/90*, Boston, MA.

Taslim, M. E., Bondi, L. A., and Kercher, D. M., 1991, "An Experimental Investigation of Heat Transfer in an Orthogonally Rotating Channel Roughened With 45 deg Criss-Cross Ribs on Two Opposite Walls," ASME JOURNAL OF TURBOMACHINERY, Vol. 113, pp. 346–353.

Taslim, M. E., and Spring, S. D., 1991, "An Experimental Investigation Into the Effects Turbulator Profile and Spacing Have on Heat Transfer Coefficients and Friction Factors in Small Cooled Turbine Airfoils," Paper No. AIAA-91-2033.

Taslim, M. E., Rahman, A., and Spring, S. D., 1991, "An Experimental Investigation of Heat Transfer Coefficients in a Spanwise Rotating Channel With Two Opposite Rib-Roughened Walls," ASME JOURNAL OF TURBOMACHINERY, Vol. 113, pp. 75–82.

Taslim, M. E., and Wadsworth, C. A., 1997, "An Experimental Investigation of the Rib Surface-Averaged Heat Transfer Coefficient in a Rib-Roughened Square Passage," ASME JOURNAL OF TURBOMACHINERY, Vol. 119, pp. 381–389.

Webb, R. L., Eckert, E. R. G., and Goldstein, R. J., 1971, "Heat Transfer and Friction in Tubes With Repeated-Rib-Roughness," *International Journal of Heat Mass Transfer*, Vol. 14, pp. 601–617.

Zhang, Y. M., Gu, W. Z., and Han, J. C., 1994, "Heat Transfer and Friction in Rectangular Channels With Ribbed or Ribbed-Grooved Walls," ASME *Journal of Heat Transfer*, Vol. 116, No. 1, pp. 58–65.

S. Mochizuki

A. Murata

M. Fukunaga

Department of Mechanical
Systems Engineering,
Tokyo University of Agriculture
and Technology,
Koganei, Tokyo, Japan

Effects of Rib Arrangements on Pressure Drop and Heat Transfer in a Rib-Roughened Channel With a Sharp 180 deg Turn

The objective of this study was to investigate, through experiments, the combined effects of a sharp 180 deg turn and rib patterns on the pressure drop performance and distributions of the local heat transfer coefficient in an entire two-pass rib-roughened channel with a 180 deg turn. The rib pitch-to-equivalent diameter ratio P/d_e was 1.0, the rib-height-to-equivalent diameter ratio e/d_e was 0.09, and the rib angle relative to the main flow direction was varied from 30 ~ 90 deg with an interval of 15 deg. Experiments were conducted for Reynolds numbers in the range 4000 ~ 30,000. It was disclosed that, due to the interactions between the bend-induced secondary flow and the rib-induced secondary flow, the combination of rib patterns in the channel before and after the turn causes considerable differences in the pressure drop and heat transfer performance of the entire channel.

Introduction

The inlet gas temperature in modern gas turbine engines continues to rise in response to an ever-increasing demand for better performance. Consequently, turbine blades are subjected to severe thermal operating conditions. Efficient blade cooling has become a necessity in order to ensure the strength and durability of the blades under high temperatures. Forced convection cooling, film cooling, impingement cooling, and combinations of these have been applied to actual high-performance air-cooling of the blades. Forced convective cooling removes the heat that has entered the blade interior by introducing the air from compressors to flow through cooling passages inside the blade.

In current advanced gas turbine blade-cooling systems, as shown in Fig. 1, the cooling airflow passages are of multipass form, where the turbulence promoters (i.e., ribs) are cast onto the two opposite walls of the internal passages. Therefore, the internal cooling passages may be modeled as serpentine passages comprising straight rectangular channels with two opposite rib-roughened walls and 180 deg bends connecting two adjacent straight channels.

Turbulent heat transfer and pressure drop performance in straight passages with repeated ribs have been studied extensively (Han et al., 1985, 1991; Prakash and Zerkle, 1993; Zhang et al., 1994). Turning flow and heat transfer in a sharp 180 deg turn of rectangular cross section with smooth walls have also been actively investigated in the past by a number of researchers (Choi et al., 1989; Chyu, 1991; Besserman and Tranrikut, 1992; Sathyamurthy et al., 1994; Ekkad and Han, 1994; Lau et al., 1994; Murata et al., 1994). Considerable data also exist for the overall performance of the entire cooling channels with 180 deg turns and rib-roughened walls (Chandra et al., 1988; Metzger et al., 1988; Han et al., 1988; Han and Zhang, 1991; Johnson et al., 1994a, b; Zhang et al., 1995; Fann et al., 1994). In spite of all these studies, however, the mechanisms of the pressure drop and heat transfer in a two-pass rectangular channel with rib turbulators have not yet been made clear. To provide information on the optimum combination of rib patterns in the before-turn and the after-turn channels, it is essential to understand the effect of the interactions of the secondary flows induced by ribs and by the sharp turn since it has an appreciable influence on the pressure drop and heat transfer of the entire channel.

The primary objective of the present study was to investigate experimentally the effect of a combination of rib patterns in the before-turn and the after-turn channels on the pressure drop and heat transfer in turbulent flow in a two-pass square channel. Emphasis was placed on examining the interactions of the two secondary flows, one induced by the ribs and the other formed in the turn.

Test Rig and Test Section

The entire experimental setup is schematically illustrated in Fig. 2. It consisted of a two-pass test section with a 180 deg sharp turn, a centrifugal turbofan, a settling chamber, a flow meter, a honeycomb flow straightener and instrumentations for pressure, temperature, and flow rate measurements. Air was supplied to the test section through an unheated smooth entrance duct that is 3 m in length and had the same cross section as that of the test section. The entrance duct served to establish hydrodynamically fully developed flow at the entrance to the test section. The air flow rate was measured by a laminar flow meter installed in a circular flow passage downstream from the settling chamber. Two static pressure ports, one 50 mm upstream and the other 20 mm downstream of the test section, were installed on the side walls of the inlet and exit ducts, respectively. They were connected to a manometer for measuring the static pressure difference from which the pressure drop between the test section inlet and exit was determined.

Figure 3 shows the schematic sketch of the test section. The test section, which was constructed of Bakelite plates (5 mm in thickness), was a two pass channel with a 44 mm × 44 mm square flow cross section (equivalent diameter $d_e = 44$ mm). The length of each of the two straight sections was 396 mm (nine times the channel equivalent diameter). The total length of the entire channel, L, measured along the channel axis was 924 mm. This gave a channel length-to-equivalent-diameter ratio $L/d_e = 21$. The distance between the two inner walls of the first and second straight pass was equal to d_e or 44 mm. From now on, the straight passes before the turn and after the turn will be called "the first pass" and "the second pass," respectively.

Contributed by the International Gas Turbine Institute and presented at Cogen-Turbo Power, Vienna, Austria, August 23–25, 1995. Manuscript received by the International Gas Turbine Institute May 15, 1995. ASME Paper No. 95-CTP-3. Associate Technical Editor: C. J. Russo.

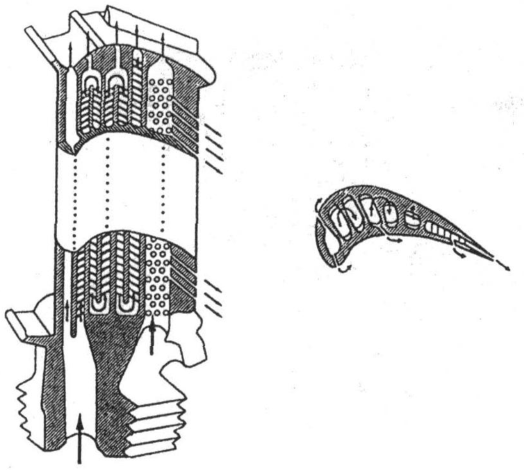

Fig. 1 Internal coolant passages of modem multipass turbine blade

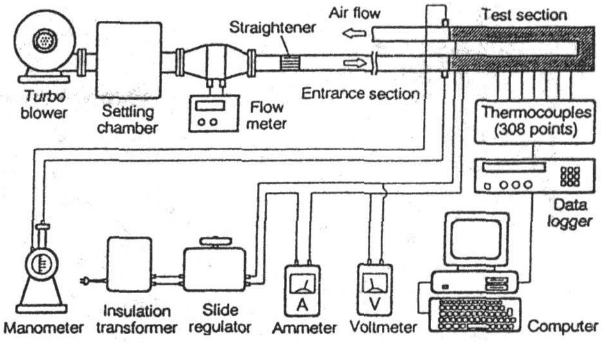

Fig. 2 Schematic of test setup

All the inside surfaces of the two straight passes of the test channel, as well as those at the 180 deg turn between them, were covered with super-invar-sheet heaters 0.05 mm thick. By applying an electric current to the sheet heaters, uniform heat flux conditions were realized. The outside surface of the entire test section was covered with fiberglass to minimize heat losses to the environment. The distribution of heating-surface temperature, T_w, was measured by means of 308 K-type (alumel-chromel) thermocouples (0.1-mm-dia), which were attached directly to the backsides of the heating sheets through spot resistance welding. K-type thermocouples were also installed at the entrance and exit of the heat transfer test section to measure the inlet and outlet air temperature, while flow mixing screens were provided at the exit of the test channel to get the bulk-mean air temperature. The locations of the thermocouples for the measurements of heating-surface temperature are indicated in Fig. 3. All thermocouple outputs were fed into a microcomputer for processing.

Rib turbulators, which comprised commercially available 4-mm square brass rods, were glued using double-stick tape (0.05 mm thick) onto the right and left surfaces of the two straight passes. The ribs were aligned such that all the ribs on the left and right walls were symmetric with each other with respect to the vertical center plane. The rib height-to-equivalent diameter ratio and the rib pitch-to-equivalent diameter ratio were $e/d_e = 0.09$ and $P/d_e = 1.0$, respectively. The rib angle with respect to the main flow direction was varied from 30 to 90 deg with an interval of 15 deg. No rib was installed in the turn region.

Figure 4 illustrates the relationship between the main flow direction and the rib orientations. If the rib angle, ϕ ($0 \leqq \phi \leqq 90$ deg) with respect to the main flow direction, was positive in the counterclockwise direction, the case was labeled "*P*" (meaning positive). Otherwise, it was labeled "*N*" (meaning negative). The rib patterns were determined by (*N* or *P*) and ϕ.

Figure 5 illustrates ten different rib arrangements (i.e., combinations of rib patterns in the first and second passes) tested in the present study. The labeling system was adopted to distinguish the rib arrangement using combinations of two characters out of the three, *P*, *N*, and *S*, where "*S*" means smooth surface or rib-free passes. The first and second characters indicate the rib pattern in the first and second passes, respectively. For example, "*NP*" arrangement refers to the channel whose first pass has the ribs of "*N*" pattern, while the second pass has those of "*P*" pattern.

Table 1 gives a total of 23 combinations of rib angle and rib pattern used in the pressure drop measurements. All angled ribs of other than $\phi = 90$ deg were in-line and the ribs with $\phi = 90$ deg were tested for both in-line and staggered arrangements. "stg" and "inl" for $\phi = 90$ deg represent "staggered" and "in-line" arrangements of the ribs, respectively. Four combinations of rib patterns designated by double circles (◎) in Table 1 were selected for heat transfer experiments.

Data Reduction

The Reynolds number was defined based on the channel equivalent diameter, d_e, as:

$$\mathrm{Re} = u_m d_e / \nu \tag{1}$$

where u_m and ν are mean velocity in the channel and kinematic viscosity, respectively. The range of the Reynolds number of the present investigation extended from 4000 to 30,000.

The friction factor, f, was defined as:

$$f = 2\Delta p (d_e/L)/(\rho u_m^2) \tag{2}$$

Nomenclature

a = side length of the square channel
A_c = cross-sectional area of the channel $= a^2$
A_h = heater-surface area
C_p = specific heat of air
d_e = equivalent diameter $= a$
e = rib height
f = friction factor, Eq. (2)
h = local heat transfer coefficient
h_r = regionally averaged heat transfer coefficient
h_m = averaged heat transfer coefficient for entire channel
k = thermal conductivity of air
L = total length of the channel
$\dot{M}$ = air mass flow rate
Nu = Nusselt number
P = rib pitch
Pr = Prandtl number of air
$\dot{q}_w$ = wall heat flux
Re = Reynolds number, Eq. (1)
T_b = local bulk mean temperature of air
T_{in} = test section inlet air temperature
T_{out} = test section outlet air temperature
T_w = wall temperature
u_m = mean air velocity in the channel $= \dot{V}/A_c$
$\dot{V}$ = volumetric flow rate of air
z = distance measured along the channel axis
Δp = pressure drop across the entire test channel
ν = kinematic viscosity of air
ϕ = rib angle with respect to mean flow direction
ϕ_0 = maximum friction rib angle
ρ = density of air

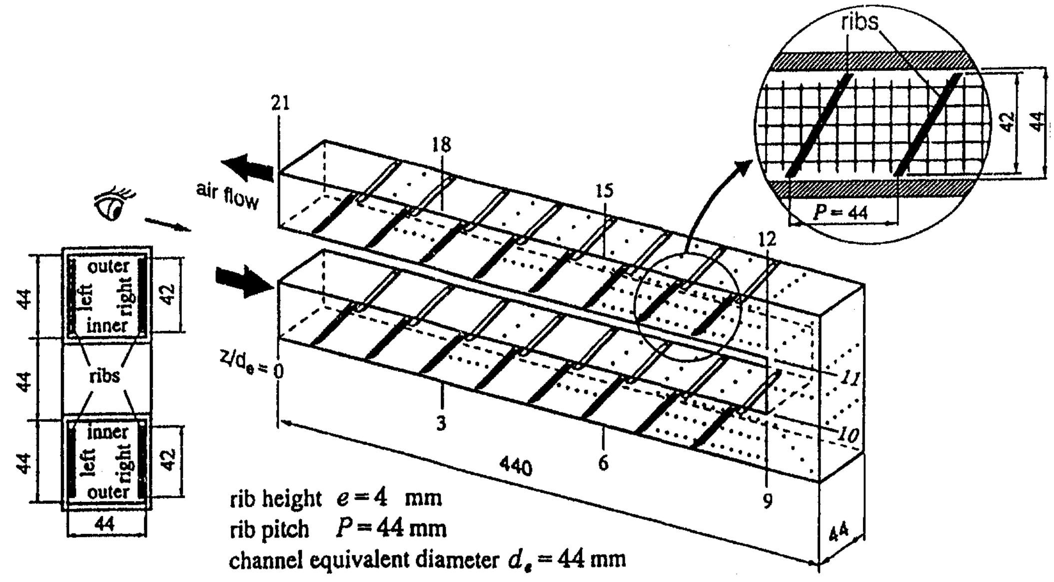

Fig. 3 Structure of test section and locations of ribs and thermocouples

where Δp was the pressure drop across the entire passage and L was the distance from the inlet to the outlet measured along the centerline of the test section. The pressure drop measurements were conducted under isothermal (nonheating) conditions.

The wall heat flux was calculated from the energy balance as:

$$\dot{q}_w = \dot{M}C_p(T_{\text{out}} - T_{\text{in}})/A_h \qquad (3)$$

where T_{in} and T_{out} were the inlet and outlet bulk air temperatures, respectively, and A_h heater-surface area. The local bulk air temperature $T_b(z)$ increases linearly with axial distance z. It was calculated from:

$$T_b(z) = T_{\text{in}} + 4az\dot{q}_w/(\dot{M}C_p) \qquad (4)$$

The local heat transfer coefficient was calculated from:

$$h = \dot{q}_w/(T_w - T_b) \qquad (5)$$

The regional-averaged heat-transfer coefficient was defined as:

$$h_r = \dot{q}_w/\Delta T_r \qquad (6)$$

where ΔT_r was the averaged-temperature difference between the heating wall and the bulk air temperature in the region. The averaging of the local temperature difference was area-weighted.

The average heat transfer coefficient for the entire test channel was calculated from:

$$h_m = \dot{q}_w/\Delta T_m$$

where ΔT_m was the averaged temperature difference between the wall and the bulk air for the region from $z/d_e = 3$ to 19.

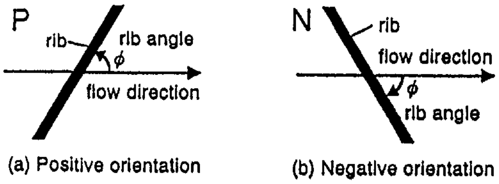

(a) Positive orientation (b) Negative orientation

Fig. 4 Rib orientations to the main flow direction

The Nusselt numbers for local, regionally averaged, and averaged for entire channel are defined respectively as:

$$\mathrm{Nu} = hd_e/k, \ \mathrm{Nu}_r = h_r d_e/k \text{ and } \mathrm{Nu}_m = h_m d_e/k$$

The uncertainties for Δp, L/d_e, and u_m were 2, 1, and 2 percent, respectively. According to the uncertainty analysis method described in *ASME Performance Test Code*, 1986, the maximum uncertainty in f was estimated to be less than 4 percent for Reynolds number greater than 10,000. The uncertainty of $\dot{q}_w$, which was calculated from Eq. (3), was 3 percent. The uncertainty of $(T_w - T_b)$ was estimated to be 7 percent. The maximum uncertainty in the heat transfer coefficient was estimated to be less than 16 percent for Reynolds number greater than 10,000.

Experimental Results and Discussion

Figure 6 shows the results of pressure drop measurements for nine different rib arrangements (from NP to SS shown in Fig. 5). For all these arrangements, the rib angle was fixed at

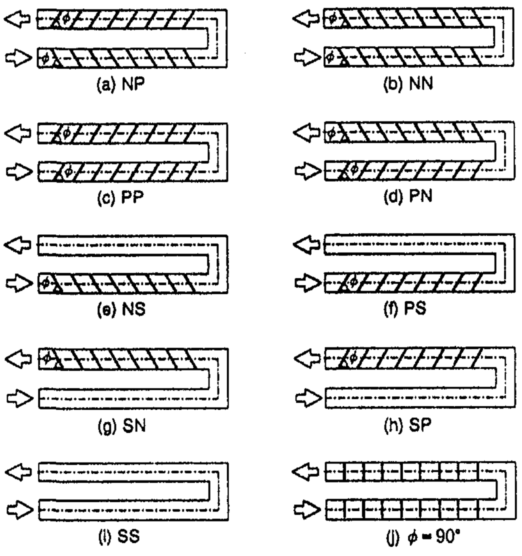

(a) NP (b) NN (c) PP (d) PN (e) NS (f) PS (g) SN (h) SP (i) SS (j) $\phi = 90°$

Fig. 5 Illustrations of rib arrangements tested

Table 1 Combinations of rib angle and rib pattern

pattern / ϕ	NP	NN	PP	PN	NS	PS	SN	SP	SS	stg	inl
no ribs	–	–	–	–	–	–	–	–	○	–	–
30°	○	○	○	○					–		
45°	○	○	○	○					–		
60°	◎	◎	◎	◎	○	○	○	○	–		
75°	○	○	○	○					–		
90°									–	○	○

○ : for pressure drop experiments
◎ : for both pressure drop and heat transfer experiments

$\phi = 60$ deg. Since L and d_e were kept constant for all the test channels in the present study, the value of f directly represents the pressure drop for a given flow rate. An examination of Fig. 6 leads to the following observations:

1 Installation of ribs causes a drastic increase in pressure drop. In the case of Re = 30,000, for example, putting ribs in either the first or the second pass (i.e., NS, PS, SN, and SP) induces 2 to 2.3 times the pressure drop of the smooth channel (SS), and the pressure drops of the channels with ribs in both passes (NP, NN, PP, and PN) become 3 to 3.5 times that of the smooth channel. Since the friction factor for a straight smooth tube, which is calculated from the empirical correlation (Incropera and DeWitt, 1990): $f = 0.184\ \mathrm{Re}^{-1/5}$, is $f = 0.023$ for Re = 30,000, it is understood that the pressure drops of the present rib-roughened two-pass channels with a 180 deg sharp turn are about 8 to 15 times that of the straight smooth tube.

2 Among the four arrangements (SP, NS, SN, and PS), where either the first or the second straight pass is rib-roughened, SP exhibits the highest pressure drop followed by NS, SN, and PS. The remarkable difference in pressure drops between SP and PS indicates that even the same rib pattern results in a different magnitude of pressure drop depending on which pass (the first or the second) it is placed in. If ribs are placed only in the first straight pass, NS pattern gives a higher pressure drop than PS, and if they are placed only in the second straight pass, SP gives a higher pressure drop than SN.

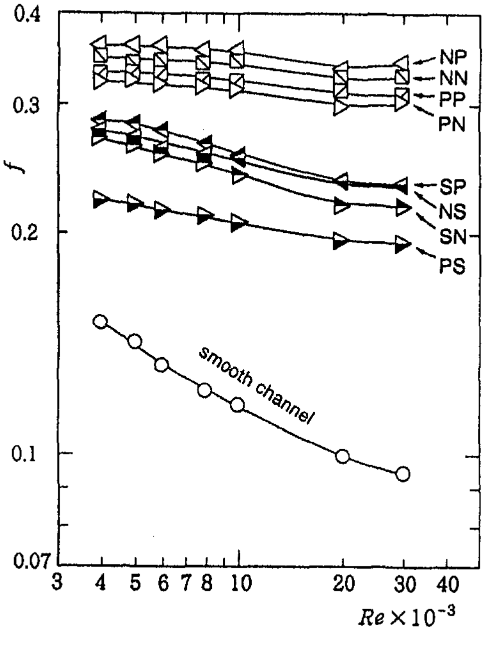

Fig. 6 Friction factor for various rib patterns, $\phi = 60$ deg

3 When both the first and second straight passes are rib-roughened, the highest pressure drop occurs in NP arrangement and the lowest in PN, with NN and PP in between. NP is the combination of SP and NS, which give the highest and the second highest f, respectively, among the four patterns described in item (2) above. On the other hand, PN is the combination of PS and SN, which are the lowest and second lowest patterns, respectively.

In the following, the pressure drop characteristics described above will be discussed based on the visualized secondary flow pattern in the 180 deg turning section. The flow visualization test was conducted by replacing the heat transfer test section with a test section made of transparent Plexiglas. Paraffin mist was used as a tracer and the laser-light sheet method was employed. The Reynolds number was 400. Since the fundamental structure (such as the formation of the circulating cells and the rotating directions of those circulations) of the secondary flow for a low Reynolds number case was considered to be similar to that of a higher Reynolds number case, as will be discussed later, the visualized results for the low Reynolds number case were used to provide the basis in interpreting the pressure drop and heat transfer characteristics.

Figure 7 shows sketches of the flows at each cross section. They were made through the observations of the video-recorded visualization results. Due to the centrifugal force, which acts on the turning flow in the bend, secondary flow is induced, forming a pair of vortices as shown in Figs. 7(a) and 7(b).

In the first pass, oblique ribs placed on opposite walls also create a secondary flow which is considered to consist of a pair of vortices (Han et al., 1985; Han and Zhang, 1991; Taslim et al., 1996). The direction of the secondary-flow-vortex circulation is dependent on the rib orientation or rib pattern. The direction of the vortex circulation created in the first pass by PS pattern coincides with that of the secondary flow formed in the 180 deg sharp turn, while that created by NS pattern gives the opposite circulation to the secondary flow in the 180 deg bend. Switching the direction of circulation causes energy loss through mixing in the flow resulting in an extra pressure drop. This is the reason why the pressure drop is higher for NS pattern, and lower for PS pattern.

The flow behavior at the exit of the turning section is extremely complicated. As shown in Fig. 7(c), more than two pairs of secondary-flow vortices may exist depending on the conditions. Although the present flow visualization results were for the case of Re = 400, the existence of two pairs of vortices (a total of four main circulation cells) was also confirmed by Choi et al. (1989), and Besserman and Tranrikut (1992) through numerical computation of turbulent flow (Re = 25,000) in a square-sectioned 180 deg bend. Besserman and Tranrikut

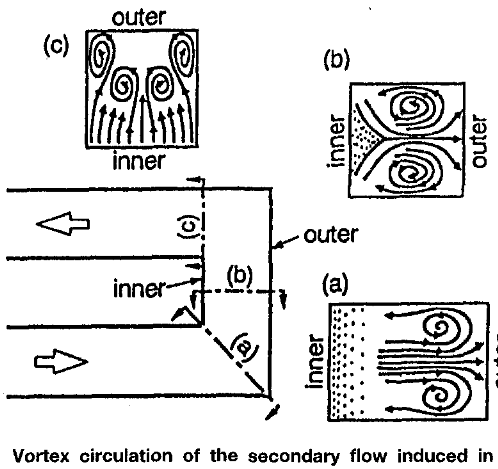

Fig. 7 Vortex circulation of the secondary flow induced in the turn (smooth channel)

(1992) also observed, through flow visualization using fluorescent dye, two and four recirculation cells at the 90 and 180 deg locations, respectively. Figure 7(*c*) indicates that upwash flows, which are the flows over the left and right wall surfaces heading from inner to outer wall, are coexisting with downwash flows. If the upwash flow is stronger than the downwash flow, SP pattern will give higher flow resistance and therefore higher pressure drop than SN pattern. This may explain the present experimental results; SP gives higher f than SN.

Figure 8 illustrates the effect of rib angle ϕ on f when both the first and second passes are rib-roughened. Since the results for NN and PP patterns always fall between those for NP and PN patterns, the data for only NP and PN patterns are plotted in the figure for brevity's sake. Figure 8 indicates that:

1 If ϕ is small, f decreases rapidly with an increase in Re, while it does not change much if ϕ is large. In other words, difference in ϕ causes appreciable difference in f for larger Reynolds numbers, while it does not change much for smaller Reynolds numbers.

2 In any rib arrangements of NP, NN, PP, and PN, and over the entire Reynolds number range tested, f increases with an increase in ϕ until it reaches 60 deg. When ϕ reaches 75 deg however, f for PN arrangement falls, while that for NP arrangement keeps rising.

3 When ϕ is 90 deg, f values for both staggered and inline arrangements fall in between the results for NP and PN arrangements with ϕ = 75 deg.

4 When ϕ is in the region of 30 ~ 75 deg, irrespective of ϕ, NP and PN give the highest and the lowest values of f, respectively.

In Fig. 9, f is plotted against ϕ for the two arrangements, NP and PN, and for Re = 30,000. It is seen from the figure that:

1 For each arrangement, there exists the rib angle, ϕ_0, that gives the maximum to f. The value of ϕ_0 is in the range of 60 to 75 deg, irrespective of NP or PN.

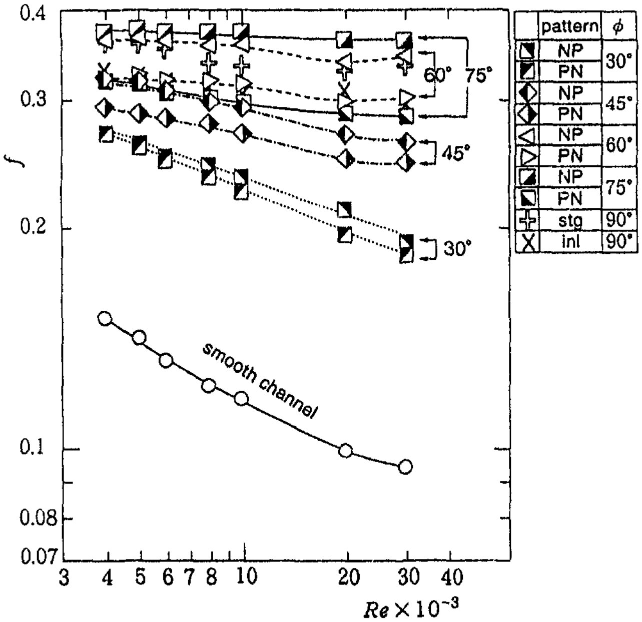

Fig. 9 Friction factor, *f*, versus rib angle, *φ*, for two different rib arrangements, NP and PN

2 Over almost the entire Reynolds number range tested, the PN arrangement shows *N*-shaped change with respect to ϕ, as is seen in Fig. 8 for the cases of Re = 30,000.

3 Difference in the rib arrangements (or the combination of rib-patterns in the first and second passes) may produce a significant difference in the entire pressure drop of the channel. For example, if ϕ = 75 deg, the pressure drop for NP arrangement is about 30 percent higher than that for PN arrangement.

Figure 10 shows a typical example of an axial distribution of the local Nusselt number on the right wall for PN arrange-

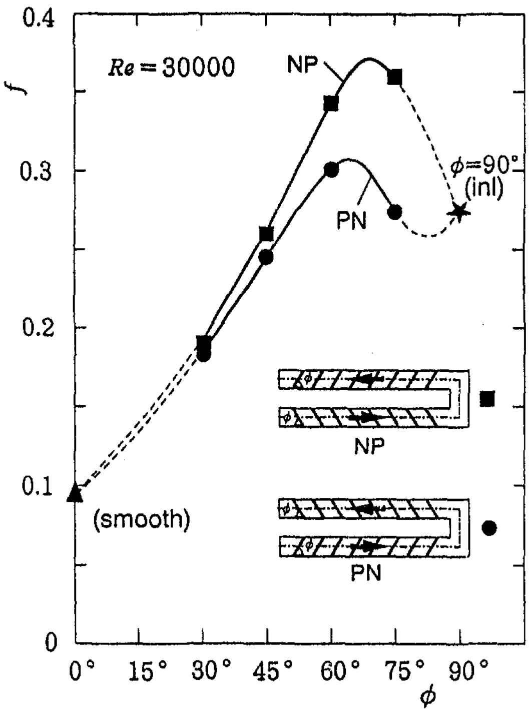

Fig. 8 Effect of rib angle on friction factor

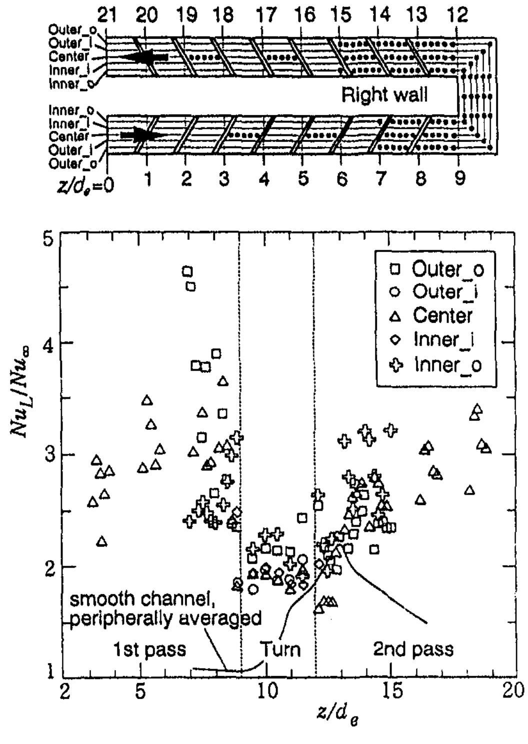

Fig. 10 Axial distribution of local Nusselt number on the right wall of PN-arrangement channel with *φ* = 60 deg and Re = 30,000

ment with $\phi = 60$ deg and for Re = 30,000. The ordinate is the ratio of the measured local Nusselt number, $\mathrm{Nu_L}$, and the Nusselt number, Nu_∞, for the hydrodynamically and thermally fully developed turbulent flow in a long straight circular tube (Kays and Crawford, 1980):

$$\mathrm{Nu}_\infty = 0.022\ \mathrm{Re}^{0.8}\mathrm{Pr}^{0.5}$$

The axial distribution of the peripherally averaged Nusselt number for a smooth channel is also plotted in the figure. The locations of the measurement stations relative to the ribs are also illustrated in the figure.

It is evident from the figure that throughout the channel the values of the ribbed-wall Nusselt number are higher than that for the smooth-channel peripherally averaged value (Murata et al., 1994), indicating the heat transfer augmentation effect brought about by the ribs. The periodic change of the local Nusselt number distribution in the first and second passes (typically represented by the triangular symbols (△), which designate the distribution along the center line) can be seen from the figure. Similar trends have been observed by Han and Zhang (1991) through mass transfer experiments. The Nusselt numbers reach their maximum values at the points of flow reattachment, which occur at some points between adjacent ribs. It should be noted that, in the first pass, the values of Nu along the outer line (□) are always higher than the corresponding values along the inner line (✙). This phenomenon is due to the secondary flow along the rib axes toward the inner wall (Chandra et al., 1988; Taslim et al., 1996). In the second straight pass, however, the difference between Nu values along outer line and those along the inner line is small compared to that in the first straight pass. This may be attributed to the complicated interaction between the two secondary flows (as described earlier): one created in the turn and the other induced by the oblique ribs in the second pass.

The average Nusselt numbers for each of the three regions (i.e., the first straight pass, turning section and the second straight pass) of the channel with $\phi = 60$ deg and Re = 30,000 are shown in Fig. 11. Results are plotted for four different rib arrangements (NP, NN, PP, and PN) as well as for a smooth channel. In the first straight pass, the Nu values for different rib arrangements coincide with each other. This is quite reasonable because the peripherally averaged effects of the secondary flows created by the rib pattern *N* are the same as those formed by the rib pattern *P*, even if the directions of the secondary-flow circulations are opposite to each other. In the turning section, however, the effect of the interaction of the secondary flows appears, resulting in the difference in Nu values. The magnitude of the difference in Nu values, which is caused by the difference of the rib arrangement, becomes a little bit larger in the second pass than in the turning section. NP and PN give the maximum and minimum Nu, respectively, as seen in the figure. The average Nu values in the second pass are higher than the corresponding values in the turning section because of the complicated interactions between the main flow from the turning section and the secondary flow formed by the ribs in the second pass. In the actual turbine-blade cooling channel, the heat transfer area of the second pass is much larger than that of the turning section. Therefore, the entire heat transfer and pressure-loss performances of the cooling channel are dominated by the performances in the second pass rather than the turning section.

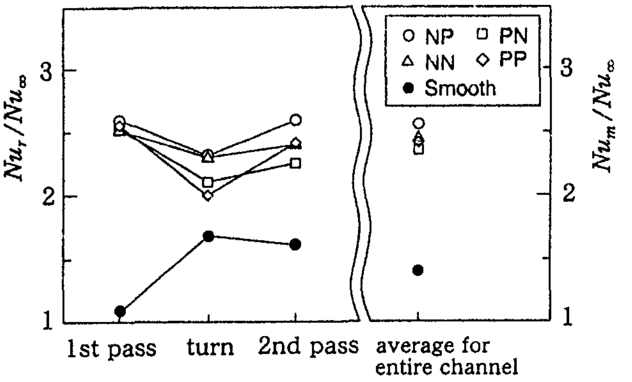

Fig. 11 Average Nusselt numbers for each of the channel regions and for the entire channel, ϕ = 60 deg and Re = 30,000

The averaged heat transfer performance, $\mathrm{Nu}_m/\mathrm{Nu}_\infty$, for the entire channel is also plotted in the right half section of Fig. 11. It is seen that NP arrangement (○) gives the highest mean heat-transfer performance followed by NN(△), PP(◇), and PN(□) arrangements. This order coincides with that of the pressure drop or *f* as was shown in Fig. 6. It is obvious that the enhancement in $\mathrm{Nu}_m/\mathrm{Nu}_\infty$, which is brought about by NP arrangement, is mainly due to the increase of heat transfer in the second pass. Compared to the smooth channel (●), NP arrangement gives about 23 percent more increase in $\mathrm{Nu}_m/\mathrm{Nu}_\infty$ than does PN.

Concluding Remarks

Pressure loss and heat transfer performance in a two-pass rib-roughened channel with a 180 deg turn were studied experimentally. The main findings are as follows:

1 Even the same rib pattern results in a different magnitude of pressure drop depending on the pass (before or after the turn) it is placed on.

2 If ribs are installed only in the first straight pass, NS arrangement gives higher pressure drop than PS, and if they are placed only in the second straight pass, SP gives higher pressure drop than SN (see Fig. 5 for the description of NS, PS, SP, and SN arrangements).

3 When both the first and the second straight passes are rib-roughened, the highest pressure drop appears in NP arrangement, with the lowest in PN.

4 For each arrangement, there exists a rib angle, ϕ_0, that gives the maximum to the pressure drop. The value of ϕ_0 is in the range of 60 to 75 deg, irrespective of NP or PN.

5 Although the average Nu values in the first pass for the rib arrangements of *P* and *N* coincide with each other, they differ one another in the turning section and in the second pass. The rib arrangements NP and PN give the maximum and minimum values of Nu, respectively. This is caused by the interactions of the secondary flows occurring both in the turning section and in the second straight pass.

6 NP arrangement gives the highest averaged heat transfer coefficient for the entire channel, followed by NN, PP, and PN. This order coincides with that of the pressure drop or *f*.

Acknowledgments

The authors would like to thank Mr. K. Tachihara for his assistance in carrying out the experiments.

References

ASME, 1986, *Measurement Uncertainty,* Performance Test Codes ANSI/ASME PTC 19.1-1985, The American Society of Mechanical Engineers, New York.

Besserman, D. L., and Tranrikut, S., 1992, "Comparison of Heat Transfer Measurements With Computations for Turbulent Flow Around a 180 deg Bend," ASME JOURNAL OF TURBOMACHINERY, Vol. 114, pp. 865–871.

Chandra, P. R., Han, J. C., and Lau, S. C., 1988, "Effect of Rib Angle on Local Heat/Mass Transfer Distribution in a Two-Pass Rib-Roughened Channel," ASME JOURNAL OF TURBOMACHINERY, Vol. 110, pp. 233–241.

Choi, Y. D., Iacovides, H., and Launder, B. E., 1989, "Numerical Computation of Turbulent Flow in a Square-Sectioned 180-Deg Bend," ASME *Journal of Heat Transfer,* Vol. 111, pp. 59–68.

Chyu, M. K., 1991, "Regional Heat Transfer and Pressure Drop in Two-Pass and Three-Pass Flow Passages With 180-deg Sharp Turns," ASME *Journal of Heat Transfer,* Vol. 113, pp. 63–70.

Ekkad, S. V., and Han, J. C., 1994, "Local Heat Transfer Measurements Near a Sharp 180° Turn of a Two-Pass Smooth Square Channel With a Transient Liquid Crystal Image Technique," *Proc. Fifth International Symposium on Transport Phenomena and Dynamics of Rotating Machinery (ISROMAC-5)*, Vol. A, pp. 701–716.

Fann, S., Yang, W. J., and Zhang, N., 1994, "Local Heat Transfer in a Rotating Serpentine Passage With Rib-Roughened Surfaces," *Int. J. Heat Mass Transfer*, Vol. 37, No. 2, pp. 217–228.

Han, J. C., Prak, J. S., and Lei, C. K., 1985, "Heat Transfer Enhancement in Channels With Turbulence Promoters," ASME *Journal of Engineering for Gas Turbines and Power*, Vol. 107, pp. 628–635.

Han, J. C., Chandra, P. R., and Lau, S. C., 1988, "Local Heat/Mass Transfer Distributions Around Sharp 180 deg Turns in Two-Pass Smooth and Rib-Roughened Channels," ASME *Journal of Heat Transfer*, Vol. 110, pp. 91–98.

Han, J. C., and Zhang, P., 1989, "Pressure Loss Distribution in Three Pass Rectangular Channel With Rib Turbulators," ASME JOURNAL OF TURBOMACHINERY, Vol. 111, pp. 515–521.

Han, J. C., and Zhang, P., 1991, "Effect of Rib-Angle Orientation on Local Mass Transfer Distribution in a Three-Pass Rib-Roughened Channel," ASME JOURNAL OF TURBOMACHINERY, Vol. 113, pp. 123–130.

Han, J. C., Zhang, Y. M., and Lee, C. P., 1992, "Influence of Surface Heat Flux Ratio on Heat Transfer Augmentation in Square Channels With Parallel, Crossed, and *V*-Shaped Angled Ribs," ASME JOURNAL OF TURBOMACHINERY, Vol. 114, pp. 872–880.

Incropera, F. P., and DeWitt, D. P., 1990, *Fundamentals of Heat Transfer*, 3rd ed., Wiley, p. 474.

Johnson, B. V., Wagner, J. H., Steuber, G. D., and Yeh, F. C., 1994a, "Heat Transfer in Rotating Serpentine Passages With Selected Model Orientations for Smooth or Skewed Trip Walls," ASME JOURNAL OF TURBOMACHINERY, Vol. 116, pp. 738–744.

Johnson, B. V., Wagner, J. H., Steuber, G. D., and Yeh, F. C., 1994b, "Heat Transfer in Rotating Serpentine Passages With Trips Skewed to the Flow," ASME JOURNAL OF TURBOMACHINERY, Vol. 116, pp. 113–123.

Kays, W. M., and Crawford, M. E., 1980, *Convective Heat and Mass Transfer*, 2nd ed., McGraw-Hill, New York, p. 260.

Lau, S. C., Russell, L. M., Thurman, D. R., and Hippensteele, S. A., 1994, "Visualization of local Heat Transfer in Serpentine Channels With Liquid Crystals," *Proc. Fifth International Symposium on Transport Phenomena and Dynamics of Rotating Machinery (ISROMAC-5)*, Vol. A, pp. 411–423.

Metzger, D. E., Fan, C. S., and Plevich, C. W., 1988, "Effects of Transverse Rib Roughness on Heat Transfer and Pressure Losses in Rectangular Ducts With Sharp 180 Degree Turns," Paper No. AIAA-88-0166.

Murata, A., Mochizuki, S., and Fukunaga, M., 1994, "Detailed Measurement of Local Heat Transfer in a Square-Cross-Section Duct With a Sharp 180-deg Turn," *International Heat Transfer Conf.*, Brighton, U. K., Vol. 4, pp. 219–224.

Prakash, C., and Zerkle, R., 1995, "Prediction of Turbulent Flow and Heat Transfer in a Ribbed Rectangular Duct With and Without Rotation," ASME JOURNAL OF TURBOMACHINERY, Vol. 117, pp. 255–264.

Sathyamurthy, P. S., Karki, K. C., and Patankar, S. V., 1994, "Prediction of Turbulent Flow and Heat Transfer in a Rotating Square Duct With a 180 Deg. Bend," ASME Paper No. 94-GT-197.

Taslim, M. E., Li, T., and Kercher, D. M., 1996, "Experimental Heat Transfer and Friction in Channels Roughened With Angled, *V*-Shaped, and Discrete Ribs on Two Opposite Walls," ASME JOURNAL OF TURBOMACHINERY, Vol. 118, pp. 20–28.

Zhang, Y. M., Gu, W. Z., and Han, J. C., 1994, "Heat Transfer and Friction in Rectangular Channels With Ribbed or Ribbed-Grooved Walls," ASME *Journal of Heat Transfer*, Vol. 116, pp. 58–65.

Zhang, Y. M., Han, J. C., Parsons, J. A., and Lee, C. P., 1995, "Surface Heating Effect on Local Heat Transfer in a Rotating Two-Pass Square Channel With 60 deg Angled Rib Turbulators," ASME JOURNAL OF TURBOMACHINERY, Vol. 117, pp. 272–280.

Jenn-Jiang Hwang
Associate Professor,
Department of Mechanical Engineering,
Chung-Hua Polytechnic Institute,
Hsinchu, Taiwan 30067

Tong-Miin Liou
Professor,
Department of Power
Mechanical Engineering,
National Tsing-Hua University,
Hsinchu, Taiwan 30043

Heat Transfer Augmentation in a Rectangular Channel With Slit Rib-Turbulators on Two Opposite Walls

The effect of slit ribs on heat transfer and friction in a rectangular channel is investigated experimentally. The slit ribs are arranged in-line on two opposite walls of the channel. Three rib open-area ratios (β = 24, 37, and 46 percent), three rib pitch-to-height ratios (Pi/H = 10, 20, and 30), and two rib height-to-channel hydraulic diameter ratios (H/De = 0.081, and 0.162) are examined. The Reynolds number ranges from 10,000 to 50,000. Laser holographic interferometry is employed to measure the local heat transfer coefficients of the ribbed wall quantitatively, and observe the flow over the ribbed wall qualitatively. The results show that the slit rib has an advantage of avoiding "hot spots." In addition, the heat transfer performance of the slit-ribbed channel is much better than that of the solid-ribbed channel. Semi-empirical correlations for friction and heat transfer are developed to account for rib spacings and open-area ratios. These correlations may be used in the design of turbine blade cooling passages.

Introduction

Turbine blade cooling is imperative in advanced aero-engines. The extremely hot gases, operating within the turbine section, require turbine blades to be cooled by using cooling circuits or straight passages. These arrangements increase engine efficiency and ensure that blade material has a longer life. To enhance the overall heat transfer inside the turbine airfoils further, turbulence promoters/ribs are often installed on the surfaces of the cooling passages. The ribs break up the viscous sublayer and promote local wall turbulence that, in turn, increases the heat transfer from both the rough and the smooth surfaces. In the past two decades, considerable works have been reported for heat transfer and pressure drop characteristics in channels/pipes with solid-ribbed walls (Burggraf, 1970; Webb et al., 1971; Han et al., 1978; Metzger et al., 1987; Chyu and Wu, 1989; Lau et al., 1991; Liou and Hwang, 1992a, b, 1993). Based on the previous studies, the effects of rib height, spacing, shape, and angle orientation on the heat transfer coefficient and friction factor over a wide range of Reynolds numbers have been well established. Moreover, semi-empirical friction and heat transfer correlations have been developed. However, engineers and designers are ceaselessly seeking ameliorative ribbed surfaces to yield optimum performance. The present study focuses on an improved rib geometry, namely, slit ribs, to apply to turbulent flow in a rectangular channel. It is of interest to determine where the channel with slit rib rougheners can perform better than that with conventional solid rib rougheners.

As for air flow over a solid-ribbed wall, the flow separates at the top edge of the rib, and then reattaches to the channel wall downstream of the rib. A conventional boundary layer and a reverse boundary layer develop from the reattachment region and grow in thickness in opposite directions. High heat transfer occurs in the vicinity of the reattachment region. However, the recirculation cells located adjacent to the upstream and downstream rib faces create the regions where wall heat transfer deteriorates. In the case of slit ribs, part of the flow goes through the rib. An interaction between the main flow and multi-plane-jet flow results in the vigorous mixing of the airflow near the rib and duct wall, and therefore, enhances the heat transfer to the airstream. To characterize the above-mentioned complex flow structures and to measure the surface heat transfer, an efficacious technique of real-time holographic interferometry is utilized. Two types of interference results are presented, i.e., finite-fringe interference for qualitative observation of the flow patterns and infinite-fringe interference for quantitative measurement of the heat transfer coefficients. This study addresses three main issues: First, experiments are conducted to determine the local heat transfer coefficient distributions along the slit-ribbed walls, which can provide an assessment of the possibility of hot spots on the slit-ribbed wall. It is important to know whether the "hot spot" can be obviated when the solid rib is replaced by the slit rib. Second, the heat transfer augmentation and friction penalty in a slit-ribbed channel are compared with those of the solid counterpart. The flow patterns around the slit and solid ribs are quite different. It is questionable whether the channel with slit ribs can provide performance superior to that with solid ribs. Finally, the roughness friction and heat transfer correlations for turbulent flow in a rectangular channel with slit ribs are developed. Based on law-of-the-wall similarity and the application of heat-momentum transfer analogy (Dippery and Sabersky, 1963), the geometrically nonsimilar roughness parameters rib pitch-to-height ratio and rib angle-of-attack were respectively correlated into the roughness functions for turbulent flow in a tube (Webb et al., 1971) and that between parallel plates (Han et al., 1978) with repeated solid ribs. In this work, this concept has been extended to correlate the data for turbulent flow in a rectangular channel with repeated slit ribs, by taking into account the rib open-area ratio.

Experimental Program

Holographic Interferometry. The real-time holographic interferometer is illustrated in detail in Fig. 1. The coherent source used is a 30 mW helium–neon laser (1). The laser beam passes through a shutter, and then is divided into two equal

---

Contributed by the International Gas Turbine Institute and presented at the 40th International Gas Turbine and Aeroengine Congress and Exhibition, Houston, Texas, June 5–8, 1995. Manuscript received by the International Gas Turbine Institute February 4, 1995. Paper No. 95-GT-41. Associate Technical Editor: C. J. Russo.

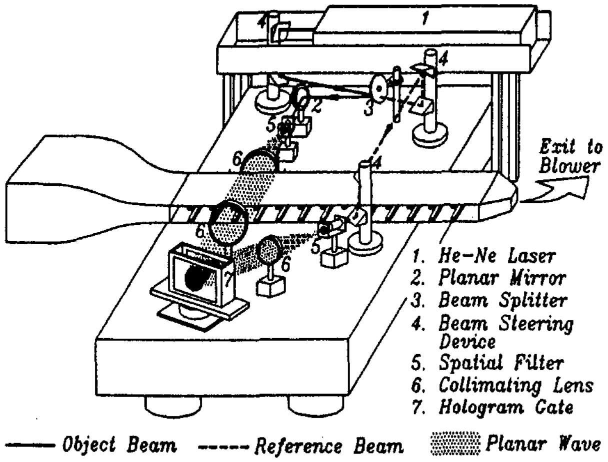

Fig. 1 Schematic drawing of a laser holographic interferometer

components by a beam splitter (3). One beam bypasses the test section and is expanded and filtered by a spatial filter (5). The spatial filter consists of a 20-fold microscope objective, and a 10 μm pinhole. The expanded wave is subsequently collimated to a planar wave by a collimating lens (6). The other beam is also expanded, filtered, and collimated to a planar wave by a spatial filter and a collimating lens. The two planar waves fall onto the holographic plate (7) situated in a liquid gate. Before the ribbed walls are heated, the hologram is exposed by which the comparison wave is recorded. As the planar object wave passes through the heated test section, it is distorted as a result of the refractive index field generated by local temperature variation in the test section. The distorted object wave is continuously interfered with by the comparison beam reconstructed by the reference wave. Consequently, an instantaneous interference field forms behind the hologram plate. The holographic film plate holder associated with a liquid gate provides in-place development of the film plate as required for subsequent real-time work. The photographic emulsion Agfa-10E75 is a suitable recording material in the present work. The instantaneous interference field is digitized by a CCD camera, which allows 512 × 512 pixel resolution with 256 grey levels per pixel and recorded on a VHS videocassette recorder for storage and further image processing.

Test Channel. The open-loop airflow system shown in Fig. 2(*a*) is operated in the suction mode and oriented horizontally. Air is drawn into the settling chamber from the temperature-controlled room; it then traverses the nozzlelike entrance, and enters the test channel. From the test channel exit, the air is ducted to a flow meter, and then to a blower. The blower is situated in a service vestibule outside the laboratory, and the heated discharge is vented from the laboratory.

The configuration and coordinate system of the test channel are illustrated in Fig. 2(*a*). The test channel is 1200 mm long and has a rectangular cross section of 160 mm by 40 mm (YZ plane). The aluminum slit ribs are attached periodically onto the top and bottom channel walls (aluminum plates, 3 mm in thickness) in an in-line manner. The rib angle of attack is 90 deg. Aluminum plates and ribs are adopted in this work because of their high conductivity and machinability. A thin thermofoil (0.18 mm in thickness) is attached uniformly between the alu-

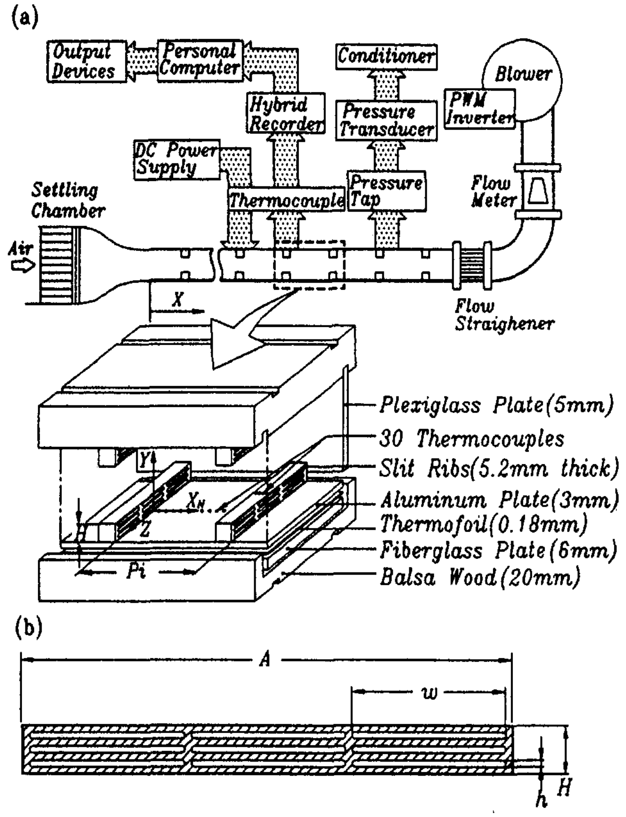

Fig. 2 Sketch of the experimental apparatus, slit-ribbed wall configuration

Nomenclature

A = channel width
B = channel height
c_p = specific heat at constant pressure
De = hydraulic diameter = $2B/(1 + B/A)$
f = friction factor
f_s = friction factor for smooth channel
H = rib height
h = slit height
k_f = air thermal conductivity
L_w = wetted length in one pitch
m_a = mass flow rate
n = number of slits in a rib
Nu = local Nusselt number
$\overline{\mathrm{Nu}}_p$ = average Nusselt number for the ribbed duct
$\overline{\mathrm{Nu}}_s$ = average Nusselt number for the smooth duct
Pi = rib pitch
Pr = Prandtl number
q_{conv} = convective heat flux from the wall
Re = Reynolds number = $U \cdot De/\nu$
St = Stanton number = $\overline{\mathrm{Nu}}_p/\mathrm{Pr} \cdot \mathrm{Re})$
T = air temperature
T_b = local bulk mean temperature of air
$\bar{T}_b$ = average bulk mean temperature of air = $\int_0^{Lw} (T_b dX)/L_w$
T_{in} = air temperature at duct inlet (i.e., room temperature)
T_w = local wall temperature
$\bar{T}_w$ = average wall temperature
U = average channel velocity without ribs
w = slit width
X = axial coordinate ($X = 0$ at channel inlet reference, Fig. 2)
X_N = axial coordinate ($X_N = 0$ at rib rear edge, Fig. 2)
Y = transverse coordinate, Fig. 2
Z = spanwise coordinate, Fig. 2
β = open-area ratio of the slit rib
ν = viscosity of the air
ρ = air density

Subscripts

b = bulk mean
s = smooth
w = wall

minum plate and a fiberglass board (6 mm in thickness), and is controlled by a DC power supply for controllable electrical heating of the test channel. In addition, a sheet of balsa wood (20 mm in thickness) is attached to the backside of the heated plate to prevent heat losses. At each of the above-mentioned interfaces, a thin layer of thermal glue (0.13 mm in thickness) is used to ensure good contact. The total thermal resistance of the glue is less than 2 percent of the total heat dissipation of the thermofoil.

For wall temperature measurements, the region between $X/De = 12$ and 14.2 is instrumented with 30 copper-constantan thermocouples, which are distributed along the spanwise centerline ($Z = 0$) of the heated plate and rib-top surfaces. The junction-beads of the thermocouple (about 0.15 mm in diameter) are carefully embedded in the wall, and then ground flat to ensure that they are flush with the surface. The temperature signals are transferred to a hybrid recorder. All of the data are then sent to a PC-486 computer via a Multi-I/O interface. The preprocessing of the raw data is carried out by using built-in software, by which the nondimensional parameter (Nu) can be calculated. As for the pressure drop measurement, two pressure taps situated at $X/De = 6$ and 17 are connected to a microdifferential transducer. The pressure signals are amplified by a conditioner and then read from a digital readout.

As shown schematically in Fig. 2(b), a number of slits with rectangular cross sections are perforated through the aluminum ribs of 5.2 mm in thickness. The rib open-area ratio (β) is defined as the ratio of the opening (slit) area and the rib facing area, and is expressed as:

$$\beta = (n\cdot w\cdot h)/(A\cdot H) \qquad (1)$$

A total of eight ribbed channels is tested in this work. Two of the channels are roughened by solid ribs. The remaining six channels are roughened by slit ribs. Detailed rib configurations and the associated parametric variations for test channels are listed in Table 1.

Experimental Conditions and Data Analysis

Experimental Conditions. Because fully developed heat transfer characteristics are of interest in the present work, the holograms are taken for the region between $X/De = 12$ and 14.2, in which hydrodynamically and thermally fully developed conditions are attained (Liou and Hwang, 1992b). Two dimensionality of the actual temperature field, thermal boundary conditions of the test section, and an analysis of the interference fringe have been described in detail by Liou and Hwang (1992a).

Heat Transfer Coefficient. The entire temperature field is revealed by the infinite-fringe interferometry, and subsequently enables the calculations of local heat transfer coefficients of the heated surface. The convection heat transfer coefficient is described in terms of the local Nusselt number Nu, which is defined as

$$\mathrm{Nu} = -(dT/dY)_w\cdot De/(T_w - T_b) \qquad (2)$$

where the air temperature gradient $(dT/dY)_w$ is determined by curve fitting, based on a least-squares method through the near wall values for temperature and fringe shift (Liou and Hwang, 1993); T_w is read from the thermocouple output; and T_b is calculated from an energy balance, $T_b = T_{in} + Q(m_a\cdot c_p)$, where Q is the quantity of heat given to air from entrance to the considered cross section of the duct and can be obtained by the integrated form of $\int_0^{Lw} [k_f\cdot(dT/dY)_w\cdot A]\cdot dX$. The maximum uncertainty of the local Nusselt number is estimated to be less than 6.5 percent by the uncertainty estimation method of Kline and McClintock (1953).

Table 1 Configurations of ribs on channel walls

Case	Rib Configuration				PR	H/De
	Type	Slit No. n	Slit Dimension w x h	β		
1	Slit	9	50x0.45mm^2	24%	10	0.081
2	Slit	9	50x0.70mm^2	37%	10	0.081
3	Slit	9	50x0.85mm^2	46%	10	0.081
4	Slit	9	50x0.85mm^2	46%	20	0.081
5	Slit	9	50x0.85mm^2	46%	30	0.081
6	Slit	15	50x1.05mm^2	46%	10	0.162
7	Solid	0	0	0	10	0.081
8	Solid	0	0	0	20	0.081

The average Nusselt number obtained by an energy balance method, and can be evaluated by the following equation:

$$\overline{\mathrm{Nu}}_p = q_{\mathrm{conv}}\cdot De/[k_f\cdot(\bar{T}_w - \bar{T}_b)] \qquad (3)$$

where q_{conv} is the convective heat flux from the ribbed wall, and is estimated by subtracting the heat losses from the supplied electrical input. Note that the q_{conv} is based on the smooth wall surface (Liou and Hwang, 1992a). The maximum uncertainty of $\overline{\mathrm{Nu}}_p$ is estimated to be less than 9.8 percent. To achieve a compact presentation with insight, the Nusselt numbers of the present study are normalized by the Nusselt number for fully developed turbulent flow in smooth circular tubes correlated by Dittus–Boelter as:

$$\mathrm{Nu}/\overline{\mathrm{Nu}}_s = \mathrm{Nu}/(0.023\cdot\mathrm{Re}^{0.8}\cdot\mathrm{Pr}^{0.4}) \qquad (4)$$

Friction Factor. The friction factor of the periodic fully developed flow is expressed as:

$$f = [(-\Delta P/\Delta L)\cdot De]/(\rho\cdot U^2/2) \qquad (5)$$

where the pressure gradient, $\Delta P/\Delta L$, is evaluated by taking the ratio of the pressure difference and the distance between two pressure taps. The maximum uncertainty of f is estimated to be less than 7.3 percent.

Roughness Functions. The friction data for turbulent flow in a rectangular duct with two opposite ribbed walls can be correlated by modified equations (Han, 1988; Liou and Hwang, 1993):

$$R(H^+) = (f/8)^{-1/2} + 2.5\ \ln\{(2H/De)\cdot[2A/(A+B)]\} + 2.5 \qquad (6)$$

where

$$H^+ = (H/De)\cdot\mathrm{Re}\cdot(f/8)^{1/2} \qquad (7)$$

Similarly, heat transfer data for fully developed turbulent flow in a rectangular channel with two opposite ribbed walls can be correlated by the following equations (Han, 1988):

$$G(H^+, \mathrm{Pr}) = (f/8)^{1/2}\mathrm{St} + 2.5\ \ln(2H/De) + 2.5 \qquad (8)$$

In the present data reduction program, Eqs. (6)–(8) are used to calculate the friction roughness function $R(H^+)$ and the heat transfer roughness function $G(H^+, \mathrm{Pr})$.

Results and Discussion

Interference Patterns. Due to the space limitations, only five representative interferograms are presented in this paper.

Figures 3(*a*) – (*c*) and (*d*) – (*e*) show the finite-fringe and infinite-fringe interferograms, respectively. Figure 3(*a*) shows a reference interferogram with an uniform temperature distribution (without heating) in the field. The fringes are parallel, and equally spaced. The disturbed finite-fringe interferograms around the solid and slit (β = 46 percent) ribs is shown in Figs. 3(*b*) and (*c*), respectively, at Re = 30,000. As for the solid rib, the fringes in the regions of the flow over and behind the rib top are highly distorted. This is because fluid turns from the channel wall into the rib contraction, subsequently introduces a strong shear layer from the rib top, and then drives the recirculating flow behind the rib. Another important finding in this interferogram is that the fringes near the channel wall behind the rib are distorted insignificantly, and roughly perpendicular to the channel wall. This signifies that the wall heat transfer is very poor. In the case of the slit rib, the tooth-shaped fringes are found behind the rib, which reveals that fluid passes partly through the rib, and consequently the recirculating cell behind the rib disappears. In addition, the distortion of the fringes near the duct wall after the rib is more notable than that after the solid rib. The transport phenomenon in this region is greatly improved when the slit rib is applied on the wall instead of the solid rib. Additional outcomes will be discussed later for comparison of local heat transfer distributions. Typical instantaneous interferograms showing the full-field isothermal lines in slit- and solid-ribbed channel flows are presented in Figs. 3(*d*) and (*e*), respectively. Because the fringes in the field are highly fluctuating and strongly time dependent, the present calculation of the local heat transfer coefficient is based on an average of 20 successive and instantaneous interferograms. It should be pointed out that a comparison of the local Nusselt number distributions between the results from 20 and 30 instantaneous interferograms shows only 2 percent in difference. Therefore, a total of 20 interferograms is enough to provide an accurate calculation of the local heat transfer coefficient in the present work.

Local Heat Transfer Coefficient. Typical results showing the local distributions of the local Nusselt number ratio for various β (0, 24, 37, and 46 percent) are presented in Fig. 4 at the same rib height (H/De = 0.081) and spacing (PR = 10). Because no wall temperature data are measured for the upstream and downstream rib faces, only the local Nusselt numbers along the rib-top and channel-wall surfaces are obtained and displayed in Fig. 4. Along the rib top surface, the $\mathrm{Nu}/\overline{\mathrm{Nu}}_s$ distributions start with a local maximum on the upstream corner of the rib due to the initiation of a secondary thermal boundary layer. Then it decreases rapidly because of the development of the thermal boundary layer. The value for the slit rib is slightly lower than that of the solid rib, and it decreases with an increase in β. This is because the rib effective conductivity is reduced as β increases, which is caused by the existence of the slit-slots on the rib. Another reason is that the augmented forced convection by flow acceleration between the rib top surfaces decreases as β increases. In fact, it is readily verified by observing the thinner distortion region of the fringes near the rib top for the slit rib as compared with that for the solid rib (Figs. 3(*b*) and (*c*)). The distribution along the solid-ribbed channel wall has been described in detail by Liou and Hwang (1992a), and is not repeated here. It is noteworthy that the local heat transfer ratio distributions downstream of the rib have similar trends for the present results and those of Tanasawa et al. (1984), upstream of the rib. For the slit-ribbed channel wall, two local maxima are located within the interrib region. The first one is located at the channel wall behind the rib. In the present work the level of turbulence intensity is not determined quantitatively.

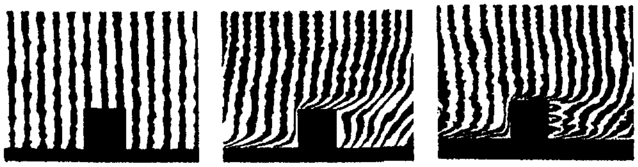

(a) UNDISTURBED FINITE FRINGE PATTERN.

(b) Re=3.0x10^4, H/De=0.081, PR=20, AND β=0.

(c) Re=3.0x10^4, H/De=0.081, PR=20, AND β=46%.

(d) Re=3.0x10^4,H/De=0.081, PR=10, AND β=0.

(e) Re=3.0x10^4,H/De=0.081, PR=10, AND β=46%.

Fig. 3 Examples of holographic interferogram for the ribbed-channel flows

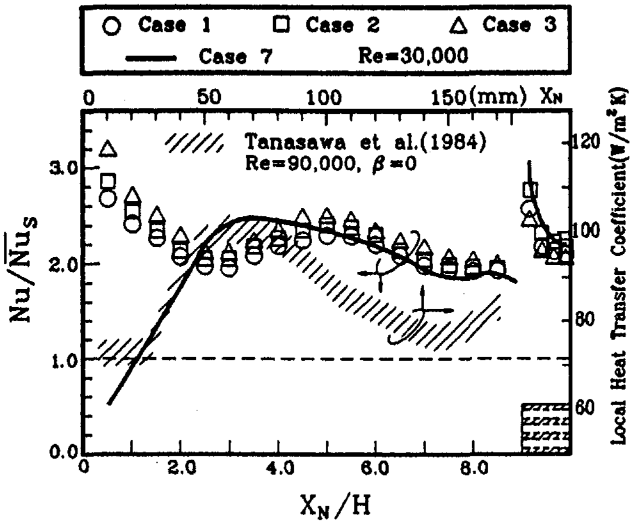

Fig. 4 Local Nusselt number ratio along the rib-top and channel wall surfaces

However, by the qualitative observation of the real-time interferogram, it is readily observed that the fringes behind the slit rib are fluctuating greatly. Therefore, the reason for the high heat transfer in this region may be due to the effect of the intense jet turbulence being generated from the rib rear face, which is more noticeable as β is larger. The second peak located in the middle of the successive ribs is considered to be the reason of an approach of the shear layer from the rib top to the duct wall. Note that the hot-spots ($\mathrm{Nu}/\overline{\mathrm{Nu}}_s < 1$) around the concave corner behind the solid rib do not occur in the slit-ribbed wall.

Average Nusselt Number and Friction Factor. The average Nusselt number ratio for the eight ribbed channels investigated is shown Fig. 5 as a function of Reynolds number. To validate the present experimental procedure and data, the present results are compared to those in previous works. Because no data could be found to compare to the present slit-rib-walled results, the present data are compared to those for the solid-rib-walled results (Han et al., 1978). As shown in this figure, the present data of cases 7 and 8 compare well with Han's data with a reasonable range of rib height and spacing. This comparison

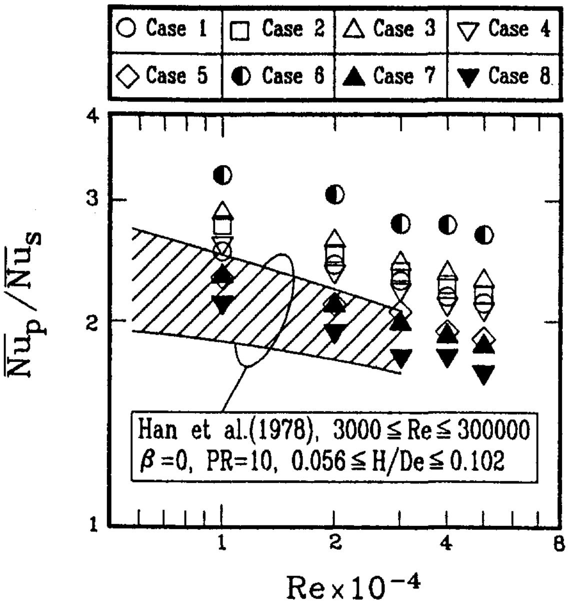

Fig. 5 Average Nusselt number ratio versus Reynolds number

confirms that the present experimental procedure is adequate and the present results are reliable. As can be observed from this figure, the heat transfer augmentation for the slit-ribbed wall (cases 1–3) is in excess of that for the solid-ribbed wall (case 7) with the same rib height (H/De = 0.081) and spacing (PR = 10), typically about 10–30 percent. It is further found that the Nusselt number ratio decreases with increasing Reynolds number, and increases with increasing rib open-area ratio and height.

The fully developed friction factor for the eight ribbed channels investigated is shown in Fig. 6. The friction factor for the slit-ribbed duct is higher than its counterpart for the smooth channel (f_s, Blasius equation), but lower than that for the solid-ribbed channel. It is essentially constant for varying Reynolds numbers. As expected, for a given Reynolds number, the friction factor decreases with increasing β because of less channel blockage for ribs with a larger β. Concerning the effect of the rib height, as shown in Fig. 6, the friction factor increases with increasing H/De. In comparison to the results of the solid-ribbed channel, the values of f are approximately 85, 70, and 65 percent for β = 24, 37, and 46 percent, respectively, at H/De = 0.081, and PR = 10 in the range of the Reynolds number investigated. A comparison of the friction factor between slit- and solid-ribbed channels with similar channel blockages is interesting. As shown in Fig. 6, the case 3 (β = 46 percent, and H/De = 0.081) has a nearly identical channel blockage to that in Han (1984) with β = 0, and H/De = 0.042. It reveals that the solid rib gives a slightly higher pressure drop than the slit rib, which may be due to the higher form drag for flow over the solid-ribbed wall. Nevertheless, the comparison gives a satisfactory agreement between these two works.

Performance Evaluations. In comparing the performance of the ribbed and smooth heat transfer passages, it is necessary to specify the constraints under which the comparison is made. There is a broad variety of constraints that may be employed (Bergles, 1969). In this paper, performance comparisons between the slit- and solid-ribbed channels are made for two sets of constraints: (1) equal airflow rate, and (2) equal blowing power. The comparison of heat transfer coefficients for the equal airflow rate constraint has already been made in Fig. 5. Attention is now turned to the equal blowing power constraint. In Fig. 7, the ratio of $\overline{Nu}_p/\overline{Nu}_s^*$ is plotted against $(f/f_s)^{1/3}\cdot Re$ (denoted as Re* in Fig. 7), where $\overline{Nu}_s^*$ is the average Nusselt number for a smooth channel with the flow rate at which the blowing power is the same as that obtained in the ribbed channel (Liou and Hwang, 1992b). Figure 7 shows that the improvement in the Nusselt number ratio of the slit-ribbed channel is more pronounced than that of the solid-ribbed channel, especially for β = 46 percent. This is reasonable because of the higher heat transfer enhancement (Fig. 5) and lower pressure drop penalty (Fig. 6) for the slit-ribbed channel. Figure 7 further shows that at a lower Reynolds number, both the slit- and solid-ribbed channels perform better than those at higher Reynolds numbers. Therefore, the usage of the slit ribs in the large rib open-area ratio and low Reynolds number range is recommended.

Roughness Friction and Heat-transfer Functions. The wall similarities based on the roughened channel analysis discussed earlier (Dippery and Sabersky, 1963) are used to corre-

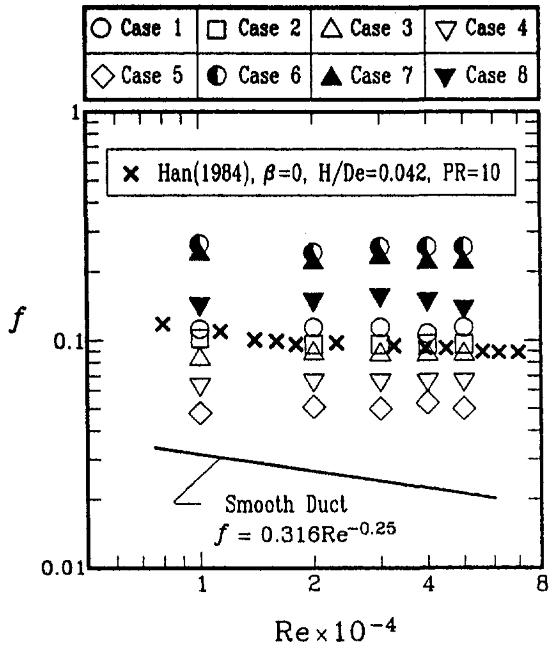

Fig. 6 Friction factor versus Reynolds number

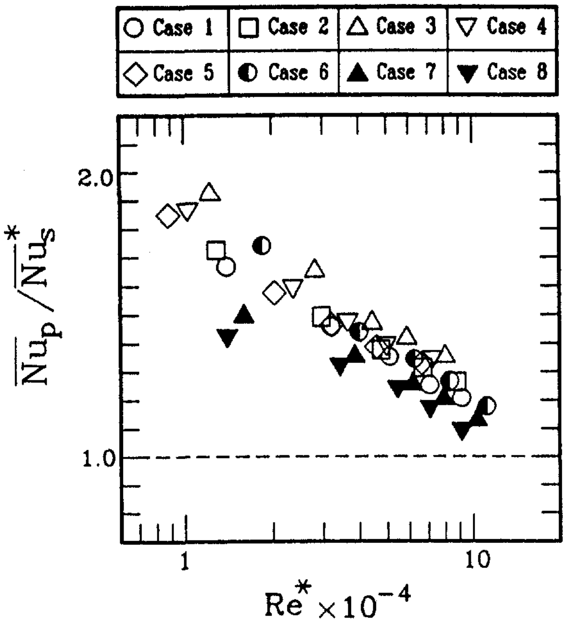

Fig. 7 Performance comparison for the constant blowing power

late the friction and heat transfer data for fully developed turbulent flow in a rectangular channels with two opposite slit-ribbed walls. According to Eqs. (6) (7), and (8), the measured friction factor, average Nusselt number, channel aspect ratio, rib height-to-channel hydraulic diameter ratio, and Reynolds number could be correlated with the friction and heat transfer roughness functions $R(H^+)$, and $G(H^+)$. Correlations of the present friction and heat transfer data shown in Figs. 8 and 9 can be expressed in the following forms:

$$R = 3.45\,(PR/10)^{0.53}\cdot(1-\beta)^{-m} \tag{9}$$

$$G = 3.65(H^+)^{0.28}\cdot(1-\beta)^{m} \tag{10}$$

where $m = 0$ for solid rib; $m = 0.78$ for slit rib. The deviations of Eqs. (9) and (10) are 8 and 5 percent for 95 percent of the total data, respectively. The R in these equations is independent of H^+ for both the slit- and solid-ribbed channels. This denotes that the average friction factor is almost independent of the Reynolds number. As for the solid-ribbed channel, Fig. 8 further shows the comparison of the present friction results (cases 7 and 8, or $m = 0$ for Eq. (9)) with the previous correlation by Webb et al. (1971) for the tube flows with solid ribs. It can be seen from this figure that these two correlations are essentially identical, with a slight change in the coefficient. In addition, as shown in Fig. 9, the heat transfer roughness function for the present solid-ribbed channel (cases 7 and 8) can be reduced as the form of $G = 3.65(H^+)^{0.28}$, which is largely identical to the previous correlation developed by Han (1988). Both these imply that the correlations given above are adequate and the present friction and heat transfer data for the solid-ribbed channels are reliable. Therefore, the data for the slit-ribbed channels (cases 1–6) are reliable. After R and G are correlated experimentally from Eqs. (9) and (10), the friction factor and Stanton number of the present cooling channels with two opposite slit-ribbed walls can be predicted from the combination of Eqs. (6), (7), and (8) for a given H/De, PR, A/B, and Re. These correlations may be helpful in the design of the cooling passages of the turbine blade.

Conclusions

Up to the present time, casting slit rib turbulators inside the cooling passages of a turbine blade has been technically difficult. However, it is important to understand the heat transfer and friction characteristics in channels with slit ribs before the actual application of such channels. In addition, information of flow over slit-ribbed walls is very useful for the general field of heat exchangers. In the present work, the effect of slit rib turbulators on heat transfer and friction in a rectangular channel has been investigated experimentally. The main findings include:

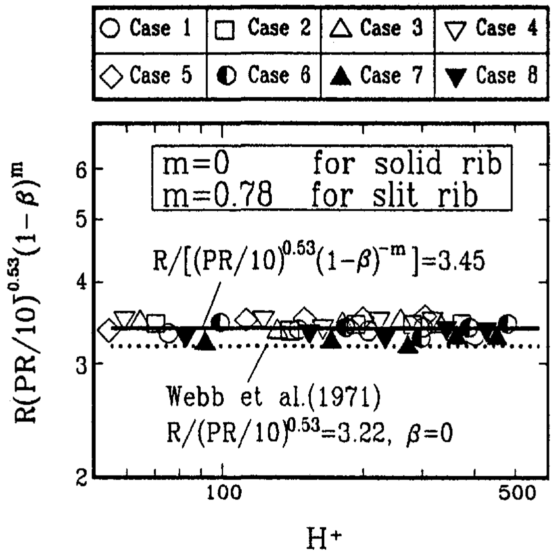

Fig. 8 Roughness friction function versus roughness Reynolds number

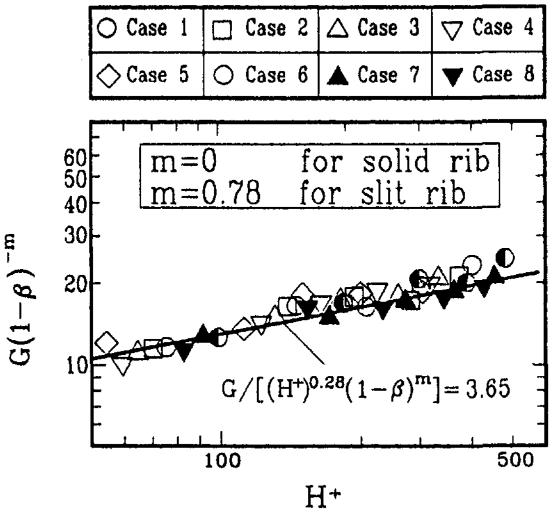

Fig. 9 Roughness heat transfer function versus roughness Reynolds number

1 The local heat transfer coefficient distributions reveal that the "hot spots" occurring in the region around the concave corner after the solid rib do not arise in the corresponding region of the slit-rib geometry.

2 As compared with conventional solid-ribbed geometry, the slit-ribbed geometry gives slightly higher heat transfer enhancement and there is a significantly lower pressure penalty for the same rib height and spacing. Consequently, the slit-ribbed geometry provides superior thermal performance to the solid-ribbed one for fixed blowing power. The heat transfer coefficient increases with an increase in the rib open-area ratio, whereas the reverse is true for the friction factor.

3 Based on the ribbed channel analysis, correlations for roughness friction and heat transfer functions are obtained for the rectangular channel with two opposite slit-ribbed walls. The parameter β, which has not been considered in the past, is taken into account in the present work.

Acknowledgments

This work was sponsored by the National Science Council of the Republic of China under contract number NSC 82-E0113-E-216-31-T.

References

Bergles, A. E., 1969, "Survey and Evaluation of Techniques to Augment Convective Heat and Mass Transfer," *Progress in Heat and Mass Transfer*, Pergamon Press, Oxford, Vol. 1, pp. 331–324.

Burggraf, F., 1970, "Experimental Heat Transfer and Pressure Drop With Two-Dimensional Discrete Turbulence Promoters Applied to Two Opposite Walls of a Square Tube," *Augmentation of Convective Heat and Mass Transfer*, E. E. Bergles and R. L. Webb, eds., ASME, New York, pp. 70–79.

Chyu, M. K., and Wu, L. X., 1989, "Combined Effects of Rib Angle-of-Attack and Pitch-to-Height Ratio on Mass Transfer From a Surface With Transverse Ribs," *Experimental Heat Transfer*, Vol. 2, pp. 291–308.

Dippery, D. F., and Sabersky, R. H., 1963, "Heat and Momentum Transfer in Smooth and Rough Tubes at Various Prandtl Number," *Int. J. Heat Mass Transfer*, Vol. 6, pp. 329–353.

Han, J. C., Glicksman, L. R., and Rohsenow, W. M., 1978, "An Investigation of Heat Transfer and Friction for Rib-Roughened Surfaces," *Int. J. Heat Mass Transfer*, Vol. 21, pp. 1143–1156.

Han, J. C., 1984, "Heat Transfer and Friction in Channels With Two Opposite Rib-Roughened Wall," ASME *Journal of Heat Transfer*, Vol. 106, pp. 774–782.

Han, J. C., 1988, "Heat Transfer and Friction Characteristics in Rectangular Channels With Rib Turbulators," ASME *Journal of Heat Transfer*, Vol. 110, pp. 321–328.

Kline, S. J., and McClintock, F. A., 1953, "Describing Uncertainties on Single-Sample Experiments," *Mechanical Engineering*, Jan., pp. 3–8.

Lau, S. C., McMillin, R. D., and Han, J. C., 1991, "Turbulent Heat Transfer and Friction in a Square Channel With Discrete Rib Turbulators," ASME JOURNAL OF TURBOMACHINERY, Vol. 113, pp. 360–366.

Liou, T. M., and Hwang, J. J., 1992a, "Turbulent Heat Transfer and Friction in Periodic Fully Developed Channel Flows," ASME *Journal of Heat Transfer*, Vol. 114, pp. 56–64.

Liou, T. M., and Hwang, J. J., 1992b, "Developing Heat Transfer and Friction in a Ribbed Rectangular Duct With Flow Separated at Inlet," ASME *Journal of Heat Transfer*, Vol. 114, pp. 565–573.

Liou, T. M., and Hwang, J. J., 1993, "Effect of Ridge Shapes on Turbulent Heat Transfer and Friction in a Rectangular Channel," *Int. J. Heat Mass Transfer*, Vol. 36, pp. 931–940.

Metzger, D. E., Vedula, R. P., and Breen, D. D., 1987, "Effects of Rib Angle and Length on Convection Heat Transfer in Rib-Roughened Triangular Duct," *Proc. ASME/JSME Thermal Engineering Joint Conference*, Honolulu, HI, Vol. 3, ASME, New York, pp. 327–333.

Tanasawa, I., Nishio, S., Takano, K., and Miyazaki, H., 1984, "High-Performance Surface for Forced-Convection Heat Transfer Using Novel Turbulence Promoters," ASME Paper No. 84-HT-69.

Webb, R. L., Eckert, E. R. G., and Goldstein, R. J., 1971, "Heat Transfer and Friction in Tubes With Repeated-Rib Roughness," *Int. J. Heat Mass Transfer*, Vol. 14, pp. 601–617.

Experimental Investigation of Steady and Unsteady Flow Field Downstream of an Automotive Torque Converter Turbine and Inside the Stator: Part I—Flow at Exit of Turbine

B. V. Marathe

B. Lakshminarayana

The Pennsylvania State University,
Department of Aerospace Engineering,
University Park, PA 16802

D. G. Maddock

Staff Development Engineer,
GM Powertrain Group,
General Motors Corporation,
Ypsilanti, MI 48198

The objective of this investigation is to understand the steady and the unsteady flow field at the exit of an automotive torque converter turbine and inside the stator with a view toward improving its performance. The measurements were conducted in a stationary frame of reference using a high-frequency response five-hole probe, and the data were processed to derive the flow properties in the relative (turbine) frame of reference. The experimental data were processed in the frequency domain by spectrum analysis and in the temporal-spatial domain by ensemble averaging technique. The flow properties (e.g., pressure and velocity) were resolved into mean, periodic, aperiodic, and unresolved components. A velocity profile similar to that of a fully developed flow was observed at all radii. The periodic data in relative reference frame revealed a small separation zone near the suction surface in the core region. The rms values of the unresolved component were found to be significantly higher in this region. The secondary flow vectors show underturning, radially inward flow in the entire passage with a small region of overturning near the separation zone. The overall flow at the turbine exit was nearly two dimensional in nature except in the zone of flow separation. The unsteady flow data show that unresolved and aperiodic components dominate the unsteadiness in the pressure, whereas the periodic components dominate the unsteadiness in velocities and flow angles. Pressure and velocity fluctuations were moderate, whereas the flow angle fluctuations were found to be high. The overall flow at the exit of turbine was found to be highly unsteady.

Introduction

The torque converter flow field is very complex. It is three dimensional, viscous, and unsteady due to the close coupling between rotor and stator elements. Additional complexities arise due to differential rotor speeds of the pump and the turbine. The unsteadiness is generated due to potential and viscous interactions at the rotor–rotor and the rotor–stator interfaces. The turbine and the pump passages are narrow, long, and dominated by viscous effects, separation, and secondary flow. The nature and magnitude of the unsteadiness varies with several parameters including spacing between two blade rows, number of blades in both the rotor and the stator, thickness of the blade trailing edge, location of flow separation, secondary flows and other geometric and operating parameters.

There have been several attempts made in recent years to investigate the torque converter flow field (e.g., Brun et al., 1996; Marathe et al., 1996; By and Lakshminarayana, 1995; Gruver et al., 1996; By et al., 1993; Browarzik and Grahl, 1992). A brief review of this is given in Marathe et al. (1995). However, none of the prior investigators report detailed steady and unsteady pressure and velocity at the exit of the turbine and inside the stator. The thrust of this paper is to understand the steady and unsteady flow field at the exit of the turbine and the stator at design operating conditions. The steady flow at the exit of the stator is presented by Marathe et al. (1996). The investigation is carried in a 230 mm torque converter using a high frequency response five-hole probe. The data at speed ratio 0.6 (design speed ratio) are reported in this paper.

Facility and Instrumentation

The torque converter test facility used in this research program is shown in Fig. 1. A detailed description of the experimental facility and static pressure distribution on the stator blade is given by By and Lakshminarayana (1995). This facility has five components: driver and absorption dynamometer, test section, oil system, and control system. The driver dynamometer is a 30-HP DC motor that delivers the precise amount of torque or rpm specified by the control system and drives the pump. The turbine is connected to the absorption dynamometer, which is controlled to maintain constant torque or rpm. The numbers of blades on the pump, turbine and stator are 27, 29, and 19 respectively. The cross section of the torque converter flow path is an elliptical torus formed by pump, turbine, and stator blades. The inner boundary of the torus is called the core and the outer boundary is called the shell. It has been observed that high oil pressure prevents cavitation inside the blade rows, and maintaining elevated temperatures enables stable flow conditions with repeatable performance. Hence, an oil system is used to keep the oil pressure and temperature constant at approximately 14 psi and 60°C, respectively. The oil used is a nonconductive,

---

Contributed by the International Gas Turbine Institute and presented at the 40th International Gas Turbine and Aeroengine Congress and Exhibition, Houston, Texas, June 5–8, 1995. Manuscript received by the International Gas Turbine Institute February 4, 1995. Paper No. 95-GT-231. Associate Technical Editor: C. J. Russo.

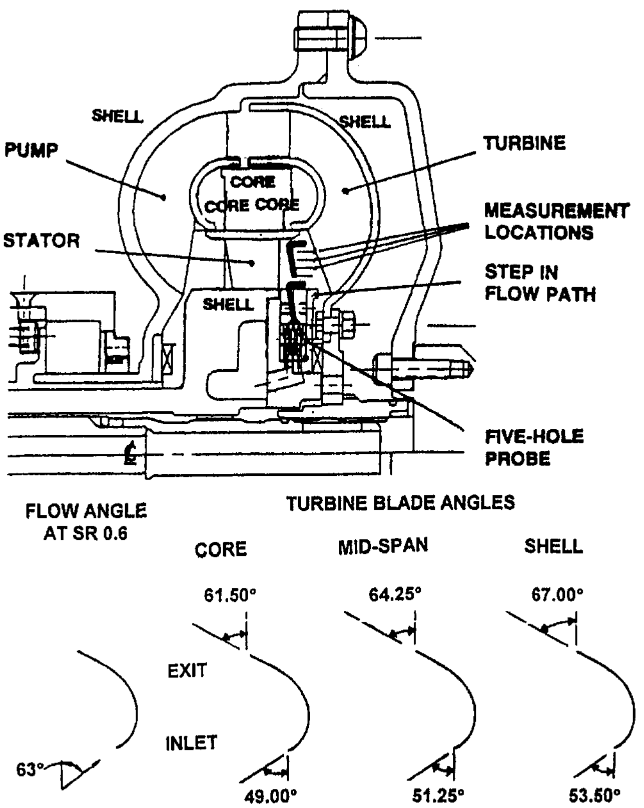

Fig. 1 Experimental facility, measurement locations, and blade angles

noncorrosive oil with a density of 857 kg/m^3 at 60°C. The performance of a torque converter is expressed in terms of torque ratio (TR) and speed ratio (SR), defined in the nomenclature.

Tests were conducted at $SR = 0.0$, 0.2, 0.4, 0.6, and 0.8 to simulate all the conditions the torque converter experiences in actual automatic transmission. The pump rpm at these speed ratios are 1050, 1070, 1090, 1160, and 1300, respectively. The design speed ratio of the torque converter is 0.6. It has a maximum efficiency at $SR = 0.8$ and minimum efficiency at $SR = 0.0$. The data acquired at the exit of the turbine at design speed ratio are presented and interpreted in this paper. The blade geometry, blade angles, and inlet flow angle (obtained from one-dimensional analysis) at this speed ratio, are shown in Fig. 1. The stator is locked for all the measurements. Measurements are carried out at six radial positions and one tangential position at 0.4276 stator axial chords upstream of the stator (or 0.068 turbine core section chord downstream of the turbine trailing edge and 0.203 turbine shell section chord downstream of the turbine trailing edge) as shown in Fig. 1. The nondimensional radial positions at the turbine shell and core will be designated by $H = 0.0$ and 1.0, respectively.

A miniature fast-response five-hole probe (1.67 mm tip diameter) was designed and fabricated to facilitate the measurements of the flow properties upstream and downstream of each of the blade rows. Details of the five-hole probe are shown in Fig. 2. Five miniature pressure transducers were mounted inside the five-hole probe. This allowed extremely small cavity volume between the probe tip and the pressure transducer. The cavity between the probe tip and the pressure transducer was filled with oil to improve the response time of the probe. The tests performed in a hydroacoustic chamber indicate a frequency response of approximately 8 kHz. This frequency response was considered sufficient since the maximum blade passing frequency is 585 Hz. A pressure tap was installed on the stator shell surface (hub) for measuring the hub static pressure. This static pressure was used for normalizing the stagnation and static pressures measured by the five-hole probe upstream and downstream of the stator. The amplified signal from the pressure transducer was acquired and recorded by the DAS-50 data acquisition system. Maximum data acquisition rate of the DAS-

Nomenclature

C = chord length
$(C_{P0})_{\mathrm{REL}} = 2((P_0)_{\mathrm{REL}} - P_{\mathrm{HUB}})/\rho V^2_{\mathrm{REF}}$
$(C_{P0})_{\mathrm{ABS}} = 2((P_0)_{\mathrm{ABS}} - P_{\mathrm{HUB}})/\rho V^2_{\mathrm{REF}}$
$C_{PS} = 2(P_S - P_{\mathrm{HUB}})/\rho V^2_{\mathrm{REF}}$
H = spanwise distance from turbine shell (hub) normalized by the turbine blade span ($H = 0$ at the shell, 1 at the core)
N_{CYC} = number of cycles in a data set
N_{BPC} = number of turbine passages in a cycle
N_{PPB} = number of data points per turbine passage
P = pressure normalized by $\rho V^2_{\mathrm{REF}}/2$
P_{HUB} = reference pressure on the hub
PS, SS = pressure and suction sides
Q_{REF} = reference dynamic head = $\rho V^2_{\mathrm{REF}}/2$
S = blade spacing
SR = speed ratio (turbine rpm/pump rpm)
TR = torque ratio (turbine torque/pump torque)
U = blade speed
V = absolute velocity normalized by V_{REF}
W = relative velocity normalized by V_{REF}
V_{REF} = normalizing velocity $(U_{\mathrm{TIP}_{\mathrm{PUMP}}}\sqrt{1 - SR})$
$\bar{V}_X$ = mass-averaged axial velocity downstream of the turbine
α = pitch angle, $\tan^{-1}(V_r/V_X)$, positive in the radial outward direction
β = yaw angle (measured from the axial direction) = $\tan(V_\theta/V_X)$, positive in the direction of rotation of turbine and pump
ρ = density of the fluid
$(\ )_{\mathrm{RMS}}$ = root mean square values of fluctuating quantities (V, P_0, P_S, α, β)
$(\hat{\ })_{\mathrm{RMS}}$ = blade periodic rms values of fluctuating quantities

Subscripts

1, 2 = inlet and exit of the stator
0, S = total/stagnation, static
ABS = absolute (stator) reference frame
REL = relative (turbine) reference frame
X, R, θ = axial, radial and tangential components
hub, tip = property at the hub and tip, respectively
Max = maximum value
RMS = root mean square value
I, J, K = subscripts defining data point number inside a blade, blade number in a cycle and cycle number, respectively (typically $I = 1-50$, $J = 1-29$, $K = 1-50$)

Superscripts

$-$ = time-averaged value (Eq. (2))
$*$ = ensemble-averaged value (Eq. (3))
$\approx$ = rotor–rotor interaction (RRI) aperiodic component (Eq. (4))
$\hat{}$ = blade periodic component (Eq. (5))
$\sim$ = blade aperiodic component (Eq. (6))
$'$ = unresolved component (Eq. (7))
$=$ = passage average value

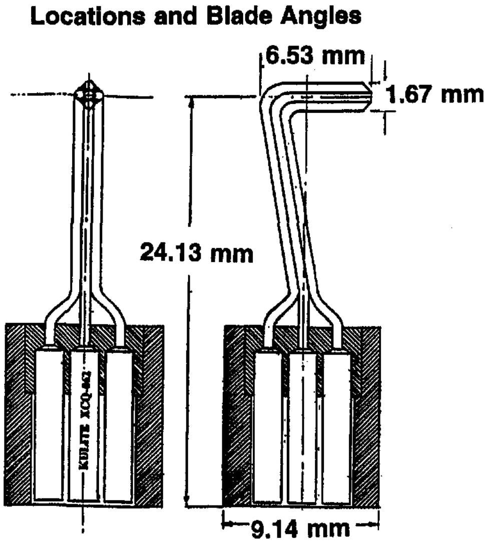

Fig. 2 Transient five-hole probe

50 system is 1 MHz. However, the data were acquired at 16.82 kHz (50 times the turbine blade passing frequency) for *SR* 0.6 to obtain 50 points in each passing turbine blade passage. A signal from the shaft encoder, mounted on the turbine shaft, was used as clocking frequency to maintain the data acquisition rate precisely at 50 times the blade passing frequency of the turbine. The data were downloaded from the DAS-50 memory buffer to a PC-486 where they were processed in both the frequency and the temporal–spatial domain. The static pressure on the stator shell was used as reference pressures for normalizing the total and the static pressures obtained from the five-hole probe.

A thermocouple was installed on the hub of the stator for accurate reference temperature. The probe calibration has an accuracy of ±1 deg in angle measurement. The pressure measurements are obtained to an accuracy of ±0.01 psi. The transducer drift introduces a maximum error of 0.5 percent. This results in a maximum 1–2 percent error in the velocities and 0.5 percent error in the static and total pressures. Corrections to the probe due to the blockage and the pressure gradient are incorporated into the data processing. The maximum cumulative error in the velocity and pressure measurements is estimated to be 2–3 percent.

Signal Processing and Averaging Technique

The method of deriving P_0, P_S, α, β from the five-hole probe data is described by Treaster and Yocum (1979). The unsteady pressure data from the five-hole probe are processed to obtain the instantaneous values of P_0, P_S, α, β. The data were processed using two different methods, described later in the paper. The signals from the pressure transducers, connected to the five-hole probe, were processed digitally and also through a spectrum analyzer to determine the dominant frequencies. The dominant frequency downstream of turbine was found to be that due to the turbine blade passing frequency. It is beyond the scope of this paper to discuss the details of the spectrum analysis.

The signal from the pressure transducer was decomposed to deterministic and unresolved components. Since the deterministic signal is generated by the relative motion between the stator and the rotor blade passages and the blade-to-blade variation of properties, it repeats over every revolution in conventional turbomachinery. However, for the torque converter, the pump and the turbine rotors have different rotational speeds. As a result, flow conditions do not repeat over one revolution of any rotor. Hence, it was necessary to find the period over which the deterministic part of the signal repeats itself. At $SR = 0.8$ the pump and the turbine shaft speeds (revolutions per second) are in 5:4 proportion. Hence, five revolutions of the pump and four revolutions of the turbine are completed in the identical time period. Since the rotational speeds are maintained with high accuracy (less than ±0.05 percent deviation in rpm), it can be assumed that the deterministic part of the signal will repeat after five revolutions of the pump or four revolutions of the turbine. It should be noted, that for speed ratios 0.6, 0.4, 0.2, and 0.0, the pump and the turbine shaft speeds are in 5:3, 5:2, 5:1, and 5:0 proportions, respectively. Therefore, the flow conditions (and relative positions of the blade) would be identical after five revolutions of the pump. The time required to complete five revolutions of the pump will be referred to as "cycle" in this paper. All deterministic signals are considered repeatable over every cycle. Hence, an ensemble-averaging technique was employed over one cycle instead of one revolution. The ensemble-average technique used by Suder et al. (1987) for LDV measurements inside an axial flow compressor was modified to incorporate once per cycle averaging in the torque converter. The technique was also adapted to process the five-hole probe data using a continuous averaging technique instead of the statistical averaging technique used for LDV data. The modified averaging procedure is as presented below.

The pressure signal from the transducer can be divided into four parts:

$$P_{IJK} = \bar{P} + \tilde{\tilde{P}}_{IJ} + \tilde{P}_{IJ} + \hat{P}_I + P'_{IJK} \tag{1}$$

where P_{IJK} is the instantaneous pressure signal measured by the five-hole probe, $\bar{P}$ is the temporal average of the signal, $\tilde{\tilde{P}}_{IJ}$ is the rotor–rotor interaction (RRI) aperiodic component, $\hat{P}_I$ is the blade periodic component, $\tilde{P}_{IJ}$ is the blade aperiodic component, and P'_{IJK} is the unresolved component. It should be noted that the subscript "I" is used for all the points in one blade passage, the "J" subscript is used for all the blade passages in one cycle, and "K" subscript is used for all the cycles in one data set. The blade periodic component $\hat{P}_I$ is generated by the blade passing frequency under consideration. The blade aperiodic component $\tilde{P}_{IJ}$ is due to the deterministic signal at frequencies other than blade passing frequency, and unresolved component P'_{IJK} includes random fluctuations and other fluctuations related to noise and vibration.

The temporal averaging is performed by taking the average of all the data points. That is,

$$\bar{P} = \frac{1}{N_{\text{cyc}}} \frac{1}{N_{\text{bpc}}} \frac{1}{N_{\text{ppb}}} \sum_{K=1}^{N_{\text{cyc}}} \sum_{J=1}^{N_{\text{bpc}}} \sum_{I=1}^{N_{\text{ppb}}} P_{IJK} \tag{2}$$

where N_{cyc} is the number of cycles per data set (1 cycle = 5 revolutions of the pump), N_{bpc} is the number of blade passages per cycle, and N_{ppb} is the number of points per blade passage. The ensemble-averaged aperiodic signal was calculated by using the equation

$$P^*_{IJ} = \frac{1}{N_{\text{cyc}}} \sum_{K=1}^{N_{\text{cyc}}} P_{IJK} \tag{3}$$

The RRI aperiodic signal is calculated as

$$\tilde{\tilde{P}}_J = \frac{1}{N_{\text{ppb}}} \sum_{I=1}^{N_{\text{ppb}}} (P^*_{IJ} - \bar{P}) \quad \text{and} \quad \tilde{\tilde{P}}_{IJ} = \tilde{\tilde{P}}_J \quad \text{for all } I \tag{4}$$

The averaging was performed by calculating blade periodic component by averaging pressure signal over number of blade passages. The equation used can be given as

$$\hat{P}_I = \frac{1}{N_{\text{bpc}}} \sum_{J=1}^{N_{\text{bpc}}} (P^*_{IJ} - \tilde{\tilde{P}}_{IJ} - \bar{P}) \tag{5}$$

The blade aperiodic fluctuating component is then calculated by subtracting the corresponding periodic component and RRI aperiodic component from the ensemble-averaged signal. The equation can be given as

$$\tilde{P}_{IJ} = P^*_{IJ} - \tilde{\tilde{P}}_{IJ} - \hat{P}_I - \bar{P} \tag{6}$$

The unresolved pressure component is then calculated by subtracting both the blade aperiodic and the blade periodic component from Eq. (1). The rms value of the unresolved unsteadiness, which includes random unsteadiness, is given by

$$(P'_{IJK})_{\text{RMS}} = \sqrt{\frac{1}{N_{\text{cyc}}}\frac{1}{N_{\text{bpc}}}\frac{1}{N_{\text{ppb}}}\sum_{K=1}^{N_{\text{cyc}}}\sum_{J=1}^{N_{\text{bpc}}}\sum_{I=1}^{N_{\text{ppb}}}(P'_{IJK})^2} \tag{7}$$

The nature of unsteadiness can thus be classified as deterministic and nondeterministic or unresolved. The deterministic unsteadiness is generated by the rotor–stator or the rotor–rotor interactions and is normally periodic over one revolution/cycle. The deterministic unsteadiness can be further divided into three categories: (1) rotor–rotor interaction (RRI) aperiodic $\tilde{\tilde{P}}_{IJ}$, (2) blade periodic component $\hat{P}_I$, and (3) blade aperiodic fluctuations $\tilde{P}_{IJ}$.

The RRI aperiodic fluctuations $\tilde{\tilde{P}}_{IJ}$ are generated due to the differential relative positions of pump and turbine blades, which are different in every passage in a cycle. The RRI aperiodic component is calculated by taking the average of ensemble-averaged signals in each passage. The blade periodic fluctuations are caused by the variation of flow properties from the suction to the pressure surface in the upstream blade passages. This component is calculated by subtracting the RRI aperiodic component from the ensemble-averaged signal and averaging the resultant component over all the passages in a cycle. The blade aperiodic fluctuations are caused by the fluctuations at shaft frequencies and also due to variations in the passage-to-passage flow due to: (1) manufacturing defects, (2) misalignment between the stator and the rotors, (3) vibrations due to eccentricity of the shaft, and (4) unsteadiness induced by the oil pump. The blade periodic unsteadiness is caused by viscous and potential interactions. Viscous interactions change the magnitude and direction of the absolute flow velocity and hence the incidence angle upstream of the stator blade row. Hence, the stator operates not only at off design inlet angles but also with considerable unsteady flow. The unresolved or nondeterministic unsteadiness is generated by free-stream turbulence and is normally random in nature. However, the unresolved unsteadiness referred to in this paper includes random unsteadiness due to turbulence and other nondeterministic/random unsteadiness generated by sources not periodic over one cycle. Various components of deterministic and nondeterministic unsteadiness derived from this procedure are illustrated in Fig. 3 for an actual signal from five-hole probe.

Two different approaches were used for processing the data to derive the mean, steady (in the relative frame), and fluctuating velocities. In the first method, the instantaneous pressure signals are processed to obtain instantaneous flow parameters (P_0, P_S, α, β, V, etc.). The instantaneous flow parameters are then processed to obtain the mean, periodic, aperiodic, and unresolved components of each flow parameter. However, this data processing method cannot incorporate spatial error (finite dimensions of the probe) corrections. As a result, the quantities obtained by this method could have a large spatial error in a highly unsteady flow field. This method is probably accurate for deriving unresolved unsteadiness. It should be noted, due to high levels of unresolved unsteadiness, approximately 10–15 percent of the total data points were out of the probe calibration range and were eliminated during the averaging process. As a result, the number of averages at each relative measurement location was different. This also introduced error in the ensemble-averaged values as the ensemble-averaged values near the calibration limits were eliminated due to the unresolved component.

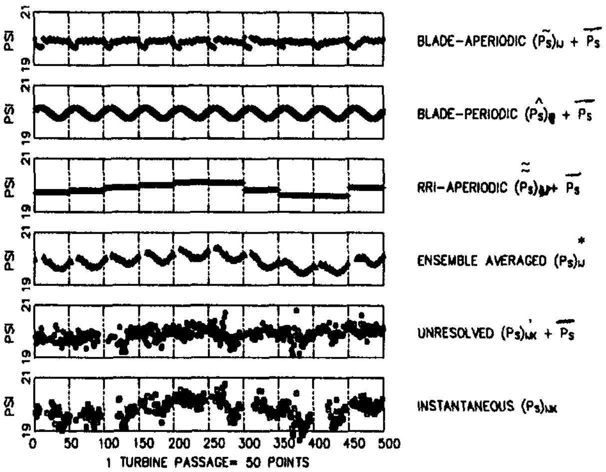

Fig. 3 Illustration of the procedure for decomposing instantaneous signal into various components

In the second method, the instantaneous pressure signals were processed to obtain ensemble (phase lock) averaged values of the pressure, removing the unresolved component from the pressure signal. The ensemble-averaged values were processed with a correction for spatial error to obtain the ensemble-averaged values of each flow parameter (P_0, P_S, α, β, V, etc.). These values are further processed to obtain mean, periodic, and aperiodic components of each flow parameter. Since the unresolved pressure component is removed from the instantaneous pressure signal, the values remain in the calibration range. However, due to large variation in pitch and yaw angles approximately 4 percent of the total data points go out of range. Since these points are near the core wake region, the flow field information could not be obtained inside the core wake region. Another advantage of this method is the possibility of applying the spatial error correction in the data processing. Hence, this method was thought to be more accurate for obtaining periodic and aperiodic components. The data presented in this paper have been processed by using the second method.

The following section discusses the passage-to-passage distribution of the important flow parameters, as well as the radial distribution of the steady and the unsteady flow properties at the exit of the entire turbine passage. Since the data obtained from the five-hole probe were in the absolute (stator, stationary) reference frame, they were further processed to obtain distribution of the flow properties in the relative (turbine, rotational) reference frame. The tangential velocity at each radial location, in the rotating frame of reference, was derived using the equation $W_\theta = U - V_\theta$, $W_X = V_X$, and $W_R = V_R$. All the velocities, in both the relative and the absolute frames of reference, were normalized by V_{REF}. The pressures were normalized by reference dynamic head Q_{REF}.

Turbine Exit Flow in Relative Reference Frame

The distribution of the ensemble-averaged relative total velocity in one quarter of turbine revolution (i.e., 7–8 consecutive blade passages) is shown in Fig. 4. The flow is nearly periodic with aperiodicity in certain regions. The blank regions represent the data points that were out of the calibration range. Approximately 13 percent of total data points are out of range and hence lost at $H = 0.7669$ and $H = 0.6443$. However, since the blank regions are at different relative locations in each blade passage only 4 percent of the total data points are lost after averaging the flow parameters over all the blade passages. The relative positions of low and high momentum regions are periodic. How-

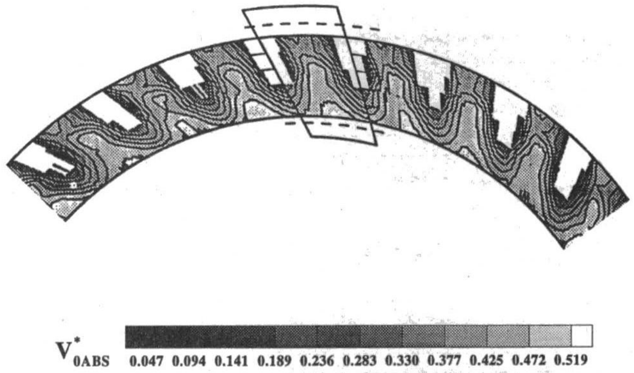

Fig. 4 Ensemble-averaged total velocity contours in one quadrant of turbine (7–8 passages)

ever, the shape and size of these regions change from passage to passage. It should be noted that the relative position of the pump blade passage is different by 0.141 passage widths for each consecutive turbine passage. As a result, the inlet flow in each blade passage is significantly different for each passage. This induces aperiodicity in the turbine exit flow field. The magnitude of the aperiodic component is comparable to the magnitude of the periodic component. However, the study of aperiodic flow properties is beyond the scope of this paper. Hence, passage-to-passage distribution of only periodic values is presented in the paper. However, the radial distribution of rms of aperiodic values is presented for comparison with the rms of periodic and unresolved components. Since the flow field under consideration is the turbine exit flow field, the properties are presented only in the relative (turbine) frame of reference. However, the radial distributions of the mass-averaged quantities are presented in both the relative and the absolute frame of reference to show the radial variation of flow properties as observed in the turbine and in the stator frames of reference. It should be noted that the flow properties change from suction surface to the pressure surface across the stator blade passage due to the inviscid effects. The data presented in this paper were obtained at the midpassage location upstream of the stator blades.

Only a small subset of data is presented and interpreted in this paper. For detailed data at other speed ratio refer to Marathe (1997).

Stagnation Pressure Coefficient at Turbine Exit. The distribution of relative stagnation pressure coefficient $(\hat{C}_{PO})_{REL}$ is shown in Fig. 5. The distribution of relative stagnation pressure shows that the stagnation pressure is nearly uniform near the shell, whereas large tangential gradients are observed near the core region. Two reasons could be cited for this type of distribution. The first reason is that distance between the probe and trailing edge of the turbine decreases with an increase in the radius (see Fig. 1). Hence, at lower radii (near shell), larger downstream distances between the probe and the turbine blade trailing edge cause larger wake decay and this results in smaller variations in the flow properties. The second reason is that the low stagnation pressure zone, near the core suction surface due to a possible corner separation bubble near the trailing edge of the turbine, generates a blockage, which accelerates the flow in midpassage near the core. Hence, relative stagnation pressure show higher gradients near both the pressure and the suction surface.

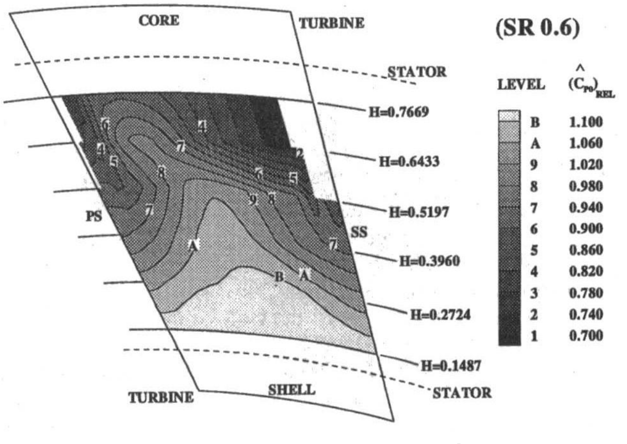

Fig. 5 Coefficient of relative stagnation pressure $(\hat{C}_{PO})_{REL}$ at SR 0.6 at the turbine exit

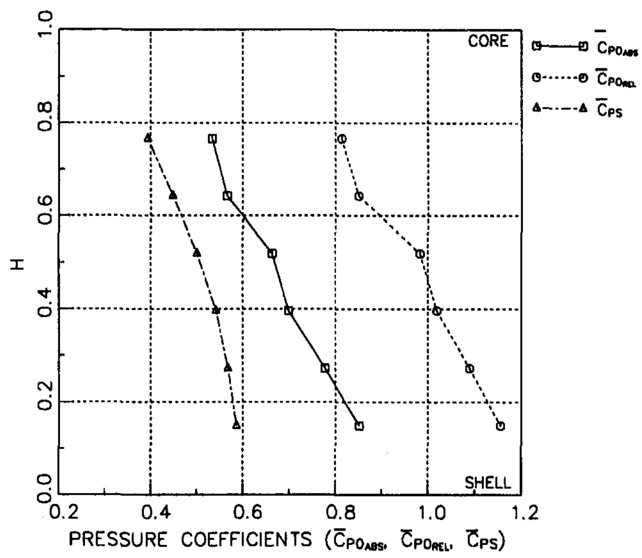

Fig. 6 Radial distribution of time-averaged absolute and relative pressure coefficients at SR 0.6 at the turbine exit

The low relative stagnation pressures observed near the core coincide with the low absolute stagnation pressures in that region (not shown). These low absolute stagnation pressures are attributed to the lower values of the static pressure and the axial velocity in that region as discussed later in the paper. Due to the small absolute flow angles and large relative flow angles, the low-velocity zones in the relative frame of reference remain as low-velocity zones in the absolute frame of reference. Also, high velocities in the relative frame remain as high velocities in the absolute frame. As a result, the velocity and pressure distribution in the relative frame of reference is very similar to that in the absolute frame of reference. The wakes near the shell region are not well defined, as the wakes dissipate before reaching the five-hole probe. The wake near the core has the smaller dissipation as the distance between the trailing edge of the turbine and five-hole probe is very small near the core. However, due to loss of data points in the wake region near the core, no conclusions could be drawn.

The radial variation of the total pressure is high from core to midspan and low from midspan to core. The low stagnation pressures near the core are attributed to the low mass flow and higher losses near the core due to the effect of curvature. The radial distribution of the mass-averaged (integrated across the blade) relative stagnation pressure coefficient (Fig. 6) shows rather smooth linear distribution from shell to core. The magnitude of $\overline{C}_{P0}$ near the core is 20–30 percent lower than the values near the shell. The presence of low relative stagnation pressures near the core is attributed to the low mass flow near the core region typical in mixed flow turbomachines as observed by Johnson and Moore (1983) and Khalil et al. (1976).

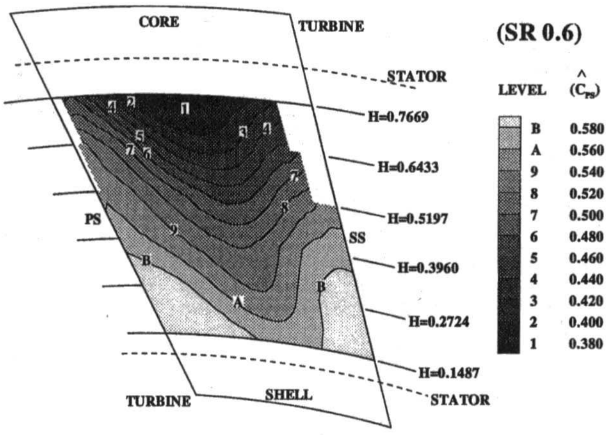

Fig. 7 Coefficient of static pressure ($\hat{C}_{PS}$) at SR 0.6 at the turbine exit

Static Pressure Coefficient at Turbine Exit. The distribution of static pressure coefficient (Fig. 7) at the exit of turbine passage shows nearly uniform tangential distribution of $\hat{C}_{PS}$ near the shell. Lower static pressures are observed at midpassage and higher values inside the blade wakes everywhere from core to shell. This is consistent with the fact that the static pressure drop across the turbine is higher away from blades. Also, the static pressures are generally higher near the pressure surface and lower near the suction surface. This is consistent with the static pressure distribution in a typical turbine blade row where higher static pressures are observed inside the blade wake. The tangential variation of static pressure is higher near the core. The radial variation of static pressure coefficient is higher near the core and lower near the shell.

The radial distributions of passage-averaged values of $\overline{(C_{P0})_{REL}}$ and $\overline{C_{PS}}$ show similar gradients from shell to core (Fig. 6). Radial distribution of mass-averaged static pressure coefficient $\overline{C_{PS}}$ (Fig. 6) shows a smooth variation of static pressure from core to shell. The static pressure decreases with an increase in the radius. This could be attributed to the curvature of the streamlines in meridional, as well as in azimuthal directions, as explained by Marathe et al. (1996).

Velocity Profiles at the Turbine Exit. The distribution of nondimensionalized relative total velocity behind the turbine $(\hat{W}_{01})_{REL}$ is shown in Fig. 8. The velocity gradients in the tangential direction are very small near the shell and significant near the core. The wakes are not well defined. The maximum wake defect near the shell is approximately 10–15 percent of free-stream value near the shell and approximately 40–50 percent of free-stream value near the core. However, due to the loss of data points inside the wakes near the core, the actual maximum velocity defect in the wake defect near the core is unknown. Since the absolute flow angles are small, the streamwise distance between the trailing edge of the turbine and tip of the five-hole probe is very small (less than 1 percent of the chord). Therefore, the wake does not dissipate before it reaches the five-hole probe. The loss of data points near the core can be attributed to the high flow angle variation in the recirculating zone/flow mixing zone. This region is also generated because of the vigorous flow mixing downstream of the separation bubble at the core–suction side corner.

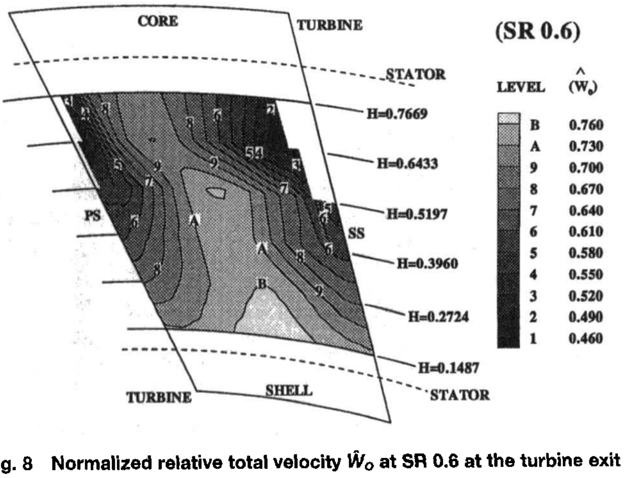

Fig. 8 Normalized relative total velocity $\hat{W}_O$ at SR 0.6 at the turbine exit

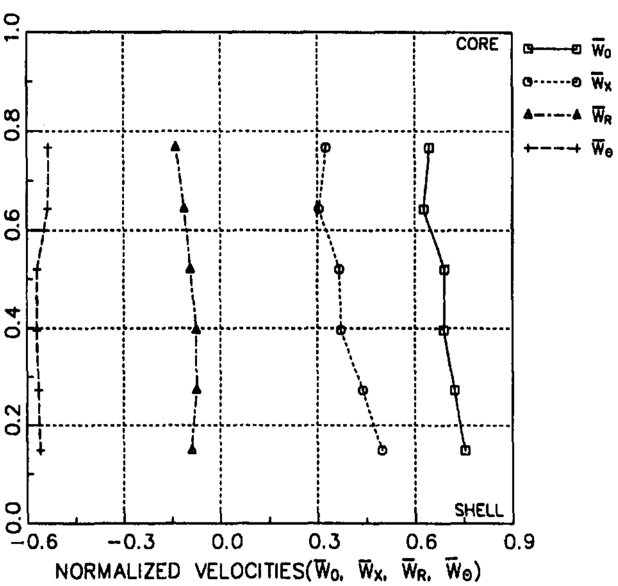

Fig. 9 Radial distribution of time-averaged normalized relative velocity components at SR 0.6 at the turbine exit

A region of low total velocity is observed near the core, which extends from $H = 0.6433$ to $H = 0.7669$ near the suction side. This region could be attributed to the possible corner separation and reattachment of flow inside the turbine passage. A similar region was observed by Brun et al. (1996) for speed ratio 0.8. It should be noted that although, in the turbine reference frame this region was observed between 64 to 77 percent of the blade spacing, in stator reference frame this region is in 72 to 88 percent of blade spacing. The overturning of the relative flow near the core-suction surface causes higher values of relative tangential velocity, which in turn causes smaller values of absolute total velocity near the wake region.

Radial distribution of the mass-averaged nondimensional relative total velocity, $\overline{(W_0)_{REL}}$ (Fig. 9), shows nearly linear variation from shell to core. The relative tangential velocity is nearly uniform from shell to core with slightly lower magnitudes near the core. Also, the magnitude of mass-averaged radial velocity is insignificant as compared to the other two components. Hence, the total velocity distribution is similar to the axial velocity distribution. The radial distribution of mass-averaged axial velocity is nearly linear from shell to core. The passage-mass-averaged axial velocity at the inlet of the stator was found to be 0.07 percent smaller than that measured by the authors at the exit of the stator.

The radial distribution of the mass-averaged radial velocities, as seen in Fig. 9, show significant negative radial velocity near the shell and the core and smaller negative radial velocity near midspan. The radial distribution of tangential velocity shows nearly uniform distribution from shell to core with slightly lower magnitude near the shell. This drop in magnitude is attributed to the small magnitudes of relative tangential velocity near the wake region (not shown). Normally, the low values of relative total velocity at the exit of a turbine represent flow

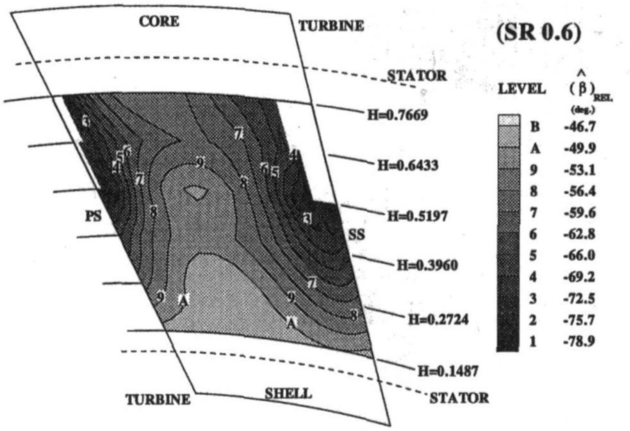

Fig. 10 Relative yaw angle $\hat{\beta}_{REL}$ (in deg) at SR 0.6 at the turbine exit

underturning. However, in the present situation, the distribution of flow angles presented later shows flow overturning in this region. This could be attributed to the very small values of axial velocities near the wake region.

Yaw Angle Profiles at Turbine Exit. The contours of the relative yaw angle (measured from the axial direction) are shown in Fig. 10. As indicated in Fig. 1, the blade outlet angle is -61.5 deg at the shell and -67 deg at the core. The distribution of relative yaw angles is nearly uniform from the core to the shell in the midpassage region. The flow is substantially underturned in this region. The flow overturns near the wakes near both the suction and the pressure surface. This could be attributed to a separation bubble near the suction surface of the trailing edge. The streamlines move around the separation bubble causing the flow to overturn in that region. This is consistent with the lower axial velocities observed in this region. The flow is substantially underturned in all regions except near the wakes. Although the relative yaw angle varies only by approximately ± 15 deg, the absolute yaw angle (not shown) varies by a larger amount. A total variation of ± 30 deg was observed in the absolute flow angles. Variation beyond these values was out of probe range and hence could not be measured. Such large fluctuation in the flow angles causes high unsteadiness in stator blade passages. The effects of these fluctuations are discussed in Part II of this paper.

The radial distribution of average relative and absolute flow angles calculated from the mass-averaged velocities is shown in Fig. 11. The relative yaw angle shows a near linear variation from shell to the core. It varies from -48 deg near shell to -60 deg near core. Thus deviation angles are significant (12 deg near the shell and 7 deg near the core). The absolute yaw angle varies from -10 deg near the shell to $+10$ deg near the core. It can be clearly observed that the radial variations of the mass-averaged pitch and yaw angles are also significant. Thus the flow field is highly three dimensional. Axial flow turbomachinery turbine blades do not show large deviation angles except in the regions of secondary flow, as reported by Zaccaria and Lakshminarayana (1995). In the axial flow turbine rotors the flow remains attached to the blade surface and the effect of secondary flow is restricted to the 20 percent blade span near hub and tip endwalls. It should be noted that although the five-hole probe measurements were taken at 40 percent axial chord upstream of the stator in the torque converter, the thick leading edge of the stator blade generates significant blockage effect at the measurement location (which is approximately two leading edge diameters upstream of the stator leading edge). As a result, the flow deviates before it reaches the five-hole probe and the yaw angle measured is higher than the actual yaw angle at the exit of the turbine. The change in the yaw angle due to the deviation of flow caused by the stator leading edge is estimated to be as high as 7 deg in the relative frame of reference. Hence, the flow deviation angle after the correction is approximately 0–5 deg near the shell. It should be noted that the flow turns by approximately 180 deg in $x-r$ plane and approximately 120 deg in $r-\theta$ plane in a turbine passage. Hence, the flow deviation angle is small compared to the overall turning of the flow. The distribution of the yaw angle shows higher yaw angles in the low-momentum core flow region. Two possible explanations for the higher yaw angles are: (1) A possible separation and reattachment of the flow near the turbine trailing edge on the suction surface near the midspan, would deviate the streamlines toward the suction surface, causing overturning of the flow in the region of low momentum fluid, or (2) presence of a passage vortex can cause a low-momentum region and the overturning in the region of low momentum fluid could be caused by the overturning arm of the passage vortex.

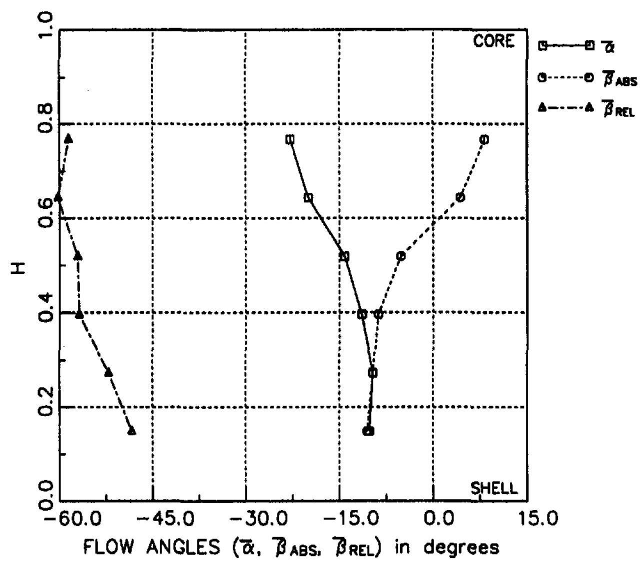

Fig. 11 Radial distribution of time-averaged absolute and relative flow angles at SR 0.6 at the turbine exit

Pitch Angle Profiles at Turbine Exit. The contours of the pitch angle ($\hat{\alpha}$) are shown in Fig. 12. The distribution of pitch angle shows nearly uniform tangential distribution near the shell and large variations in α from the pressure to the suction side near the midspan and the core. The largest variation in the pitch angle is near $H = 0.7669$ where pitch angles are approximately $+6$ deg adjacent to the pressure surface, approximately -41

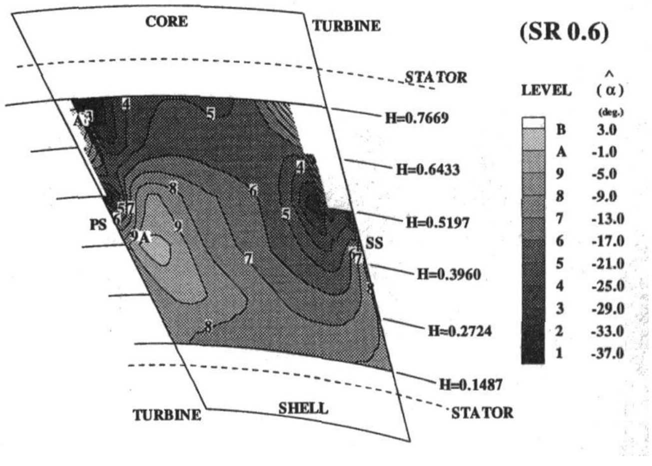

Fig. 12 Pitch Angle $\hat{\alpha}$ (in deg) at SR 0.6 at the turbine exit

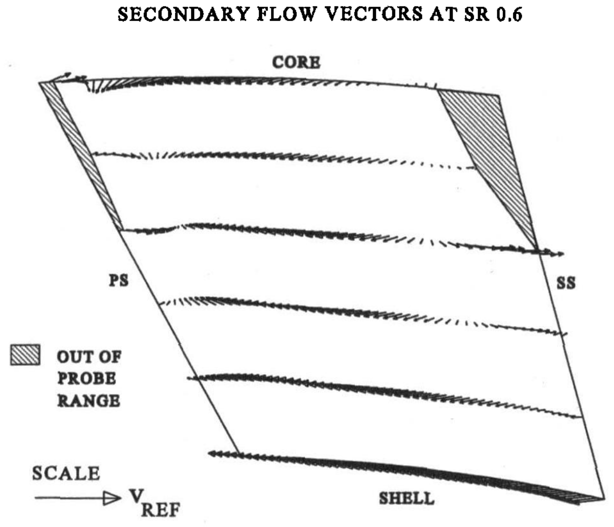

Fig. 13 Secondary flow vectors at SR 0.6 at the turbine exit

deg in a small region near the pressure surface, nearly uniform at −17 deg throughout the passage and approximately +6 deg near the suction surface. These large variations are attributed to the corner separation bubble near core suction surface. The radial velocities are positive in the wake/separation regions due to radial positive pressure gradient. The blockage generated by corner separation bubble deviates the streamlines downward in the near wake region. This causes high negative radial flow in the near wake region.

Secondary Flow Vectors at Turbine Exit. The secondary flow vectors (in the relative frame of reference) at the exit of the turbine blade passage are shown in Fig. 13. The secondary flow pattern in the turbine passage is complex due to the presence of meridional and longitudinal curvature, as well as rotation, as analyzed by Lakshminarayana and Horlock (1973). The presence of streamwise vorticity at the inlet to the turbine (from the pump) causes the secondary flow to deviate considerably from those observed in isolated rotors or cascades. The secondary flow velocity W_{SEC} is defined as

$$W_{\text{SEC}} = \mathbf{i}_\theta[(W_\theta)_{\text{MEASURED}} - (W_\theta)_{\text{IDEAL}}] + \mathbf{i}_\mathbf{R} W_R \tag{9}$$

where ideal tangential velocity $(W_\theta)_{\text{IDEAL}}$ is calculated by using blade outlet angles as ideal flow outlet angles. The secondary flow vectors show flow underturning in the entire passage except near the wake region near the core. The flow deviation angles calculated from mass-averaged velocities from the experimental data show approximately 3 deg deviation near the core, approximately 7 deg deviation near the midspan, and approximately 15 deg deviation near the shell. The flow underturning can be explained using velocity triangles at the exit of the turbine. The flow path cross-sectional area decreases from the turbine exit to the stator inlet. Hence, the flow accelerates in the axial gap between the turbine and the stator. The axial velocity increases, but the tangential velocity remains unaffected. As a result, the flow angle decreases from the turbine exit to the stator inlet. Since the five-hole probe is closer to the turbine trailing edge near the core and farther from the turbine trailing edge near the shell, the effect of angle change due to flow acceleration is higher near the shell and smaller near the core. Therefore, the deviation is higher near the shell and lower near the core.

A small region of flow overturning is observed near the wake region near the core. This flow overturning is probably caused by the separation bubble at the corner of the suction surface near the trailing edge. The flow streamlines bend over the separation bubble and hence have higher flow angle in the small region next to the separation bubble. When the measurement location is far downstream of the blade passage, the overturning is not usually observed as the flow mixing changes the direction of these streamlines. However, for the present case, the measurement location is 1.5 mm downstream of the turbine blade. Hence, the flow overturning is clearly observed near the separation zone near the core. No other significant secondary flow was observed in the entire passage.

Distribution of Unresolved Unsteadiness Downstream of Turbine Rotor

The distribution of rms values of the unresolved component of the flow properties was calculated using the ensemble-averaging technique described earlier in the paper. The rms values at each tangential and radial measurement location were obtained using the equation

$$\widehat{(Q_I)'_{\text{RMS}}} = \frac{1}{N_{\text{cyc}}}\frac{1}{N_{\text{bpc}}}\sqrt{\left(\sum_{K=1}^{N_{\text{cyc}}}\sum_{J=1}^{N_{\text{bpc}}} Q'^{2}_{IJK}\right)} \tag{10}$$

where $\widehat{(Q_I)'_{\text{RMS}}}$ is the blade periodic rms component. Q refers to the derived quantities such as C_{P0}, V_0, α, β, etc. The contour plots of all quantities $\widehat{(Q_I)'_{\text{RMS}}}$ are presented in this section. The rms values of velocity components are normalized by the local periodic component of the total velocity. The rms values of the pressures are normalized by the local dynamic head $(\frac{1}{2}\rho V_0^2)$. The radial distribution of the rms values of each of the unsteady components (periodic, aperiodic and unresolved) downstream of the turbine (upstream of the stator) are also presented in this section. The rms values in the radial distribution plots are normalized by the reference velocity or reference dynamic head. All the quantities presented here are in the absolute frame of reference. These quantities represent the unsteady flow properties perceived by the stator.

Distribution of rms Unsteadiness in Absolute Stagnation Pressure and Static Pressure. The distribution of the rms values of the unresolved component of absolute stagnation pressure coefficient is shown in Fig. 14. The values are normalized by the local dynamic head. The variation of the stagnation pressure coefficient is significant. In the midpassage region near the core the rms values are small (approximately 20–24 percent of the local dynamic head). The rms values of stagnation pressure fluctuations increase to approximately 62 percent of local dynamic head near the core. The higher values of unsteadiness near the core can be attributed to the following two factors: (1) As the probe tip is closer to the turbine trailing edge near the

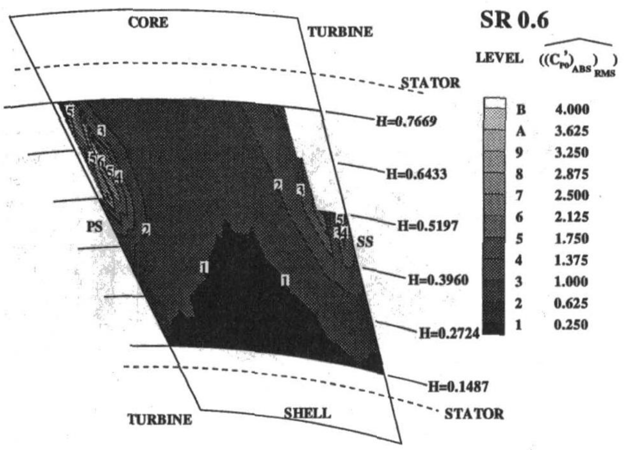

Fig. 14 Distribution of blade periodic rms value of fluctuations in unresolved absolute stagnation pressure coefficient $\widehat{((C'_{P0})_{\text{ABS}})_{\text{RMS}}}$ normalized by local absolute dynamic head at SR 0.6 at the turbine exit

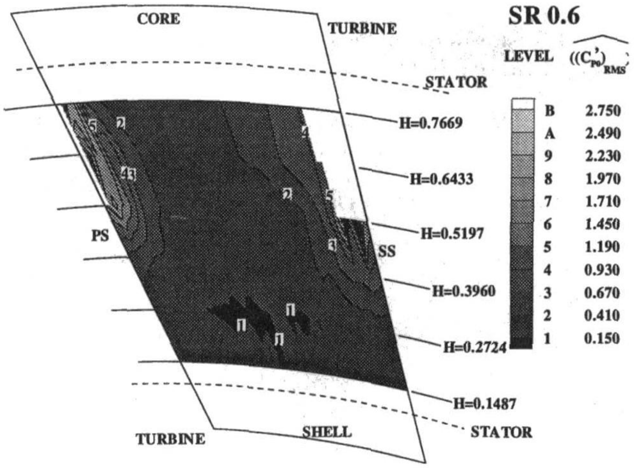

Fig. 15 Distribution of blade periodic rms value of fluctuations in unresolved static pressure coefficient $\widehat{((C'_{PS})_{RMS})}$ normalized by local absolute dynamic head at SR 0.6 at the turbine exit

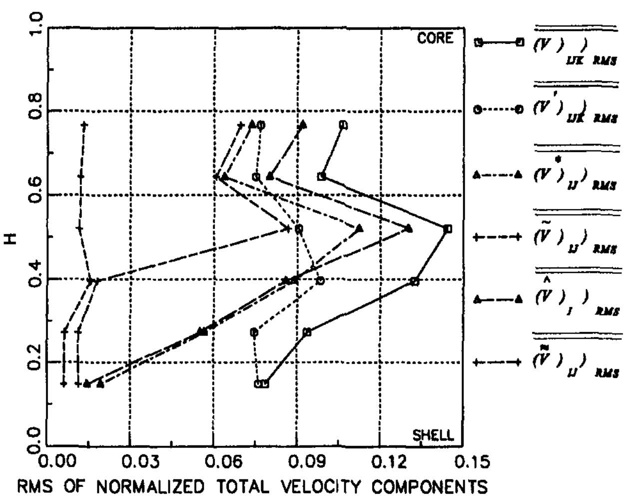

Fig. 17 Radial distribution of passage-averaged value of rms of normalized absolute total velocity fluctuations at SR 0.6 at the turbine exit

core, the flow mixing and dissipation are smaller near the core. As a result, the random fluctuations are higher near the core and smaller near the shell. (2) In the mixed flow machines, the flow near the core region experiences higher losses due to the adverse pressure gradients, caused by the flow path curvature, as explained by Johnson and Moore (1983). This causes lower mass flow and higher turbulence in the region near core. Near the separation zone of the core region, the rms values are significantly higher (approximately 100–400 percent of the local dynamic head) than those observed in the midpassage region.

The distribution of the rms values of unresolved unsteadiness in static pressure, as shown in Fig. 15, indicates small values (less than 15 percent of the local dynamic head) of rms near the shell region. The rms values of the static pressure increase smoothly from shell to core. In the entire passage (except near the wake region) the rms values remain smaller than 41 percent of the local dynamic head. The wake/separation region shows very high unsteadiness. However, the rms static pressure coefficient values are 40 percent lower than the rms stagnation pressure coefficient in this region.

Distribution of the rms of the Velocity Components and the Flow Angles. The distribution of the rms values of unresolved total velocity, as shown in Fig. 16, indicates high values of unsteadiness in the entire passage. The distribution of unresolved unsteadiness in axial, tangential, and radial velocities is given by Marathe (1997). The unsteadiness is lower near the shell (15 percent of local dynamic head for V_0) and is uniform from suction side to the pressure side. The unsteadiness in the core (away from the wake region) varies from 15 to 20 percent from shell to core. The near wake regions show high values of unsteadiness (65 percent of Q_{REF} for V_0 and V_X, 72 percent of Q_{REF} for V_R, and 48 percent of Q_{REF} for V_θ). However, it should be noted that the local total velocity in this region is small (30 percent of the free-stream velocity). Therefore, the unsteadiness in this region is also approximately 20 percent of the free-stream value. Therefore, it can be concluded that unresolved unsteadiness is approximately 20 percent of the free-stream velocity in the entire passage. Maximum values of unsteadiness are observed near the pressure side.

The radial distribution of the passage-averaged rms value of the unsteadiness in total velocity is shown in Fig. 17. Here, $\overline{\overline{((V_0)_{IJK})_{\mathrm{RMS}}}}$ is the rms of absolute total velocity minus the time-averaged value, $\overline{\overline{((V'_0)_{IJK})_{\mathrm{RMS}}}}$ is the rms of fluctuations in the unresolved absolute total velocity, $\overline{\overline{((V'_0)_{\mathrm{rms}}}}$ is the rms of fluctuations in the ensemble-averaged absolute total velocity minus the time-averaged value, $\overline{\overline{((\hat{V}_0)_I)_{\mathrm{RMS}}}}$ is the rms of fluctuations in the blade periodic absolute total velocity, $\overline{\overline{((\tilde{V}_0)_{IJ})_{\mathrm{RMS}}}}$ is the rms of fluctuations in the blade aperiodic absolute total velocity, and $((\tilde{\tilde{V}}_0)_{IJ})_{\mathrm{RMS}}$ is the rms of fluctuations in the RRI aperiodic absolute total velocity. The deterministic components (periodic and aperiodic) are more dominant. The RRI aperiodic component is found to be the smallest among all the components of unsteadiness. The blade periodic unsteadiness is also high near 55 percent stator span due to higher gradients in the velocity components near the wake region at this location. The lower values of unsteadiness at 71 and 88 percent stator span are due to the loss of the data points in the high velocity gradients and high unsteadiness regions of the wake. A slight increase in the unsteadiness near core region is caused by the flow acceleration in the midpassage caused by flow separation. Flow acceleration generates higher velocity gradients and hence, higher values of blade periodic and blade aperiodic unsteadiness in that region. The values of total unsteadiness are high (approximately 30 percent of the mean total velocity, V_{01}) near the core due to the reasons explained earlier. Other types of mixed flow turbomachinery also exhibit low velocities near the convex shroud endwall due to flow separation. The flow field near the convex side separates due to curvature and the adverse pressure gradient. This results in the higher losses and lower velocities near the

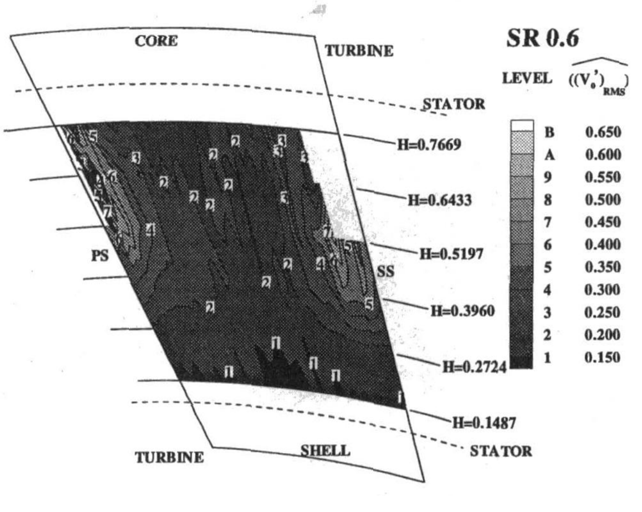

Fig. 16 Distribution of blade periodic rms value of fluctuations in unresolved absolute total velocity $\widehat{((V'_0)_{RMS})}$ normalized by local absolute total velocity at SR 0.6 at the turbine exit

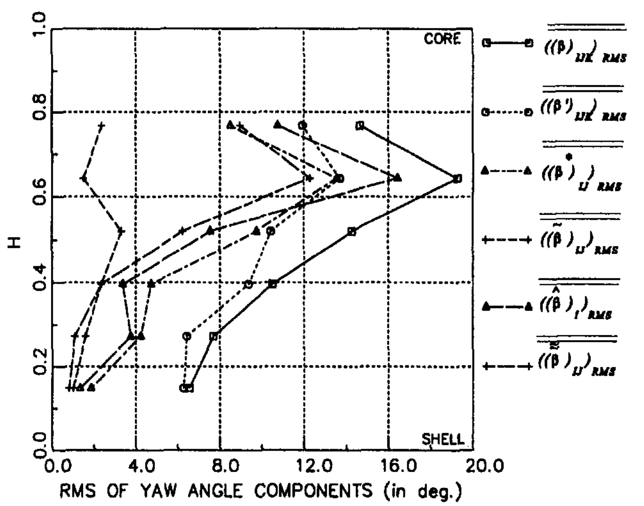

Fig. 18 Radial distribution of passage-averaged value of rms of absolute yaw angle fluctuations (in deg) at SR 0.6 at the turbine exit

convex endwall, as observed by Khalil et al. (1976) and Johnson and Moore (1983). The influence of the endwall boundary layers on the flow field is more pronounced in the mixed flow turbomachinery than in the axial flow turbomachinery. As a result, the flow separation and reattachment of the flow near the core could result in high turbulence intensity, and hence high values of unresolved component.

The radial distribution of passage-averaged rms values of unsteady axial velocity (presented in Marathe, 1997) was found to be nearly identical to that of the total velocity, as the axial velocity component is the dominant component (80–90 percent) of the total velocity. The radial distribution of radial and tangential unsteady velocities is different than that for the total velocity. The magnitude of the blade periodic and blade aperiodic unsteadiness is found to be significantly lower than the unresolved unsteadiness in the total velocity.

The radial distribution of the passage-averaged rms values of yaw angles, shown in Fig. 18, indicates highest rms values (12 to 15 deg) in all components, except the RRI aperiodic component, near the core region. The total fluctuation in the yaw angle is ±20 deg at 71 percent stator span. The magnitude of this total fluctuation reduces to approximately ±6 deg near the shell. Thus the stator experiences significant fluctuations in incidence angle and velocity due to the upstream turbine rotor.

Concluding Remarks

The distribution of flow properties at the exit of the turbine of an automotive torque converter, in the relative reference frame, shows a highly nonuniform flow field near the core and a nearly uniform flow field near the shell region. The blade wakes are thin and the wake decay is very rapid near the shell. A velocity profile similar to that of a fully developed flow is observed at most radii, and this is more pronounced near the core. Turbine blade wake is observed near the core, with a small zone of very low velocities near the suction surface, possibly caused by the flow separation inside the turbine passage. Secondary flow patterns show flow overturning in the separation region near the core, flow underturning in the rest of the passage, and radial negative velocity in the entire passage. The flow underturning is probably caused by flow acceleration, due to reduction in the cross-sectional area from the turbine exit to the stator inlet. This increases axial velocity, but the tangential velocity remains unaffected. As a result, the flow angle decreases from the turbine exit to the stator inlet.

The instantaneous unsteady flow property was decomposed into four components; time mean, periodic, aperiodic, and unresolved. The unresolved unsteadiness of all properties dominates the unsteady flow field. The unresolved unsteadiness in the velocity at the stator inlet is high (approximately 20 percent of the mean value) near the core and moderate near the shell (approximately 15 percent of the mean value). These magnitudes indicate very high levels of turbulence at both the core and the shell regions. The periodic component due to the blade-to-blade distribution of the steady-state flow properties in the turbine reference frame is significant. Due to the closed-loop circuit path and close spacing of the blade rows, the pump flow field influences the unsteady component at the inlet to the turbine generating unsteadiness at frequencies that are combinations of the blade passing frequencies. As a result, significant aperiodic component is generated.

The fluctuations in the flow angle are high in both the pitch and the yaw directions. The average rms value of the pitch and the yaw angle fluctuation was found to be 15 deg near the core and 10 deg near the shell. Thus, the stator experiences significant fluctuations in incidence angle and the velocity, which results in large unsteadiness inside the stator passage. The fluctuations in the incidence angle contribute significantly to the unsteady surface static pressure on the stator blade and this is dealt with in Part II of the paper.

It can be concluded that the flow field inside a torque converter is highly three dimensional, viscous, turbulent, and unsteady. Hence, the effects of three dimensionality and unsteady effects should be incorporated in the design of the torque converter elements to achieve improved performance.

Acknowledgments

This work was sponsored by Powertrain Division of General Motors Corporation. The authors wish to express their gratitude to R. By for his assistance, advice, and comments on the experimental program. Assistance by Y. Dong in the data acquisition is also acknowledged.

References

Browarzik, V., and Grahl, K. G., 1992, "Non-steady Flow Measurements Inside a Hydrodynamic Torque Converter by Hot-Film Anemometry," ASME Paper No. 92-GT-161.

Brun, K., Flack, R. D., and Gruver, J. K., 1996, "Laser Velocimeter Measurements in the Pump of an Automotive Torque Converter: Part II—Unsteady Measurements," ASME JOURNAL OF TURBOMACHINERY, Vol. 118, pp. 570–577.

By, R. R., and Lakshminarayana, B., 1995, "Measurement and Analysis of Static Pressure Field in a Torque Converter Turbine," ASME *Journal of Fluids Engineering*, Vol. 117, pp. 473–478.

By, R. R., Kunz, R. F., Lakshminarayana, B., 1995, "Navier–Stokes Analysis of the Pump Flow Field of an Automotive Torque Converter," ASME *Journal of Fluids Engineering*, Vol. 117, pp. 116–122.

Gruver, J. K., Flack, R. D., and Brun, K., 1996, "Laser Velocimeter Measurements in the Pump of an Automotive Torque Converter: Part I—Average Measurements," ASME JOURNAL OF TURBOMACHINERY, Vol. 118, pp. 562–569.

Johnson, M. W., and Moore, J., 1983, "Secondary Flow Mixing Losses in a Centrifugal Impeller," ASME *Journal of Engineering for Power*, Vol. 105, pp. 24–32.

Khalil, I. M., et al., 1976, "Losses in Radial Inflow Turbines," ASME *Journal of Fluids Engineering*, Vol. 98, pp. 364–373.

Lakshminarayana, B., and Horlock, J. H., 1973, "Generalized Expressions for Secondary Vorticity Using Intrinsic Coordinates," *Journal of Fluid Mechanics*, Vol. 59, pp. 97–115.

Marathe, B. V., 1997, "Investigation of Three-Dimensional, Unsteady, Viscous Flow Field Inside an Automotive Torque Converter," Ph.D. Thesis, Dept. of Aerospace Engineering, The Pennsylvania State University.

Marathe, B. V., Lakshminarayana, B., and Dong, Y., 1996, "Experimental and Numerical Investigation of Stator Exit Flow Field of an Automotive Torque Converter," ASME JOURNAL OF TURBOMACHINERY, Vol. 118, pp. 835–843.

Suder, K. L., et al., 1987, "Measurements of the Unsteady Flow Field Within the Stator Row of a Transonic Axial Flow Fan. I—Measurement and Analysis Technique," ASME Paper No. 87-GT-226.

Treaster, A. L., and Yocum, A. M., 1979, "The Calibration and Application of Five-Hole Probes," *ISA Transactions*, Vol. 18, No. 3, pp. 23–34.

Zaccaria, M., and Lakshminarayana, B., 1995, "Investigation of Three-Dimensional Flow Field at the Exit of a Turbine Nozzle," *Journal of Propulsion and Power*, Vol. 11, p. 55.

B. V. Marathe

B. Lakshminarayana

The Pennsylvania State University,
Department of Aerospace Engineering,
University Park, PA 16802

D. G. Maddock
Staff Development Engineer,
GM Powertrain Group,
General Motors Corporation,
Ypsilanti, MI 48198

Experimental Investigation of Steady and Unsteady Flow Field Downstream of an Automotive Torque Converter Turbine and Inside the Stator: Part II—Unsteady Pressure on the Stator Blade Surface

The stator flow field of an automotive torque converter is highly unsteady due to potential and viscous interactions with upstream and downstream rotors. The objective of this investigation is to understand the influence of potential and viscous interactions of the upstream rotor on the stator surface pressure field with a view toward improvement of the stator design. Five miniature fast-response pressure transducers were embedded on the stator blade. The measurements were conducted at three locations near the leading edge and two locations near the trailing edge at the midspan location. The upstream flow field was measured using a fast response five-hole probe and is described in Part I of this paper. The experimental data were processed in the frequency domain by spectrum analysis and in the temporal-spatial domain by the ensemble-averaging technique. The flow properties were resolved into mean, periodic, aperiodic, and unresolved components. The unsteady amplitudes agreed well with the pressure envelope predicted by panel methods. The aperiodic component was found to be significant due to the rotor–rotor and rotor–stator interactions observed in multistage, multispool environment.

Introduction

The unsteady pressure field on the stator blade is generated due to potential and viscous interactions at the rotor–rotor and the rotor–stator interfaces. The nature and magnitude of the unsteadiness depend on several parameters including the spacing between two blade rows, the number of blades in both the rotor and the stator, the thickness of the blade leading and trailing edges, the location of flow separation, secondary flows, and other geometric and the operating parameters. The objective of this investigation is to understand the effect of the upstream turbine rotor unsteady flow field on the unsteady pressure on the stator blade, with a view toward improvement in the performance of the stator. Another objective was to determine the effect of change in the speed ratio (which changes incidence angle and mass flow) on the various components of unsteady pressure. Understanding the rotor–stator interaction would lead to better design of both blade rows.

Many successful attempts have been made in the past to measure the unsteady flow field inside the axial and radial flow turbomachinery elements. Schulz et al. (1990) measured the unsteady three-dimensional flow and pressure field in an annular compressor cascade. The wakes generated by the rotating cylinder cage generated a highly unsteady pressure field near the leading edge of the cascade. The unsteadiness is found to decay rapidly from the leading edge to the trailing edge of the annular cascade blade with faster decay occurring on the pressure surface than on the suction surface. These observations are consistent with the present data. The unsteady surface pressure measurements by Manwaring and Fleeter (1992) also show faster decay on the pressure surface than on the suction surface. These authors also observe that the effect of the upstream wake is carried downstream to the second stage of the compressor. This is also consistent with the present data. Several other researchers have measured unsteady flow inside the axial flow turbomachines. However, very few attempts have been made to measure the steady and the unsteady flow field inside the torque converter. Some recent attempts (Browarzik and Grahl., 1992, Brun et al., 1996, etc.) on unsteady flow measurements inside the torque converter have been mentioned in the first part of this paper. However, the present knowledge of the unsteady flow field inside the torque converter is very inadequate for successful implementation of this effect in the design process.

Facility and Measurement Program

The torque converter test facility used in this research program is described in the first part of this paper. The unsteady data acquired inside the stator blade at SR = 0.065, 0.2, 0.6, and 0.8 are presented and interpreted in this paper. The effect of the speed ratio on the stator flow unsteadiness is also presented. The stator blade geometry, blade angles, and inlet flow angle (obtained from one-dimensional analysis), at speed ratios 0.065 and 0.6 are shown in Fig. 1. The stator inlet and exit flow angles for SR = 0.2 are identical to those for SR = 0.065. The flow angles for SR 0.8 have been presented by Marathe et al. (1996). Upstream flow measurements carried out at 0.4276

Contributed by the International Gas Turbine Institute and presented at the 40th International Gas Turbine and Aeroengine Congress and Exhibition, Houston, Texas, June 5–8, 1995. Manuscript received by the International Gas Turbine Institute February 4, 1995. Paper No. 95-GT-232. Associate Technical Editor: C. J. Russo.

stator axial chords upstream of the stator using five-hole probe have been presented in Part I of this paper. The blade static pressure measurements were carried out at five chordwise locations (three near the leading edge and two near the trailing edge) at midspan of the stator blade surface. These locations are designated as *LE*, *LE*(*PS*), *LE*(*SS*), *TE*(*SS*), *TE*(*PS*) in Fig. 1. The unsteady pressures are acquired using miniature fast-response pressure transducers mounted inside the stator blade, as shown in Fig. 1. The pressure transducers have natural frequency of 100 kHz. However, due to cavity volume between the blade surface and the pressure sensing area, the frequency responses of the pressure transducers were approximately 30 kHz. A pressure tap, on the stator shell surface (hub), at mid-pitch location, was used for measuring the reference static pressure. This static pressure was subtracted from the stagnation and the static pressures measured by the five-hole probe and also from the stator blade unsteady pressure. All the pressures were normalized by reference dynamic head Q_{REF}. The detailed method of data processing has been described in Part I of this paper. A thermocouple was installed on the hub of the stator for accurate reference temperature. The pressure measurements are obtained to an accuracy of ±0.01 psi. The transducer drift introduces a maximum error of 0.5 percent. This results in 0.5 percent error in the static and total pressures.

The unsteady flow field upstream of the stator is reported in Part I of this paper. The unsteady blade static pressures measured on the stator blade (due to upstream flow distortions caused by the turbine) are reported in this paper.

Analysis of the Unsteady Blade Static Pressure Signal

Two different methods were used to process the unsteady blade static pressure data on the stator blade. In the first method, the signal was decomposed in the frequency domain (Fourier analysis) and the contributions to the unsteadiness from various sources were analyzed. In the second method the signal was decomposed in the time domain using ensemble averaging technique. The details of both the techniques have been discussed in Part I of this paper.

Fourier Analysis. Fourier analysis of the pressure signal reveals several dominant frequencies in the pressure signal. They can be classified as follows:

1. Pump shaft frequency (P_S) and its harmonics.
2. Turbine shaft frequency (T_S) and its harmonics.
3. Pump blade passing frequency relative to stator (P) and its harmonics.
4. Turbine blade passing frequency relative to stator (T) and its harmonics.
5. Difference between P and T frequencies ($P - T$) and its harmonics.
6. Difference between T and $P - T$ frequencies $\{T - (P - T)\}$.
7. Ball bearing vibration frequencies (normally between 0–100 Hz for present analysis).

The shaft frequencies of pump and turbine (P_S and T_S) are generated as the entire flow field repeats after every revolution. They are also generated due to the vibration of the test section at that frequency.

The blade passing frequencies of pump and turbine (P, T, $P - T$, and $T - (P - T)$) are generated by the viscous and inviscid interactions of blade rows. The unsteadiness generated at one blade row is convected downstream to the next blade row. However, the subsequent blade row senses the unsteadiness propagated from the first blade row in the relative frame. Therefore, the frequency of unsteadiness in the next blade row is

Nomenclature

C = chord length
$C_{P0} = 2(P_0 - P_{\text{HUB}})/\rho V^2_{\text{REF}}$
$C_{PS} = 2(P_S - P_{\text{HUB}})/\rho V^2_{\text{REF}}$
LE = leading edge
$LE(PS)$ = leading edge pressure side (4.2 percent axial chord downstream)
$LE(SS)$ = leading edge suction side (13.3 percent axial chord downstream)
$(\hat{N})$ = amplitude of the periodic properties (V_0, C_{P0}, C_{PS}, α, β) defined as $(\hat{N}_{\text{MAX}} - \hat{N}_{\text{MIN}})/2$
(N^*) = amplitude of the ensemble-averaged properties (V_0, C_{P0}, C_{PS}, α, β) defined as $(N^*_{\text{MAX}} - N^*_{\text{MIN}})/2$
P = pump blade passing frequency
P_{HUB} = reference pressure on the hub
P_{LE} = leading edge pressure at stator midspan (used as a reference pressure for normalizing time mean and panel code pressures)
P_S = pump shaft frequency
PS, SS = pressure and suction side/surface
Q_{REF} = reference dynamic head = $\rho V^2_{\text{REF}}/2$
S = blade spacing
SR = speed ratio (turbine rpm/pump rpm)
T = turbine blade passing frequency
TE = trailing edge
T_S = turbine shaft frequency
U = blade speed
V = absolute velocity normalized by V_{REF}
V_{REF} = normalizing velocity $(U_{\text{TIP}_{\text{PUMP}}}\sqrt{1 - SR})$
$\bar{V}_X$ = mass-averaged axial velocity upstream of the turbine
X = distance from leading edge of stator blade
$(\ )_{\text{RMS}}$ = root mean square values of fluctuating quantities (V_0, C_{P0}, C_{PS}, α, β)
α = pitch angle, arctan (V_r/V_X), positive in the radial outward direction
β = absolute yaw angle (measured from the axial direction) $\tan^{-1}(V_\theta/V_X)$, positive in the direction of rotation of the pump and the turbine
β_{REL} = relative yaw angle (measured from the axial direction) $\tan^{-1}(W_\theta/V_X)$, positive in the direction of rotation of the pump and the turbine
ρ = density of the fluid

Subscripts

1, 2 = inlet and exit of the stator
0, S = total/stagnation, static
ABS = absolute (stator) reference frame
REL = relative (turbine) reference frame
X, R, θ = axial, radial, and tangential components
hub, tip = property at the hub and tip, respectively
Max = maximum value
RMS = root mean square value

Superscripts

$-$ = time-averaged value (Eq. (2), Part I)
$*$ = ensemble-averaged value (Eq. (3), Part I)
$\approx$ = rotor–rotor interaction (RRI) aperiodic component (Eq. (4), Part I)
$\hat{}$ = blade periodic component (Eq. (5), Part I)
$\sim$ = blade aperiodic component (Eq. (6), Part I)
$'$ = unresolved component (Eq. (7), Part I)

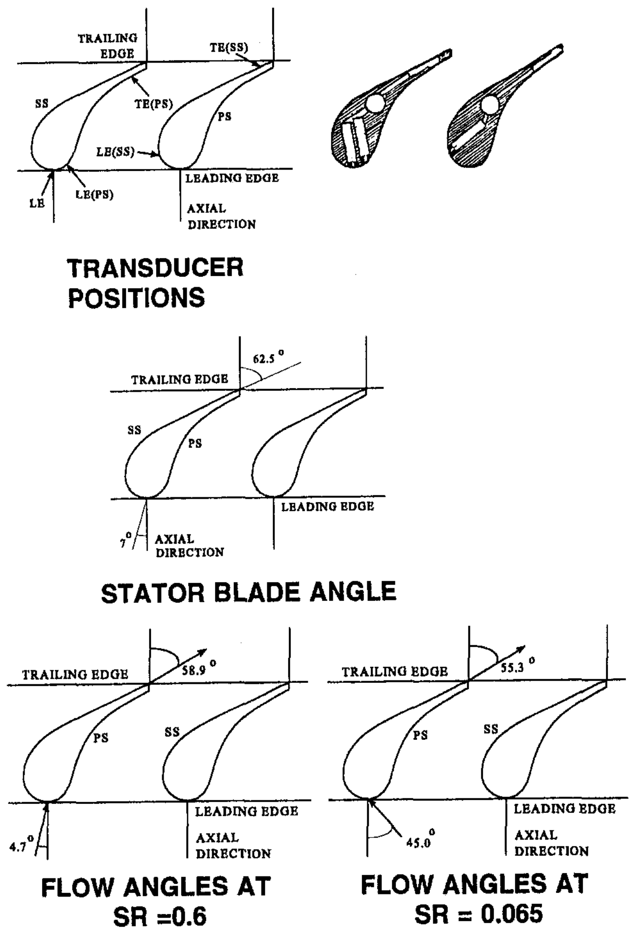

Fig. 1 Stator blade geometry, transducer locations, and flow angles at *SR* = 0.6 and 0.065

equal to the difference between the frequency of unsteadiness in the first blade row and the blade passing frequency of the next blade row. Thus unsteadiness frequency $(P - T)$ in the turbine blade row is sensed by the stator as frequency $T - (P - T)$.

The bearing frequencies are generated by the vibration of the ball bearings. These frequencies are sensed by the transducer through the mechanical vibration of the test facility. A test was performed to determine the correlation between the mechanical vibration of the test facility and the signal from the transducer. An accelerometer was placed at four different locations on the test facility. A high coherence was found between the bearing vibrations and the signal sensed by transducer at these frequencies. Therefore, it is concluded that the vibrations induced by the bearings are responsible for the transducer signal at these frequencies. The bearing vibrations are at low frequency (less than 200 Hz), and were removed by digital notch filtering.

The superposition of these different frequencies generates a composite wave. At speed ratio 0.6, the pump and turbine shaft speeds (revolutions per second) are in 5:3 proportion. Therefore, five revolutions of the pump and three revolutions of the turbine are completed in identical period. Since all the frequencies listed above are directly related to the pump and the turbine shaft speed, it is evident that the composite wave, generated by the superposition, will have identical period as that required for five revolutions of the pump or three revolutions of the turbine. It should be noted that for speed ratios 0.8, 0.4, 0.2, and 0.0 the pump and the turbine shaft speeds will be in 5:4, 5:2, 5:1, and 5:0 proportions respectively. Hence, the flow field for all the speed ratios will repeat after five revolutions of the pump. In this paper, the five revolutions of the pump will be called a *cycle*. The signal at different frequencies repeat several times in each cycle. The number of repetitions of waves at each frequency in one cycle are as given in Table 1.

Thus, the signal at the pump blade passing frequency "P" repeats 135 times in one cycle and pump shaft frequency "P_S" repeats 5 times in each cycle. It should be noted that at speed ratio 0.0, the composite wave will have a period equivalent to that of one revolution of the pump instead of five revolutions. However, to maintain the consistency with the other speed ratios the cycle will be considered as five revolutions of the pump.

Ensemble-Averaging Technique and Definition of Terminology. The ensemble-averaging technique used in processing unsteady blade pressure data is described in Part I of this paper. This technique is used to determine mean, periodic, aperiodic, and unresolved components of fluctuating pressure on the stator blade. Periodic fluctuations are introduced from the turbines wakes upstream of the stator blade row.

The nature of unsteadiness can be classified as deterministic and nondeterministic or unresolved. The deterministic unsteadiness is generated by the rotor–stator or the rotor–rotor interactions and is normally periodic over one revolution/cycle. The deterministic unsteadiness can be further divided into three categories: (1) Rotor–Rotor interaction (RRI) aperiodic $\tilde{\tilde{P}}_U$, (2) blade periodic component $\hat{P}_I$, and (3) blade aperiodic fluctuations $\tilde{P}_U$. The RRI aperiodic fluctuations $\tilde{\tilde{P}}_U$ are generated due to the differential relative positions of the pump and the turbine blades, which are different in every passage in a cycle. The RRI aperiodic component is calculated by taking the average of the ensemble-averaged property in each passage. The blade periodic fluctuations are caused by the variation of flow properties across the blade passages upstream of the stator. This component is calculated by subtracting the RRI aperiodic component from the ensemble-averaged property and averaging the resultant component over all the passages in a cycle as indicated in Part I of the paper.

The blade aperiodic fluctuations are caused due to flow variations in the passage-to-passage flow as described in Part I of this paper. The blade periodic unsteadiness is caused by viscous and potential interactions. Viscous interactions change the magnitude and direction of the absolute flow velocity and hence the incidence angle upstream of the stator blade row. Therefore, the stator operates not only at off-design inlet angles but also with considerable unsteady flow. The unresolved or nondeterministic unsteadiness is generated by free-stream turbulence and is normally random in nature. However, the unresolved unsteadiness referred to in this paper includes random unsteadiness, due to turbulence and other nondeterministic/random unsteadiness generated by sources not periodic over one cycle. Various components of deterministic and nondeterministic unsteadiness derived from this procedure, for an actual signal from a five-hole probe, are illustrated in Fig. 3 of Part I of this paper. A similar procedure is used to process the unsteady blade static pressure data.

Table 1

SR	P_S	T_s	P	T	P-T	T-(P-T)	T-2 (P-T)
0.8	5	4	135	116	19	97	78
0.6	5	3	135	87	48	39	9
0.4	5	2	135	58	77	19	96
0.2	5	1	135	29	106	77	193

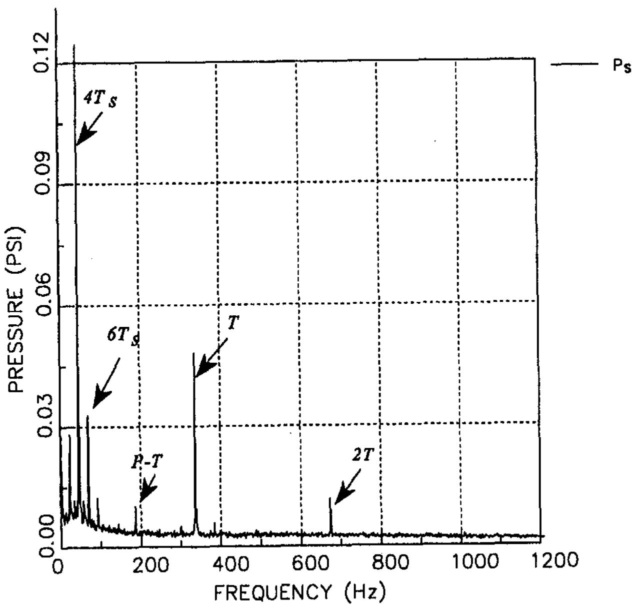

Fig. 2(*A*) FFT of upstream static pressure at *SR* = 0.6

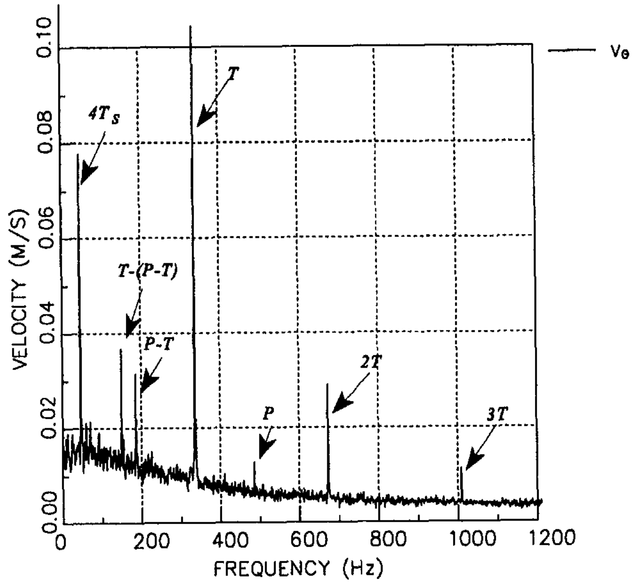

Fig. 2(*B*) FFT of upstream absolute tangential velocity at *SR* = 0.6

Comparison of Power Spectra of Unsteady Static Pressure Upstream and on the Stator Surface

The power spectrum of the unsteady inlet static pressure, acquired upstream of the stator, at the design speed ratio, is shown in Fig. 2(*A*). The data were acquired from a five-hole probe at midspan and processed using Fast Fourier Transform (FFT). The plot shows that the upstream flow field is dominated by the turbine shaft and the turbine blade passing frequencies. The second, fourth, sixth, and eighth harmonics of shaft frequency are significantly higher than the first, third, fifth, and seventh harmonics. Also, the fourth harmonic of the turbine shaft frequency shows the highest amplitude. The vibration studies conducted by authors (not presented here) show very high coherence between the vibration of the turbine shaft and the pressure signal at $4T_S$ frequency. The high amplitude of shaft vibration, at four times the turbine shaft frequency, is attributed to the number of roller bearing elements. Two harmonics of the turbine blade passing frequency, one harmonic of pump blade passing frequency, and one harmonic of combination $(P - T)$ frequency were also found to have significant magnitudes. However, turbine blade passing frequency is the most dominant one, followed by combination $(P - T)$ frequency and pump blade passing frequency.

The absence of the pump shaft frequencies in the upstream flow data suggests that the pump shaft frequencies are not propagated upstream of the stator and are not directly sensed by the five-hole probe. Since the pump flow field affects the stator flow field through inviscid interactions, the unsteady pressure signal transmitted upstream from the pump–stator interface is dissipated before reaching the location of the five-hole probe. Hence, the pressure fluctuations, sensed by the five-hole probe at the pump shaft and the pump blade passing frequencies, are not significant.

The existence of the combinations of blade passing frequencies (e.g., $P - T$, $T - (P - T)$, etc.) can be explained as follows: Since the torque converter has a closed-loop flow path, the viscous and inviscid interactions at one interface would be carried to the next interface through the blade passage. The flow inside the blade passage would experience unsteadiness at the rotor–stator/rotor–rotor interaction frequency. This frequency will be perceived by the second interface as the frequency of upstream unsteadiness. Thus, the unsteadiness generated due to the turbine–stator interaction at frequency T will be perceived by the downstream pump as unsteadiness at frequency $P - T$. Thus, due to the two rotating frames of reference and the one stationary frame of reference, several combinations of the frequencies ($(mP - nT)$, where m and n are integers) occur. The dominating frequency depends on the rate of dissipation of fluctuations, the levels of unsteadiness in the upstream and the downstream blade rows at each frequency, and the pressure gradient inside the upstream and the downstream blade rows.

The power spectrum of tangential velocity upstream of the stator shown in Fig. 2(*B*), indicate significant amplitudes of combination frequencies $(P - T)$ and $(T - (P - T))$ and pump blade passing frequency P. The fourth harmonic of turbine shaft frequency is the only significant shaft frequency observed in the spectrum. The third harmonic of the turbine blade passing frequency is also observed. The spectrum of the static pressure (Fig. 2(*A*)) and the tangential velocity (Fig. 2(*B*)) indicate that the turbine blade passing frequency dominates the stator upstream/turbine downstream flow field at the midradius.

The power spectrum of the unsteady stator blade static pressure near the leading edge of the stator (*LE*) is plotted in Fig. 3(*A*). The combination frequency $(P - T)$ is the most dominant in the spectrum, followed by the turbine blade passing frequency, pump blade passing frequency, and other combination frequencies (e.g., $2(P - T)$, $T - (P - T)$, $2(T - (P - T))$ etc.). Similarly, at the trailing edge of the stator, frequency $P - T$ is the most dominant (Fig. 3(*B*)) followed by the pump blade passing frequency, the turbine blade passing frequency, and other combination frequencies. The potential interactions between the pump and the turbine seem to have a dominant influence, due to their close spacing.

Arranging the dominant frequencies observed, with the descending order of magnitude, the following sequence was observed:

- At the stator leading edge: P_S, $P - T$, T, $4T_S$, P, $T - (P - T)$, $2T$ and other frequencies
- At the stator trailing edge: P_S, $P - T$, $4T_S$, P, T, $2P$, $8T_S$, $T - (P - T)$, $2(P - T)$, $2T$ and other frequencies

The presence of the pump shaft frequency is attributed to the vibration of the pump shaft. Since the transducers inside the stator blade are mounted on a rigid support, the vibrations of the rig are sensed by the transducers. The high amplitude of the pressure fluctuations (Fig. 3(*B*)) at the $P - T$ frequency is attributed to the fact that the sources of unsteadiness at this frequency are present at each interface. The downstream pump pressure field has less influence near the stator leading edge.

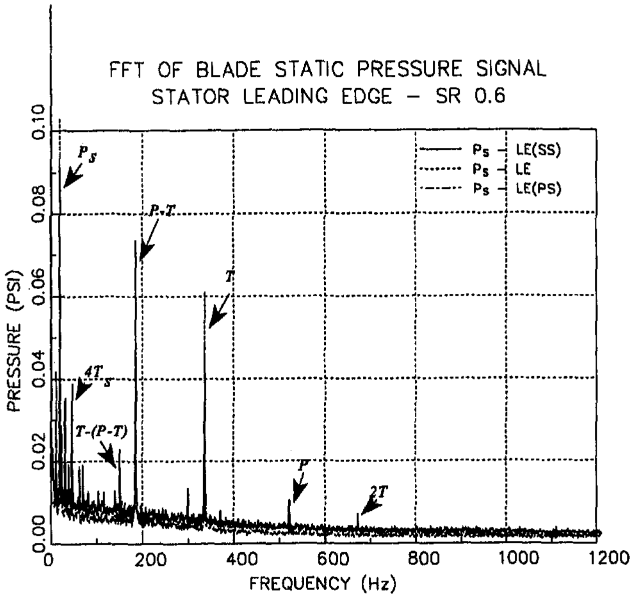

Fig. 3(*A*) **FFT of blade static pressure near the stator leading edge at *SR* = 0.6**

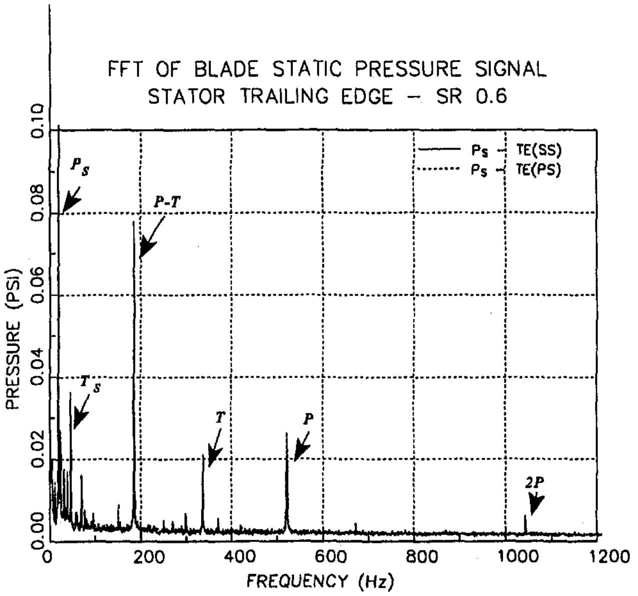

Fig. 3(*B*) **FFT of blade static pressure near stator trailing edge at *SR* 0.6**

Large flow accelerations near the leading edge of the stator generate large magnitudes of unsteadiness at the $P - T$ frequency, even though the variations in the inlet flow conditions may be small. However, these pressure fluctuations are not sensed by the upstream five-hole probe, as the turbine exit flow is not adversely affected by the downstream inviscid effects due to the pump. Therefore, large values of unsteadiness are observed at the *P-T* frequency on the stator blade, but not upstream of the stator blade.

Stator Inlet and Stator Blade Surface Properties at Different Speed Ratios

Since all the unsteady pressure measurements on the stator blade were acquired at the midspan location, the inlet flow distortion and the-ensemble averaged blade static pressure, at this spanwise location, will be presented here. A comparison of the authors' time-averaged data with the steady stator blade pressure data, due to By and Lakshminarayana (1991), will also be presented.

A panel code developed by McFarland (1984, 1993), for the prediction of unsteady flow in multistage turbomachinery, was effectively used by Dunn and Haldeman (1994), for the prediction of unsteady surface pressure in a two-stage turbine. This code uses unsteady pressures, flow angles, and velocities from the exit of the upstream stage, to calculate the pressure and the velocity distribution on the blade surface. A similar technique was used in the present investigation where the flow parameters measured upstream of the stator (V_0, β) were used as input for the code, and the maximum and minimum C_{PS} envelope on the stator blade was calculated using a panel method code developed by McFarland (1984). A comparison of the authors' time-averaged data with the steady-state static pressure data, on the stator blade, predicted by the panel method code will also be presented. The amplitude of the unsteady pressure envelope predicted by the panel method code will be compared against the amplitude of the ensemble-averaged pressures. Hub static pressure (P_{HUB}) is subtracted from the turbine exit pressure measurements. The blade static pressure at the stator leading edge (P_{LE}) is subtracted from the time mean measured pressure and from the surface pressure distribution predicted by panel code. All the pressures are normalized by reference dynamic head Q_{REF}. The blade static pressures from panel code and data (By and Lakshminarayana, 1991) are normalized using the blade static pressure at the leading edge of the stator, as the value of hub static pressure was unknown for these data sets. The velocities are normalized by the reference velocity V_{REF}.

The inlet distortion affects the blade pressure distribution in two ways: (1) The upstream unsteady static pressure introduces unsteady blade static pressure near the blade leading edge. Also, the unsteady dynamic head affects the blade pressure due to fluctuation in surface velocity on the stator blade. (2) The time-dependent incidence angle results in unsteady pressure on the blade surface. It also affects the position of the stagnation point, the location of the transition/separation, strength and location of the secondary flows, and the pressure gradient across the passage. Typically, in axial flow turbomachinery, the change in the incidence angle has more pronounced effect on the downstream blade than that due to a change in the upstream static pressure or change in the upstream velocity.

Flow Properties at Speed Ratios 0.065 and 0.2. The inlet flow distortion acquired by the fast response probe (described in Part I), at midspan of the stator at speed ratio 0.065, is presented in Fig. 4(*A*). The plot shows the ensemble-averaged values of five important flow parameters, namely the ensemble-averaged values of C^*_{P0}, C^*_{PS}, V^*_0, α^*, and β^* in the four adjacent flow passages. The total velocity and stagnation pressure profiles show that the maximum fluctuation is approximately 15–20 percent of the mean value. The static pressure is nearly uniform. This could be attributed to the wake dissipation caused by the large streamwise distance between the trailing edge of the turbine and the measurement location, and also due to the high levels of turbulence at *SR* 0.065. Maximum variation in the static pressure is approximately 0.05 Q_{REF}, maximum variation in the stagnation pressure is approximately 0.15 Q_{REF}, maximum variation in the yaw angle is approximately 10 deg, and maximum variation in the total velocity is approximately 0.15 V_{REF}. These fluctuations are small compared to the fluctuations at the speed ratios 0.6 and 0.8 as presented later in the paper. However, variation in the upstream stagnation pressure has more dominant effect on the blade static pressure near the leading edge. The pressure fluctuations on the stator surface are also influenced by the steady-state C_{PS} distribution on the blade surface. As a result, the pressure fluctuations at the leading edge were found significant as discussed later in the paper. It should also be noted that the large design incidence angle (45 deg), at this speed ratio, generates very high flow acceleration on the

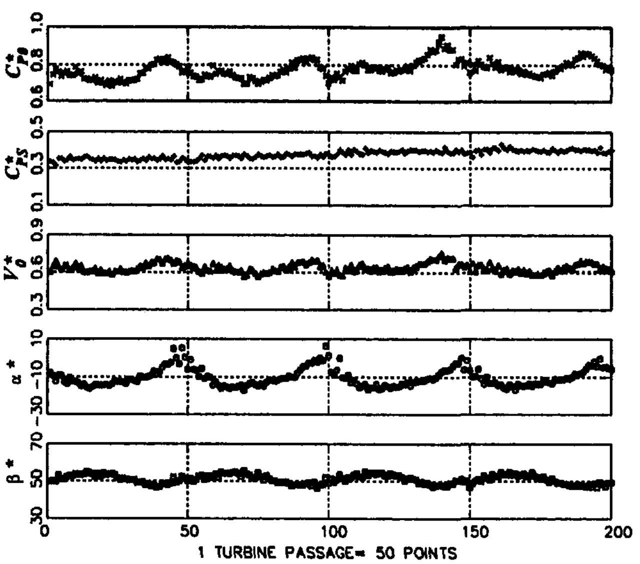

Fig. 4(*A*) Stator inlet flow distortion in four turbine passages at *SR* = 0.065 (ensemble-averaged value, α^* and β^* are in deg)

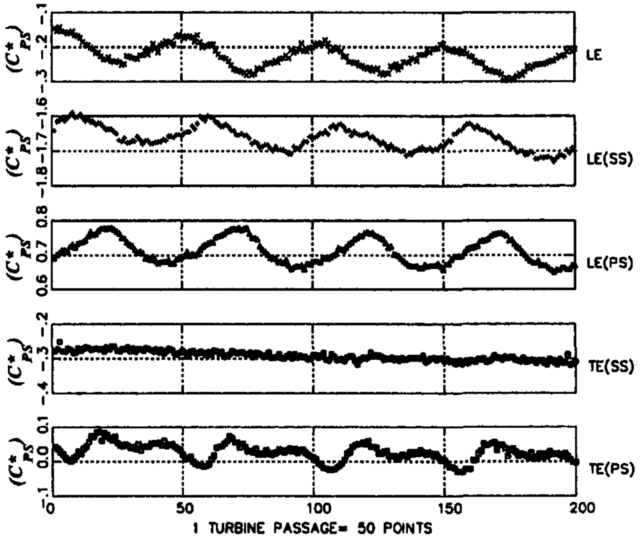

Fig. 4(*B*) Stator blade pressure variation at five transducer locations at *SR* = 0.065 (ensemble-averaged value)

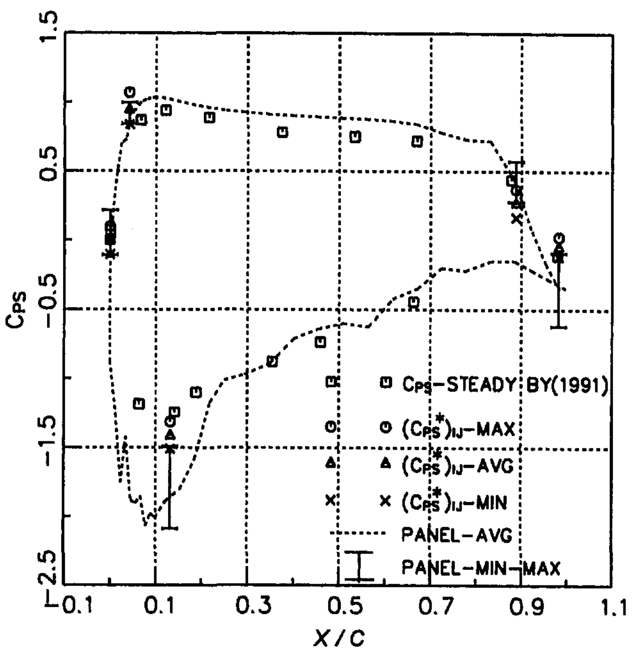

Fig. 4(*C*) Comparison of experimental data with the panel method predictions at *SR* = 0.065

suction surface. Therefore, any small change in the incidence angle results in a large change in the stator blade pressure distribution. This results in very high pressure fluctuations observed at the suction surface at this speed ratio.

At $SR = 0.065$, the magnitude of the upstream unsteady static pressure is very small (Fig. 4(*A*)) compared to the unsteady static pressure amplitude at the leading edge of the stator (Fig. 4(*B*)). The major contribution to the unsteady pressure on the stator blade at this speed ratio is from the unsteady total pressure and the unsteady yaw angle upstream of the blade. The amplitude of the unsteady static pressure at the leading edge of the stator is approximately equal to the amplitude of upstream stagnation pressure. The pressure history from the transducer, at the leading edge pressure surface, shows the smallest time lag compared to upstream C_{po} (gust), followed by those at the leading edge and the leading edge suction surface. This indicates that the stagnation point is closest to the transducer at the leading edge pressure surface (*LE*(*PS*)). This agrees with the flow angle distribution presented in Fig. 4(*A*). Since the streamwise distance between the stagnation point and the transducer at the leading edge pressure surface is small, the amplitude of the pressure signal from the transducer at the leading edge pressure surface is significant. This also explains the reason for higher periodicity exhibited by the blade static pressure at the leading edge pressure surface (*LE*(*PS*)), as compared to that at the trailing edge suction surface. The amplitude of the pressure fluctuation at the trailing edge suction surface is very small and nearly aperiodic in nature. This aperiodicity is caused by the potential effect of the downstream pump rotor.

Comparison of the time mean values with the steady-state measurements of By and Lakshminarayana (1991) reveal (Fig. 4(*C*)) good agreement. The comparison of the measured C_P variation with that predicted by the panel method solution is also shown in Fig. 4(*C*). The symbol $(C^*_{PS})_{IJ}$ – MAX denotes the maximum value of ensemble-averaged static pressure coefficient on the stator blade surface, measured by high response pressure transducers mounted on the stator blade. Similarly, $(C^*_{PS})_{IJ}$ – MIN and $(C^*_{PS})_{IJ}$ – AVG indicate the minimum and time-averaged values of the ensemble-averaged static pressure coefficient on the stator blade surface. The PANEL-AVG denotes the time-averaged C_{PS} distribution predicted by the panel code with minimum and maximum values predicted by the panel code denoted by PANEL-MIN-MAX. The amplitude of the pressure fluctuation measured near the trailing edge on the pressure side agrees well with the pressure envelope calculated by the panel method, indicating that the major contributor to the pressure fluctuations at the trailing edge is the incidence angle change upstream. However, near the leading edge the amplitude of measured pressure fluctuation is much smaller than the calculated pressure envelope. This is consistent with the observation that the upstream stagnation pressure fluctuation and incidence angle are out of phase and therefore the combined effect results in lower amplitude of unsteadiness compared to the individual contribution from each of these sources. Thus, it is concluded that the unsteady blade pressures, near the leading edge, are influenced by the variation of both the upstream stagnation pressure and the incidence angle, whereas the unsteady blade pressures near the trailing edge are mainly influenced by the incidence angle variations at the inlet.

The inlet flow distortion for $SR = 0.2$, shown in Fig. 5(*A*), is nearly identical to the inlet flow distortion at $SR = 0.065$ (Fig. 4(*A*)). The mean values of C^*_{Po}, C^*_{PS}, and V^*_0 are nearly identical to those at $SR = 0.065$. However, the amplitudes of

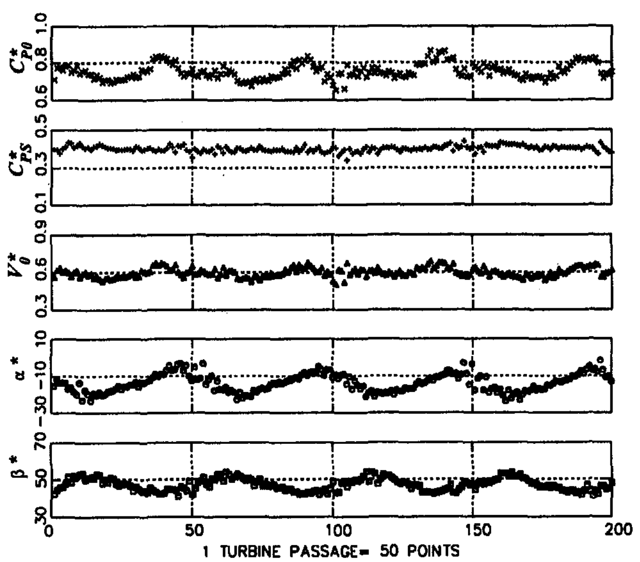

Fig. 5(*A*) Stator inlet flow distortion in four turbine passages at *SR* = 0.2 (ensemble-averaged value, α^* and β^* are in deg)

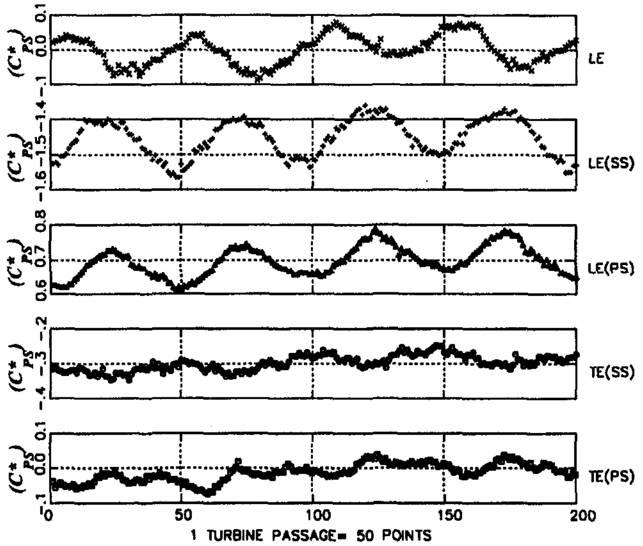

Fig. 5(*B*) Stator blade pressure variation at five transducer locations at *SR* = 0.2 (ensemble-averaged value)

fluctuations are different. The amplitude of C^*_{P0} variation is 15–20 percent less than that at $SR = 0.065$. The amplitudes of static pressure coefficient, normalized total velocity, and pitch angle variation are nearly identical. However, the amplitude of yaw angle variation is higher at $SR = 0.2$ than that at $SR = 0.065$. It should also be noted that although the normalized total velocity is identical for both the speed ratios, the actual total velocity at $SR = 0.2$ is significantly higher than that at $SR = 0.065$, as the reference velocity V_{REF} is higher at $SR = 0.2$ than at $SR = 0.065$.

The combined effects of higher velocity and flow angle fluctuations upstream induce higher values of unsteady pressure on the stator blade surface (Fig. 5(*B*)) at $SR = 0.2$ as compared to those at $SR = 0.065$. Higher amplitudes of unsteady pressure are observed at all the transducer locations except near the trailing edge pressure surface (*TE*(*PS*)). The lower magnitude of fluctuations at *TE*(*PS*) is attributed to the lower mean flow inlet angle that shifts the stagnation point farther away from the *TE*(*PS*) at $SR = 0.2$. The phase lag for $SR = 0.2$ was found identical to that at $SR = 0.065$. A comparison of the time mean values with steady-state data at $SR = 0.2$ from By and Lakshminarayana (1991) shows (Fig. 5(*C*)) good agreement. A comparison of the time mean with the panel method prediction also shows good agreement. The time mean pressure at *TE*(*PS*) is slightly lower than steady-state value and the predictions by panel method. However, the amplitude of the pressure fluctuations is accurately predicted by the panel method code. The predicted values of amplitude of pressure fluctuations agree well with the experimental data.

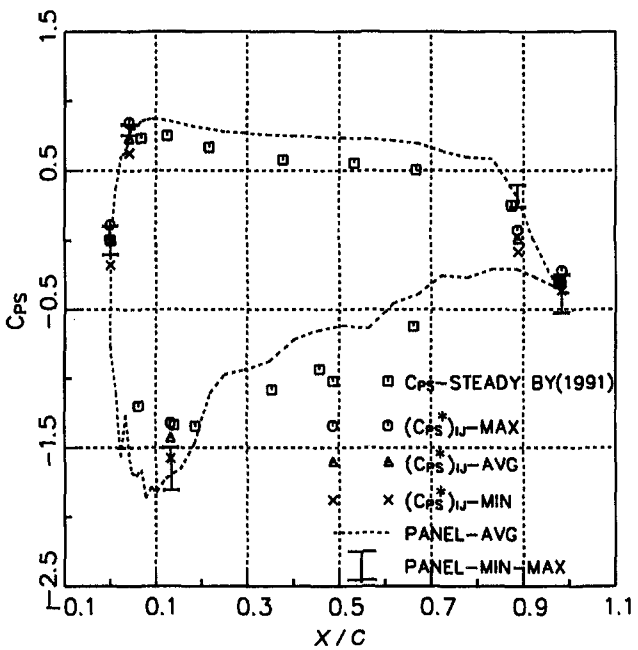

Fig. 5(*C*) Comparison of experimental data with the panel method predictions at *SR* = 0.2

Flow Properties at the Design Speed Ratio ($SR = 0.6$). The inlet flow distortion measured by the fast response probe (described in part-I), at mid-span of the stator at the design speed ratio is presented in fig. 6(*A*). The plot shows five important flow parameters namely C^*_{P0}, C^*_{PS}, V^*_0, α^* and β^* in the four adjacent flow passages. A nearly periodic flow can be observed in these blade passages. As indicated in Part I, a small portion of the signal is lost, as the data were out of the probe range in that region. Total velocity and stagnation pressure profiles show a nearly fully developed flow, with maximum velocity variation of approximately 0.5 V_{REF}, maximum static pressure variation of approximately 0.1 Q_{REF}, maximum stagnation pressure variation of approximately 0.2 Q_{REF} and approximately 35 deg maximum variation in the yaw angle across the turbine passage. Since the pressure transducers, at the leading edge (*LE*) and at the leading edge suction surface (*LE*(*SS*)), are very close to the stagnation point, the variation in the upstream stagnation pressure and the yaw angle have a dominant influence on the unsteady static pressure on the stator blade.

The ensemble-averaged values of unsteady blade static pressure at the stator midspan at five chordwise locations on the stator blade surface (Fig. 1) are shown in Fig. 6(*B*). The ensemble-averaged unsteady static pressure variation on the stator blade, in the period required for passing of the four turbine passages, is shown. The amplitude of the ensemble-averaged property near the leading edge is dominantly influenced by the variation of the upstream total pressure and the flow angle (Fig. 6(*A*)). These two effects have an opposing effect, as they are not in the phase (Fig. 6(*B*)). Hence, the amplitude of the static pressure variation near the leading edge is smaller than the amplitude of the upstream stagnation pressure variation. A comparison of the unsteady pressure history, at the chordwise locations *LE*, *LE*(*PS*), and *LE*(*SS*), shows a phase difference between these three signals. This phase lag is due to the time lag

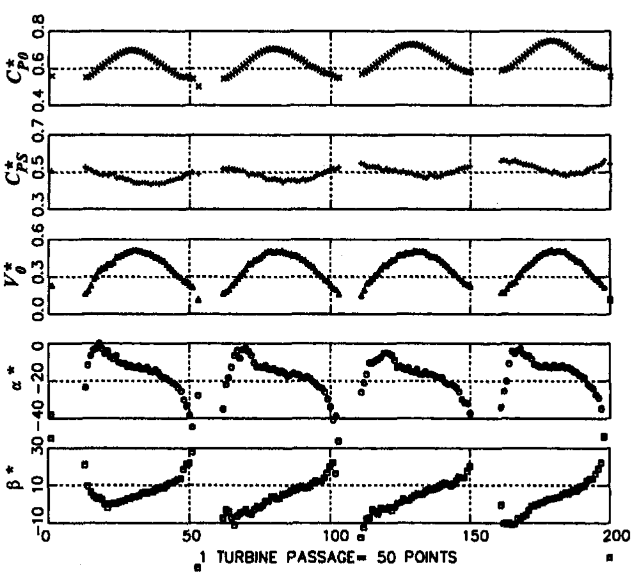

Fig. 6(*A*) Stator inlet flow distortion in four turbine passages at $SR = 0.6$ (ensemble-averaged value, α^* and β^* are in deg)

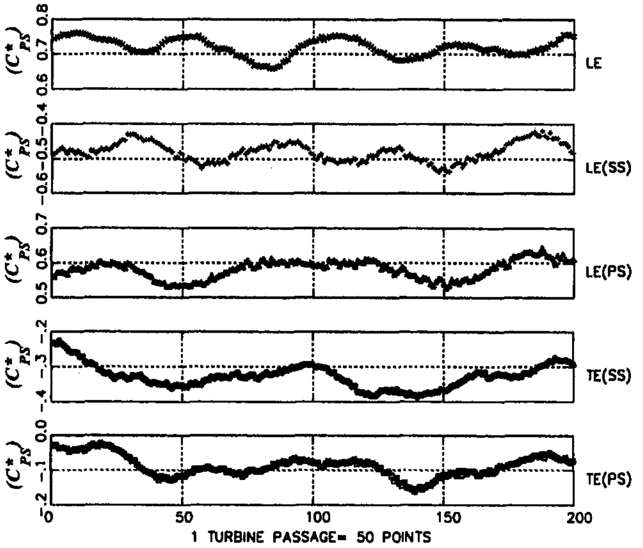

Fig. 6(*B*) Stator blade pressure variation at five transducer locations at $SR = 0.6$ (ensemble-averaged value)

required for propagation of the unsteady property through the blade passage. The time lag depends on the convective velocity of the gust, streamwise distance relative to the transducers from the upstream measurement location. The pressure history from the transducer at the leading edge suction surface (*LE*(*SS*)) showed the smallest time lag, followed by those at the leading edge (*LE*) and the leading edge pressure surface (*LE*(*PS*)). This is consistent with the fact that the stagnation point is closest to the transducer, at the leading edge suction surface. This is also consistent with the upstream yaw angle distribution presented in Fig. 6(*A*). The ensemble-averaged static pressure at the stator trailing edge showed a very high magnitude of aperiodicity, caused by the potential effects of the downstream pump rotor. The aperiodic property, at the stator trailing edge, is due to the signal at frequencies *P* and *P*-*T*, as described earlier in the paper.

A comparison of the measured time mean values of static pressure with that predicted by the Panel method solution is shown in Fig. 6(*C*). The amplitude of the pressure fluctuation measured at the trailing edge agrees well with the pressure envelope calculated by the panel method, indicating that the major contributor to the pressure fluctuations at the trailing edge is the incidence angle change upstream. However, near the leading edge, the amplitude of the measured pressure fluctuation is much smaller than the calculated pressure envelope. This is consistent with the observation that the upstream stagnation pressure fluctuation and incidence angle are out of phase and therefore the combined effect results in lower amplitude of unsteadiness compared to the individual contribution from each of these sources. Thus it can be concluded that the unsteady blade pressures near the leading edge are influenced by the variation of both the upstream stagnation pressure and incidence angle, whereas the unsteady blade pressures near the trailing edge are mainly influenced by the incidence angle variations at the inlet.

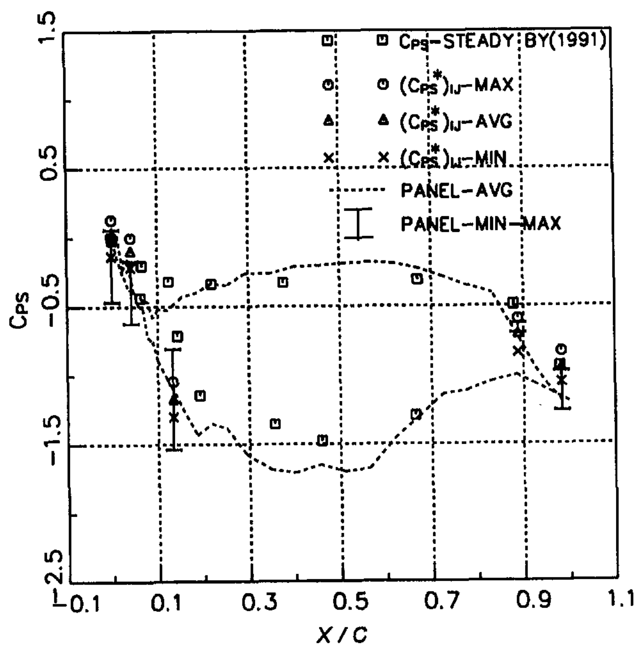

Fig. 6(*C*) Comparison of experimental data with the panel method predictions at $SR = 0.6$

The magnitude of unsteadiness in blade surface pressure is nearly identical (approximately $\pm$ 0.1 Q_{REF} at all five transducer locations for $SR = 0.6$); whereas, at $SR = 0.065$ the unsteady blade pressures, near the leading edge (*LE*, *LE*(*PS*), *LE*(*SS*)), show similar amplitudes, but their values near the trailing edge are significantly lower ($\pm 0.05 Q_{\text{REF}}$). This is attributed to the higher fluctuations of upstream stagnation pressure and smaller fluctuations in the incidence angle at $SR = 0.065$.

Flow Properties at Speed Ratio 0.8. The inlet flow distortion for $SR = 0.8$ is presented in Fig. 7(*A*). The variation in the stagnation pressure coefficient, C_{P0}, is nearly identical to that observed at $SR = 0.6$ (approximately 0.2 Q_{REF}). The variation in the static pressure coefficient is also nearly identical. However, variation of the total velocity at $SR = 0.8$ is much smaller than that at $SR = 0.6$. This can be attributed to the higher values of static pressures in the midpassage and lower values of static pressures near the core. The higher static pressures in the midpassage are caused by lower pressure drop in the turbine. Unsteadinesses of all properties (C^*_{P0}, C^*_{PS}, V^*_0, α^*, β^*) are all in phase for this speed ratio.

The static pressure fluctuations shown in Fig. 7(*B*) indicate high periodic fluctuations on the leading edge and the leading edge suction surface but aperiodic pressure variation on the leading edge pressure surface. This aperiodic variation is attributed to the possible flow separation on the pressure side of the stator, which was also observed by Bahr et al. (1990). Due to high flow acceleration on the suction surface, low mass flow

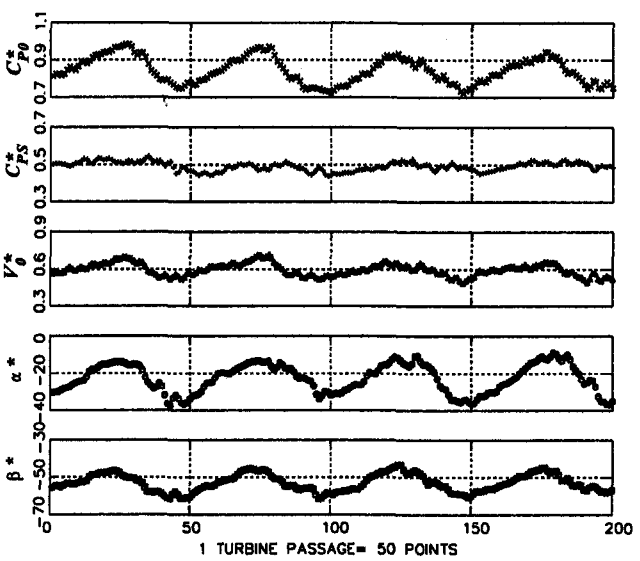

Fig. 7(*A*) Stator inlet flow distortion in four turbine passages at *SR* = 0.8 (ensemble-averaged values, α^* and β^* are in deg)

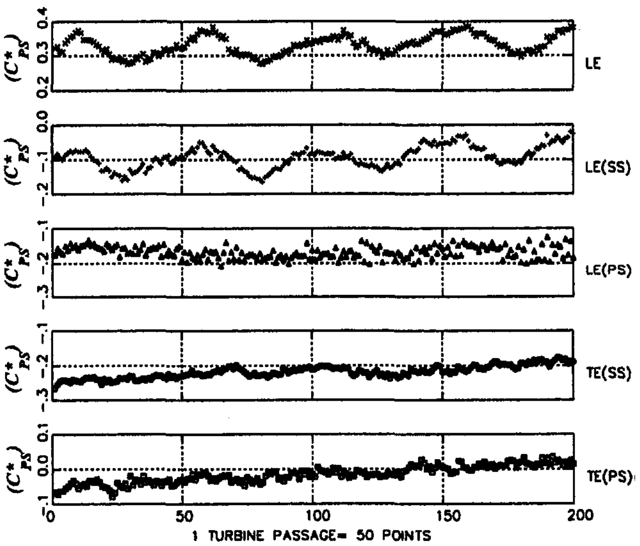

Fig. 7(*B*) Stator blade pressure variation at five transducer locations at *SR* = 0.8 (ensemble-averaged value)

rate, and possible separation at the *TE*(*SS*) and *TE*(*PS*), as observed by Bahr et al. (1990), the pressure variation near the trailing edge (*TE*(*SS*) and *TE*(*PS*)) is aperiodic. The phase lag between the pressure data at the leading edge suction side (*LE*(*SS*)) and the leading edge (*LE*) is negligible indicating that the stagnation point is midway these two positions.

A comparison of the time mean unsteady data with the steady-state data of By and Lakshminarayana (1991) shows good agreement (Fig. 7(*C*)). The agreement between predictions and data of steady-state blade static pressure is poor. The viscous effects have dominant influence on the flow at *SR* = 0.8. However, the amplitudes of unsteady pressure fluctuations agree well with the panel code prediction, except near the leading edge pressure surface (*LE*(*PS*)).

Variation of Unsteadiness With Speed Ratio

The nature and magnitude (amplitude) of unsteadiness, both upstream and on the blade surface, at various speed ratios, are compared in this section.

Upstream Flow Distortion. A comparison of the amplitude of upstream unsteadiness at different speed ratios is shown in Fig. 8(*A*). The amplitude of the ensemble-averaged

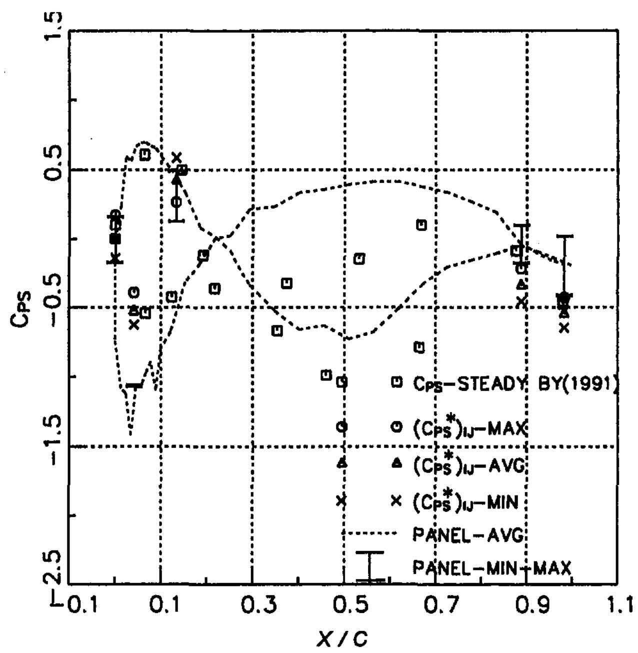

Fig. 7(*C*) Comparison of experimental data with the panel method predictions at *SR* = 0.8

$(C^*_{P0})_{IJ}$ and the blade periodic properties $(\hat{C}_{P0})_I$ are shown in each figure. The ensemble-averaged values are the phase-locked average of the flow properties as explained in part I, Eq. (3). The blade periodic values represent the blade-to-blade distribution of the flow properties in the turbine reference frame as explained in part I, Eq. (5). Since the static pressure on the stator blade surface is directly influenced by the passing turbine blades, the ensemble-averaged values and the blade periodic values of the blade static pressures give a direct correlation between the passing turbine wakes and the fluctuations in the pressure field on the stator blade. The difference between the ensemble-averaged values and the blade periodic values is equal to the amplitude of the aperiodic values. The variation in amplitude of the total pressure coefficient shows (Fig. 8(*A*)) that the amplitude of the blade periodic variation increases linearly with the speed ratio. This increase is attributed to the increased pressure drop across the turbine as the speed ratio is increased. Higher pressure drop results in higher pressure and velocity gradients across the turbine passage in the relative frame of reference. This results in higher amplitudes of the periodic pressure fluctuations on the stator blade. This accounts for an increase in the amplitude of periodic $(\hat{C}_{P0})$ with speed ratio.

Both the aperiodic and the periodic components of unsteady stagnation pressure decrease from *SR* = 0.065 to *SR* = 0.2 (Fig. 8(*A*)). This can be explained as follows: The reference velocities are 9.316, 11.525, 8.835, and 7.001 m/s for speed ratios 0.065, 0.2, 0.6, and 0.8, respectively. Hence, the normalizing factor increases by 25 percent from *SR* = 0.065 to *SR* = 0.2. However, the drop in the total pressure remains nearly identical for both the speed ratios. As a result, the normalized values of the unsteady pressure are higher for *SR* = 0.065 than for *SR* = 0.2.

The amplitude of both the blade periodic and the aperiodic value of static pressure coefficient increases with the speed ratio (Fig. 8(*B*)) from *SR* = 0.065 to *SR* = 0.6. This is similar to the variation of total pressure coefficient. The amplitude of periodic unsteadiness in C_{PS} decreases from *SR* = 0.6 to *SR* = 0.8. This is attributed to a significant drop in the magnitude of the periodic fluctuations in the velocity from *SR* 0.6 to *SR* 0.8, as discussed later in the paper. The magnitude of the aperiodic component of C_{P0} and C_{PS} is significantly higher than the magni-

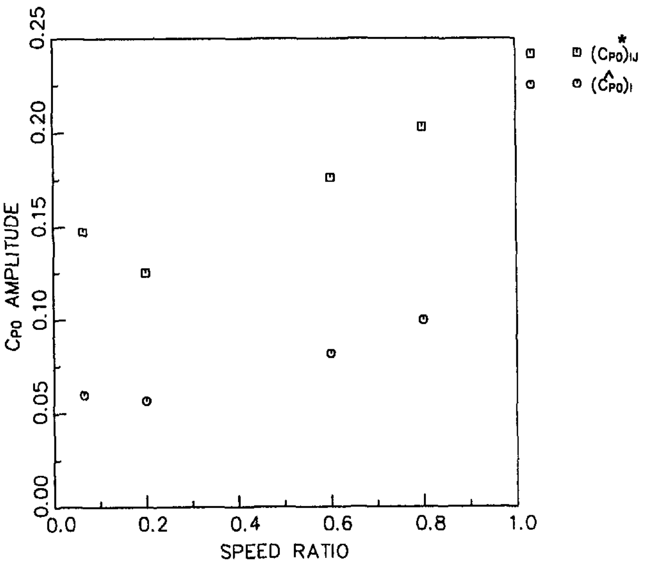

Fig. 8(*A*) Variation of upstream C_{Po} amplitude with speed ratio

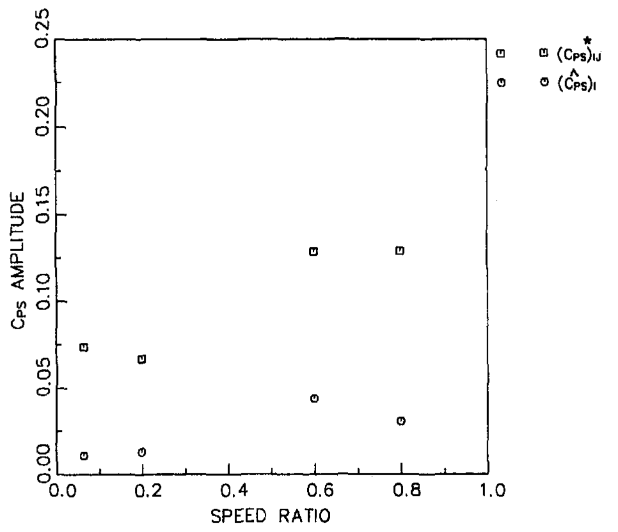

Fig. 8(*B*) Variation of upstream C_{PS} amplitude with speed ratio

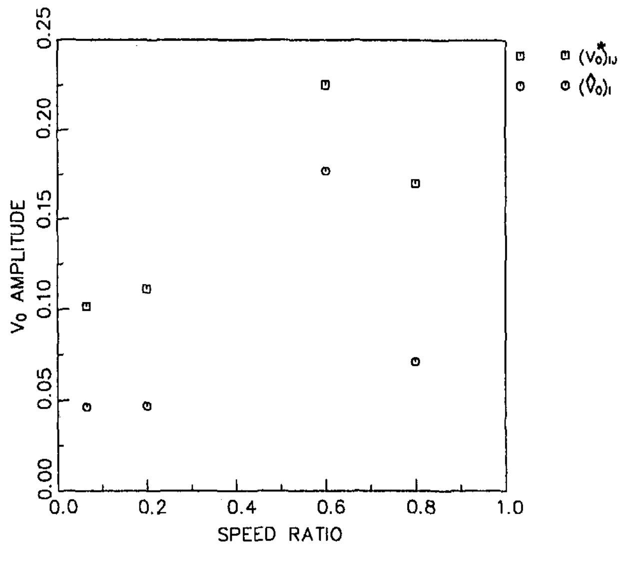

Fig. 8(*C*) Variation of upstream V_0 amplitude with speed ratio

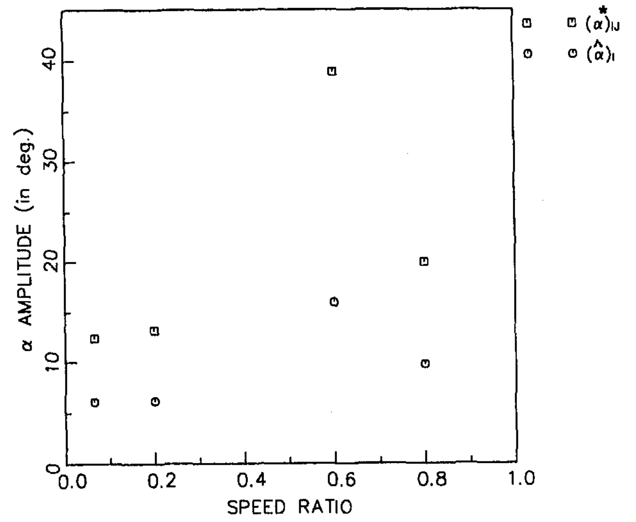

Fig. 8(*D*) Variation of upstream pitch angle (α) amplitude with speed ratio

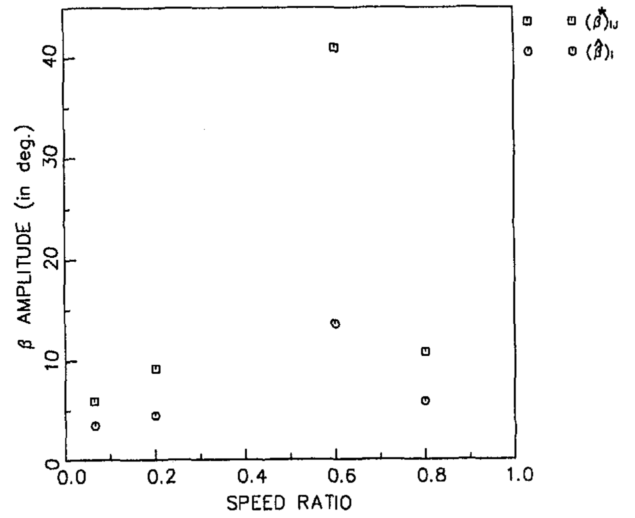

Fig. 8(*E*) Variation of upstream yaw angle (β) amplitude with speed ratio

tude of the periodic component. The aperiodicity in the flow field is introduced due to the differential relative positions of the pump and the turbine blade, and due to aperiodic nature of trailing edge separation and Von-Karman type vortices generated in the turbine exit flow.

The amplitudes of the blade periodic and aperiodic components of the absolute total velocity show (Fig. 8(*C*)) significant variation with the speed ratio. The amplitude of the blade periodic velocity shows large increases ($0.05V_{REF}$ for *SR* 0.2 to $0.18V_{REF}$ for *SR* 0.6) from $SR = 0.2$ to $SR = 0.6$ and a large drop from $SR = 0.6$ to $SR = 0.8$. This change is attributed to the static pressure distribution at $SR = 0.8$ as explained earlier in the paper. The higher static pressure in the midpassage and lower static pressure near the wake region causes lower magnitudes of velocity fluctuations. Also, since the aperiodic wake dissipation (flow mixing) is less at the design speed ratio, the amplitude of aperiodicity is smaller for $SR = 0.6$ than for other speed ratios. Therefore, the aperiodic component increases from *SR* 0.065 to 0.2, decreases from $SR = 0.2$ to 0.6 and increases again from $SR = 0.6$ to 0.8.

The amplitudes of pitch and yaw angle fluctuations show (Figs 8(*D*), 8(*E*)) variations similar to those observed for velocity. However, the amplitude of the aperiodic fluctuations in the flow angle is nearly twice the periodic amplitude at *SR*

= 0.6. The aperiodic angle fluctuations are caused by the trailing edge separation. The aperiodic fluctuations diminish with an increase in the streamwise distance due to flow mixing downstream of the turbine.

Unsteady Stator Blade Static Pressure. The magnitude of the static pressure fluctuations at the leading edge shows (Fig. 9(*A*)) an increase in the aperiodic fluctuations with the speed ratio. The aperiodic component dominates the unsteadiness on the stator blade pressure at all speed ratios and at all five measurement locations. The viscous and inviscid effects from upstream and downstream blade rows dominate the pressure field inside the torque converter. The closed-loop flow path and differential relative blade positions of the pump and the turbine induce large magnitudes of aperiodic fluctuations on the stator blade.

The magnitude of periodic component does not show any systematic variation with the speed ratio near the leading edge of the stator. The magnitude increases from $SR = 0.065$ to 0.2, decreases from $SR = 0.2$ to 0.6 and increases again from $SR = 0.6$ to 0.8. This variation is attributed to the stator blade surface pressure distribution. The unsteady pressures on the stator blade are related to the mean pressure distribution on the stator blade. From $SR = 0.065$ to $SR = 0.2$, the incidence angle remains nearly identical (approximately 40–45 deg), but the mass flow increases. Increased mass flow increases the dynamic head, which increases the pressure coefficients near the leading edge. This results in higher unsteadiness at the leading edge. From $SR = 0.2$ to 0.6, the incidence angle changes from 40 to -10 deg. Also, the mass flow is significantly lower for SR 0.6. As a result, the blade loading on the stator reduces significantly. As a result, the periodic fluctuations are smaller for SR 0.6. From $SR = 0.6$ to $SR = 0.8$, the incidence angle changes from -10 to -40 deg. The blade loading is significantly lower. However, negative incidence angles cause flow acceleration on the pressure surface (Fig. 9(*C*)) and flow deceleration on the suction surface near the leading edge (Fig. 9(*B*)). This causes reversal of pressure distribution near the leading edge with higher pressures on the suction surface and lower pressures on the pressure surface. The region of reversal of pressure distribution (Fig. 7(*C*)) is very sensitive to the small change in dynamic head and flow angles. Therefore, any small fluctuations in the upstream flow properties would cause significant pressure fluctuations near the leading edge at $SR = 0.8$. This increases unsteady pressure fluctuations near the leading edge. The trailing edge region is not affected significantly by the upstream flow changes. Therefore, the periodic pressure fluctuations increase from $SR = 0.6$ to 0.8 near the leading edge, but decrease from $SR = 0.6$ to 0.8.

It should be noted that the leading edge pressure fluctuations are influenced largely by the location of the stagnation point, the mass flow, and the upstream pressure fluctuations. The location of the stagnation point shifts from pressure surface for SR 0.065, to near the leading edge for SR 0.6, to the suction surface for SR 0.8. As a result, at SR 0.8 and SR 0.6 higher fluctuations are observed (Fig. 9(*A*)) at leading edge and leading edge suction surface (Fig. 9(*B*)); whereas, at the leading edge the pressure surface shows (Fig. 9(*C*)) small magnitudes of fluctuations. Similarly, for SR 0.065 the fluctuations on the leading edge pressure surface (*LE*(*PS*)) and the leading edge (*LE*) show higher magnitudes of fluctuation than those observed on the suction surface. Near the trailing edge, the magnitude of the pressure fluctuation is influenced by the flow inside the blade passage. Since the overall flow turning inside the blade passage decreases with the speed ratio, the amplitude of the periodic property also decreases (Figs. 10(*A*) and 10(*B*)) with the speed ratio. However, the aperiodic component is influenced largely not only by the aperiodic pressure field upstream but also due to the pump downstream. Therefore, the aperiodic

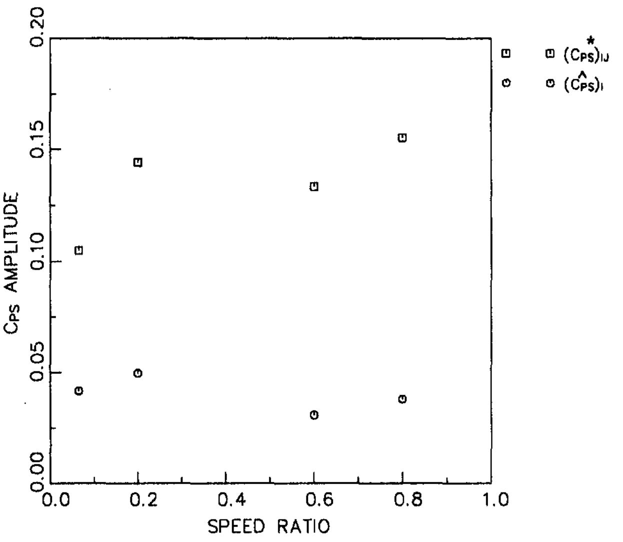

Fig. 9(*A*) Variation of blade C_{PS} amplitude with speed ratio at leading edge (*LE*)

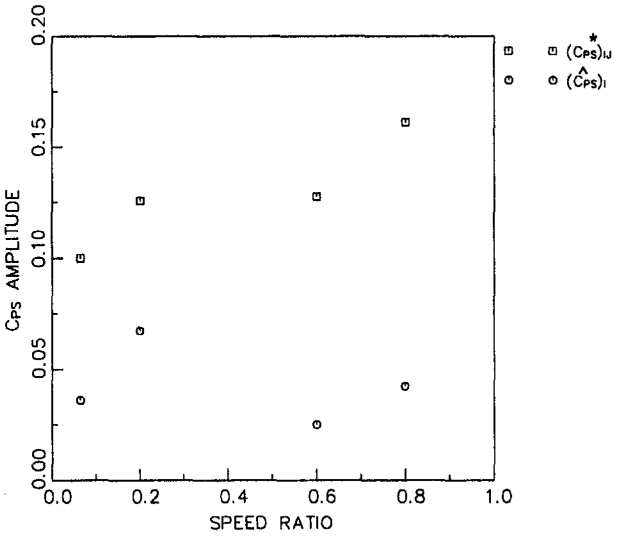

Fig. 9(*B*) Variation of blade C_{PS} amplitude with speed ratio at *LE*(*SS*)

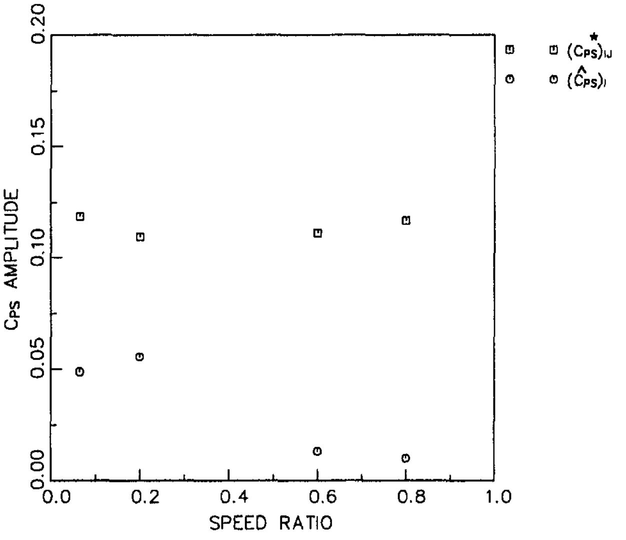

Fig. 9(*C*) Variation of blade C_{PS} amplitude with speed ratio at *LE*(*PS*)

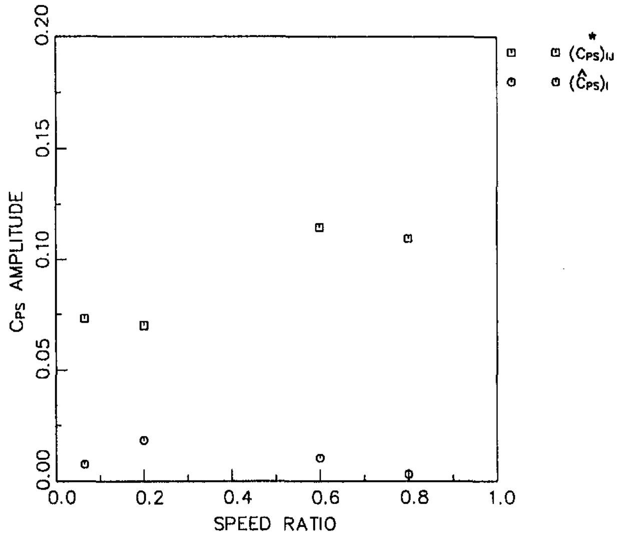

Fig. 10(*A*) Variation of blade C_{PS} amplitude with speed ratio at *TE*(*SS*)

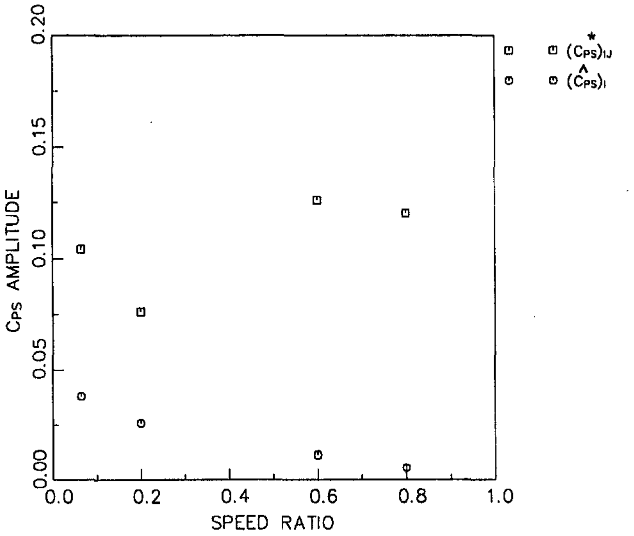

Fig. 10(*B*) Variation of blade C_{PS} amplitude with speed ratio at *TE*(*PS*)

component increases with the speed ratio at the trailing edge of the stator.

Concluding Remarks

The analysis of the data in the frequency domain revealed several frequencies of unsteadiness. The closed-loop flow path generates combination of the pump and the turbine blade passing frequencies. The shaft frequencies of the pump and the turbine (P_S and T_S) and the blade passing frequencies (P, T) dominate the unsteady flow field. However, the magnitude of combination of blade passing frequencies ($P - T$, $T - (P - T)$, etc.) was also found to be significant. The blade passing frequencies of the turbine and pump are dominant only at the respective interfaces (viz., turbine–stator, pump–stator).

Flow unsteadiness at the stator inlet (or the turbine exit) has significant influence on the unsteady pressure on the surface of the stator. Unsteadiness in stagnation pressure and flow angle has dominant influence on the stator blade pressure field. The potential effects of downstream pump influence the trailing edge pressure distribution.

The unsteady pressure envelope calculated by using the panel method and upstream flow parameters shows good agreement with the experimental data. The unsteadiness in upstream flow angles and steady-state stator blade loading have dominant influence over the unsteadiness near the trailing edge; whereas, unsteadiness in the upstream stagnation pressure and the inlet flow angles have dominant influence on the amplitude of the unsteady blade static pressure near the leading edge.

Acknowledgments

This work was sponsored by Powertrain division of General Motors Corporation. The authors wish to express their gratitude to R. R. By for his assistance, advice, and comments on the experimental program. Assistance by Y. Dong in the data acquisition is also acknowledged.

References

Bahr, H. M., et al., 1990, "Laser Velocimeter Measurements in the Stator of a Torque Converter," SAE Paper No. 901769.

Browarzik, V., and Grahl, K. G., 1992, "Non-steady Flow Measurements Inside a Hydrodynamic Torque Converter by Hot-Film Anemometry," ASME Paper No. 92-GT-161.

Brun, K., Flack, R. D., and Gruver, J. K., 1996, "Laser Velocimeter Measurements in the Pump of a Torque Converter: Part II—Unsteady Measurements," ASME JOURNAL OF TURBOMACHINERY, Vol. 118, pp. 570–577.

By, R. R., and Lakshminarayana, B., 1991, "Static Pressure Measurements in a Torque Converter," SAE Paper No. 911934.

Dunn, M. G., and Haldeman, C. W., 1994, "Phase-Resolved Surface Pressure and Heat-Transfer Measurements on the Blade of a Two-Stage Turbine," *Unsteady Flows in Aeropropulsion,* ASME AD-Vol. 40, pp. 13–25.

Marathe, B. V., Lakshminarayana, B., and Dong, Y., 1996, "Experimental and Numerical Investigation of Stator Exit Flow Field of an Automotive Torque Converter," ASME JOURNAL OF TURBOMACHINERY, Vol. 118, pp. 835–845.

McFarland, E. R., 1984, "A Rapid Blade-to-Blade Solution for Use in Turbomachinery Design," ASME *Journal of Engineering for Gas Turbines and Power,* Vol. 106, pp. 376–382.

McFarland, E. R., 1993, "An Integral Equation Solution for Multi-stage Turbomachinery Design Calculations," ASME Paper No. 93-GT-41.

Manwaring, S. R., and Fleeter, S., 1992, "The Unresolved Unsteady Flow in Multistage Compressor Blade Rows," *Experimental Thermal and Fluid Science,* Vol. 5, pp. 225–234.

Schulz, H. D., Gallus, H. E., and Lakshminarayana, B., 1990, "Three Dimensional Separated Flow Field in the Endwall Region of an Annular Compressor Cascade in the Presence of Rotor-Stator Interaction: Part 2—Unsteady Flow and Pressure Field," ASME JOURNAL OF TURBOMACHINERY, Vol. 112, pp. 679–690.

Laser Velocimeter Measurements in the Turbine of an Automotive Torque Converter: Part I—Average Measurements

K. Brun

R. D. Flack

Mechanical, Aerospace, and Nuclear
Engineering Department,
University of Virginia,
Charlottesville, VA 22903

The three-dimensional average velocity field in an automotive torque converter turbine was examined. Two significantly different operating conditions of the torque converter were tested: the 0.065 and 0.800 turbine/pump speed ratio. Velocities were measured using a one-directional, frequency-shifted laser velocimeter. The instantaneous angular positions of the torque converter turbine and pump were recorded using digital shaft encoders. Shaft encoder information and velocities were correlated to generate average velocity blade-to-blade profiles and velocity vector plots. Measurements were taken in the inlet, quarter, mid, and exit planes of the turbine. From the experimental velocity measurements, mass flows, turbine output torque, average vorticities, viscous dissipation, inlet incidence flow angles, and exit flow angles were calculated. Average mass flows were 23.4 kg/s and 14.7 kg/s for the 0.065 and 0.800 speed ratios, respectively. Velocity vector plots for both turbine/pump speed ratios showed the flow field in the turbine quarter and midplanes to be highly nonuniform with separation regions and reversed flows at the core-suction corner. For the conditions tested, the turbine inlet flow was seen to have a high relative incidence angle, while the relative turbine exit flow angle was close to the blade angle.

Introduction

The torque converter is a hydrodynamic, recirculating, multicomponent turbomachine. Torque converters are commonly used in cars, buses, locomotives, and construction equipment as a means of smooth torque transmission between the engine and the automatic transmission and to provide torque amplification during start-up conditions. They are also often used as a smooth clutch to engage gas turbines. The typical torque converter consists of a pump, a turbine, and a stator, employing oil as the working fluid. Rotational energy is introduced into the fluid by the pump and extracted by the turbine, thus providing a ''soft'' fluid coupling between the input pump shaft and output turbine shaft. The stator is placed between the turbine exit and the pump inlet, its function being ideally to create zero incidence angle flow into the pump at the turbine/pump design speed ratio and to act as a torque reactor at low speed ratios (allowing torque amplification). Since all three torque converter components have high radial and tangential blade turning angles and rotate at different angular speeds, the internal flow field is highly complex and three dimensional.

The only nonintrusive measurement method that has been successfully used in turbomachines to measure internal velocities accurately is laser velocimetry. Velocities obtained from laser velocimetry can be employed in two ways as design tools: (1) Measured velocities help to identify flow regions that cause large inefficiencies (losses) such as separation regions or highly nonuniform velocity fields. (2) They can be applied as boundary conditions for computational flow prediction codes and as validations of the computational results.

Previous Experimental Torque Converter Studies. In the past, a number of researchers have studied the torque converter flow employing both analytical and experimental methods. A comprehensive review of relevant torque converter literature was included in papers by Bahr et al. (1990) and Gruver et al. (1996). For the sake of brevity only recent papers are reviewed herein.

Browarzik and Grahl (1992) and Browarzik (1994) used hot-film anemometry to examine the nonsteady flow field at the inlet and outlet of a pump and turbine of a Föttinger type torque converter. The effect of the pump–turbine interaction on the flow field was studied in detail. A frequency spectrum showing the relative magnitudes of velocities at the turbine and pump exit was included. Blade-to-blade velocity profiles and flow angles as a function of the pump–turbine blade interaction frequency were also presented.

By and Lakshminarayana (1991, 1993) and By et al. (1993) measured steady pressures in the stator and the pump of a torque converter and compared it to viscous and potential flow predictions. Good agreement was obtained. Separation regions at the core and suction sides and rotational secondary flows were predicted for the pump mid and exit planes.

More recently, Marathe et al. (1996) measured pressures at the exit of a torque converter stator using a five-hole probe and compared results with predictions from a two-dimensional Navier–Stokes code. Significant secondary flow was observed at the stator exit. Also, the flow near the stator shell side was seen to be separated. Predictions from the Navier–Stokes code were in good agreement with the pressure measurements.

Previous Laser Velocimetry Studies in Torque Converters. The same geometry as described by By et al. (1993) was used by Bahr et al. (1990) to measure the three-dimensional velocity field throughout the stator of the torque converter. For the study, a one-directional laser velocimeter was employed and the torque converter was machined entirely from Plexiglas. Digital shaft encoders were used to measure the instantaneous angular positions of the turbine and the pump. Laser velocimeter velocities were correlated with the shaft encoder information to generate blade-to-blade profiles and vector plots. The inlet, $\frac{1}{4}$, mid, $\frac{3}{4}$, and exit planes were examined for the 0.065 and 0.800

Contributed by the International Gas Turbine Institute and presented at the 40th International Gas Turbine and Aeroengine Congress and Exhibition, Houston, Texas, June 5–8, 1995. Manuscript received by the International Gas Turbine Institute March 10, 1995. Paper No. 95-GT-292. Associate Technical Editor: C. J. Russo.

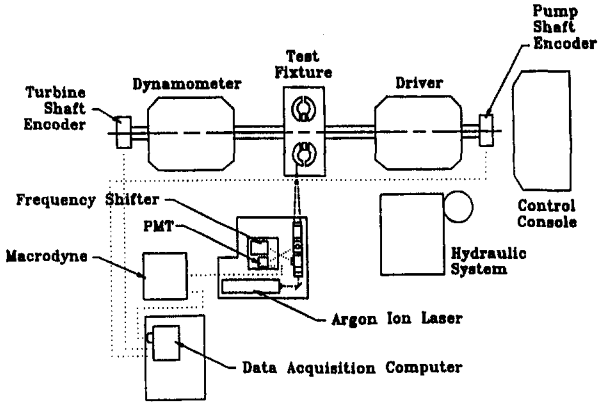

Fig. 1 Experimental setup

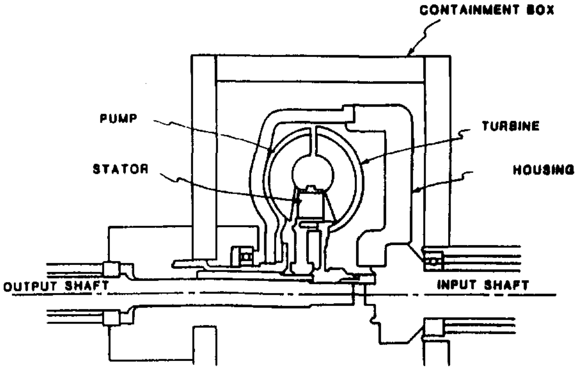

Fig. 2 Plexiglas torque converter in containment box

turbine/pump speed ratios. At the 0.800 speed ratio, a separation region was observed in the midplane at the pressure and core sides. For the same speed ratio another separation region was observed in the exit plane at the suction and shell sides. The measured velocities and calculated torque distributions were found to be poorly distributed from the core to shell sides.

Gruver et al. (1996) and Brun et al. (1996) used the same experimental facility to measure velocities throughout the torque converter pump. Average and unsteady velocities were measured in the pump inlet, mid, and exit planes. Strong rotational secondary flows were observed in the mid and exit planes. The mid and exit planes showed large flow separation regions at the core and suction sides at both speed ratios. Unsteady measurement results showed strong velocity fluctuations at the pump inlet and smaller fluctuations at the pump exit plane.

Objectives. For this research the same experimental facility and torque converter as described by Bahr et al. (1990), Gruver et al. (1996), and Brun et al. (1996) were utilized to measure the three-dimensional flow field in the turbine of a torque converter. Velocities were analyzed in detail in four planes of the turbine: inlet, quarter, mid, and exit planes. Vector plots are included to demonstrate the nature of the internal flow field. From the measured velocities the mass flow, output torque, average vorticity, viscous dissipation, incidence angle, and exit angle were calculated. Results included in this paper represent the most complete and detailed flow data for the torque converter turbine available in the literature to date. With the experimental results as a benchmark, better computational modeling of the internal torque converter flow field can be achieved, and the geometries can be optimized to improve the efficiency.

Experimental Apparatus

A schematic of the experimental test rig is shown in Fig. 1. The torque converter test fixture, support rig, laser velocimeter, signal processor, and data acquisition system are described below. This experimental apparatus is described in detail by Bahr et al. (1990), Gruver et al. (1996), and Brun et al. (1996). The facility is summarized herein.

Torque Converter Test Fixture. A standard automobile Trilok-type torque converter design was manufactured entirely of Plexiglas and installed in an oil-filled Plexiglas containment box, which is optically accessible from all sides (Fig. 2). Performance curves for the torque converter showing power efficiency (output power/input power) and torque ratio (output torque/input torque) versus speed ratio (turbine speed/pump speed) are presented in Fig. 3. One should note that in an automotive torque converter, the power efficiency increases linearly with speed ratio above the stator decoupling point ($SR \approx 0.8$ in this design) to reach almost 100 percent efficiency at a speed ratio of unity. The relevant outside dimensions of the torque converter are shown in Fig. 4. The torque converter pump consisted of 27 identical blade passages, the turbine of 29 identical blade passages, and the stator of 19 identical passages. Pump and turbine blades had a constant thickness of 1.1 mm, while the stator blades were airfoil shaped with a chord length of 22.5 mm and a maximum thickness of 7.5 mm. The detailed dimensions of the torque converter and blade passage geometries were previously documented by By (1993) and by By and Lakshminarayana (1991, 1993). Thus, the measurement geometry and the test conditions can be reconstructed from information in this manuscript and from the above references.

The index of refraction of Plexiglas was nominally 1.490. To reduce undesired laser beam scattering and bending, the refractive index of the oil and the Plexiglas had to be closely matched. Shell-Flex 212 oil was used as the flow medium, which has an index of refraction of 1.489 at 25°C and 1.480 at 50°C. However, perfectly matching the index of refraction of the oil and the Plexiglas was impossible because of thermal transients and gradients in the oil during torque converter operation and because of the birefringent properties of Plexiglas, especially after machining. The density of the oil at 25°C was 899.1 kg/m^3, and the viscosity was 1.98×10^{-3} kg/m·s and 1.29×10^{-3} kg/m·s at 25°C and 40°C, respectively. The oil was seeded with metallic coated glass particles, which have an

Nomenclature

A = measurement plane area
dm/dt = mass flow rate
g = gravity
h_l = steady viscous dissipation head loss per chord length
r = radius from shaft center
SR = speed ratio
T_θ = torque flux
u, v, w = x, y, z-direction velocity in rotating turbine frame
V = total velocity vector in stationary frame
v_θ = tangential velocity in rotating turbine frame
V_θ = tangential velocity in stationary frame
V_z = axial velocity
x = core to shell side direction (rotating frame)
y = pressure to suction side direction (rotating frame)
z = throughflow direction
β = angle (rotating frame) with respect to the axial direction
μ = dynamic viscosity
ξ = average vorticity
ϕ = viscous dissipation function
ω_{pump} = pump angular speed
ω_{turbine} = turbine angular speed

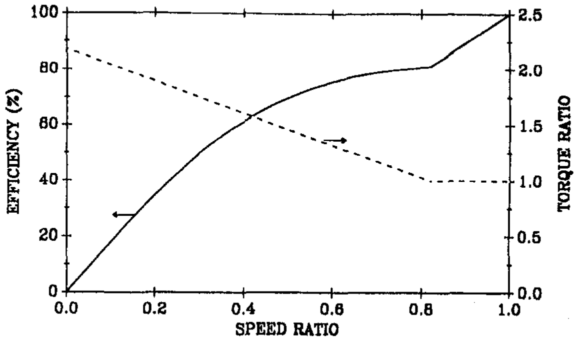

Fig. 3 Torque converter power efficiency and torque ratio

average diameter of 12 μm and a specific gravity of 2.6. The specific gravity of the particles was sufficiently close to the oil's specific gravity (0.9) so that particle lag was not a problem. Maximum errors due to particle lag in turbulent flow were calculated to be 0.005 m/s. The seeding density was approximately 4000 particles per cubic centimeter of oil.

For the remainder of this paper the torque converter cylindrical coordinate system is defined as follows: axial—along the torque converter shaft, tangential—in the torque converter rotational direction, and radial—perpendicular to the shaft.

Torque Converter Support Rig. The support rig is shown in Fig. 1. It consisted of an 18 kW electric motor to drive the torque converter pump and a 130 kW eddy-current dynamometer to absorb the rotational energy from the torque converter turbine. The rotational speeds of the pump and turbine shafts were controlled to within 1 rpm. The motor and dynamometer were cooled and lubricated by a hydraulic system. Oil pressures and temperatures were measured throughout the test fixture and support system. Load cells on the shafts were used to measure the input and output torques of the torque converter.

Shaft Encoders and Angular Resolution. Two 10-bit (1024 circumferential sectors) shaft encoders were attached to the pump and turbine shafts to record the pump and turbine instantaneous angular positions. Since the turbine had 29 blade passages, this leads to an angular resolution of 35 sectors per turbine blade passage. The pump and stator passages had resolutions of 37 and 54 angular sectors, respectively.

Laser Velocimeter. The measurement system was a commercially available one-directional frequency shifted backscatter laser velocimeter. A 2 W argon-ion laser operating at a wavelength of 514.5 nm was the emission source and a photomultiplier tube (PM tube) was used to measure the laser-Doppler signals. The effective probe volume (measurement location) was 72 μm in diameter and 793 μm long, and the focusing (and collecting) lens had a focal length of 250.8 mm. Frequency shifting of the beams was incorporated to distinguish positive from negative velocities.

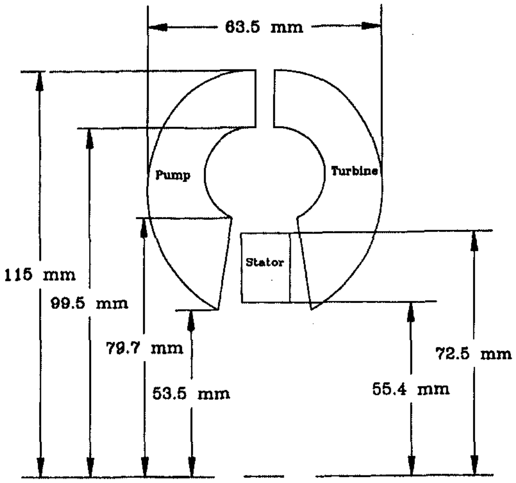

Fig. 4 Relevant torque converter dimensions, (mm)

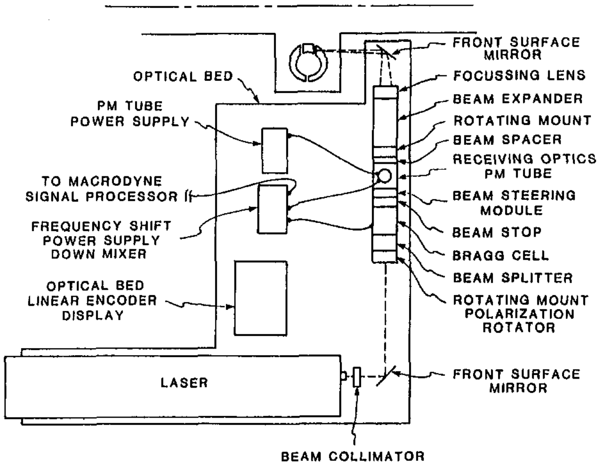

Fig. 5 Laser velocimeter and optics

Both laser and optics were mounted on a mill table to ensure a stable position. To move the LV probe volume, the mill table was automatically traversed in Cartesian directions using stepper motors. The mill table positions were monitored by linear encoders and a digital read-out (accuracy of 0.005 mm). Laser and optics mounted on the mill table are shown in Fig. 5.

Signal Processing and Data Acquisition. Laser velocimeter signals from the PM tube were bandpass filtered to eliminate noise and then converted to velocity signals using a burst counter-type processor. The processor employed a minimum threshold setting and a $\frac{5}{8}$ peak counter comparator to validate signals. The minimum threshold eliminated low-voltage noise and the $\frac{5}{8}$ peak count comparator rejected signals from multiple particles in the probe volume. Velocity signals were then sent to a dedicated data acquisition computer via a high-speed digital I/O card. The instantaneous angular positions of the pump and turbine given by the shaft encoders were read into the data acquisition system simultaneously with each velocity signal.

Measurement Uncertainties and Errors. Typical turbulence intensities in the torque converter flow were 20–30 percent (Bahr et al., 1991). Hence, errors due to laser velocimeter individual realization biases were (according to Flack, 1982) approximately 3 percent and could be neglected.

Uncertainties in the measured velocities were due to beam crossing angle deviations, digital processing of the burst signals, shaft encoder uncertainty, and the averaging of a finite number of samples. The combined uncertainty of these factors was typically ±0.05 m/s. Furthermore, uncertainties in probe volume positioning translate into velocity uncertainties when velocity gradients are present in the flow. The uncertainty of the probe volume position is affected by small index of refraction changes and also by the number of Plexiglas–oil interfaces a laser beam has to cross. For example, to measure velocities in the turbine inlet the beams had to cross four interfaces and the positioning uncertainty was 0.3 mm. On the other hand, for turbine exit plane measurements the beams had to cross eight interfaces and the positioning uncertainty was 0.6 mm. Typical velocity uncertainties due to positioning were 0.05 m/s and 0.08 m/s for the inlet and exit planes, respectively. Thus, the total velocity

Table 1 Test conditions

	Condition #1	Condition #2
Speed Ratio:	0.065	0.800
Pump Speed:	800 rpm	1100 rpm
Turbine Speed:	52 rpm	880 rpm
Stator Speed:	0 rpm	0 rpm
Input Torque:	25 Nm	34 Nm
Output Torque:	27 Nm	16 Nm
Power efficiency:	13.0%	82.0%

uncertainty calculated from all factors noted above was 0.08 m/s for the inlet, quarter, and midplanes, and 0.10 m/s for the exit plane.

Experimental Procedure

Optical Alignment and Probe Volume Positioning. Although the LV system was one-directional, all three velocity components were obtained by realigning the optics and accessing the torque converter at Cartesian angles in independent measurements. The axial and tangential velocity components were measured by aligning the laser velocimeter beams perpendicularly to the torque converter shaft, while for the radial component the beams were aligned parallel to the shaft (Fig. 1 shows the arrangement to measure the axial component and Fig. 5 shows the arrangement to measure the radial component). Measurement locations in the turbine were accurately determined using marked reference points and the known torque converter dimensions.

Measurement Procedure. The torque converter was run at two significantly different operating conditions. These conditions are shown in Table 1. Before each set of data was taken, the test rig was run for an hour so that temperatures and pressures within the system could stabilize. The probe volume was then positioned at the desired measurement location and velocity signals were read into the computer.

Velocity measurements were taken in the inlet, quarter, mid, and exit planes of the torque converter turbine as shown in Fig. 6. Each blade passage was defined by a pressure and a suction side as well as a core and a shell side.

In all measurement planes, ten evenly spaced measurement locations were accessed between the core and the shell sides and were set by traversing the mill table. For each measurement location the three velocity components were measured. As the turbine rotated by the stationary laser velocimeter probe volume, all 29 turbine blade passages were accessed. Approximately 30,000 valid velocity samples were collected. This procedure was followed for all 10 core-to-shell positions. Using the turbine shaft encoder information, blade-to-blade profiles were generated for all 29 turbine blade passages.

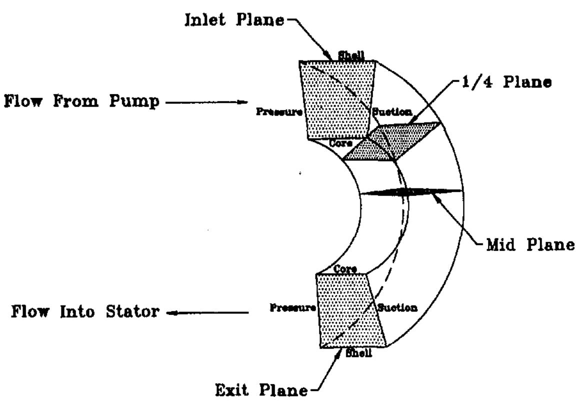

Fig. 6 Turbine blade passage and measurement planes

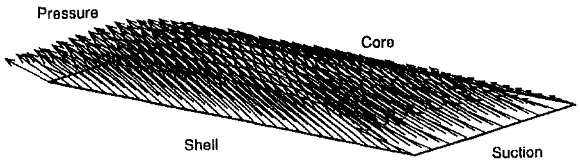

Fig. 7 Inlet plane average velocity vector plot for 0.065 speed ratio

Blade-to-blade profiles were shown to be identical within their measurement uncertainty. Hence, the 29 blade-to-blade profiles were superimposed and averaged to obtain one time-averaged blade-to-blade profile for each core to shell position. The average blade-to-blade profiles were then arranged by their core-to-shell measurement locations and three-dimensional vector plots were generated using commercially available plotting routines. For each of the measured blade-to-blade positions, more than 500 valid velocity samples were collected. Repeatability studies and histograms showed this to be a sufficient sample size for a high confidence in the average velocities. Typical 95 percent confidence intervals of the average velocities were ±0.05 m/s.

Measurement Results

Turbine time-averaged velocity results are presented and discussed for four measurement planes and two speed ratios. Flow field results are shown as vector plots, secondary flow (velocities tangent to the measurement plane) plots, and throughflow contour plots. For the remainder of this paper throughflow velocity is defined as the velocity component normal to a given measurement plane. All velocities are presented relative to the rotating turbine frame. From the measurement results, the turbine output torques, average vorticity, viscous dissipation, incidence angles, and exit angles were calculated. All of the above are discussed. Although only time-averaged relative velocities are presented herein, Brun and Flack (1993) reported unsteady effects for the same apparatus.

Flow Field at the 0.065 Speed Ratio. Typical velocity results for the 0.065 speed ratio are shown in Figs. 7–12. The inlet, quarter, mid, and exit plane flow fields are presented. These plots illustrate general flow trends in the torque converter turbine.

Figure 7 shows a vector plot of the turbine inlet flow field. For this case the flow enters the turbine with a strong secondary flow component from the suction to the pressure side. The pump operates at a higher rotational speed than the turbine ($\omega_{\mathrm{pump}} - \omega_{\mathrm{turbine}} = 750$ rpm), causing the pump exit flow to enter the turbine with preswirl. This preswirl appears in the turbine inlet as a secondary flow component from the suction to the pressure side. Typical secondary flow (preswirl) velocities for this case are 6 m/s. The throughflow velocity distribution for the inlet plane can be observed in Fig. 8. Peak throughflow velocities of 4.0 m/s are located at the shell side and centered between the pressure and suction sides. The throughflow velocity gradually decreases toward the core side, with minimum velocities of 0.2 m/s located directly at the core. Earlier measurements of the pump flow field by Gruver et al. (1996) showed a similar trend in the pump exit plane. The velocity deficit at the pump exit core side was found to be due to flow separation caused by the high radial to axial flow turning angle in the pump. Thus, flow separation in the pump has a noticeable effect on the downstream turbine flow field.

The quarter plane flow field for the 0.065 speed ratio is shown in Figs. 9 and 10. The vector plot (Fig. 9) shows that the flow, which was relatively uniform in the inlet plane, has become nonuniform with large throughflow velocity gradients as it

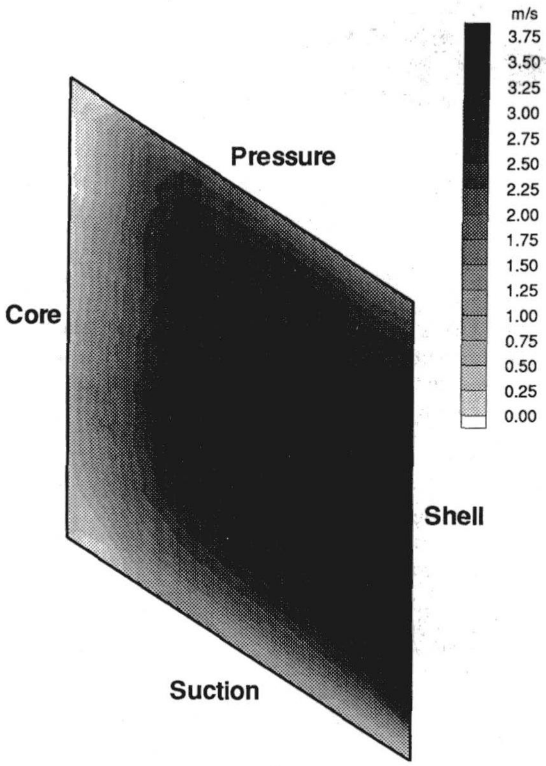

Fig. 8 Inlet plane average throughflow contour plot for 0.065 speed ratio

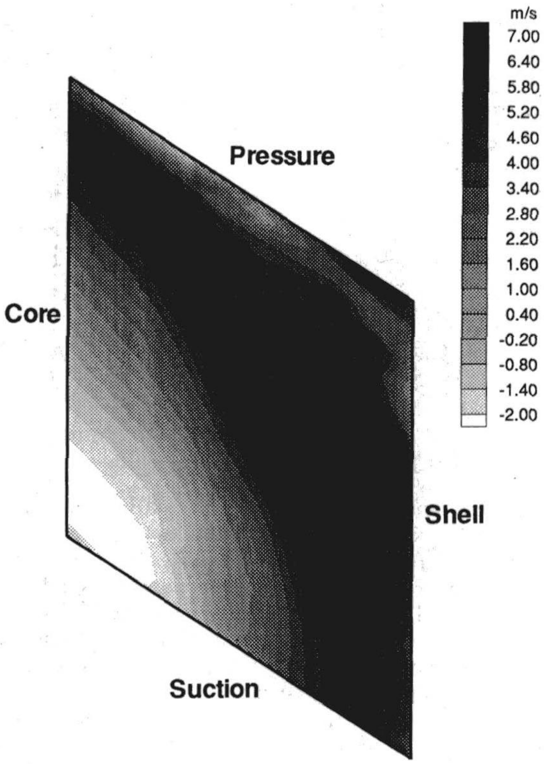

Fig. 10 Quarter plane average throughflow contour plot for 0.065 speed ratio

moved downstream into the quarter plane. A large separation region (about 30 percent of the flow area) with strong reversed flows of up to 2.0 m/s can be observed at the core and suction sides.

The cause of this separation is the high incidence flow into the turbine inlet. The flow stalls and separates at the leading edges of the turbine blades and is not able to reattach because of the high radial flow turning angle in the turbine. Typical secondary flow magnitudes for this case are 2.1 m/s. Figure 10 shows the quarter plane throughflow velocity distribution. Peak velocities of 6.2 m/s are observed close to the pressure and shell sides, while the largest negative (reversed flow) velocities are located in the core-suction corner.

Figures 11, 12, and 13 present the midplane flow field for the 0.065 speed ratio. A separation region at the core-suction corner can be observed (Fig. 11). The general flow trends in the midplane are similar to those in the quarter plane. Figure 12 shows peak throughflow velocities of 5.5 m/s near the pressure and shell sides and reversed flow velocities of 0.5 m/s at the core–suction corner. The overall flow field has become more uniform between the quarter and the midplane. The area of separated flow covers only about 15 percent of the flow area. For this case the flow in the plane (secondary flow) is shown in Fig. 13. The secondary flow is approximately divided along a diagonal line from the pressure–core corner to the shell–suction corner. Below the diagonal the flow is predominantly directed toward the core–suction corner ($\approx$0.5 m/s) and feeds into the reversed throughflow region, while above the diagonal the flow is toward the pressure–shell corner ($\approx$1.0 m/s) and feeds the peak through flow region in that corner.

Figure 14 presents the turbine exit flow field. Peak throughflow velocities are 3.3 m/s, and are located at the shell. The throughflow velocities decrease gradually toward the core side with smallest velocities of 0.8 m/s directly at the core. The throughflow velocity deficit at the core is a residual effect generated by the upstream flow separation in the quarter and midplanes. For this case, typical secondary flow velocities are from the pressure to the suction side with magnitudes of 4.0 m/s.

Flow Field at the 0.800 Speed Ratio. Typical velocity results for the torque converter turbine at the 0.800 speed ratio are shown in Figs. 15–18. The general velocity trends for the 0.800 speed ratio are similar to those observed at the 0.065 speed ratio.

Figure 15 shows a vector plot of the turbine inlet plane flow field. The throughflow velocity is seen to decrease from the shell ($\approx$3.0 m/s) to the core ($\approx$0.0 m/s) side. For this case, the difference between pump and turbine rotational speeds ($\omega_{\text{pump}} - \omega_{\text{turbine}} = 220$ rpm) is not as large as it was for the 0.065 speed ratio. Consequently, the flow enters the turbine with less preswirl. Typical secondary (preswirl) velocities are 1.3 m/s from

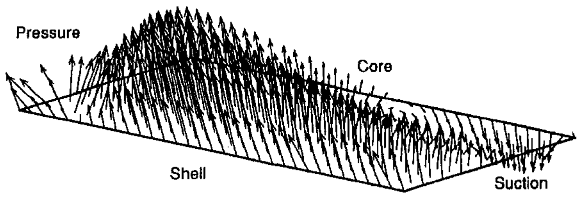

Fig. 9 Quarter plane average velocity vector plot for the 0.065 speed ratio

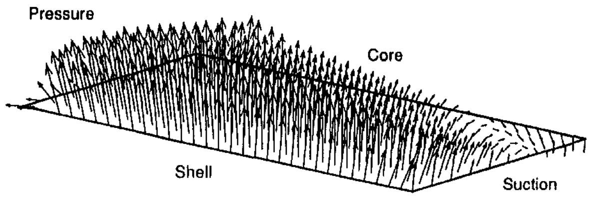

Fig. 11 Midplane average velocity vector plot for 0.065 speed ratio

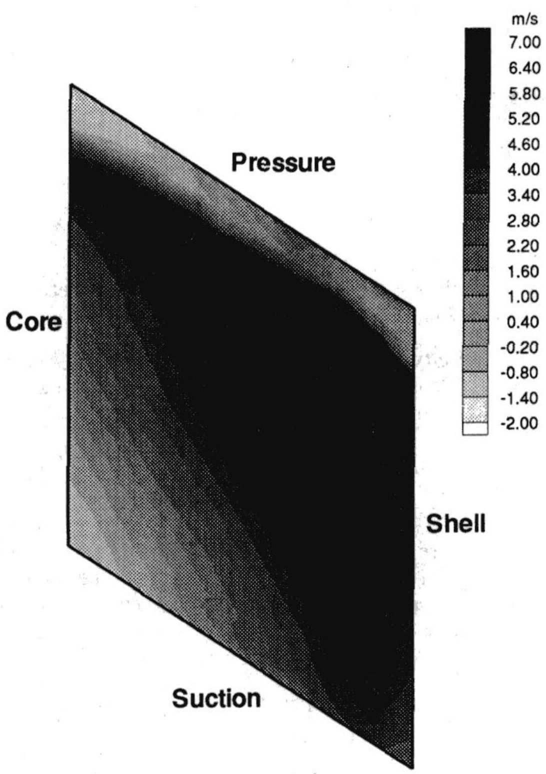

Fig. 12 Midplane average throughflow plot for 0.065 speed ratio

the suction to the pressure side. Throughflow maximum and minimum velocities are 3.0 m/s at the shell and 0.0 m/s at the core, respectively. The quarter plane flow field is presented in Fig. 16. No flow separation can be seen, but a low-velocity region (deficit) is apparent at the core–suction corner. Minimum throughflow velocities here are 0.5 m/s. Peak throughflow velocities (3.5 m/s) occur close to the pressure and shell sides. Typical secondary velocity magnitudes for this case are 2.0 m/s.

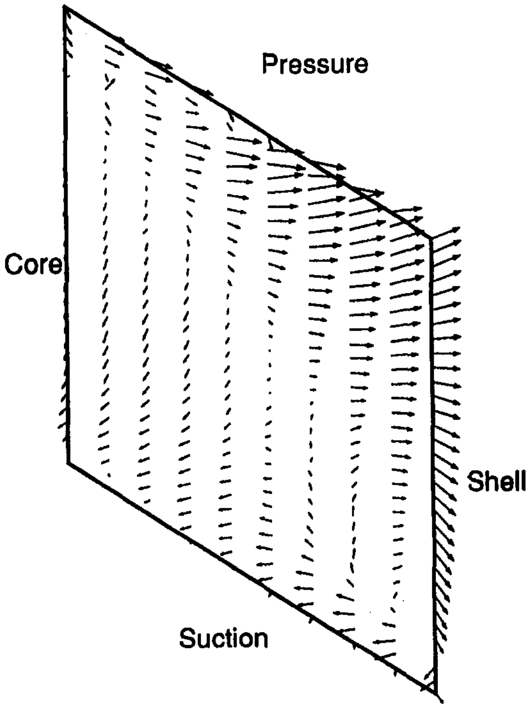

Fig. 13 Midplane average secondary velocity plot for 0.065 speed ratio

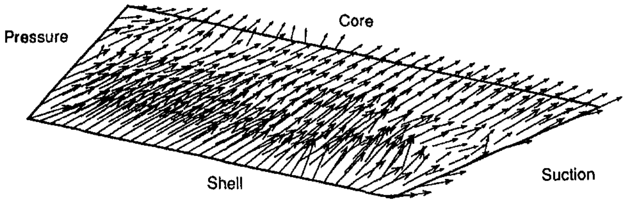

Fig. 14 Exit plane average velocity vector plot for 0.065 speed ratio

In Fig. 17 the turbine midplane flow field is presented. The velocity field is relatively uniform and no separation regions are noticeable; no significant velocity deficit can be identified on the core side. The flow has almost fully recovered the velocity deficit that was seen at the quarter plane core–suction corner for this case. Maximum and minimum velocities are 3.3 m/s at the core and 0.7 m/s at the pressure side, respectively. Typical secondary velocity magnitudes here are 1.0 m/s.

Finally, the turbine exit velocity field is presented in Fig. 18. The flow exits the turbine uniformly and the flow is well aligned with the turbine exit blades. Typical secondary velocity magnitudes are 2.5 m/s, and the maximum and minimum velocities are approximately 2.0 m/s and 0.5 m/s, respectively.

Mass Flow Rates. Mass flow rates (*dm*/*dt*) for inlet, quarter, mid, and exit planes were calculated by numerically integrating in two directions the average throughflow velocities

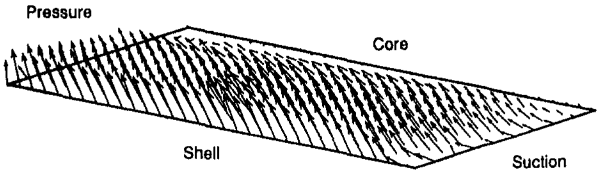

Fig. 15 Inlet plane average velocity vector plot for 0.800 speed ratio

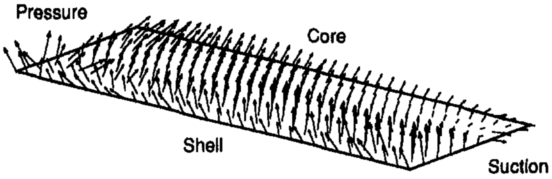

Fig. 16 Quarter plane average velocity vector plot for 0.800 speed ratio

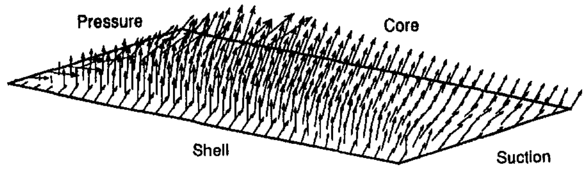

Fig. 17 Midplane average velocity vector plot for 0.800 speed ratio

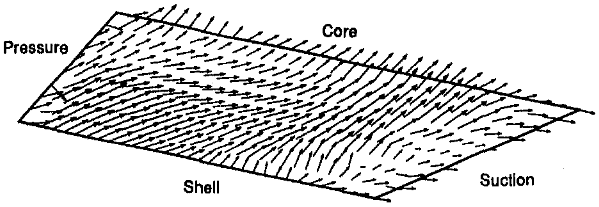

Fig. 18 Exit plane average velocity vector plot for 0.800 speed ratio

Table 2 Mass flows (kg/s)

	0.065 Speed Ratio	0.800 Speed Ratio
Inlet Plane:	22.3 ± 1.7	15.1 ± 1.3
1/4 Plane:	24.2 ± 2.3	14.4 ± 1.2
Mid Plane:	24.9 ± 2.2	15.9 ± 1.4
Exit Plane:	21.6 ± 3.9	12.7 ± 2.3

(w_i), the incremental flow areas (A_i), and the oil density (ρ) across the passage:

$$\frac{dm}{dt} = \sum \frac{dm_i}{dt_i} = \sum w_i A_i \rho$$

Small differences in mass flows were observed. To evaluate the accuracy of the data, an uncertainty analysis of the mass flow rate was performed based on both the uncertainty of the throughflow velocities and the uncertainties of the measurement locations. Results are shown in Table 2. Measurement results agree well with earlier measurements in the pump by Gruver et al. (1996).

Turbine Torques. The output torque flux of the turbine was calculated using Euler's form of the angular momentum equation:

$$T_\theta = \iint r V_\theta \rho V \cdot dA$$

where r is the radius from the shaft center, V_θ is the tangential velocity component in the stationary frame, V is the total velocity, and ρ is the fluid density. The surface integral was evaluated numerically for all four measurement planes:

$$T_\theta = \sum \sum [\rho r_j V_{\theta ij} w_{ij}] \Delta x \Delta y$$

where w is the throughflow component of the velocity. The total output torque is the difference between the inlet and the exit torque flux. Results of the torque between the inlet and mid-planes, between the mid and exit planes, and the total output torque (between inlet and exit) are presented in Table 3. Torques measured from the shaft load cells are also presented.

The total output torque at the 0.065 speed ratio is 5.5 Nm higher than at the 0.800 speed ratio. For 0.065 speed ratio the chordwise torque distribution is uneven; 82 percent (20 Nm) of the total torque (24.2 Nm) is extracted between the inlet and the midplane; while for the 0.800 speed ratio the torques are more evenly distributed with 62 percent (11.6 Nm) of the total torque (18.8 Nm) extracted between the inlet and the midplane. The calculated torques agree to within the measurement uncertainty with the torque from the shaft load cells.

The uneven torque distribution at the 0.065 speed ratio is caused by the strong tangential velocity component (preswirl) in the secondary flow entering the turbine. For the 0.065 speed ratio case, this flow component is approximately 6 m/s faster than the turbine blade speed. Hence, the tangential flow must be decelerated and redirected by the blades, causing a significant momentum exchange and torque generation on the blades. The momentum exchange occurs primarily in the first half of the blade passages between the inlet and midplanes. Thus, significantly more torque is extracted between the inlet and midplanes than between the mid and exit planes. For the 0.800 speed ratio the tangential velocity magnitude is smaller (≈1 m/s) and consequently the torque is more evenly distributed between the inlet and exit planes.

Table 3 Turbine torque [Nm]

	0.065 Speed Ratio	0.800 Speed Ratio
Inlet-Mid Plane:	20.0 ± 2.4	11.6 ± 2.1
Mid-Exit Plane:	4.2 ± 2.1	7.1 ± 1.9
Total Output:	24.2 ± 3.1	18.8 ± 2.8
Load Cell Torque:	25.8 ± 1.1	16.1 ± 0.9

Table 4 Average vorticity (s^{-1})

	0.065 Speed Ratio	0.800 Speed Ratio
Inlet Plane:	13.2	87.8
1/4 Plane:	6.4	43.1
Mid Plane:	28.0	45.7
Exit Plane:	79.0	44.4

Flow Vorticity. To quantify the secondary flow components in the planes, the average vorticity (ξ) was calculated using the following equation:

$$\xi = -\frac{1}{A}\iint (\nabla \times V)\cdot dA = -\frac{1}{A}\iint \left(\frac{\partial v}{\partial x} - \frac{\partial u}{\partial y}\right) dA$$

where x and y are in the plane directions, u and v are secondary flow velocities in the plane of interest, and A is the plane area. The component u is in the core to shell direction and v is in the pressure to suction direction. To integrate the experimental velocity data the expression was rewritten in numerical form:

$$\xi = -\frac{1}{A}\sum\sum\left[\frac{v_{i+1} - v_i}{\Delta x} - \frac{u_{i+1} - u_i}{\Delta y}\right]\Delta x \Delta y$$

The average vorticity was obtained by integrating across an entire measurement plane.

Results are presented for the turbine inlet, quarter, mid, and exit planes and for both speed ratios in Table 4. The magnitude of the average vorticity is generally higher at the 0.800 speed ratio than at the 0.065 speed ratio.

Steady-State Viscous Dissipation. The steady-state viscous dissipation function, ϕ, is an indicator of the nonuniformity of the time-averaged velocity field. ϕ is the term of the energy conservation equation that contains the energy losses in the fluid due to viscous internal shear stresses; it is effectively a summation of the absolute velocity gradients in the flow field. Neglecting chordwise velocity gradients ($\partial/\partial z \approx 0$), the dissipation function for incompressible, steady-state fluids can be written as:

$$\phi = 2\mu\Bigg(\bigg(\frac{\partial u}{\partial x}\bigg)^2 + \frac{\partial v}{\partial y}\bigg)^2\Bigg) + \mu\Bigg(\bigg(\frac{\partial u}{\partial y} + \frac{\partial v}{\partial x}\bigg)^2 + \bigg(\frac{\partial w}{\partial x}\bigg)^2 + \bigg(\frac{\partial w}{\partial y}\bigg)^2\Bigg)$$

The steady-state viscous head loss, h_l, per chord length is calculated by integrating the viscous dissipation function over a measurement plane and dividing it by the weight flow rate:

$$h_l = \frac{\iint \phi dA}{\left(\frac{dm}{dt}\cdot g\right)}$$

where g is gravity. This was determined by numerically integrating across a measurement plane, similar to the vorticity calculation above. The steady-state viscous head loss per chord length is a dimensionless parameter, which quantifies the pressure loss in the fluid due to laminar velocity gradient shear stresses.

Since the calculation was performed for the time-averaged flow field only, viscous dissipation due to unsteadiness and turbulence is not included in the head loss term. Typically the shear losses due to turbulence and unsteadiness are significantly larger than the viscous dissipation for the time-averaged flow field (Stepanoff, 1948). Thus, the steady-state viscous head loss does not represent total viscous flow losses; it only demonstrates the magnitudes of the viscous losses due velocity gradients and nonuniformities in the time averaged flow field. Table 5 shows head loss results for both speed ratios.

For both speed ratios the steady-state viscous losses are seen to be comparatively small in the inlet plane (0.39, 0.56 for *SR* = 0.065, 0.800, respectively) and large in the quarter plane (2.72, 3.29 for *SR* = 0.065, 0.800, respectively). This corresponds to observations of a uniform flow field in the inlet and a highly nonuniform flow field in the quarter plane for both cases. Mid and exit plane steady-state losses are seen to be smaller again. The magnitudes of the overall steady state viscous dissipation losses for both speed ratios are similar.

Turbine Inlet and Exit Flow Angles. Knowledge of the turbine interface flow angles is essential for a one dimensional flow analysis. Thus, the average relative inlet and exit flow angles, β, were calculated from the measured velocities using:

$$\beta = \tan^{-1}\left(\frac{v_\theta}{V_z}\right)$$

where V_z is the axial velocity and v_θ is the weighted tangential velocity in the rotating turbine frame. The weighted relative tangential velocity was obtained by averaging the tangential components and weighing the value proportionally to the mass flux across a plane. Results are presented in Table 6. Angles are given in the relative rotating frame with respect to the axial direction and also with respect to the inlet and exit blades (in brackets).

Results show that the inlet and exit flow at the 0.800 speed ratio is well aligned with the blades (−5.8 and 7.4 deg, respectively). At the 0.065 speed ratio the flow enters the turbine with a high incidence angle (26.8 deg), which is caused by the significant amount of preswirl the flow experiences from the pump. The 0.065 speed ratio exit flow angle is small (1.2 deg) and the flow is thus comparatively well aligned with the blades.

Because of the high incidence angle at which the flow enters the turbine for the 0.065 speed ratio, it separates at the leading edge of the inlet blades. The separation bubble that consequently develops on the suction side of the blades extends all the way through the quarter plane into the midplane. Figures 9–12 show this separation bubble. For the 0.800 speed ratio the incidence angle is small and consequently no leading edge separation or separation bubble can be observed (Figs. 15–17).

Conclusions

A laser velocimeter was used to measure the three-dimensional flow field in the inlet, quarter, mid, and exit planes of the turbine of an automotive torque converter. Time-averaged velocities are presented and analyzed. Results in this paper embody the most detailed velocity measurements in torque converters available to date. Important conclusions drawn from this investigation are:

1 At the 0.065 speed ratio the flow enters the turbine at a high incidence angle (26.8 deg) and with a significant amount of preswirl ($\approx$6 m/s), causing it to separate at the leading edge of the suction blade. Because of the rapid radial flow turning in the turbine the flow is not able to reattach before the midplane. Evidence of the separated flow are large regions (25 percent of the flow area) of reversed flow at the suction/core sides in the quarter and midplanes.

2 For the 0.800 speed ratio the flow enters the turbine with a small incidence angle (−5.8 deg) and preswirl velocities of less than 1 m/s. No separation or reversed flow can be seen for this case, but velocity deficits are still observed at the core side of the quarter and midplanes.

3 For both speed ratios the flow in the exit plane is attached and leaves the turbine uniformly and well aligned with the blades (1.2 and 7.4 deg exit angles for 0.065 and 0.800 speed ratios, respectively).

4 The turbine mass flow rates are approximately 22 kg/s and 15 kg/s for the 0.065 and 0.800 speed ratios, respectively. These results agree well with earlier pump measurements by Gruver et al. (1996).

5 The turbine output torque, calculated using the angular momentum equation, are 24.2 Nm and 18.7 Nm for the 0.065 and 0.800 speed ratios, respectively. The torque are very unevenly distributed at the 0.065 speed ratio; 82 percent of the torque is extracted between the inlet and midplanes. For the 0.800 speed ratio, the torque are approximately evenly distributed; only 62 percent of the torques are extracted between inlet and midplane.

6 The steady-state viscous dissipation head loss was calculated from the experimental data. The steady-state dissipation is an indicator of the nonuniformity of a flow field. Largest steady-state head losses are observed in the quarter plane for both speed ratios. This corresponds to the observation of a highly nonuniform flow field in this plane.

Table 5 Steady viscous head loss per chord length

	0.065 Speed Ratio	0.800 Speed Ratio
Inlet Plane:	0.39	0.56
1/4 Plane:	2.72	3.29
Mid Plane:	1.21	0.99
Exit Plane:	1.29	1.46

Table 6 Average turbine inlet and exit flow angles

	Inlet Plane	Exit Plane
0.065 Speed Ratio:	78.8° (26.8°)	61.2° (1.2°)
0.800 Speed Ratio:	46.2° (-5.8°)	67.4° (7.4°)

Acknowledgments

This research was sponsored in part by General Motors Corporation's NAO Engineering Center in Warren, MI, the GM Powertrain Division in Ypsilante, MI, and the Rotating Machinery and Controls (ROMAC) Industrial Program at the University of Virginia. The authors wish to express their gratitude to Don Maddock for his support and involvement.

References

Bahr, H. M., Flack, R. D., By, R. R., and Zhang, J. J., 1990, "Laser Velocimeter Measurements in the Stator of a Torque Converter," *SAE Trans., Journal of Passenger Cars,* Vol. 99, pp. 1625–1634.

Browarzik, V., and Grahl, K. G., 1992, "Non-steady Flow Measurements Inside a Hydrodynamic Torque Converter by Hot-Film Anemometry," ASME Paper No. 92-GT-161.

Browarzik, V., 1994, "Experimental Investigation of Rotor/Rotor Interaction in a Hydrodynamic Torque Converter Using Hot-Film Anemometry," ASME Paper No. 94-GT-246.

Brun, K., and Flack, R. D., 1993, "Laser Velocimetry Measurements in a Turbine of an Automotive Torque Converter," University of Virginia, SEAS Report No. UVA/532811/MANE93/102.

Brun, K., Flack, R. D., and Gruver, J. K., 1996, "Laser Velocimeter Measurements in the Pump of an Automotive Torque Converter: Part II—Unsteady Measurements," ASME JOURNAL OF TURBOMACHINERY, Vol. 118, pp. 570–577.

Brun, K., and Flack, R. D., 1995, "A Method to Measure Periodic Velocity Fields in Multi-element Turbomachines With Discrete Sampling," *Journal of Physics E, Meas. Sci. Technol.,* Vol. 5, pp. 418–425.

By, R. R., 1993, "An Investigation of Three-Dimensional Flow Fields in the Automotive Torque Converter," Doctoral Dissertation, Department of Aerospace Engineering, The Pennsylvania State University, PSU-AERSP #93-002.

By, R. R., and Lakshminarayana, B., 1991, "Static Pressure Measurements in a Torque Converter Stator," SAE Paper No. 911934.

By, R. R., and Lakshminarayana, B., 1993, "Measurement and Analysis of Static Pressure Fields in a Torque Converter Pump," *Second ASME Pumping Machinery Symposium,* ASME FED-Vol. 154, pp. 253–264; accepted for publication in ASME *Journal of Fluids Engineering.*

By, R. R., Kunz, R. F., and Lakshminarayana, B., 1993, "Navier–Stokes Analysis of the Pump of an Automotive Torque Converter," *Second ASME Pumping Machinery Symposium,* ASME FED-Vol. 154, pp. 264–274; accepted for publication in ASME *Journal of Fluids Engineering.*

Flack, R. D., 1982, "Influence of Turbulence Scale and Structure on Individual Realisation Laser Velocimeter Biases," *Journal of Physics E: Scientific Instrumentation,* Vol. 15, pp. 1038–1044.

Gruver, J. K., Flack, R. D., and Brun, K., 1996, "Laser Velocimeter Measurements in the Pump of a Torque Converter: Part I—Average Measurements," ASME JOURNAL OF TURBOMACHINERY, Vol. 118, pp. 562–569.

Marathe, B. V., Lakshminarayana, B., and Dong, Y., 1996, "Experimental and Numerical Investigation of Stator Exit Flow Field of an Automotive Torque Converter," ASME JOURNAL OF TURBOMACHINERY, Vol. 118, pp. 835–843.

Stepanoff, A. J., 1948, *Centrifugal and Axial Flow Pumps,* Wiley, New York.

Laser Velocimeter Measurements in the Turbine of an Automotive Torque Converter: Part II—Unsteady Measurements

K. Brun

R. D. Flack

Mechanical, Aerospace, and Nuclear
Engineering Department,
University of Virginia,
Charlottesville, VA 22903

The unsteady velocity field found in the turbine of an automotive torque converter was measured using laser velocimetry. Velocities in the inlet, quarter, mild, and exit planes of the turbine were investigated at two significantly different turbine/pump rotational speed ratios: 0.065 and 0.800. A data organization method was developed to visualize the three-dimensional, periodic unsteady velocity field in the rotating frame. For this method, the acquired data are assumed to be periodic at synchronous and blade interaction frequencies. Two shaft encoders were employed to obtain the instantaneous angular position of the torque converter pump and turbine at the instant of laser velocimeter data acquisition. By proper "registration" of the velocity data, visualizing the transient interaction effects between the turbine, pump, and stator was possible. Results showed strong cyclic velocity fluctuations in the turbine inlet plane as a function of the relative turbine-pump position. These fluctuations are due to the passing of upstream pump blades by the slower rotating turbine blades. Typical fluctuations in the throughflow velocity were 3.6 m/s. Quarter and midplane velocity fluctuations were seen to be lower; typical values were 1.5 m/s and 0.8 m/s, respectively. The flow field in the turbine exit plane was seen to be relatively steady with negligible fluctuations of less than 0.03 m/s. From the velocity data, the fluctuations of turbine performance parameters such as flow inlet angles, root-mean-square unsteadiness, and output torque per blade passage were calculated. Incidence angles were seen to vary by 3 and 6 deg for the 0.800 and 0.065 speed ratios, respectively, while the exit angles remained steady. The turbine output torque per blade passage fluctuated by 0.05 Nm for the 0.800 speed ratio and 0.13 Nm for the 0.065 speed ratio.

Introduction

The automotive torque converter is a recirculating hydrodynamic turbomachine with three independent blade cascade elements that govern the internal flow field. These three elements are the pump (connected to the automobile's engine), which drives the fluid and adds energy to the flow, the turbine (connected to the automobile's transmission shaft), which extracts energy from the flow and translates it into output torque, and the stator, which redirects the turbine exit flow back into pump. Torque converters thus couple the automobile's engine to the automatic transmission and provide smooth torque transmission. The pump and the turbine are rotating at different speeds, while the stator is either locked or allowed to float freely, depending on the design. Due to the interaction between the three independent elements, the internal flow field is highly unsteady and three dimensional. Especially at the element interfaces, turbine–pump, turbine–stator, and pump–stator, the flow field experiences strong velocity fluctuations. These fluctuations can have a significant influence on the performance characteristics of the torque converter. For example, fluctuations of the turbine inlet and exit flow angles will directly affect the torque converter output power. Thus, to fully understand the internal flow field and reliably predict the performance of a torque converter, one cannot solely rely on average velocity measurements, but one must also visualize the unsteady effects generated by the element interactions.

One nonintrusive technique that has been successfully used to measure velocities accurately in turbomachines is burst laser velocimetry. Unfortunately, a burst laser velocimeter is a discrete sampling type instrument and is typically only employed to measure steady-state flow phenomena. However, the flow field in the torque converter is periodically unsteady and is solely dependent on the instantaneous angular positions of the pump, turbine, and stator. Thus, to visualize the unsteady flow field in the torque converter, a method must be employed to correlate discrete laser velocimeter data samples that were collected over many cycles of the torque converter to the relative angular positions of the turbine, pump, and stator.

Previous Research of Unsteady Flows in Turbomachines. A method was described by Brun and Flack (1997) to visualize an unsteady flow field in a multi-element turbomachine using discrete sampling measurements. The method was demonstrated for the turbine inlet velocity field of an automotive torque converter. Velocities were measured with a burst laser velocimeter for a turbine/pump speed ratio of 0.800. Results showed a strong influence of the pump on the turbine inlet flow field, with a jet/wake region migrating through the turbine inlet at the blade interaction frequency.

Other researchers have visualized unsteady velocity fields in single element turbomachine geometries in which data analysis is simpler. For example, Hamkins and Flack (1987) used a laser velocimeter to measure blade-to-blade profiles in a four-bladed impeller centrifugal pump. For these measurements data repeated periodically at a frequency of four times per impeller revolution. A synchronous fluctuation was not present in these data. The authors identified steady flow reversals in the impeller for low flow rates. Later Beaudoin et al. (1992) used the same

---

Contributed by the International Gas Turbine Institute and presented at the 40th International Gas Turbine and Aeroengine Congress and Exhibition, Houston, Texas, June 5–8, 1995. Manuscript received by the International Gas Turbine Institute March 10, 1995. Paper No. 95-GT-293. Associate Technical Editor: C. J. Russo.

experimental facility to measure blade-to-blade profiles in a four-bladed impeller centrifugal pump, in which the impeller synchronously orbited with a fixed orbit size. For these measurements data repeated periodically one time per revolution. Conversely, a precise 4X synchronous (or blade pass) variation was not present in these data. For this case unsteady separation regions were identified for low flow rates.

Eckardt (1979) and Krain (1981) utilized a laser-2-focus (L2F) system and a shaft timer to investigate the flows in several radial compressor impellers. For one of the impellers, velocities at the exit were fairly uniform. Kannemans (1980) used a single-component laser velocimeter and a slotted disk on the shaft for timing to study the velocities in a pump impeller. At design, experimental results agreed well with potential theory predictions. Sideris and Van de Braembussche (1987) used the same rig and velocity measurements were coupled with pressure measurements to show the influence of the volute on the flow field.

A number of studies on the unsteady flow field in axial flow turbomachines have been completed at NASA-Lewis. Powell et al. (1982) utilized a backscatter laser velocimeter to measure velocities in a compressor rotor. Shaft encoder information was used to develop blade-to-blade velocity profiles. Strazisar (1985) used a laser velocimeter and a variable clock that was phase locked to the shaft to investigate the flow field between the blades in a transonic fan. An oscillating shock was seen. Suder et al. (1987) employed a laser velocimeter to measure the unsteady flow field within the stator row of a fan. Unsteady flow field features were resolved, and both rotor wake generated and random unsteadiness were identified.

Previous Studies of Torque Converter Internal Flows. By and Lakshminarayana (1991, 1993) measured average static pressures on the blades of an automotive torque converter stator and pump, respectively. Their results showed that the static pressure distribution is generally poor at the blade core section, that centrifugal force has a dominant effect on the static pressure rise in the pump, and that potential flow theory can approximately predict the static pressure distribution at the blade midspan, but not at the core and shell sections. Later, By et al. (1993) developed a three-dimensional, incompressible, viscous flow code to predict the flow field of a torque converter pump. Results showed that the pump rotation has a major effect on the secondary flow field and that the inlet velocity profiles have a profound effect on the mass-averaged total pressure loss.

The average velocity flow field in the stator of an automotive torque converter was described by Bahr et al. (1990). A torque converter was machined entirely from Plexiglas and a laser velocimeter was employed to measure velocities. Detailed velocity profiles for five planes in the stator and for two speed ratios are presented. Separation regions were observed in the pressure side/midchord/core side and suction side/trailing edge/shell side regions of the stator at a speed ratio of 0.800.

Gruver et al. (1996) and Brun et al. (1996) used the same experimental facility to determine the average and unsteady flow field in the pump of an automotive torque converter. Average velocity plots showed separation regions at the core-suction side in the pump mid and exit planes for the 0.065 speed ratio. The unsteady flow field was demonstrated for the pump inlet and exit planes. Significant unsteadiness was observed in both planes; typical velocity fluctuations in the inlet and exit planes were 90 and 30 percent of the average throughflow velocity, respectively.

Brun and Flack (1997) also used the same experimental facility to measure the average flow field in the turbine of an automotive torque converter. Blade-to-blade profiles were generated using a laser velocimeter and an angular encoder on the pump shaft. Velocity vector plots for the inlet, quarter, mid, and exit planes were presented for the 0.065 and 0.800 speed ratios. A region of separated flow with recirculation at the core and pressure sides was observed for the 0.065 speed ratio. Mass flows, output torque, vorticity, viscous dissipation, and flow angles were also presented.

Objectives. For this research the same experimental facility and torque converter as described by Bahr et al. (1990), Gruver et al. (1996), and Brun and Flack (1997) were utilized to measure the flow field in the inlet, quarter, mid, and exit planes of the torque converter turbine at the 0.065 and 0.800 turbine/pump speed ratios. The method described by Brun and Flack (1994) was employed to correlate laser velocimeter data with shaft encoder information to visualize the turbine unsteady velocity field. Detailed studies are included herein to demonstrate the unsteady effect the pump has on the turbine inlet, quarter, mid, and exit plane flow. Stator effects on the turbine flow were studied but were found to be negligible and are thus not included herein. Velocity vector plots and blade-to-blade profiles are presented to show the dependence of the turbine flow field on the relative pump position. Unsteady inlet flow angles, root-mean-square unsteadiness, and torque fluctuation per blade passage are also included. This paper provides the most complete and detailed data of the unsteady flow field in the torque converter turbine published to date. Results presented offer not only a basic understanding of the torque converter turbine flow field, but also serve as a benchmark for unsteady mixed flow turbomachinery computational flow codes.

Experimental Facility and Data Organization

Test Facility. A one-directional backscatter burst laser velocimeter was used to measure velocities in the turbine of a Trilok type automotive torque converter. Two 10-bit binary shaft encoders (1024 sectors per revolution) accessed the instantaneous angular positions of the torque converter turbine and pump. Both angular positions were recorded simultaneously with the instantaneous velocities on the computer.

Nomenclature

A = measurement plane area
N = number of relative angular position combinations ($N = 37$)
N_T = turbine blade passage angular position (1-35)
N_P = pump blade passage angular position (1-37)
rms = average root-mean-square unsteadiness per plane
r = radius from shaft center
T_θ = torque flux per blade passage
u, v, w = x, y, z-direction velocities in rotating turbine frame
w_{avg} = time-averaged throughflow velocity
v_θ = tangential velocity in rotating turbine frame
V_θ = tangential velocity in stationary frame
V_z = axial velocity
V = total velocity vector
x = core to shell side direction (rotating turbine frame)
y = pressure to suction side direction (rotating turbine frame)
z = throughflow direction in rotating turbine frame
β = angle (rotating frame) with respect to the axial direction
Δ = relative angular position between pump and turbine blade passages (0 to 36)

The torque converter turbine consisted of 29 identical blade passages with an angular resolution of 35 sectors apiece. Pump and stator blade passages had angular resolutions of 37 and 54 sectors, respectively. Velocities were measured in the turbine inlet, quarter, mid, and exit plane. In each plane 10 core-to-shell side positions were accessed with the laser velocimeter probe volume and 30,000 velocity samples were collected. As the pump rotated by the stationary probe volume, all 35 turbine passage blade-to-blade positions were accessed at each core-to-shell location. Measurements were taken for both the 0.065 and the 0.800 speed ratios.

The entire experimental facility, data acquisition procedure, and measurement uncertainties were described by Bahr et al. (1990), Gruver et al. (1996), and Brun and Flack (1997). The detailed dimensions of the torque converter and passage geometries were given by By and Lakshminarayana (1993) and By (1993). Thus, the measurement geometry and test conditions can be reconstructed from the above references.

Data Organization Principles. The principles and methodology involved to determine the unsteady flow field in a multi-element turbomachine using discrete sampling was described in detail by Brun and Flack (1994). For the sake of brevity only the main concepts and procedure are included herein.

In a torque converter, the velocity at any location in the fluid path can depend on the instantaneous angular positions of the turbine, pump, and stator. Hence, to obtain complete knowledge of the velocity at one measurement location in the torque converter, one must collect velocity samples for all possible relative angular position combinations between the turbine, pump, and stator. The relative angular position (Δ) is defined here as the difference between the absolute angular positions in the stationary frame.

Also, the torque converter flow field is not only synchronously periodic, but can be assumed to be periodic over the cycle of a blade passage within the elements. This simplifying assumption holds for most turbomachines where the blade passages are geometrically identical and where the orbits of the elements are centered around the turbomachine's centerline. Consequently, velocity samples from all blade passages within an element can be superimposed and averaged to obtain one representative blade passage. Velocity samples thus need not be collected for all relative position combinations between the entire elements, but only for all relative position combinations between the blade passages of the elements. This assumption significantly reduces the number of samples required for the measurements.

Finally, in the torque converter turbine, the transient influence of the stator on the flow field was found to be negligible. Measurements in the turbine inlet, mid, and exit planes showed that the throughflow velocities at the center of the blade passages fluctuated by 0.002 m/s, 0.005 m/s, 0.008 m/s, respectively, as a function of the relative position between the turbine and stator. Since these fluctuations were smaller than the measurement uncertainty (typically 0.05 m/s), one can assume that the stator does not have a transient influence on the turbine flow field, and one can neglect the stator for the transient analysis. Consequently, velocities measured in the turbine only need to be organized by their blade passage position and by the relative angular position between turbine and pump blade passages.

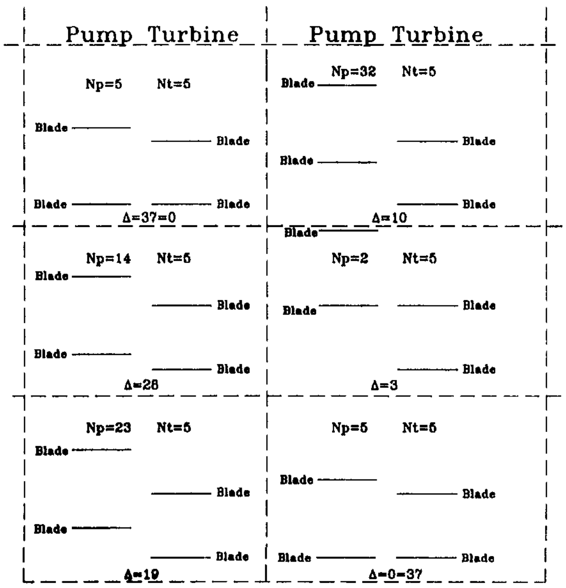

Fig. 1 Pump and turbine blade passages shown at six possible relative angular positions (Δ)

Data Organization Procedure. Each collected velocity sample has a corresponding pump angular position N_P between 1 and 37 and a turbine angular position N_T between 1 and 35. Figure 1 shows six representative relative angular positions between pump and turbine. The relative angular position is thus defined as:

$$\Delta = N_T - N_P$$

The value of Δ for each valid signal ranges between -37 and 36. Figure 1 shows 6 relative angular positions and the corresponding Δ values for a case in which N_T is kept constant and N_P is varied. This would be the case if the turbine was held stationary and the pump was rotating. Values of Δ from -37 to 36 represent two complete passes of turbine-pump blade passages. Since each pass of the turbine-pump blade passages contains the same velocity information, Δ values from -37 to -1 can be combined with Δ values from 0 to 36 to increase the sample size, namely

$$\Delta = \Delta + 37 \quad \text{for} \quad \Delta < 0$$

Individual velocity samples can now be organized into groups in a 37×35 matrix using the relative angular position Δ and the turbine position N_T. Velocities in the organized groups are averaged. Individual velocities in an organized group that are 2.5 standard deviations or more from the sample mean are omitted and the mean is recalculated. This procedure is repeated for 10 turbine core-to-shell positions. As a result, for 37 different values of Δ, velocity fields with a resolution of 10 core-to-shell and 35 pressure-to-suction measurement points are obtained.

A simplified explanation of the result of the procedure is as follows. The pump rotates at a higher speed than the turbine. Pump blades pass the turbine at a constant speed. Since each value of Δ is a relative angular position, the series of variations of Δ from 36 to 0 represents one pump blade passing by on turbine blade passage. The result is that one can visualize the effect the rotating pump blades have on the slower rotating turbine inlet, quarter, mid, and exit plane velocity fields, as if one is rotating with the turbine passage. Thus, the flow field is demonstrated at the pump–turbine blade interaction frequency.

Unsteady Velocity Results

As previously described, velocity data in the turbine inlet, quarter, mid, and exit planes were recorded and analyzed for the 0.065 and 0.800 speed ratios. The unsteady flow field in the turbine inlet plane is of primary interest for turbine performance analysis and hence is discussed in greater detail. Also, turbine relative inlet flow angles, root-mean-square unsteadiness, and output torque per blade passage were determined as a function of the relative position between turbine and pump (Δ). For the remainder of this manuscript, all velocities are given with respect to the rotating turbine reference frame and throughflow

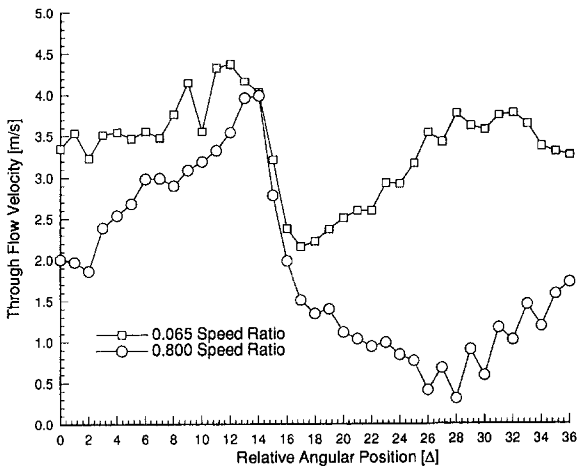

Fig. 2 Throughflow velocity versus Δ at the center position in the turbine inlet plane

velocity is defined as the velocity component normal to a given measure plane.

Turbine Inlet Plane. The pump exit is located 3 mm upstream from the turbine inlet and hence has a strong influence on the turbine flow field. To demonstrate this influence, unsteady velocity results for the turbine inlet plane at both speed ratios are presented in Figs. 2–4. Figure 2 shows the upstream influence of the pump on the velocity at one center location in the turbine blade passage. For this case, throughflow velocities at the 50 percent core-to-shell side position and the 50 percent pressure-to-suction side position ($N_T = 17$) in the turbine inlet are plotted versus the relative angular position between the pump and turbine (Δ). Strong fluctuations of the throughflow velocity can be observed for both speed ratios. Peak velocity fluctuations are 3.6 m/s and 2.1 m/s for the 0.800 and 0.065 speed ratios, respectively. Peak velocity fluctuations are defined here as the difference between highest and lowest throughflow velocities. Significantly more unsteadiness is seen for the 0.800 speed ratio than for the 0.065 speed ratio. This observation is consistent throughout the turbine.

Instead of just looking at fluctuations at one individual measurement location, one can qualitatively observe the unsteadiness of an entire plane by generating velocity vector or contour plots for several fixed Δ values and compare them. Velocity vector plots for four representative Δ values are presented in Figs. 3(*a*) through 3(*d*) for the 0.800 speed ratio. Figure 3(*a*) depicts the turbine inlet flow field at the instant when a pump exit blade and a suction side turbine inlet blade are perfectly aligned (0 percent relative position, $\Delta = 37$). Figure 3(*b*), 3(*c*), and 3(*d*) show the turbine inlet velocity field when the pump exit blade is at the 25, 50, and 75 percent ($\Delta = 29$, 19, 10) relative position between the turbine inlet blades, respectively. The 100 percent relative blade position, for which the pump exit blade is again perfectly aligned with the turbine inlet plane ($\Delta = 0 = 37$), is also shown in Fig. 3(*a*). Namely, the 100 percent relative blade position is identical to the 0 percent relative blade position.

Figures 3(*a*) through 3(*d*) show a strong jet/wake region migrating through the inlet plane from the suction to the pressure sides as the pump blades pass the turbine inlet blade passage (from 0 to 100 percent relative position). For example, in Fig. 3(*a*) ($\Delta = 37$) the jet ($V \approx 3.6$ m/s) center is near the shell side and 30 percent of the pressure to suction side distance. The wake region ($V \approx 0$) is near both the suction and pressure sides, i.e., it is centered on the leading edge of the blade. Also, a very high velocity gradient between the two regions is near the pressure side. In Fig. 3(*b*) ($\Delta = 29$) the jet is well defined directly at the pressure side. Next, Fig. 3(*c*) ($\Delta = 19$) shows that the jet center is now near the shell side and 75 percent of the pressure-to-suction side distance, while two high velocity gradients are seen between 55 to 65 percent and 90 to 100 percent. For $\Delta = 10$ (Fig. 3(*d*)) the jet center is at 50 percent of the pressure to suction side distance. Finally, for $\Delta = 0$ the flow field returns to the field as shown in Fig. 3(*a*). By observing Figs. 3(*a*) through 3(*d*) and back to 3(*a*) as a series, the progression of the center of the jet is easily observed to move from approximately 30 to 0 to 75 to 50 percent and to 30 percent, respectively. Earlier measurements by Gruver et al. (1996) showed a high-velocity region in the pump exit plane at the pressure side and a very low-velocity region at the suction side of the pump blades. These velocity regions directly correspond to the jet and the wake entering the turbine inlet plane. Since the distance between pump exit and turbine inlet is small, nonuniformities and high velocity gradients in the pressure-to-suction side direction of the pump exit flow field propagate directly downstream into the turbine inlet and cause significant unsteadiness.

A similar analysis of the flow field was performed for the 0.065 speed ratio turbine inlet plane. Throughflow contour plots for Δ values of 37, 29, 19, and 10 are presented in Figs. 4(*a*) through 4(*d*). Again, a jet/wake region can be observed to migrate through the turbine inlet plane as the pump exit blades rotate by the turbine blade passage. Peak velocities in the jet were 4.5 m/s and minimum velocities in the wake were 2.5 m/s. For this case the overall velocity field is seen to fluctuate less than for the 0.800 speed ratio; the 0.065 speed ratio flow field is steadier. This observation is again consistent with measurements by Gruver et al. (1996), which showed that the pump exit velocity profile is more uniform in the pressure-to-suction side direction for the 0.065 than for the 0.800 speed ratio; i.e., less unsteadiness propagates into the turbine inlet for this case.

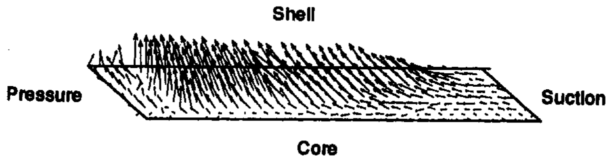

Fig. 3(*a*) Turbine inlet velocity field for 0 percent pump–turbine relative position (Δ = 37) at the 0.800 speed ratio

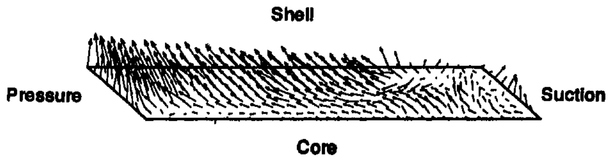

Fig. 3(*b*) Turbine inlet velocity field for 25 percent pump–turbine relative position (Δ = 29) at the 0.800 speed ratio

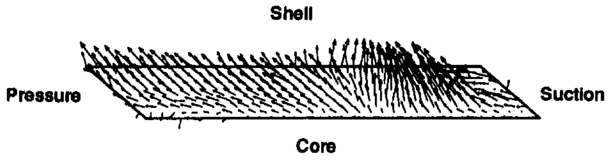

Fig. 3(*c*) Turbine inlet velocity field for 50 percent pump–turbine relative position (Δ = 19) at the 0.800 speed ratio

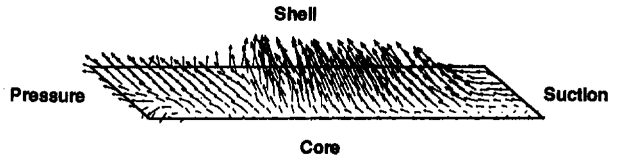

Fig. 3(*d*) Turbine inlet velocity field for 75 percent pump–turbine relative position (Δ = 10) at the 0.800 speed ratio

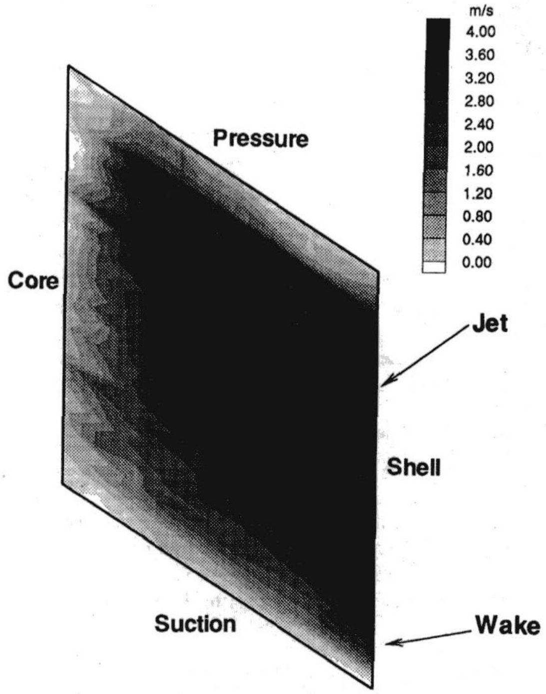

Fig. 4(*a*) Turbine inlet velocity field for 0 percent pump–turbine relative position (Δ = 37) at the 0.065 speed ratio

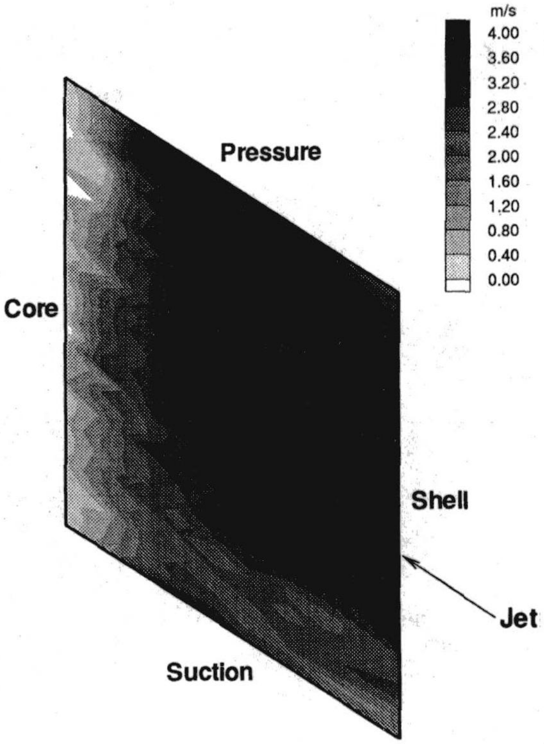

Fig. 4(*b*) Turbine inlet velocity field for 25 percent pump–turbine relative position (Δ = 29) at the 0.065 speed ratio

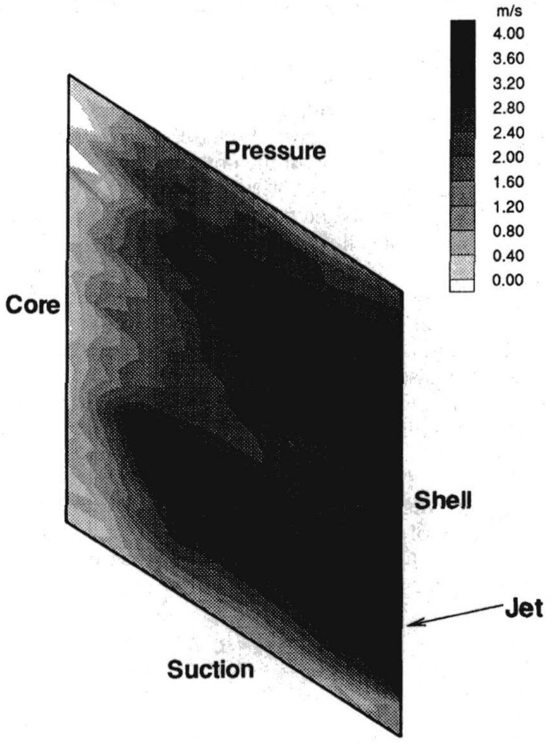

Fig. 4(*c*) Turbine inlet velocity field for 50 percent pump–turbine relative position (Δ = 19) at the 0.065 speed ratio

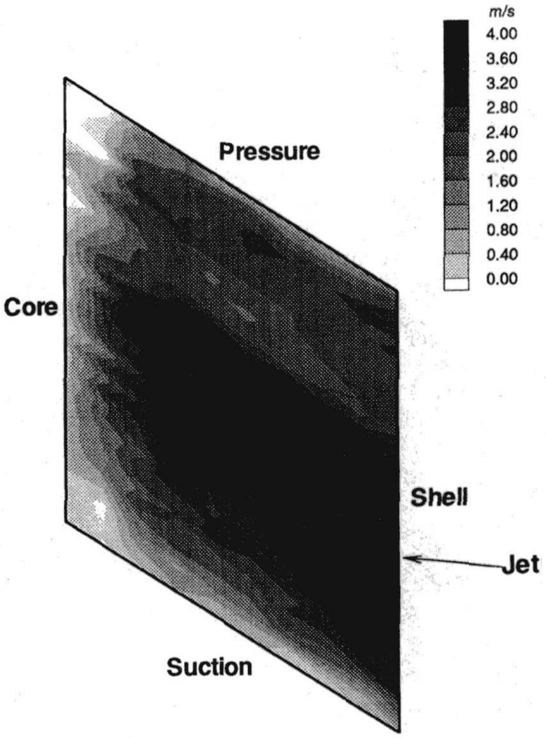

Fig. 4(*d*) Turbine inlet velocity field for 75 percent pump–turbine relative position (Δ = 10) at the 0.065 speed ratio

Turbine Quarter Plane. Figure 5 shows the throughflow velocity at the center location of the turbine quarter plane as a function of the relative pump–turbine position (Δ). Significant velocity fluctuations are observed for both speed ratios. Peak fluctuations are 1.5 m/s and 1.4 m/s for the 0.800 and 0.065 speed ratios, respectively. The overall fluctuations in the quarter plane are seen to be significantly lower than fluctuations in the inlet plane. This is due to the fact that the quarter plane is farther downstream than the inlet plane and the flow is allowed to undergo some additional mixing. Consequently, pressure-to-suction side gradients in the flow field are washed out and the overall flow field is more uniform by the time it reaches the quarter plane.

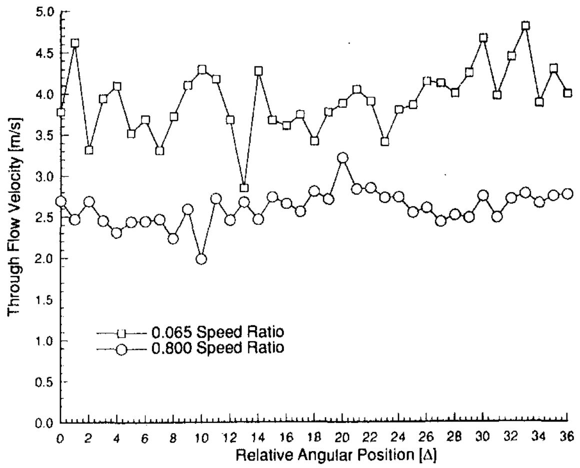

Fig. 5 Throughflow velocity versus Δ at the center position in the turbine quarter plane

Turbine Midplane. Figure 6 shows the throughflow velocity at the center of the midplane as a function of Δ. Velocity fluctuations for this plane are significantly smaller than for the inlet and quarter planes. This is again explained by the added mixing and damping that the flow undergoes between the quarter and midplanes. Peak velocity fluctuations are 0.8 m/s for the 0.800 speed ratio and 0.6 m/s for the 0.065 speed ratio. Hence, 75 percent of the unsteadiness observed in the inlet plane is damped out by the time the flow reaches the midplane. Vector/contour plots for both the quarter and the midplanes show very little qualitative changes in the overall velocity trends for different Δ values; they are not included for the sake of brevity.

Turbine Exit Plane. The turbine exit was analyzed for a stator and a pump influence. Peak velocity fluctuations were found to be smaller than the typical measurement uncertainty (0.05 m/s). For example, the passage center peak throughflow velocity fluctuation is 0.03 m/s and 0.01 m/s for the 0.800 and the 0.065 speed ratios, respectively. Velocity fluctuations from the pump are completely damped out by the time they reach the turbine exit, and stator fluctuations do not propagate far enough upstream to affect the turbine. Thus, the flow field in the turbine exit plane is steady.

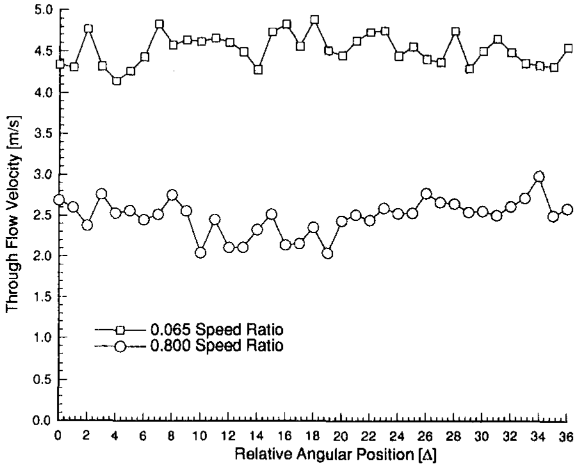

Fig. 6 Throughflow velocity versus Δ at the center position in the turbine midplane

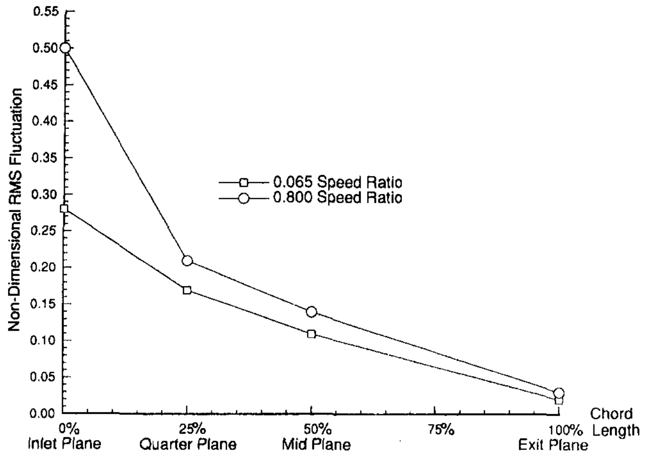

Fig. 7 Nondimensional root-mean-square unsteadiness

Root-Mean-Square (rms) Unsteadiness. To quantitatively evaluate the overall unsteadiness in a measurement plane, the average rms unsteadiness per plane was calculated from the experimental data using the following equation:

$$\mathrm{rms} = \frac{1}{A}\iint\left(\frac{1}{N}\sum_{i=0}^{N=36}(w_{\mathrm{avg}} - w_i)^2\right)^{1/2} dA$$

$$= \frac{1}{A}\sum\sum\left(\frac{1}{N}\sum_{i=0}^{N=36}(w_{\mathrm{avg}} - w_i)^2\right)^{1/2} \Delta x \Delta y$$

This expression was numerically integrated across all four measurement planes for both speed ratios. Results were nondimensionalized by the average throughflow velocity in each plane. Figure 7 shows a plot of the nondimensional results. The rms unsteadiness is seen to be very high in the inlet plane: 0.50 for the 0.800 speed ratio and 0.28 for the 0.065 speed ratio. As anticipated, the unsteadiness decreases between the inlet and the quarter, the quarter and the mid, and the mid and the exit planes. In the exit plane the rms unsteadiness is 0.04 and 0.03 for the 0.800 and 0.065 speed ratios, respectively. Hence, rms results are consistent with earlier observations: The flow unsteadiness decreases with chord length in the downstream direction of the turbine. Again, this can be attributed to the fact that the velocity fluctuations are damped as they passes through the turbine.

Inlet Flow Angle. An important parameter for the performance analysis of a turbine is the inlet flow angle. The relative inlet flow angle β was determined from the measured velocities for all 37Δ values and both speed ratios using:

$$\beta = \tan^{-1}\left(\frac{v_\theta}{V_z}\right)$$

where V_z is the axial velocity and v_θ is the weighted relative tangential velocity. The weighted relative tangential velocity is obtained by averaging the tangential components and weighing the value proportionally to the mass flux across a plane. All angles are given in the relative rotating frame with respect to the axial direction. Unsteady inlet angle results are shown in Fig. 8. For the 0.065 speed ratio the relative angle varies between −73 and −70 deg and for the 0.800 speed ratio the angle varies between −42 and −48 deg. The blade angle of the test turbine is −52 deg. Hence, the inlet flow is seen to fluctuate more for the 0.800 than for the 0.065 speed ratio, which agrees with earlier vector/contour plot observations.

Output Torque. The fluctuation of the output torque per blade passage is an important design parameter since it directly affects the fatigue life of the turbine. Torque flux can be calculated using Euler's form of the angular momentum equation:

$$T_\theta = \int\int r V_\theta \rho V \cdot dA$$

where r is the radius from the shaft center, V_θ is the tangential velocity component in the stationary frame, V is the total velocity, and ρ is the fluid density. The surface integral was evaluated numerically for the inlet and the exit planes:

$$T_\theta = \sum \sum (\rho r_j V_{\theta ij} w_{ij}) \Delta x \Delta y$$

where w is the throughflow component of the velocity. The output torque per blade passage is the difference between the exit and inlet torque flux. Figure 9 is a plot of the output torque per passage versus the relative angular position (Δ). Results show that the torque fluctuates significantly more for the 0.065 than for the 0.800 speed ratio; the 0.800 speed ratio fluctuations are 0.05 Nm, while the 0.065 speed ratio fluctuations are 0.13 Nm. Thus, for the 0.065 speed ratio, the torque converter turbine is not only subjected to a higher blade interaction frequency than for the 0.800 speed ratio, but the amplitude of the torque due to this interaction is also 2.6 times greater.

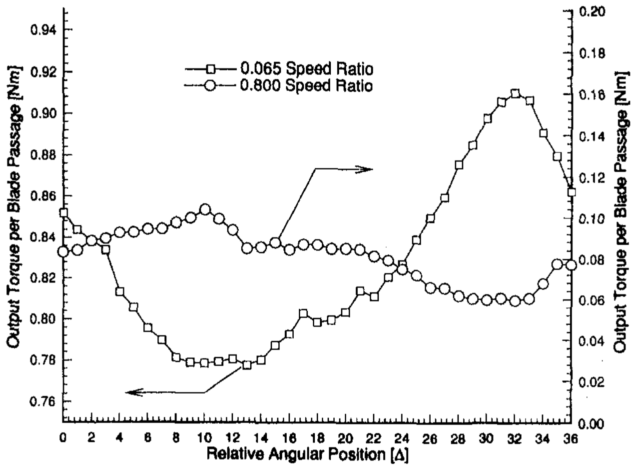

Fig. 9 Output torque per turbine blade passage versus Δ

Summary and Conclusions

The unsteady velocity field found in the turbine of a torque converter was measured for the 0.065 and 0.800 turbine/pump rotational speed ratios. Velocities in four planes of the torque converter turbine were studied: inlet, quarter, mid, and exit planes. Analysis of the flow field indicates the following:

1 Significant velocity unsteadiness was seen in the inlet, quarter, and midplanes for both speed ratios. This unsteadiness was solely due to the pump–turbine blade interaction.

2 In all measurement planes more unsteadiness was observed for the 0.800 than for the 0.065 speed ratio. Typical peak throughflow velocity fluctuations in the turbine inlet were 3.6 m/s for the 0.800 speed ratio and 2.1 m/s for the 0.065 speed ratio.

3 Negligible unsteadiness was observed in the exit plane. Typical velocity fluctuations were smaller than the measurement uncertainty (0.05 m/s). Hence, the fluctuations from the pump–turbine interaction were completely damped out by the time they reached the turbine exit plane.

4 The unsteadiness due to the stator did not propagate far enough upstream to affect the turbine. Peak throughflow velocity fluctuations in the turbine exit plane due to the stator–turbine interaction were 0.008 m/s, which was significantly smaller than the measurement uncertainty.

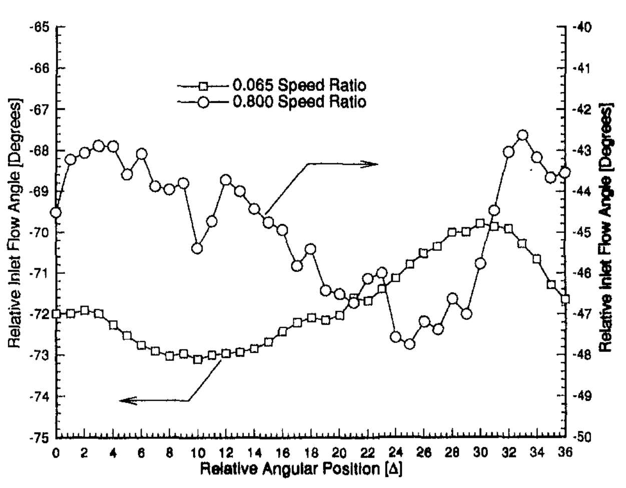

Fig. 8 Turbine inlet relative flow angles versus Δ

5 The overall unsteadiness decreased between inlet and quarter, quarter and mid, and mid and exit planes. For example, at the 0.800 speed ratio, typical peak throughflow velocity fluctuations were 3.6 m/s, 1.5 m/s, 0.8 m/s, and 0.03 m/s for the inlet, quarter, mid, and exit planes, respectively. Hence, the velocity fluctuations were damped out as they passed through the turbine.

6 Velocity vector/contour plots of the turbine inlet plane flow field showed strong jet/wake regions migrating through the inlet plane at the pump–turbine blade interaction frequency. These jet/wake regions correspond directly to high and low-velocity regions in the pump exit plane that are washed downstream into the turbine.

7 The root-mean-square (rms) unsteadiness was calculated from the velocity results for all four measurement planes and both speed ratios. Nondimensionalized rms values for the turbine inlet plane were 0.28 and 0.50 for the 0.065 and 0.800 speed ratios, respectively. The rms values were seen to decrease in the turbine downstream direction.

8 The relative inlet flow angle was seen to fluctuate by 6 and 3 deg for the 0.065 and 0.800 speed ratios, respectively. Output torque per blade passage fluctuated by 0.13 Nm for the 0.065 speed ratio and by 0.05 Nm for the 0.800 speed ratio. Hence, operating the torque converter at a lower speed ratio results in larger cyclic forces on the blades.

Acknowledgments

This research was sponsored in part by General Motors Corporation's NAO Engineering Center in Warren, MI, the GM Powertrain Division in Ypsilante, MI, and Rotating Machinery and Controls (ROMAC) Industrial Research Program at the University of Virginia. The authors wish to express their gratitude to Don Maddock for his support and involvement.

References

Bahr, H. M., Flack, R. D., By, R. R., and Zhang, J. J., 1990, "Laser Velocimeter Measurements in the Stator of a Torque Converter," SAE Paper No. 901769; *SAE 1990 Transactions, Journal of Passenger Cars*, Vol. 99, Section 6, pp. 1625–1634.

Beaudoin, R. J., Miner, S. M., and Flack, R. D., 1992, "Laser Velocimeter Measurements in a Centrifugal Pump With an Orbiting Impeller," ASME JOURNAL OF TURBOMACHINERY, Vol. 119, pp. 340–358.

Brun, K., and Flack, R. D., 1994, "A Method to Measure Periodic Velocity Fields in Multi-element Turbomachines With Discrete Sampling," *Journal of Physics—E, Meas. Sci. Technol.*, Vol. 5, pp. 418–425.

Brun, K., Flack, R. D., and Gruver, J. K., 1996, "Laser Velocimeter Measurements in the Pump of a Torque Converter: Part II—Unsteady Measurements," ASME JOURNAL OF TURBOMACHINERY, Vol. 118, pp. 570–577.

Brun, K., and Flack, R. D., 1997, "Laser Velocimeter Measurements in the Turbine of an Automotive Torque Converter: Part I—Average Measurements," ASME JOURNAL OF TURBOMACHINERY, Vol. 119, this issue, pp. 649–653.

Brun, K., 1993, "Laser Velocimetry Measurements in the Turbine of an Automotive Torque Converter," Master's Thesis, University of Virginia, May.

By, R. R., 1993, "An Investigation of Three-Dimensional Flow Fields in the Automotive Torque Converter," Doctoral Dissertation, Department of Aerospace Engineering, The Pennsylvania State University, PSU-AERSP #93-002.

By, R. R., and Lakshminarayana, B., 1991, "Static Pressure Measurements in a Torque Converter Stator," SAE Paper No. 911934.

By, R. R., and Lakshminarayana, B., 1993, "Measurement and Analysis of the Static Pressure Field in a Torque Converter Pump," *2nd ASME Pumping Machinery Symposium,* ASME FED-Vol. 154, pp. 253–264; accepted for publication in the ASME *Journal of Fluids Engineering.*

By, R. R., Kunz, R. F., and Lakshminarayana, B., 1993, "Navier–Stokes Analysis of the Pump Flow Field of an Automotive Torque Converter," *2nd ASME Pumping Machinery Symposium,* ASME FED-Vol. 154, pp. 264–274; accepted for publication in the ASME *Journal of Fluids Engineering.*

Eckardt, D., 1979, "Flow Field Analysis of Radial and Backswept Centrifugal Compressor Impellers, Part 1: Flow Measurements Using a Laser Velocimeter," *Performance Prediction of Centrifugal Pumps and Compressors,* ASME, New York, pp. 77–86.

Gruver, J. K., Flack, R. D., and Brun, K., 1996, "Laser Velocimeter Measurements in the Pump of a Torque Converter: Part I—Average Measurements," ASME JOURNAL OF TURBOMACHINERY, Vol. 118, pp. 562–569.

Hamkins, C. P., and Flack, R. D., 1987, "Laser Velocimeter Measurements in Shrouded and Unshrouded Radial Flow Pump Impellers," ASME JOURNAL OF TURBOMACHINERY, Vol. 109, pp. 70–78.

Kannemans, H., 1980, "Radial Pump Impeller Measurements Using a Laser Doppler Velocimeter," ASME Paper No. 80-GT-94.

Krain, H., 1981, "A Study on Centrifugal Impeller and Diffuser Flow," ASME *Journal of Engineering for Power,* Vol. 103, pp. 688–697.

Powell, J. A., Strazisar, A. J., and Seasholtz, R. G., 1981, "Efficient Laser Anemometer for Intra-Rotor Flow Mapping in Turbo Machinery," ASME JOURNAL OF TURBOMACHINERY, Vol. 103, pp. 424–429.

Sideris, M. T., and Van de Braembussche, R. A., 1987, "Influence of a Circumferential Exit Pressure Distortion on the Flow in an Impeller Diffuser," ASME JOURNAL OF TURBOMACHINERY, Vol. 109, pp. 48–54.

Strazisar, A. J., 1985, "Investigation of Flow Phenomena in a Transonic Fan Rotor Using Laser Velocimetry," ASME *Journal of Engineering for Power,* Vol. 107, pp. 427–435.

Suder, K. L., Hathaway, M. D., Okiishi, T. H., Strazisar, A. J., and Adamczyk, J., 1987, "Measurement of the Unsteady Flow Field Within the Stator Row of a Transonic Axial-Flow Fan," ASME Paper No. 87-GT-226.